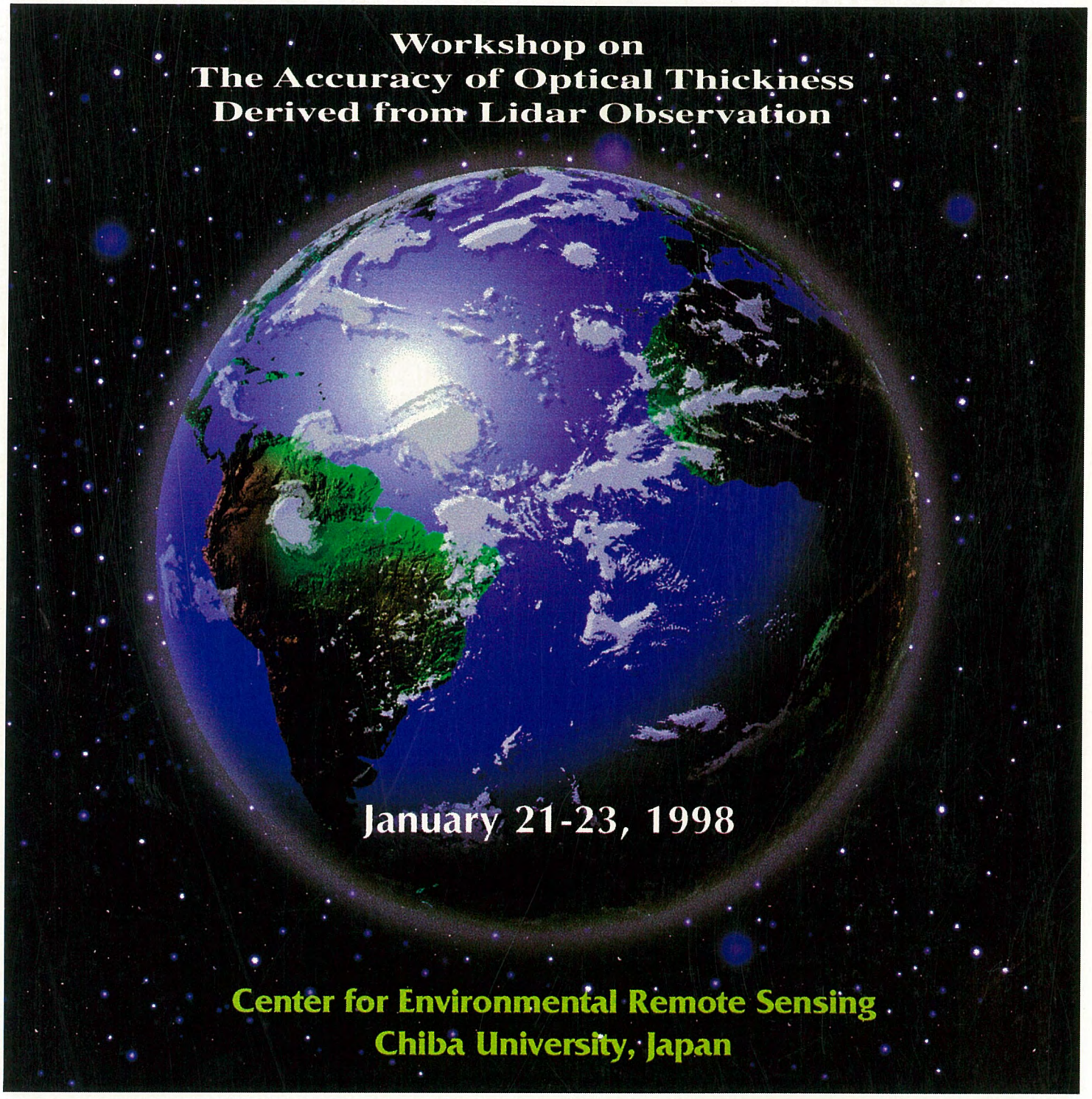
Proceedings of the International Symposium on The Atmospheric Correction of Satellite Data and Its Application to Global Environment



CEReS

Published by Center for Environmental Remote Sensing (CEReS)
Chiba University, Chiba-shi, 263-8522 Japan

This compilation ©1998 CEReS, Chiba University, Japan
Authors retain all rights to individual manuscript.
Printed in Japan

Proceedings of the

CEReS International Symposium on The Atmospheric Correction of Satellite Data and Its Application to Global Environment

Workshop

The Accuracy of Optical Thickness Derived from Lidar Observation

January 21 (Wed.) -23 (Fri.), 1998
Keyaki Hall, Chiba University

Editors : Nobuo Takeuchi
Tamio Takamura
Hiroaki Kuze

Preface

It is a great honor for me to greet the participants from all over the world to the international symposium on

The Atmospheric Correction of Satellite Data and Its Application to Global Environment,

and the associated workshop on

The Accuracy of Optical Thickness Derived from Lidar Observations.

Recently, world-wide abnormal weather is a hot topic. Last week we had a large amount of snowfall in Tokyo and Chiba area. This might be one of the unexpected outcome of such an effect. Also in tropical area its influence is conspicuous. In this symposium we have a special session on 'Indonesian Forest Fire Impact' from the viewpoint of the satellite observations. It is widely believed that the aerosol particles emitted from the forest fire greatly influence not only the local climate but the global warming.

Under these circumstances I believe it quite suitable to have a symposium in which a number of distinguished scientists take part from around the world. The discussions in this symposium will produce fruitful results toward the future study of global environment.

I would like to express my respects to Professor Tomio Asai and other colleagues who promoted this symposium. At the same time I hope every participant attending here could take this opportunity to share scientific ideas with each other, and stay comfortably in Chiba.

Koscak Maruyama

Koscak MARUYAMA

President of Chiba University
January 21, 1998


The CERES
International
Symposium on
The Atmospheric
Correction of
Satellite Data and
Its Application to
Global Environment

The international symposium on The Atmospheric Correction of Satellite Data and Its Application to Global Environment

January 21-23, 1998, Chiba University

CONTENTS

I. Optical Properties of the Atmosphere

New Breakthrough in Far-wing Line Shapes : Application to CO_2 and H_2O
R.H.Tipping and Q.Ma..... 3

Measurement of Spatial Coherence of the Light Influenced by Turbulence
Hiroshi Okayama and Li-Zhong Wang..... 11

Evaluation of Optical Properties of Atmospheric Aerosols Based on Chemical Characterization
Sachio Ohta and Naoto Murao 17

Line Strengths and Half-widths of CO_2, CO, and N_2O in the Near Infrared Region at Room Temperature
Masashi Fukabori, Tadao Aoki, and Teruo Aoki 25

II. Remote Sensing of Aerosol over Land and Ocean

(Invited Paper)
An Inversion Algorithm for Simultaneous Determination of Vegetation Reflectance and Aerosol Optical Depth Using Satellite Radiance Data
Qiu Jinhuan 31

Day and Night Detection of Volcanic Clouds and Aerosol by NOAA/AVHRR Data
K.Kinoshita, N.Iino, I.Uno, A.Mori, and J.Kohno.....37

Polarimetric Investigation of the Aerosols over the Ocean for the Atmospheric Correction
K.Masuda, M.Sasaki, T.Takashima, and H.Ishida.....45

Two Channel Analyses of the Aerosol Optical Properties Using NOAA/AVHRR
Akiko Higurashi and Teruyuki Nakajima.....51

Retrieving Aerosol Parameters from Advanced Visible and Near Infrared Radiometer (AVNIR) Multispectral Images of Mount Etna's Aerosol Plume
I.M.Watson and C.Oppenheimer.....55

III. Satellite Data Application to Environment

Using Double-channel and Double-angle ATSR Data in the Evaluation of Land Surface Temperatures
Jiemin Wang, Massimo Menenti, Akihiko Kondoh, and Donqi Liu.....59

Construction of GPS Vapor Information System for Interdisciplinary Studies
Akihiko Kondoh, Isao Naito, Ryu Otani, Tetsuya Iwabuchi, and Shin-ichi Miyazaki.....65

Study on the Minimum Representative Area on a Test Site
Hirokazu Yamamoto, Yoshiaki Honda, and Koji Kajiwara.....71

Retrieval of Cloud Physical Parameters on a Global Scale using NOAA/AVHRR
Kazuaki Kawamoto and Teruyuki Nakajima.....77

Diurnal Variation of Cloud Cover on 1996 from GMS-5 Images
Itaru Okada, Tamio Takamura, Kiyofumi Ogino, and Hideki Tamaru.....81

IV. Atmospheric Correction over Land and Ocean

(Invited Paper)
Correction Methods for Aerosol and Thin Cirrus Effects on Remote Sensing
Yoram J. Kaufman..... 89

Atmospheric Correction of Satellite Data Using Aerosol Information Derived from Multi-wavelength Lidar Observation
Mitsuo Minomura, Jianfei Ru, Hiroaki Kuze, and Nobuo Takeuchi.....102

Cirrus Cloud Correction for Retrieval of Sea Surface Temperature by Satellite IR Measurements
Lisheng Xu, T.Takamura, G.Zhang, and J.Ding.....106

Cross Calibration Between ADEOS/AVNIR and OCTS - Error Budget Analysis and the Results from the Field Campaign -
Kohei Arai..... 112

Bathymetric Mapping using Landsat TM - Case Study in Indonesia -
Katsutoshi Kozai and Winardi.....121

(Invited Paper)
Experiences in Atmospheric Correction for ADEOS/OCTS Ocean Color Data
Hajime Fukushima, Mitsuhiro Toratani, Yasushi Mitomi, and Toshimitsu Noguchi 125

Assesment of ERBE Scene ID by Using the Collocated AVHRR Data
Toshiro Inoue 132

Atmospheric Correction for Ocean Color Sensors : ADEOS/OCTS and POLDER
Sonoyo Mukai, Itaru Sano, and Kazuhiko Masuda 136

V. Algorithm of Physical and Statistical Models

(Invited Paper)
Applied Mathematical Problems of Atmospheric Correction and Filtration of Multispectral Satellite Data
Oleg I.Smokty 143

Single- and Multiple-scattering Properties of Ice Crystals in 1.38 μm Wavelength and Their Potential Applications in Satellite Remote Sensing
Lisheng Xu, T.Takamura, G.Zhang, and J.Ding 151

Effects of Adjacent Clouds to Satellite Fields of View on the Measurements of the Surface Reflectivity
T.Kobayashi, K.Masuda, and M.Sasaki 157

Sensitivity Analysis of Temperature - Emissivity Separation Relevant to the Atmospheric Correction
Masao Moriyama 161

(Invited Paper)
A New Algorithm for Estimating Aerosol Optical Thickness from Satellite Image Data and Its Accuracy
Y.Kawata, A.Yamazaki, M.Imanaka, and K.Mouri 165

A Parameterized Model for the Atmospheric Correction of Satellite Data
Qiu Jinhuan 171

Snow Surface Bidirectional Reflectance Effects on Atmospheric Correction Based on Doubling-Adding Method
Satoshi Tsuchida 177

VI. Remote Sensing of Indonesian Forest Fire

(Invited Paper)
Forest / Land Fire Impact in Indonesia
Muchlisin Arief and Bambang S.Tejasukmana.....183

(Invited Paper)
Relation between Continuity of Forest Fire and Forest Types in Indonesia
Haruo Sawada, Naoki Mitsuzuka, and Tomoyuki Ueda 188

The Effect of Indonesian Forest Fire on Local Tropospheric Aerosol Optical Thickness by Using NOAA AVHRR data
Jianfei Ru, Mitsuo Minomura, Hiroaki Kuze, Nobuo Takeuchi, Akiko Higurashi, and Teruyuki Nakajima 195

Climate-relevant Aerosol Parameters of South-East-Asian Forest Fire Haze
Wolfgang von Hoyningen-Huene 201

VII. Ground-based and Airborne Monitoring

(Invited Paper)
Lidar Measurements of Stratospheric Aerosol over Hefei, China during 1991-1996
H.Hu, J.Zhou, and Y.Wu 211

Lidar Measurements Synchronized with Satellite Overflights Acquired at 14.64N, 121.07E
L.dela Fuente, S.Dorado, N.Lagrosas, C.Enaje, J.Holdsworth, and M.Alarcon 214

Climate Change and ENSO in Southern Thailand
Absornsuda Siripong and Phuwieng Prakhammintara 228

Tracking Urban Planetary Boundary Layer of Hong Kong by Aerosol Monitoring
K.M. Leung, T.M. Mok, K.Y. Chan, A.H.P. Ho, C. N. Ng, J.C.L. Chan, and J.L. Gao 242

Retrieval of aerosol Characteristics by Combining Ground-based and Airborne Measurements
S.Kaneta, T.Takamura, and N.Takeuchi 250

An Attempt for a Ground Truth Validation of MOS-B Radiance Data
Wolfgang von Hoyningen-Huene 254

Lidar Network for Observation of Asian Dust (Kosa) in Japan
T.Murayama, M.Abo, H.Adachi, K.Aoki, K.Arao, K.Asai, M.Fujiwara, R.Imasu, K.Kai, T.Kawahara, R.Koga, H.Kuze, S-A Kwon, A.Nomura, I.Matsui, Y.Saito, T.Sakai, K.Shiraishi, N.Sugimoto, and N.Takeuchi 264

Preliminary Study on the Evaluation of Atmospheric Effect to Interferometric SAR Measurement
Kazuya Saito, Tamio Takamura, Kunihisa Takimoto, and Johta Yamamoto 270

Measurement of Stratiform Cloud Liquid Water Path from Airborne Microwave Radiometer
Yozo Takayama and JACCS Aircraft Observation Group 276

Observational Study on the Radiative Properties of Atmospheric Aerosols over China
G.-Y Shi, T.Nakajima, T.Takamura, T.Hayasaka, L.Xu, B.Wang, X.Jin, X.-B.Fan, R.-M.Hu, P.Zhang, L.-S.Zhang, X.-H.Wang, L.-X.Wang, and H.Zhang.....280

Atmospheric Aerosol Properties over Lunar Lake, Nevada Using the Ground Based Spectro-polarimeter
Tsutomu Takashima and Kazuhiko Masuda 284

Continuous Observation of Aerosols and Clouds with Ground Based Lidars in Tsukuba, Japan and in Jakarta, Indonesia
Nobuo Sugimoto, Ichiro Matsui, Mego Pinandito, Ii Hydayat, Imam Rosananto, and Muharyan Syamsudin 288

Satellite Workshop : The Accuracy of Optical Thickness Derived from Lidar Observation

January 23, 1998

Calibration of the Vertical Lidar Measurement of Tropospheric Aerosol Extinction Coefficients
H.Kinjo, H.Kuze, H.Matsushima, and N.Takeuchi 295

H-S Method for Deriving Aerosol Extinction Coefficient Profile from Lidar Observation
Qiu Jinhuan 299

Lidar Measurements of Tropospheric Aerosol over Hefei
Jun Zhou 303

Diurnal Measurements of the Planetary Boundary Layer over Hong Kong Derived From Lidar Observations
K.M. Leung and T.M. Mok 309

Lidar Monitoring of Atmospheric Aerosols in Seoul Using a Micro Pulse Lidar
Soon-Chang Yoon and Jae Guang Won 315

INDEX 323

I. Optical Properties of the Atmosphere

NEW BREAKTHROUGH IN FAR-WING LINE SHAPES: APPLICATION TO CO_2 AND H_2O

R. H. Tipping
Department of Physics and Astronomy
University of Alabama
Tuscaloosa, AL 35487

and

Q. Ma
Department of Applied Physics
Columbia University and
Institute for Space Studies, Goddard Space Flight Center
New York, NY 10027

ABSTRACT

Within the formalism developed previously for the calculation of the far-wing line shape for molecular systems, most of the computer resources were used to diagonalize the anisotropic potential-energy matrix whose size is determined by the number of states included. For systems of interest in atmospheric studies, e.g. CO_2 and H_2O, this limited the number of states that could be included and the accuracy attainable. Recently, a new formalism has been developed in which the eigenfunctions of the orientations of the system are chosen as the basis functions. Both the anisotropic interaction and the dipole moment function are diagonal in this system and as many states as desired can be included. In this new formalism the sums over the initial and final states of the system become integrals over the orientational variables. By choosing reasonable resolutions of the integrands, one can carry out the calculations within modest computational time. Results for self- and foreign-broadened CO_2 and H_2O have been obtained. Using these results one can then easily calculate the corresponding far-wing absorption, and new results will be presented and compared with experiment.

INTRODUCTION

In order to make forward calculations of the effects of the Earth's atmosphere on the transmission of radiation and to use these to extract useful atmospheric profiles from measurements, one must have a transmission code (for instance, a line-by-line code such as FASCOD3, or lower resolution codes such as MODTRAN or LOWTRAN) and a molecular data base (for instance, HITRAN96). This data base must contain information on the frequencies and intensities for all the transitions of interest for the atmospheric species, together with information about the line shape. For many applications one can assume pressure-broadened Lorentzian line

shapes (or possibly Voigt profiles) and one must then know the temperature-dependent half widths and pressure shifts. However, in some cases, the above information is not sufficient to calculate accurate synthetic spectra; in particular, in the regions of Q-branches or in the far wings of the rotational or vibration-rotational bands. In the former case, the phenomenon of line-mixing[1] must be included, while in the latter case, the significant deviation of the true line shape from a Lorentzian shape must be known.[2] In practice, most of the radiation codes truncate the wings of the Lorentzian line shapes (e.g. at $\pm$ 25 cm^{-1} from the line center) and incorporate the remaining absorption that varies smoothly with frequency as a "continuum" correction. In this regard, the self- and N_2-broadened continua are the most important and lead to significant improvements in the modeling.[3] In the present work, we outline some recent theoretical calculations of the far-wing line shape and calculate the corresponding absorption for CO_2 and H_2O to illustrate the importance of these types of calculations.

THEORY

Before presenting the results, we present a brief description of the theory. The absorption coefficient $\alpha(\omega)$ per unit volume at frequency ω (cm^{-1}) for a gas at temperature T is given by

$$\alpha(\omega) = \frac{4\pi^2 \, n_a \, \omega}{3\hbar c} \tanh(\beta\hbar\omega/2) \, [F(\omega) + F(-\omega)] \qquad (1)$$

where $\beta = 1/kT$ and n_A is the number density of absorbers. The spectral density $F(\omega)$ is the Fourier transform of the dipole moment correlation function

$$F(\omega) = \frac{1}{2\pi} \int_{-\infty}^{\infty} C(t) \, e^{-i\omega t} \, dt \qquad (2)$$

$$C(t) = Tr [\rho \, \mu^{\dagger}(0) \cdot \mu(t)], \qquad (3)$$

where

$$\vec{\mu}(t) = e^{iHt/\hbar} \, \vec{\mu}(0) \, e^{-iHt/\hbar} \qquad (4)$$

and

$$\rho = \frac{e^{-\beta H}}{Tr [e^{-\beta H}]} \, . \qquad (5)$$

By introducing the Liouville operator L for the total Hamiltonian, H, defined by

$$L\,\vec{\mu}(t) = [\,H,\ \vec{\mu}(t)\,]/\hbar \quad , \tag{6}$$

one can formally write the spectral density as

$$F(\omega) = \frac{1}{\pi}\,\mathrm{Re}\,\mathrm{Tr}\int_0^{\infty} \vec{\mu}^{\dagger}(0)\cdot\sqrt{\rho}\;e^{i(\omega - L)t}\,\sqrt{\rho}\;\vec{\mu}(0)\;dt \quad . \tag{7}$$

Then for the far-wing case, one makes the quasistatic approximation in which the translational motion is treated classically. Furthermore, assuming that all the lines have the same (band-average line shape), one can write $F(\omega)$ in the form[4]

$$F(\omega) = \pi^{-1}\sum_{\omega_{ij}>0} e^{-\hbar(\omega - \omega_{ij})/2kT}\left\{\frac{1}{(\omega - \omega_{ij})^2}\,\chi(\omega - \omega_{ij}) + \frac{1}{(\omega + \omega_{ij})^2}\,\chi(\omega + \omega_{ij})\right\} . \tag{8}$$

The χ functions can be calculated from first principles from knowledge of the interaction potential. In the present work,[5] this is carried out by a multi-dimensional integration.

RESULTS

The results for the line shape function $\chi(\omega)$ for H_2O - H_2O for T = 296 K is shown in Fig. 1. As can be seen from Eq. (8) above, if the shape were Lorentzian in the far wing, $\chi(\omega)$ would be a horizontal line; clearly this is not the case as the far wing shape falls off exponentially with frequency displacement. Furthermore, it is super-Lorentzian in the near wing. In Fig. 2 we compare the corresponding theoretical absorption (denoted by the Δ) to the experimental laboratory results of Burch et al.[6] for the high frequency wing of the pure rotational band. This region is important in the atmosphere because the Earth's blackbody curve peaks in this region. As can be seen, there is substantial agreement over several orders of magnitude, and given the difficulty of measuring the very weak absorption near the minimum around 1000 cm^{-1}, one sees that the agreement is very good overall. Because the empirical "continuum" corrections in the existing radiative transfer codes are based primarily on this data, one concludes that the theoretically calculated continuum is in good agreement with the current models. Similar comparisons for CO_2 - CO_2 at two different temperatures are shown in Fig. 3 and compared to laboratory measurements denoted by the + symbol) in the high-

frequency wing of the ν_3 band. This spectral region is important in the retrieval of CO_2 abundances and distribution. Also shown are the results for the absorption calculated assuming a Lorentzian shape (dashed line). It is clear from this figure that one calculates far too much absorption in the wing of the band by using the Lorentzian shape, and that for accurate modeling in this spectral region, one needs to use a more accurate line shape for CO_2.

CONCLUSIONS

In order to calculate accurate absorption in the wings of the pure rotational and vibration-rotational bands, one has to utilize a line shape that deviates substantially from that of the Lorentzian shape which gives good results only near the band centers. For atmospheric spectra, this is important for H_2O and CO_2 bands as these dominate the infrared spectral absorption. These line shapes can then be used to calculate the "continuum" correction necessary in radiative transfer codes in order to get agreement between atmospheric spectra and synthetic spectra. Until recently, such corrections had to be made using empirical data and often had to be extrapolated to atmospheric conditions. Recently, by calculating the line shape within the quasistatic approximation by carrying out multidimensional integrals, one can now obtain accurate theoretical results which can be used to refine the empirical continuum corrections.

REFERENCES

1. A. Levy, N. Lacome, and C. Chackerian, Jr., *Collisional Line Mixing*, in *Spectroscopy of the Earth's Atmosphere and Interstellar Medium*, Eds. K. Narahari Rao and A. Weber, Academic Press, San Diego, 1992.

2. R. M. Goody and Y. L. Yung, *Atmospheric Radiation*, Oxford University Press, New York, 1989.

3. S. A. Clough, F. X. Kneizys, and R. W. Davies, *Line Shape and the Water Continuum*, Atm. Res. 23, 229 (1989).

4. Q. Ma and R. H. Tipping, *A Far Wing Lineshape Theory and its Application to the Water Continuum Absorption in the Infrared Region. I*, J. Chem. Phys. 95, 6290 (1991); Q. Ma and R. H. Tipping, *A Far Wing Lineshape Theory and its Application to the Water Vibrational Bands. II*, J. Chem. Phys. 96, 8655 (1992); Q. Ma and R. H. Tipping, *A Far Wing Lineshape Theory and its Application to Foreign Broadened Water Continuum Absorption. III*, J. Chem. Phys. 97, 818 (1992).

5. Q. Ma and R. H. Tipping, *The Distribution of Density Matrices Over Potential-Energy Surfaces: Application to the Calculation of the Far-Wing Line Shapes for CO_2*, J. Chem. Phys. Mar., 1998.

6. D. E. Burch and D. A. Gryvnak, *Method of Calculating H_2O Transmission between 333 and 633 cm^{-1}*, AFGL-TR79-0054, 1979; D. E. Burch and R. A. Alt, *Continuum Absorption by H_2O in the 700 - 1200 cm^{-1} and 2400 - 2800 cm^{-1} Windows*, AFGL-TR-84-0128, 1984.

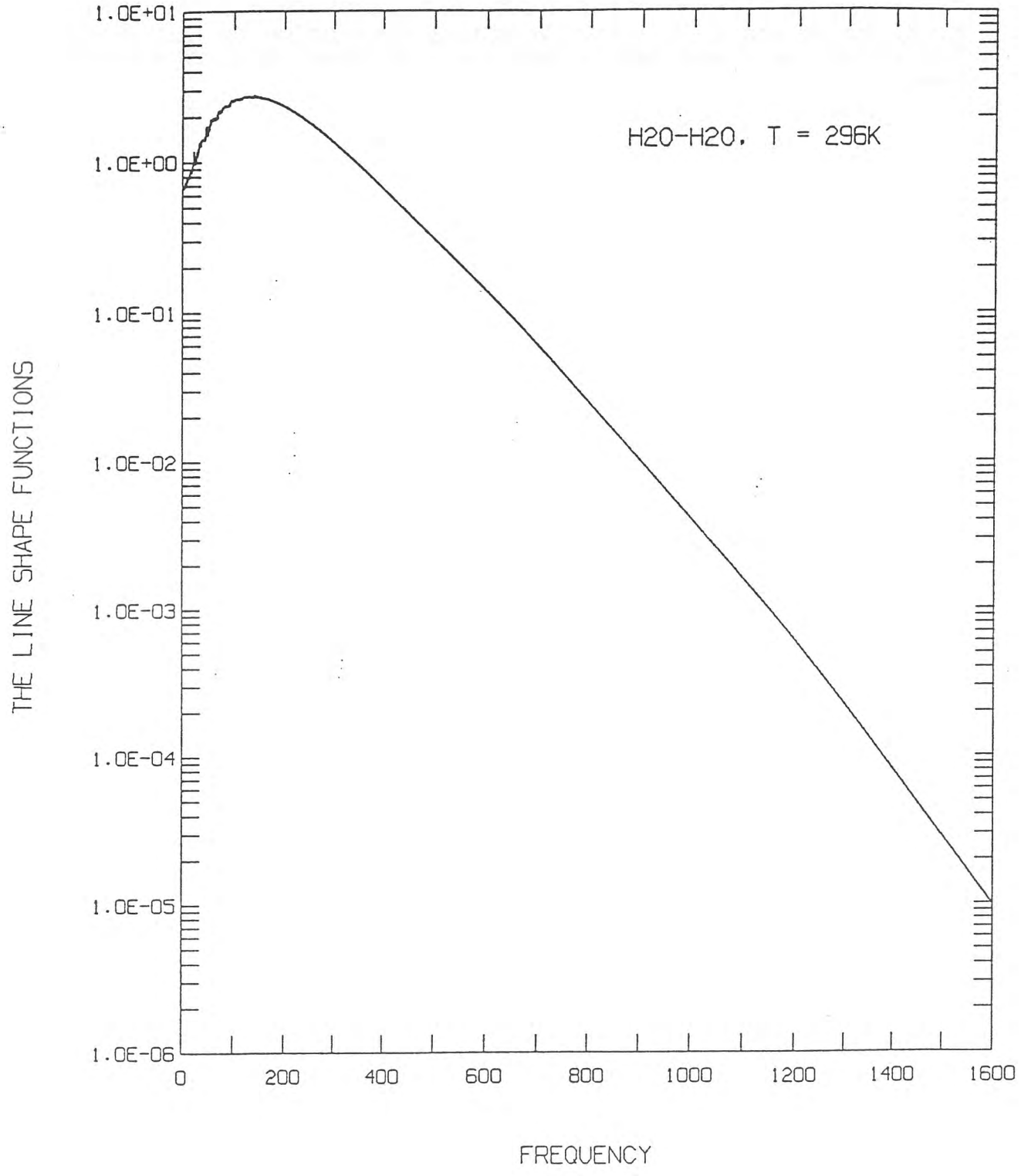


Figure 1. The band-average line shape function for H_2O - H_2O.

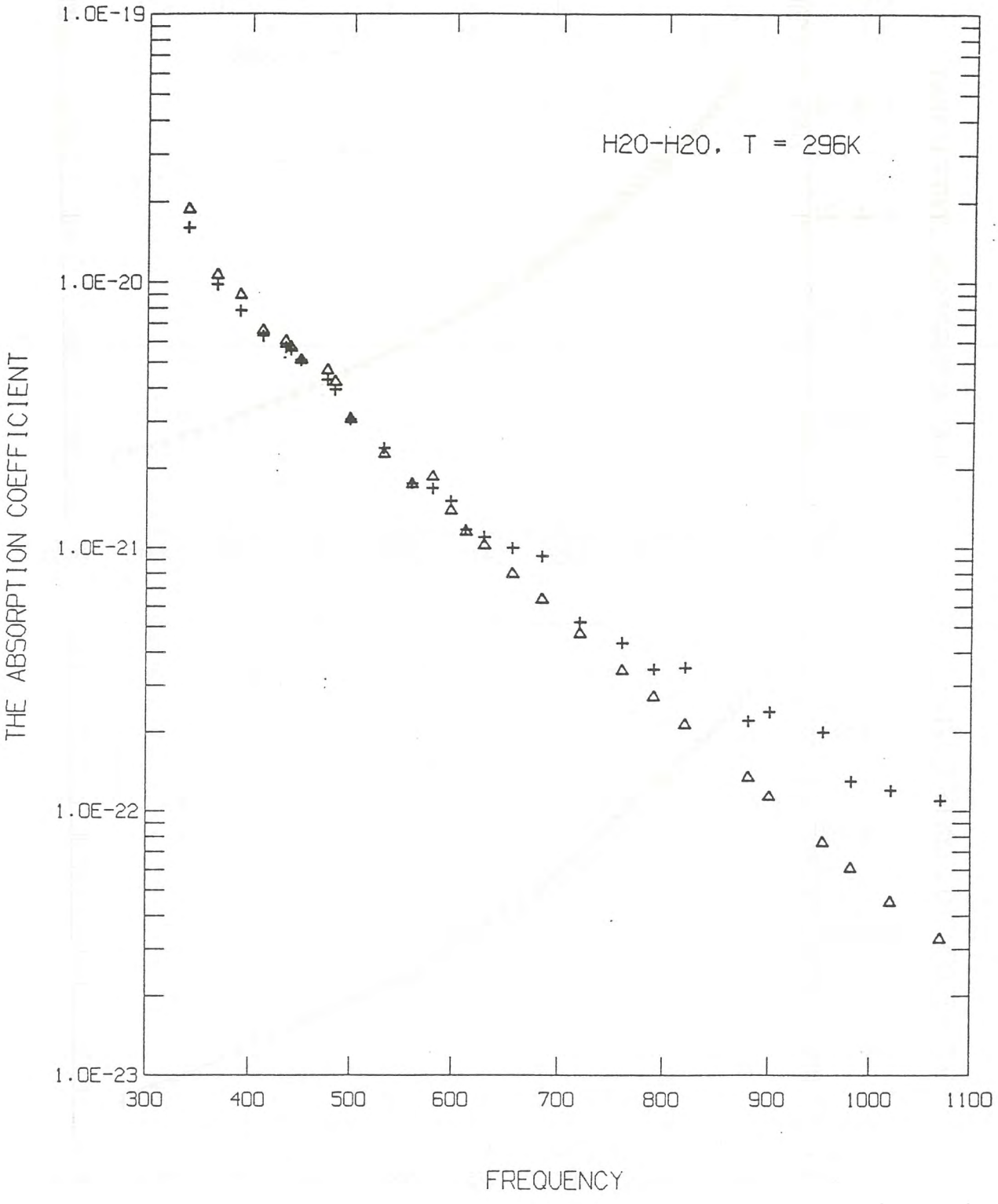


Figure 2. The absorption coefficient $\alpha(\omega)$ in units of cm^2 $molecule^{-1}$ atm^{-1} versus frequency in cm^{-1} for H_2O - H_2O at T = 296 K.

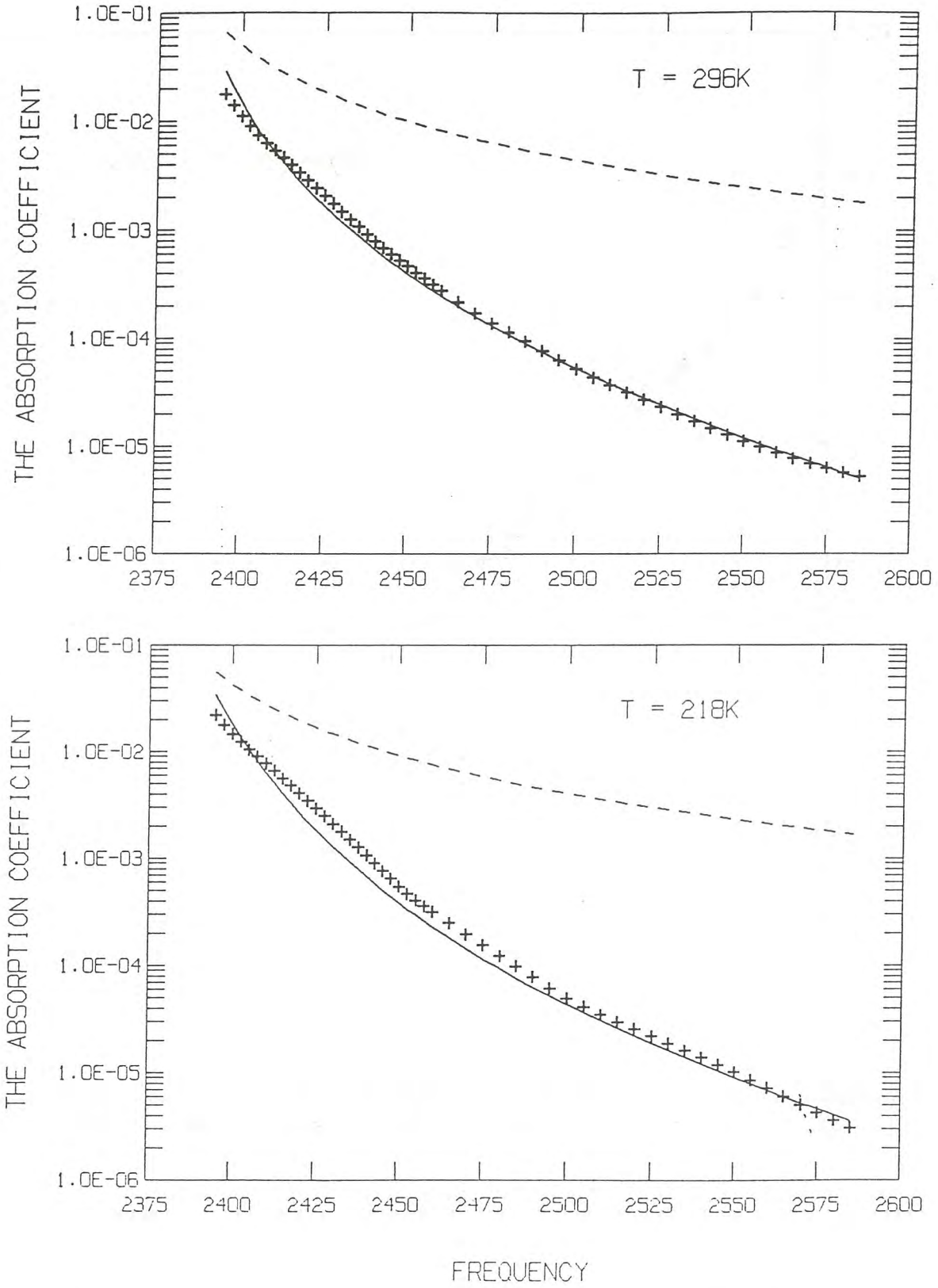


Figure 3. The absorption coefficient $\alpha(w)$ in units of cm^{-1} amagat^{-2} versus frequency in cm^{-1} for CO_2 - CO_2 at two temperatures.

Measurement of Spatial Coherence of the Light Influenced by Turbulence

Hiroshi Okayama and Li-Zhong Wang

Center for Environmental Remote Sensing, Chiba University
1-33 Yayoi cho, Inage-ku Chiba 2638522 Japan

ABSTRACT

For right evaluation of the earth surface by a sensor on the satellite, it is important to correct the atmosphere and atmospheric turbulence is one of the correction factors.

The spatial coherence of the light influenced by the turbulence was measured by use of a simulator equipped with a multiple reflection system in the laboratory. The turbulence was generated by changing the ambient temperatures from 32° C to 48° C. It has been found that in measurement results the spatial coherence of the light which has passed through the turbulent region decreases with the increase of the temperature. The analysis of interference fringes caused by double slits was made by use of the photographic method.
The visibility of the interference fringes depends on the degree of turbulence, and the dependency is theoretically described.

1. Introduction

Atmospheric turbulence artificially generated in a remote sensing simulator is used for experiment.
When the earth's surface is exactly estimated by remote sensing, the satellite data must be corrected for the turbulence of atmosphere although an adequate correction method has not been found yet. In this paper the resulted of an optical measurement of turbulence is described. Regarding turbulence there are many theoretical papers, but few papers have reported on the experiments on degradation of spatial coherence. The degradation of coherence by turbulence was reported by Ho [1] and Andrews [2].

We visualize the problem physically as follows. A beam of a monochromatic wave is emanating from the plane Z = 0, its irradiance profile being Gaussian. We assume that the minimum scale of the turbulence is much larger than the wave length of the beam. We specify the coherence function in the plane z = 0, and try to find the coherence function in the plane Z = L. The turbulence is measured by use of a double slits. The degradation of coherence is estimated by the measurement of spatial coherence.

2. Turbulence and coherence

Because the average irradiance of a Gaussian beam varies in the plane Z = L, it is more meaningful to describe the coherence degradation in a random medium by the degree of coherence than by the mutual coherence function itself. The degree of coherence is defined as

$$\gamma(x_1, x_2) = \left\{\hat{\Gamma}(x_1, x_2)\right\} \Big/ \left[\left\{\hat{I}(x_1)\right\}\left\{\hat{I}(x_2)\right\}\right]^{\frac{1}{2}}, \qquad (1)$$

where $\hat{\Gamma}(x_1, x_2)$ is a mutual coherence function and $\hat{I}(x)$ is average irradiance. The mutual coherence function is represented as follows :

$$\left\{\hat{\Gamma}(x_1,x_2)\right\}_L = \left\{\hat{V}(x_1)\hat{V}^*(x_2)\right\}_{Z_1=Z_2=L} , \tag{2}$$

where $\hat{V}(x)$ shows a scaler wave field.

$$\begin{aligned}\left\{\hat{\Gamma}\right\}_L = \left\{\hat{\Gamma}_0\right\}_L \Big(1-\frac{1}{2}\pi k^2 \int_0^L dp \int_0^\infty d\eta\, \eta\tilde{\phi}(\eta)\Big) \\ \times \Big\{1-J_0\left[\beta_r(p)\eta r_{12}\right] \\ \times \exp\left[-\eta^2(L-p)^2/k^2a^2|B(L)|^2\right]\Big\}\Big),\end{aligned} \tag{3}$$

and

$$\begin{aligned}\left\{\hat{I}\right\}_L = \left\{\hat{I}_0\right\}\Big(1-\frac{1}{2}\pi k^2 \int_0^L dp \int_0^\infty d\eta\,\eta\tilde{\phi}(\eta) \\ \times\Big\{1-I_0\left[2\beta_i(p)\eta r\right] \\ \times\exp\left[-\eta^2(L-p)^2/k^2a^2|B(L)|^2\right]\Big\}\Big) ,\end{aligned} \tag{4}$$

where $x_1 = -x_2$, $y_1 = -y_2$ and $z_1 = z_2 = L$. J_0 is Bessel function, and r_{12} is the distance between the two observation points. a is effective radius of Gaussian beam. L is the propagation length.

$$\tilde{\beta}_r(p) = 1+\left[\frac{\left(1-L/r_c\right)}{|B(L)|^2}-1\right]p , \tag{5}$$

$$\tilde{\beta}_i(p) = -\left[\frac{L}{ka^2|B(L)|^2}\right]p , \tag{6}$$

$$|B(L)|^2 = \left(1-L/r_c\right)^2+L^2/k^2a^4 , \tag{7}$$

$$\begin{aligned}\gamma(r_{12},L) \approx \exp\Big(-\frac{1}{2}\pi k^2\int_0^L dp\int_0^\infty d\eta\,\eta\tilde{\phi}(\eta) \\ \times\left\{-J_0\left[\beta_r(p)\eta r_{12}\right]+I_0\left[\beta_i(p)\eta r_{12}\right]\right\} \\ \times\exp\left[-\eta^2(L-p)^2/k^2a^2|B(L)|^2\right]\Big) ,\end{aligned} \tag{8}$$

where $r_{12} = 2r$. For turbulent atmosphere

$$\left\{\tilde{\Gamma}\right\}_L \approx \left\{\tilde{\Gamma}_0\right\}_L \exp\left[-4.35 C_n^2 k^2 L \eta_m^{-\frac{5}{3}} \times F\left(r_{12}\eta_m ; \frac{L\eta_m^2}{k}, \frac{L}{ka^2}, \frac{L}{r_c}\right)\right] , \tag{9}$$

where η is of the order of $1/l_m$ and C_n is the structure constant of the refractive index.

$$\left\{\hat{I}\right\}_L \approx \left\{\hat{I}_0\right\}_L \exp\left\{ -4.35 C_n^2 k^2 L \eta_m^{-\frac{5}{3}} \times H\left[r/a|B(L)| ; \theta\right]\right\} , \tag{10}$$

$$\therefore \ \gamma\left(r_{12}, L\right) \approx \exp\left[-4.35 C_n^2 k^2 L \eta_m^{-\frac{5}{3}} \times Q\left(r_{12}\eta_m ; \frac{L\eta_m^2}{k}, \frac{L}{ka^2}, \frac{L}{r_c}\right)\right] , \tag{11}$$

where

$$Q\left(r_{12}\eta_m ; \frac{L\eta_m^2}{k}, \frac{L}{ka^2}, \frac{L}{r_c}\right) = \int_0^1 dp \left(1+\theta^2 p^2\right)^{\frac{5}{6}} \times \left\{ {}_1F_1\left[-\frac{5}{6}, 1, -\frac{1}{4}\beta_r^2(p) r_{12}^2 \eta_m^2 / \left(1+\theta^2 p^2\right)\right] - {}_1F_1\left[-\frac{5}{6}, 1, \frac{1}{4}\tilde{\beta}_i^2(p) r_{12}^2 \eta_m^2 / \left(1+\theta^2 p^2\right)\right]\right\} , \tag{12}$$

where

$$\theta^2 = L^2 \eta_m^2 \Big/ k^2 a^2 |B(L)|^2 , \tag{13}$$

${}_1F_1$ is the confluent hypergeometric function.

The solution for a collimated beam can be obtained by setting $L/r_c = 0$, where r_c is radius of wave-front curvature. Let us first consider two limiting cases, the case of a spherical wave, where $L/ka^2 \to \infty$.

When $L/ka^2 \to 0$, we have

$$\gamma(r_{12},L)=\exp\left(-4.35C_n^2k^2L\eta_m^{-\frac{5}{3}}\times\left\{{}_1F_1\left[-\frac{5}{6},1,-\frac{1}{4}r_{12}\eta_m^2\right]-1\right\}\right) . \tag{14}$$

For $1/4\cdot r_{12}^2\ \eta_m^2 >> 1$ we get

$$\gamma(r_{12},L)\approx\exp\left(-1.455C_n^2k^2Lr_{12}^{\frac{5}{3}}\right) . \tag{15}$$

When $L/ka^2\to\infty$, we have

$$\gamma(r_{12},L)=\exp\left(-4.35C_n^2k^2L\eta_m^{-\frac{5}{3}}\int_0^1 dp\times\left\{{}_1F_1\left[-\frac{5}{6},1,-\frac{1}{4}(1-p)^2r_{12}^2\eta_m^2\right]-1\right\}\right) . \tag{16}$$

For $1/4\cdot r_{12}^2\ \eta_m^2 >> 1$ we get

$$\gamma(r_{12},L)\approx\exp\left(-0.546C_n^2k^2Lr_{12}^{\frac{5}{3}}\right) . \tag{17}$$

When $L/ka^2 << 1$, $L^2\eta_m^2/k^2a^2 << 1$, and $1/4\cdot r_{12}^2\ \eta_m^2 >> 1$,

$$\gamma(r_{12},L)\approx\exp\left[-1.455C_n^2k^2Lr_{12}^{\frac{5}{3}}\left(1-\frac{5}{6}L^2/k^2a^4\right)\right], \tag{18}$$

which shows that a collimated beam has a higher degree of coherence than an infinite plane wave.

In order to see how the degree of coherence changes as the value of L/ka^2 varies from 0 to ∞, the integral Q is evaluated numerically for $L/r_c = 0$ and a prescribed $L\eta_m^2/k$. The results are shown in Fig. 1.

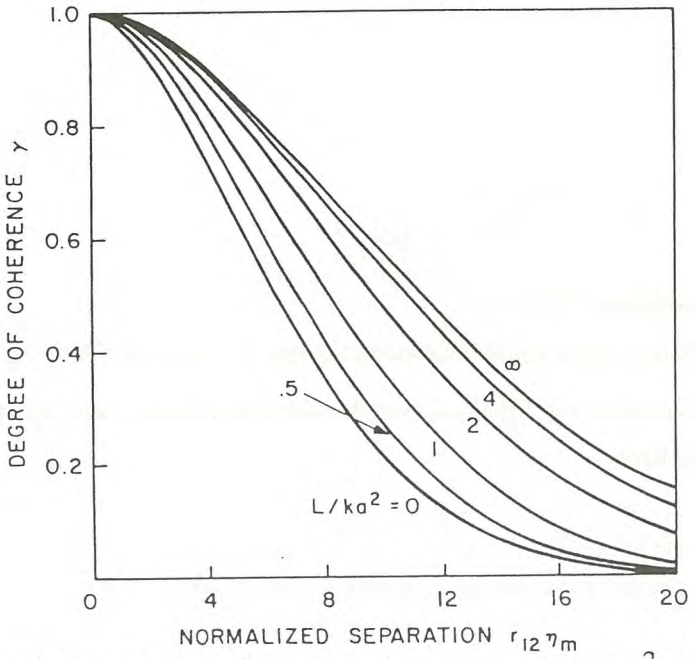


Fig. 1. Degree of coherence of a collimated gaussian beam, for $L/k\,l\,m^2 = 1$, $C_m^2\,k^2\,L\,\eta_m^{-5/3} = 0.025$, where $\eta_m = 5.91/l\,m$.

3. Experimental apparatus

A chamber (240 cm × 75 cm × 30 cm) was made to simulate the atmosphere. To measure the turbulence optically, a long optical pass was insured by multiple reflection in the chamber. The optical system of the chamber is shown in Fig. 2. There are four heat sources of nichrome line in the chamber. To send a hot wind uniformly steel and styrenes filters were used. The double slits were used to measure the spatial coherence. The slits were 25 μm wide and 50 μm apart from each other. The given interference fringes were recorded on the photographic film. The densities of the interference fringes were measured by use of a micro densitometer. The visibility of the interference fringes was calculated by use of the following equation :

$$\gamma = \frac{I_{max} - I_{min}}{I_{max} + I_{min}}, \tag{19}$$

where I_{max} and I_{min} are maximum and minimum values of the effective exposure, respectively. Here the visibility of the interference fringe represents the degree of coherence.

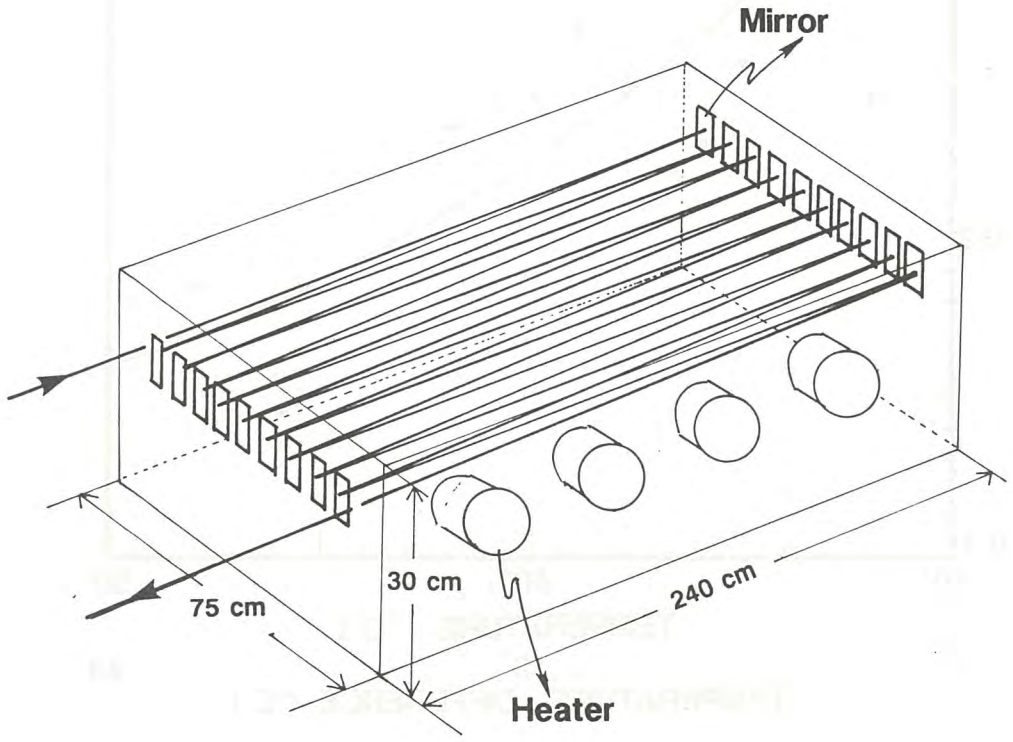


Fig. 2. A simulator of atmospheric turbulence with optical system of multiple reflection.

4. Experimental Results

The degradation of coherence by turbulence is theoretically clear from Fig. 1. The experimental results by turbulence of air are shown in Fig. 3. From Fig. 3 the coherence degree reduces with increasing temperature of air. When the temperature increases from 30° C to 40° C, the degree of coherence reduces by 0.136.

The temperature outside the chamber is 27 °C. The temperature differences between inside and outside of the chamber are shown on the horizontal in Fig. 3.

Possible causes for turbulence occurrence are the aerosol and temperature difference for the chamber, but the aerosol effect was ignored in this experiment.

5. Conclusions

For this experiment, a simulator with an optical multiple reflection system was made. The temperatures of the air were changed from 32° C to 48° C. The degradation of coherence was evaluated by measurement of the spatial coherence. In the future it would be necessary to measure turbulence in a larger temperature range. Then it might be possible to make atmospheric correction of satellite data from our experimental results.

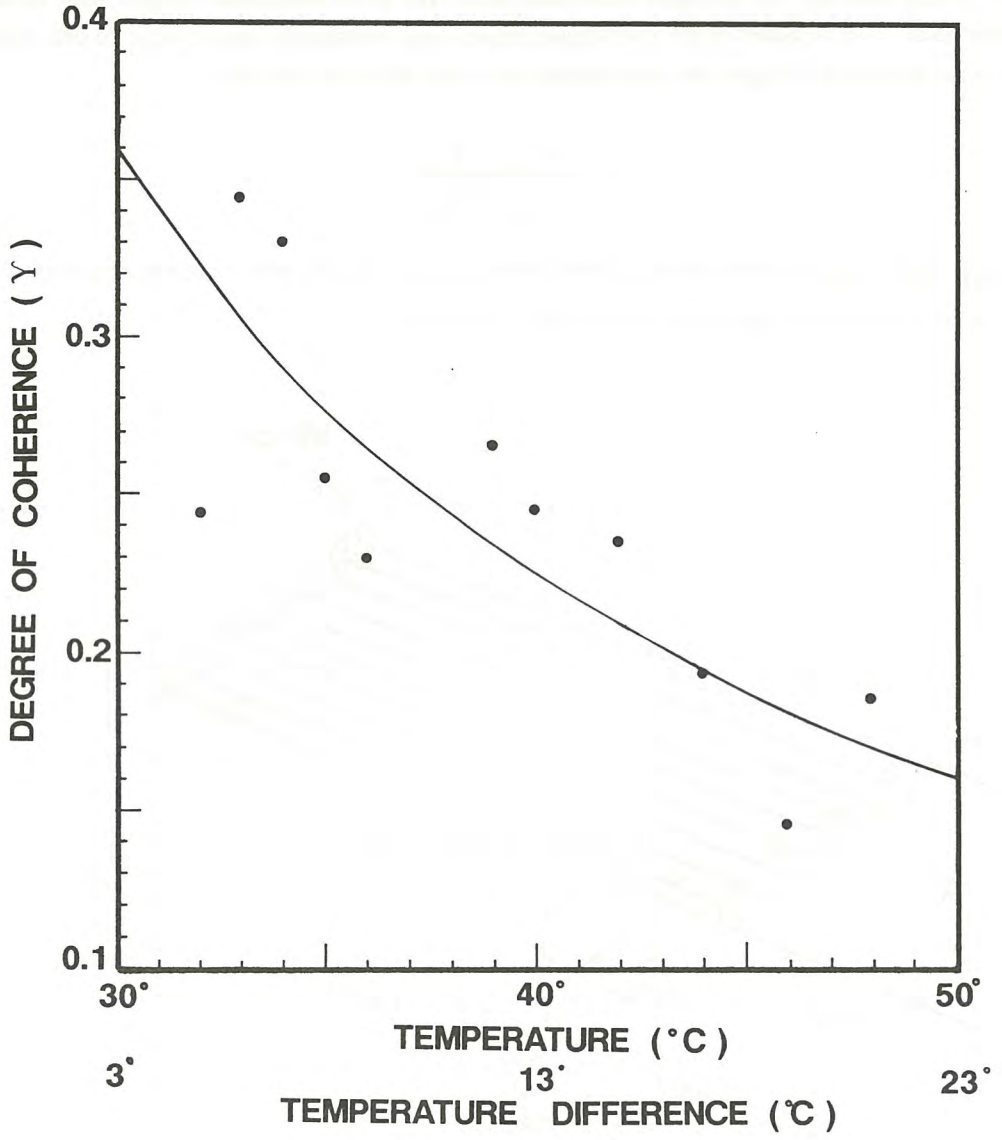


Fig. 3. Degree of coherence of turbulent air from experimental result.

References

1. T. L. Ho, "Coherence Degradation of Gaussian Beams in a Turbulent Atmosphere", Journal of The Optical Society of Am., **60**, 665 (1970).

2. L. C. Andrews, W. B. Miller and J. C. Ricklin, "Spatial coherence of a Gaussian-beam wave in weak and strong optical turbulence", Journal of The Optical Society of Am. A, **11**, 1653 (1994).

EVALUATION OF OPTICAL PROPERTIES OF ATMOSPHERIC AEROSOLS BASED ON CHEMICAL CHARACTERIZATION

Sachio OHTA and Naoto MURAO
Division of Environment Resources Engineering
Graduate School of Engineering, Hokkaido University
Sapporo 060-0813, JAPAN
FAX: 81-11-706-7890, E-mail: ohta@sany.hokudai.ac.jp

ABSTRACT

Atmospheric fine particles, aerosols less than 2μm in diameter, were collected on filters and chemically analyzed in Sapporo, Okinawa island in Japan and Ester-Dome, Alaska in U.S.A. They were made up of nine components such as elemental carbon, organics, sulfate, nitrate, ammonium, sea-salt cations, soil and water.

Based on the chemical characterization, it was assumed that atmospheric aerosols comprise seven species of particles such as elemental carbon, organics, ammonium sulfate, ammonium nitrate, sea-salt, soil particles and mixed nuclei which have inner core of elemental carbon and outer shell of sulfate. Using log-normal size distribution, complex index of refraction and atmospheric concentrations of each chemical species particles, single scattering albedo and volume extinction coefficient of aerosols were evaluated by calculation with Mie scattering theory.

Keywords; chemical characterization of aerosols, Mie scattering theory, single scattering albedo, volume extinction coefficient, mixed nuclei

1. INTRODUCTION

In remote sensing of ocean color, vegetation or surface reflectivity of land surface, it is necessary to determine optical thickness, size distribution and single scattering albedo of atmospheric aerosols. But, it is difficult, in particular, to measure the single scattering albedo by a handy measuring instrument. We have developed a method to estimate the single scattering albedo based on chemical characterization of the atmospheric aerosols. In this paper, we present the chemical characterization of atmospheric aerosols, and evaluation of the single scattering albedo based on the characterization in Sapporo and Okinawa island in Japan, and Ester-Dome near Fairbanks, Alaska in U.S.A.

2. CHEMICAL CHARACTERIZATION OF ATMOSPHERIC AEROSOLS IN SAPPORO

2.1. Experimental

Atmospheric fine particles, aerosols less than 2 μm in diameter, were collected on two types of filters such as Teflon and quartz fiber filters simultaneously, equipped with a cyclone separator whose 50% cut off diameter was 2 μm at a flow rate of 20 ℓ min^{-1}. The samplings were carried out every half month, continuously for 14 days, from November 1991 to October 1992 on a roof top of our office building at a height of 26m above the ground in the University Campus in Sapporo.

We analyzed chemical species of the fine particles colleced on both Teflon and quartz fiber filters as in Ohta and Okita (1990) except for total particulate mass (TPM), water content and aluminum (Al). TPM was determined by weighing Teflon filters on an electric balance in a dry box with silica gel. Before and after the sampling, the Teflon filters were left in the dry box for more than 24 hours at a relative humidity less than 30%, and then weighed them by the electric balance.

The amount of water associated with aerosols on the Teflon filter was determined by Karl-Fischer method. The water was vaporized in a water evaporator, introduced in an aqua-counter, and titlated coulometrically in the Karl-Fischer reagent solution.

We used Al as a tracer material of soil. The amount of Al on the sampled Teflon filter was determined with particle induced X-ray emission (PIXE) method (Kasahara et al., 1993).

2.2. RESULTS

Atmospheric concentrations of chemical components of the aerosols were determined in elemental carbon (EC), organic carbon (OC), sulfate (SO_4^{2-}), nitrate (NO_3^-), ammonium (NH_4^+), chloride (Cl^-), sodium (Na^+), calsium (Ca^+), alminum (Al) and water.

By using above results, we calculated the following chemical species concentrations in the atmosphere.

The amount of organics was determined by multiplying the amount of organic carbon (OC) by 1.20 according to Countess et al.(1980),

$$\text{Organics} = 1.20 \times \text{OC}.$$

We denoted SS.Ci as the sum of sea-salt cations (Na^+, Mg^{2+}, Ca^{2+}, K^+ and Sr^{2+}). Since Na^+ consists of 83.7% of the sum of the sea-salt cations, we obtained SS.Ci as follows,

$$\text{SS.Ci} = (1/0.837) \times Na^+.$$

The mass fraction of Al in Sapporo soil was 8.6% (Ohta and Okita, 1990). The amount of soil particles was, then, calculated by

$$\text{Soil particles} = (1/0.086) \times \text{Al}.$$

Figure 1 shows semimonthly mass balance of atmospheric fine particles in Sapporo.

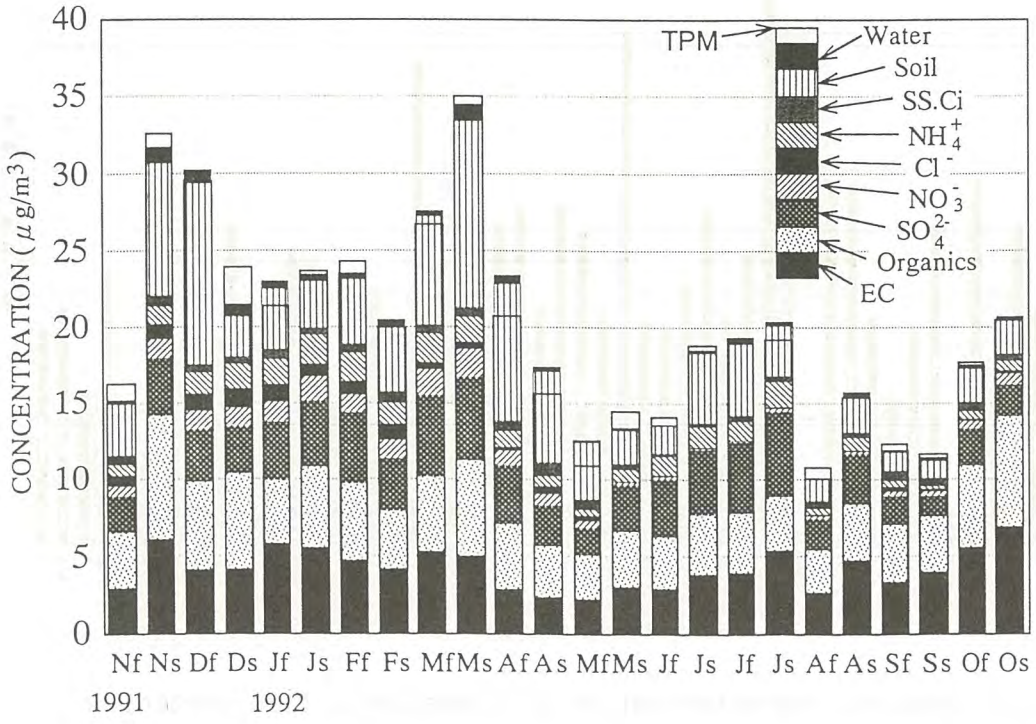


Fig.1 Semimonthly mass balance of atmospheric fine particles in Sapporo from November 1991 to October 1992. TPM, ss.Ci and EC are semimonthly concentrations of totla particulate mass, the sum of sea-salt cations and elemental carbon, respectively. Sampling periods, e.g. Nf and Ns represent the first and second half of November, respectively.

We defined the sum total of chemical components (TCC) as

$$TCC = EC\ (\text{elemental carbon}) + OC + SO_4^{2+} + NO_3^- + Cl^- + NH_4^+ + SS.Ci + \text{soil particle} + \text{water}$$

The ratio of the sum total of chemical components (TCC) to the total particulate mass (TPM) ranged from 90 to 116 %. We, thus, concluded that atmospheric fine particles in Sapporo almost consisted of nine components such as elemental carbon, organics, SO_4^{2-}, NO_3^-, Cl^-, NH_4^+, sea-salt cations, soil particles and water. Under the condition of relative humidity less than 30%, in particular, the water content was negligible.

3. CHEMICAL CHARACTERIZATION OF ATMOSPHERIC AEROSOLS IN OKINAWA ISLAND AND ESTER-DOME, ALASKA.

We measured atmospheric concentrations of chemical species of fine particles, aerosols less than 2μm in diameter, weekly from May 1995 to September 1996 at Okinawa island in Japan, and monthly from August 1991 to August 1992 at Ester-Dome near Fairbanks, Alaska, U.S.A. The chemical characterization of the fine particles at Okinawa island and Ester-Dome are shown in Figure 2 and 3, respectively.

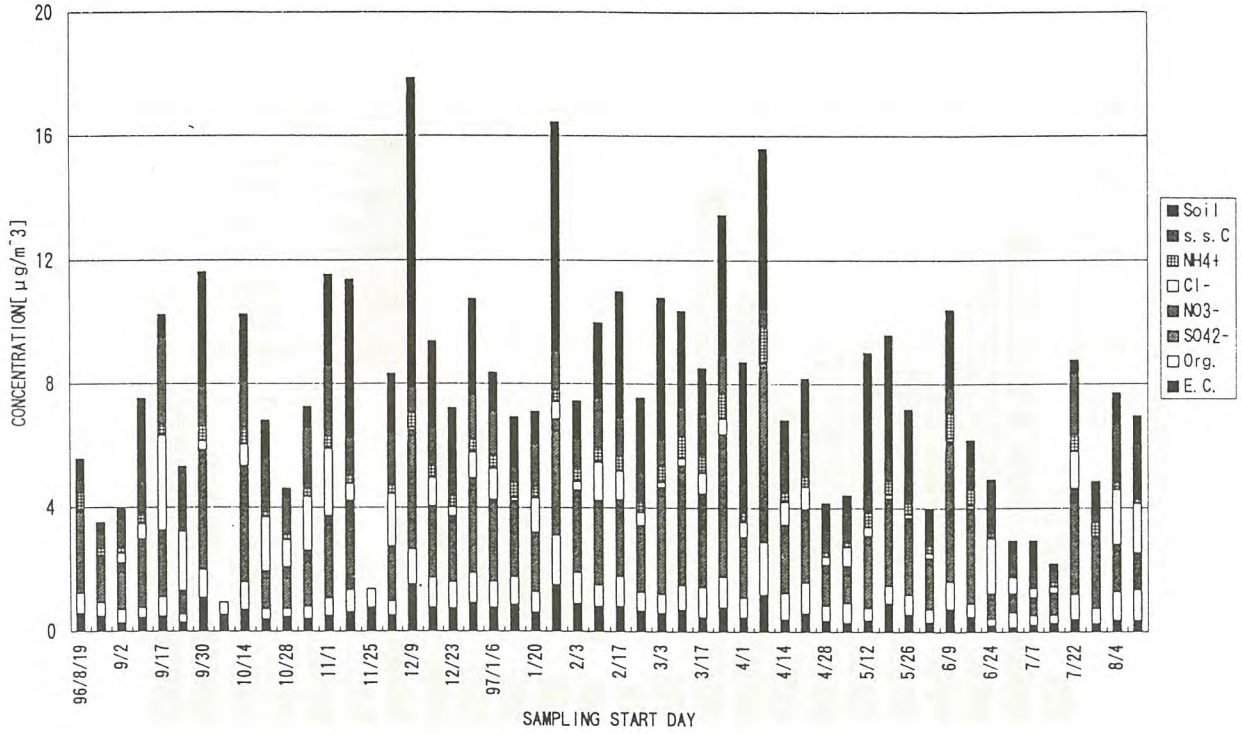


Fig.2 Chemical characterization of atmospheric fine particles in Okinawa island.

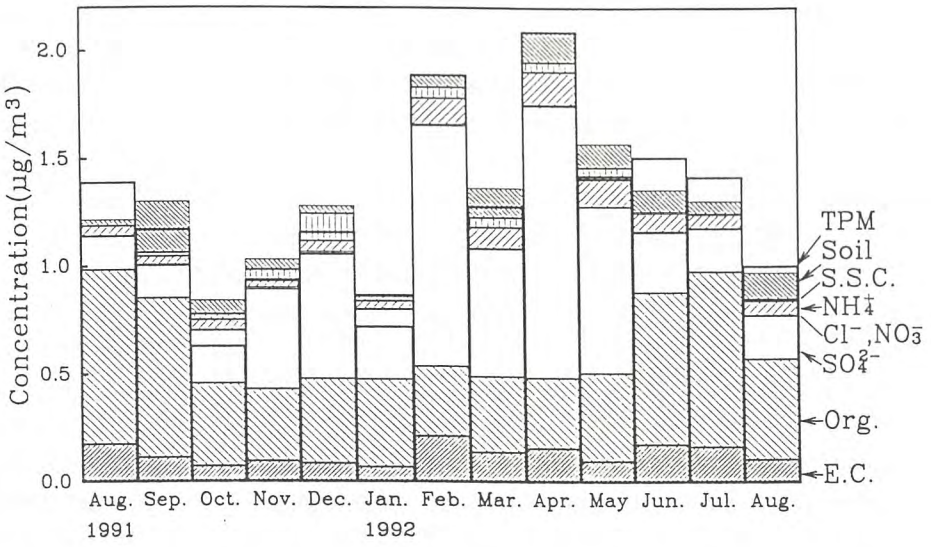


Fig.3 Chemical characterization of atmospheric fine particles at Ester-Dome near Fairbanks in Alaska.

4. EVALUATION OF OPTICAL PROPERTIES OF ATMOSPHERIC AEROSOLS BASED ON CHEMICAL CHARACTERIZATION

On the basis of the chemical characterization, we assumed that atmospheric aerosols had two kinds of mixing condition such as external mixture and internal half mixture. The external mixture comprises six species of

particles such as elemental carbon (EC), organics, $(NH_4)_2SO_4$, NH_4NO_3, sea-salt and soil particles. Whereas internal half mixture contains mixed nuclei in addition to above six species of homogeneous particles. The mixed nuclei are assumed to have an inner core of elemental carbon and outer shell of sulfate, formed with half amount of EC and half amount of sulfate in the atmosphere.

The particles of elemental carbon, organics, $(NH_4)_2SO_4$, NH_4NO_3 and the mixed nuclei belong to the fine particles less than $2\mu m$ in diameter and sea-salt and soil particles belong to the coarse particles which had a size distribution in volume with a peak in the $2\text{-}20\mu m$ region.

We adopted the size distribution of each species of particles as log-normal in number distribution,

$$dN/d\ln D = N_0/(\sqrt{2\pi}\ln\sigma_G)\cdot\exp[-(\ln D-\ln D_{GN})^2/(2\ln^2\sigma_G)]$$

where dN is the number density of particles of diameter between D and D+dD, N_0 is the total number density, D_{GN} is the geometric number mean diameter and σ_G is the geometric standard deviation of the distribution.

The geometric number mean diameter and the standard deviation were assumed to be $0.11\mu m$ and 2.10 for the fine particles, and $0.98\mu m$ and 2.15 for the coarse particles, respectively. We took account of the condensational growth of hygroscopic particles such as $(NH_4)_2SO_4$, NH_4NO_3 and sea-salt for monthly mean relative humidity. The growth of each species of particles was calculated according to the experimental studies by Tang et al.(1977).

Since we sampled aerosols by the system equipped with the cyclone separator whose 50% cut off diameter was $2\mu m$, we measured the whole fine particles, but only small fraction of the coarse particles.

The complex index of refraction at $0.50\mu m$ wavelength was assumed to be 1.50-0.55i for EC, 1.55-0.00i for organics, 1.55-0.00i for $(NH_4)_2SO_4$, NH_4NO_3 and sea-salt, and 1.55-0.008i for soil particles.

Using above size distribution and complex index of refraction for each species of particles i, the volume extinction coefficients σ_{Ei} and the volume scattering coefficient σ_{Si} were calculated by the Mie scattering theory. Those for the mixed nuclei we calculated following Toon and Ackerman (1981).

Thus, the total volume extinction coefficient σ_E of the atmospheric aerosols was obtained as the sum of volume extinction coefficients of each species of particles σ_{Ei},

$$\sigma_E = \Sigma\sigma_{Ei},$$

and the total volume scattering coefficient σ_S was similarly obtained as

$$\sigma_S = \Sigma\sigma_{Si}.$$

The single scattering albedo ω of the atmospheric aerosols was defined as the ratio of the total volume scattering coefficient to the total volume extinction coefficient,

$$\omega = \sigma_S / \sigma_E.$$

5. OPTICAL PROPERTIES OF ATMOSPHERIC AEROSOLS

Figures 4 and 5 show the semimonthly mean single scattering albedo and volume extinction coefficient of the atmospheric aerosols in external mixture and internal half mixture, respectively, at the wavelength of 0.5 μm in Sapporo from November 1991 to October 1992. In Figure 4 the single scattering albedo and the volume extinction coefficient in external mixture ranged from 0.73 to 0.85 and from 5.8×10^{-7} to 1.47×10^{-6} cm^{-1}, respectively. In the calculation there were no mixed nuclei, that is, EC and sulfate suspended in isolation in the atmosphere. Whereas, in the internal half mixture shown in Figure 5 which had mixed nuclei formed with half amount of EC and half amount of sulfate in the atmosphere, the single scattering albedo and the volume extinction coefficient ranged from 0.68 to 0.78 and from 5.8×10^{-7} to 1.46×10^{-6} cm^{-1}, respectively. Thus, the calculated single scattering albedo decreased by 0.05 to 0.07 compared with that in the external mixture.

Figur 6 shows weekly single scattering albedo and volume extinction coefficient of atmospheric aerosols in internal half mixture in Okinawa island. The single scattering albedo and volume extinction coefficient ranged from 0.80 to 0.95 and 1.5×10^{-7} to 8.0×10^{-7} cm^{-1}, respectively. Whereas, in external mixture condition, the single scattering albedo increased in the range of 0.87 to 0.97.

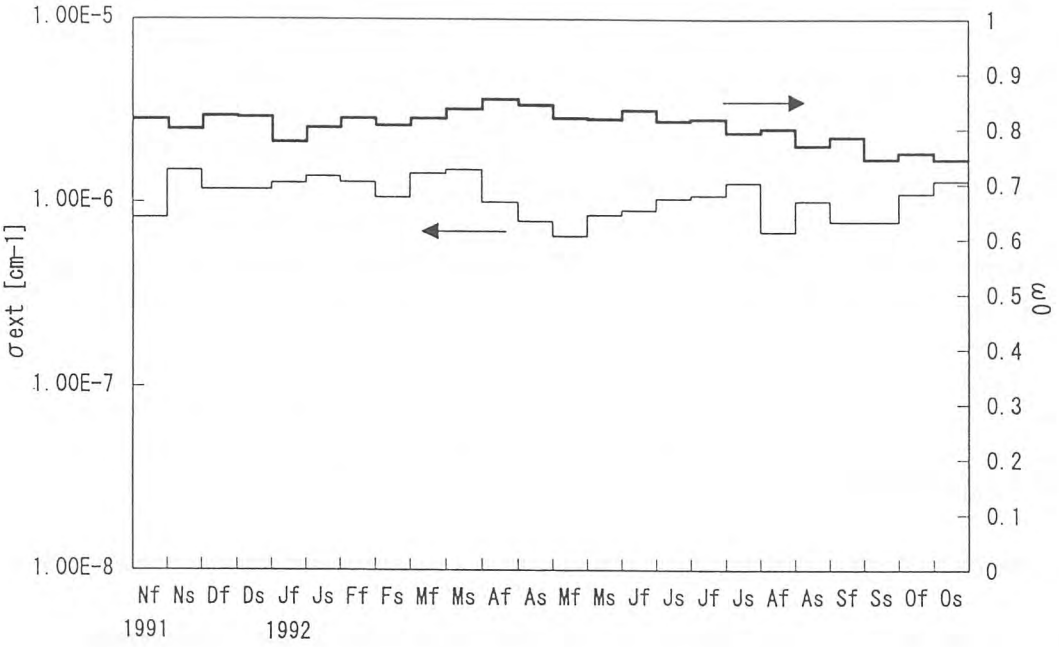


Fig.4 Semimonthly mean single scattering albedo and volume extinction coefficient of atmospheric aerosols in external mixture in Sapporo

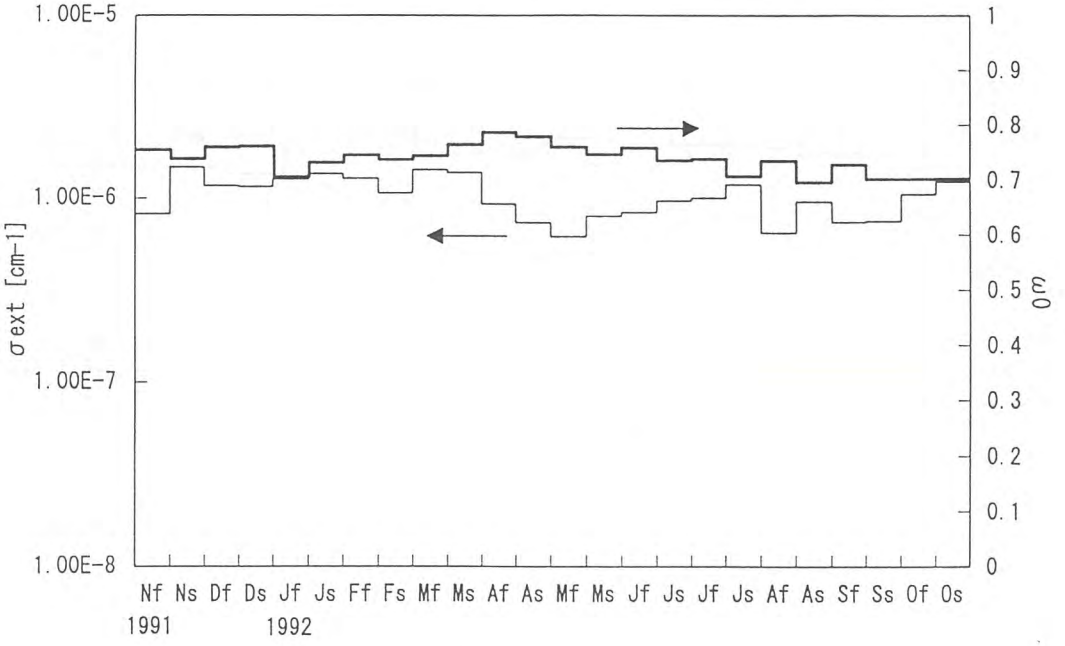


Fig.5 Semimonthly mean single scattering albedo and volume extinction coefficient of atmospheric aerosols in internal half mixture in Sapporo.

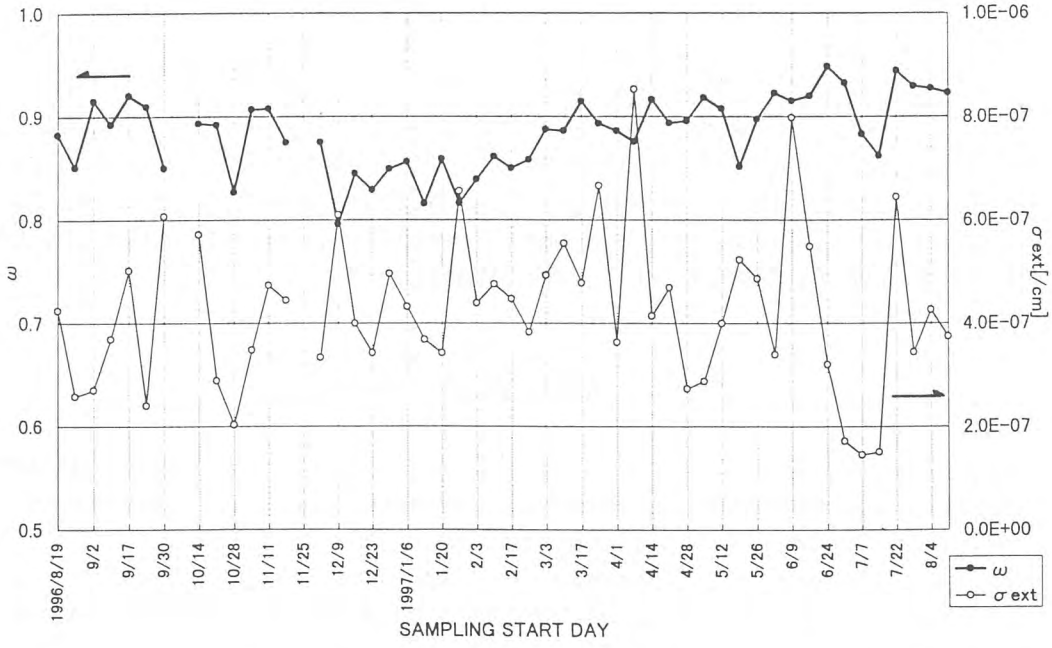


Fig.6 Weekly mean single scattering albedo and volume extinction coefficient of atmospheric aerosols in internal half mixture in Okinawa island.

Figure 7 shows the monthly mean single scattering albedo and volume extinction coefficient of atmospheric aerosols in internal half mixture at Ester-Dome, Alaska. The single scattering albedo ranged from 0.83 to

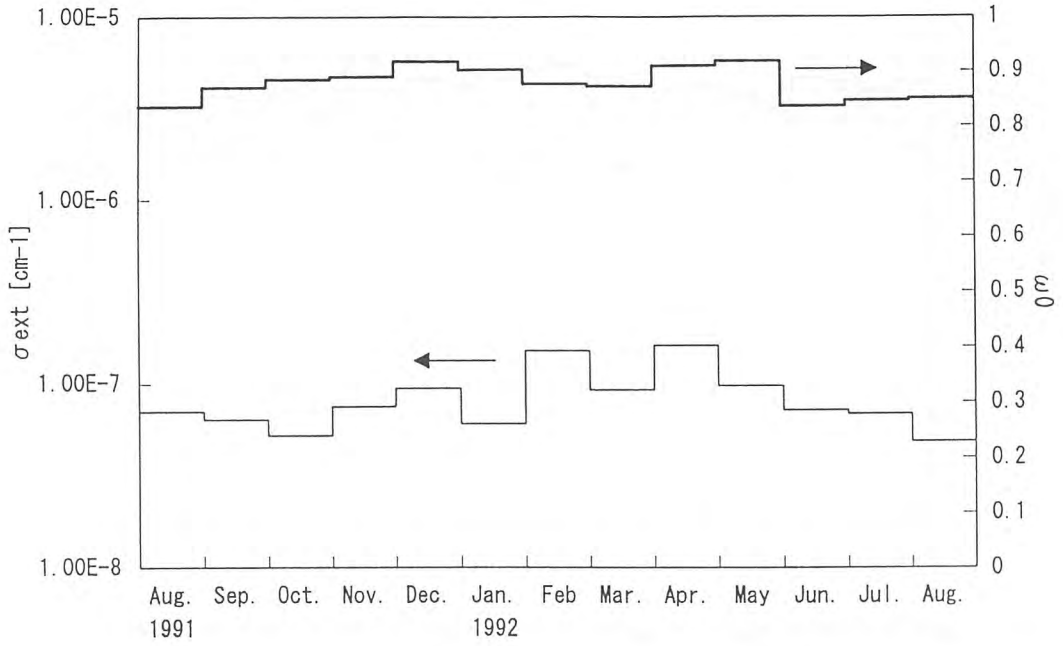


Fig.7 Monthly mean single scattering albedo and volume extinction coefficient of atmospheric aerosols in internal half mixture at Ester-Dome near Fairbanks, Alaska.

0.92 and from 5.2×10^{-8} to $1.7\times^{-7}cm^{-1}$, respectively. In the external mixture condition, the single scattering albedo ranged from 0.88 to 0.96.

We found that there were differences of 0.04 to 0.07 in the single scattering albedo between in the external mixture and the internal half miture aerosols. Thus it is important, hereafter, to determine the concentration of the mixed nuclei in the atmosphere.

REFERENCES

Countess, R.J., Wolff, G.T. and Cadle, S.H. (1980): The Denver winter aerosol: a comprehensive chemical characterization. Journal of Air Pollution Control Association, Vol.30, 1194-1200.

Kasahara, M., Shinoda, K., Takahashi, K. and Yoshida, K. (1993): Characterization of road-side aerosols by PIXE and SEM-EDX analysis. International Journal of PIXE, Vol.3, 313-318.

Ohta, S. and Okita, T. (1990): A chemical characterization of atmospheric aerosol in Sapporo. Atmospheric Environment, Vol.24A, 815-822.

Tang, I.N., Nunkelwitz, H.R. and Davis, J.G. (1977): Aerosol growth studies-II. Preparation and growth measurements of monodisperse salt aerosols. Journal of Aerosol Science, Vol.8, 149-159.

Toon,O.B. and Ackerman,T.P. (1981): Algorisms for calculation of scattering by strastified spheres. Appl. Optics, Vol.20, 3657-3660.

Line strengths and half-widths of CO_2, CO, and N_2O in the near infrared region at room temperature

Masashi Fukabori, Tadao Aoki, and Teruo Aoki
Meteorological Research Institute
Tsukuba, Ibaraki 305, Japan

Hideyuki Ishida, and Takeshi Watanabe
Toray Research Center Inc.
Otsu, Shiga 520, Japan

ABSTRACT

The absorption spectra of CO_2, CO, and N_2O in the near infrared region were measured with a high-resolution Fourier transform spectrometer at room temperature to examine the uncertainties of the line parameters of the spectroscopic database. The line strengths and half-widths of these molecules were determined by a nonlinear least squares technique. We compared our results with the values compiled in the HITRAN databases. Large differences between the measured line strengths and the compiled ones in the HITRAN databases were found for the weak bands of each molecule. Air-broadened half-widths of CO_2, CO, and N_2O, which were calculated with measured N_2- and O_2-broadened half-widths, were close to the values of the HITRAN96 database. Self-broadened half-widths of CO_2 and N_2O agreed with the HITRAN96 values;while self-broadened half-widths of CO were different from the HITRAN96 values.

1. INTRODUCTION

In order to obtain the vertical profiles and column amounts of trace gases, which are related to the global warming and ozone depletion, solar spectra have been measured with ground-based high-resolution spectrometers by many investigators. Accurate absorption line parameters such as line center positions, line strengths, and half-widths are necessary for the analysis of solar spectra, whereas the uncertainties of the line parameters are still large, especially in the near infrared region. Many absorption lines from the visible to the far infrared region have been compiled in the spectroscopic databases. Among the spectroscopic databases, the HITRAN database(Rothman *et al.*, 1983;Rothman *et al.*, 1987;Rothman *et al.*, 1992;Rothman, 1996) has been mostly used for the radiative transfer calculation of the Earth's atmosphere. The accuracy of absorption line parameters is estimated to be 10%, that is not sufficient to retrieve the vertical profiles of trace gases. To examine the uncertainties of the line parameters of HITRAN, we measured the absorption spectra of trace gases with a high-resolution Fourier transform spectrometer.

2. EXPERIMENT

The absorption spectra were obtained using a Bruker IFS–120HR Fourier transform spectrometer with a KBr beam splitter, a tungsten lamp and an InSb detector. The spectral resolution was set at 0.008–0.02 cm^{-1}, depending on the gas pressure to be measured. We used the several kinds of absorption cells according to the line strengths of trace gases. The purity of the absorbing gases was above 99.9%. The N_2 and O_2 samples of high purity were used for the buffer gases. Pressure measurements were made with MKS Baratron pressure transducers designed for 0–100 torr and 0–1,000 torr ranges. All spectra were measured at room temperature. The variation of the sample gas temperature was controlled within ± 1 K during the measurement. The signal to noise ratio was better than 200 for each measurement.

3. ANALYSIS

The line strengths, self-, N_2-, and O_2-broadened half-widths of CO_2, CO, and N_2O were determined with a nonlinear least squares procedure. An iterative method was used to minimize the sum of the squares of the difference between the measured spectrum and calculated one with the appropriate line parameters. At lower pressures of the sample gas, the Voigt profile was assumed as a line shape.

The line strengths in a vibration-rotation band of the linear molecule are expressed by

$$S(m) = \frac{8\pi^3 N_T}{3hcQ_{rot}}\omega(m)exp\left[-\frac{hcE_{rot}(m)}{kT}\right]g_{J'l'}\left|U^{J'l'}_{J''l''}\right|^2\left|M^{v'J'l'}_{v''J''l''}\right|^2\left[1-exp\left(-\frac{h\omega}{kT}\right)\right], \quad (1)$$

$$N_T = \frac{N_L T_0}{Q_{vib}T}, \quad (2)$$

where $|U^{J'l'}_{J''l''}|$ is the matrix element of the dipole moment of a pure rotational transition, $|M^{v'l'J'}_{v''l''J''}|$ is the matrix element of the dipole moment of the vibrational transition, and the other symbols have their usual meanings. The square of the matrix element of the vibrational transition can be expressed as

$$|M^{v'l'J'}_{v''l''J''}|^2 = |R^{v'l'}_{v''l''}|^2 F(m), \tag{3}$$

where $F(m)$ is the factor that accounts for the vibration-rotation interaction and $|R^{v'l'}_{v''l''}|$ is the matrix element of the pure vibrational transition. For a linear molecule, $F(m)$ may be expressed as function of the running index m by,

$$F(m) = 1 + am + bm^2, \tag{4}$$

where

$$m = \begin{cases} J''+1 & \text{for the R–branch,} \\ -J'' & \text{for the P–branch.} \end{cases} \tag{5}$$

The air-broadened half-widths were calculated from experimental values for N_2-broadened and O_2-broadened half-widths assuming the relation

$$\gamma^0_{\text{abs–air}} = 0.79\gamma^0_{\text{abs–}N_2} + 0.21\gamma^0_{\text{abs–}O_2}. \tag{6}$$

4. RESULTS AND DISCUSSION

4.1 CO_2

Absorption spectra were measured for the (30011–00001), (30012–00001), (30013-00001), and (30014–00001) bands of CO_2 in the 1.6 μm region. Figure 1 shows the self-broadened half-widths of the (30012–00001) band. The measured half-widths agreed well with the HITRAN92(Rothman *et al.*, 1992) values which were based on the recent high-resolution experiments(Jones, 1987; Dana *et al.*, 1989; Dana *et al.*, 1992). Our results were also in good agreement with the values reported by Margottin-Maclou *et al.*(1988). Self-broadened half-widths of the HITRAN86(Rothman *et al.*, 1987) database were larger than those of the HITRAN92 database and our results for $7 \leq m \leq 46$. Figure 2 shows the N_2-broadened half-widths of the (30012–00001) band. Our results were very close to the values of the recent high-resolution experiments(Johns, 1987; Dana *et al.*, 1989; Margottin-Maclou *et al.*, 1988). Similar results were observed in the other three bands for the self- and N_2-broadened half-widths.

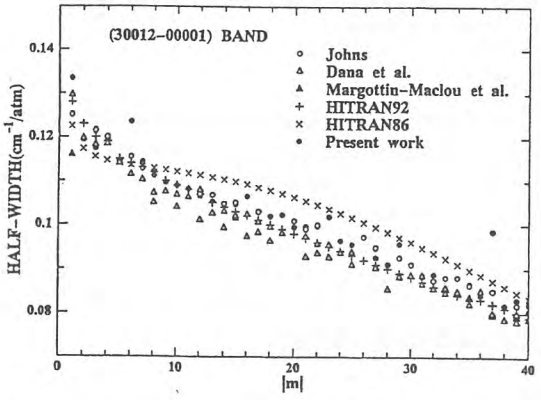


Fig.1 Self-broadened half-widths of the (30012–00001) band of CO_2.

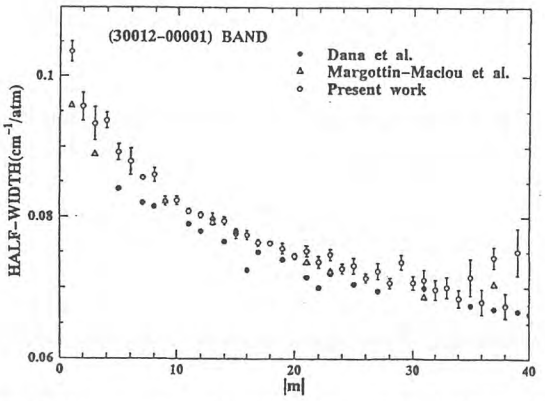


Fig.2 N_2-broadened half-widths of the (30012–00001) band of CO_2.

Figures 3 and 4 show the comparisons of the measured line strengths with the HITRAN values for the (30011–00001) and (30012–00001) bands of CO_2, respectively. The line strengths of the HITRAN92 database for the four bands in the 1.6 μm region are based on the experimental results carried out in the 1970's(Valero and Suarez, 1978; Suarez and Valero, 1978a; Suarez and Valero, 1978b). The line strengths obtained for the (30011–00001) band agreed well with the AFGL82(Rothman *et al.*, 1983) values, but the large difference between our results and the recent HITRAN values was found. For this weak band, the line strengths reported by Valero and Suarez were about 10–15% larger than those obtained by Toth *et al.*(1971). However, for the (30012–00001) band, our results were close to the HITRAN92 values, though the measured strengths of the R-branch were a few percent smaller than those of HITRAN. Similar results were found for

the other weak and strong bands. In the HITRAN96 database(Rothman, 1996), the line strengths of only the (30011–00001) band were revised and agreed with our results.

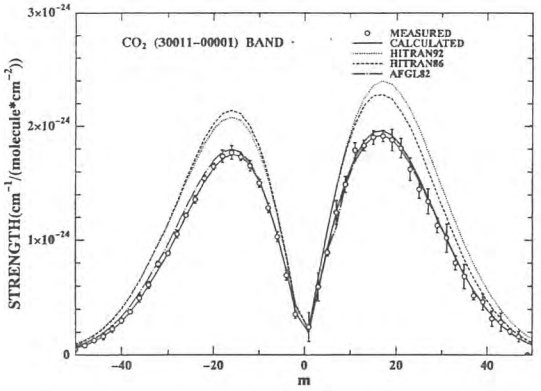


Fig.3 Line strengths of the (30011–00001) band of CO_2.

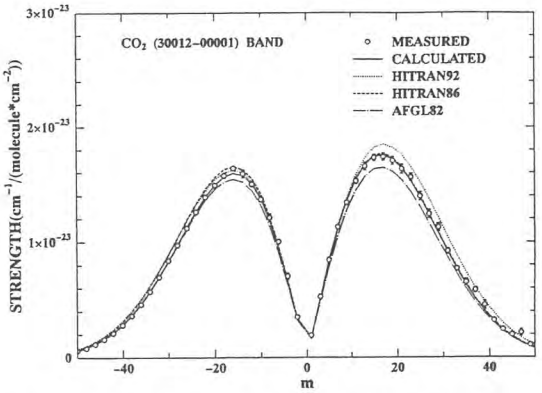


Fig.4 Line strengths of the (30012–00001) band of CO_2.

4.2 CO

Absorption spectra were measured for the (2-0) band of CO. Figure 5 shows the N_2- and O_2-broadened half-widths of the (2-0) band. O_2-broadened half-widths were very close to the values obtained by Nakazawa and Tanaka(1982), though N_2-broadened half-widths were slightly different from their results around m=10. N_2-broadened half-widths measured by the recent high-resolution experiments(Anselm *et al.*, 1993;Hamdouni *et al.*, 1993) agreed quite well with our results. Self-broadened half-widths were 5-8% smaller than the HITRAN96 values.

The measured line strengths agreed well with the values of HITRAN92 and HITRAN96 within the experimental error shown in Fig.6. The vibration-rotation coupling function obtained in this study was

$$F(m) = 1 + 5.08 \times 10^{-3} m + 3.52 \times 10^{-5} m^2. \quad (7)$$

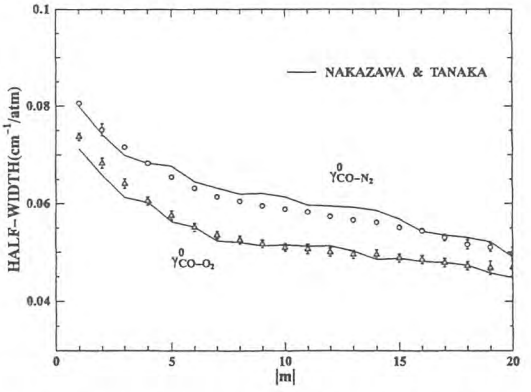


Fig.5 N_2- and O_2-broadened half-widths of the (2-0) band of CO.

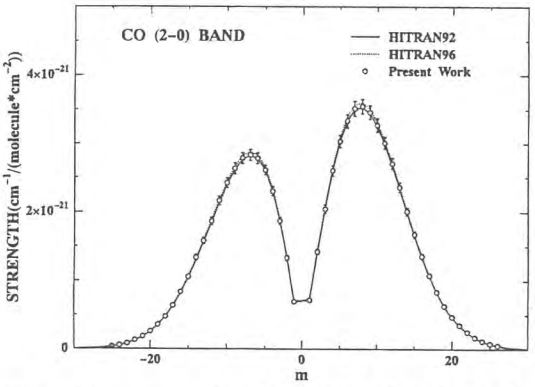


Fig.6 Line strengths of the (2-0) band of CO.

4.3 N_2O

Absorption spectra were measured for several bands of N_2O in the 2.0, 2.1, 2.3, 2.5, 2.6, and 2.9 μm regions. Since all lines of the R-branch in the (0002-0000) band do not blend with lines of other bands, the R-branch of this band is the appropriate region to determine the half-widths. Self-, N_2-, and O_2-broadened half-widths of N_2O were obtained for lines of this R-branch. Figure 7 shows the comparison of the measured self-broadened half-widths with the values obtained by other workers(Toth, 1971;Margolis, 1972;Lacome *et al.*, 1984;Toth, 1993) and of HITRAN92. Our results were close to the values obtained by Lacome *et al.*(1984) and Toth(1993) for the self-broadened half-widths. The values reported in the 1970's, which were obtained by the low-resolution spectra using a grating spectrometer, were about 25% larger than our values around m=16.

Figure 8 shows the comparison of the measured line strengths with the HITRAN values for the (4000-0000) band in the 2.3 μm region. The measured line strengths agreed well with the HITRAN96 values in the

R-branch, but the measured line strengths were about 5% less than the HITRAN96 values in the P-branch. Similar to the (4000-0000) band, the measured line strengths of the other bands were slightly different from the HITRAN96 values.

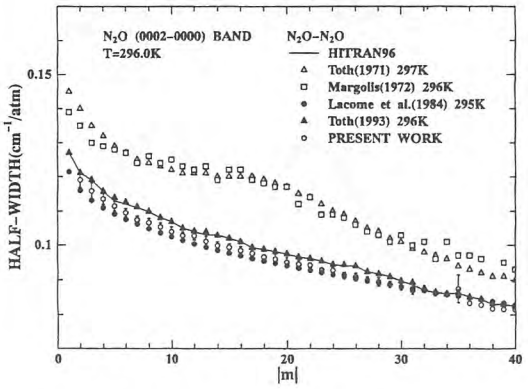


Fig.7 Self-broadened half-widths of the (0002-0000) band of N_2O.

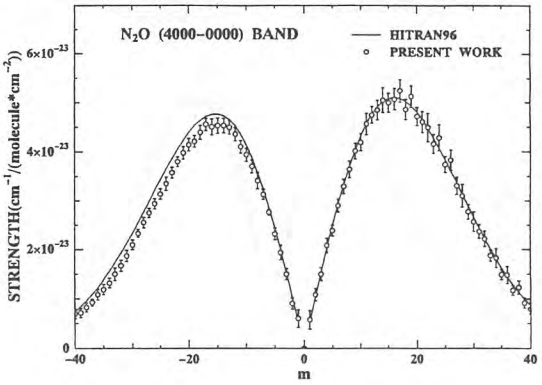


Fig.8 Line strengths of the (4000-0000) band of N_2O.

REFERENCES

Anselm, N., K.M.Yamada, R.Schieder, and G.Winnewisser, 1993:Measurements of foreign gas gas pressure shift and broadening effects in the (1-0) band of CO with N_2 and Ar, *J. Mol. Spectrosc.*, **161**, 284–296.

Dana, V., A.Valentin, A.Hamdouni, and L.S.Lothman, 1989:Line intensities and broadening parameters of the 11101←10002 band of $^{12}C^{16}O_2$, *Appl. Opt.*, **28**, 2562–2565.

Dana, V., J.-Y. Mandin, G. Guelachvili, Q. Kou, M. Morillon-Chapey, R.B. Wattson, and L.S. Rothman, 1992:Intensities and self-broadening coefficients of $^{12}C^{16}O_2$ lines in the laser band region, *J. Mol. Spectrosc.*, **152**, 328–341.

Hamdouni, A., A.Barbe, J.-J.Plateaux, V.Langlois, V.Dana, J.-Y.Mandin, and M.Badaoui, 1993:Measurements of N_2-induced shifts and broadening coefficients of lines in CO fundamental from Fourier transform spectra, *J. Quant. Spectros. Radiat. Transfer*, **50**, 247–255.

Johns, J.W.C., 1987:Absolute intensity and pressure broadening measurements of CO_2 in the 4.3-μmm region, *J. Mol. Spectrosc.*, **125**, 442–464.

Lacome, N., A.Levy and G.Guelachvili, 1984:Fourier transform measurement of self-, N_2, and O_2-broadening of N_2O lines: temperature dependence of linewidths. *Appl. Opt.*, **23**, 425–435.

Margolis, J.S., 1972:Intensity and half width measurements of the (00^02–00^00) band of N_2O, *J. Quant. Spectros. Radiat. Transfer*, **12**, 751–757.

Margottin-Maclou, M., P. Dahoo, A. Henry, A. Valentin, and L. Henry, 1988:Self-, N_2, and O_2-broadening parameters in the ν_3 and $\nu_1+\nu_3$ band of $^{12}C^{16}O_2$, *J. Mol. Spectrosc.*, **131**, 21–35.

Nakazawa T., and M.Tanaka, 1982:Measurements of intensities and self- and foreign-gas-broadened half-widths of spectral lines in the CO fundamental band, *J. Quant. Spectros. Radiat. Transfer*, **28**, 409–416.

Rothman, L.S., R.R. Gamache, A. Barbe, A. Goldman, J.R. Gillis, L.R. Brown, R.A. Toth, J.-M. Flaud, C.Camy-Peyret, 1983:AFGL atmospheric absorption line parameters compilation: 1982 edition, *Appl. Opt.*, **22**, 2247–2256.

Rothman, L.S., R.R.Gamache, A.Goldman, L.R.Brown, R.A.Toth, H.M.Pickett, R.L. Poynter, J.-M.Flaud, C.Camy-Peyret, A.Barbe, N.Husson, C.P. Rinsland, and M. A. H. Smith, 1987:The HITRAN database: 1986 edition, *Appl. Opt.*, **26**, 4058–4097.

Rothman, L.S., R.R.Gamache, R.H.Tipping, C.P.Rinsland, M.A.H.Smith, D.Chris Benner, V. Malathy Devi, J.-M.Flaud, C.Camy-Peyret, A.Perrin, A.Goldman, S.T.Massie, L.R.Brown, and R.A.Toth, 1992:The HITRAN molecular database: edition of 1991 and 1992, *J. Quant. Spectros. Radiat. Transfer*, **48**, 469–507.

Rothman, L.S., 1996:HITRAN 1996(CD-ROM), private communication.

Suarez, C.B., and F.P.J.Valero, 1978a:Absolute Intensity Measurements at different Temperatures of the $C^{12}O_2^{16}$ bands $30^01_{\ I} \leftarrow 00^00$ and $30^01_{\ IV} \leftarrow 00^00$, *J. Quant. Spectros. Radiat. Transfer*, **19**, 569–578.

Suarez, C.B., and F.P.J.Valero, 1978b:Intensities, self-broadening by Ar and N_2 for the $30^01_{\ III} \leftarrow 00^00$ band of CO_2 measured at different temperatures, *J. Mol. Spectrosc.*, **71**, 46–63.

Toth, R.A., 1971:Line strengths of N_2O in the 2.9 micron region. *J. Mol. Spectrosc.*, **40**, 588–604.

Toth, R.A., 1993:Line strengths (900–3600 cm^{-1}), self-broadened linewidths, and frequency shifts (1800-2360 cm^{-1}) of N_2O, *Appl. Opt.*, **32**, 7326–7365.

Valero, F.P.J., and C.B.Suarez, 1978:Measurement at different temperatures of absolute intensities, line half-widths, and broadening by Ar and N_2 for the $30^01_{\ II} \leftarrow 00^00$ band of CO_2, *J. Quant. Spectros. Radiat. Transfer*, **19**, 579–590.

II. Remote Sensing of Aerosol over Land and Ocean

An inversion algorithm for simultaneous determination of vegetation reflectance and aerosol optical depth using satellite radiance data

Qiu Jinhuan
Institute of Atmospheric Physics. Chinese Academy of Sciences.Beijing 100029. China

Abstract

Based on the property of vegetation reflectance spectra in the range from near-ultraviolet to near-infrared and the sensitivity of outgoing radiance to the reflectance and aerosol optical depth. a so-called iteration-correlation inversion algorithm is proposed to simultaneously derive the reflectance and aerosol optical depth. According to numerical inversion simulations. effects of the measurement error in radiance. the error in aerosol imaginary index and the vegetation ununiform on inversion results are analyzed. As shown in inversion simulations. as the error in the imaginary index is within 0.01. standard deviations of solutions of the reflectance and the optical depth for 14 wavelength channels are less than 0.063 and 0.023. and under 2% error of radiance. they are less than 0.023 and 0.0056. respectively. showing a satisfactory accuracy.

I. INTRODUCTION

Atmospheric aerosol optical depth and vegetation reflectance spectra properties are important to research environment and climate change. space-to-earth remote sensing and so on. Vegetation reflectance spectra properties can indicate vegetation growing status and season changes and affects the earth radiation budget. it is also one of the theoretical bases of space-to-earth remote sensing application. and it has been widely used in remote sensing information spotting. environment pollution monitoring. plant diseases and insect pests monitoring. crop yield estimating and geological minerals locating[1-3]. Atmospheric aerosol optical depth is an important parameter characterizing atmospheric turbidity and a crucial factor determining aerosol radiance-climate effect. Spaceborne remote sensing is the sole means to determine aerosol optical depth and earth surface reflectance in the global scale. In the recent 20 years. research in spaceborne remote sensing of aerosol optical depth and earth surface reflectance has made important progress. Now there are two main methods for spaceborne remote sensing of aerosol optical depth. One is occultation method in which stratospheric optical depth is determined by measuring the solar direct radiation at sunrise and sunset with radiometer. The other is to retrieve atmospheric column aerosol optical depth from outgoing radiance information measured in space. which is mainly applied under the situation of ocean underlying surface[4-5]. In the case of land surface. its reflectance is very complicated. and it is generally bigger than that of ocean. and so it has stronger effect on upward sky radiance. Therefore. spaceborne remote sensing of continent aerosol optical depth remains a question unresolved. Based on the vegetation reflectance properties from near ultra-violet to near infrared and the extraterrestrial radiance sensitivity to vegetation reflectance and atmospheric aerosol optical depth. a method for spaceborne remote sensing of the reflectance and the optical depth is proposed in this paper. and the corresponding iteration-correlation inversion algorithm is developed.

2. ANALYSIS OF SENSITIVITY

(1) Characteristics of vegetation reflectance

Whether surface reflectance and aerosol optical depth can be simultaneously retrieved from upward radiance information is crucially dependent on surface reflectance spectra characteristics. The bigger the surface reflectance is. the more it affects the radiance. and the more unfavorable it is to extract the optical depth out of the radiance. but the more favorable it is to retrieve surface reflectance.

Fig.1 shows average value. standard error. maximum and minimum of fifty sorts of the vegetation reflectance spectra from 410nm to 1000nm in Tong's book[3]. In the 50 sorts of vegetation. 18 sorts are rice or wheat. 26 are different trees. and the rest is grassland or reed. Fig.2 shows 12 sorts of the vegetation reflectance spectra in the range of 410-1000nm. The 12 sorts of vegetation are rice. wheat. cotton. rape. sweet potato. astragalus sinicus. Chinese pine. Spruce. cypress. cedar. white poplar and grassland. respectively.

According to Figs.1-2. some characteristics of vegetation reflectance can be seen as follows:

(a) In the wavelength range of 410-500nm. reflectance is relatively smaller. being 2-65 times smaller than. near infrared reflectance. Some of them is even smaller than sea water reflectance. The average of fifty sorts of

vegetation reflectance is less than 0.05, their standard deviation is less than 0.02, and the reflectance change comparatively little from 0.008 to 0.101.

(b)There are maximums of the reflectance in 550-560nm, which change within 0.05-0.3, and minimums of the reflectance can be found around 680nm.

(c) From 680 to 740nm, the reflectance increases obviously when the wavelength increases, and when it is bigger than 740nm in near infrared, the reflectance is usually very high. The average of fifty sorts of reflectance is larger than 0.38, the standard deviation is larger than 0.2, and the reflectance changes in the range of 0.19-0.84. The features above are identical with the research conclusions by Kontratyev (1969). The method of synthetic remote sensing for surface reflectance and aerosol optical depth proposed in this paper is just based on these features of vegetation reflectance.

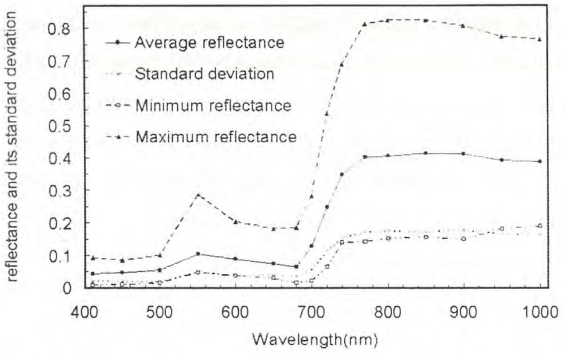


Fig.1 Average values, maximums, minimums and standard deviations of 50 sorts of vegetation reflectance

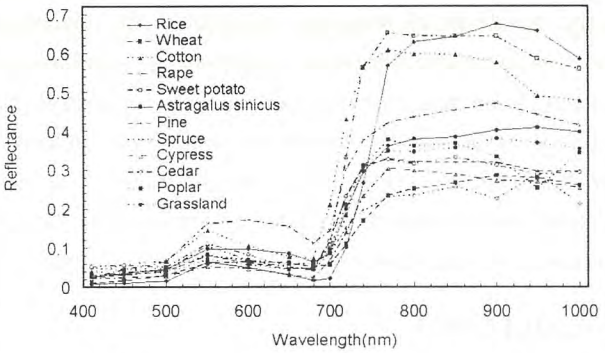


Fig.2 Twelve sorts of vegetation reflectance spectra

(2) *Sensitivity of sky radiance to surface reflectance and aerosol optical depth*

In this paper, Guass-Seidel iteration algorithm presented is adopted to solve radiation transfer equation, $I(\tau,\mu,\varphi)$ stands for radiance, τ_a is aerosol optical depth, μ is cosine of zenith angle,φ is azimuth angle, μ_0 is cosine of solar zenith angle.

As discussed above, the vegetation reflectance in the wavelength less than 680nm and near infrared has different properties, so sensitivity of upward radiance at the representative wavelengths of 500nm and 800nm to surface reflectance and aerosol optical depth is emphatically analyzed in Fig.3 and Fig.4.

Fig.3 illustrates change of upward radiance at 500nm and 800nm with reflectance. In the figure, radiance is unity when surface reflectance is zero, meaning the radiance is relative. Here aerosol size distribution is Deirmendjian (1969) continental model[6], and aerosol refractive index is 1.5-0.01i. It can be seen from Fig.3 that:

(a)The radiance increases when the reflectance increases.

(b)The radiance is very sensitive to the change of the reflectance, especially at the 800nm wavelength. Under the condition that μ_0=1.0, μ=1.0, $\phi=0^{o}$ and τ_a=0.2, when vegetation reflectance changes between 0 and 0.8, the radiation at 500nm and 800nm increases respectively 12 and 36 times. Additionally, because the vegetation reflectance in the wavelength less than 500nm is ordinarily less than 0.1, while the near infrared reflectance can change in a wide range of 0.18 to 0.85. So, the radiance channel in the wavelength less than 500nm is rather less sensitive to vegetation reflectance than near infrared channel, and it is favorable to retrieve aerosol optical depth.

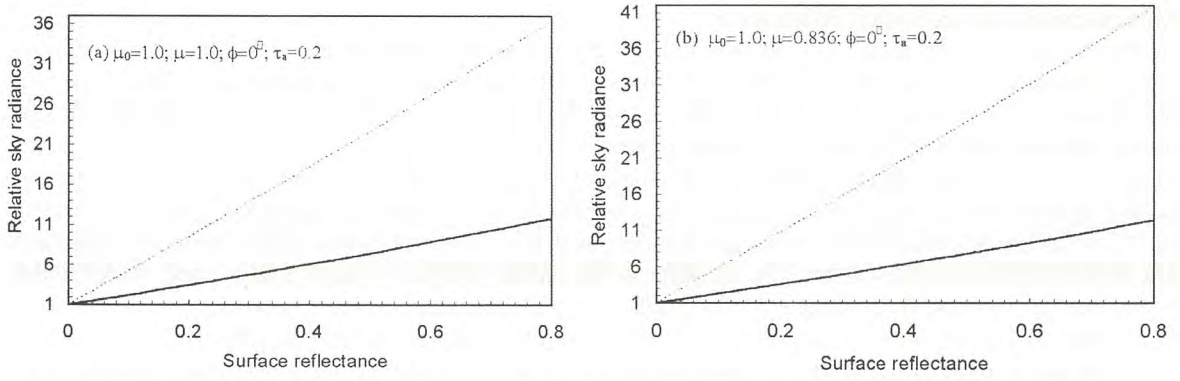


Fig.3 Sky radiance verse surface reflectance. Solid line: λ=500nm; dash line: λ=800nm

Fig.4 shows change of the upward radiation at 500nm and 800nm with aerosol optical depth. Here the radiance is set as 1 when the optical depth is zero, the reflectance for two wavelengths of 500nm and 800nm are average values of fifty sorts of vegetation reflectance as shown in Fig.2, being respectively 0.051 and 0.405. Aerosol size distribution is continental Diemendjian distribution, and aerosol complex refractive index is 1.5-0.01i. It can be seen from Fig.4:

(a) The 500nm radiance is more sensitive to the aerosol optical depth than the 800nm radiance.

(b) Sky radiance is more sensitive to the surface reflectance than the aerosol optical depth.

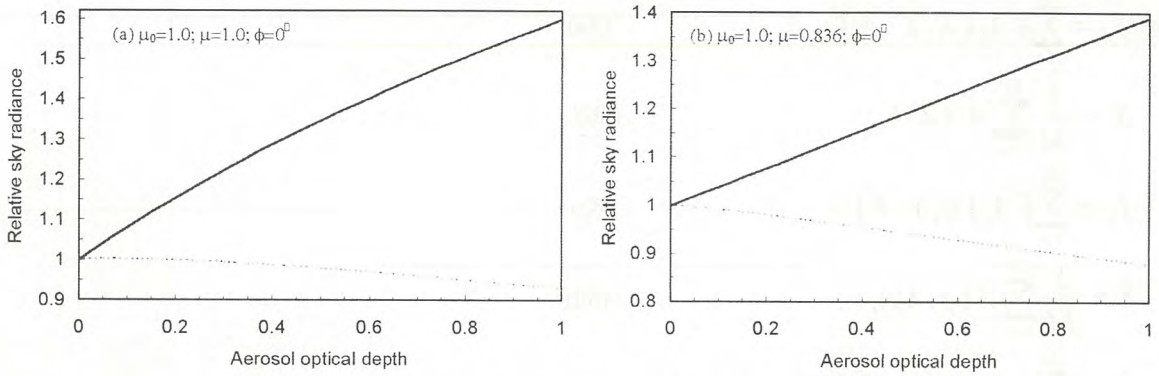


Fig.4 Sky radiance verse aerosol optical depth. Solid line:λ=500nm; dash line: λ=800nm

Because the upward radiance is more sensitive to surface reflectance than the aerosol optical depth, how to get the depth is the key of synthetic remote sensing. In brief, in the channels near the wavelength of 680nm and less than 500nm, vegetation reflectance is small, and for some channel it may even be less than sea water reflectance.Thus, these radiance channels have relatively weaker sensitivity to vegetation reflectance. Generally, it is more sensitive to aerosol optic depth than near infrared radiance. Furthermore, the change of vegetation reflectance in the wavelength less than 680nm (especially less than 500nm) is small. Hence, these channels are applicable to retrieve atmospheric aerosol optical depth by spaceborne remote sensing. Therefore, it is feasible to get the aerosol optical depth from upward radiance in the spectral channels of near 680nm and less than 500nm. Once aerosol optical depth is known, it can be used to improve vegetation reflectance retrieval.

III. RETRIEVAL ALGORITHM

According to the above sensitivity analyses, in the case of vegetation cover, there are two kinds of channel selections suitable for the inversion of aerosol optical depth. one is to choose two or more channels in the wavelength range of 400nm to 500nm, and another is to select several channels in the range of 400nm to 500nm plus the 680nm channel. The advantage of the first choice is that the change of vegetation reflectance of the channels between 400nm and 500nm is small. But by the consideration of sensitivity, the second choice is better. In the following numerical experiments, we used the second choice and selected three channels of 450nm, 500nm and 680nm, marked as λ_{a1}, λ_{a2} and λ_{a3}. Because upward radiance is more sensitive to surface reflectance than aerosol optical depth, it is very important to find an appropriate method to determine reflectance of the three wavelengths. In this paper, an iteration-correlation retrieval algorithm is proposed. In the algorithm, optimum reflectance solution of the three wavelengths is obtained by process of iteration and analysis the relationship between the reflectance solution and all the specimens in the reflectance library. The inversion steps goes like this:

(1)According to known information of surface reflectance measured, build a reflectance library covering a lot of vegetation kinds, in which the reflectance samples are marked as A(j, λ_I), j=1,⋯,⋯, N, i=1,⋯,⋯, M. Here N is the total number of samples, λ_i is wavelength, M represents the total number of spectral channels.

(2) Assume Junge aerosol size distribution in inversion given by: $n(r) = cr^{-(v^*+1)}$,

Under the assumption of Junge distribution, aerosol optical depth can be written as:

$$\tau_a(\lambda) = \tau_a(\lambda_0 = 500nm)(\lambda_0/\lambda)^{2-v^*}, \quad (7)$$

(3)Suppose that v_0 is the initial value of v^*, τ_0 is the initial value of $\tau_a(\lambda_0=500nm)$, and the refractive index

of aerosol is known, then compute aerosol scattering phase functions and optical depths for M channels.

(4)Use the computed aerosol scattering phase functions and optical depths to search reflectance solutions for M channels by solving radiation transfer equation, written as $A_S(\lambda_i)$.

(5)Compute the correlation coefficient between $A_S(\lambda_i)$ and all the samples in the reflectance library as follows:

$$C_f(j) = \frac{f_{xy}}{\sqrt{f_x f_y}}, \tag{8}$$

where: $f_x = \sum_{i=1}^{M}[A_s(\lambda_i) - X]^2$, (8a)

$$X = \frac{1}{M}\sum_{i=1}^{M} A_s(\lambda_i), \tag{8b}$$

$$f_y = \sum_{i=1}^{M}[A_s(\lambda_i) - Y]^2, \tag{8c}$$

$$Y = \frac{1}{M}\sum_{i=1}^{M} A(j,\lambda_i), \tag{8d}$$

$$f_x = \sum_{i=1}^{M}[A_s(\lambda_i) - X][A(j,\lambda_i) - Y], \tag{8e}$$

(6)If reflectance specimen j=k makes $C_f(j)$ the largest, corresponding with the best correlation to reflectance solution, then the reflectance of the three wavelengths λ_{a1}, λ_{a2} and λ_{a3}, corresponding to this specimen, are taken as their solution, written as A_{S1}, A_{S2} and A_{S3}, respectively.

(7) By solving radiation transfer equation, and using A_{S1}, A_{S2} and A_{S3}, to compute the solution of λ_{a1}, λ_{a2}, and λ_{a3} aerosol optical depths, written as τ_{a1}, τ_{a2} and τ_{a3}, respectively.

(8)Using τ_{a1}, τ_{a2} and τ_{a3}, by the least square regression algorithm, to fit a Junge parameter ν^*, written as ν_S.

(9)Using ν_S, compute aerosol scattering phase function, and according to equation (6) determine the optical depths of M channels except λ_{a1}, λ_{a2}, and λ_{a3}, again. Repeat steps (3) to (8). When the difference of optical depths between two iteration processes is less then a given value ε, iteration is ended.

5. NUMERICAL EXPERIMENTS

The iteration-correlation retrieval algorithm requires to build a vegetation reflectance library. In this paper, the library has 90 specimens, all gotten from the Ref.[3]. The twelve vegetation reflectance spectra in Fig.2 are chosen as true spectra in numerical experiments. Define the standard errors of aerosol optical depth and vegetation reflectance solutions in the twelve sets of numerical experiments using these reflectance spectra as:

$$\delta_a(\lambda_i) = \sqrt{\frac{1}{12}\sum_{j=1}^{12}[\tau_a(j,\lambda_i) - \tau_a^*(\lambda_i)]^2}. \tag{9}$$

$$\delta_s(\lambda_i) = \sqrt{\frac{1}{12}\sum_{j=1}^{12}[A(j,\lambda_i) - A^*(j,\lambda_i)]^2}. \tag{10}$$

where j is the ordinal number of the twelve kinds of vegetation. $\tau_a^*(\lambda_i)$ and $A^*(j, \lambda_i)$ is the true aerosol optical depth and vegetation reflectance for wavelength λ_i. $\tau_a(j, \lambda_i)$ and $A(j, \lambda_i)$ are their solutions, respectively. There are fourteen inversion channels, i.e. 410, 450, 500, 550, 600, 650, 680, 700, 720, 740, 770, 800, 850 and 900nm, among which the three channels of 450nm, 500nm and 680nm are used to retrieve aerosol optical depth. In inversion, the real part of the complex refractive index is supposed to be 1.5, the imaginary part is zero, and the initial value of optical depth is zero.

The following is to analyze the standard errors $\delta_a(\lambda_i)$ and $\delta_S(\lambda_i)$ in optical depth and reflectance solutions of the fourteen channels, according to Figs.5-6, where true aerosol size distribution is Junge distribution of ν^*=3, The aerosol complex index of 1.5-0i, two values of $\tau_a(\lambda$=500nm) being 0.1 and 0.5 are selected.

As shown in From Figs.5-6, for all the wavelengths, standard errors of aerosol depth solutions are <0.026,

standard errors of reflectance solutions are <0.03. Inversion results are quite satisfactory. Under the condition of μ_0=1.0 and μ=1.0, in the range of 500nm to 800nm, the larger the wavelength, the less the standard errors of optical depth and reflectance solutions. But to the other three conditions, the larger the wavelength, the larger the standard errors.

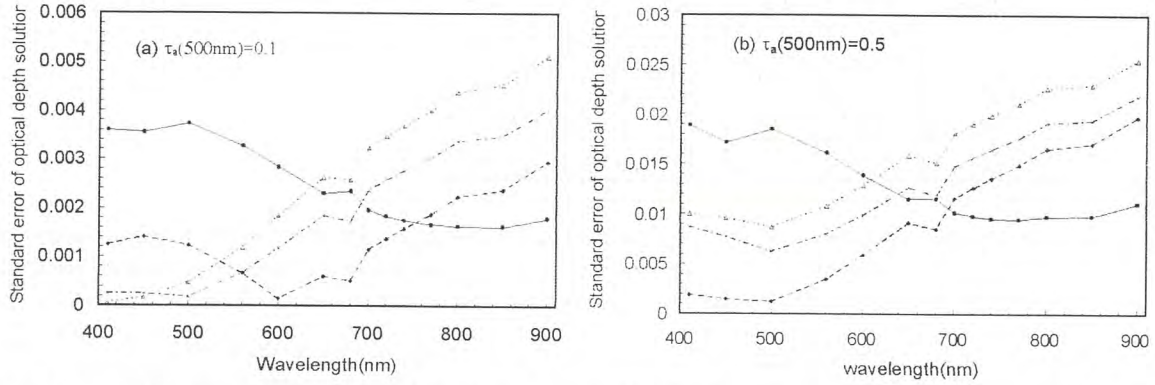


Fig.6 Standard error of aerosol optical depth solution under the Junge size distribution. •: μ_0=1.0, μ=1.0; ◆: μ_0=1.0, μ=0.836; Δ: μ_0=0.5, μ=1.0; ×: μ_0=0.5, μ=0.836.

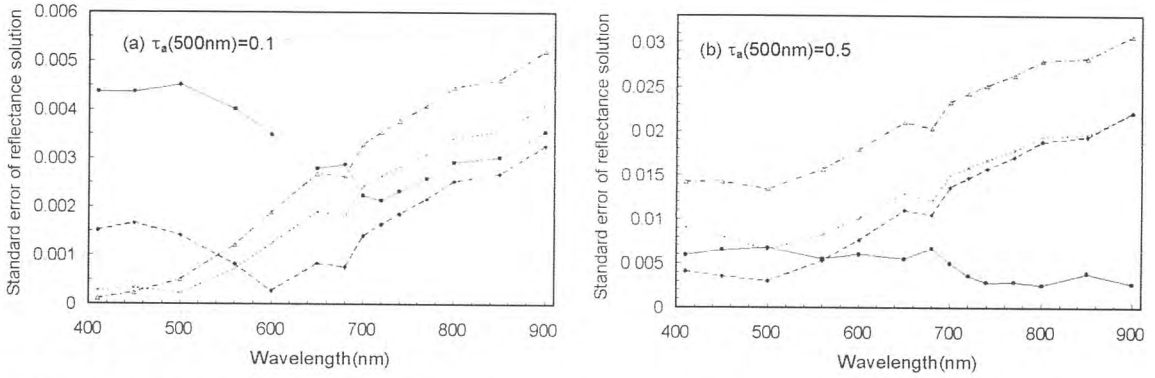


Fig7 Standard error of vegetation reflectance solution under the Junge size distribution. •: μ_0=1.0, μ=1.0; ◆: μ_0=1.0, μ=0.836; Δ: μ_0=0.5, μ=1.0; ×: μ_0=0.5, μ=0.836.

Next, the effect of error in the aerosol imaginary index to optical depth and reflectance solutions is analyzed according to Table 2. Here σ_a and σ_s are standard errors of optical depth and reflectance solutions for fourteen channels, given by:

$$\sigma_a = \sqrt{\frac{1}{14}\sum_{i=1}^{14}[\tau_a(\lambda_i) - \tau_a^*(\lambda_i)]^2}\ . \qquad (15)$$

$$\sigma_s = \sqrt{\frac{1}{14}\sum_{i=1}^{14}[A(\lambda_i) - A(\lambda_i)]^2}\ . \qquad (16)$$

In Table 2, κ is true aerosol imaginary index, and ν_S is solution of Junge parameter ν^*, fitted from aerosol optical depth solutions for three wavelengths of 450nm, 500nm and 680nm. The true vegetation reflectance spectrum is a rice reflectance spectrum, the true aerosol distribution is Junge distribution of ν^*=3, and the aerosol real index is 1.5. In inversion, the aerosol imaginary index is supposed to be zero. As shown in Table 1, as the imaginary index is larger, errors of aerosol optical depth, its size distribution and vegetation reflectance solutions are all lager. The larger the depth is, the distinct the error effect. In the condition of the imaginary index within 0.01, the solutions are idealistic. For example, when $\tau_a(\lambda$=500nm)=0.1 and κ=0.01, σ_a, σ_S and ν_S is 0.0157, 0.0035 and 2.6, respectively, errors being small. But when κ is equal to 0.05, σ_a, σ_S and ν_S is 0.0312, 0.0136 and 2.3, respectively. The errors are larger obviously. In the case of $\tau_a(\lambda$=500nm)=0.5, as κ=0.0, σ_a, σ_S and ν_S is 0.0141, 0.0026 and 2.95, respectively, implying good precision; as κ=0.01, σ_a and σ_S is 0.079 and 0.0223, respectively, the solutions being reasonable; but as κ=0.05, σ_a and σ_S is 0.222 and 0.0721, respectively,

the errors being much larger.

Table 1 Effect of Error in Aerosol Imaginary Index on Optical Depth and Reflectance Solution. μ_0=0.5, μ=1.0.

τ_a(500nm)	0.1	0.1	0.5	0.5	0.5
k	0.01	0.05	0	0.01	0.05
σ_a	0.0157	0.0312	0.0141	0.0619	0.2215
σ_s	0.0035	0.0136	0.0026	0.0223	0.0721
ν_s	2.6	2.3	2.95	2.4	2.0

In the case of spaceborne remote sensing, it is possible that vegetation sort in the field of view can be not single. Thus, the following analyses the inversion results under the condition of mixed vegetation spectrum reflectance from Table 2. Here the right reflectance spectrum is mixed of two rice reflectance spectra by the ratio of 7 to 3, the true aerosol complex index is 1.5-0.0i, J3 represents Junge distribution of ν^*=3, DL represents continental Deirmenjian distribution[6]. μ_0=0.5 and μ=1.0. As shown in Table 3, when $\tau_a(\lambda$=500nm)=0.1, the standard errors of aerosol optical depth and surface reflectance are $\leq$ 0.0096 and 0.00333 for J3 and DL distributions, and when $\tau_a(\lambda$=500nm)=0.5, they are $\leq$ 0.0516 and 0.00677, respectively, both of them have fairly good precision.

Table 2 Standard errors of optical depth reflectance solutions in the condition of a mixed surface.

	σ_a		σ_s	
J3	0.0096	0.0243	0.00224	0.00677
DL	0.0061	0.0516	0.00333	0.00418
$\tau_a(\lambda$=500nm)	0.1	0.5	0.1	0.5

Next, effect of the radiance error on inversion results is analyzed from Table 3. Here true wheat reflectance spectrum (as shown in Fig.2), and Junge distribution of ν^*=3 are taken. μ_0=0.5 and μ=1.0. As shown in Table 3, in the case of 2% radiance error, when $\tau_a(\lambda$=500nm)=0.1, the standard errors of aerosol optical depth and surface reflectance solutions are 0.0054 and 0.0032, and when $\tau_a(\lambda$=500nm)=0.5, they are 0.0226 and 0.0056, respectively. The errors are small.

Table 4 Standard Errors of Optical Depth and Reflectance Solutions Caused by Radiance Error.

$\tau_a(\lambda$=500nm)	σ_a	σ_r	σ_a	σ_r
0.1	0.0034	0.0016	0.0054	0.0032
0.5	0.0181	0.0068	0.0226	0.0056
Measurement error (%)	1		2	

REFERENCES

[1]Collins, w., 1978, Remote sensing of crop type and maturity, Photogrammetric Engineering and Remote Sensing, 44(1), pp.43-55.

[2]Horloor, D.N.H. et al.,1983, The red edge of plant leaf reflectance, Int. J. Remote Sensing, 4(2), 273-288.

[3]Tong Qingxi et al., 1990, Spectra and Analysis of Typical Earth Objects of China, Science Press, pp632.

[4]Menghua Wang and Howard R. Gordon, 1994, Estimating aerosol optical properties over the oceans with the multiangle imaging spectrodiometer: Some preliminary studies, Appl. Opt., 33, 18, 4042-4057.

[5] Nakajima T. and A. Higurashi, 1997, AVHRR remote sensing of aerosol optical properties in the Persian Gulf region, summer 1991, J. Geophy. Res., Vol.102, 16935-16946.

[6] Deirmendijan, D., 1969,Electromagnetic Scattering on Spheric Polydispersions, Elsevier, New York.

Day and Night Detection of Volcanic Clouds and Aerosol by NOAA/AVHRR Data

K. KINOSHITA*, N. IINO*, I. UNO**, A. MORI# and J. KOHNO##

*Kagoshima University, Kagoshima 890
**National Institute for Environmental Studies, Tsukuba 305
#Nagasaki Prefectural Institute of Public Health and Environmental Sciences, Nagasaki 852
##Kagoshima Environmental Research and Service, Kagoshima 890

Abstract: Volcanic clouds in Kyushu, Japan in NOAA/AVHRR and other satellite images were analyzed during August-November 1989 when the air pollutants concentration measurement was carried out at the Unzen-Nodake(1142m). The results confirm that high concentration events of SO_2 were frequently detected because of the long-range transport of volcanic gas from the Aso and Sakurajima Volcanoes. Detectability of very thin clouds and aerosol from volcanoes are also discussed.

1. Introduction

There are many active volcanoes in south-west Japan belonging to the west-Japanese volcanic belt. Some of them eject ash clouds and aerosol, as observed by earth observation satellites such as LANDSAT. The NOAA satellites are effective in detecting this large scale extension. Thus, the dispersion of volcanic clouds may be regarded as tracer experiments on a gigantic scale which provide information on the atmospheric dynamics of upper and boundary layers.

In this report we discuss the detection of volcanic clouds and aerosol in NOAA/AVHRR data and others during August-November 1989, when the air pollutants concentration measurement was carried out at the Unzen-Nodake(1142m). In this measurement[1], many high concentration events of SO_2 were found, which were probably due to the long-range transport of volcanic gas from the Aso and Sakurajima Volcanoes, as inferred from meteorological conditions. It must be very valuable to study satellite images of volcanic clouds which may well be accompanied by volcanic gas. In a recent work[2], we have analyzed the morning data of NOAA-10/AVHRR processed by Japan Weather Association. Here we extend the analysis to all relevant raw data of NOAA-10 and 11 during this period archived by the Institute for Industrial Science, University of Tokyo[3]. There are four opportunities for observation in a day, taking altogether the descending and ascending paths of two NOAA satellites. We also discuss the satellite detection of very thin clouds and aerosol ejected from volcanoes after a brief introduction concerning their activities.

2. Volcanic activity in Kyushu and Ryukyu Islands

Let us briefly discuss volcanic activity in south-west Japan(see Fig. 1)[4]. Among the volcanoes in Mainland Kyushu, Mt.Sakurajima is the most active on the average, with ash clouds sometimes exceeding 100 km[5]. Since the year of 1972, volcanic plumes have been ejected almost daily from the summit crater(1040 m), mixed with occasional big eruptions. The plumes flow at altitudes around 1000-2000 m, depending on the ejection strength and wind velocity, with a vertical thickness of 200-800 m. The pattern of horizontal dispersion is sensitive to the vertical profile of wind direction and velocity. Typical patterns of dispersion are

as follows:

(1) Linear advection with small spread under strong wind, around or over 10 m/s.

(2) Wide angle spread of fan type under weak wind with large vertical shear.

(3) Belt type dispersion under medium wind with indefinite shear.

Some intermediate patterns are also seen, such as the narrow angle or conical type. An extreme limit of case (2) is the flat plate type when the wind is almost nil. In many cases, these features are well reproduced by a vertical shear model with upper level wind data as inputs[6].

Aso Volcano in central Kyushu was very active during June 1989-January 1991. Volcanic clouds observed in the satellite images were with scales comparable to or sometimes exceeding those of Sakurajima Volcano. Especially, in the autumn of 1989, heavy ash-falls from Mt.Aso seriously damaged agriculture and badly affected traffic inside the caldera and its neighboring regions. It is quite plausible that this volcano was an important source of SO_2 observed at the Unzen-Nodake(70 km westward from Mt. Aso).

A big topic recently has been the eruption of Unzen Volcano starting from 17 November 1990, and the pyroclastic flows from the Fugendake lava dome from May 1991 until the beginning of 1995. There are many data of ash clouds of 10-40 km taken by the remote sensing satellites. However, in 1989 when the air pollutants concentration measurement was carried out at the Unzen-Nodake near-by, Fugendake was quite dormant without any effect.

In the Ryukyu Islands south of Kyushu, there are many volcanic islands. Among them, a white spot of cloud was often seen above the vent of Satsuma-Iwojima Volcano, indicating that the volcano was continuously ejecting white plumes which were diminished in the dry air. As for Suwanosejima Volcano, such a white spot was rarely seen.

Instead, it occasionally becomes very active ejecting plumes of considerable scale. However, during the term August-November 1989, the level of its activity was not so high, with short plumes in NOAA data[2].

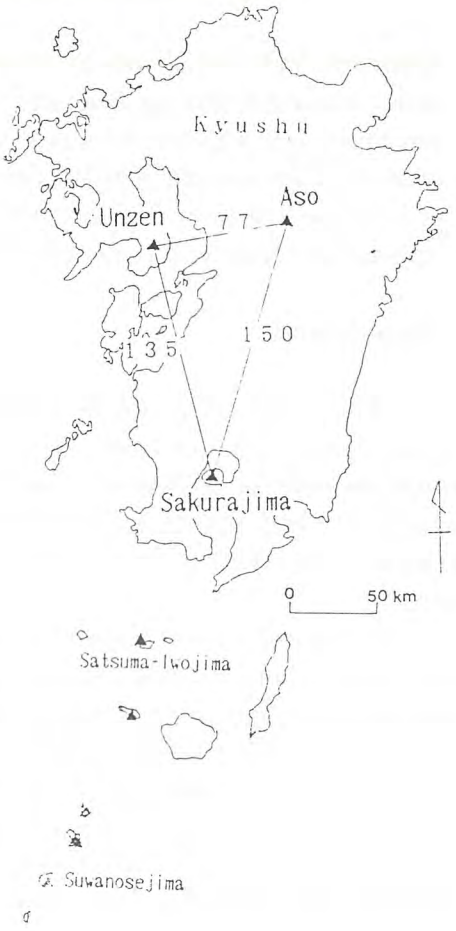


Fig. 1. Prominent active volcanoes in Kyushu and Ryukyu Islands. The distances between the three mountains are indicated in km.

3. Satellite imagery of volcanic clouds

In general, volcanic clouds are composed of volcanic ash, water vapor and other chemical substances such as CO_2, SO_2, HCl and H_2S. During the downstream advection, coarse grained ashes fall off and water vapors evaporate in dry air, but very fine ashes and aerosol of sulfuric acid converted from the oxidation of SO_2 in the air remain. They form very thin tails of volcanic clouds. On the other hand, in the case of wet air, volcanic ejecta may be subject to rain out and wash out. However, in the satellite images with many series of cumulus clouds on the land, volcanic plumes are often recognized with somewhat vague boundaries and extensions over the

sea. Thus, the spatial pattern and geographical situation are important in the detection of volcanic clouds and in the distinction from meteorological clouds. Keeping these points in mind, let us discuss the detection problem of volcanic clouds according to the wavelength of the satellite sensors. The home page of SiNG-Kagoshima shows several color images combining different bands[7].

3.1. Visible, NIR and SWIR images

In the daytime satellite images, the volcanic clouds appear as relatively bright objects in visible, near infrared(NIR) and also short-wave infrared(SWIR) images. Thick ash clouds are easily detectable in all of these bands, but thin ash or fumarolic plumes are difficult to see in NIR and SWIR bands. The thin volcanic clouds are somewhat transparent in the NIR band, and relatively insensitive to the SWIR bands. Diffused clouds over the sea, however, are often detectable even in SWIR bands. The sensitivity of semi-transparent clouds according to the wavelength may provide information on grain size distribution. Fig. 2(a) shows a LANDSAT/TM-1 image on 21 Nov. 1989 when a large angle spread of thin volcanic cloud was observed from the ground; the data values of the TM bands are shown along the line AB.

The detection of thin volcanic clouds over land is difficult in the NIR band because of strong reflection from vegetation. On the other hand, the visible band with shorter wave length is more sensitive to thin clouds, since vegetation appears as a dark background as shown in Fig. 2(a).

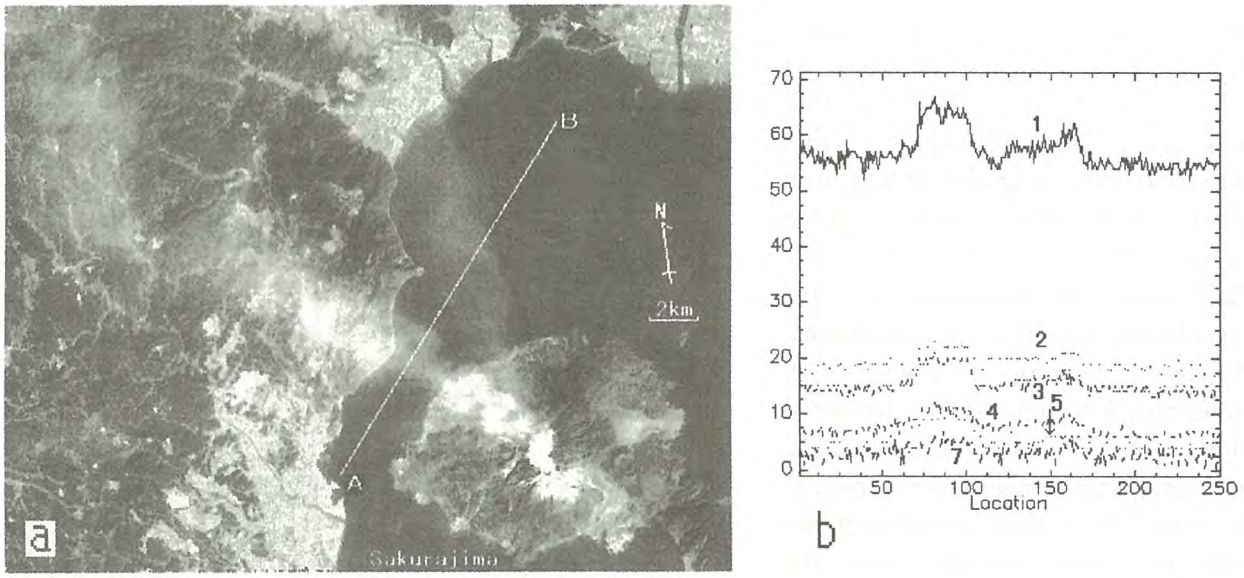


Fig. 2. (a) A LANDSAT/TM-1 image of a Sakurajima plume on 21 Nov. 1989. **(b)** The data values of TM-*n* sensors along the line AB in (a), where the channel number *n* is indicated in the graph.

3.2. Thermal images

Thick volcanic clouds are recognized as cold objects in thermal infrared(TIR) images of NOAA/AVHRR and LANDSAT/TM sensors, as the surface of volcanic cloud becomes in equilibrium with the ambient atmosphere at altitudes of about 1-3 km. Semi-transparent clouds also shield partially the infrared radiation from the surface of the earth. These features are common to day and night time observations, especially for clouds extending over the sea. The AVHRR-3 images in the medium infrared band, 3550-3930 nm, also exhibit similar properties at nighttime, in contrast to the daytime images dominated by solar reflection.

For the NOAA-11 data, the split-window method taking the difference of AVHRR-4 and 5 may be useful for the discrimination of meteorological and volcanic clouds, as confirmed in daytime images under various conditions[8]. This is due to the different spectral properties of the clouds around 11 and 12 μ m, while further distinction between lithic dust and aerosol of sulfuric acid in the volcanic clouds is not possible.

The above methods are useful to study the extension of volcanic clouds over the sea. However, detection over the land is not always easy in the thermal band because of the non-uniformity, the decrease of temperature at night, and the similarity of bare land with ash clouds in the split-window images.

Finally, let us mention the detection of thermal anomalies due to volcanism in TIR images. The LANDSAT-5/TM-6 sensor is useful both in daytime and nighttime with a resolution of 120 m, although it cannot measure very high temperatures above a saturation limit of about 70℃. There are also problems of calibration and absorption correction due to vapors above a vent. The spatial resolution of NOAA/AVHRR sensor with 1.1 km at best is considered to be too poor to detect thermal anomalies. However, we did find several single pixel anomalies due to volcanism(see 4(iii) and Table 1).

4. High SO_2 concentration events and NOAA images

When the air pollutants concentration measurement was carried out at the Unzen-Nodake during Aug.-Nov. 1989[1], the concentration of sulfur dioxide revealed the strongest time variation exceeding the background level, compared with other components such as SO_4^{--} and Ca^{++}. The latter two exhibited positive correlation with SO_2, in accord with volcanic origin. The SO_2 concentration has been measured also at Aso Volcano Museum(1150 m). The high concentration events detected there were attributed not only to Aso Volcano with the crater at 3 km east but also to Sakurajima Volcano at 150 km SSW[9]. Since volcanic plumes tend to keep their altitudes during the advection without much vertical dispersion as observed from the ground[5] and aircraft[10], mountain site measurements are good for detecting their long-range transport. In the following, we discuss the SO_2 concentrations at these stations together with

Table 1. Volcanic clouds at Aso and Sakurajima, with the direction Dir, length L and the type denoted as Lin., Long, Belt, Con., Fan and Stag. for linear or long advections, belt type dispersion, small angle dispersion of conical type, fan type spread and stagnation, respectively. The marks - and X denote cases without signal, and unobservable cases due to cloud coverage, respectively. The mark * denotes thermal anomaly at the vent in ch. 3.

		Sakurajima			Aso		
Date	JST	Dir	L	Type	Dir	L	Type
9/10	8:15	NW	125	Long		-	
	19:34	W	84	Lin.		X	
9/11	2:45	NW	82	Lin.		X	
	7:53	NW-NNW	129	Long		X	
	14:10	N	82	Lin.		-	
	19:11	NW	62	Fan		X	
10/27	7:23	W-SW	46	Fan	WSW-SSW	51	Fan
10/29	8:18	SSW-SW	86	Lin.	SW	44	Con.
	14:10	SW-SE	227	Belt	SW	50	Con.
	19:30	W	125	Long		-	
10/30	2:35		-*			-*	
	7:55	E-NW	65	Lin.	NE-E	53	Lin.
	14:00	NNW	23	Fan	NE-E	93	Long
	19:13	NW	77	Fan		-*	
11/03	1:52		-*			-	
	8:06	W-SSW	27	Stag	NE	46	Lin.
	13:16	NW	20	Fan		X	
11/04	1:42		-*			-*	
	7:43	N	39	Lin.	NNE	103	Lin.
	13:06	NNW	187	Long	NNE	213	Long
	19:01	NNW	60*	Lin.		-	
11/05	7:21	N	18	Lin.	NE	102	Lin.

satellite images.

In August, there were several high concentration events of SO_2 with one hour values exceeding 30 ppb at two stations. However, corresponding image data by satellites were not obtained because of the cloud coverage and the lack of good timing, though there were Sakurajima plumes extending more than 100 km on other days.

During September-November 1989, there were 18 morning data of NOAA-10, LANDSAT-5, MOS-1 and SPOT, which were relevant to the high concentration events at two stations[2]. In addition, we found altogether 26 candidates of NOAA-10 in the evening plus NOAA-11 in the midday and midnight. Here we discuss three prominent groups of them as listed in Table 1 with 19 candidates and other images.

(i) September 10-11 scenes

In these days, Kyushu area was at the north-west boundary of the Pacific high pressure system with typhoons No.19 in SW and No.20 in SE seas, as seen from the geopotential height and wind field at 850 hPa shown in Fig. 3(a). The meso-scale weather conditions were relatively stable, and isentropic forward trajectories starting from Mt.Sakurajima at 1500 m at 9, 21 JST on 10 Sept. and 5 JST on 11 Sept. exhibited similar behavior, with the starting direction at WNW and NNW, and then curved slowly towards NE as in Fig. 3(b). There are six NOAA images, all with volcanic plumes from Sakurajima, as summarized in Table 1. Their directions and the curved shapes are consistent with the computed trajectories, and the detected scales of about 40-130 km are enough to suggest their effects on high SO_2 concentration on 11 Sept. shown in Fig, 4 in two stations. Fig. 5 illustrates NOAA/AVHRR images at 7:53 and 14:10 on 11 September. We can see that Sakurajima plumes in these images are in accord with the trajectories in Fig. 3(b). On the other hand, plumes from Aso Volcano were not observed in NOAA images, partly because of the cloud coverage. The high SO_2 concentration on 10 Sept. observed only at Aso Volcanic Museum may be attributed to Aso Volcano as inferred from the westward direction of Sakurajima plume.

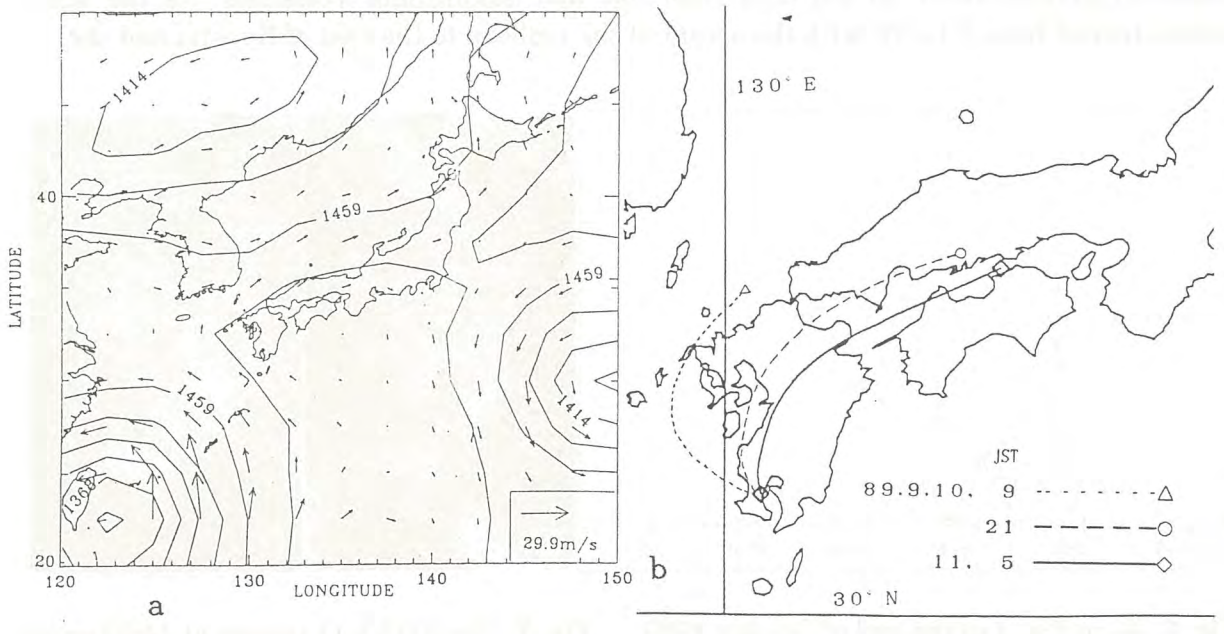


Fig. 3. (a) Geopotential height and wind field at 850 hPa at 9 JST on 11 Sept. 1989.
(b) Forward trajectories from Sakurajima at height 1500 m and starting times indicated in the graph for 24 hours.

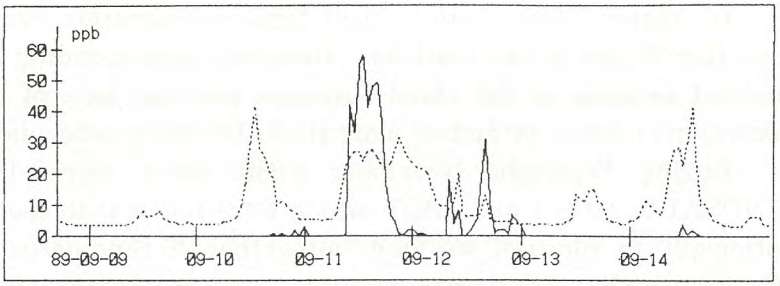


Fig. 4. One hour values of the SO_2 concentration at Unzen-Nodake(solid line) and Aso Volcano Museum(dotted line) for 9-14 Sept. 1989.

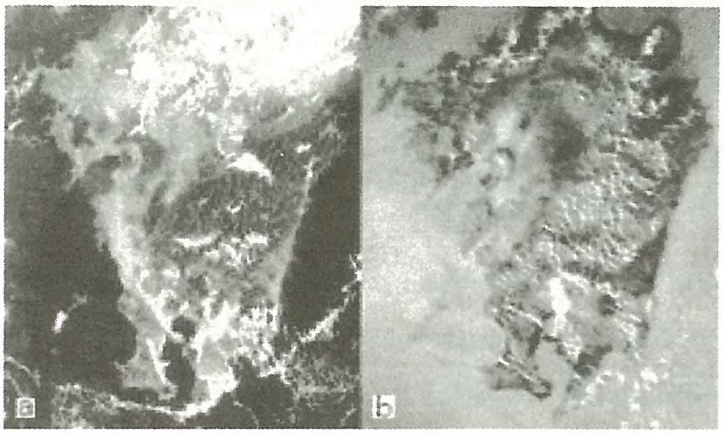


Fig. 5. NOAA/AVHRR images on 11 Sept. 1989. **(a)** ch. 1 at 7:53. **(b)** The difference of raw data values of ch. 4 and 5 at 14:10.

(ii) October 27-30 scenes

Very high concentrations of SO_2 at both stations on 27 October, shown in Fig. 6, are evidently attributed to Aso Volcano, because of the east wind due to the typhoon No.28 approaching Kyushu from the south. The NOAA-10 data in this morning exhibited westward diffusion of plumes about 50 km both from Aso and Sakurajima Volcanoes. As the wind direction turned from E to NE with the ascent of the typhoon to the east of Kyushu and the

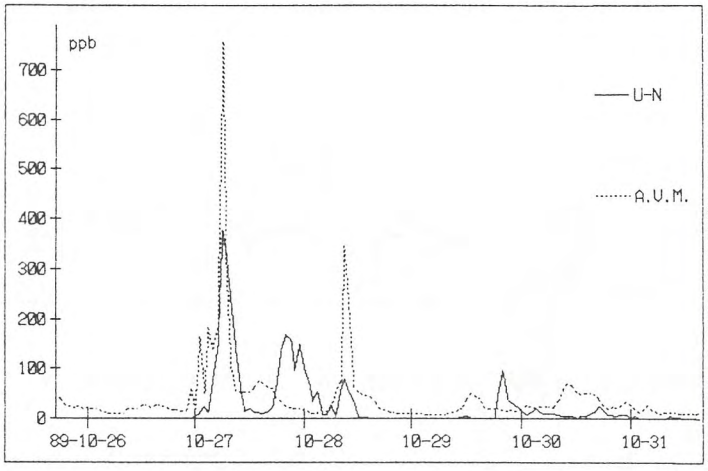


Fig. 6. As in Fig. 4 in the end of October 1989.

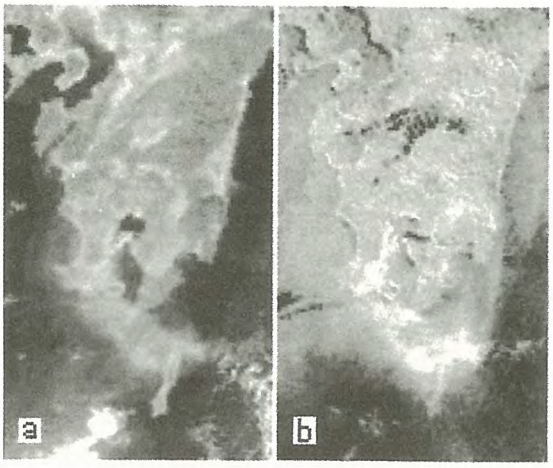


Fig. 7. The NOAA-11 images at 14:00 on 29 Oct. 1989. **(a)** AVHRR-1. **(b)**The difference as in Fig. 5(b).

approaching of a high pressure system from the west, the SO_2 concentrations of both stations once decreased to the background levels. Then, as the high pressure system moved to the east, the wind direction turned south to bring volcanic gas from Mt.Sakurajima, resulting again in high SO_2 concentrations at both stations. The NOAA data on these days are in accord with the above inspection as listed in Table 1. Fig. 7 illustrates a comparison of visible band image(a) and the split window method applied to the raw data(b). We see that the volcanic clouds from Mt.Sakurajima are very much enhanced in Fig. 7(b), while a thick cloud from Aso Volcano is not, suggesting the water rich properties. The enhancement of ash-rich cloud is also seen in Fig. 5(b) in contrast to meteorological clouds.

(iii) November 3-5 scenes

A traveling high pressure system approached Kyushu from west on 3 November, resulting in flat plate type stagnation of volcanic clouds over Mt.Sakurajima in the morning, and slowly passed east on the next day. Then southern winds dominated and continued further, bringing volcanic gas from Mt.Sakurajima and resulting in SO_2 concentrations shown in Fig. 8. There are NOAA images with Sakurajima plumes such as shown in Fig. 9. However, there are clear scenes of volcanoes without plumes as listed in Table 1. We should bear in mind that transparent gas with high SO_2 concentration might be ejected in such cases. In such clear scenes at nighttime, hot spots are seen at the vents of volcanoes in ch. 3 as indicated by the mark * in Table 1. Fig. 9 shows an Aso plume exceeding that of Sakurajima, but directed to NE without affecting the high SO_2 concentrations in two stations.

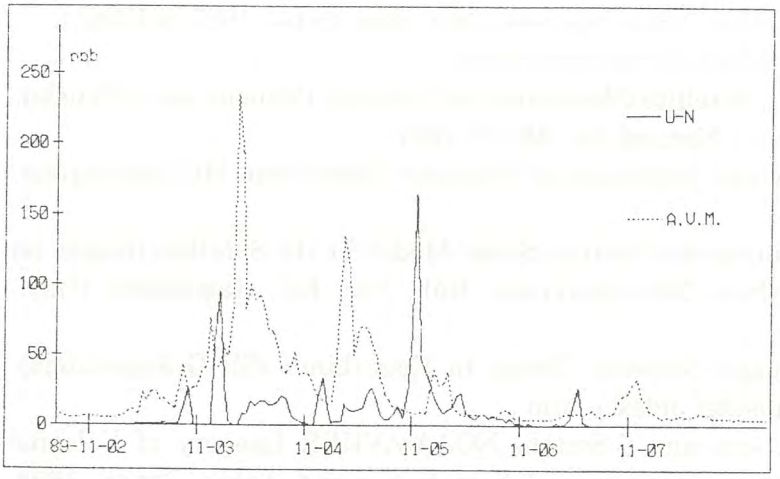


Fig. 8. As in Fig. 4 in early November.



Fig. 9. The NOAA-11/AVHRR-4 image at 13:06 on 4 Nov. 1989.

6. Concluding remarks

We have found that the directions of the plumes from Aso and Sakurajima Volcanoes found in NOAA images are well understood by the wind field and the geopotential height at 850 hPa, which are closely related with the weather chart on the ground. As for Sakurajima plumes, this is also in accord with the ground observations[5].

Mountain site measurements of the SO_2 concentrations in Kyushu can be considered as very good measures for the long-range transport of volcanic gas in this area. The NOAA data, with a high frequency of observation interval, may be good information to study this problem.

As for the dispersion pattern of the volcanic plumes, the vertical shear model[6] was found to describe gross features in most cases studied here. It is very interesting to apply the Lagrangian particle model[11] to describe quantitative aspects of plume dispersion. We can also understand the emission rate of SO_2 and its time variation by means of the correlation spectrometer measurements from the ground[12].

It also remains to estimate quantitatively the particle sizes and densities of volcanic clouds and aerosol from satellite data.

Acknowledgments

This work was supported in part by the Grant-in-Aide for Scientific Research(C-2, No.08680555) of Ministry of Education, Science and Culture of Japan. We are indebted to Dr.T.Nemoto, Institute of Industrial Science, University of Tokyo, for very kind help in extracting the NOAA/AVHRR data from the archive. We are grateful to Mr.S.Ikebe for providing the SO_2 data of Aso Volcano Museum. We thank very much to Prof. M.Gore for careful reading of the manuscript.

References

("J." = Papers in Japanese)

[1] A.Mori, I.Uno, S.Wakamatsu and K.Murano, SO_2 Concentration and Aerosol Compositions observed at the Mt.Unzen Nodake, submitted to J. Jpn. Soc. Atmos. Env.(J.).

[2] K.Kinoshita, N.Iino, A.Mori and I.Uno, Detection of Volcanic Plumes by NOAA Images and Comparison with Air Pollution Data, Proc. 23th Japanese Conf. Rem. Sens., 1997, p.133(J.).

[3] See http://www.tkl.iis.u-tokyo.ac.jp/SatIAN/welcome.html .

[4] K.Kinoshita, S.Ikebe and K.Isogai, Satellite Observation of Volcanic Phenomena in Kyushu, Japan, Bull. Fac. Ed., Kagoshima Univ., Natural Sci. **48**, 37, 1997.

[5] K.Kinoshita. Observation of Flow and Dispersion of Volcanic Clouds from Mt. Sakurajima, Atmos. Env. **30**, 2831, 1996.

[6] N.Iino and K.Kinoshita, Investigation of a Vertical Shear Model for the Satellite Images on the Dispersion of Volcanic Clouds from Mt.Sakurajima, Bull. Fac. Ed., Kagoshima Univ., Natural Sci. **47**, 1, 1996(J.).

[7] The home page of Satellite Image Network Group in Kagoshima (SING-Kagoshima): http://www-rk.edu.kagoshima-u.ac.jp/sing/ index_e.htm .

[8] K.Kinoshita, S.Hosoyamada, A.Goto and S.Saitoh, NOAA-AVHRR Imagery of Volcanic Clouds in Kyushu, Japan, Proc. 13th Int. Geosci. and Remote Sensing, Tokyo, Japan, 1993, p.1824.

[9] H.Naoe, K.Kinoshita and S.Ikebe, Analysis of Long-Range Transport of Volcanic Gas in Kyushu, Tenki **40**, 671, 1993(J.).

[10] I.Uno et al., Behavior of Secondary Pollutants and Volcanic SO_2 over Kyushu during Spring Time High Pressure System, J. Jpn. Soc. Atmos. Env. **32**, 404, 1997(J.).

[11] I.Uno and S.Wakamatsu, Analysis of the Mt.Sakurajima SO_2 Volcanic Plume Transport and Diffusion Processes, Dobokugakkai Ronbunshu **552**/VII-1, 53, 1996(J.).

[12] K.Ohta et al., Emission Rates of Sulfur-Dioxide from Some Volcanoes in Japan, Proc. Kagoshima Int. Conf. on Volcanoes, Kagoshima, 1988. p.420.
S.Fujita, Y.Tonooka and K.Ohta, Annual Contribution of Volcanic Sulfur Dioxide Emissions to the Atmosphere in Japan, J. Jpn. Soc. Air Pollut. **27**, 336, 1992(J.).

Polarimetric Investigation of the Aerosols Over the Ocean for the Atmospheric Correction

Kazuhiko Masuda[1)], Masayuki Sasaki[1)],
Tsutomu Takashima[2)] , and Hiroshi Ishida[3)]

1) Meteorological Research Institute
1-1, Nagamine, Tsukuba, Ibaraki 305
2) National Space Development Agency of Japan
1-9-9, Roppongi, Minato, Tokyo, 106
3) Maritime University of Kobe
5-1-1, Fukae-minami, Higashi-naga, Kobe, 658

ABSTRACT

Measurements of the sky radiation at a scattering angle of 90° were made by a multichannel polarimeter as well as the direct solar radiation at wavelengths of 443nm, 490nm, 565nm, 670nm, 765nm, and 865nm over the Pacific Ocean in August 1997, and over the Inland Sea of Japan in September 1997. To investigate the feasibility of the use of the degree of polarization to retrieve the optical properties of atmospheric aerosols over the ocean, radiative transfer calculations were performed using the doubling-adding method for a realistic atmosphere-ocean model. Aerosols were assumed to be composed of "water soluble" and "oceanic" models where these components are externally mixed. Particles are assumed to be spherical, and the size distributions are also assumed to be expressed by the log-normal functions. A look-up table of the degree of polarization at a scattering angle of 90° (p_{90}) was created with parameters of the solar zenith angle, the aerosols optical thickness at λ=550nm ($\tau_{a,550}$), and the Ångström coefficient (α). $\tau_{a,550}$ and α were simultaneously retrieved using the look-up table. Most of the differences between the $\tau_{a,550}$ retrieved from p_{90} and those derived from the direct solar radiation were within 0.03.

1. Introduction

Since radiation detected at satellite sensors over the ocean is significantly influenced by the radiation from atmospheric scatterers such as aerosols and molecules, it is essential to correct their effects to quantitatively derive the oceanic information. The atmospheric correction requires precise information of atmospheric aerosols. Atmospheric correction techniques first estimate the aerosol model and its optical thickness from the longer wavelength bands of a ocean color sensor then derive oceanic information from the shorter wavelength bands (for example, Gordon, 1997; Fraser *et al.*, 1997). For this purpose, it is necessary to prepare appropriate aerosol models. However, there are not so many measurements of the solar and sky radiation over the ocean from vessels (Hoppel *et al.*, 1990; Takayama *et al.*, 1991; Korotaev *et al.*, 1993; Villevalde *et al.*, 1994). The purpose of this paper is to investigate the feasibility of using the degree of polarization to retrieve the optical properties of aerosols over the ocean and to find a candidate aerosol model for the atmospheric correction.

2. Atmosphere-Ocean System Model

Downward radiation just above the ocean surface was computed by the doubling-adding method for wavelengths (λ) of 443nm, 490nm, 565nm, 670nm, 765nm, and 865nm. The computational method is the same as used by Masuda and Takashima (1988) where multiple scattering and polarization are taken into account. A plane-parallel and vertically inhomogeneous atmosphere is simulated by four homogeneous sub-layers (0-2km, 2-5km, 5-13km, 13-100km). The optical thickness of molecular scattering and absorbent constituents such as ozone were obtained by LOWTRAN7 (Kneizys *et al.* 1988) for the mid-latitude summer model. The depolarization factor of atmospheric molecules is 0.0295 according to Kneizys *et al.* (1980). The basic components of the maritime aerosol model are generally the "oceanic" model (OC) for the particles generated at the sea surface and the "water soluble" model (WS) for aerosols soluble in water and

consisting of a mixture of sulfate, nitrate, and organic components (WCP-112, 1986). These two types of aerosol component models are considered in this study where they are assumed to be externally mixed. The size distribution for each aerosol model is expressed by the log-normal function,

$$\frac{dn(r)}{d\ln r} = \frac{1}{\sqrt{2\pi}\ln\sigma}\exp\left(-\frac{\left(\ln r - \ln r_m\right)^2}{2\ln^2\sigma}\right), \quad (1)$$

where r_m is the mode radius and $\ln\sigma$ is the standard deviation. The aerosol particles are assumed to be spherical. The scattering matrices are computed by the Mie scattering theory for the radius ranging from 0.001μm to 10.0μm. The OC model is adopted from the Radiation Commission report (WCP-112, 1986) where (r_m, σ) are (0.3μm, 2.51μm). The refractive indices at λ=443nm and 865nm are $1.384\text{-}i8.01\times10^{-9}$, $1.372\text{-}i1.21\times10^{-6}$. The WS models is adopted from the WCP-55 report (WCP-55, 1983) with (r_m, σ) of (0.0285μm, 2.015μm) where σ is decreased by 10% from the original value. The refractive indices λ=443nm and 865nm are 1.53-i0.005, 1.52-i0.012. The Ångström coefficients (α) of the OC-WS mixed aerosol model is shown in Fig. 1 as a functions of a ratio of the WS component (f_w) to the optical thickness (WS+OC) at λ=550nm ($\tau_{a,550}$).

The ocean surface is simulated by multiple facets whose slopes vary according to the wind speed over the ocean (Cox and Munk, 1954). Wind speed is assumed to be 5m/sec. The effect of the white caps is not taken into account.

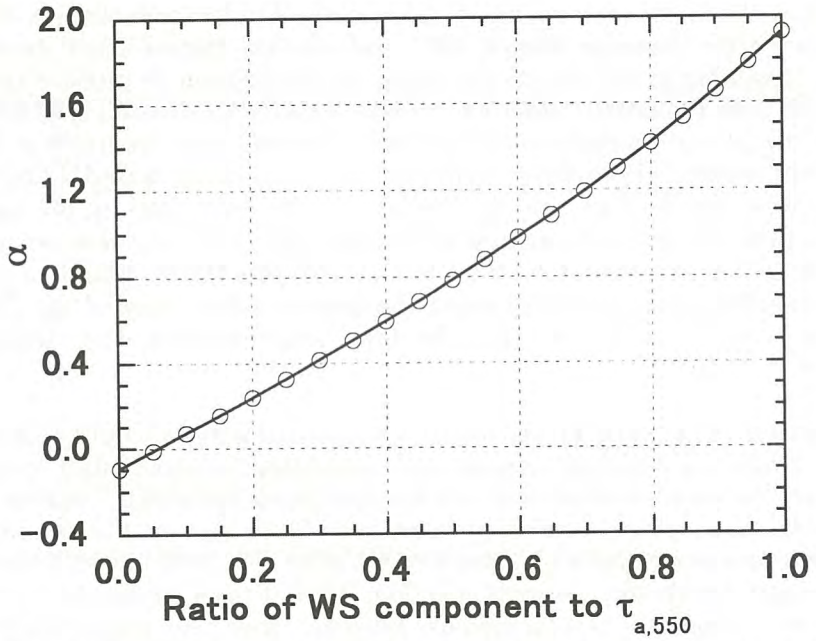


Fig. 1 Ångström coefficient (α) as a function of a ratio of water-soluble component to the aerosol optical thickness at λ=550nm.

3. Instruments and Measurements

FPR1000 (Opto Research Corporation) is a portable multichannel polarimeter to measure the diffused sky radiation as well as the direct solar radiation. The specification and calibration of FPR1000 is described in Masuda and Sasaki (1997). A brief description is given here. FPR1000 has six interference filters whose central wavelengths (half transmission bandwidth) in nm are 443 (20), 490 (20), 565 (20), 670 (20), 765 (40), and 865 (40). These wavelength regions correspond to those of POLDER and the Ocean Color and Temperature Scanner (OCTS) sensors on board ADEOS. A Glan-Thompson prism is installed in front of the interference filters. The field of view is 2°. The detector is a silicon photodiode. The accuracy of polarization measurements is estimated to be about 1% in polarization units (Masuda and Sasaki, 1997). Calibration constants for the direct solar radiation measurements were determined by the modified Langley plot at Mauna Loa Observatory (Masuda and Sasaki, 1997) in December 1996 and in December 1997. FPR5000 is similar to the FPR1000 except that the rotation of the polarizer is controlled by a step

motor which makes it easier to measure the sky radiation.

The sky radiation was measured over the Pacific Ocean from Kobe, Japan to Honolulu, Hawaii by the training ship (Seiun-maru) of the Institute for Sea-Training, Ministry of Transport of Japan in August 1997. Similar measurements were made over the Inland Sea of Japan by the training ship (Fukae-maru) of the Maritime University of Kobe in September 1997. We refer to these cruises as the PO and the IS cruises, respectively. The degree of polarization (p_{90}) were measured by the FPR5000 at a 90° angle from the solar direction in the principal plane, where the degree of polarization is generally maximum. This enables us to get stable values despite ship motions. The direct solar radiation was also measured by the FPR1000. Figure 2 shows the observational areas presented in this paper. The solar zenith angles (SZA) were from 27.6° to 57.9° (PO) and from 38.8° to 57.2° (IS).

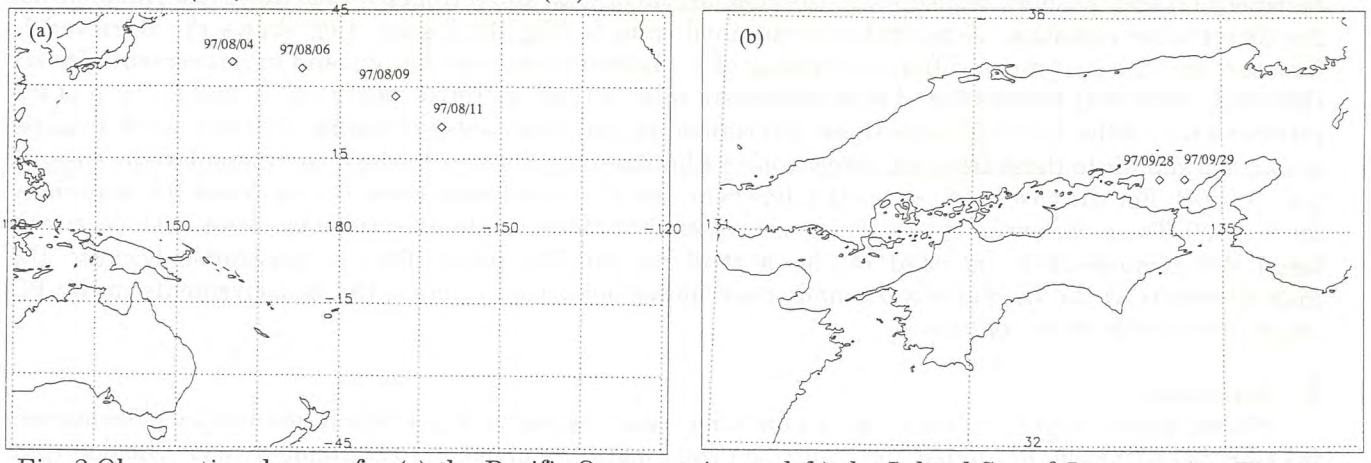


Fig. 2 Observational areas for (a) the Pacific Ocean cruise and (b) the Inland Sea of Japan cruise. Figures denote year/month/day.

4. Results

The relationship of p_{90} between λ=443nm and 865nm is shown in Fig. 3 as a function of $\tau_{a,550}$ and f_w. The SZA is fixed to 45.8°, but p_{90} is not significantly influenced by SZA. In our calculations, p_{90} differs less than 1% in polarization units for 22.5°<SZA<60° from p_{90} at SZA=45.8°. The measurements are also plotted in the figures where circles denote measurements in the PO cruise, and crosses the IS cruise.

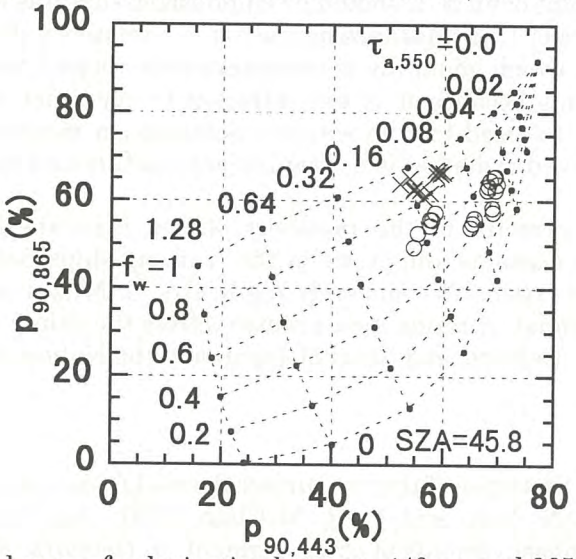


Fig. 3 Relationship of the degree of polarization between 443nm and 865nm as a function of $\tau_{a,550}$ and a ratio of the water-soluble component to $\tau_{a,550}$ for SZA=45.8°.Dotted lines denote the calculations, whereas circles (crosses) denote measurements in the Pacific Ocean cruise (the Inland Sea of Japan cruise).

$\tau_{a,550}$ and α were retrieved from the p_{90} at six wavelengths. First, the calculated p_{90} was interpolated with respect to the cosine of the SZA at the time of measurement. A two-dimensional table of p_{90} was then created for $\tau_{a,550}$=0.0 to 1.28 (step=0.01), and f_w=0.0 to 1.0 (step=0.05) by interpolating the calculations for eight $\tau_{a,550}$ (0.0, 0.02, 0.04, 0.08, 0.16, 0.32, 0.64, and 1.28) and six f_w (0.0, 0.2, 0.4, 0.6, 0.8, and 1.0), using the cubic spline interpolation method. We selected ($\tau_{a,550}$, f_w) pair which minimizes the following equation as the most probable aerosol model.

$$\sum_{i=1}^{6}\left(p_{90,calc}\left(\lambda_i,\tau_{a,550},f_w\right)-p_{90,meas}\left(\lambda_i\right)\right)^2 . \qquad (2)$$

Figures 4 (a) and (b) show, respectively, the comparison of $\tau_{a,550}$ and α from p_{90} with those determined from the direct solar radiation. Note that α is obtained from f_w (Fig. 1). Figure 4 (c) shows the retrieved f_w (crosses) and the root mean difference (rms_{90}) of p_{90} between the calculations and measurements for six channels. rms_{90} may be considered as a measure of reliability of the retrieval of $\tau_{a,550}$, α, and f_w. Most of the retrieved $\tau_{a,550}$ differ by <0.03 from those determined by the direct solar radiation. The retrieved α values ($\alpha_{(p90)}$) are similar to those from the direct solar radiation ($\alpha_{(dir)}$) for α>1.0 which correspond to the cases of $\tau_{a,550\,(dir)}$>0.1. For the cases of $\tau_{a,\,550,\,dir}$<0.1, however, the $\alpha_{(p90)}$ are larger than $\alpha_{(dir)}$ by about 0.5, especially for $\alpha_{(dir)} \fallingdotseq 0$. The α values for the IS cruise are larger than those for the PO cruise by about > 0.5 because a large WS component is included in the aerosol for the IS cruise. This is reasonable because the measurements in the IS cruise were made near industrial areas, whereas the measurements in the PO cruise were made on the open sea.

5. Conclusion

Sky radiation as well as direct solar radiation were measured with portable multichannel polarimeters over the Pacific Ocean in August 1997, and over the Inland Sea of Japan in September 1997. The degree of polarization was measured at a 90° angle from the solar direction in the principal plane. We calculated the radiative transfer using the doubling-adding method to create a look-up table with three parameters (SZA, $\tau_{a,550}$, and α). $\tau_{a,550}$ and α were retrieved from p_{90} using the look-up table. Differences between $\tau_{a,550}$ retrieved from p_{90} and those determined from the direct solar radiation were mostly within 0.03. Since α values are directly related to a ratio of the WS component to $\tau_{a,550}$, the size distribution of the aerosol model is constructed, which may be a candidate aerosol model for the atmospheric correction in the regions without very absorptive aerosols.

From an observational point of view, it should be emphasized that it is easier to measure the degree of polarization than the radiance or transmittance because it is a relative value for which critical calibration is not required. Further, p_{90}, which generally is maximum with respect to the observation direction, can easily be measured from ships because it is not influenced very much by ship motions. The method described in this paper may be used for the satellite polarization measurements for some geometrical conditions in which the observed radiation is not significantly influenced by the sun glint.

Acknowledgments. We are grateful to the members of the Institute for Sea-Training, Ministry of Transport of Japan, and the captains and crews of the training ships Seiun-maru and Fukae-maru for their cooperation to the observations. We sincerely thank Drs. S. Mukai and I. Sano of Kinki University for their helpful discussions on interpreting measurements from the ship. Part of this study was supported by the Ministry of Education, Culture, and Sport of Japan and the National Space Development Agency of Japan.

REFERENCES

Cox, C., and W. Munk, 1954: Statistics of the sea surface derived from sun glitter. *J.Mar. Res.*, 13,198-227.

Fraser, R. S., S. Mattoo, E-N. Yeh, and C. R. McClain, 1997: Algorithm for atmospheric and glint corrections of satellite measurements of ocean pigment. *J. Geophys. Res.*, 102, 17107-17118.

Gordon, H. R., 1997: Atmospheric correction of ocean color imagery in the Earth Observing System era. *J. Geophys. Res.*, 102, 17081-17106.

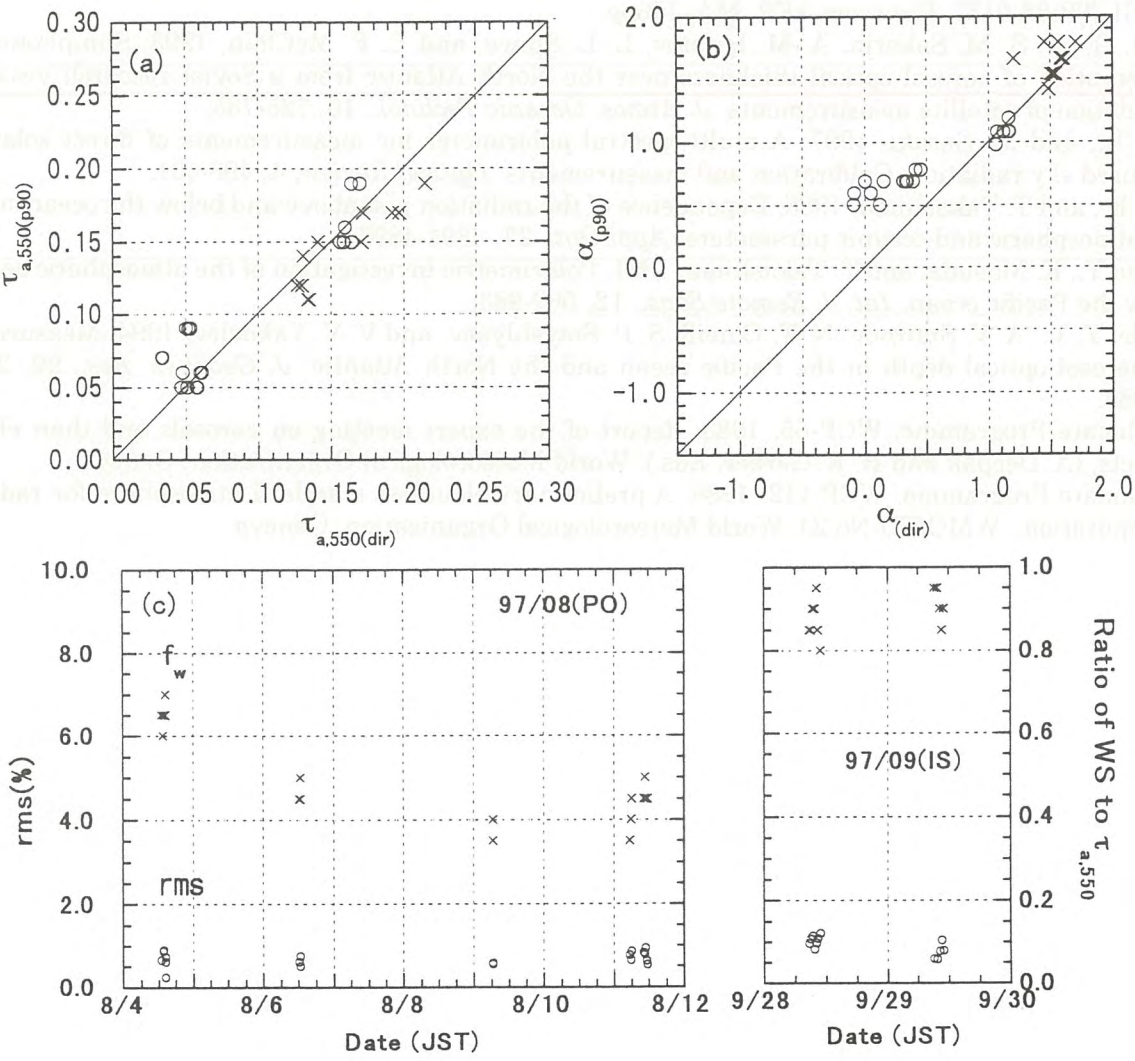


Fig. 4 (a) Comparison of the optical thickness of aerosols at λ=550nm ($\tau_{a,550}$) derived from p_{90} at at six channels with $\tau_{a,550}$ determined from the direct solar radiation. (b) The same as (a) but for the Ångström coefficient (α). Circles (crosses) denote the PO cruise (the IS cruise).
(c) Root mean square difference of p_{90} between measurements and calculations in polarization units (circles) and the retrieved ratio of water-soluble component to $\tau_{a,550}$ (crosses).

Hoppel, W. A., J. W. Fitzgerald, G. M. Frick, and R. E. Larson, 1990: Aerosol size distributions and optical properties found in the marine boundary layer over the Atlantic ocean. *J. Geophys. Res.*, **95**, 3659-3686.

Kneizys, F. X, and coauthors, 1980: Atmospheric Transmittance/Radiance: Computer Code LOWTRAN5. Air Force Geophysics Laboratory, AFGL-TR-80-0067, Hanscom AFB, MA, 233pp.

Kneizys, F. X, and coauthors, 1988: Users guide to LOWTRAN7. Air Force Geophysics Laboratory, AFGL-TR-88-0177, Hanscom AFB, MA, 146pp.

Korotaev, G. K., S. M. Sakerin, A. M. Ignatov, L. L. Stowe, and E. P. McClain, 1993: Sun-photometer observation of aerosol optical thickness over the North Atlantic from a Soviet research vessel for validation of satellite measurements. *J. Atmos. Oceanic Technol.*, **10**, 725-735.

Masuda, K., and M. Sasaki, 1997: A multi-spectral polarimeter for measurements of direct solar and diffused sky radiation: Calibration and measurements. *Optical Review*, **4**, 496-501.

Masuda, K., and T. Takashima, 1988: Dependence of the radiation just above and below the ocean surface on atmospheric and oceanic parameters. *Appl. Opt.*, **27**, 4891-4898.

Takayama,Y., K. Masuda, and T. Takashima, 1991: Polarimetric investigation of the atmospheric aerosols over the Pacific ocean. *Int. J. Remote Sens.*, **12**, 969-983.

Villevalde, Y. V., A. V. Smirnov, N. T. O'neill, S. P. Smyshlyaev, and V. V. Yakovlev, 1994: Measurement of aerosol optical depth in the Pacific ocean and the North Atlantic. *J. Geophys. Res.*, **99**, 20983-20988.

World Climate Programme, WCP-55, 1983: Report of the expert meeting on aerosols and their climate effects, (A. Deepak and H. E. Gerber, Eds.), World Meteorological Organization, Geneva.

World Climate Programme, WCP-112, 1986: A preliminary cloudless standard atmosphere for radiation computation., WMO/TD-No.24, World Meteorological Organization, Geneva.

Two channel Analyses of the Aerosol Optical Properties Using NOAA/AVHRR

Akiko Higurashi and Teruyuki Nakajima

Center for Climate System Research, University of Tokyo
4-6-1 Komaba, Meguro-ku, Tokyo 153, Japan

Abstract

We estimated the global distribution of the aerosol optical thickness and Ångström exponent using NOAA/AVHRR channel-1 and -2 radiance data for four months in 1990. The global distributions of those aerosol parameters look consistent with our knowledge on the distribution of desert-derived, biomass-burning, and anthropogenic pollutant aerosols. Especially, we found that thin anthropogenic aerosols can be identified easily with large Ångström exponent values. Retrieved values of the aerosol optical thickness and Ångström exponent were validated with AERONET (AEresol Robotic NETwork) data, which are ground-based measurement data with sunphotometer by NASA.

1. Introduction

The aerosol effect on the earth's climate is one of the greatest uncertainties in climate modeling(Kiehl and Briegleb, 1993; Taylor and Penner, 1994). For accurate quantitative estimation of the effect, it is necessary to improve our knowledge of aerosol characteristics on a global scale, such as the size distribution, total content, absorptivity and so on. For this purpose, use of satellite data, which are acquired on a daily and global basis, is very efficient. National Oceanic and Atmospheric Administration (NOAA) has been producing global maps of aerosol optical thickness, which is retrieved assuming other aerosol optical parameters with channel-1 of NOAA/AVHRR(Stowe et al., 1992). Next step should be a use of multi-channel radiance data.

In this study, we present an analysis of aerosol optical thickness and Ångström exponent using NOAA/AVHRR channel-1 and 2.

2. Satellite Data Analysis

We developed the algorithm to retrieve the aerosol optical thickness and Ångström exponent from NOAA/AVHRR channel-1(0.64μm) and -2(0.83μm) radiance data(Nakajima and Higurashi, 1997; Higurashi and Nakajima, 1997). The algorithm is based on the relationship between channel-1 and 2 reflectances at the TOA(top of the atmosphere) of an atmosphere-ocean surface system as shown by Fig. 1. We assume 1.5-0.005*i* for the aerosol refractive index and the following bimodal size distribution,

$$\frac{dv}{d\ln r} = \sum_{n=1}^{2} c_n \exp\left[-\frac{1}{2}\left(\frac{\ln r - \ln r_{m,n}}{\ln s_n}\right)^2\right]. \qquad (1)$$

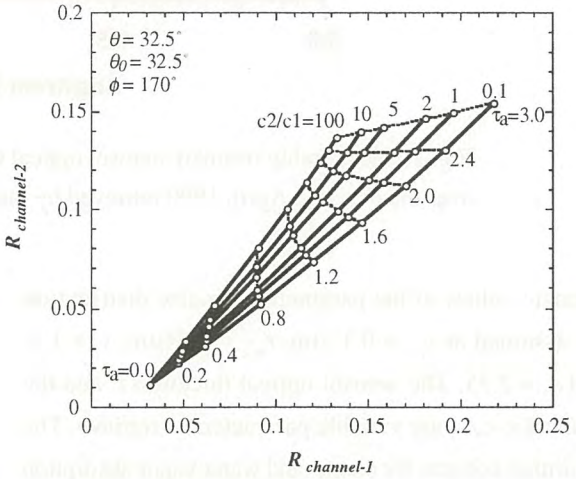
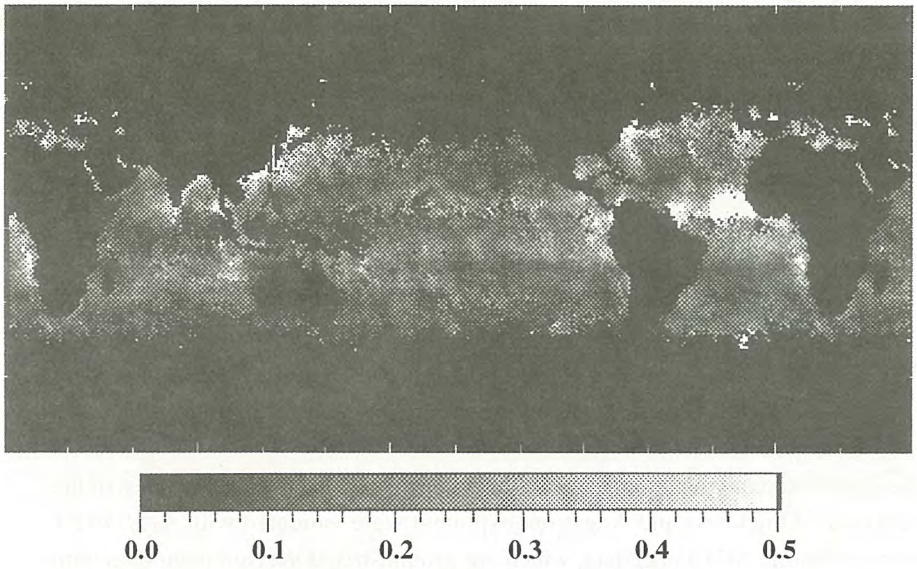


Fig. 1 Relation ship between AVHRR channel 1 and channel 2 reflectance with coutours of fixed optical thickness(solid lines)and fixed c_2/c_1 of size distribution (dashed lines).



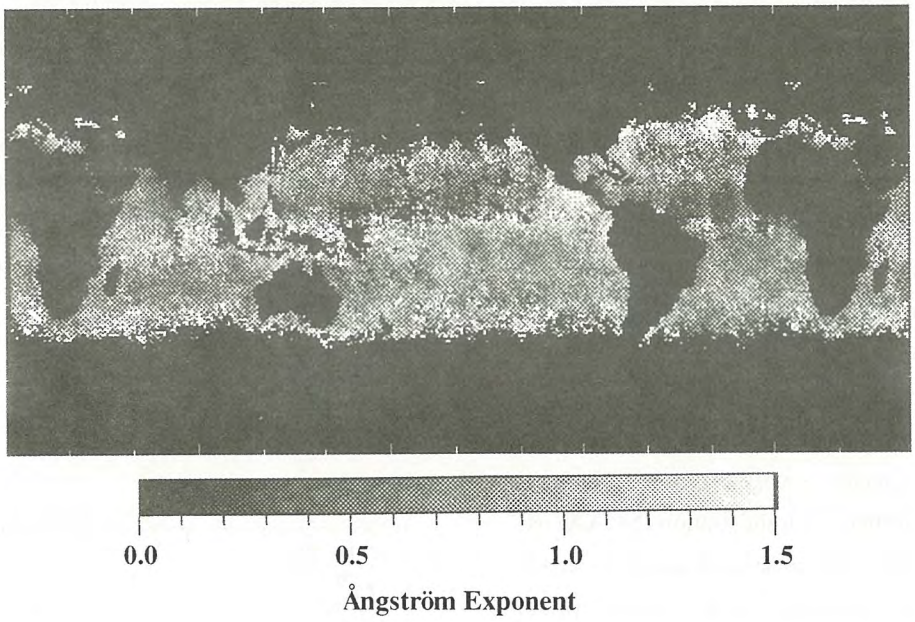


Fig. 2 The monthly mean of aerosol optical thickness at 0.5μm and Ångström exponent over the ocean in April, 1990 retrieved by our algorithm from AVHRR channel 1 and 2.

Climate values of the parameters for size distribution are assumed as $r_{m,1}$ = 0.17μm, $r_{m,2}$ = 3.44μm, s_1 = 1.3, and s_2 = 2.75. The aerosol optical thickness τ and the peak ratio c_2/c_1 are variable parameters to retrieve. The algorithm corrects for ozone and water vapor absorption using TOMS retrieval data and ECMWF objective analysis data, and for surface reflectance by assuming a rough-ocean surface with NCEP objective analysis data. We analyzed a selected pixel data in each 0.5°x0.5° segment data as clear-sky. To avoid solar specular reflection from ocean surface, data within 30° half cone angle centered on the flat ocean specular ray are excluded. Also, we except data with high wind speed , that is, greater than 12m/s, because on that conditions, the effect of the reflection by form on the retrieval is getting large.

Figure 2 shows the global map of the aerosol optical thickness and Ångström exponent, which is

Table 1. Selected AERNET data stations

Stations	Lat.	Lon.	Period
Ascension Island	S 7.58'	W 14.24'	Mar.-Dec., 1996
Barbados	N 13.00'	W 60.00'	May, Sep.-Oct., Dec., 1996-Jul., 1997
Bermuda	N 32.22'	W 64.41'	Mar.-Nov., 1996
Cape Verde	N 16.43'	W 22.56'	Oct. 1994-May 1995, Oct. 1996-Jun. 1997
Dry Tortugas	N 24.36'	W 82.47'	Mar.-Oct 1996, Jun.-Jul. 1997
Guadeloup	N 16.00'	W 58.30'	Mar.-Apr. 1996
Izana	N 28.18'	W 16.18'	Jun-Jul. 1997
Lanai	N 20.49'	W 156.59'	Nov. 1995 - Dec. 1996, July 1997
MALE	N 04.11'	E 73.31'	Sep. 1996 - Apr. 1997
Sandy Hook	N 40.26'	W 73.59'	May - Sep. 1996
St Nicolas	N 33.19'	W 119.30'	Jun.-Jul. 1996
Tromelin	S 15.53'	E 54.31'	Jul. - Nov. 1996
Wallops	N 37.56'	W 75.28'	Aug. - Sep., 1995, Jun. - Aug. 1996
Zenith	N 32.28'	W 64.34'	Jul., Nov. 1996

monthly mean in April, 1990, retrieved by this algorithm. We can find large quantities of soil dust are transported out of North Africa across the North Atlantic Ocean to Caribbean. Small Ångström exponents in this region consist with this fact, because small Ångström exponent indicates the large contribution of big particles. Off South Africa, Central America, the east coast of America, Europe, and East Asia, aerosol optical thickness is also comparatively large, however Ångström values is large that means the contributions of small particles are large. This is supported by that there are the high density of pollutant sources in North America and Europe and biomass burning is carried out extensively in Zaire and Central America in the spring(Andreae, 1993).

3. Validation with AERONET data

For the validation of retrieved results from satellite, we used the AERONET data, which is the network of aerosol optical measurement by sunphotometer on the global scale and opened as the daily and monthly-mean aerosol optical thickness at 340, 440, 670, and 1020nm at each stations, We selected

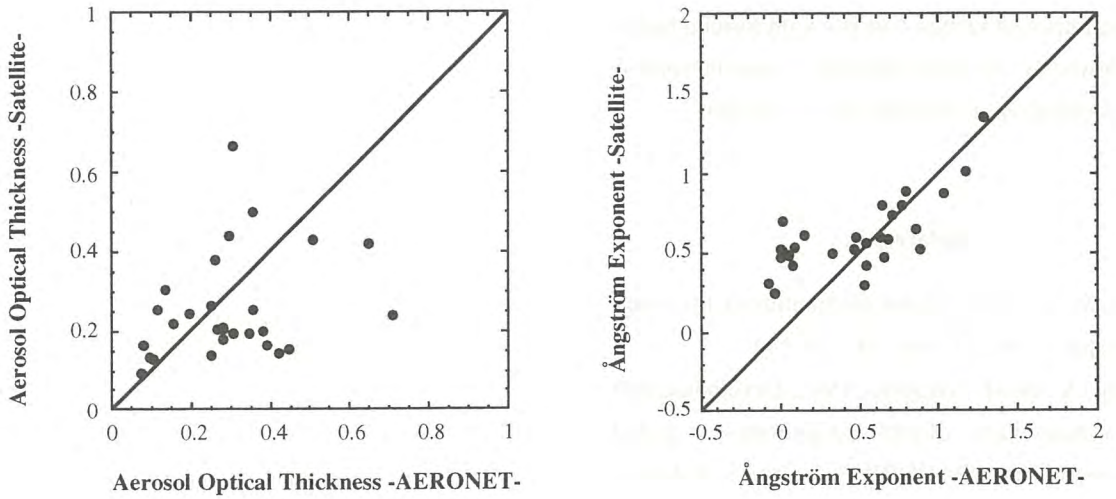


Fig. 3 The correlation between derived aerosol optical parameters, that is, optical thickness and Ångström exponent, from ground based measurement and retrieved values.

daily-mean data at stations over the ocean, which are listed in Table 1.

We calculated the aerosol optical thickness at 500nm and Ångström exponent, following the Ångström law, that is,

$$\tau_{a,\lambda} = \beta\lambda^{-\alpha}, \quad (2)$$

where $\tau_{a,\lambda}$ is the aerosol optical thickness at each wavelength λ, and α and β show the Ångström exponent and coefficient for daily-mean values and then monthly-mean are calculated. Figure3 shows the correlation between aerosol optical thickness and Ångström exponent derived from AERONET data and retrieved with AVHRR. Although they vary a little widely because the analyzed period is different, they are seems to be consistence except the retrieved results for Ångström exponent by AERONET data less than 0.2. For such affected by large particles like desert dust case, it may be difficult to express by assumed aerosol model and necessary to introduce other model.

4. Summary

We retrieved aerosol optical thickness and Ångström exponent by two channel algorithm with NOAA/AVHRR channel-1 and 2 radiance data in 1990. The important aerosol sources are desert dust, biomass burning, and pollutant. Anthropogenic aerosols are clearly distinguished with high Ångström exponent, although their loading are low as compared with soil dust. The retrieved results consists with ground based values, however, for large particles, it may be needed more investigation of assuming aerosol model.

References

Andreae, M. O., 1993: Global distribution of fires seen from space, , *EOS Trans.*, **74**, 129-144.

Higurashi, A., and T. Nakajima, 1997: Development of a two channel aerosol retrieval algorithm on global scale using NOAA/AVHRR. *Submitted to J. Atmos. Sci.*

Kiehl, J. T., and B. P. Briegleb, 1993: The relative role of sulfate aerosols and greenhouse gases in climate forcing, *Science*, **260**, 311-314.

Nakajima, T., and A. Higurashi, 1997: AVHRR Remote Sensing of Aerosol Optical Properties in the Persian Gulf Region, the Summer of 1991, *J. Geophys. Res.*, **102**, 16935-16946.

Stowe, L. L., R. M. Cavoy, and P. P. Pelliguino, 199: Monitoring the Mt. Pinatubo aerosol layer with NOAA-11/AVHRR data, *Geophys. Res. Lett*, **19**, 159-162.

Taylor, K. E., and J. E. Penner, 1994: Response of the climate system to atmospheric aerosols and greenhouse gases, *Nature*, **369**, 734-737.

Retrieving Aerosol Parameters from Advanced Visible and Near Infrared Radiometer (AVNIR) multispectral images of Mount Etna's aerosol plume.

I.M.Watson and C.Oppenheimer

Department of Geography, University of Cambridge, Downing Place, Cambridge, CB2 3EN, UK
Tel: +44 1223 333396. Fax: +44 1223 333392
E-mail: imw22@cus.cam.ac.uk/co200@cam.ac.uk

Abstract

Two multispectral images acquired on 28 March 1997 and 23 May 1997 by the Advanced Earth Observation Satellite (ADEOS) sensor AVNIR will be analysed in each of the four multispectral channels to retrieve aerosol optical thicknesses. The 28 March image provides the opportunity to retrieve optical parameters above snow, unvegetated basaltic lava flows and East Sicilian coastal waters. The heterogeneity of the plume can be clearly seen and could provide an insight into short term changes in rates of emission by Etna's active craters and near-source topographic effects.

The 23 May image provides a useful comparison by showing two distinct plumes; a relatively homogeneous plume from the southern complex of the Bocca Nuova, Voragine and Southeast craters and a distinctive 'beaded' plume from the Northeast crater. Analysis of the separate plumes will allow remotely sensed data to help categorise the differing eruptive activity of the two sites. Proximal and distal sections through the plume may also provide insight into temporal evolution of the aerosol phase.

Introduction

On 17 August 1996 the Advanced Earth Observing Satellite (ADEOS) was launched containing several remote sensors, including the Advanced Visible and Near Infra-red Radiometer (AVNIR). The AVNIR sensor contains four multispectral bands and one panchromatic band with at NADIR spatial resolutions of sixteen and eight metres respectively.

Two multispectral images have been obtained dated 28 March 1997 and 23 May 1997. In the 28/03/97 image a cloud free plume can be observed travelling south east over snow at the summit, then old basaltic lava flows and then out over the Ionian Sea. This provides an opportunity to derive aerosol parameters, primarily optical depth, over three spectrally different but well defined backgrounds which will enable the suitability of these backgrounds to volcanic aerosol retrievals to be studied.

The second image, 23/05/97, captured substantially more orographic cloud though the summit area still remains clear. Two distinct plumes can be observed, one emanating from the central Bocca Nuova and Voragine complex and the Southeast crater, and one from the Northeast crater. The plume generated by the Northeast crater has a pulsed nature with a periodicity of 40 s (for a wind speed of 5 m s^{-1}) while the primary plume can be seen to be much more consistent. The volcanic activity at the time of the images involved 'Strombolian' explosive activity at the Bocca Nuova and Southeast crater with quieter floor vent degassing from the Voragine and Northeast craters. The two plumes merge at 4 km from the summit.

Methodology

The images are to be atmospherically corrected using the minimum digital count level algorithm (Kawata, 1997). This method of estimating atmospheric optical thickness was developed specifically for the AVNIR sensor. First the minimum digital count level, (DC_{min}) is found for each of the four multispectral bands (i). The $DC_{min}(i)$ is then converted into the minimum radiance, ($PR_{min}(i)$). Then an appropriate meteorological range V(i) is then found for a given minimum radiance which is passed to MODTRAN code to calculate the atmospheric optical thickness for each band.

Once the atmospheric optical thickness is calculated for the non aerosol atmosphere the measured at-satellite radiance can be seen to contain contribution from the land/ocean surface and the volcanic aerosol. The true background signal can be calculated by removing the atmospheric contribution in an area of the image not contaminated by the volcanic aerosol. From this an approximate optical depth of the aerosol can be calculated. With this optical depth, the plume height, calculated using the brightness temperature, and the solar zenith angle, the extinction of incoming solar radiation on the background can be modelled. The subsequent albedo will be imposed iteratively until convergence criteria are met.

A routine for calculating the aerosol optical thickness, particle size and single scattering albedo will be developed to utilise a the pair of images (Kaufman, 1990). Both AVNIR and the Ocean Color and Temperature Scanner (OCTS) will be used to retrieve aerosol parameters, and SO_2 burden retrievals will also be attempted using OCTS. A simultaneous retrieval of both aerosol parameters and SO_2 gas burden would enable the generation of an accurate tropospheric volcanic box model.

Discussion

Aerosol parameters such as optical depth, mean scattering radius and single scattering albedo enhance understanding of the chemistry of volcanic plumes. The nature of volcanic hazards dictate remote measurement of gases and aerosols. An understanding of plume chemistry is therefore vital in utilising any remote measurements made. The inherent reactivity associated with high temperature release, and the presence of multiphase reactive conditions necessitate modelling of such conditions if realistic conclusions are to be drawn from spectroscopic and radiometric measurements at distances of kilometres from the vent. The investigation of Mount Etna is partly involved in a larger remote sensing project the EU Framework IV Environment and Climate Programme, aimed at mitigating volcanic risk in Europe with Mt. Etna, Europe's largest volcano and Mt. Versuvius, potentially Europe's most dangerous volcano. It is hoped that the aforementioned methodology can be used in both European and other volcanoes as a source of information directly related to the individual volcanoes volcanic activity.

References

Oppenheimer *et al.* 1997 AVNIR observations of Mount Etna's Aerosol Plume (*In press*)

Ravishankara. 1997. Heterogeneous and multiphase chemistry in the troposphere. *Science Vol. 27 pp 1058-1065*

Lynch 1996. Multispectral remote sensing of aerosols. *Acta Astronomica. No 12 pp 947-953*

Kaufmann *et al.* 1990. Satellite measurements of air pollution-method. *J.G.R. 95 D7 pp-9898-9909*

III. Satellite Data Application to Environment

Using Double-channel and Double-Angle ATSR Data In the Evaluation of Land Surface Temperatures

Jiemin WANG [1] Massimo MENENTI [2]
Akihiko KONDOH [3] Dongqi LIU[1]

[1] Lanzhou Institute of Plateau Atmospheric Physics,
Chinese Academy of Sciences, Lanzhou, Gansu 730000, China
[2] DLO Winand Staring Centre for Integrated Land, Soil and Water
Research, P.O.Box 125, 6700 AC Wageningen, The Netherlands
[3] Center for Environmental Remote Sensing, Chiba University,
Yayoi-cho, Inage-ku, Chiba 263, Japan

Introduction

Land surface temperature (LST) is the most important parameter to be estimated from satellite remote sensing in the study of energy and water budget on land surfaces. There are two major difficulties associated with satellite estimates of land surface temperature: a) the evaluation of atmospheric effects on the measurements from a satellite based sensor; b) the evaluation of emissivity of the land surface. The characteristics of land surface are much more complicated compared with the sea surface. The emissivity of land surfaces varies with landuse type, with vegetation cover and its structure; it may be substantially lower than one, may vary strongly from one point to another, and may have large spectral and angular variation. Consequently, the land surface temperature itself may vary strongly over small distances, within a pixel, leading to difficult average procedure and to some problems in the definition of LST itself.

The split-window method, by using of a linear combination of the radiometric temperatures in channel 4 (11 μm) and channel 5 (12 μm) of the AVHRR, or the similar thermal infrared bands of the Geostationary satellite data, has been fully studied in the estimation of sea surface temperature (SST). Similar simple algorithm was also tried in the estimation of land surface temperature (LST) (Becker and Li, 1990). The task becomes difficult because we still have less knowledge on the variation of the land surface emissivities.

The new ERS-ATSR (Along Track Scanning Radiometer) data consist of 11 μm and 12 μm thermal IR bands (as well as bands at 1.6 and 3.7 μm) and nadir and forward (~54°) measurements, at nearly the same time, which doubles the information as compared with AVHRR. The view geometry for the infrared radiometer of ATSR is shown in Figure 1. One area along the satellite track, with resolution about 1 km for nadir and a little larger for forward, is viewed twice during about two minutes. Assuming the atmosphere is horizontally stratified and stable in this short period, the atmospheric correction should be more accurately determined than by previous methods. Some authors have tried to promote an operational scheme in the estimation of land surface temperatures very recently (e.g. Sobrino et al, 1996).

One set of ATSR data has been used for the algorithm study on deriving surface temperature for a heterogeneous area in Northwest China, where the Heihe River Basin Field Experiment on Land Surface-Atmospheric Interaction (HEIFE, 1990-1993) has been carried out. The experiment region is mainly a large area of Gobi and sand desert with various scales of oasis dispersed along the river and irrigation canals. Surface data

collected during the HEIFE intensive observations, as well as previous studies by using of Landsat TM and NOAA AVHRR are used for the intercomparison. To evaluate the atmospheric effect including atmospheric transmissibility and slant path radiation at the satellite altitude and both of the IR channels of ATSR, the ModTran radiative transfer model has been operated.

Theory & Double-Angle/Double-Channel Technique

Radiance measured on board of the satellite, $B(T_{\lambda\theta})$, as normally expressed,

$$B(T_{\lambda\vartheta}) = \varepsilon_{\lambda\vartheta} B_{\lambda}(T_s)\tau_{\lambda\vartheta} + R_{atm,\lambda\vartheta\uparrow} + R_{ref,\lambda}\tau_{\lambda\vartheta} \quad (1)$$

Where T is temperature (K), ε is the surface emissivity, τ is the atmospheric transmissibility, the subscript λ denotes the wave band, θ denote the view angle, s denotes the land surface. The second in the right hand of Eq. 1 is the path radiance of the atmosphere, while the third term is the contribution of the surface reflected downward atmospheric radiance. Both terms can be simplified based on minor assumption (Sobrino et al, 1996):

$$R_{atm,\lambda\vartheta\uparrow} = (1-\tau_{\lambda\vartheta})B_{\lambda}(T_a) \quad (2)$$

$$R_{ref,\lambda} = (1-\varepsilon_{\lambda\vartheta})(1-\tau_{\lambda,53})B_{\lambda}(T_a) \quad (3)$$

Where T_a is the mean temperature of the atmosphere. For Nadir and Forward of ATSR bands IR3 (10.8μm) & IR4 (12μm), and assuming the transmissibility at 53° is equal to that of forward view, four equations can be Written as following:

$$B(T_{11n}) = \varepsilon_{11n}B(T_s)\tau_{11n} + (1-\tau_{11n})B(T_{a,11n}) + (1-\varepsilon_{11n})(1-\tau_{11f})\tau_{11n}B(T_{a,11n}) \quad (4)$$

$$B(T_{11f}) = \varepsilon_{11f}B(T_s)\tau_{11f} + (1-\tau_{11f})B(T_{a,11f}) + (1-\varepsilon_{11f})(1-\tau_{11f})\tau_{11f}B(T_{a,11f}) \quad (5)$$

$$B(T_{12n}) = \varepsilon_{12n}B(T_s)\tau_{12n} + (1-\tau_{12n})B(T_{a,12n}) + (1-\varepsilon_{12n})(1-\tau_{12f})\tau_{12n}B(T_{a,12n}) \quad (6)$$

$$B(T_{12f}) = \varepsilon_{12f}B(T_s)\tau_{12f} + (1-\tau_{12f})B(T_{a,12f}) + (1-\varepsilon_{12f})(1-\tau_{12f})\tau_{12f}B(T_{a,12f}) \quad (7)$$

The unknowns in the left side of Eq. 4-7, besides the required surface temperature T_s, there are four ε's related to the two wavebands / two view angles (if the atmospheric parameters can be evaluated by observation and transfer models). We must make assumption to reduce the unknowns. Like generally accepted, we first assume that $\varepsilon_{11} = \varepsilon_{12}$, and $\Delta\varepsilon_{\theta} = \varepsilon_n - \varepsilon_f$.
For easier solution, the separation of T_s and ε is necessary in the above simultaneous equations. Applying the first order Taylor series expansion of the Plank Function B(T), Eq. 4-7 can be rearranged as a function of temperature and emissivity (Sobrino, et al, 1996):

$$T_s = T_{11n} + A_{11}(T_{11n} - T_{11f}) - B_{0,11} + (1-\varepsilon_n)B_{1,11} - \Delta\varepsilon_{\vartheta}B_{2,11} \quad (8)$$

$$T_s = T_{12n} + A_{12}(T_{12n} - T_{12f}) - B_{0,12} + (1-\varepsilon_n)B_{1,12} - \Delta\varepsilon_{\vartheta}B_{2,12} \quad (9)$$

Where

$$A_{11} = (1-\tau_{11n})/(\tau_{11n} - \tau_{11f}) \quad (10)$$

$$B_{0,11} = A_{11}(1-\tau_{11f})(T_{a,11n} - T_{a,11f}) \quad (11)$$

$$B_{1,11} = [(1-\tau_{11n}\tau_{11f})/(\tau_{11n}-\tau_{11f})](T_{11n}-T_{11f}) + \tau_{11f}L_{n,11} \quad (12)$$

$$B_{2,11} = \tau_{11f}A_{11}B_{1,11} \quad (13)$$

$$L_{11n} = B(T_{11n})/[\partial B(T)/\partial T]_{T_{11n}} \cong \lambda T_{11n}^2/C_2 \quad (14)$$

There is a similar set of the coefficients for band 12 μm.

Equation 8 and 9 are used for the computation of T_s and ε. However, the unknowns (T_s, ε, and Δε) are still more than the equations. Further estimation of ε by other method is still needed.

The operation of ModTran

The Modtran radiative transfer model was used to calculate the atmospheric transmissibility and radiances for IR3 (11 μm) and IR4 (12 μm) of ERS-1 ATSR at the satellite altitude with the appropriate channel filter functions. The model inputs, particularly the temperature and humidity profiles, are mainly from field measurements at two contrasting stations, one in desert, another in the middle of oasis. The profiles are a composition of following sources:

Surface-1000m: Tethered-balloon sounding
1000-2000m: Low Level Sounding
1000-14000m: Aerological radiosounding
15000m up: Mid-Latitude Summer Model

Total vertical water contents of the atmosphere were calculated to be 1.992 and 1.970 g/cm^2 for oasis and desert respectively. The 'Desert extinction' in the Modtran options is chosen for aerosol attenuation.

The model outputs are summarized in Table 1.

Table 1. Model Outputs for the time when ERS-1 passing (11:30, August 19, 1991)

		11μm		12μm	
		Oasis	Desert	Oasis	Desert
Transmitance	Nadir	0.8632	0.8671	0.7678	0.7728
	Forward	0.7874	0.7933	0.6662	0.6735
Path Radiation W/cm^{2}Sr	Nadir	7.72E-5	7.51E-5	1.27E-4	1.24E-4
	Forward	1.20E-4	1.16E-4	1.86E-4	1.82E-4

The Estimation of Land Surface Emissivity

There were some laboratory and field works on surface emissivity evaluation, but no specific measurements for this during HEIFE. Van de Griend and Owe (1993) proposed a relation between surface emissivity and the satellite sensed vegetation index NDVI, $\varepsilon = 1.009 + 0.047\ln(NDVI)$. We have used it in the regional energy balance study with Landsat TM combined with HEIFE surface observations (Wang et al, 1995). For this study a slightly modified formula is used,

$$\varepsilon = 1.009 + 0.047\ln(NDVI + 0.3) \quad (15)$$

Which seems better particularly for the desert region. On the other hand, Rubio et al (1996)

have investigated large varieties of vegetation, soil and rocks, and postulated a simpler relation for 8-14 μm waveband:

$$\varepsilon_\lambda = a\varepsilon_m + b \qquad (16)$$

Where ε_m is the mean effective emissivity for this band, a and b are coefficients given in Table 2 for 11 μm and 12 μm narrow band. In this study, two areas in rather homogeneous part of both desert and oasis in HEIFE region have been chosen respectively, each has 10×10 pixels. Following values are calculated from (16):

Oasis: ε_{11}=0.987 ε_{12}=0.987

Desert: ε_{11}=0.954 ε_{12}=0.971

The values at oasis are similar with that from Eq. 15; while for desert, it is shown here that $\varepsilon_{11} \neq \varepsilon_{12}$. We used a mean value of ε_{11} and ε_{12} in the surface temperature calculations.

Table 2. Mean values and the coefficients of Eq.16 for emissivity calculation in 8-14 μm wavebands by Rubio et al (1997)

	Vegetation			Soil			Rocks		
	a	B	σ	a	b	σ	A	B	σ
11μm	1.619	-0.608	±0.006	0.240	0.742	±0.004	0.231	0.737	±0.02
12μm	1.467	-0.458	±0.009	0.047	0.932	±0.005	0.078	0.898	±0.009
ε_m	0.985±0.002			0.958±0.003			0.936±0.03		

The deficiencies of the ATSR forward view: 'Edge Effect'

The surface resolution for ATSR nadir view is 1 km × 1 km, while that for forward view is 1.5 km × 2 km. The lower resolution of the forward view causes the lower contrast in the T_f images compared with that of T_n, which is clearer for HEIFE area in the boundary of the oasis. Besides, more unrealistic is that if we check the $(T_n - T_f)$ images we found abnormal values at both the north edge and south edge of the oases. At the north edge, when satellite enters over the oasis from the desert, $(T_n - T_f) < 0$. The values of T_f were even 5~8 K lager than T_n at some pixels. Oppositely, at the south edge, when satellite leaves oasis and passes over the Gobi desert, $(T_n - T_f) > 0$, but abnormally large (Figure 2). The normal values are: In the 'training area' of desert, $(T_n - T_f) \approx 0.7$ K for 11 μm and 2.4 K for 12 μm; In the training area of oasis, $(T_n - T_f) \approx 3.7$ K for 11 μm and 4.0 K for 12 μm. As we know that the surface temperature of desert is about 20 K higher than oasis. The phenomenon mentioned above, called it 'Edge effect' temporally, looks like a kind of delay of response in the ATSR forward view.

To prevent large errors in the surface temperature estimation by using of Eq. 8 and 9, we should pay more attention at the pixels near the edge of the oasis. Some threshold values were set according to following analysis: If we assume

$$(T_n - T_f) = a - b\,T_n \qquad (17)$$

Then from the training areas, we have:

Oasis:

11μm $(T_n - T_f) = -211.7278 + 0.7123 T_n$

12μm $(T_n - T_f) = -241.6689 + 0.8149T_n$

Desert:

11μm (Tn=310.8) $(T_n - T_f) = -341.1525 + 1.1T_n$

12μm (Tn=314.0) $(T_n - T_f) = -984.4949 + 3.14\ T_n$

An iteration algorithm also used to improve the final estimates.

Results and discussion

The estimated surface temperature of the Heihe River Basin, with method mentioned above, is shown in Figure 3, with a relevant histogram shown in Figure 4. The results have been compared with observations and the previous results from Landsat TM analysis, as shown in Table 3.

Table 3. Comparison of Land Surface Temperatures Observed and Calculated at four HEIFE Stations

Station	*Desert*	*Zhangye*	*AWS013*	*AWS015*
Observation 08/19/1991	44.8	33.4	45.2	47.0
Cal. By Using ATSR	45.0	34.0	50.0	49.0
Observation 07/09/1991	44.8	22.8	17.9	46.5
Cal. By Using Landsat TM	46.5	17.0	16.0	43.7

Concluding Remarks

Using double-channel and double angle IR measurements can improve the evaluation of surface temperature, when compared with the split-window method. This is essential for land surface processes study. To use Eq. 8 and 9, a combination with operation of radiative transfer model is necessary. The evaluation of surface emissivity $\varepsilon(\lambda,\theta)$ is most important in this study. It is necessary to continue the multi-channel (still in the 11~12 μm) multi-view angle space measurements. If the view angle can be add to 3~5, the equations can be solved analytically. For processing ATSR data, the deficiency in the forward view was noticed.

References

Becker, F., and Li, Z., 1990: Towards a local split window method over land surfaces. International Journal of Remote Sensing, 11, 369-394

Rubio, E., V. Caselles, and C. Badenas, 1997: Emissivity measurements of several soils and vegetation types in the 8-14 μm wavebans. Analysis of two field methods. Remote Sensing of Environment, 50, 400-521

Van de Griend, A. A., and M. Owe, 1993: On the relationship between thermal emmisivity and the NDVI for natural surfaces. International Journal of Remote Sensing, 14, 2449-2460.

Wang J., Y. Ma, M. Menenti, W. Bastiaanssen, and Y. Mitsuta, 1995: The scaling-up of processes in the heterogeneous landscape of HEIFE with the aid of satellite remote sensing. Journal of the Meteorological Society of Japan, 73, 6, 1235-1244

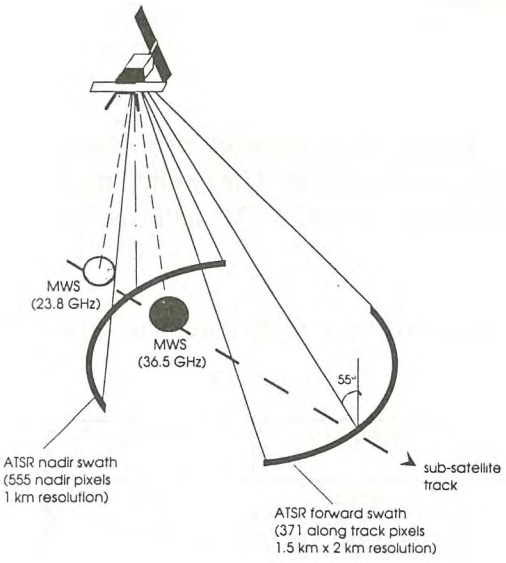


Figure 1. ATSR view geometry

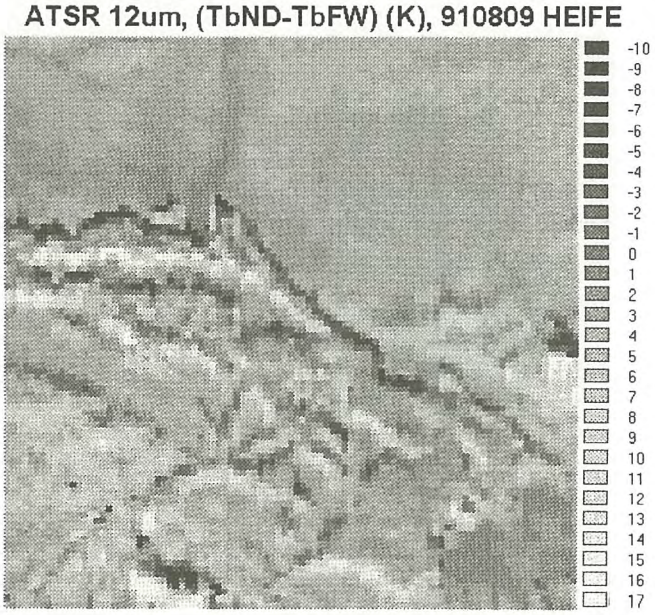


Figure 2. The distribution of brightness temperature difference (T_n-T_f) for 12 μm.

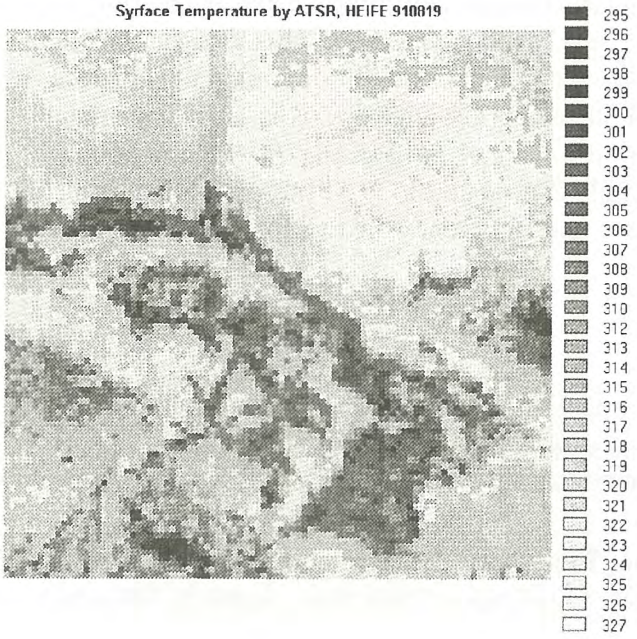


Figure 3. Surface temperature distribution in HEIFE region, calculated by using of ATSR data.

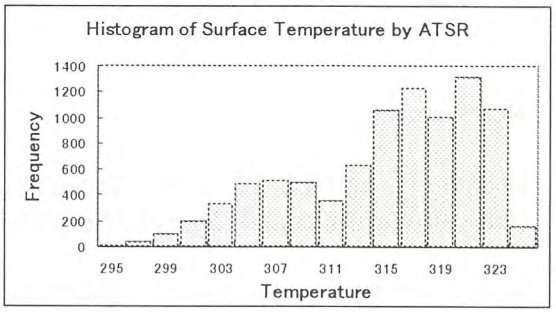


Figure 4. Histogram of surface temperature distribution in Figure 3.

CONSTRUCTION OF GPS VAPOR INFORMATION SYSTEM FOR INTERDISCIPLINARY STUDIES

Akihiko Kondoh[1], Isao Naito[2], Ryu Otani[3], Tetsuya Iwabuchi[4], Shin-ichi Miyazaki[5]

[1] CEReS, Chiba University, [2] Earth Rotation div., Mizusawa Astorogeodynamics Observatory/NAO
[3] Department of Earth and Planetary Physics, Graduate School of Science, Univ. of Tokyo
[4] The Graduate University for Advanced Studies, [5] Geographical Survey Institute

INTRODUCTION

GPS Meteorology is the study that includes the observation of precipitable water, its application to weather forecast or observation of global warming by using Global Positioning System(Businger, 1996; Ware *et al.*, 1996; Naito, 1996). Recent developments of the accuracy of satellite orbit forecasting and of software for analyzing GPS data enable the estimation of precipitable water(PW). Precipitable water data from GPS stations by Geographical Survey Institute(GSI), of which number of stations are compatible with AMeDAS stations, are available in Japan(Hatanaka *et al.*, 1996; Aonashi *et al.*, 1997).

This paper outlines the data base construction for interdeciplinary use of GPS water vapor information for environmental sciences. The objectives of GPS Meteorology Project(GPS/MET JAPAN) started this year, characteristics of GPS vapor information by GSI and the changes in vapor over Japan islands detected by GPS are also explained in the paper.

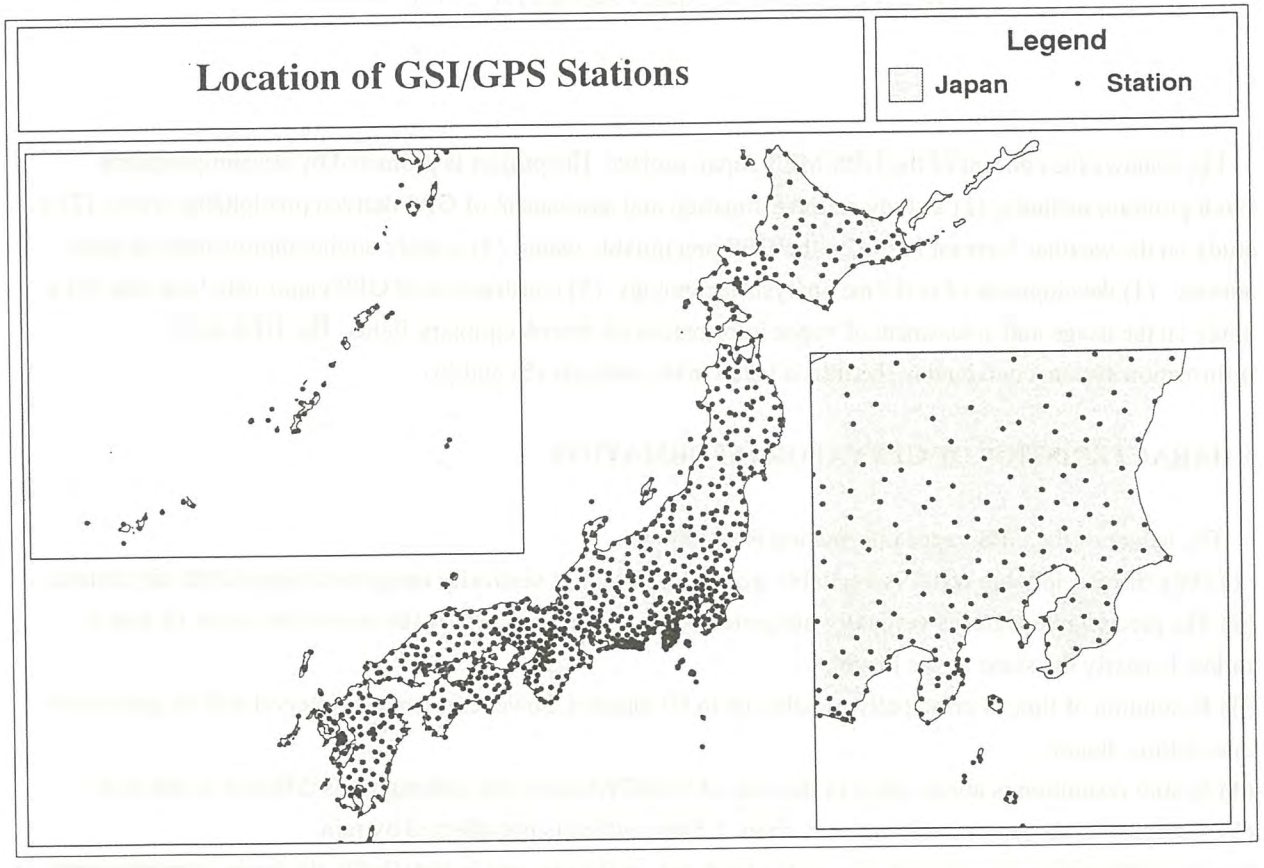


Fig.1 The locations of GPS Stations by GSI, Japan.

OBJECTIVES OF GPS/MET JAPAN

Fig.1 shows the locations of GSI/GPS stations. GPS/MET Japan utilizes the data from these densely distributed GPS stations. It is rare in other countries, and it will enable the distinctive studies in Japan.

There are several objectives in GPS/MET JAPAN as follows:

- To combine GPS vapor information to the numerical weather forecast system of Japan Meteorological Agency(JMA), and uses for meso scale weather forecast.
- To feedback weather forecast data to land surveys, and to improve accuracy of space geodetic methods, including GPS and VLBI.
- To construct vapor information data base for the interdisciplinary research, such as environmental sciences.

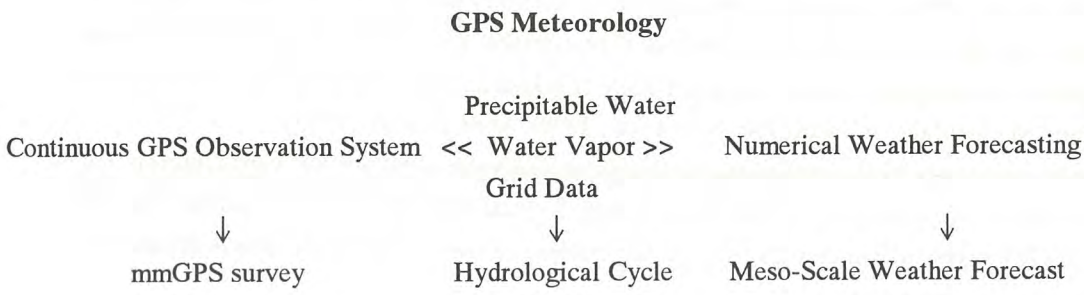


Fig.2 A concept of GPS/MET Japan(STA, 1997).

Fig.2 shows the concept of the GPS/MET Japan project. The project is promoted by six sub-programs. Each program includes, (1) a study on the estimation and assessment of GPS derived precipitable water, (2) a study on the weather forecast based on the GPS precipitable water, (3) a study on the improvement of space surveys, (4) development of real time analysis technology, (5) construction of GPS vapor data base and (6) a study on the usage and assessment of vapor information for interdeciplinary fields. The GPS vapor information system contained in the title is taken in the subjects (5) and (6).

CHARACTERISTICS OF GPS VAPOR INFORMATION

The nature of the GPS vapor information is as follows:

(1) Only the precipitable water is available from GPS, which is vertically integrated vapor of the air column.
(2) The precipitable water is vertically integrated water vapor averaged by the area of the circle of which radius is nearly the same as the height.
(3) Resolution of time is principally possible up to 10 minutes, however, an actual interval will be practically one or three hours.
(4) Spatial resolution is about 25km in the case of GSI/GPS networks, although it is different in the area.
(5) Accuracy of the precipitable water is about 1.5mm, which is not affected by rain.
(6) The GPS stations are located only on the land, not on the sea, and is installed in the basin in mountainous

area.

Above are the characteristics of GPS precipitable water itself. As the construction of vapor information based on the 4DDA data from numerical weather forecast system of JMA is one of the objectives in GPS/MET Japan, three-dimensional vapor information will be available in near future.

ACTUAL CONDITIONS OF PRECIPITABLE WATER DEPICTED BY GSI/GPS OBSERVATION

Fig.3 is the comparison of precipitable water estimated from the radiosonde and from GPS observations at Tsukuba. The zenith hydrostatic delay, which can be calculated from atmospheric pressure, is subtracted from zenith neutral delay to calculate zenith wet delay. It can be converted to precipitable water by applying a constant. The correlation is considerably high. The average difference between them is 0.4mm, and standard deviation is 2.1mm. It shows that the GPS is functioning well as a vapor sensor. Small disagreement will be disappearing by introducing vapor oriented GPS analysis system.

Fig.4 denotes the time changes in precipitable water at Shionomisaki station. Sudden increases in precipitable water are clearly delineated, while regular observation of the radiosonde could not detect such abrupt changes.

Fig.5 shows the transition of precipitable water when the autumnal rain front slowly passed over the Japan island, which is calculated from regular GIS/GPS observation data. Although the zenith hydrostatic delay is not excluded in Fig.5, almost all the variation can be explained by precipitable water because the change in atmospheric pressure is within several hPa at that time. The location of the front is clearly delineated as dark parts in the figure, which means humid.

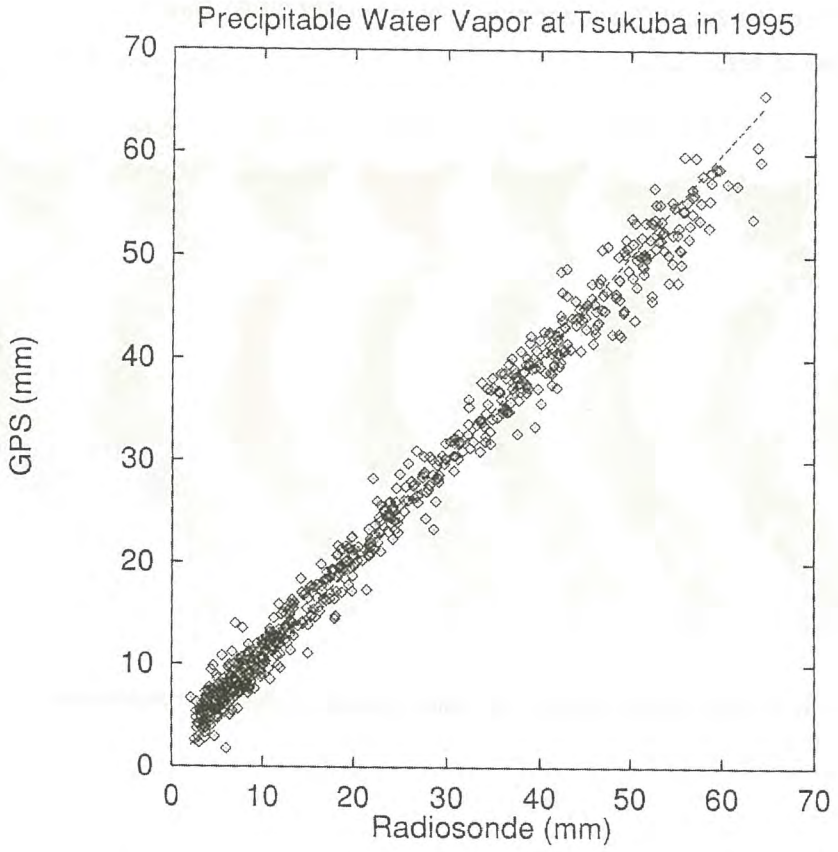


Fig.3 Comparison between observed and GPS derived precipitable water at Tateno, Tsukuba.

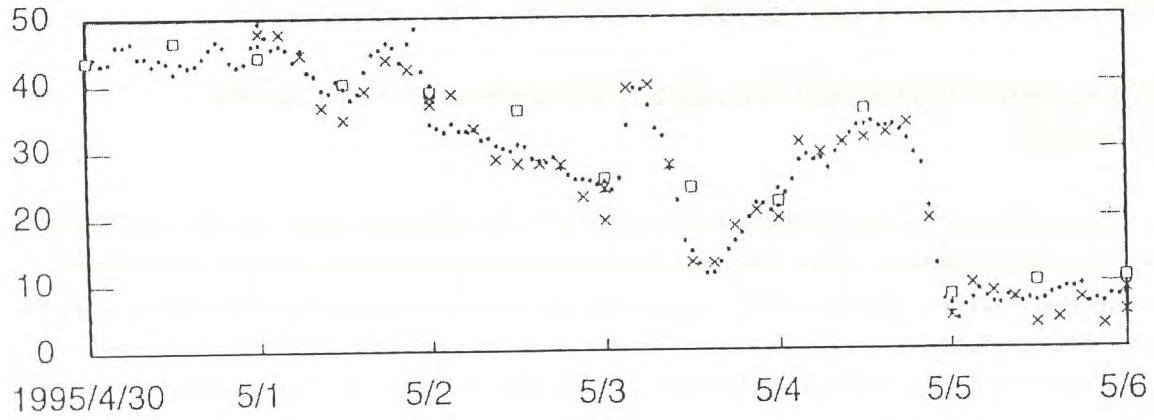


Fig.4 Time change in precipitable water at Shionomisaki station. ● and × show the precipitable water calculated from GIPSY and GAMITT softwares respectively. □ denotes the radiosonde derived precipitable water.

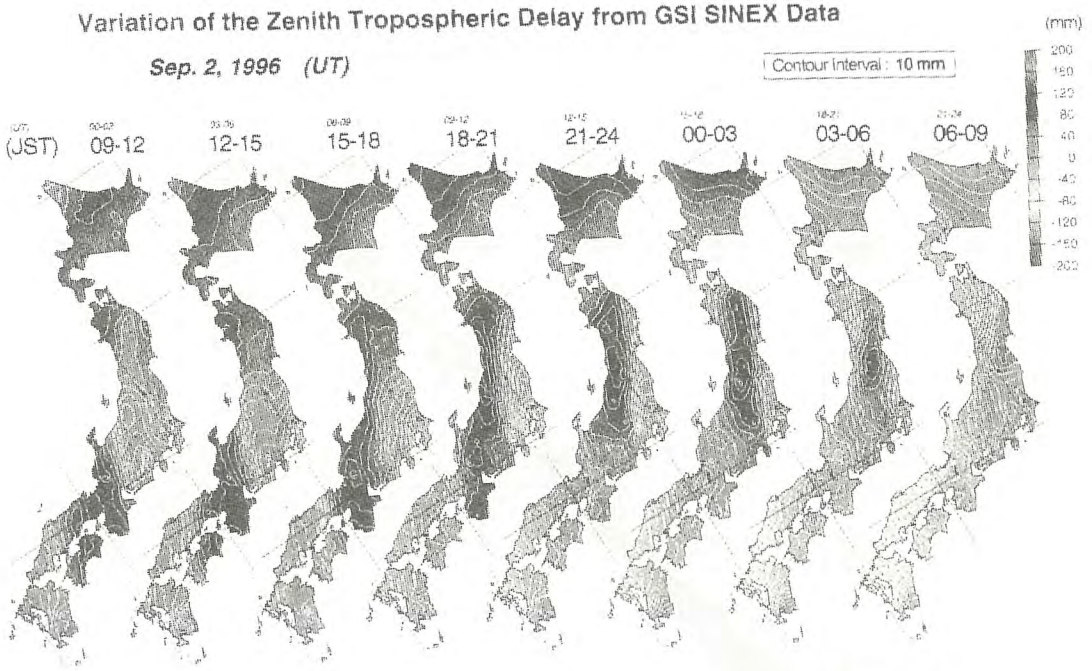


Fig.5 An example of time changes in the zenith tropospheric delay over Japan island.

CONSTRUCTION OF GPS VAPOR INFORMATION DATA BASE

GPS information in GSI is archived in two formats. One is RINEX file, which is raw observational data. The other is SINEX file. It is the analyzed data by the GPS software. The use in vapor information is based on SINEX file. Users can access the data through a computer network.

The large capacity data archive system was installed in the center for environmental remote sensing(CEReS) in Chiba University. It is originally designed to store satellite data directly received in CEReS, which are NOAA and GMS. Various geographic information including meteorological data is also planning to archive in it, and to construct a data base system.

GPS vapor information is one of the geographic information, namely it has the information on the location it is observed. The geographic information should be stored and analyzed on the geographic information system(GIS). Fig.1 is drawn by using GIS, and it enables the spatial analysis.

For example, Fig. 6 shows the location of GSI/GPS Stations on the land use map. GPS vapor variations inherent in the local characteristics, such as land use, topography, etc., can be analyzed by superimposing various spatial information on the GPS vapor data. The GIS oriented GPS water vapor information system is currently planning to construct in CEReS, Chiba University, for interdisciplinary environmental studies.

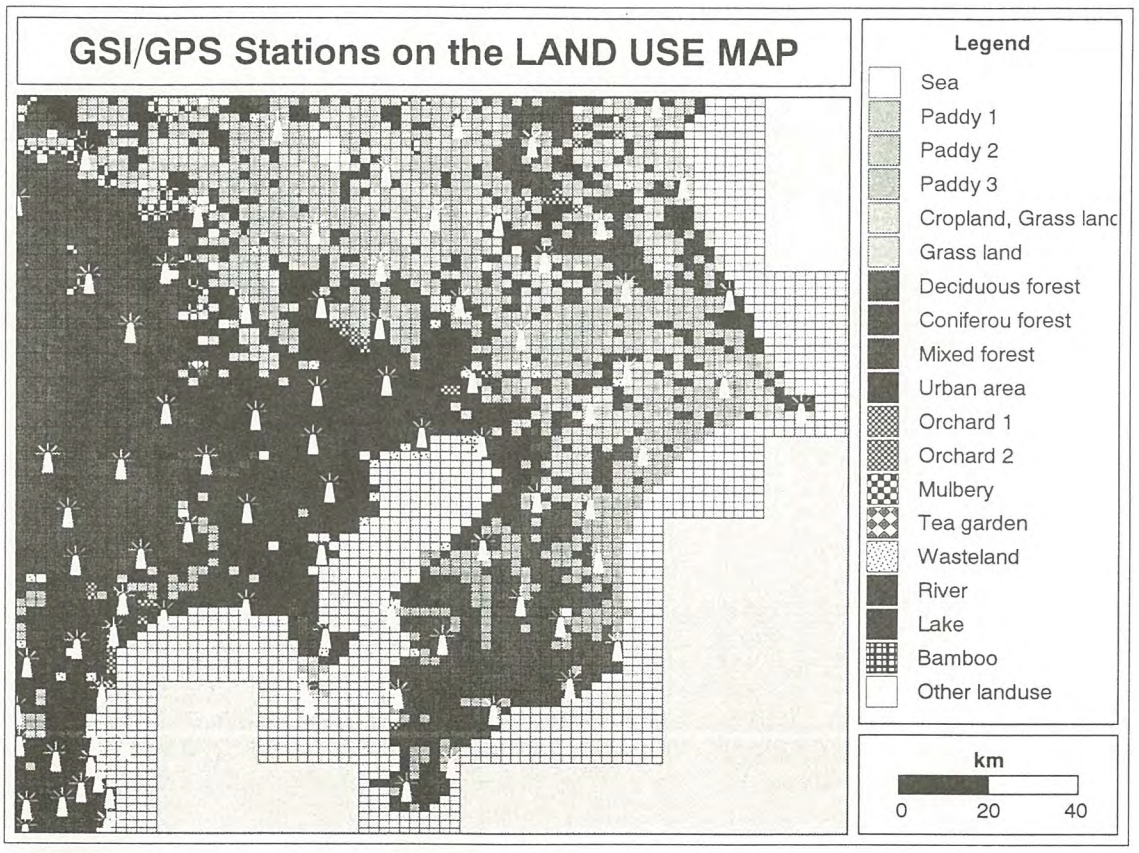


Fig.6 GPS stations in Kanto Palin, Japan over land use map.

CONCLUDING REMARKS

There is another project in the field of GPS meteorology in USA. Its objective is to observe the vertical profiles of air temperature and vapor by GPS receiver on board low orbit satellite. These projects are in complementary relationship with GPS/MET Japan in the spatial scale treated. It is certain that both projects contribute to the monitoring the global warming and its influences. GPS gets a great expectation in that it will be a indispensable sensor to monitor the changes in Earth system.

REFERENCES

Businger, C., (1997): The promise of GPS in atmospheric monitoring. *Bull. Am. Meteor. Soc.*, **77**, 5-18.

Duan, J., Bevis, M., Fang, P. Bock, Y., Chiswell, S., Businger, S., Rocken, C., Solheim, F., Hove, T. V., Ware, R., McClusky, S., Herring, T. A. and King, R. W.(1996): GPS meteorology: Direct estimation of the absolute value of precipitable water. *J. Appl. Meteorol.*, **35**, 830-838.

Ware et al.(1996): GPS sounding of the atmosphere from low orbit: Preliminary results. *Bull. Am. Met. Soc.*, **77**, 19-40.

Study on the Minimum Representative Area on a Test Site

Hirokazu YAMAMOTO, Koji KAJIWARA and Yoshiaki HONDA

Center for Environmental Remote Sensing(CEReS), Chiba University
1-33 Yayoi-cho, Inage-ku, Chiba, 263 Japan
Fax :+81-43-290-3857
E-mail:kath@rsirc.cr.chiba-u.ac.jp

Abstract

It is necessary to use the ground observational data to calculate physical value in a wide survey unit (1km×1km) in order to verify the reliability of the algorithm for speculating physical variable from 1km satellite data. Since it is difficult to conduct the ground observation within whole wide area survey unit in short time, the minimal survey area which can represent a wide survey unit has to be determined. The objective of this study is to find the minimal representing area of a wide survey unit through the car survey and radio-controlled helicopter survey we developed in Mongolian grassland. As a result, it can be said that these systems used in the research are a good way to calculate the minimal representing area of a wide survey unit.

1. Introduction

In Earth System Science(1984) proposed by NASA, various information on earth is gathered during first decade and it is made some models for various phenomena arised on earth during second decade. Especially, in recent years, it is interested in estimating vegetation amount quantitatively from satellite data which has the characteristics of lower spatial resolution and higher time-frequency. Global quantitative analysis using satellite data is very important for understanding water and energy flow in the arid and semiarid region.

It is necessary to understand relation between spectral reflectance and physical parameter of the objects because satellite sensor fundamentally obtain only reflected spectral radiance energy. But each pixels of satellite data have not only ground reflectance but also atmospheric information. Therefore atmospheric correction is often conducted on satellite image processing, and ground data for verification are needed for global quantitative land analysis using satellite data .

Generaly, it is often tried to get the ground truth data, which should be satisfied with condition of scale as same as satellite data and condition of simultaneity for satellite data. But it is difficult to collect the ground truth data in the short time in the area which is the same as low spatial resolution of satellite sensor (ex. NOAA AVHRR, ADEOS OCTS, in future ADEOS-II GLI、EOS-AM MODIS data). If the study area looks like very homogeneous area, it is needed to confirm whether the site is actually uniform area or not. For example, in sparse vegetated area, it cannot be regarded as homogeneous area in small scale because ground may vary the condition of some objects at each observation units. Therefore, it is needed to clarify how large the area can be regarded as one unit.

2. Objective

The aim of this study is to estimate the minimum representative area in Mongolian grassland, which is very flat and homogeneous area, and to verify data obtained by the system we developed.

3. Methods and Results

In this study, we tried to obtain spectral information and video images by our two developed system. One is car survey system (Figure 1.) and the other is Radio-Controled Helicopter (RC Heli) survey system (Figure 2.). Both can get so many video images and spectral information in the short time. The detailed statement of these system is explained in section 3.1 and 3.2.

The study area where we observed is Mongolian grassland, which is located at about N47.3 deg E106.3 deg , and which is very homogenous and flat area. The terrain type is almost gravel or sandy, and vegetation density is thin, plant height is from about 1.0cm to about 22.5cm. The distribution of measurement point is shown in the Figure 3 . The measurement was conducted in 14 Aug. 1996 and 15 Aug. 1996(Table 1.). Both systems are able to obtain spectral information and video images at the same time. In this study, there may have possibility of difference of change for spectral information affected by difference of siol condition (soil moisture content etc.) between car survey and RC-heli survey, because each measurement date is different. Therefore this study does not compare spectral refrectance directly, but compare minimum area using vegetation coverage ratio derived from each measurements.

3.1 Measurement using Car Survey System

The arm of this system juts from the roof of car and move with car, and it observes the gound condition quickly. CCD camera, multichannel spectrometer S2320(Soma Optics, Ltd.), GPS receiver, and GPS Camera (made by Konica) are mounted on the tip of the observation tower all together. GPS Camera can save information (date,time, longitude and latitude, and azimuth and observation angle) in the upper side of the photograph. Before optical fiber, there is a diaphragm, which can be set the sensor's field of view (FOV) continuously. FOV in this video image is the same as sensor looking position and the sensor's FOV. The center of sensor is coincident with the optical center of sensor. White standard reference board we used is barium sulphate panel. This panel is made by baraita paper plus $BaSO_4$, which is superior cost performance, geometric dependancy. This system can avoid shadow of measurement system itself by the revolving stand on the car-top. This system can obtain one data every one minute, and in this study, we measured 100 points in 1km×2.5km area(Figure 2.).

Figure 4 depicts vegetation coverage ratio (VCR) of 100 measurement points. VCR is derived from video images obtained by the above system. This diagram shows that the virtical axis is vegetation coverage ratio and the horizontal axis is measurement number. it can be seen that grassland which looks like homogeneous area has big variability. For this figure, Figure 5. is shown moving averaged VCR from 5 points to 35 points. It has become smaller variability over about 25 points. Figure 6 is shown diagram for the variance and standard deviation of moving averaged VCR each moving averaged number. From over 25 moving averaged number for measurement points, standard deviation and variance become small and practically constant value. Therefore it is clear that the set of 25 measurement points removes the variability. The measurement area S for one measurement point is expressed by FOV and observation height of spectrometer and CCD camera:

$$S = \pi \times 2.16^2[m^2] \times \tan^2(\frac{22^\circ}{2}) \cong 0.554[m^2] \quad (1)$$

The set of 5×5 measurement points which put out the variety is represented as approximately satellite ground spatial resolution 1km×1km(in this study, NOAA AVHRR), therefore the minimum representative area S' derived from car survey measuremet is shown below:

$$S' = 0.554[m^2] \times 5 \times 5 \cong 13.9[m^2] \quad (2)$$

3.2 Measurement Using Radio-controled Helicopter

We developed the radio-controled helicopter (RC-heli) measurement system. This system has spectrometer, GPS receiver, CCD camera and micro-computer, and it can change the observation height from about 1m to 150m. In this study, the measurement height of RC-heli is about 55m. The result of section 3.1 occasionally may measure the only same gound condition. Therefore we observed the wide range of ground condition using RC-heli system in 30 measurement points. The area S' measured by spectrometer and CCD camera mounted on RC-Heli is calculated with measurement condition:

$$S = \pi \times 55^2[m^2] \times \tan^2(\frac{22^\circ}{2}) \cong 359[m^2] \quad (3)$$

By using this, the variety of measurement value is confirmed whether about 359m^2 area is regarded as one unit or not. CCD camera mounted on RC-Heli takes ground condition such like the car survey system, but it is difficult to calculate vegetation coverage ratio directly because video image has many noise and unclearness in one pixel. Therefore, at first, we conducted simple regression analysis between NDVI and VCR obtained by car survey, and then NDVI obtained RC-Heli survey is substituted for relationship between VCR and NDVI obtained car survey. Calculated simple regression equation is the following:

$$VCR = 1.3537 \cdot NDVI - 0.24867 \quad (4)$$

VCR :Vegetation Coverage Ratio

NDVI:Normarized Difference Vegetation Index

NDVI value obtained by RC-heli system is substituted for the above equation and then we calculated VCR at each points. Figure 6 depicts defference of VCR at each measurement points. Vertical axis shows VCR and horizontal axis shows measurement point number. This diagram expresses small variabirity of VCR at each measurement points. In this case, variance is 0.0006 and standard deviation is 0.024. Therefore, we could confirm that the area measured by RC-heli system in this study is regarded as one unit area. Observed variety of VCR observed by RC-Heli is smaller than that of VCR observed by car survey.

4. Discussion

When we try to get ground data using car survey system with the same variance measured by RC-Heli survey system, the moving averaged number of data should be 31 (see Figure 6.).

$$S' = 0.554[m^2] \times 31 \cong 17.2[m^2] \quad (5)$$

$$359[m^2] \div 17.2[m^2] \cong 21 \quad (6)$$

This result shows that the measurement area of spectrometer and CCD camera mounted on RC-heli is about the 21 times as large as the area measured by car survey. It is better that the area 17.2km^2 which dose not cause vriety is identified as the minimum representative area than 25 measurement points of car survey. Therefore it is said that the minimum representative area for the wide area (1km$\times$ 1km) is about 17.2km^2. And the result of section 4.2 indicates that RC-heli survey system is very useful tool because it can be measured objects which has large variety in the large area all at once.

5. Conclusion

In this study, we could calculate minimum representative area, which is about 17.2km^2 in flat and homogeneous wide grassland in Mongolia (1km×1km), by using car and RC-heli system. The car survey system which has high efficiency of observation needs about two hours for 100 points measurement, but RC-heli system needs 5 minutes for 30 points measurement. It is evident that RC-heli survey is very useful for changeability of incident solor radiance and so on. This system is conducted ground truth efficiently because this system can estimate minimum representative area in the short time by changing observation height. When ground observation and satellite observation are conducted at the same time without changing solor incident radiance, it is very important to shorten the total time of observation. From this point of view, it is also said that RC-heli is very useful tool. Data obtained by using these systems we developed in this study can be used as verification data after atmospheric correction for satellite data.

In future, it is thought to obtain some samples of biomass etc. in the minimum representative area calculated by using method we developed in this study. Moreover, it is also needed to prove representativity of minimum area derived from some vegetation indeces (NDVI etc.) statistically. In order to prove this, it is important to develop the method of acquisition of biomass etc. in small error.

6. References

[1] Yamamoto, H.,Kajiwara, K., Honda, Y.:Car Survey Measurement in Mongolian Grassland, Proceeding of the Symposium of the Japan Society of Photogrammetry and Remote Sensing, 241-244, 1995.(in Japanese)

[2] Yamamoto, H.,Kajiwara, K., Honda, Y.:The Estimation of Vegetation Coverage Ratio by Car Survey --- The Experience in Mongolian Grassland ---, Proceeding of the Symposium of the Japan Society of Photogrammetry and Remote Sensing,241-244, 1996.(in Japanese)

[3] Yamamoto, H., Honda, Y., Kajiwara, K., Okano, C., Huang, S. and Matsuoka, .:The Analysis of Field Data Measured in Grassland for Biomass Monitoring Using Satellite Data, Journal of the Japan Society of Photogrammetry and Remote Sensing, Vol.36, No.4, 1997.(in Japanese)

[4] Honda Y.and Kajirawa K.:Testing of Instant Aero Survey, Proceeding of the International Symposium on "The Role of Remote Sensing for The Environmental Issues in Arid and Semi-Arid Regions", 29-32,1997.

[5] Honda, Y:Grassland Biomass Monitoring using NOAA AVHRR, International Symposium on Remote Sensing on Remote Sensing, EMSEA, KSRS, 31-34, 1994.

[6] Honda, Y.:Ground Truth Database for Global Scale Research-Grassland Biomass Monitoring using NOAA AVHRR and Ground Truth-, Proceedings of the symposium on vegetation Monitoring, 178-186, 1995.

[7] Honda, Y., Kajiwara, K., Kimura, Y.:Ground Truth Image Data for Global Scale Research, Proceedings of International Symposium on Remote Sensing, 140-143, 1995.

[8] Kajiwara, K. and Kimura, Y.:Ground Truth Database for Global Scale Research International Archives of Photogrametry and Remote Sensing, Vol.XXXI, Part B7, 291-297, 1996.

[9] Kajiwara, K.:Instant Aero Surveying, Proceedings of International Symposium on Remote Sensing, 121-124, 1996.

[10] Kajiwara, K. and Kimura, Y.:Ground Truth Database Development, Proceedings of The Interregional Semminar on Global Mapping for Implementation of Multinational Environmental Agreements, 1996.

Table 1. Measurement Condition

Date	14 Aug. 1996	15 Aug. 1996
Time	15:44～17:30	12:05～12:10
Accumulation Count	10	10
Integration Time	0.08 sec	0.16 sec
The Numberof	1024ch	512ch
Spectral Resolution	0.68nm/ch	1.37nm/ch
Observation Angle	Nadir	Nadir
Field of View	Approx. 22 deg	Approx. 22 deg
Sensor Height	2m16cm	Approx. 55m
The Numberof	100 points	30 points



Figure 1. The Appearance of Car Survey System

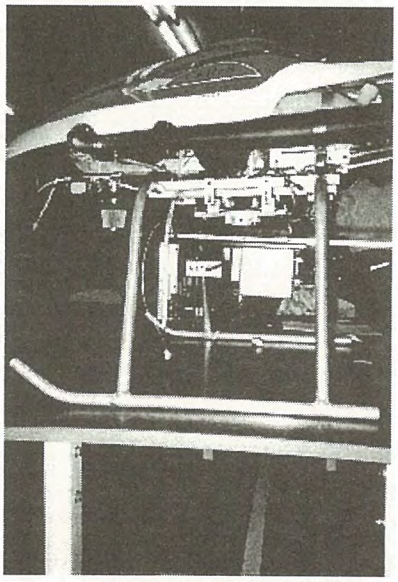


Figure 2 The Appearance of Radio-controled Helicopter System

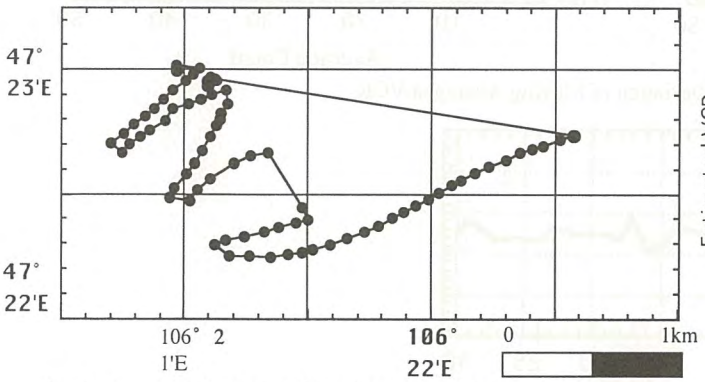


Figure 3. Distribution of Measurement Points by Car Survey

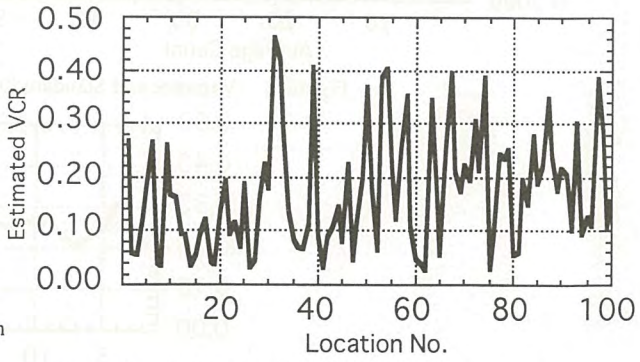


Figure 4. Difference of VCR obtained by car survey

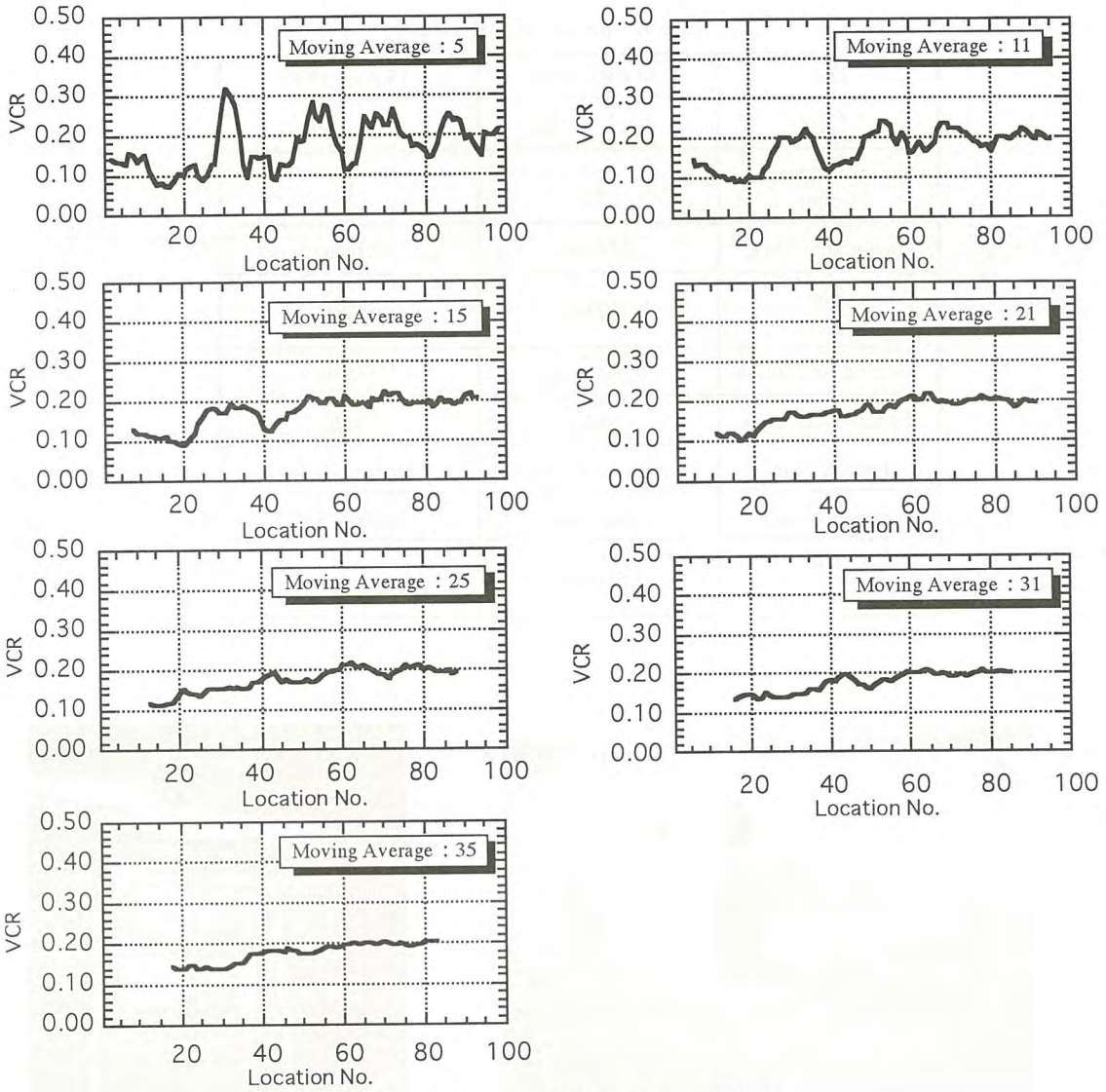


Figure 5. Difference of Moving Averaged VCR

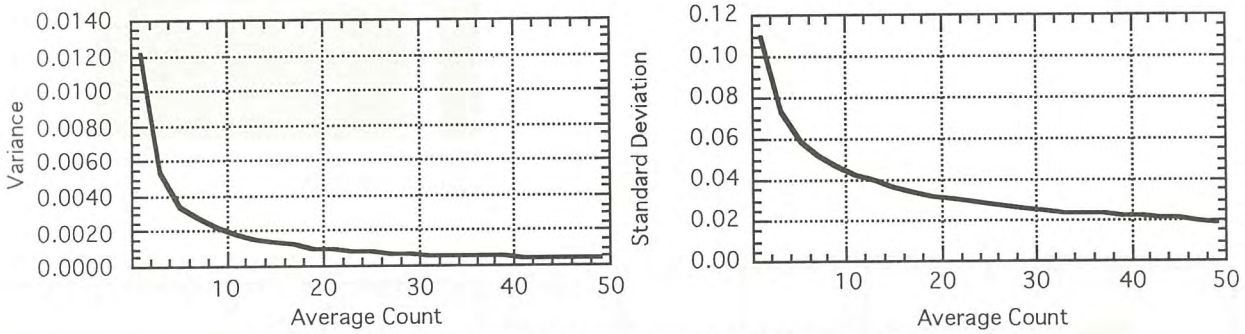


Figure 6. Variance and Standard Deviation of Moving Averaged VCR

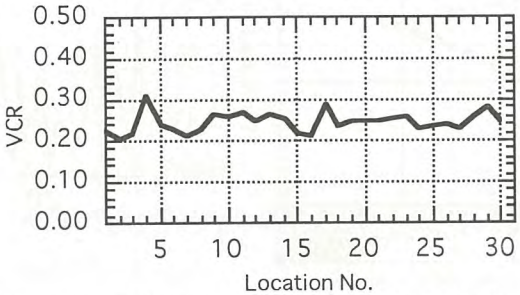


Figure 7. Difference of VCR Obtained by RC-heli survey

Retrieval of Cloud Physical Parameters on a Global Scale using NOAA/AVHRR

Kazuaki Kawamoto and Teruyuki Nakajima
Center for Climate System Research, University of Tokyo
4-6-1 Komaba, Meguro-ku, Tokyo 153, Japan

1. Introduction

Clouds actually occupy about 60% coverage of the earth's surface and play a considerably important role for formation of the climate through radiative processes. Their large variations both in horizontal and vertical extent make situations more complex. In order to evaluate the effects of clouds on the earth's radiation budget, it is important to observe globally not only the macroscopic variables, such as cloud amount and height, but also cloud optical and microphysical properties such as cloud optical thickness and effective particle radius (hereafter cloud physical parameters), which are more closely related to the radiation budget.

Motivated by this background, we have developed a retrieval algorithm which can be expanded into global scale based on Nakajima and Nakajima (1995) for cloud physical parameters .

2. Retrieval Principles

We use cloud-reflected solar radiation for retrieving cloud physical parameters. The fact that the cloud optical thickness is mainly a function of channel-1 (visible, ch1. 0.63 μm) signal, while the effective particle radius is mainly a function of channel-3 (near-infrared, ch3. 3.73 μm) signal is applied to analysis. Both signals, however, contain undesirable components for determination; in ch1, surface reflection, in ch3, surface reflection and thermal emissions from the ground, the cloud layer, and the atmospheric layers. These undesirable components must be removed from observed signals. Moreover, water vapor absorption affects ch3 signal, while it is negligible in ch1.

In actual data analysis, we adopted a look-up table (LUT) method. LUT is sets of solutions of radiative transfer equations under various conditions of geophysical and angular parameters, such as cloud optical thickness, effective particle radius, cloud top height, cloud geometrical thickness, satellite zenith and solar zenith and relative azimuth angles. As mentioned above, since ch3 has water vapor absorption, LUT for ch3 is made to be feasible for various water vapor amount. So our LUT, or algorithm is independent of atmospheric conditions. It means its applicability of expanding into global scale analysis. The ancillary data such as temperature, humidity, and geopotential height are from NCEP reanalysis objective analysis data. Observed radiance corrected and theoretical radiance stored in LUT are compared, and an iteration is continued until the optimal solutions will be obtained.

3. Comparison with In situ measurements

In order to verify the accuracy of the algorithm, we compare satellite retrievals to which this algorithm is applied with in situ measurements synchronous to satellite observations.

We have surveyed in situ cloud microphysical measurements with aircrafts and balloons conducted from 1981 to 1992, and among them, the ones whose location and time had been close to satellite passage were only selected.

Fig.1 shows the result of the comparison. Within satisfactory errors are retrieved the effective particle radii of both stratiform and convective clouds. As error sources in analyzing actual satellite data, we can cite cirrus contamination, partial cloud cover, and cloud inhomogenity argued in Han et al.(1994), sensor discretization and calibration uncertainties summarized in Pincus et al.(1995), slight gaps between satellite imagery and in situ measurement point temporally and spatially, and uncertainties of meteorological parameters taken from the ancillary data.

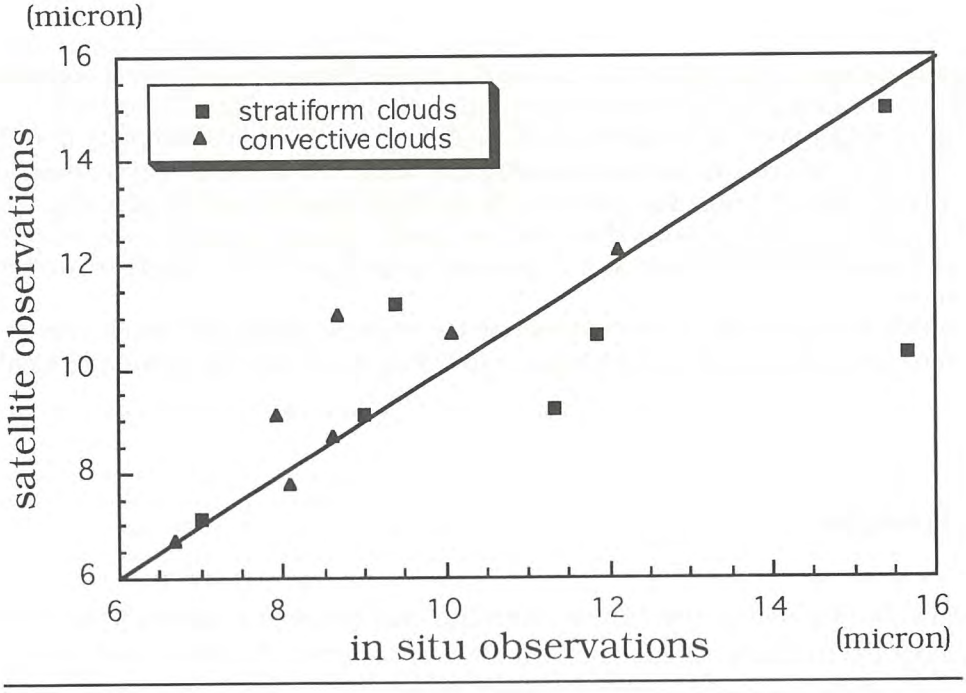


Fig.1

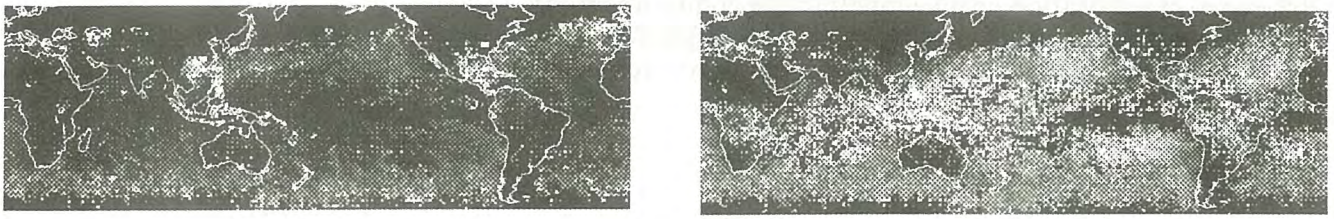
4. Global Analyses

We have performed global analyses of cloud physical parameters of Jan., Apr., Jul., and Oct. in 1987. Fig. 2 shows maps of cloud physical parameters in Jan. and Jul., and Fig.3 illustrates the latitudinal distribution of cloud physical parameters, along with Han et al. (1994) 's result, which analyzed also 1987 case. Since these figures are monochromatic, see Kawamoto et al. (under preparation) in datail.

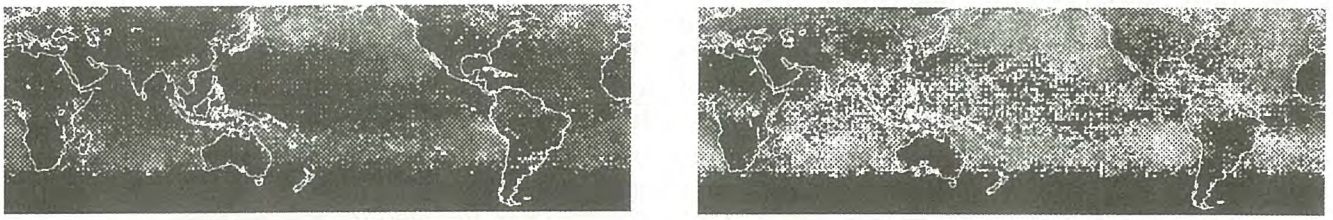
As for cloud optical thickness, differences of summer stratus clouds, which occur around 40~50 (deg.) over the summer hemispheric ocean, and optically thick clouds due to ocean upwelling regions such as off Peru between Jan. and Jul. are apparent. While as for effective particle radius, generally the values over ocean are larger than those of land, suggesting difference of aerosol abundance. In coastal regions, even over ocean, the values are similar to those of land. This may be caused by continental airmass flown into ocean. The seasonal variation over equatorial Africa and Amazon basin can be explained by the difference of rainfall, since CCN (cloud condensation nuclei) removal due to rainfall (precipitation scavenging) would increase cloud droplet radius. GPCP(Global Precipitation Climatology Project) results (not shown) support this idea.

1987

January



July



Cloud Optical Thickness

Effective Particle Radius



Fig. 2

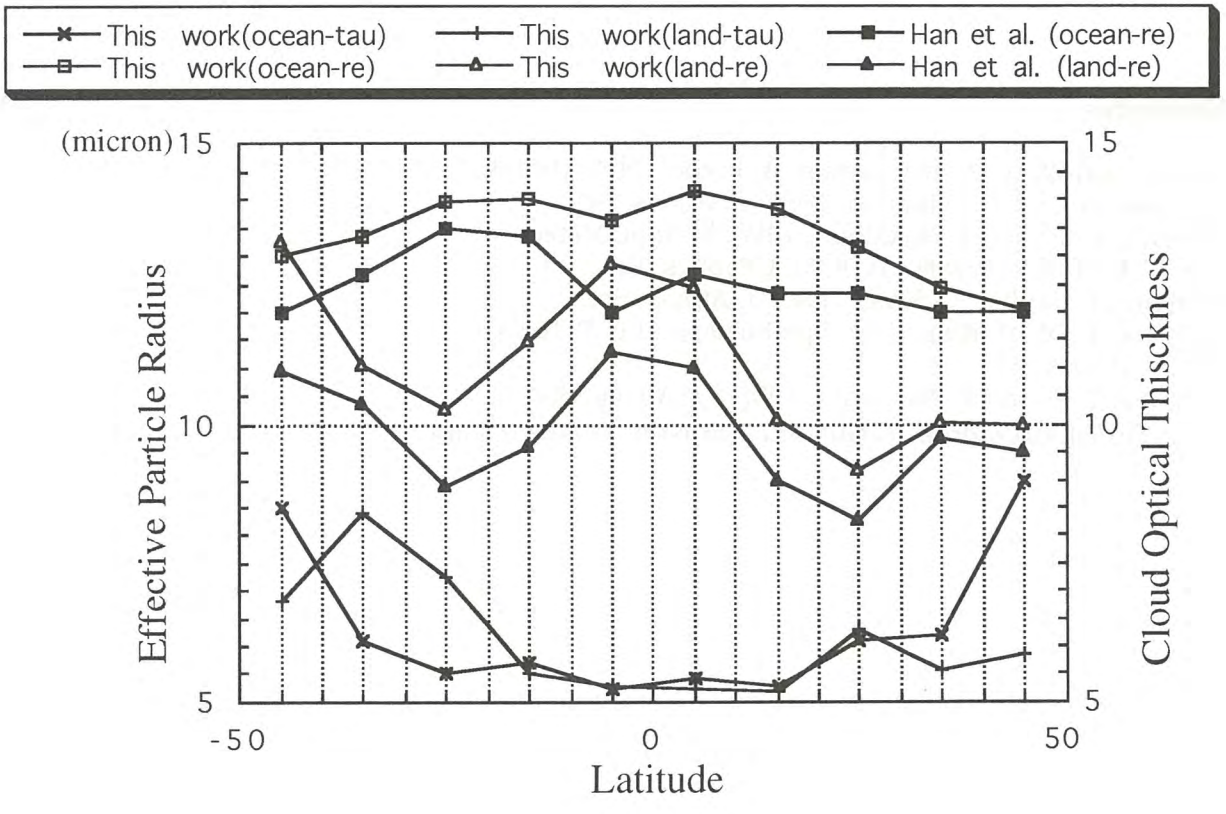


Fig. 3

From Fig.3 about effective particle radius, Han et al.'s result and ours are very similar in shapes, but ours is larger by about 1.5 μm than theirs. Han himself said it caused by the difference of calibration coefficients (private communication).
About cloud optical thickness, the values in higher latitudes tend to be larger. This feature may be caused by 3-D effect of clouds which are remarkable in larger solar zenith angles. (Loeb and Davies, 1996)

5. Concluding Remarks

We have developed the algorithm which is capable of global scale analysis of cloud physical parameters, and performed global analyses in a seasonal time scale. Some features of cloud physical parameters were described such as ocean-land contrast, near coastal regions influenced by different characteristics of airmass, and seasonal variation of effective radius caused by rainfall difference. Then the result of Han et al. (1994) and our result were compared. Their result is smaller by 1.5 μm than ours.

Recently, the research of aerosol-cloud interactions with satellite remote sensing has begun (e.g. Kaufman and Nakajima, 1993) . Our algorithm can be used for the purpose effectively combined with aerosol optical properties from Higurashi and Nakajima (1998).

Acknowledgement

The authors are grateful to Dr. C. J. Tucker at NASA/GSFC and Dr. R. Imasu at NIRE for providing AVHRR/GAC data, and Mr. A. Sinpo at Univ. of Tokyo for handling NCEP reanalysis data. Aircraft measurements data were provided by Meteorological Research Institute/Aircraft measurements group.

References

Han, Q., and W. B. Rossow, and A. A. Lacis, 1994: J.Clim.
Higurashi, A. and T. Nakajima, 1998: J. Atmos. Sci.
Kaufman, Y. J., and T. Nakajima, 1993: J. Appl. Meteor.
Loeb, N. G. and R. Davies, 1996: J. Geophys. Res.
Nakajima, T., and M. D. King, 1990: J. Atmos. Sci.
Nakajima, T., M. D. King, J. D. Spinhirne, and L. F. Radke, 1991: J. Atmos. Sci.
Nakajima, T. Y. and T. Nakajima, 1995: J. Atmos. Sci.
Pincus, R., M. Szczodrak, J. Gu, and P. Austin, 1995: J.Clim.

Diurnal variation of cloud cover on 1996 from GMS-5 images

Itaru OKADA, Tamio TAKAMURA, Kiyofumi OGINO, and Hideki TAMARU
(Center for Environmental Remote Sensing, Chiba University)

1. Introduction

Cloud is an important component for global and local climate. Its distribution and variation express an integration of atmospheric conditions. Cloud also directly affects to local climate through radiative process. Final purpose of the present study is to estimate radiative flux at the surface from geostationary meteorological satellite images. Diurnal variation of radiative flux has large amplitude. Hence it is important to make nature of the variation of clouds clear.

In the present study, 1 hourly cloud cover data, which is processed from GMS-5 (Geostationary Meteorological Satellite) of Japan Meteorological Agency, is introduced. As famous cloud data set, ISCCP (International Satellite Cloud Climatology Project) is distributing global 3 hourly data. However it is more valuable to produce 1 hourly data, because incoming solar radiation changes quickly. And the ambiguity of plus minus 1.5 hour is often insufficient for meteorological research on local phenomenon.

2. Data and analysis

GMS-5 image data is received at Institute for Industrial Sciences, University of Tokyo, and is processed by Prof. Kikuchi at Kochi University. Only 10.5 - 11.5 micro meter infrared window channel is used for the present study, though GMS-5 has 3 infrared channels, because this work will be extend to the past data of GMS-3 and GMS-4, which have only one infrared channel.

Two formats for GMS-5 data are used in the present study, because the data had been supplied temporally with different format. One format covers from 70 degree N 70 degree E to 70 degree S 150 degree W (140 square degree), the other is from 60 degree N 80 degree E to 60 degree S 160 degree W (120 square degree). This data also includes some geometrical deformations. These situations will be improved soon. Prof. Kikuchi has released corrected data recently.

NCEP reanalysis data is used for deciding air temperatures at 400 hPa and 700 hPa, that is produced by US National Center for Environment Prediction. It is handled by Mr.Sinpo at University of Tokyo in Japan.

Northern hemisphere weekly snow cover and sea ice extent is also used, that is supplied

by US National Snow and Ice Data Center.

As cloud determination method, following procedures are applied. This method is almost same with infrared part of ISCCP cloud detection (Rossow and Garder, 1993). The stages are composed of 3 steps.

a. Picking up clear sky pixels from temporal and spatial variation analysis

The pixel is compared with surrounding pixels in the same day and also compared with same pixel in the day before and after.

b. Screening clear sky pixels and deciding clear sky radiation temperature.

The extremely low values are rejected. If averaged clear sky radiation temperature for some time series is too lower than maxima of them, the average is contaminated by cloud pixels. In such case, maxima is used as clear sky temperature with some negative bias. The biases belongs to surface conditions, open sea, sea ice, high land, snow, and other land covers. The clear sky radiation temperature is decided every 5 days at every hour.

c. Comparing each pixels with the clear sky radiation temperature.

If radiation temperature of a pixel is too lower than the clear sky radiation temperature, it is decided as cloudy pixel. The threshold belongs to surface conditions as above.

3. Results

a. Geographycal distribution of cloud cover and clear sky radiation temperature

Fig. 1 shows that distributions of total cloud cover each season. In South-east Asia, cloud activity is most prominent. ITCZ (Intertropical convergence zones) are also clearly seen. Contrast between summer and winter is remarkable on the Asian continent. Clouds due to cold serge is dominant near Japan islands on winter. Cloud stays on Sichuan basin through the year.

Secondly, cloud pixels are classified by its radiation temperature, although broken cloud, cirrus, or much water vapor in tropical region may make error. The radiation temperatures are divided into 3 layers; the low layer is below 700 hPa, the middle layer is above 700 hPa and below 400 hPa, and the high layer is above 400 hPa. Air temperature at 400 hPa and 700 hPa are given by climatology of NCEP reanalysis data. The figures of each levels are not shown.

In the high layer, ITCZ and Polar front are shown clearly through the year. Convectional band extends from the Asian Continent to Japan Islands in July. In middle layer, it should noted that some parts of the layer is covered by clouds in the high layer. Therefore, some area looks less cloud cover than real condition. Cloud covers on Sichuan basin are clearly shown through the year. In the low layer, cloud cover shows large contrast between ocean and land. More strict threshold was applied to land area than ocean area, therefore the

result shows fewer cloud cover in land area. ISCCP results show very similar pattern. This problem may induce unnatural radiation balance between land and ocean.

Thirdly, clear sky radiation temperature map was created. This figure is not shown. This map composed of rest of all the pixels without cloudy ones. It does not include only true clear pixel, but may include cloudy pixels which were not discriminated as cloud. For example, convectional area in the bay of Bengal shows too low temperature near 260 K as clear sky. And water vapor absorption and decreasing surface emissivity may make large effects to the temperature. Therefore, edge of the map shows lower value than the center. However it should be noted here that these figures can show large seasonal variations on the continents and small variations on the ocean. It means this map can be used as a kind of index of surface temperature.

b. Diurnal variations of cloud cover and clear sky temperature

Diurnal variations of cloud covers and clear sky radiation temperature are described at 4 regions. These regions are Mongol area as semi-arid surface (38N100E-43N110E), the Northwestern Pacific as ocean surface (35N150E-40N160E), Hua-Bei plane as vegetated surface (32N114E-37N117E), and Australian desert (18S130E-23S140E).

In Mongol area, diurnal variations of total cloud cover show peaks in afternoon in every seasons. These peaks are affected from cloud covers in the low layer. The reason is derived to be effects from diurnal variation of vertical structure of air temperature profile, and the tendency is also certified in ISCCP data. In daytime, the surface temperature is higher than that in night , so it makes cloud detection easier. However, in July, total variation includes cloud in the high layer. The high layer cloud has peak in the evening.

In the Northwestern Pacific, the variations of cloud cover are very stable. In April, cloud in the high layer is decreasing in morning and increasing in afternoon. Summer depression in July may be caused from migration of the extra-tropical high.

Fig. 2 shows the diurnal variations of cloud cover at Hua-Bei plane. The variations are very stable in July. The variations in the low level have maximum in afternoon in the other seasons. These maximum are considered to be same case like Mongol. Diurnal variation of total cloud cover in January is characteristic. The variation in the middle layer leads the total variation. In April, the high layer shows fewer cloud cover in early morning. In October, the total variation increases in afternoon, and more remarkably in evening, while the low layer does not contribute.

In Australian desert, the diurnal variation in January is very remarkable in the low layer. Depression of cloud cover in the middle layer in daytime may emphasis to increase cloud cover in the low layer. In April there is also the depression. While, there

looks really no cloud in July.

For clear sky radiation temperature, diurnal variations in each seasons were also described like cloud cover. In the Northwestern Pacific, the diurnal variation of clear sky radiation temperature is very stable. The variation has maximum in early afternoon and stable minimum in 6 - 7 o'clock at local time in Australian Desert through the year. While The variation in Mongol as semi arid area has maximum in early afternoon and minimum through the night. The variation in Hua-Bei plane shows different variations between summer and other seasons. In July it looks stable like that in the ocean, and in other seasons it is like that in Mongol. It is derived that much precipitation in July and vegetation opposed to change the surface temperature quickly.

4. Concluding remarks

Hourly cloud data set from GMS-5 images is produced. This data set shows distribution and variation of cloud cover in the middle layer and the high layer well. The cloud cover in the low layer still remains problem. This problem should be solved in order to use this data for radiation estimation. Hourly changed threshold for cloud determination may improve the problem.

Regional description about diurnal variation of cloud cover and clear sky radiation temperature also shows interesting properties. Physical explanation should be given from further studies.

To extend this analysis to longer term including GMS-3 and GMS-4 will show regional properties of interannual variations of cloud cover.

The product of cloud covers in the present study will open to public in near future.

References

Bergman, J.W. and M.L. Salby, 1996: Diurnal variations of cloud cover and their relationship to climatological conditions. J. Climate, 9, 2802-2820.

Rossow, W.B. and L.C. Garder, 1993: Cloud detection using satellite measurements of infrared and visible radiances for ISCCP. J. Climate, 6, 2341-2340.

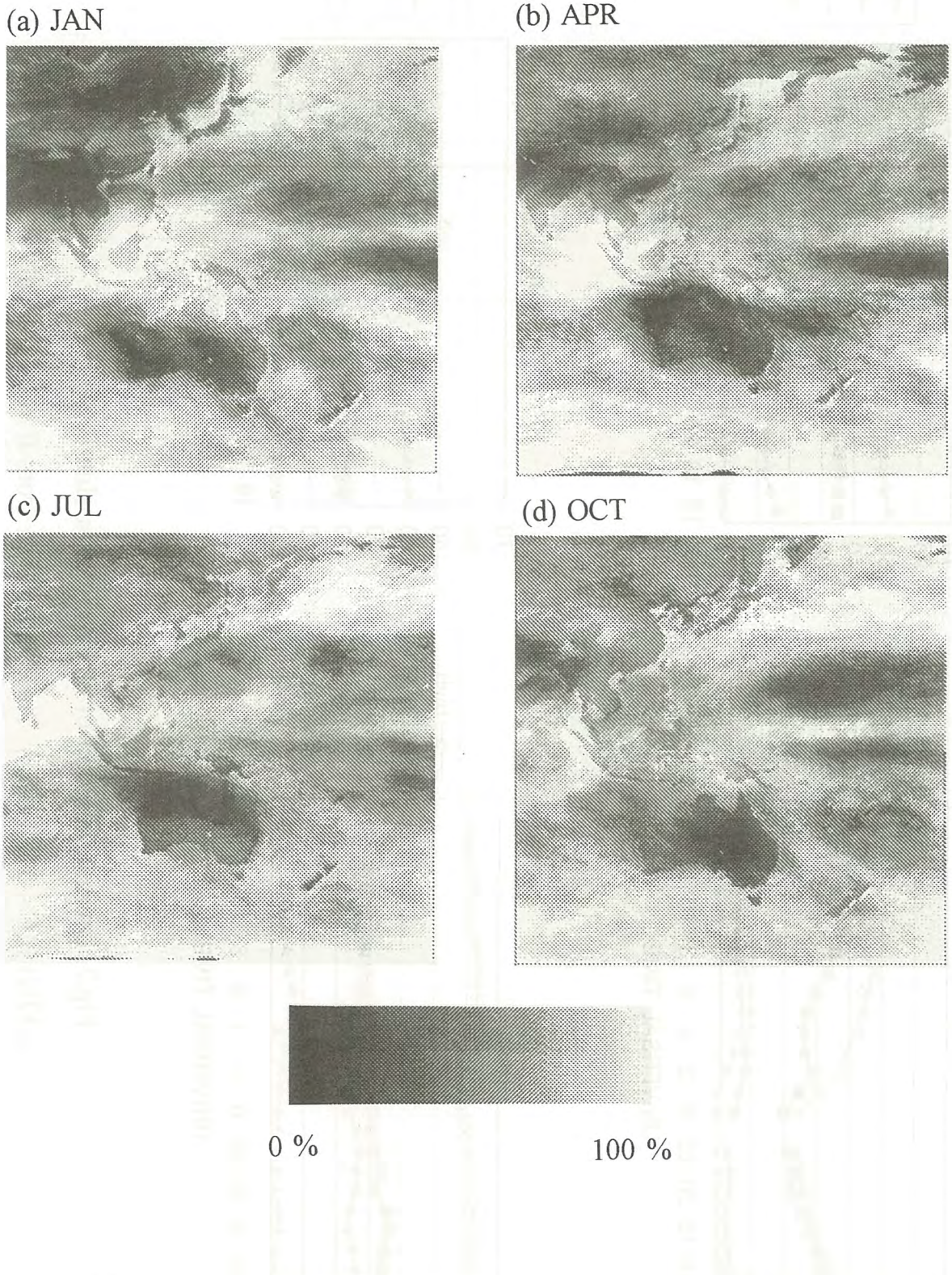


Fig. 1. Total cloud cover of (a) January, (b) Feburary, (c) July, and (d) October.

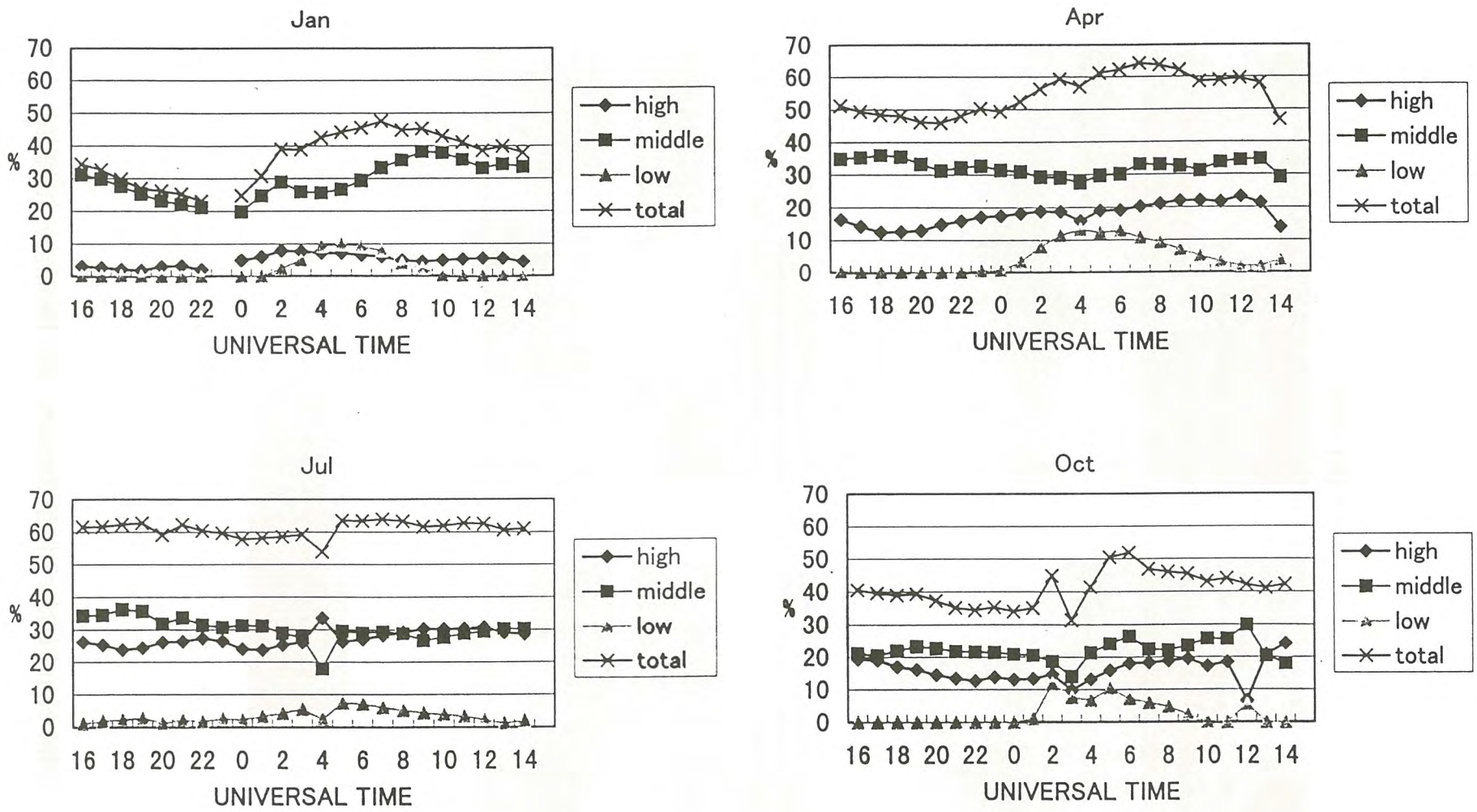


Fig.2. Diurnal variation of cloud cover in Hua-Bei plane (32N114E - 37N117E). Time series start from 0 hour at local time.

IV. Atmospheric Correction over Land and Ocean

Correction methods for aerosol and thin cirrus effects on remote sensing

Yoram J. Kaufman

NASA/Goddard Space Flight Center, code 913
Greenbelt, MD 20771

ABSTRACT

Aerosol and cirrus clouds affect the reflected solar radiation detected by satellite sensors. Both aerosol and cirrus increase the apparent reflectance over dark surfaces such as vegetation in the visible channels by scattering sunlight to the sensor. Aerosol reduces the apparent reflectance over bright surfaces (e.g. vegetation and soils in the near IR) by absorbing reflected solar radiation on its way down to the surface and on its way up to the sensor. Correction, removal or avoidance of the atmospheric effects due to aerosol and thin cirrus clouds (we cannot correct for the effect of thick cirrus) can take several pathways:

- Direct correction for aerosol and thin cirrus: The effect of aerosol or cirrus on radiation is determined first and then used for direct correction of the measured radiance to derive the surface spectral reflectance.
- Indirect correction for aerosol: No direct correction is applied but the remote sensing functions designed to find the surface properties (e.g. the NDVI) are redesigned in order to minimize their dependence on the aerosol presence.
- Circumvention of the aerosol effect: In case of heavy aerosol, switching the remote sensing investigation to longer wavelengths, where the aerosol is transparent and has only a small effect, while the details of the surface cover are still evident.

We shall review these techniques and bring some new insight on their applications and limitations, mainly in light of the launch in the summer of 1998 of the MODIS instrument on the NASA Earth Observing System with an array of spectral channels that will allow these correction processes.

Introduction

With the launch of the Earth Observing System (EOS) AM in summer 1998, and parallel efforts in Japan (ADEOS) and Europe (ENVISAT) we are entering a new era in studying the earth as an interrelated system rather an assembly of independent parameters. The Earth Observing system will have an unprecedented spectral and spatial remote sensing capability with scientific instruments that were designed, characterized, and calibrated for the purpose. For example MODIS on EOS-AM will have 5 spectral bands designed for aerosol and land remote sensing in the solar spectrum with resolution of 500m (470 nm, 550 nm, 1.2 μm, 1.6 μm, 2.1 μm) and 2 additional bands with resolution of 250m (650 nm and 860 nm). MODIS will

have a special channel at 1.375 μm for highly sensitive remote sensing of cirrus clouds that together with shorter wavelength channels can be used to derive the cirrus radiative effects and to correct for their presence.

One of the main reason for this large investment in remote sensing is the recognition that climate change research based on the effects of greenhouse gases alone is not sufficient to understand climate change and we need to bring in elements with high spatial and temporal variability like aerosol, changes in land use, clouds and water vapor and ocean productivity. The only way to measure these variable effects is from satellites that can provide daily high resolution data. In this respect the introduction of the new satellite systems starts a new stage in the 160 year old climate change research, from the first recognition by Fourier in 1824 that greenhouse gases in the atmosphere can warm the surface, to the first calculations of the effect of doubling of CO_2 and the water vapor feedback by Arrhenius in 1896, based on the IR spectrum of CO_2 and water vapor derived from Langley's precise measurements of the moon IR emission (see review by Ramanathan and Vogelmann, 1997). Presently it is recognized that the greenhouse gases by themselves cannot solve the climate problem and highly varying processes have to be studied. Satellites are uniquely suitable for studying spatially highly variable processes, but they require high accuracy including accurate derivation of the surface properties.

The atmosphere affects remote sensing of the earth surface from space by scattering and absorption by aerosol particles (e.g. micron size dust particles or submicron pollution particles suspended in the air) and molecules in the atmosphere. The effect of aerosol and molecular scattering is stronger in the shorter solar wavelengths where the particle size is similar to the radiation wavelength. Absorbing gases (e.g. water vapor, ozone and oxygen) absorb in specific spectral bands (e.g. Tanré et al., 1992). Aerosol scattering is broader, it increases the apparent surface reflectance over dark surfaces while aerosol absorption reduces the apparent brightness of bright surfaces (Fraser and Kaufman, 1985; Kaufman, 1989). While the concentrations of atmospheric gases do not vary significantly, the concentration of aerosol and water vapor can vary by more than an order of magnitude.

Correction for the effect of molecular scattering, ozone and oxygen absorption is important, since even though their concentration does not change substantially from climatologic values, their effect on radiation detected by the satellite and on the apparent surface reflectance will vary as a function of the view and illumination direction (e.g. Tanré et al., 1992). The effect of water vapor absorption is very significant for the NOAA-AVHRR near IR channel, that is used together with the visible channel to derive the normalized vegetation index (NDVI) used to monitor the dynamics of global vegetation (Tucker et al., 1985; Holben, 1986; Tanré et al., 1992). The newly designed space instruments, e.g. MODIS, have narrower channels that are almost not sensitive to water vapor absorption. Review of the aerosol

properties on remote sensing is given by Kaufman (1989), review of the effect of aerosol and gases on remote sensing from AVHRR by Tanré et al. (1992). The detection of cirrus clouds by MODIS was introduce by B.-C. Gao (e.g. Gao et al., 1996).

Direct correction for the aerosol effect

Direct correction of the aerosol effect is based on determination of the aerosol opacity (expressed by the optical thickness and the resulting path radiance) from specific pixels in the image and applying it to correct the same image (Kaufman and Sendra, 1988; Holben et al., 1992; Vermote et al., 1997). Once the optical thickness is determined, the atmospheric correction can proceed using inversion of the basic radiative transfer equation (e.g. Vermote et al., 1997). To determine the aerosol optical thickness, the surface reflectance, ρ, has to be small and known with good accuracy (e.g. within uncertainty of $\Delta\rho=\pm 0.005$). Vegetated surfaces are dark in the red and blue parts of the spectrum (Kaufman et al., 1997a) and their reflectance can be estimated using their reflectance in the mid-IR (2.15 or 3.75 μm - Kaufman and Remer, 1994; Kaufman et al., 1997b). This method of using the mid-IR reflectance for correction in the visible channels, is possible for two reasons:

- Aerosol is mostly transparent in the long wavelengths, because the optically active particles are small in case of biomass burning or urban/industrial emissions. For dust the particles are large but their refractive index is significantly smaller in the mid IR reducing their backscattering (see Fig. 1) and atmospheric effect at 2.1 μm.

- There is a good correlation between the surface reflectance in the visible channels and the mid-IR channels (Kaufman et al., 1997a). The correlation is caused by shadows introduced by vegetation in all the wavelengths. Also while vegetation introduces chlorophyll absorption in the red and blue channels, it introduces liquid water absorption in the mid-IR. Apparently the vegetation chlorophyll and liquid water content are correlated to some extend. In general it was found in several ecosystems that the surface reflectance in the red (0.66 μm) is half of that at 2.1 μm for dark surfaces with reflectance at 2.1 less then 0.15 (Kaufman et al., 1997a).

To derive the aerosol optical thickness from the satellite measured radiance and to use it in atmospheric correction, it is important to apply the same aerosol model in both cases and to have a model that represent the total column of ambient aerosol. For this purpose the aerosol model has to be based on inversion of sky and sun radiance measured from the ground (Kaufman and Holben, 1996; Kaufman and Tanre, 1996). Such model was developed recently for smoke and urban/industrial aerosol (Remer et al., 1996). The model is dynamic in the sense that the composition of the aerosol modes varies with the aerosol loading represented by the aerosol

optical thickness. Table 1 summarizes these models. The models are given graphically in Fig. 2.

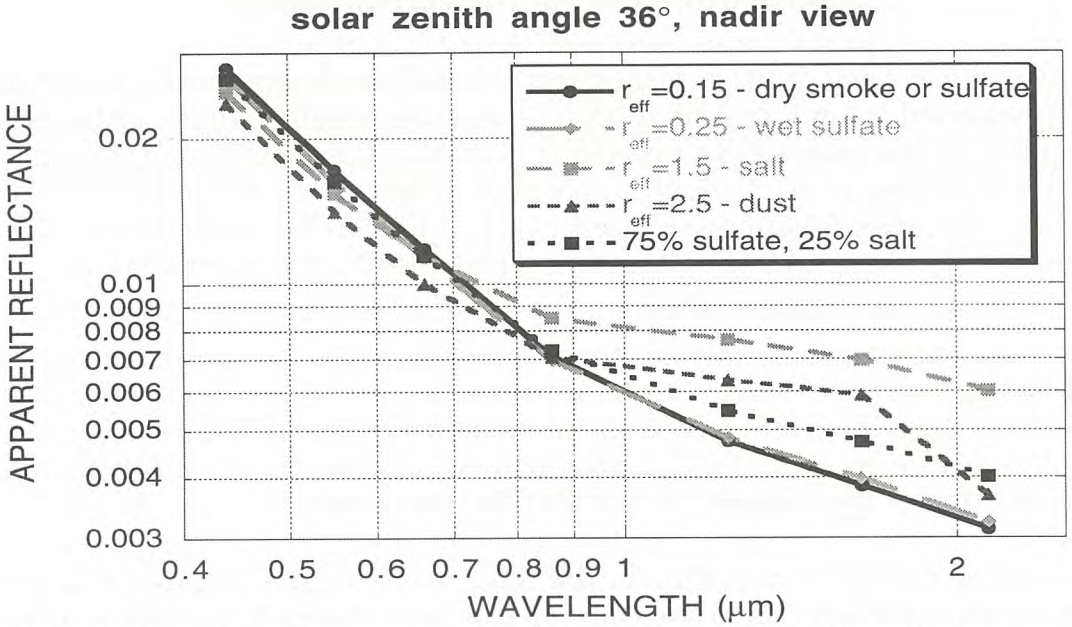


Figure 1: Typical spectral radiance (normalized to apparent reflectance by multiplying the radiance by π/F_0 - F_0 is the solar flux) for aerosol optical thickness of 0.2 at 0.86 μm over a black surface, for several aerosol types: small accumulation mode particles that correspond to smoke or dry urban/industrial aerosol ("sulfate"); wet larger "sulfate" particles, salt, dust, and a mixture of sulfate and salt (Tanré et al., 1997). Note the reduction with wavelength of the apparent reflectance for all aerosol types. Most aerosol types have a very small effect on the apparent reflectance at 2.1 μm due to small particle size (smoke and sulfates) or small refractive index (dust).

Indirect corrections

In the direct correction for the aerosol effect, the measured radiances is directly corrected for the aerosol effect by deriving the surface reflectance from the measured radiance for the measured aerosol loading and optical properties. In the indirect corrections, a remote sensing function, designed for remote sensing of the surface properties (such as the NDVI used for remote sensing of vegetation - Tucker et al., 1985) is redefined in a new form that minimizes the dependence on the aerosol loading. The aerosol loading and optical properties are no longer needed. One such function is the Atmospheric Resistant Vegetation Index (ARVI) that replaces the red channel used in the NDVI, with a combination of the red and blue channels (Kaufman an Tanré, 1992; 1996). This redefinition of the NDVI as ARVI retains a similar information about the surface properties while being significantly less sensitive to the aerosol effect. We can demonstrate the ability of ARVI to reject the aerosol effects with the following simple calculations. The NDVI is defined by the

normalized difference between the apparent reflectance of the surface at 0.86 μm, ρ_{86}, and that at 0.66 μm, ρ_{66}:

$$NDVI = \frac{\rho_{86} - \rho_{66}}{\rho_{86} + \rho_{66}}.$$

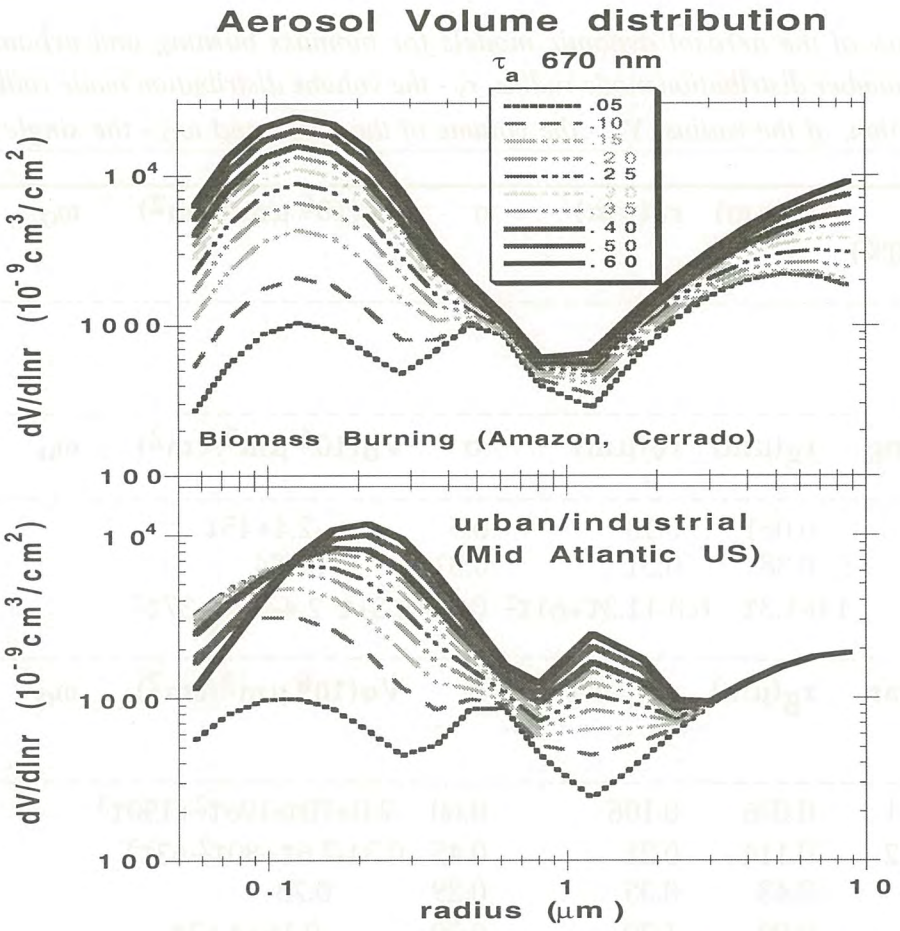


Fig. 2: Aerosol volume distribution for the aerosol models derived from AERONET 1993 deployments, in the Amazon - smoke aerosol and in the Mid Atlantic region of the US - industrial/urban aerosol (Remer et al., 1996). The modes are for: r<0.3 μm - accumulation mode (organic smoke or sulfates); for 0.3 μm<r<0.8 μm stratospheric aerosol; for 0.8 μm<r<2.5 μm maritime salt particle mode; for 2.5 μm<r the coarse particle mode.

The apparent reflectance is the radiance measured in the top of the atmosphere, L, normalized to reflectance units ($\pi L/F_o\mu_o$) using the solar spectral flux F_o and the cosine of the solar zenith angle μ_o. In this definition the aerosol effect can double the apparent reflectance of vegetation at 0.66 μm for moderate aerosol loading. Therefore a new function is defined, ARVI, based on the same principle of remote sensing of vegetation as NDVI, but replacing the problematic apparent reflectance at

0.66 μm with a corrected reflectance:

ρ_{66} --> $\rho_{RB} = 2\rho_{66} - \rho_{47}$, and therefore: $ARVI = \frac{\rho_{86} - \rho_{RB}}{\rho_{86} + \rho_{RB}}$,

Note that the apparent reflectances of ARVI are defined after corrections for molecular scattering (Kaufman and Tanré, 1992).

Table 1: Summary of the aerosol dynamic models for biomass burning and urban/industrial aerosol. r_g - the number distribution mode radius, r_v - the volume distribution mode radius, σ - the std. of the logarithm, of the radius, V_O - the volume of the mode and ω_O - the single scattering albedo

continental aerosol (RH=70%)	**r_g(μm)**	**r_v(μm)**	**σ**	**$V_o(10^6\ \mu m^3/cm^2)$**	**ω_o**
accumulation					
coarse					
biomass burning	**r_g(μm)**	**r_v(μm)**	**σ**	**$V_o(10^6\ \mu m^3/cm^2)$**	**ω_o**
accumulation	0.061	0.13	0.5	$-2.4+45\tau$	
stratospheric	0.38	0.51	0.31	0.984	
coarse	$1.0-1.3\tau$	$6.0-11.3\tau+61\tau^2$	$0.69+0.81\tau$	$2.4-6.3\tau+37\tau^2$	
industrial/urban aerosol	**r_g(μm)**	**r_v(μm)**	**σ**	**$V_o(10^6\ \mu m^3/cm^2)$**	**ω_o**
accumulation 1	0.036	0.106	0.60	$-2.0+70\tau-196\tau^2+150\tau^3$	
accumulation 2	0.114	0.21	0.45	$0.34-7.6\tau+80\tau^2-63\tau^3$	
stratospheric	0.43	0.55	0.29	0.73	
salt	0.99	1.30	0.30	$-0.16+4.12\tau$	
coarse	0.67	9.50	0.94	1.92	

Why should introduction of the blue channel, heavily contaminated by aerosol reduce ARVI dependence on the aerosol effect? The main reason ARVI is useful is that the aerosol decreases with wavelength while vegetation reflectance is unchanged and soil reflectance increases with wavelengths. Consider a representative case of aerosol with the aerosol effect in the blue twice of that in the red. The effect of aerosol at 0.86 μm is considered to be negligible due to net zero balance between the aerosol scattering and absorption effects above the bright

surface. We assume the vegetation reflectance to be the same in the red and blue channels. Therefore aerosol causes the following transformations:

$\rho_{66} \Rightarrow \rho'_{66} = \rho_v + 0.02$, $\rho_{47} \Rightarrow \rho'_{47} = \rho_v + 0.04$, $\rho_{86} \Rightarrow \rho'_{86} = \rho_{86}$

and therefore:

$\rho_{RB} \Rightarrow \rho'_{RB} = \rho_v$ is unchanged and

ARVI ==> ARVI' = ARVI is also unchanged

The transformation would change NDVI:

$NDVI = (\rho_{86} - \rho_v)/(\rho_{86} + \rho_v) \Rightarrow NDVI' = (\rho_{86} - \rho_v + 0.02)/(\rho_{86} + \rho_{66} + 0.02)$

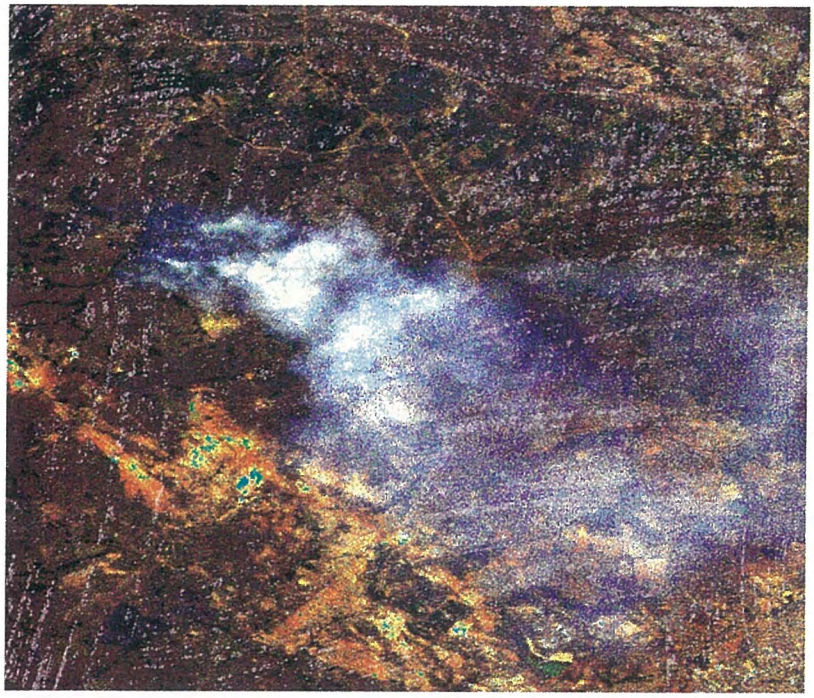
While NDVI changed, ARVI is not influenced in this case by the aerosol presence.

Avoiding the aerosol effect- spectrally

Alternative technique to eliminate the aerosol effect instead of the atmospheric direct or indirect corrections is avoidance of the atmospheric aerosol effect by using wavelengths longer than 1 micron, where the aerosol effect is minimal. In the range of 1.2-1.6 μm the land surface is bright, and the aerosol opacity is smaller then in the visible wavelengths. Therefore the net aerosol effect on the apparent surface reflectance is very small (Fraser and Kaufman, 1985; Kaufman et al., 1997a). At 2.1 μm the aerosol effect is very small even for dark surfaces (see Fig. 1). The use of spectral bands beyond 1 μm for remote sensing of vegetation was not demonstrated in general but its capability is shown in Fig. 3. Here a heavy smoke covering the region around Cuiaba, Brazil prohibits the surface observations in an otherwise very clear image. A color image in the longer wavelengths depicts clearly the river, vegetation, bare soils and burn scars and is almost completely independent of the presence of the smoke.

Correction for cirrus clouds using the 1.37 μm channel

Remote sensing in the solar channels traditionally avoided the water vapor absorption bands looking for atmospheric windows to observe the land, ocean, aerosol and clouds. But absorption bands also provide valuable information, in a similar way to the applications of absorption bands in the IR. The 0.89 -0.96 μm water absorption region is used on POLDER and MODIS instruments on ADEOS and EOS respectively for remote sensing of total precipitable water vapor. This technique uses the reflected sunlight that travels through the atmosphere to the surface and back to space through the water vapor to measure the total precipitable water vapor concentration in the vertical column (e.g. Kaufman and Gao, 1992). The 1.375 μm strong water vapor absorption band, discovered by Bo-Cai Gao and adopted for MODIS (Gao et al., 1996) will be used mainly to derive the reflective properties of cirrus clouds and to correct for their optical effects on remote sensing of land, ocean, aerosol and low altitude clouds (Gao et al., 1998). Figure 4 demonstrates this remote sensing application. While the atmospheric window at 0.65 μm allows the observation of the land, ocean and the cirrus clouds, the opacity of the lower troposphere at 1.375 μm due to the strong water vapor absorption, does not allow light to penetrate to the surface and we observe only scattered light from higher altitudes by the cirrus clouds. If the cirrus clouds would not have been present the image would be black. This information can be used to subtract the cirrus effect on the path radiance as shown in the bottom of Fig. 4. But the cirrus cloud effect on the path radiance at wavelengths shorter then 1.375 μm is stronger then that at 1.375 μm due to the effect of the residual water absorption in this channel. Over ocean the effect of the unknown amount of water vapor on the reflection of sunlight by the cirrus clouds can be derived from scatter plots of the cirrus reflectance at the 1.375 μm and the nearby 1.2 μm channel. Since the reflectance of the cirrus crystals does not change substantially between these two wavelengths due to their large size, and spectrally stable refractive index, the ratio between the cirrus effect at 1.375 μm and 1.2 μm is the water vapor transmitance in the viewing and illumination directions of the particular image. Over the land a similar method can be used only if there are some dark surface pixels, e.g. vegetation at 0.66 μm. Fig. 4, following Gao et al. (1998), demonstrates this correction.



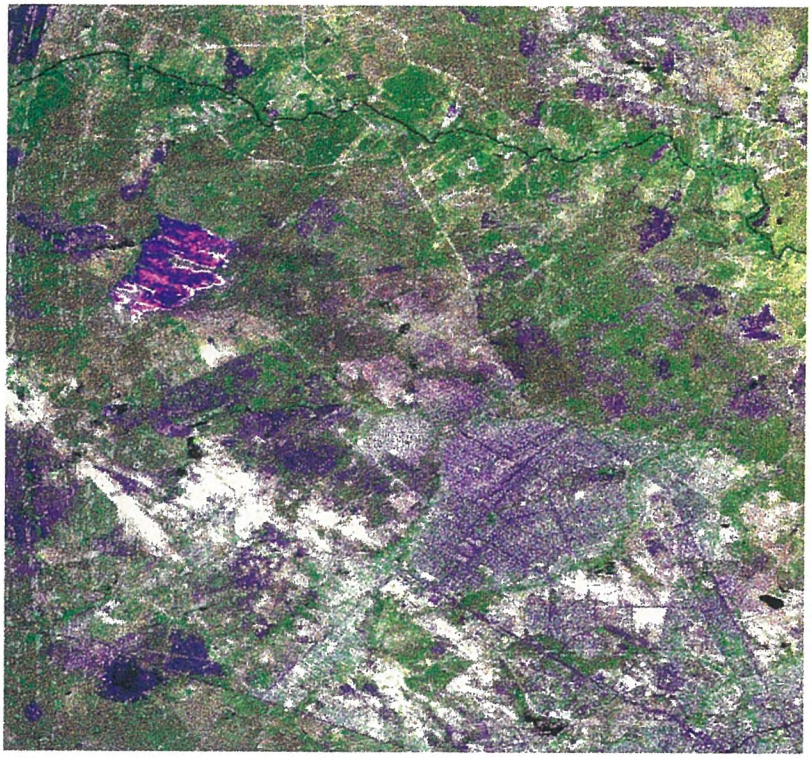


Fig. 3: Large fire near Cuiaba on Aug. 25, 1995 taken from the ER-2 AVIRIS instrument during the SCAR-B experiment. The image is 10x20 km and 20 m resolution. Top image - heavy smoke emitted from the fire and flowing over Cuiaba. The image resembles human vision and is composed of 0.47 μm (blue), 0.55 μm (green) and 0.66 μm (red). Bottom image - is for 2.1 μm (blue), 1.2 μm (green) and 1.65 μm (red). The smoke is almost transparent in these longer wavelengths and the fire is clearly seen with its 3 main temperatures zones (blue - glowing, purple - smoldering - emitting the heavy smoke, and white - the fire front. Note that it is much easier to observe the surface features in the long wavelengths that penetrates the smoke. The solar zenith angle is 36°. The AVIRIS data were provided by Robert Green from JPL.

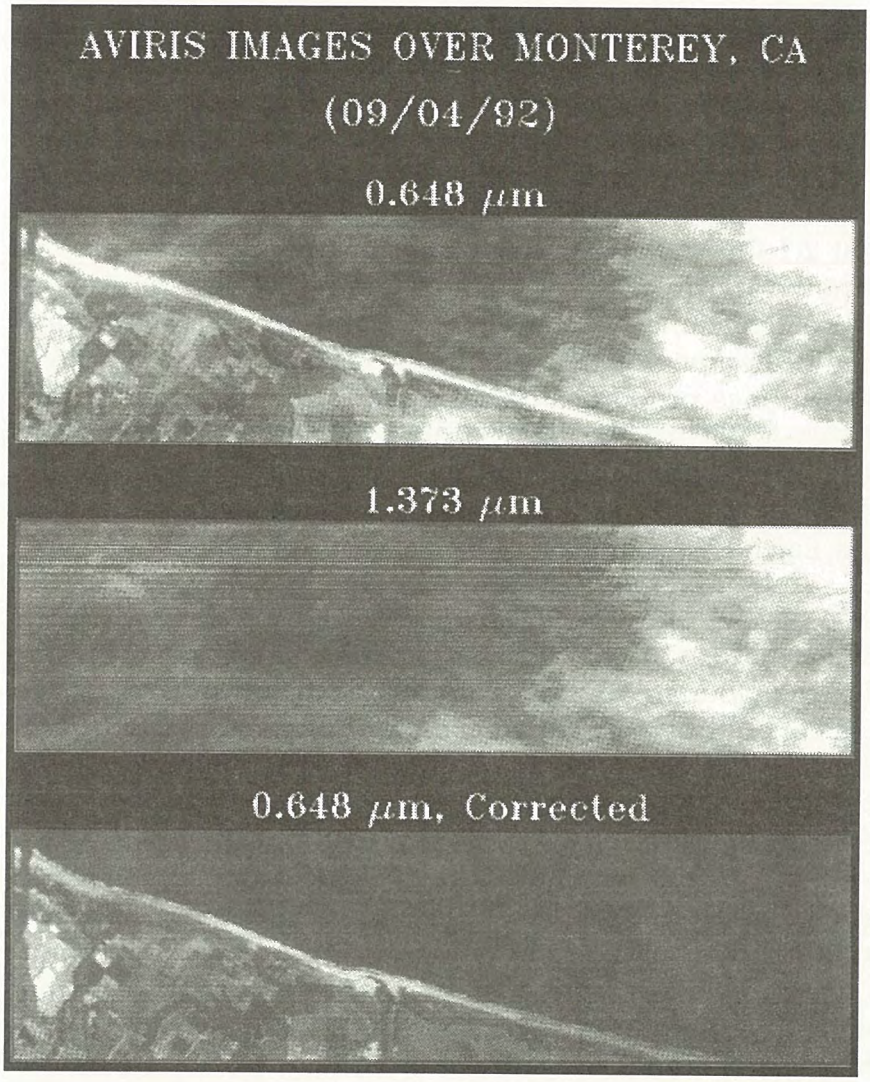


Fig 4: Application of the MODIS new 1.375 μm cirrus channel, using AVIRIS data. Top: image of an ocean-land region at 0.65 μm, indicating the presence of thin clouds over the land and ocean. Middle image - image from the 1.375 μm cirrus channel, observing high clouds only, no land-ocean signal. The difference between the land and ocean reflectance is eliminated by the strong water vapor absorption in the lower troposphere in this channel. Bottom image - is the same as the top image but corrected for the cirrus effect (After Gao et al., 1998).

Conclusions

AEROSOL: Although direct corrections for the aerosol effect over the land are possible, they do not constitute the only, or the best possibility to reduce or get rid of the aerosol effect on remote sensing of the surface. Indirect corrections by redefining functions that represent the surface properties, but are less dependent on the aerosol presence is one possibility. Switching to remote sensing in longer wavelengths (1.2 μm to 2.1 μm) where aerosol has a small effect may be another possibility. Note that the longer wavelengths are not sensitive directly to the chlorophyll concentration but rather to the liquid water in the vegetation associated with it. Thus application of the longer wavelengths for remote sensing of vegetation requires additional studies. The image presented here and others from Brazil show excellent ability to distinguish between different vegetation densities, and lack of

sensitivity to the presence of even very heavy and nonhomogneous smoke. The direct correction for the aerosol effect is also helped by the low optical effects of the aerosol in long wavelengths, e.g. 2.1 μm. For smoke or urban/industrial aerosol the high transparency at 2.1 μm is due to the small particle size of the accumulation mode relative to the wavelength. The accumulation mode is the dominant mode affecting the solar radiation. For dust the transparency is due to the low real refractive index of the dust at 2.1 μm. Application for dust of this method was not demonstrated yet. The method for direct correction is completed by finding a correlation between the surface reflectance at the visible channels and the 2.1 μm channel, for part of the pixels in the image (e.g. vegetation). In this way a complete circle is achieved in which the surface properties of some pixels are observed in the mid IR, and used in the visible to derive the aerosol amount and to perform the correction of the entire image. Applications of this technique were performed so far only in limited scope and full demonstration and evaluation awaits the launch of the MODIS instrument on the Earth Observing System.

CIRRUS CLOUDS: The newly found and implemented cirrus cloud channel in the middle of the strong water absorption band at 1.375 μm was shown to be very sensitive to the presence of cirrus clouds. We anticipate to find from MODIS that a larger fraction of the earth is covered by thin cirrus clouds that were not detected with previous satellite systems. To use this channel for atmospheric corrections two steps are needed. For correction for the increase in the path radiance (the radiance measured by satellite for zero surface reflectance) the signal in 1.375 μm needs to be corrected for the residual effect of water vapor. This is done with the help of correlation with the 1.2 μm over water and 0.65 μm over vegetation. But for correction of the cirrus clouds for their effect on attenuation of the solar radiation reflected from the surface, a complete evaluation of the optical properties of the cirrus clouds in needed. Due to the high altitude of the clouds, the presence of the cloud in one pixel affects the observation of the surface in another pixel. A method to correct for these effects still awaits the ingenuity of young scientists.

References:

Gao, B.-C. and Y. J. Kaufman, Selection of the 1.375 μm MODIS channel for remote sensing of cirrus clouds and stratospheric aerosols from space, *J. Atmos. Sci, 52,* 4231-4237, 1996;

Gao, B.-C., Y.J. Kaufman, W. Han and W.J. Wiscombe, Correction of thin cirrus path in the 0.4-1.0 μm spectral region using the sensitive 1.375 μm cirrus detection channel, .submitted to JGR, 1998

Holben, B.N., Characteristics of maximum value composite images for temporal AVHRR data, Int. J. Remote Sens., 7, 1417-1437, 1986;

Holben B.N., Vermote E., Kaufman Y.J., Tanré D., Kalb V., 1992: Aerosols retrieval over land from AVHRR data- Application for atmospheric correction, *IEEE Transactions on Geoscience and Remote Sensing, 30,* 212-222.

Fraser, R.S. and Y.J. Kaufman, 1985: 'The relative importance of aerosol scattering and absorption in remote sensing', *IEEE J. Geosc. Rem. Sens., GE-23,* 525-633.

Kaufman, Y. J. , The Atmosphere Effect on Remote Sensing and its Correction, Chapter 9 in *Optical Remote Sensing, technology and application,"* G. Asrar, Ed., Wiley, 1989.

Kaufman, Y.J. and B.C. Gao: Remote Sensing of Water Vapor in the Near IR from EOS/MODIS, IEEE *Geosci. and Rem. Sens.*, 30, 871-884, 1992.

Kaufman, Y.J., and B. N. Holben, Hemispherical Backscattering By Biomass Burning And Sulfate Particles Derived From Sky Measurements, special issue of JGR-Atmospheres on Carbonaceous Aerosol. 101, 19433-19445, 1996.

Kaufman, Y. J. and C. Sendra, 1988: 'Algorithm for atmospheric corrections', *Int. J. Rem. Sens., 9,* 1357-1381.

Kaufman, Y.J., D. Tanré, L. Remer, E. Vermote, A. Chu, and B.N. Holben, Remote Sensing of Tropospheric Aerosol from EOS-MODIS Over the Land Using Dark Targets and Dynamic Aerosol Models, JGR-Atmosphere, special issue on remote sensing of aerosol and atmospheric corrections, 102, 17051-17067, 1997a

Kaufman, Y. J. and L. Remer, 1994: 'Remote Sensing of Vegetation in the mid-IR: the 3.75 μm channels', *IEEE J. Geosc. and Rem. Sens. 32*, 672-683.

Kaufman, Y.J. , D. Tanré, L. Remer, E. Vermote, A. Chu, and B.N. Holben, Remote Sensing of Tropospheric Aerosol from EOS-MODIS Over the Land Using Dark Targets and Dynamic Aerosol Models, JGR-Atmosphere, special issue on remote sensing of aerosol and atmospheric corrections, 102, 17051-17067, 1997b

Kaufman Y.J., and D., Tanré, 1992: Atmospheric Resistant Vegetation Index, *IEEE J. Geosc. Rem. Sens.,*, 30, 261-270.

Kaufman, Y. J., D. Tanré: Direct and Indirect Methods for Correcting the Aerosol Effect on Remote Sensing, *Rem. Sens. of Environ.*, 55, 65-79, 1996.

Ramanathan V., and A.M. Vogelmann, Greenhouse effect, atmospheric absorption and the earth's radiation budget: from the Arrhenius-Langley era to the 1990s, *Ambio*, 26, 38-46, 1997.

Remer, L. A., Y. J. Kaufman, B. N. Holben, *Global Biomass Burning,* Ed. J. Levin, p. 519, The MIT press, Cambridge MA, 1996;

Tanré D., B.N. Holben and Y.J. Kaufman, 1992, Atmospheric correction algorithm for NOAA-AVHRR products, theory and application, *IEEE J. Geosc. Rem. Sens.*, 30, 231-248.

Tanré, D. ,Y.J. Kaufman, M. Herman and S. Mattoo, Remote sensing of aerosol over oceans from EOS-MODIS, *J. Geophys. Res. , 102D,* 16971-16988, 1997;

Tucker C.J., J.R.G. Townshend and T.E. Goff, 1985: "African land cover classification using satellite data", Science N.Y., 227, 369.3587-3594.

Vermote, E.F. , N. El Saleous, C.O. Justice, Y.J. Kaufman, J.L. Privette, L. Remer, J.C. Roger , and D. Tanré, Atmospheric correction of visible to mid-IR EOS-MODIS data over land surface, background, operational algorithm and validation, JGR special issue on remote sensing of aerosol, 102, 17131-17141, 1997.

Atmospheric correction of satellite data using aerosol information derived from multi-wavelength lidar observation

Mitsuo Minomura, Jianfei Ru, Hiroaki Kuze, and Nobuo Takeuchi
Center for Environmental Remote Sensing(CEReS),
Chiba University, 1-33, Yayoi-cho, Inage-ku, Chiba, 263 Japan
mino@rsirc.cr.chiba-u.ac.jp

January 22, 1998

1 Introduction

The radiative transfer codes, for example MODTRAN3, employ the standard atmospheric models. However the actual conditions of atmosphere, especially those of aerosol particles, change both spatially and temporally. It is highly desirable to make use of the relevant data measured simultaneously to perform the atmospheric correction on the satellite data.

The lidars are quite useful to obtain aerosol information under in-situ conditions. A multi-wavelength lidar system (1064, 756, 532, and 355 nm) was constructed at the Center for Environmental Remote Sensing (CEReS), Chiba University in March, 1996 and it has been applied to the atmospheric correction of satellite data.

We compare the results obtained with aerosol profiles based on the multi-wavelength lidar measurements and those obtained by using the standard atmospheric models.

2 Multi-wavelength lidar data and MODTRAN3 code

The block diagram of our multi-wavelength lidar system is shown in Fig.1. The 1064, 532, and 355 nm wavelengths are generated by a single Nd:YAG laser, and the 756 nm wavelength by a Ti-sapphire laser pumped by another Nd:YAG laser. The total energy of the output pulses is about 1.2 J with the repetition rate of 10 Hz. The back-scattered light is collected by a Newtonian telescope with 0.47 m^2 effective mirror area. Photomultipliers are used for 756, 532, and 355 nm and an avalanche photodiode for 1064 nm. The sampling rate of the time-of-flight signals is 50 MHz, which corresponds to a spatial resolution of 3 m. The resulting aerosol extinction profiles are applied to the atmospheric correction of satellite data.

An example of such profiles is exhibited in Fig.2. These data were collected on June 27, 1997 during the overflight of NOAA-14. The lidar signal (so-called A scope) for each wavelength is analyzed up to the altitude of 4 km using the Fernald method. The lidar parameter, defined as the ratio between the aerosol extinction coefficient and its back-scattering coefficient, is assumed to be 30 sr^{-1} for all the three wavelengths. The extinction coefficient profile at 550 nm is interpolated from other three profiles, which is then incorporated into the MODTRAN3 code to calculate the radiation transmission.

In MODTRAN3, there is an option of the user-defined aerosol profile where up to 34 layers can be

arbitrarily assigned. In the present case we assume 26 layers between 0 to 4 km, keeping the upper 8 layers between 5 and 100 km same as the standard model (urban aerosol, spring-summer). This profile yields the optical thickness and radiances used in the atmospheric correction on the basis of the lidar data.

In the calculation based on the standard aerosol profile, the value of the ground visibility is adjusted to obtain the same optical thickness as the lidar case for each channel (No. 1 and 2) of NOAA AVHRR. The resulting effect of atmospheric correction is compared with that of the lidar-based correction.

3 Atmospheric correction

The equations of atmospheric correction[1] employed here are as follow:

$$\rho^{(1)} = \frac{1}{a_0}\left[\frac{\pi d^2}{E_s(\lambda_i)\cos\theta_s}\{c_0(i) + c_1(i) \times DN\} - a_0\right], \quad (1)$$

$$a_0 = \frac{\pi d^2}{\cos\theta_s}\frac{\int_{\lambda_1}^{\lambda_2} L_0(\lambda)\Phi(\lambda)d\lambda}{\int_{\lambda_1}^{\lambda_2} E_s(\lambda)\Phi(\lambda)d\lambda}, \quad (2)$$

$$a_1 = \frac{d^2}{\cos\theta_s}\frac{\int_{\lambda_1}^{\lambda_2} E_g[\tau_{dir}(\lambda) + \tau_{dif}(\lambda)]\Phi(\lambda)d\lambda}{\int_{\lambda_1}^{\lambda_2} E_s(\lambda)\Phi(\lambda)d\lambda}, \quad (3)$$

$$\rho^{(2)} = \rho^{(1)} + q(\rho^{(1)} - \bar{\rho}^{(1)}), \quad (4)$$

$$q = \int_{\lambda_2}^{\lambda_1} \frac{\tau_{dif}(\lambda)}{\tau_{dir}(\lambda)}\Phi(\lambda)d\lambda, \quad (5)$$

and

$$\bar{\rho}^{(1)} = \frac{1}{N^2}\sum_{j=1}^{N^2} \rho_j^{(1)}. \quad (6)$$

In eq.(1), $\{c_0(i) + c_1(i) \times DN\}$ is the radiance received by the satellite sensor, $\Phi(\lambda)$ the sensor response function, $\tau_{dir}(\lambda)$ and $\tau_{dif}(\lambda)$ the direct and diffusive transmittance from the ground to the sensor, respectively, E_s and E_g the extraterrestrial and ground irradiance, respectively, d the Earth-Sun distance in astronomical units, θ_s solar zenith angle, $\rho^{(1)}$ the surface albedo derived from this first-step calculation, q the measure of the strength of the adjacency effect, $\bar{\rho}^{(1)}$ the average reflectance in an $N \times N$ pixel window centered on the considered pixel, and $\rho^{(2)}$ the surface albedo after the correction of adjacency effect.

If, for simplicity, the response function $\Phi(\lambda)$ is assumed to be constant, these equations are reduced into

$$\rho^{(1)} = \rho\frac{L_{pix} - L_0}{L_{tot} - L_0}, \quad (7)$$

$$\rho^{(2)} = \rho^{(1)} + \frac{L_p - L_0}{L_g}(\rho^{(1)} - \bar{\rho}^{(1)}), \quad (8)$$

where L_{pix}, L_0, L_{tot}, L_p and L_g are the radiance of the pixel, path radiance for the dark ground ($\rho = 0$), total radiance, path radiance for the atmosphere, and directly transmitted radiance after the reflection at the ground. These radiances are calculated using MODTRAN3 with an appropriate ground surface albedo of ρ (~ 0.2). In eq.(7), $(L_{tot} - L_0)$ consists of the direct and diffusive radiance reflected at the ground. In Fig.3, the albedo dependence of each radiance component calculated with the lidar-derived data is shown. One can see that $(L_{tot} - L_0)$ is proportional to ρ, so that this assumption of $\rho = 0.2$ does not affect the resulting albedo in eq.(1).

From the images of NOAA-14 AVHRR channel 1 and 2, we have selected 140 × 140 pixels including Chiba Prefecture as a test area. For the adjacency area in eq.(6) we have put $N = 3$ in the present example, which is an area of about 3×3 km^2.

4 Results

Each radiance component of L_0, L_p and L_g is calculated with MODTRAN3 using lidar-derived and standard atmospheric model data. The results show that among the radiance components, the multiple

[1] Richter, R., A fast atmospheric correction algorithm applied to Landsat TM images, Int. J. Remote Sensing, 1990, 11(1), pp.159–166.

scattering component, the ground reflected radiance L_g, and the dark-target path radiance L_0 are similar for both correction schemes. On the contrary there is a small difference for the atmospheric path radiance L_p, which is due to the diffusive scattering. As shown in Fig.4, the difference of L_p between the two schemes depends on the number of streams assumed in the calculation.

The images of raw data, the albedo after the first step correction, and that after the adjacency effect correction are compared in Fig.5 for NOAA AVHRR channel 1. For both the images corrected with standard atmospheric model and with lidar-derived data, there are clear differences between raw data (no correction) and corrected data ($\rho^{(1)}$ and $\rho^{(2)}$). Although the difference between the two correction schemes is small, Fig.6 shows that the aerosol profile affects the result through the adjacency effect.

5 Summary

The Atmospheric Data Correction Lidar (ADCL) is used to obtain the vertical aerosol extinction profile during the satellite overflight. The lidar-derived data and standard atmospheric data are compared in the correction of the NOAA AVHRR image.

The MODTRAN3 code is employed to calculate the radiance components using the lidar-derived and standard-model profiles. Both profiles yield similar results, yet some difference is detectable in the adjacency effect, which is related to the path radiance from the atmosphere.

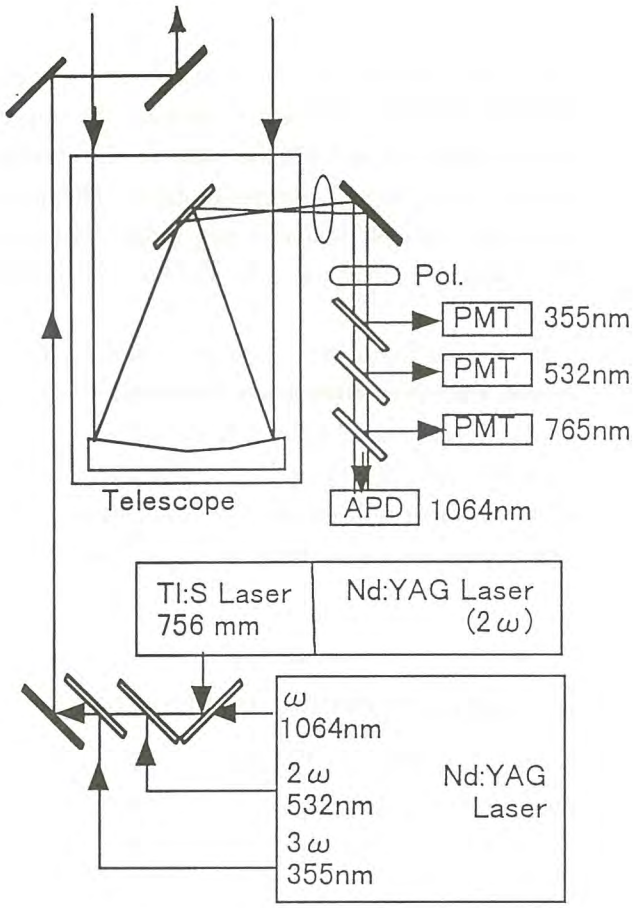


Fig.1 Block diagram of multi-wavelength lidar system

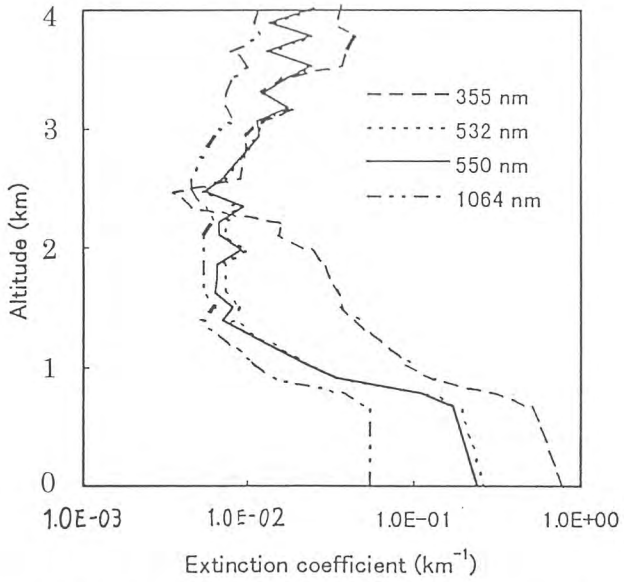


Fig.2 Vertical profiles of extinction coefficient derived from multi-wavelength lidar on June 27, 1997. The profile of 550 nm is interpolated from other three wavelengths.

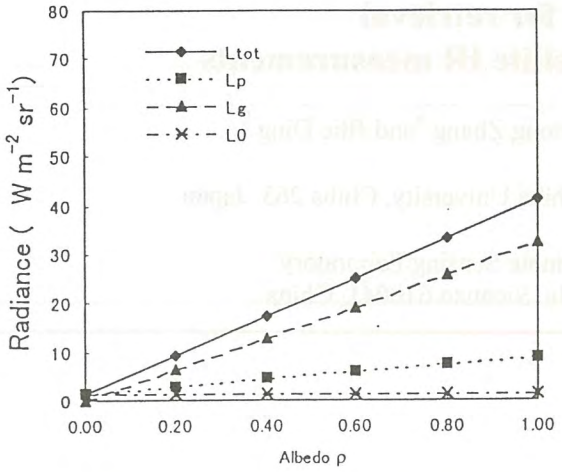


Fig.3 Albedo dependence of each radiance component, NOAA AVHRR channel 1.

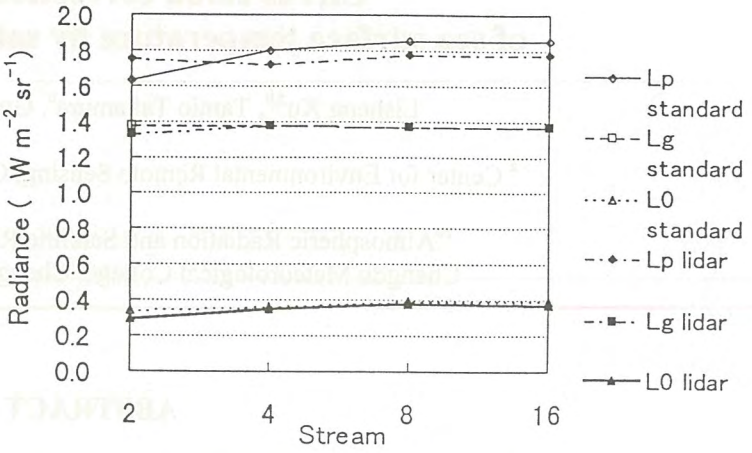


Fig.4 Multiple scattering component for each correction, NOAA AVHRR channel 1. The abscissa is the number of streams, a parameter related to multiple scattering in the MODTRAN3 code.

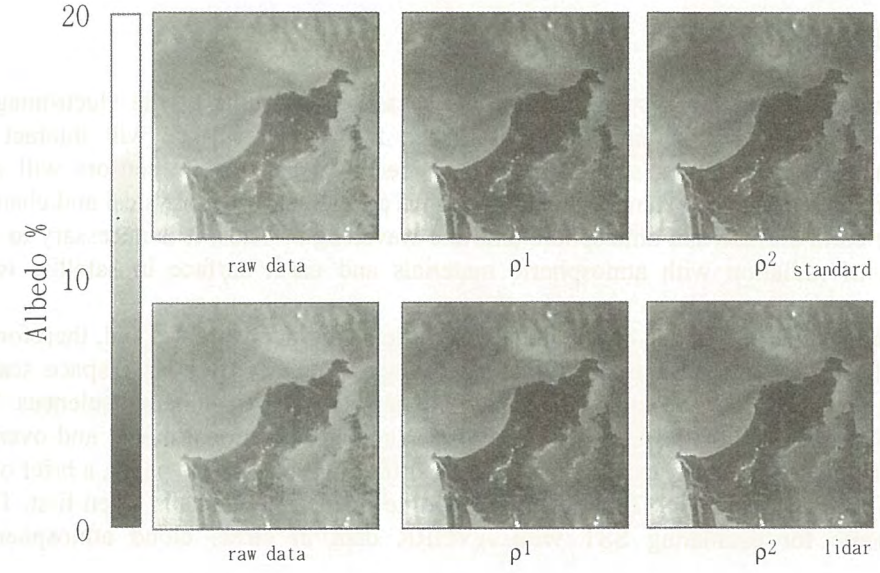


Fig.5 Atmospheric correction for standard atmospheric model and lidar-derived data, channel 1, 27 June 1997, 4 stream.

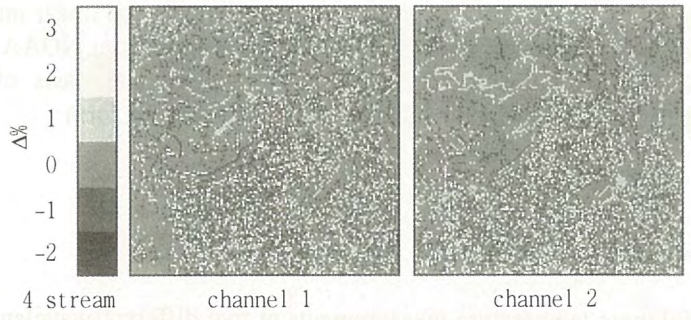


Fig.6 Difference of $\rho^{(2)}$ between the results with standard atmospheric model and lidar-derived data, ratio to the original digital numbers in percent.

Cirrus cloud correction for retrieval of sea surface temperature by satellite IR measurements

Lisheng Xu[a,b], Tamio Takamura[a], Guotong Zhang [b]and Jilie Ding [b]

[a] Center for Environmental Remote Sensing, Chiba University, Chiba 263, Japan

[b]Atmospheric Radiation and Satellite Remote Sensing Laboratory
Chengdu Meteorological College, Chengdu, Sichuan 610041, China

ABSTRACT

A brief review of the basic developments in retrievals of sea surface temperature (SST) from satellite IR measurements is presented first. Then, using a semi-empirical / theoretical method, a nonlinear correction scheme for SST retrievals in cirrus cloud atmospheres is developed.

1. INTRODUCTION

All satellite remote sensing systems include the measurement units of the electromagnetic radiation. The upward radiation emitted and reflected from earth surface will interact with atmospheres in their propagation, so that the signals received by satellite sensors will suffer degradation and distortion. The extent of the interaction is a function of the physical and chemical structure of the earth surface and atmosphere ,and the wavelength. Thus, it is necessary to study the interaction of radiation with atmospheric materials and earth surface in satellite remote sensing.

It is well known that SST is one of climatically significant surface variables and, therefore, the ability of satellite to monitor SST fluctuations and changes regularly over large space scales is very important for contemporary studies in climatology and other environmental sciences. Thus, since the 1970's a great effort has been invested to produce an operational model and overcome many factors that make obtaining accurate temperature difficult[1-14]. In this paper, a brief outline of the atmospheric correction of SST retrievals by satellite IR measurements is given first. Then a correction scheme for estimating SST with AVHRR data in cirrus cloud atmospheres is developed.

2. BRIEF REVIEW

Since late 1981, the NOAA NESDIS has performed operationally the linear multichannel sea surface temperature (MCSST) retrievals with AVHRR data obtained from NOAA polar-orbiting satellites[1]. As shown by McMillin and Crosby [2], the theoretical basis of the MCSST algorithms was developed in 1970's, which results in an algorithm of the form

$$Ts = T_j + \gamma (T_i - T_j) \quad (1)$$

$$\gamma = k_j / (k_j - k_i) \quad (2)$$

where T_i and T_j are brightness temperature measurements at two different wavelengths in the 11-12 μm window spectral region, k_i and k_j the water vapor absorption coefficients. Eg.(1) indicates that the temperature deficit in one channel, $Ts - T_j$, due to atmospheric water vapor absorption is a linear function of the brightness temperature difference ($T_i - T_j$). Thus, with data taken from more than one channel the differential absorption technique can be used to correct water vapor

sorption in clear atmospheres, with a constant γ parameter.

In practical uses, however, the simplifying assumptions leading to Eg. (1) are suspect . Since 1980s, to relate the output signal to SST more accurately, many authors[3-7] have investigated the effect of atmospheric water vapor on satellite-derived SSTs. Walton[5] has developed a nonlinear multichannel algorithm, which is called the cross product sea surface temperature (CPSST) solution with the form

$$CPSST(i,j) = \frac{SST_j - T_j}{SST_j - T_j + T_i^* - SST_i}(T_i^* - T_j) + T_j \quad (3)$$

$$SST_i = A_i T_i + B_i \quad (4)$$

$$T_i^* = T_i + C \quad (5)$$

for the dual window and split window combinations of channels. For triple window channels, the CPSST solution can be derived as

$$CPSST(3,4,5) = T_{11} + \gamma(T_{3.7} - T_{12} + C) \quad (6)$$

$$\gamma_t = \gamma_d(1-\gamma_s)/(1-\gamma_s-\gamma_d) \quad (7)$$

Since 1980s, world-wide volcanic activities frequently occur, major changes in the stratospheric aerosol content and desert dust storms greatly alter the normal atmospheric spectral absorption characteristics and have a dramatic impact on SST measurements from satellites. Therefore, the MCSST algorithms have been rapidly developed for atmospheric aerosol corrections [8-13]. Walton [9] pointed out that all the two-window correction algorithms produce significant errors in the presence of volcanic aerosols. Three AVHHR window channels can provide an alternate solution that corrects stratospheric aerosols as well as water vapor absorption. Xu and Smith [10] further theoretically showed that it is better to use the VAS four-window channel algorithm for stratospheric aerosol correction. In addition, Griggs [8] suggested a technique of aerosol correction to the AVHRR MCSST algorithms by using the aerosol optical thickness τ_c. May et al. [11] developed a technique that incorporates an aerosol optical thickness term directly into the CPSST algorithm to correct Saharan dust aerosol contamination, which is called AERSST.

Although atmospheric correction for SST retrievals in clear and aerosol atmospheres have made such as progress, the correction in the condition of cirrus clouds still have severely limited because of the complexities and difficulties of the problem. Recently, Xu and Sun [14] and Xu et al. [13]have studied this subject theoretically and demonstrated some important characteristics for remote sensing of SSTs using VAS IR observations in cirrus cloud combined stratospheric aerosol atmospheres, and revealed the nature and limitation of the MCSST algorithms in these conditions. However, adequate operational cirrus cloud correction algorithm is still lack. In the following we present our preliminary results toward the realization of this aim.

3. MODELS

All particles in the atmosphere–atomic, molecular, and various liquid and solid particles, interact with radiation. For satellite remote sensing of SST in IR region, the major errors result from water vapor absorption, and the effects of aerosols and cirrus clouds. In the present study, we mainly emphasize the effects of cirrus clouds.

Two specific crystal habits, i.e., hexagonal columns and plates are considered. Twenty particle size distributions with every one including a superposition of two modified Γ - function distributions are constructed . The cloud ice - water content (IWC) ranges from 3×10^{-5} to 0.25 gm^{-3}, and the corresponding effective particle size r_e ranges from 30 to 325 μm for columns and

from 42 to 449 μm for plates.

It is assumed that ice crystals of cirrus clouds are randomly oriented in space. The single-scattering properties of ice crystals are computed by the improved ray-optics theory [15-16] and Mie theory with the critical dimension Lc = 45 μm .

The cloud layer is considered as plane-parallel, horizontally homogeneous and vertically inhomogeneous with an improved two-layer ice model [17] being used. For multiple scattering radiative transfer calculations the adding/doubling method [18] is employed, and the analytic Henyey - Greenstein phase function is used .

Four atmospheric models, namely, i.e., Standard Atmosphere, Tropical, Midlatitude Summer, and Midlatitude Winter are considered. Molecular scattering and absorption with the background stratospheric aerosols are taken into account, and calculated by LOWTRAN 7 Code [19].

4. CORRECTION SCHEME

As shown in Fig. 1, the brightness temperature of channel 4, T_b (11), is related linearly to that of channel 5, T_b (12). This relationship is considered in our formulation of SST retrieval algorithms. Fig. 2 shows that determination of a suitable function relation of the cloud optical thickness τ_{11} and ΔT_b (3.7 − 11), i.e., $\tau_{11} = f$ [ΔT_b (3.7 − 11)], is very important for establishing the retrieval model. In the present study, we simply use the following expression :

$$\tau_{11} = a - (T_{11} - T_{3.7} + b)^{1/2} \tag{8}$$

In formulation of the retrieval formulas, the parameter b needs to be changed gradually so that the errors of the retrieval formulas are reduced to a minimum.

To investigate the cirrus cloud correction on satellite-derived SSTs, a semi-empirical / theoretical method is employed. The satellite data were taken from NOAA-11 AVHRR measurements, with three days in 1993 being found to be influenced by cirrus clouds in the 15^0 - 32^0 N latitude band. The brightness temperatures retrieved by using the NOAA NESDIS CLAVR(Clouds- from- AVHAA) global program [20]are employed to get the estimate values of SST. Meanwhile, numerous brightness temperatures "observed" by the three AVHRR IR channels in different atmospheric models with different macro- and micro-physics of cirrus clouds, and different satellite zenith angle (0^0--60^0) can be calculated. Then, the theoretical simulation data combined with satellite observation data together are used to set up the SST retrieval equations for three different SST climate regions by stepwise regression analyses, respectively.

For 297.0 ≤ SST ≤ 304.0 K, we have

$$\begin{aligned} SST = {} & a_0 + a_1(T_{11} - T_{12}) + a_2(T_{3.7} - \alpha)T_{12} + a_3(T_{3.7} - T_{11})\times \\ & (T_{11} - T_{3.7} + \beta)^{1/2} + a_4(T_{11} - T_{12}) / (1 - \sin\varphi) \\ & + a_5(T_{11} - T_{12})(\sec\theta - 1) \end{aligned} \tag{9}$$

where α and β should be changed in each stepwise regression so that a minimum standard error is obtained, which are referred to as "the control parameters", lastly α= 520 and β= 35; a_0= 331.964, a_1= 6.68847, a_2= 0.00043, a_3= -0.0199, a_4= -4.2924, a_5= 0.13848.

For 291 ≤ SST ≤ 299 K, after numerous tests, the model is determined as

$$\begin{aligned} SST = {} & 0.0051T_{3.7} + 1.39368(T_{11} - T_{12}) - 0.00299T_{12}(T_{3.7} - 538) \\ & + 0.24312(T_{3.7} - T_{11})(T_{11} - T_{3.7} + 35)^{1/2} - 0.36696\times \\ & (T_{11} - T_{12})/ (1 - \sin\varphi) - 0.1265T_{3.7}(\sec\theta - 1) \\ & + 77.533 \quad . \end{aligned} \tag{10}$$

For 284 ≤ SST ≤ 291 K, performing a lot of numerical experiments, we have the model as

$$\begin{aligned} SST = {} & a_0 + a_1T_{11} + a_2T_{12} / (1 - \sin\varphi) + a_3T_{3.7}(T_{11} - T_{12}) \\ & + a_4(T_{11} - T_{12} + \alpha)\sin\varphi + a_5(T_{3.7} - T_{11} + \beta)^{1/2}(\sec\theta - \gamma) \end{aligned} \tag{11}$$

where $a_0 = 226.78037$, $a_1 = 0.24901$, $a_2 = -0.13805$, $a_3 = -0.00711$, $a_4 = 5.70107$, $a_5 = -0.17797$; the control parameters $\alpha = 18$, $\beta = 200$, $\gamma = 7$.

Xu et al.[13] have analyzed the influences of cirrus clouds combined with different stratospheric aerosols on VAS SST retrievals and the limitation of MCSST algorithms, which pointed out that for such as high nonlinear SST retrieval problems, one way for improving the retrieval accuracy is a further increase in IR window channels. For VAS sensor, for instance, the optimal MCSST retrieval equation that corrects the effects of cirrus clouds combined with stratospheric aerosols and atmospheric gases is a five-IR window channel algorithm. For AVHRR sensor, however, there are only three IR window channels. Furthermore, as shown in Fig. 1, the brightness temperature of channel 4, $T_b(11)$, is related linearly to that of channel 5, $T_b(12)$. These indicate that in general it is not easy to establish a MCSST algorithm with satisfactory accuracy using the AVHRR three IR window channels under cirrus cloud conditions. In the present study, we have developed a technique to set up a nonlinear SST retrieval algorithm to correct the effects of tenuous or moderate cirrus clouds ($\tau_c \leq 3.6$). The effects of the satellite observation angle θ and the latitude φ are considered, with $\theta \leq 45^0$ and $\varphi \leq 45^0$. Furthermore, to increase the retrieval accuracy , we formulated the equations for three different SST climate regions. These mean that the influences of cirrus clouds and atmospheric conditions in different regions and different SST climatology have been taken into account. Clearly, our nonlinear retrieval method is different from the CPSST algorithm[5].

5. CONCLUTIONS

By using a semi-empirical / theoretical method, a nonlinear correction scheme for SST retrievals in cirrus cloud atmospheres has been proposed. In the theoretical simulation, two shapes of ice crystals, i.e., hexagonal columns and plates, are considered, and twenty particle size distributions are constructed. A suitable scattering model for nonspherical particles is employed. Meanwhile, NOAA-11 AVHRR observation data are used. For three different SST climate regions in the latitude $\varphi \leq 45^0$, and the cloud optical thickness $\tau_c \leq 3.6$ and the satellite zenith angle $\theta \leq 45^0$, a set of the nonlinear retrieval equations (9), (10) and (11) has been set up, with the standard deviations, σ, being 0.668, 0.669, and 0.659, respectively. The preliminary results demonstrate that the nonlinear correction technique is feasible.

ACKNOWLEDGMENTS

The research is supported by the National Natural Science Foundation of China under Grant NSFC-49675255 and the Foundation of Ministry of Education, Science, Sports and Culture of Japan under Grant N0. 08241104 .

REFERENCES

1. McClain, E. P., 1981, Multiple atmospheric-window techniques for satellite-derived sea surface temperatures . In Oceanography from Space, J. F. R. Gower,ed., (New York: Plenum), pp. 73-85.
2. McMillin, L. M. and Crosby, D. S.,1984, Theory and validation of the multiple window sea surface temperature technique . J. Geophys. Res., 89, 3655-3661.
3. Barton, I. J., 1983, Dual channel satellite measurements of sea surface temperature . Quart. J. Roy. Meteor. Soc., 109, 365-378.
4. Barton, I. J., 1985, Transmission model and ground-truth investigation of satellite-derived sea surface temperature. J. Climate Appl. Meteor., 24, 508-516.
5. Walton, C. C., 1988, Nonlinear multichannel algorithms for estimating sea surface temperature with AVHRR satellite data . J. Appl. Meteor., 27, 115-124.
6. Barton, I. J., and Co-authors, 1989, Theoretical algorithms for satellite-derived sea surface temperatures. J.Geophys. Res., 94, 3365-3375.

7. Barton, I. J., 1992, Satellite-derived sea surface temperature–A comparison between operational, theoretical, and experimental algorithms . J. Appl. Meteor., 31, 433-442 .
8. Griggs, M. 1985, A method to correct satellite measurements of sea surface temperature for the effects of atmospheric aerosols . J. Geophys. Res. , 90, 12,951-12,959.
9. Walton, C. C., 1985, Satellite measurements of sea surface temperature in the presence of volcanic aerosols . J.Climate Appl. Meteor., 24, 501-507.
10. Xu, L. and Smith, W. L., 1986, Numerical simulation of the influence of volcanic aerosols on VAS derived SST determinations . Appl. Opt., 25, 1137-1144.
11. May, D. A., and Co-authors, 1992, A correction for Saharan dust effects on satellite sea surface temperature measurements . J. Geophys. Res., 97, 3611-3619.
12. Reynolds, R. W., 1993, Impact of Mount Pinatubo aerosols on satellite-derived sea surface temperatures . J. Climate, 6, 768-774.
13. Xu, L., Zhang, J., Zhang, G., and Chen, H., 1994, Simulation of remote sensing of sea surface temperature from space : Influence of cirrus clouds and stratospheric aerosols on sea surface temperatures derived from the VISSR Atmospheric Sounder . Int. J. Remote Sens., 15, 2599-2614.
14. Xu, L. and Sun, B., 1991, Influence of cirrus clouds on the VISSR atmospheric sounder-derived sea surface temperature determinations . Appl. Opt., 30, 1525-1536.
15. Zhang, J. and Xu, L., 1995, Light scattering by absorbing hexagonal ice crystals in cirrus clouds. Appl. Opt., 34, 5867-5874.
16. Xu, L. and Zhang, J., 1996, Light scattering by randomly oriented hexagonal ice crystals : Improved diffraction computations and diffraction properties of ice crystals . Optik , 101, 161-165.
17. Xu, L. and Zhang, J., 1992, Simulation of retrieval of the base height and thickness of cirrus clouds from satellite data . J. Opt. Soc. Am. A 9, 1536-1546.
18. Lenoble, J., ed., 1985, Radiative Transfer in Scattering and Absorption Atmospheres : Standard Computational Procedures (Hampton : A. Deepak).
19. Kneizys, F. X., and Co-authors, 1988, Users Guide to LOWTRAN 7 . AFGL-TR-88-0177, AFGL/OPS, Hamscom AFB, MA01731, U.S.A.
20. Stowe, L. L., and Co-authors, 1991, Global distribution of cloud cover derived from NOAA/ AVHRR operational satellite data . Advan. Space Res., 11, 51-54.

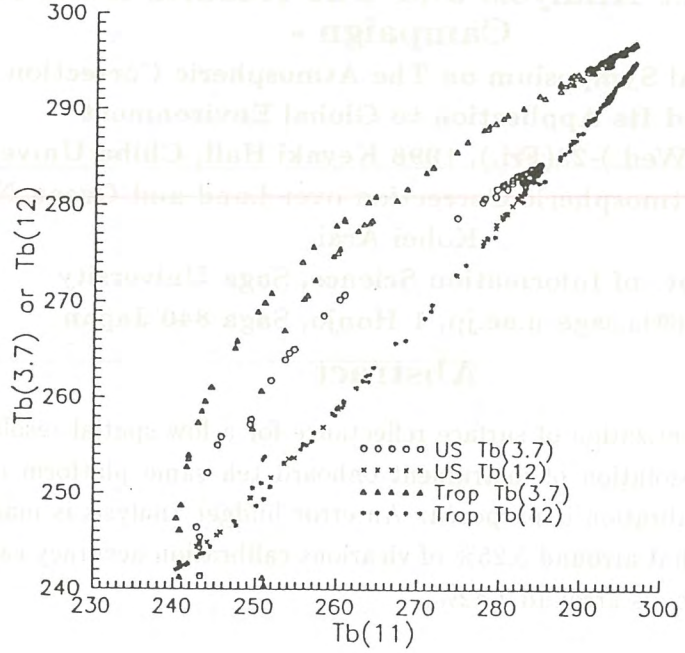


Figure 1. The brightness temperature T_b (3.7) and T_b (12) vs T_b (11) in cirrus cloud atmospheres.

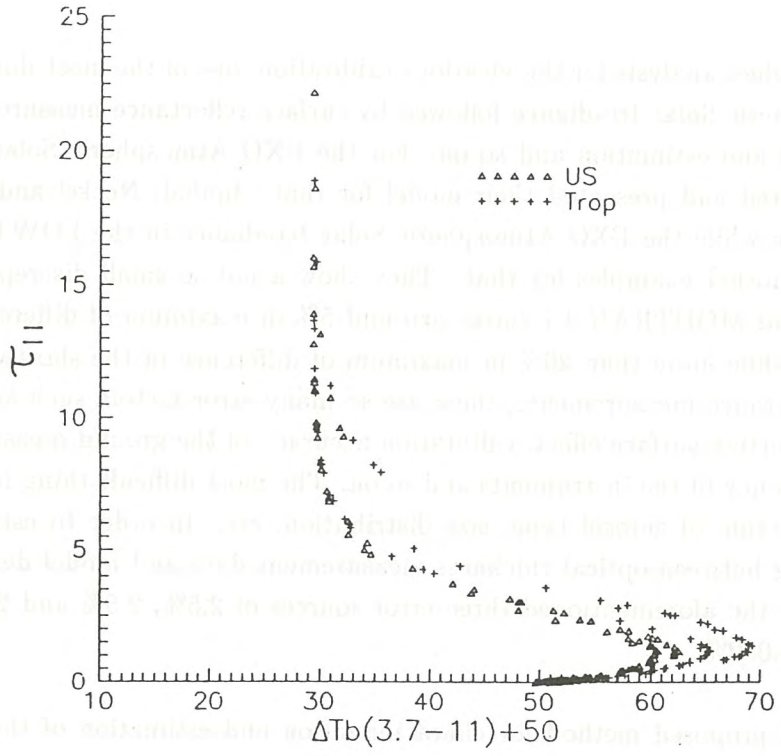


Figure 2. The cloud optical thickness at 11μm, τ_{11}, vs the brightness temperature differences, ΔT_b (3.7 – 11) .

Cross Calibration Between ADEOS/AVNIR and OCTS - Error Budget Analysis and The Results from the Field Campaign -

The CEReS International Symposium on The Atmospheric Correction of Satellite Data and Its Application to Global Environment
January 21(Wed.)-23(Fri.), 1998 Keyaki Hall, Chiba University
Session 4 : Atmospheric Correction over Land and Ocean No.4-4

Kohei Arai
Dept. of Information Science, Saga University
arai@is.saga-u.ac.jp, 1 Honjo, Saga 840 Japan

Abstract

A method for the characterization of surface reflectance for a low spatial resolution of instrument data with a high spatial resolution of instrument onboard teh same platform of low resolution of instrument for vicarious calibration is proposed. An error budget analysis is made for the proposed method. The result shows that arround 5.25% of vicarious calibration accuracy can be achieved if the vicarious calibration accuracy is arround 4.42%.

Keywords: Atmospheric code, ADEOS, AVNIR, OCTS, Vicarious calibration, Field Campaign, Size distribution of aerosol, Aerosol type, Mie Phase function

1 Introduction

According to the error budget analysis for the vicarious calibration, one of the most dominant error source is the EXO Atmospheric Solar Irradiance followed by surface reflectance measurements, optical thickness measurements and estimation and so on. For the EXO Atmospheric Solar Irradiance, so many researchers measured and presented their model for that. Iqubal, Neckel and Labs, Gao, Flierich, Shaw are exampels while the EXO Atmospheric Solar Irradiance in the LOWTRAN-7 and MODTRAN-2 and 3 are another examples for that. They show a not so small discrepancy among them. For instance, Gao and MODTRAN-3.7 shows arround 5% in maximum of difference between both in the visible region while more than 20% in maximum of difference in the shortwave infrared region. In the surface reflectance measurements, there are so many error factors such as stability of the instruments, non-Lambertian surface effect, calibration accuracy of the ground measuring instruments, temperature dependency of the instruments and so on. The most difficult thing in the optical thickness estimation is selection of aerosol type, size distribution, etc. In order to estimate those, we used to use curve fitting between optical thickness measurement data and model derived optical thickness. If we think only the aforementioned three error sources of 2.5%, 2.5% and 2%, then the Root Sum Square error is 4.062%.

This paper describes the proposed method for characterization and estimation of the surface re-

flectance for the area corresponding to one pixel of the low resolution of instrument with simultanuously observed high spatial resolution of instrument data. Error budget analysis will be followed beginning with error budget analysis of the vicarious calibration for high spatial resolution of instruments followed by sampling error(including mis-registration) and the difference of spectral responses between the two instruments(high and low spatial resolution of instruments) in terms of Atmosphric influences and spectral surface reflectances.

2 The Proposed Method

In particular, it is suspected that a large error in the surface reflectance measurements for a low spatial resolution of instrument such as AVHRR, MODIS as well as OCTS because it takes a long time to measure the surface reflectance and BRDF for the areas corresponding to the one pixel of the low resolution of instruments, 700 m x 700 m for OCTS and 1,000 m x 1,000 m for MODIS. This imply that more than 2.5% of error is caused by the characterization and estimation of the surface reflectance. In order to reduce the error, the following method is proposed. Instead of making measurements for surface reflectance for the wide areas, characterization and estimation of the surface reflectance with simultanuously observed high spatial resolution of instrument data and the measured surface reflectance for the areas corresponding to the one pixel of a low resolution of instrument is capable. The error factors in the proposed method are

- Vicarious calibration for the high spatial resolution of the instrument
- Sampling error and registration error between high and low spatial resolution of instruments
- Different atmospheric influences and spectral reflectances between both instruments caused by the different spectral responses.

3 Error Budget Analysis

3.1 Vicarious calibration accuracy for the high spatial resolution of instrument

3.1.1 Vicarious Calibration

The methods for a vicarious calibration so called the radiance based, the reflectance based and the improved reflectance based methods were proposed by several *institutes*[1,2,3].
Essentially the reflectance and the improved reflectance based methods use Sunphotometer data derived optical thickness of the atmosphere and the BRDF and the spectral reflectance of the surface of interest as well as an atmospheric code including a Radiative Transfer Code, RTC. Based on the BRDF and the spectral reflectance and the optical thickness of the atmosphere, the radiance at the top of the atmosphere so called TOA radiance is estimated with the atmospheric code. On the other hand, the radiance based method uses aircraft data. The difference between the estimated radiance at the certain altitude(the aircraft altitude) with the BRDF, the spectral reflectance and the optical

thickness and the measured radiance(the aircraft data) is compensated in the TOA radiance estimation. A sensitivity analysis was conducted and reported for the aerosol complex refractive index, the aerosol size distribution and so on. Meanwhile Aureolemeter gives the phase function with some error. In the calculation of multiple scattering due to aerosol particles with the doubling method, some approximations for Mie phase function are *required*[4,5].
In this paper, the sensitivities of the atmospheric parameters and the geometric relationship among the ground cover target, the sun and the satellite are evaluated with field campaign data for the vicarious calibration of ADEOS/AVNIR(one of the examples of high spatial resolution of instrumnets).

3.1.2 Error Budget Analysis for the Vicarious Calibration

Table 1 shows the results from the error budget analysis for the vicarious calibration.

Table 1 Error budget for the vicarious calibration for ADEOS/AVNIR

Error Source	Error in %	Remarks
Optical Thickness Measurement	1	
Curve Fitting for Size Distribution and Refraction Index Estimation	2	
Surface Reflectance Measurement including BRDF Measurement and Correction	2	For both the Standard Panel and the surface of test site
EXO Atmospheric Solar Irradiance	2.5	
Mis-Registration	1	
Accuracy of Radiative Transfer Code	1	
Root Sum Square Error	4.15%	

3.1.3 The field campaign for the vicarious calibration of ADEOS/AVNIR

AVNIR is the high spatial resolution of visible to near infrared instrument onboard ADEOS satellite for multi-purpose mission including agricultural and forest inventory, land use, digital elevation model and so on. The satellite was launched in August 1996 and was terminated in June 1997 due to mulfuntion of the solor panel.

One of the post launch calibration activities is the field campaign for the vicarious calibration of the AVNIR and was conducted three times, at the Calfornia offshore in November 1996, at the Rogers Dry Lake and Ivanpah Playa in Feburary and March 1997 and the Calfornia offshore in May 1997. In the field campaign at Ivanpah Playa on March 4 1997, our team measured solor irradiance with our Sunphotometer(5 channels), sky light with the Aureolemeter, surface reflectance, surface BRDF as well as standard panel of Labsphere Spectralon. Weather condition was not so good because two days before that day, we had the rainfall so that the atmospheric condition is not stable and the surface was getting dry gradually. Therefore I took the modefied Langley Plot other than Langley Plot. On the day for vicarious calibration, March 4 1997, we had a dry atmosphere.

Table 2 Conditions on the field campaign for vicarious calibartion of AVNIR in March 1997

Date	Location	Sunrise	Overpass time	Solor Noon	Pointing Angle
1997/3/4	Ivanpah Playa	6:07	10:49:59	11:52	3.6
Surface Pressure	Humidity	Temp.	Solor Az.	Solor Zenith	
930(mb)	48(%)	284(K)	156.8	45.0	

Fig.1 to 6 show the location of the test site, Ivanpah playa, Nevada USA, the surface reflectance, Optical thickness due to molecular, aerosol and total, and TOA radiance normalized by Solar irradiance rpovided by MODTRAN-3.7, so called Normalized TOA radiance, respectively. Through a comparison between the calculated TOA radiance(45.25, 52.63, 69.64, 110.02(W/m^2srum) for AVNIR band 1 to 4)and the converted AVNIR radiance from AVNIR Digital Count Value(43.25, 51.00, 68.11, 104.15(W/m^2srum) for AVNIR band 1 to 4), there were -4.5, -3.1, -2.2, -5.6(%) of differences between them.

3.2 Characterization and Estimation of Surface Reflectance

The next thing we have to do is to register the high spatial resolution of instrument data onto the low spatial resolution of instrument data. Through a visual matching between the two imagery data on the display, two instrument data are registered with a few 10th of pixel of error.

3.3 Difference of Spectral Responses Between Two Instruments

Fig.7 and 8 show the spectral responses of AVNIR and OCTS, respectively. Both are overlapped so that it is possible to generate AVNIR spectral response with OCTS spectral response through weighted linear combination of OCTS spectral response. Using MODTRAN-3.7, the weights for the linear combination are calculated and are 27.7, 39.8 and 32.5 for OCTS band 1, 2 and 3, respectively for the generation of AVNIR band 1 and are 56.8 and 43.2 for OCTS band 4 and 5 for the generation of AVNIR band 2. Fig.9 and 10 show the relationship between the generated AVNIR band 1 from OCTS band 1, 2 and 3 and the generated AVNIR band 2 from OCTS band 4 and 5, respectively. Fig.11, 12 and 13 show the original AVNIR image(false colored), the simulated OCTS band 1+2+3 image from AVNIR by averaging over 44 by 44 pixels and the real OCTS band 1+2+3 image of Ivanpah Playa in Nevada, U.S.A. on March 4 1997. Using these OCTS band 1+2+3 and OCTS band 4+5 data from AVNIR data as well as a virtual center wavelength of OCTS band 1+2+3 and band 4+5, we can estimate OCTS band 1 to 5 from AVNIR data. Then we can conduct vicarious calibration of OCTS using the calibrated AVNIR.

3.4 Calibration Accuracy for the Proposed Method

Taking Root Sum Square for the aforementioned factors, we concluded that the calibration accuracy of the proposed method is arround 5.02%(Vicarious Calibration Accuracy of 4.15%, Characterization and Estimation of Surface Reflectance Including Mis-Registration of 2% and Difference of Spectral Responses(Atmospheric Influences and Spectral Reflectance) of 2%).

4 Concluding Remarks

Through the field campaign, the radiance from ADEOS/AVNIR was comfirmed with some discrepancy within +/-5.5(%) against the vicarious calibration data. According to the reflectance based method, around 5(%) is the most possible accuracy so that +/-5.5(%) difference is not so large. Through the sensitivity analysis, it is confirmed that the most significant factor on the TOA calculation in the vicarious calibration is the imagenary part of the complex refractive index of aerosol followed by phase function so that the accuracy of Aureolemeter is very important. It is also fount that the calibration accurcay of the proposed method is arround 5.02%.

References

1.P.N.Slater, S.F.Biggar, K.J.Thome, D.I.Gellman, P.R.Spyak, Vicarious Radiometric Calibration of EOS Sensors, JAOTEC, Vol.13, No.2, 349-359, 1996.

2.S.F.Biggar, P.N.Slater, D.I.Gellman, Uncertainties in the in-flight calibration of sensors with reference to measured ground sites in the 0.4 to 1.1um range, Remote sensing of Environment, 1993.

3.C.L.Grotbeck, R.P.Santer, S.F.Biggar, P.N.Slater, Solar Aureole and Optical Depth Inversion Techniques for Atmospheric Radiative Transfer Calculations, JAOTEC,

4.J.E.Hansen, L.D.Travis, Light scattering in planetary atmosphere, Space Science Review, Vol.16, 527-610, 1974.

5.J.H.Joseph, W.J.Wiscombe, J.A.Weinman, The delta-Eddington approximation for radiative flux transfer, Journal of Atmospheric Science, Vol.33, 2452-2459, 1976

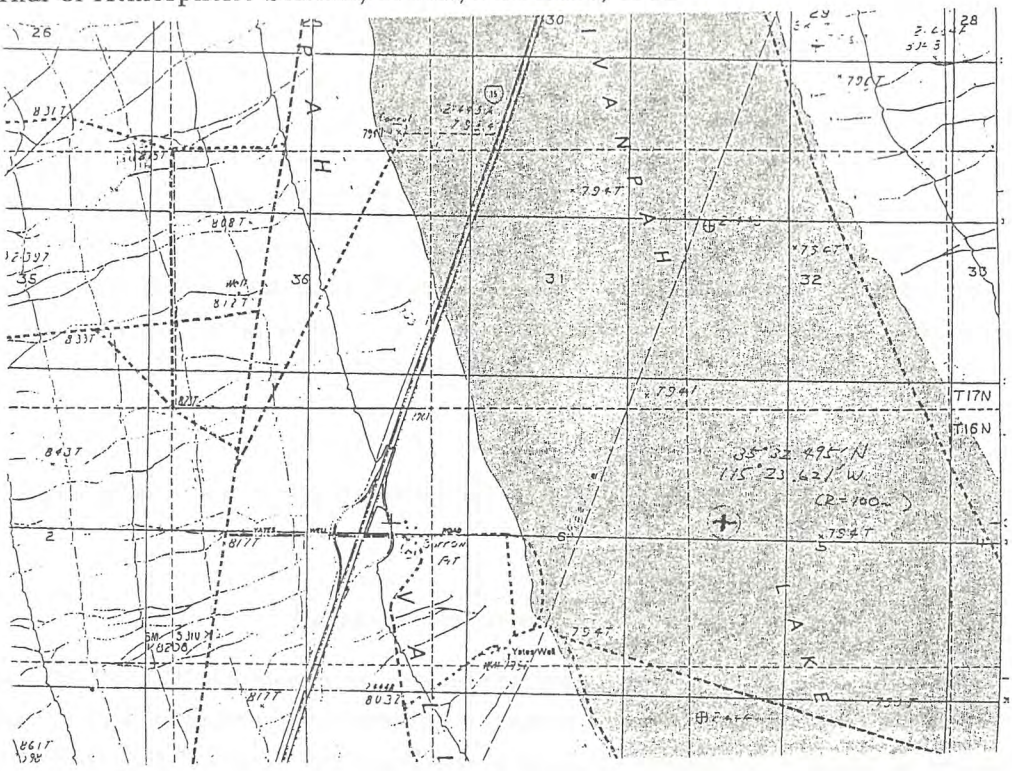


Fig.1 Location of test site,Ivanpah playa in Nevada, U.S.A.

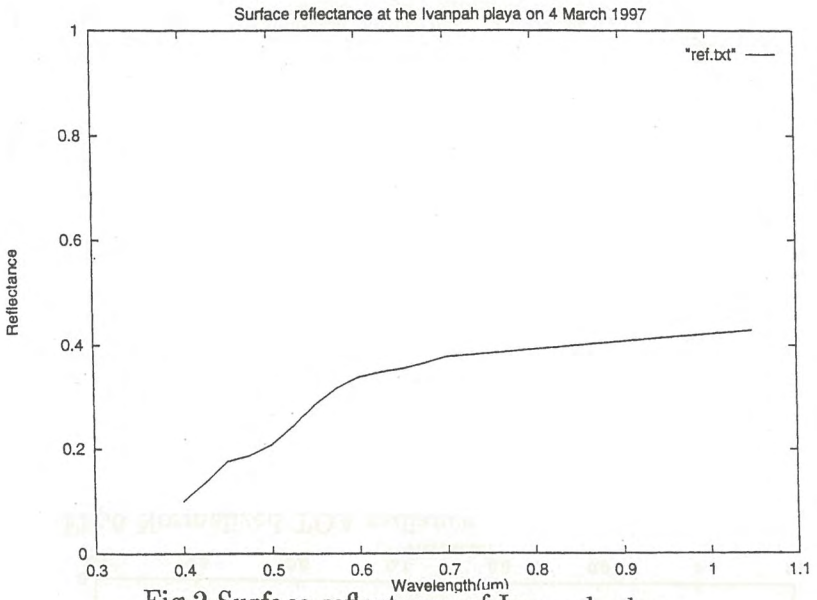


Fig.2 Surface reflectance of Ivanpah playa.

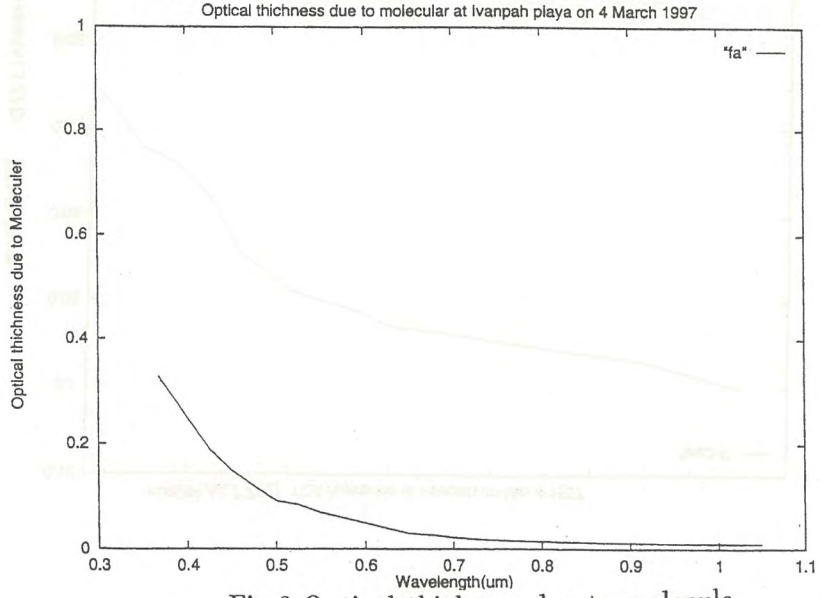


Fig.3 Optical thickness due to molecule.

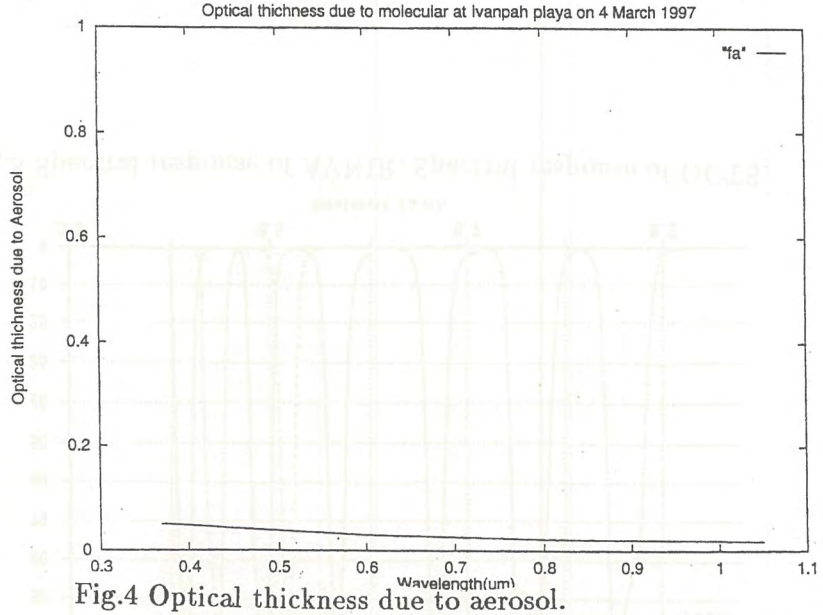


Fig.4 Optical thickness due to aerosol.

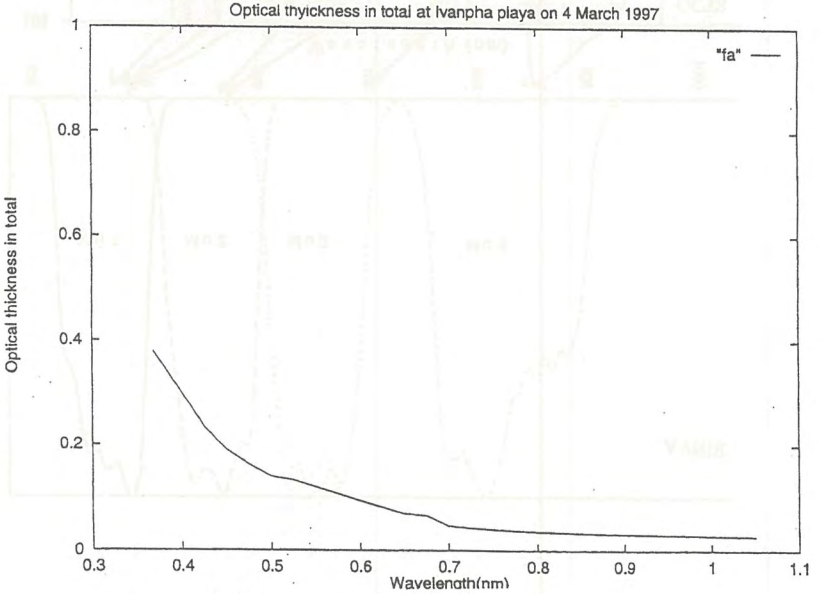


Fig.5 Optical thickness in total.

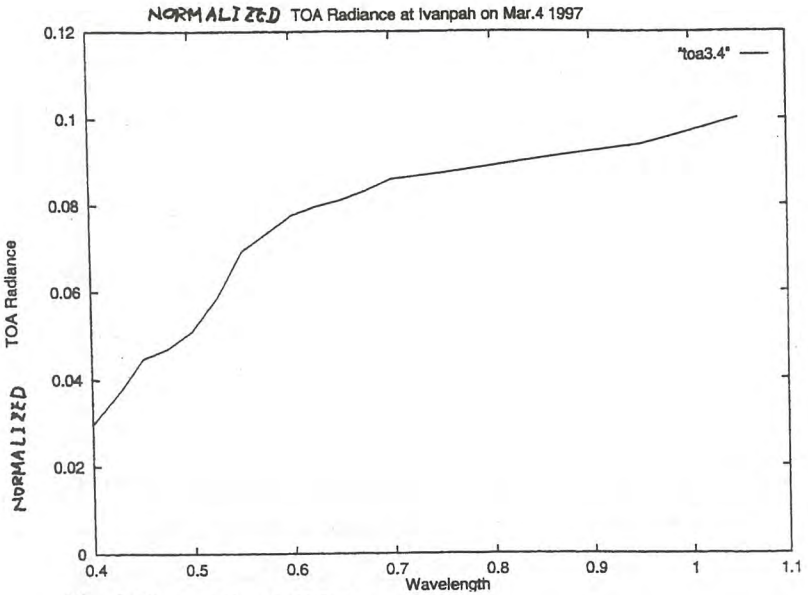


Fig.6 Normalized TOA radiance.

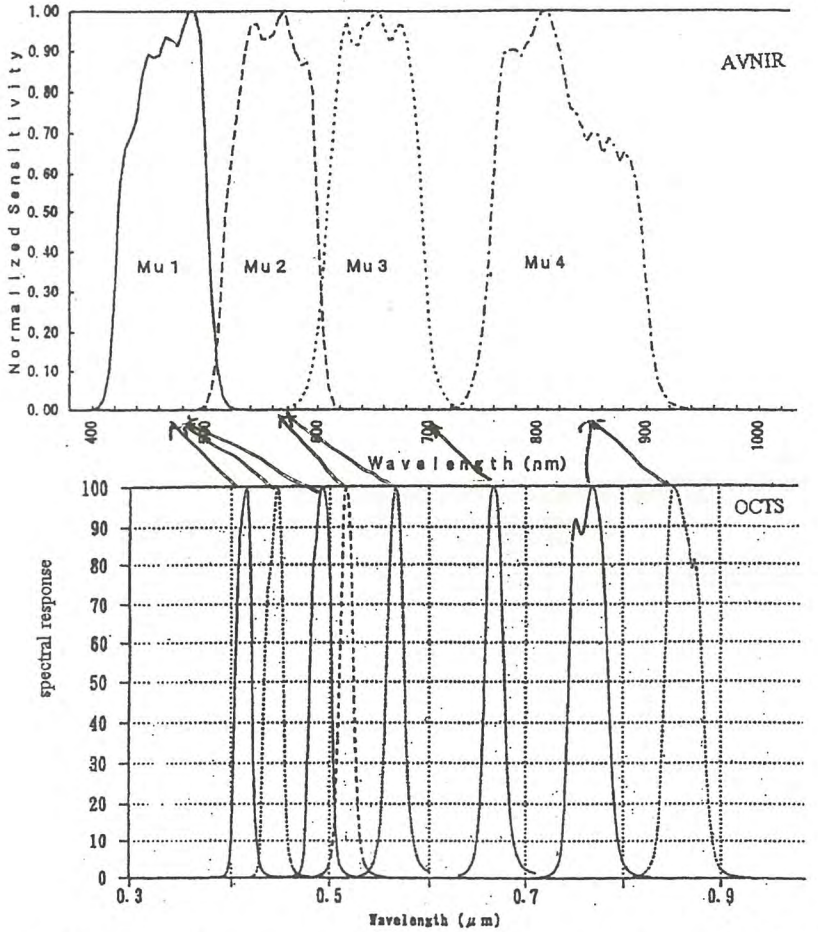


Fig.8 Spectral response of AVNIR. Spectral response of OCTS.

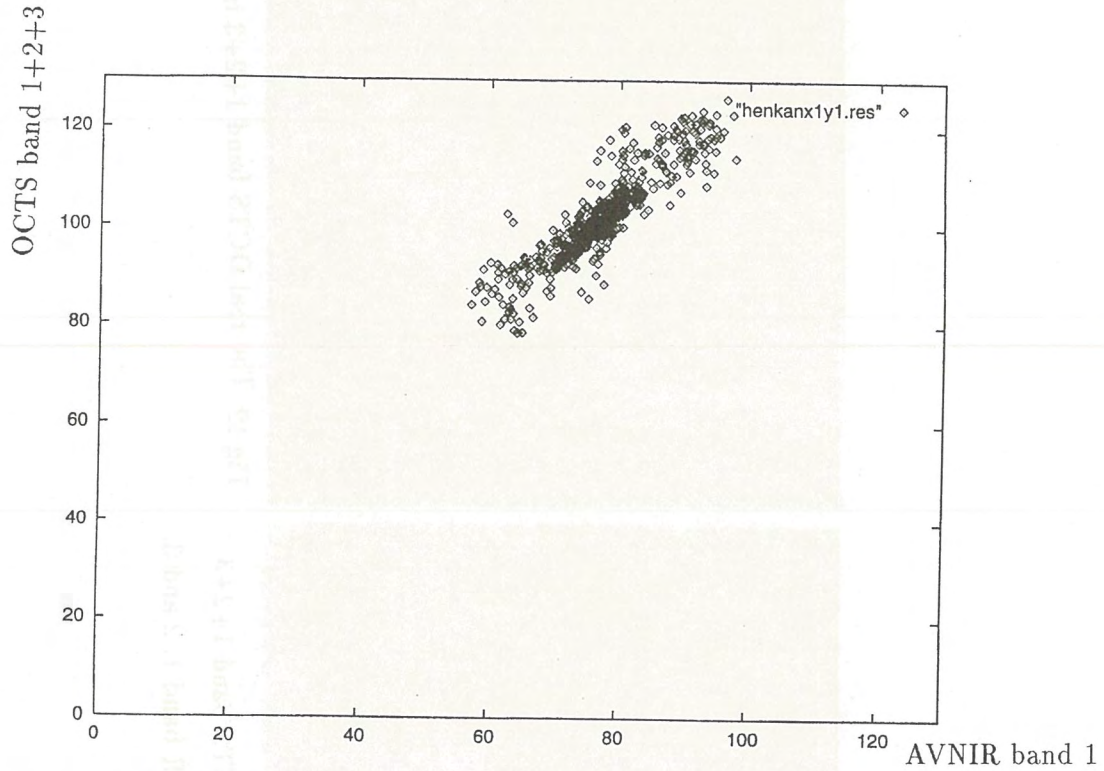


Fig.9 A relationship between the generated AVNIR band 1 and OCTS band 1+2+3.

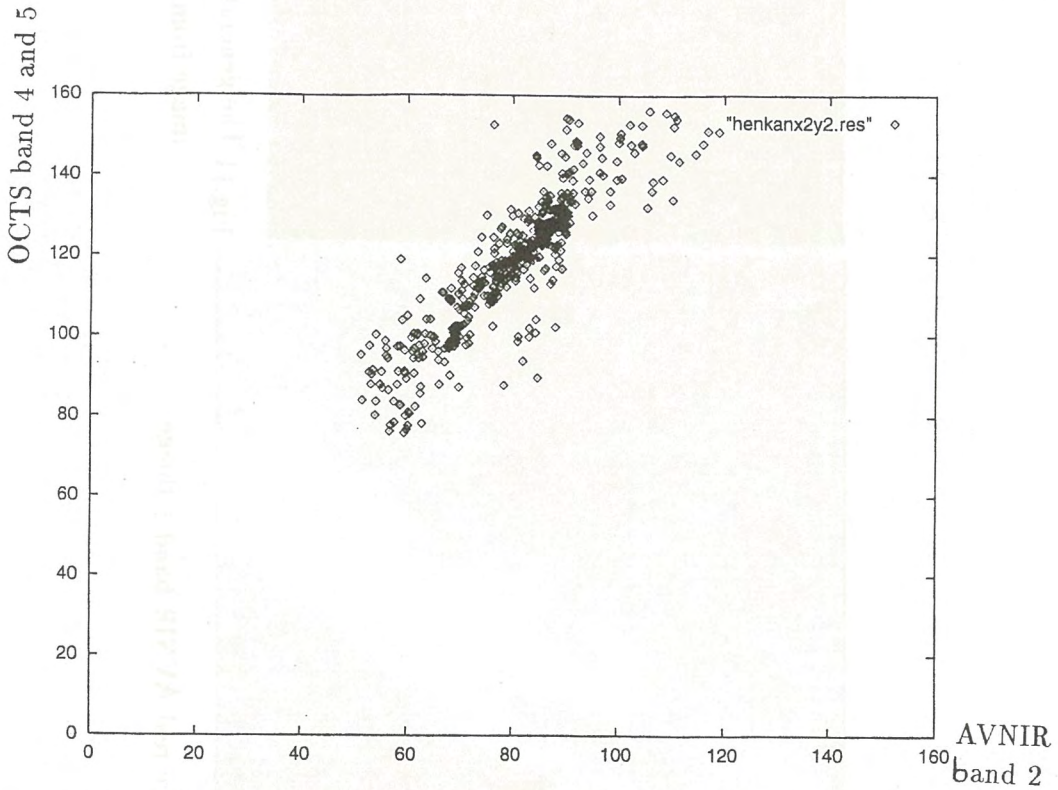


Fig.10 A relationship between the generated AVNIR band 2 and OCTS band 4 and 5.

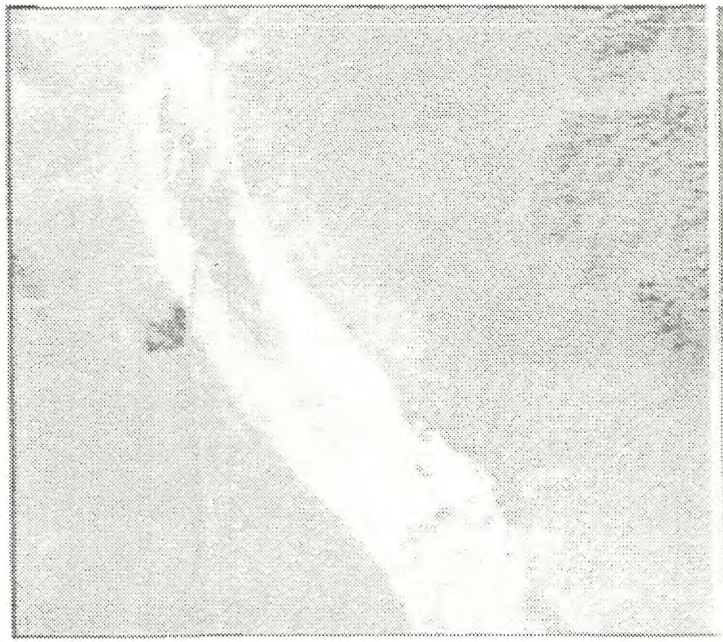


Fig.13 The real AVNIR band 1 image

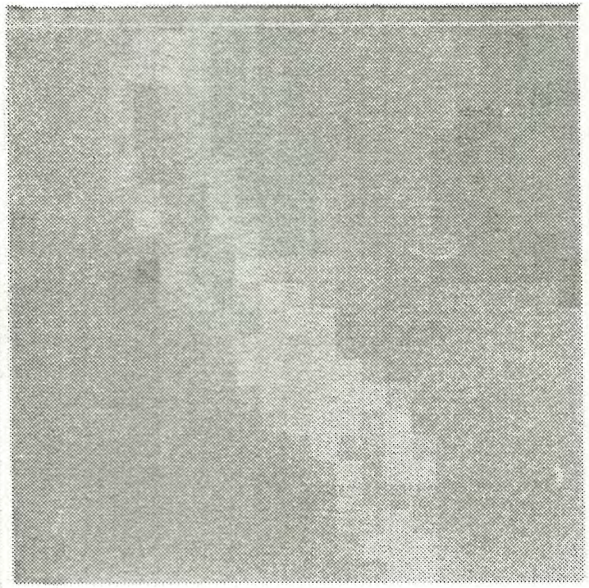


Fig.11 The generated OCTS band 1+2+3 image from AVNIR band 1, 2 and 3.



Fig.12 The real OCTS band 1+2+3 image

BATHYMETRIC MAPPING USING LANDSAT TM
- CASE STUDY IN INDONESIA -

Katsutoshi KOZAI (Kobe Univ. Mercantile Marine)
Winardi(Kobe Univ.Mercantile Marine & LIPI/PPPO)

1. Introduction

Protecting fragile shallow water ecosystems and managing maritime development and planning activities in the eastern region of Indonesia is one of the high priorities for the Government of Indonesia. In order to fulfill these basic needs, observations were carried out around Padar, a small island located between Sumbawa and Flores, to collect the basic data of shallow waters such as depths and bottom types in September, 1994.Landsat Thematic Mapper(abbreviated to TM)image covering the in situ study area is used for spatially analysing depths and bottom types. The purpose of this study is to estimate and evaluate bathymetry around Padar island using Landsat TM.

2. Satellite and In situ data

Fig.1 shows the study area around Padar island taken from Landsat TM. Padar island is located at the northwest section of the study area and in situ observation is made on the northern part of the island(indicated as optically shallow water, bottom visible).Optically deep water area(bottom not visible) is also illustrated at the southwest section of the study area where the depth is more than 200 meters. Table 1 shows the observed depths and bottom types around Padar Bay. Depth is ranging from 0.75 to 17 meters and four bottom types including dead and live corals are identified. Since maximum detectable depths are 6.4, 3.0 and 2.1 meters for TM band1,2 and 3 respectively[1], depths ranging from 0.75 to 5 meters are used for modeling and verification purposes.

As indicated in Fig.1, the geometrically corrected Landsat TM image (taken on Aug.26, 1993, band 1 to 4) covers 25 x 25 km area and is resampled at 25 x 25 meters per pixel.

3. Method

Several bathymetric models using Landsat TM were tested and a multiband-multilinear model[2] with two water-penetrating bands(TM band 1, 0.45~0.52 μ m and TM band 2, 0.52~0.6 μ m) was selected for model verification because of high multiple correlation coefficient of 0.74. This model assumes a generalized ratio[3] defined as follows.

$$(R_{1A})^{c1} x (R_{2A})^{c2} = (R_{1B})^{c1} x (R_{2B})^{c2} = \alpha \qquad (1)$$

where R_{1x} is the reflectance of the sea bottom in channel 1 over bottom type

x. Based on this assumption and TM two bands of information, the exponential attenuation model is given as follows.

$$z=w_1\{\ln(R_{1B})-X_1\}/2k_1+w_2\{\ln(R_{2B})-X_2\}/2k_2 \quad (2)$$

where z is depth, $X_i=\ln(L_i-L_{i\infty})$, L_i=radiance in TM band i and $L_{i\infty}$ is the radiance in band i over optically deep water(bottom not visible); k_1 and k_2 are the effective attenuation coefficients for each band. The weights w_1 and w_2 satisfy that $w_1+w_2=1$. So the multiband-multilinear model is described as follows.

$$z=M_0+M_1X_1+M_2X_2 \quad (3)$$

where the constants, M_0, M_1, M_2 are determined by multiple regression analysis for the known water depths. Fig.2 shows the spectral dependence of variable X_i on the observed depths.

4. Results

Based on the dataset above a model is adopted as follows.

$$z=-3.42+5.04X_1-2.1X_2 \quad (4)$$

Multiple correlation coefficient is 0.92.Standard error of estimated depth of the model is about 59 cm for the depth range of 5 meters.In order to evaluate the model performance the residual versus observed depth is illustrated in Fig.3.High residuals are found most in the specific region where the mixed bottom type exists.Influences of bottom type on the model performance including the generalized ratio assumption is under investigation.

Acknowledgements

This work is carried out by the joint research program of CEReS, Chiba University(9-5).

References

1) Ji,W, D.L.Civco and W.C.Kennard (1992): Satellite Remote Bathymetry: A New Mechanism for Modeling, Photogrammetric Engineering and Remote Sensing, Vol.58, No.5, pp545-549.

2) Paredes,J.M. and R.E.Spero (1983): Water depth mapping from passive remote sensing data under a generalized ratio assumption, Applied Optics, Vol.22, pp1134-1135.

3) Clark,R.K.,T.H.Fay,H.V.Miller and C.L.Walker (1990):Thematic Mapper Band Selection for Bathymetric Measurements, Proceedings of Ocean Optics X,Vol.1302, pp.630-640.

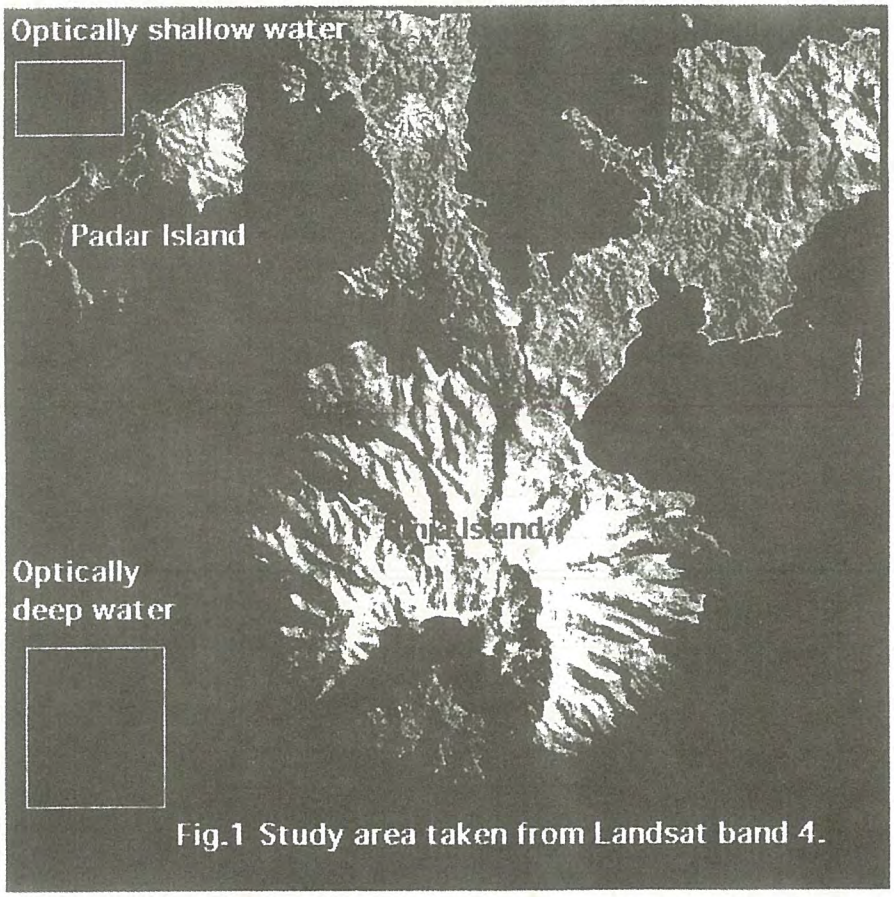


Fig.1 Study area taken from Landsat band 4.

Table 1. Observed depths and bottom types around Pulau Padar Bay waters.

No.	Longitude (deg. E)	Latitude (deg. S)	Depth (meter)	Bottom type
1	119.5626	8.6511	2.4	dead corals
2	119.5630	8.6505	10.5	live corals
3	119.5640	8.6512	2.5	live corals
4	119.5651	8.6513	1.5	seagrass
5	119.5661	8.6525	0.8	seagrass
6	119.5670	8.6534	1.3	seagrass
7	119.5675	8.6532	10.1	sand
8	119.5678	8.6540	2.1	live corals
9	119.5681	8.6541	4.5	sand
10	119.5694	8.6547	1.5	seagrass
11	119.5721	8.6509	1.1	dead corals, etc
12	119.5721	8.6498	1.9	seagrass
13	119.5725	8.6491	1.0	seagrass
14	119.5720	8.6484	4.2	seagrass
15	119.5735	8.6473	0.9	live corals
16	119.5714	8.6475	5.0	live corals, etc
17	119.5696	8.6483	1.5	sand, etc
18	119.5687	8.6474	17.0	live corals
19	119.5706	8.6442	15.0	live corals

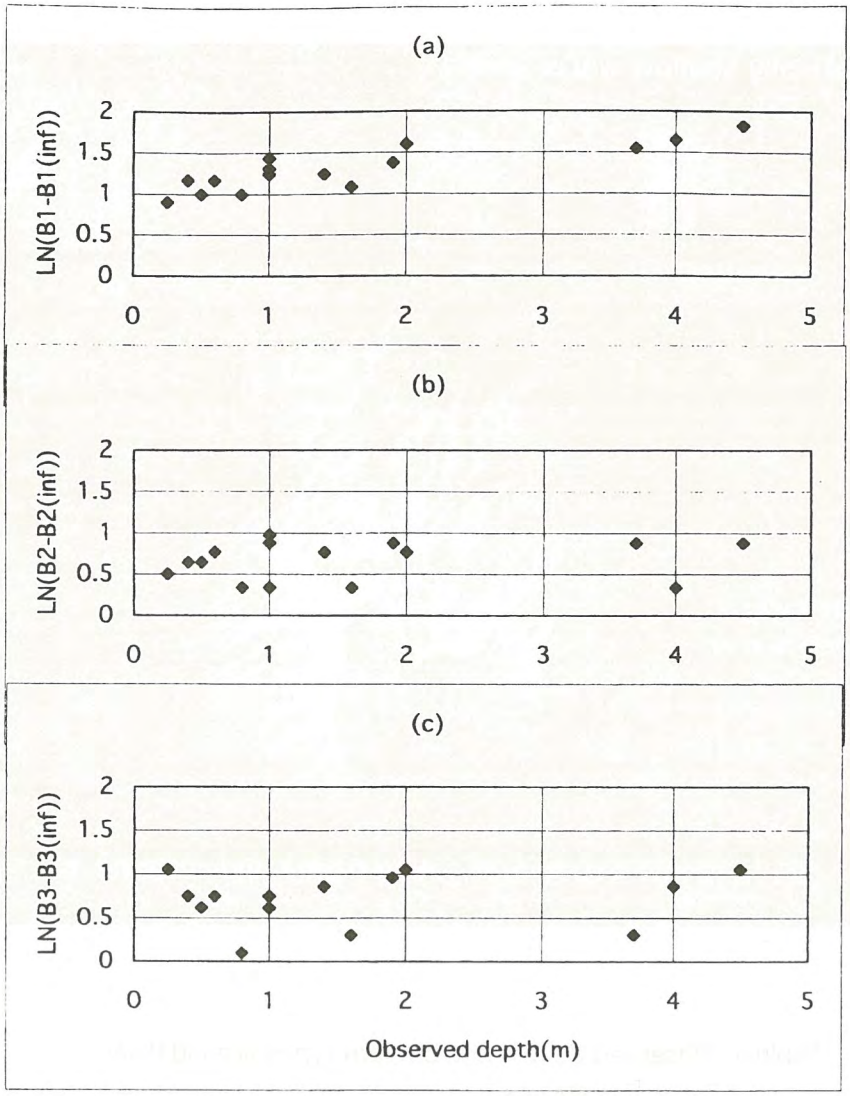


Fig.2 Observed depth versus LN(Bi-Bi(inf)). (i=band No.)

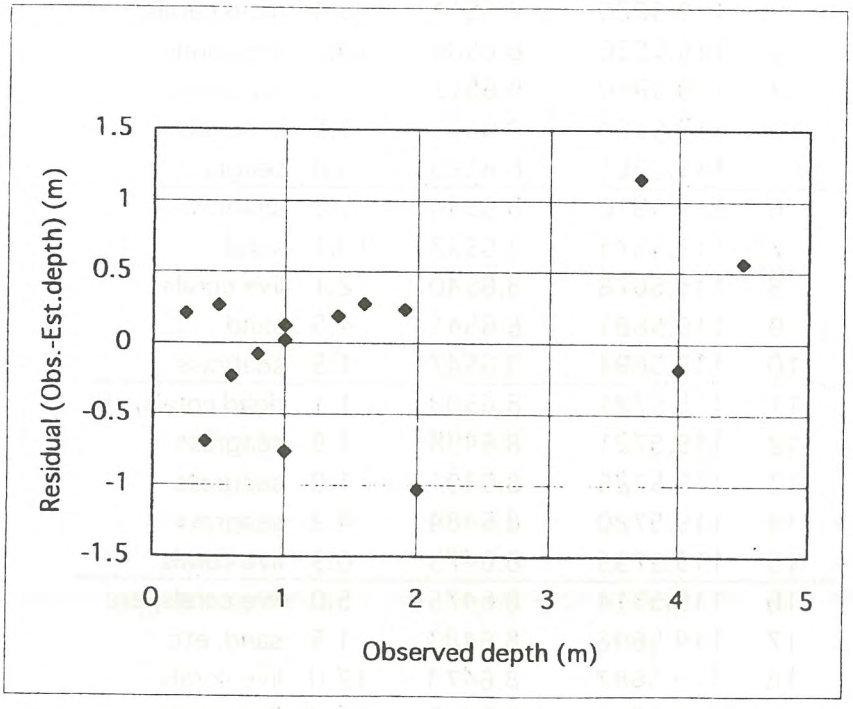


Fig.3 Residual versus observed depth.

Experiences in Atmospheric Correction for ADEOS/OCTS Ocean Color Data

Hajime Fukushima[†], Mitsuhiro Toratani[†], Yasushi Mitomi[‡], and Toshimitsu Noguchi[†]

[†]*School of High-Technology for Human Welfare, Tokai University*
[‡]*Earth Observation Research Center, National Space Development Agency*
E-mail: hajime@fc.u-tokai.ac.jp Fax: +81-559-68-1155

Abstract. We first describe the atmospheric correction algorithm for OCTS (Ocean Color and Temperature Scanner) that has been used for the standard product generation at NASDA/EOC (Earth Observation Center). During the pixel-wise processing, the algorithm selects 2 aerosol models out of 10 candidate models and determines the " interpolation ratio" based on the estimated spectral ratio of aerosol optical thickness at 670 and 865 nm bands. We then discusses several variants of the aerosol model selection scheme and compares the performance of the schemes by simulating the atmospheric correction process in use of modeled aerosol signals. The results suggest the superiority of a scheme that iteratively determines the final candidate aerosol models. We finally compares the OCTS algorithm and the old CZCS algorithm in use of a data set of 32 in-situ observation that were conducted contemporaneously with the satellite observation. While the OCTS algorithm gives smaller estimation error in the normalized water-leaving radiances, the CZCS algorithm attaines similar performance of errer factor 2 in terms of the satellite-derived chlorophyll-a concentration. This is considered due to the nature of the estimation algorithm that relies on the ratio of the water-leaving radiances.

1. Introduction

Correction of the atmospheric effect is very important for qualitative ocean color remote sensing. As it is often pointed out, the portion of " water-leaving radiance" to the total observed radiance can be as low as few percent, while radiance due to aerosol particles varies over a range similar to that of water-leaving radiance. This demonstrates the difficulty of the problem.

Ocean color atmospheric correction, however, is not impossible if we utilize near infra-red band observation where we can retrieve information of atmosphere exclusively. For CZCS data, Gordon *et al.* (1983) proposed an algorithm based on the single scattering approximation. The algorithm was widely accepted (see Feldman *et al.*, 1989, for example) and gave us satisfiable results for most of the cases.

For OCTS (Ocean Color and Temperature Scanner) and SeaWiFS, much improvement in the performance is endeavored because these instruments observe the ocean surface over factor-2 wide spectral range (412~865nm) with higher radiometric resolution (10bits). Gordon an Wang (1994) proposed an algorithm for SeaWiFS data that takes the following elements, (a) pixel-wise aerosol-type variability, and (b) multiple scattering that involves aerosol, into accounts. The atmospheric correction algorithm used since April, 1997 at NASDA/EOC for the OCTS standard data products is based on that algorithm with some modifications. In this paper, we first describe the OCTS algorithm that uses ten aerosol models including that of Asian dust. The algorithm selects an appropriate pair of aerosol models and determines the interpolation ratio between the aerosol reflectances of the two models based on the observed aerosol reflectances in the NIR bands. We will briefly discuss the performance of the algorithm in comparison with the CZCS algorithm, which assumes constant aerosol type over at least whole image.

We will then discuss some variants in the scheme for the model selection and the interpolation ratio determination. Simulations are conducted to evaluate and compare the performances of three different schemes.

2. OCTS atmospheric correction algorithm

OCTS aboard ADEOS satellite had been routinely operated from November 1st, 1996 to June 30, 1997, collecting global ocean color data that amounts far more than the CZCS data set. The instrument has 8 observation bands centered at 412, 443, 490, 520, 565, 670, 765, and 865 nm. The nominal bandwidths for 412-670 nm bands are 20 nm while 765 and 865 nm bands have 40 nm width.

The current OCTS algorithm is based on the SeaWiFS algorithm (Gordon and Wang, 1994) but differs from it mainly in the following aspects.

(a) OCTS algorithm uses a table that relates aerosol reflectance $\rho_A+\rho_{MA}$ (multiple scattering included) to aerosol optical thickness, while the SeaWiFS algorithm uses a different table that relates $\rho_A+\rho_{MA}$ to a ρ_{AS}, the aerosol reflectance under the single scattering approximation.

(b) It determines two candidate aerosol models and the interpolation ratio based on the spectral ratio of the aerosol optical thickness rather than ε, or the ratio of single scattering reflectance.

(c) It uses 670 and 865 nm bands for atmospheric correction while the SeaWiFS project will use 765 and 865 nm bands.

Radiative transfer model

In what follows, we describe the current OCTS atmospheric correction algorithm briefly. For precise description, see NASDA/EOC (1997).

The satellite-observed radiance ρ_T is modeled as follows.

$$\rho_T(\lambda) = \rho_M(\lambda) + \rho_A(\lambda) + \rho_{MA}(\lambda) + t(\lambda)\rho_W(\lambda) , \quad (1)$$

where λ is wavelength, ρ_M is reflectance due to gas molecules, ρ_A is aerosol reflectance, ρ_{MA} is reflectance due to the interaction between molecules and aerosol particles, ρ_W is reflectance of the ocean, t is transmittance between ocean surface and the satellite. Note that the model equation here is expressed in terms of reflectance rather than radiance, but radiance L and reflectance ρ is easily converted with each other by the following relation,

$$\rho(\lambda) = \frac{\pi L(\lambda)}{F_0'(\lambda)\cos\theta_0} , \quad (2)$$

where F_0' is extraterrestrial solar irradiance that takes two times of ozone absorption into account, and θ_0 is the solar zenith angle for that pixel.

In comparing the OCTS model equation (1) with that of the CZCS algorithm, it is noted that the new element introduced is ρ_{MA}, the interaction between gas molecules and aerosol particles.

Aerosol Models

Since the water reflectance ρ_W can be discarded in the NIR (670~865nm) bands, we can obtain the aerosol reflectance including the interaction part as follows,

$$\rho_A(\lambda) + \rho_{MA}(\lambda) = \rho_T(\lambda) - \rho_M(\lambda) . \quad (3)$$

We need to estimate $\rho_A+\rho_{MA}$ for band 1~5 but it is not straight forward since the spectral relation of $\rho_A+\rho_{MA}$ over the whole visible and near IR region is dependent on θ_0, θ, the satellite zenith angle, and $\Delta\phi$, the relative azimuth angle between the sun and the satellite. Similar to the method proposed by Gordon and Wang (1994), we introduces a table that stores the relation between the aerosol reflectance $\rho_A+\rho_{MA}$ and aerosol optical thickness τ_A for each band and uses that table to determine the magnitude of $\rho_A+\rho_{MA}$ in the shorter wavelength's based on the estimated spectral ratio of τ_A between two NIR bands. Since the relation between $\rho_A+\rho_{MA}$ and τ_A is also dependent on the aerosol model, OCTS algorithm has the following ten models:

- Tropospheric aerosol: (Models 1, 2, and 3) with R.H. of 50, 80, and 90%
- Coastal aerosol: (Models 4, 5, and 6) with R.H. of 50, 80, and 99%
- Maritime aerosol: (Models 7, 8, and 9) with R.H. of 50, 80, and 99%
- Asian dust aerosol: (Model 10)

The definition of these models are based on Shettle and Fenn (1979), with the " Coastal type" being a composite of 99.5% of tropospheric and 0.5% of oceanic aerosol, each in terms of number of particles.

The size distribution of Asian dust was determined from ground observations conducted in Nagasaki (Nakajima *et al.*,1989) while the refractive index was given by S.Ohta (private communication) from the absorption measurement of soil particles sampled at Chinese dessert area.

Fig.1 shows $\varepsilon(\lambda,856)$ for all the 10 models, under a typical scan geometry. ε is defined as

$$\varepsilon(\lambda,865) = \frac{\omega_A(\lambda)P_A(\psi,\lambda)\tau_A(\lambda)}{\omega_A(865)P_A(\psi,865)\tau_A(865)} \quad (4)$$

where ω_A is aerosol single scattering albedo, $P_A(\psi,\lambda)$ is aerosol scattering phase function, ψ is the scattering angle.

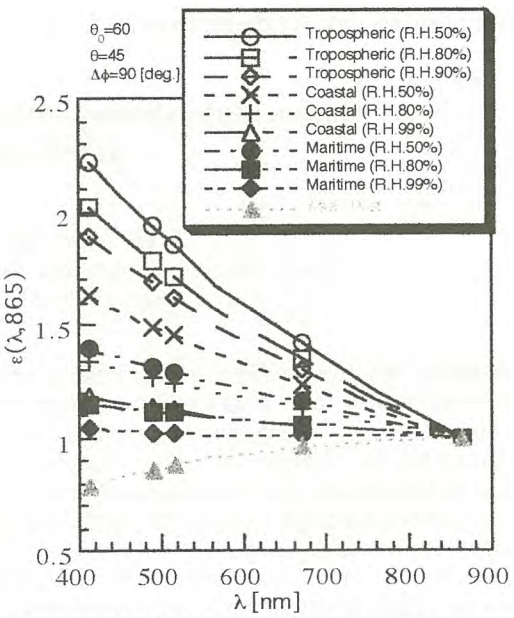


Figure 1. Spectral dependency of $\varepsilon(\lambda, 865)$ for the aerosol models used in OCTS atmospheric correction algorithm. Scan geometry was set to $\theta 0 = 60°$, $\theta = 45°$, $\Delta\phi = 90°$.

Note that $\varepsilon(\lambda,856)$ varies as wide factor of 2 or more in the shorter wavelength region.

Lookup tables

The actual atmospheric corrections implemented to the data processing system at NASDA/EOC has following lookup tables.

(1) ρ_M table that gives $\rho_M(\lambda)$ for the given θ_0, θ, and $\Delta\phi$.

(2) " $\rho_A+\rho_{MA}$ vs. τ_A" table that contains the coefficients a_1, a_2, and a_3 in the equation,

$$\rho_A(\lambda)+\rho_{MA}(\lambda) = a_1\tau_A(\lambda) + a_2\tau_A(\lambda)^2 + a_3\tau_A(\lambda)^3 , \quad (5)$$

for all $(\theta_0, \theta, \Delta\phi)$ and for all aerosol types. We will call this " main aerosol look-up table".

(3) ω_A table that has $\omega_A(\lambda)$ values for all the aerosol models.

(4) K_{ext} table that contains the values of extinction coefficients for all aerosol models.

(5) P_A table that retains aerosol scattering phase functions for all the aerosol models.

The entries for these tables were all generated by rstar5b code developed by T.Nakajima and his group.

Procedure of pixel-wise data processing

The pixel-wise procedure for the atmospheric correction is described as follows. In what follows, $\gamma'(M)$ means the estimated value of the spectral ratio of τ_A between 670 and 865 nm bands for an assumed aerosol model M, while $\gamma(M)$ is the theoretically derived value of K_{ext} ratio for a model M.

(1) Get $\rho_A(\lambda)+\rho_{MA}(\lambda) = \rho_T(\lambda)-\rho_M(\lambda)$ at 670 and 865 nm.

(2) Estimate τ_A at 670 and 865 nm for each assumed aerosol model(M) by solving the cubic equation (5) in reference to the main aerosol look-up table).

(3) Calculate γ'_{ave} by

$$\gamma'_{ave} = \sum_{M=1}^{10} \gamma'(M) , \quad (6)$$

to select a pair of aerosol models A and B that have closest $\gamma'(M)$ values to γ_{ave}', such that $\gamma'(A) < \gamma_{ave}'$ and $\gamma'(B) > \gamma_{ave}'$. If γ_{ave}' has higher (or lower) value than all the γ valus, go to the step (6). Define interpolation ratio r as $(\gamma_{ave}' - \gamma'(A))/(\gamma'(B) - \gamma'(A))$.

(4) For models A and B, obtain $\tau_A(\lambda,M)$ for band 1~5 (412~565 nm) by

$$\tau_A(\lambda, M) = \frac{K_{ext}(\lambda, M)}{K_{ext}(865, M)} \tau_A(865, M) . \quad (7)$$

Derive $\rho_A(\lambda)+\rho_{MA}(\lambda)$ for the models A and B in use of the aerosol LUT.

(5) Obtain final $\rho_A(\lambda)+\rho_{MA}(\lambda)$ by interpolating the $\rho_A+\rho_{MA}$ values for the models A and B.

(6) (In case γ_{ave}' is higher (or lower) than all the $\gamma(M)$ values) Select model 1 (or model 10) to determine $\rho_A(\lambda)+\rho_{MA}(\lambda)$ in the same way as described above but for the single model.

Example of processed imagery

Figure 2 shows an example of atmospherically corrected OCTS imagery. Plate (a) is aerosol radiance at the 865 nm band defined as

$$L_A(865) = L_T(865) - L_M(\lambda) = \frac{1}{\pi}(\rho_T(865) - \rho_M(865))F_0'(865)\cos\theta_0 . \quad (8)$$

Plate (b) shows $\gamma'_{ave}(670,865)$ derived from the satellite observation. Normalized water-leaving radiance at 490 nm band defined as

$$nL_W(490) = \frac{L_W(490)}{t_0(490)\cos\theta_0} = \frac{F_0'(865)\rho_W(490)}{\pi t_0(490)} , \quad (9)$$

where t_0 is the transmittance between the sun and the sea surface is shown in plate (c). Note that nL_W image has little or no correlation with L_A image, showing that the atmospheric correction was conducted satisfactorily for this particular data. The resulted image of the estimated chlorophyll-a (C) concentration is shown in image (d), using the OCTS standard in-water algorithm,

$$C = 0.2818\{\frac{L_W(520) + L_W(565)}{L_W(490)}\}^{-3.497} . \quad (10)$$

Comparison with the CZCS algorithm

We will study here the superiority of the OCTS algorithm compared to that of CZCS. The purpose of our analysis is to evaluate the error in derived L_W that would be induced by disregarding the pixel-wise variability of aerosol type as exercised by the CZCS algorithm. For simplicity, we will adopt the following radiative transfer model that was used for the CZCS algorithm.

$$L_T(\lambda) = L_M(\lambda) + L_A(\lambda) + t(\lambda)L_W(\lambda) , \quad (11)$$

where L_T is the total radiance, L_M is the radiance due to the molecular scattering, L_W is the water-leaving radiance. This simple model is enough for the analysis since we are only concerned with the difference in L_W. We also assume the single scattering approximation holds for the aerosol radiance $L_A(\lambda)$, which is given as

$$L_A(\lambda) = \frac{\omega_A(\lambda) P_A(\psi, \lambda)\tau_A(\lambda)F_0'(\lambda)}{4\pi\cos\theta} . \quad (12)$$

Combining (4) with (12) gives

$$L_A(\lambda) = \varepsilon(\lambda, \lambda_0)L_A(\lambda_0)\frac{F_0'(\lambda)}{F_0'(\lambda_0)} , \quad (13)$$

where λ_0 is a reference NIR wavelength such as 865 nm. Assuming $L_W(\lambda_0)$ is 0, we have

$$L_W(\lambda) = \frac{1}{t(\lambda)}\{L_T(\lambda) - L_M(\lambda) - \varepsilon(\lambda, \lambda_0)L_A(\lambda_0)\frac{F_0'(\lambda)}{F_0'(\lambda_0)}\} . \quad (14)$$

In OCTS algorithm, ε is variable pixel-wise while for CZCS it is often assumed to be unity or at least constant over the whole image. Let $\Delta L_W(\lambda)$ be the error due to the difference $\Delta\varepsilon(\lambda, \lambda_0)$. Then,

$$-\Delta L_W(\lambda) = \frac{\Delta\varepsilon(\lambda, \lambda_0)L_A(\lambda_0)}{t(\lambda)}\frac{F_0'(\lambda)}{F_0'(\lambda_0)} . \quad (15)$$

As an example, let us evaluate ΔL_W for the case λ=490nm and λ_0=865nm, when $t(\lambda)\approx 0.9$ and $F'_0(490)/F'_0(865)=1.97$. Analyses of several OCTS images predict that $\varepsilon(490,865)$ varies about ± 0.2 over the entire image. It we take that variability as $\Delta\varepsilon$ and assume $L_A(865)$ of $0.4\mu W/cm^2/nm/sr$ (moderate aerosol under clear sky condition), ΔL_W will be $\pm 0.18\mu W/cm^2/nm/sr$. The resulted error is significantly large, considering that $L_W(490)$ for waters with high pigment concentration could be as low as $0.2\mu W/cm^2/nm/sr$.

3. Modifications of the aerosol type selection scheme

In the standard algorithm described above, γ'_{ave}, required for selection of the two candidate models and for determination of the interpolation ratio, was determined by simply averaging $\gamma'(M)$ over all aerosol models assumed. Since a preliminary analysis of the process shows that, under some conditions, this standard scheme results in significant errors in estimating $\rho_A(\lambda)+\rho_{MA}(\lambda)$ in shorter wavelength bands, we propose here following variants of the scheme.

"Weighted average" scheme

Instead of taking simple average, γ'_{ave} is given by the weighted average,

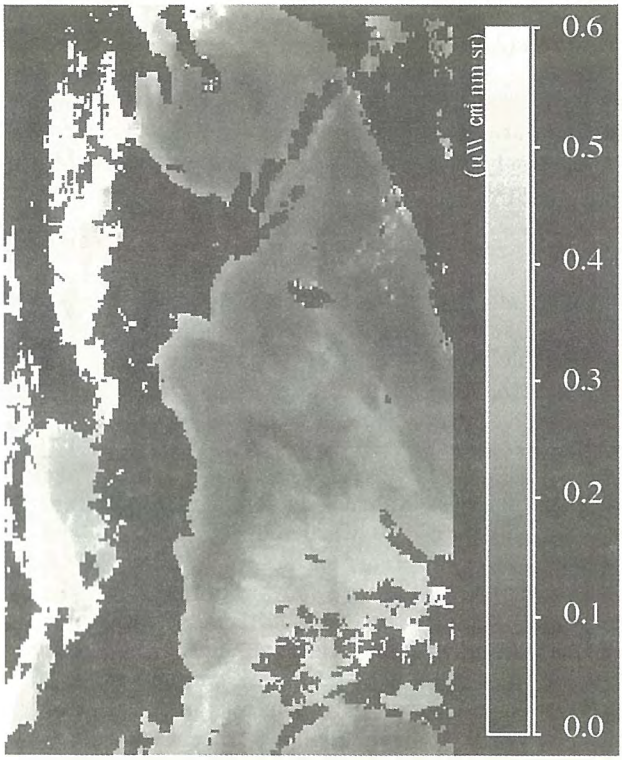
$$\gamma'_{ave} = \frac{\sum_{M=1}^{10} w_M \gamma'(M)}{\sum_{M=1}^{10} w_M} , \quad (16)$$

where $$w_M = \frac{1}{|\gamma'(M) - \gamma(M)|} . \quad (17)$$

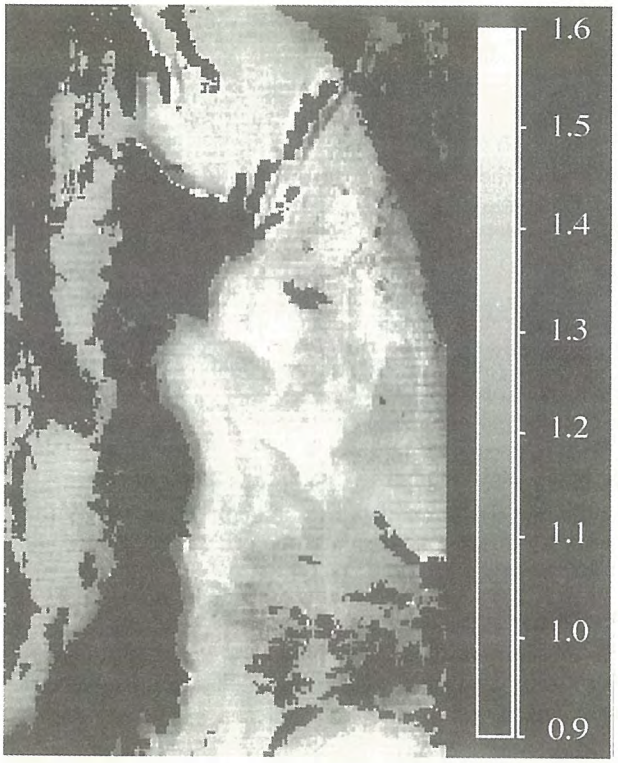
The reason to take the weight as the reciprocal of the difference between estimated and theoretical γ values is to put highest weight to the model that gives the closest estimated value to its theoretical value. In other words, if the satellite observes aerosol of that type (say, M), we will have $\gamma'_{ave} = \gamma(M)$. The rest of the algorithm stays just the same as the standard algorithm.

"Weighted average with iteration" scheme

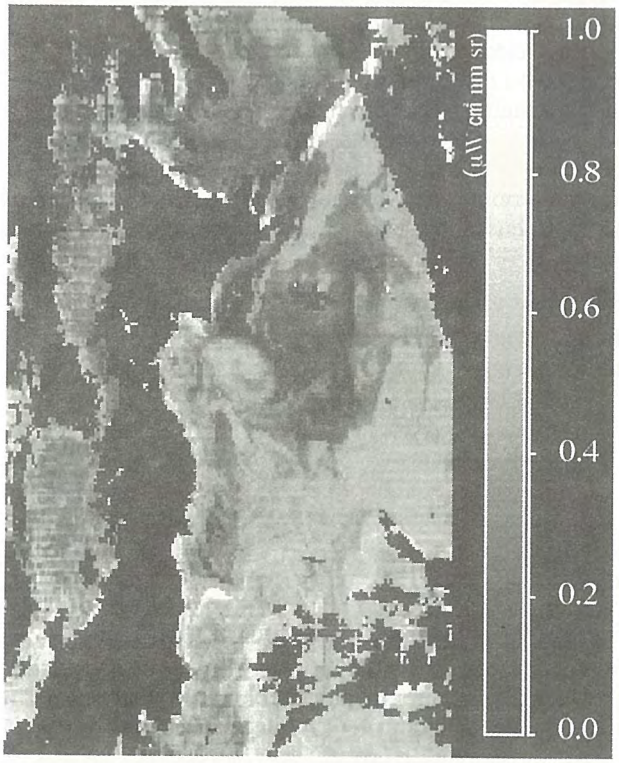
This scheme is to iteratively drop two models to update γ'_{ave} based on new candidate aerosol models. That is, we calculate γ'_{ave} by



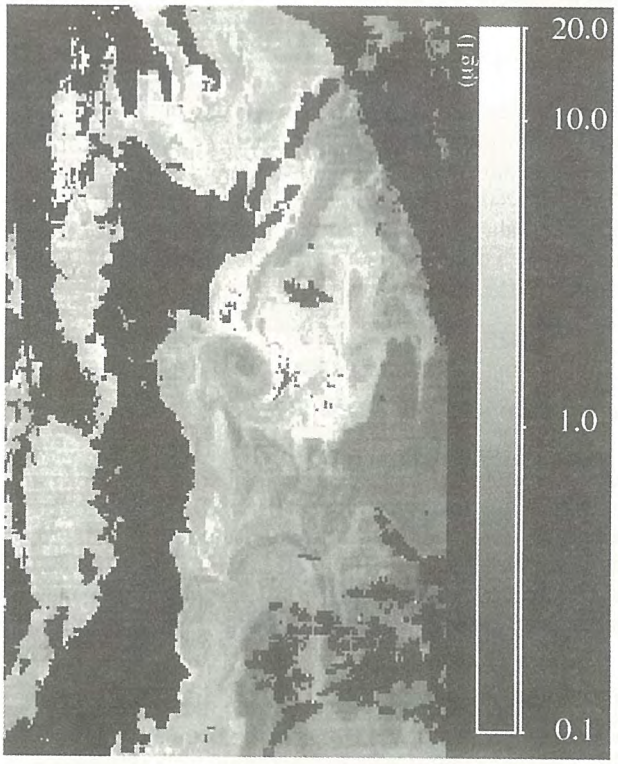
(a) $L_A(865)$



(b) $\gamma'_{AVE}(670,865)$

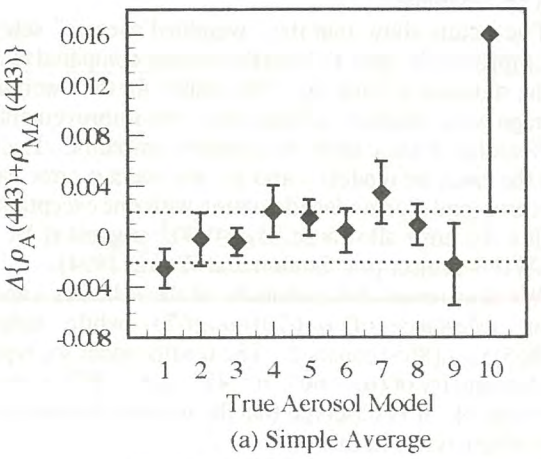


(c) $nL_W(490)$

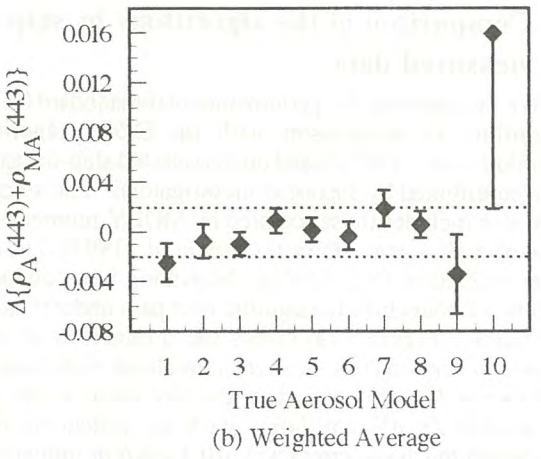


(d) Chl-a

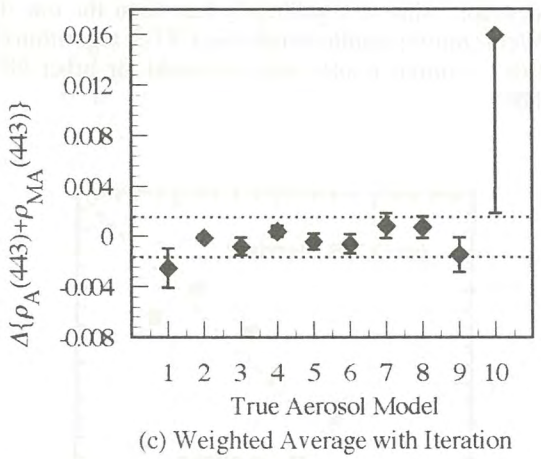
Figure 2. Atmospherically corrected images of OCTS data obtained on April 26,1997. (a) Aerosol radiance at 865nm. (b) $\gamma'_{ave}(670,865)$ defined as the ratio of estimated aerosol radiance between 670nm and 865nm. (c) Derived normalized water-leaving radiance at 490nm. (d) Derived estimate of chlorophyll-a concentration.



(a) Simple Average

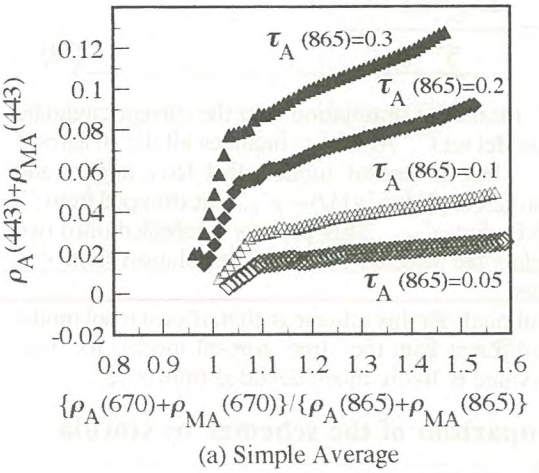


(b) Weighted Average

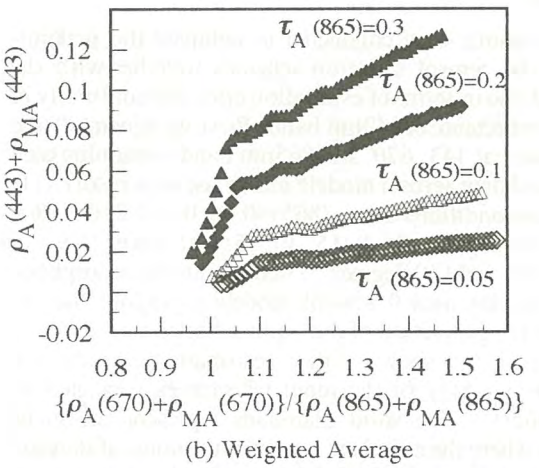


(c) Weighted Average with Iteration

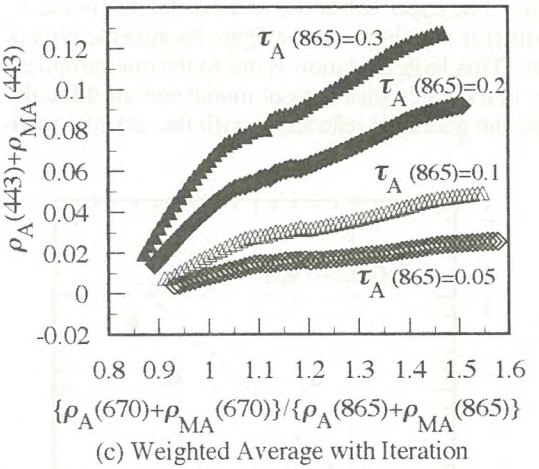
Figure 3. Estimation error in aerosol reflectance at 443nm for different schemes. "True aerosol model" in the abscissa corresponds to the aerosol model used to generate input reflectances for the atmospheric correction. (a) The results for the standard scheme. (b) The same but for the "weighted average" scheme. (c) For the weighted average with iteration.



(a) Simple Average



(b) Weighted Average



(c) Weighted Average with Iteration

Figure 4. Continuity on estimated aerosol reflectance at 443nm band for different aerosol selectionscheme. $\rho_A(443)+\rho_{MA}(443)$ represents output of the atmospheric correction algorithm for vaiable spectral ratio of near infra-red aerosol reflectance between 670nm band and 865nm band. Scan geometry was θ_0=0°, θ=45°, $\Delta\phi$=90°.

(a) The results for the simple average scheme. (b) The same but for the weighted average. (c) For the weighted average with iteration.

$$\gamma'_{ave} = \frac{\sum_C w_M \gamma'(M)}{\sum_C w_M} , \qquad (18)$$

where Σ_C means the summation over the current candidate aerosol model set C. At first, C includes all the 10 aerosol models. Then, 2 aerosol models that have largest and second largest $\Delta\gamma(M) = |\gamma(M) - \gamma'_{ave}|$ are dropped from C, resulting in new γ'_{ave}. This process is repeated until two final models are selected and the interpolation ratio r is determined.

The rationale for this scheme is that, if an aerosol model is much different from the "true" aerosol model, its theoretical g value is likely much deviated from γ'_{ave}.

4. Comparison of the schemes by simulation

Simulations were conducted to compare the performance of the aerosol selection schemes together with the standard one in terms of estimation error and continuity in aerosol reflectance of 443nm band. First we generate "true reflectance" at 443, 670, and 865nm bands assuming each of 10 candidate aerosol models and in use of aerosol LUT, under the conditions that $\tau_A(865)$=0.05, 0.1, 0.2, 0.3, θ_0 = 20, 40, 60 degrees, θ = 0, 15, 30, 45, 60 degrees, $\Delta\phi$ = 0, 30, 60, 90, and 120 degrees. Then we run the atmospheric correction that uses 9 aerosol models excluding the one used for the generation of the input reflectances.

Figure 3 shows the estimation error in $\rho_A(443)+\rho_{MA}(443)$ for the input reflectances generated by each model. The solid diamonds represent the grand average where the error bars represent the range of standard deviation. The upper half of the error bar for the model 10 (Asian dust) is not shown in the figure because the error is too large. This large deviation is due to the unique optical property of the Asian dust aerosol model and the difficulty to handle the generated reflectance with the rest of 9 models. This is also true for the model 1 because that model is also an "extreme".

The results show that the "weighted average" scheme (b) improves the error 18% on the average compared to that of the standard scheme (a). The results for the "weighted average with iteration" scheme show the improvements of 58% on the average from the standard procedure. Excluding the cases for models 1 and 10, the average error for all the cases (and the standard deviation with one exception) is within the error allowance $|\Delta\rho| \leq 0.002$ suggested by the SeaWiFS project (see Gordon and Wang, 1994).

We also tested the continuity of the schemes varying input reflectance of $\rho_A(670)+\rho_{MA}(670)$ while keeping $\rho_A(865)+\rho_{MA}(865)$ constant. The results under the typical scan geometry of (θ_0 = 60°, θ = 45°, $\Delta\phi$ = 90°) is shown in Figure 4. It is observed that the iterative scheme gives smoothest result in this test.

5. Comparison of the algorithms by ship-measured data

We evaluate here the performance of the standard OCTS algorithm, in comparison with the CZCS algorithm (Gordon *et al.*, 1983) based on the selected ship-measured data contributed by Japanese investigators. The selected data also includes those acquired by MOBY moored buoy deployed off Lanai, Hawaii (Clark *et al.*, 1997). The data were selected so that the ship observation was conducted within 12 hours from the satellite over pass under clear sky condition. Figure 5 (a) shows the comparison of ship-measured and satellite-derived normalized water-leaving radiance at 443 nm band where the root mean square error is about 0.23 μW/cm^2/nm/sr with no systematic bias. Although much less error level of 0.1 μW/cm^2/nm/sr or so is desirable, this is significantly less than the one (0.32 μW/cm^2/nm/sr) resulted under the CZCS algorithm (Fig. 5 (b)). Similar results were obtained for other OCTS bands.

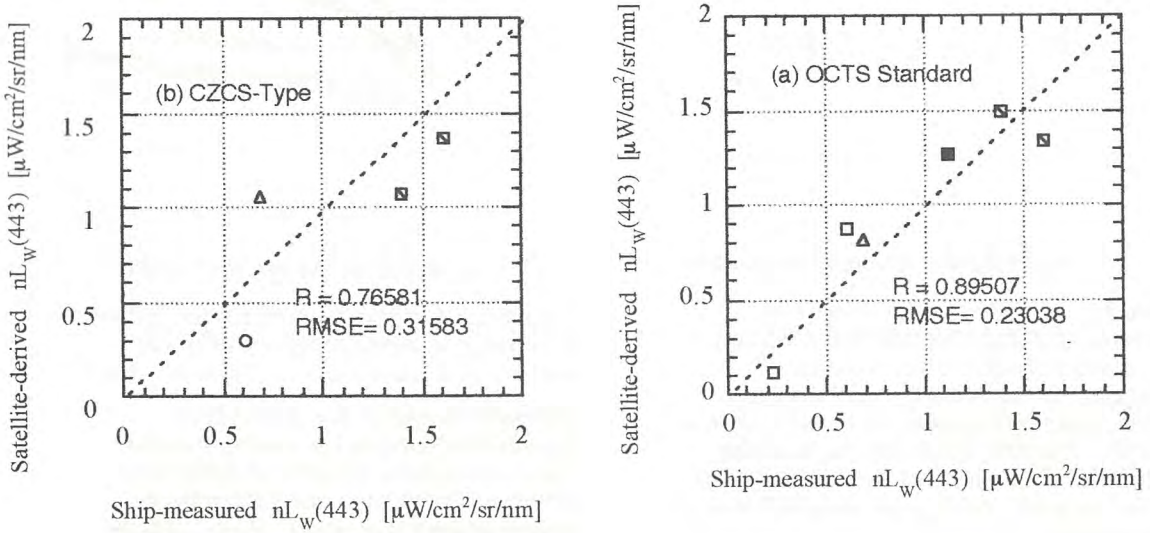


Figure 5 Comparison of ship-measured and satellite-derived normalized water-leaving radiance at 443 nm band under (a) OCTS standard and (b) CZCS-type atmospheric correction algorithms.

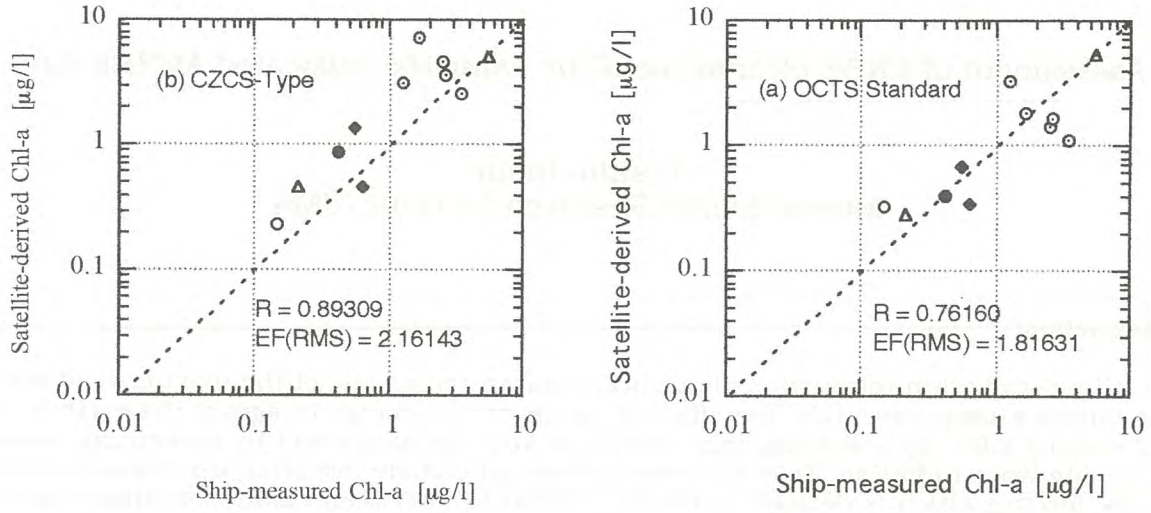


Figure 6 Comparison of ship-measured and satellite-derived Chlorophyll-a concentration under (a) OCTS standard and (b) CZCS-type atmospheric correction algorithms.

Figure 6 shows similar comparison but for Chlorophyll-a concentration. The root mean square error in reference to the perfect fit line is about 1.8 (+80% or -45%) for the OCTS algorithm and about 2.2 (+120% or -55%) for the CZCS algorithm, showing the superiority of the former.

6. Conclusion

To update the current software for OCTS standard product generation at NASDA/EOC, the "weighted average" scheme will be implemented into the "version 3" software which is supposed to be completed by the end of October, 1997. The "iterative scheme" was developed after the decision had been made and may be implemented in the future.

Acknowledgment

The authors thank Dr. T.Nakajima, Ms. A.Higurashi, Mr. Y.Mitomi, Mr. T.Tanaka, and the engineers at NEC Corp. and NEC Aerospace Systems, *Ltd.*, who jointly worked for the development and the implementation of the OCTS atmospheric correction algorithm. They also thank Japanese and international colleagues who have contributed their in-situ data to NASDA for calibration and validation of OCTS. This work received support from the National Space Development Agency of Japan (NASDA) under contract PSPC-20117.

References

Clark, D. K., H. R. Gordon, K. J. Voss, Y. Ge, W. Broenkow, and C. Trees, Variation of atmospheric correction over the ocean, J. Geophys. Res., 102, D14, 17209-17217, 1997.

Feldman, G. C., N. Kuring, C. Ng, W. Esaias, C. McClain, J. Elrod, N. Maynard, D. Endres, R. Evans, J. Brown, S. Walsh, M. Carle, and G. Podesta, Ocean color: availability of the global data set, Eos Trans. AGU, 70(23), 634-635, 640-641, 1989.

Gordon, H.R., D. K. Clark, J. W. Brown, O. B. Brown, R. H. Evans, and W. W. Broenkow., Phytoplankton pigment concentrations in the Middle Atlantic Bight: comparison of shop determinations and CZCS estimates, Appl. Opt., 22(1), 20-36, 1983.

Gordon, H. R., J. W. Brown, and R. H. Evans., Exact Rayleigh scattering calculations for use with the Nimbus-7 coastal zone color scanner, Appl. Opt., 27(5), 862-871, 1988.

Gordon, H.R., and M. Wang., Retrival of water-leaving radiance and aerosol optical thickness over the oceans with SeaWiFS: a preliminary algorithm, Appl. Opt., 33(3), 443-452, 1994.

Nakajima, T., M. Tanaka, M. Yamamoto, M. Shiobara, K. Arao, and Y .Nakanishi, Aerosol optical characteristics in the yellow sand events observed in May, 1982 at Nagasaki - part II models, J. Meteor. Soc. Japan, 67, 279-291, 1989.

NASDA/EOC, Advanced Earth Observing Satellite (ADEOS): OCTS Data Processing Algorithm Description, Ver. 2.0.1, 1997, Anonymous FTP site, ftp://ftp2.eorc.nasda.go.jp/pub/format/OCTS/PDF/ALGORITHM/, 1997.

Shettle, E. P., and R. W. Fenn., Models for the aerosols of the lower atmosphere and the effects of humidity variations on their optical properties, AFGL-TR-79-0214, 675, 94pp, 1979.

Assessment of ERBE clear scene ID by using the collocated AVHRR data

Toshiro Inoue
Meteorological Research Institute/JMA

1. Introduction

Cloud-radiation interactions have been considered as one of the most critical areas in global climate change research. The effect of clouds on the energy budget of the earth is in the way of cooling effect by reflecting solar radiation and warming effect by preventing the earth-emitted long-wave radiation. To study cloud effects on climate, we often use the term of cloud radiative forcing which is defined as the flux difference between cloudy condition and clear condition. We understand that the reliability of cloud radiative forcing is depending on how accurately we can estimate the clear radiance.

In this study, collocated ERBE and AVHRR data are used to compare ERBE short-wave and long-wave fluxes at the top of the atmosphere, and cloud/cloud-free information by AVHRR data within the footprint of the ERBE. The ERBE S-8 data include scene ID which indicates clear, partly cloudy and overcast within a footprint. We used this scene ID for selecting cloud free data for the ERBE data. On the other hand, the spatial uniformity and mean brightness temperature of 11 μm of AVHRR within the ERBE footprint are used to identify ERBE cloud free scene. To assess these clear scene ID and clear scene determined from AVHRR we compared with visible reflectivity and short-wave fluxes .

2. Data

This study makes use of collocated AVHRR and ERBE observations made from the NOAA-9 polar orbiting satellite, over the eastern Pacific (15S-35S, 75W-100W) for the years 1985 and 1986. The NOAA-9 nominal equator crossing times are 0900 UTC and 2100 UTC.

The AVHRR data used in this study is the Global Area Coverage (GAC) data which has a nominal resolution at nadir of 4 km. The AVHRR has five spectral bandpasses: Channel 1 (0.56-0.68 (μm); Channel 2 (.725-1.1 (μm); Channel 3 (3.55-3.93 (μm); Channel 4 (10.3-11.3 (μm); and Channel 5 (11.5-12.5 (μm). These five channels are located in spectral regions where atmospheric gases are characterized by weak absorption. The AVHRR data are therefore good for studying surface properties, such as sea surface temperature and vegetation properties, and cloud top properties. Inoue (1987) developed a cloud type classification, referred to as the split window technique, based on the equivalent brightness temperature in Channel 4 (BT11) and the temperature difference between Channel 4 and 5 (BTD). The BTD is essential to classify cloud free,optically thin cirrus and optically thick clouds.

ERBE observations are used to specify the broadband energy budget at the top of the atmosphere. At nadir the ERBE footprint is approximate 35 km. The ERBE scanning instrument has been discussed by Kopia (1986). The method of inverting the instantaneous scanner observations to the top of the atmosphere fluxes is discussed in Barkstrom et al (1989), and Smith et al (1986).

Collocation of the AVHRR pixels with the ERBE footprint is accomplished based on the method developed by Ackerman et al. (1992), Ackerman and Inoue (1994). The method is based on the scanning geometry of both instruments.

3. Clear Data Analysis

The first step is to determine the clear-sky thresholds of brightness temperature for 11μm(BT11) and brightness temperature difference between the 11μm and 12μm(BTD) for each 2.5x2.5 latitude/longitude region within the area of study. This is accomplished through analyze of 3x3 groups of AVHRR pixels. In step 1, a first guess threshold of BT11 is determined using the spatial coherence approach of Coakley and Bretherton (1982). The spatial coherence method is used to estimate the clear-sky thresholds for BT11, specified as the foot of the 'foot' of the clear-sky arch.

In the second pass through the data, only those 3x3 groups of pixels that have a standard deviation less than 0.4C and a mean BT11 that is greater than the initial threshold selected by

the spatial coherence analysis are considered. Each group of AVHRR pixels is assigned an appropriate 2.5 by 2.5 degree grid box. The mean BT11 and mean BTD for each grid box are then computed and assigned the clear-sky thresholds values.

Having selected a clear-sky threshold that is a function of month and geographic region, a third pass through the data is made. In this final pass, each individual AVHRR pixel that lies within and ERBE footprint is classified using the predetermined clear BT11 and BTD according to the split window technique.

4. Results

The clear scene ID is compared with the average visible reflectivity computed from collocated AVHRR pixels. The clear scene determined from the collocated AVHRR is also compared with the visible reflectivity. In determination of cloud free footprint, only infrared data is used as was stated before. Figure 1-a shows the bivariate histogram for scene ID and visible reflectivity. The scene ID of 10 indicates cloud free, and 60 indicates partly cloudy. We can see most of the clear scene ID indicates the visible reflectivity is less than 5%. Same features are seen in Figure1-b for the data which cloud cover within the footprint is less than 5%. However, there are some data for the higher visible reflectivity even for the clear scene ID and the cloud cover less than 5%, although cloud cover less than 5% shows smaller number of data than that of clear scene ID.

Figure 2 shows scatter plots of visible reflectivity and scene ID for the data of January in 1986 (b) and other date(a). Figure 3 shows scatter plots of visible reflectivity and cloudiness(%). We can see relatively higher visible reflectivity for both clear scene ID and cloud cover less than 5 % for the case of January in 1986. Other data show much lower visible reflectivity than this. We simply consider that some bad data are included for the data in January. Further study is required to study this reason. Generally speaking, both scene ID and cloud cover less than 5 % show reasonable agreement with visible reflectance.

Figure 4 shows the short-wave flux (W/m*m) and long-wave flux (W/m*m) at the top of the atmosphere retrieved from ERBE observations for the clear scene ID (a) and clear scene by AVHRR (b). This indicates smaller SW for the cloud cover less than 5 % than clear scene ID. This suggest the use of AVHRR shows less contaminated with clouds.

Figure 5-a represents the histogram of cloud cover determined from the collocated AVHRR for the clear scene ID footprint. This means most of clear scene ID corresponds to cloud cover is less than 10% but some are contaminated by cloud up to 100% by the cloud cover estimate from collocated AVHRR. The higher cloud cover might be caused by optically thin cirrus clouds. Figure 5-b shows the histogram of scene ID (10 is clear and 60 is partially cloudy) for the ERBE footprint which is covered by cloud less than 5% determined from collocated AVHRR data. The 90% of the clear scene determined by AVHRR agree with clear scene ID of 10.

5. Summary

The reliability of cloud radiative forcing is depending how clear data is accurate, since the cloud radiative forcing is defined as the flux difference between cloudy conditions and clear conditions. The clear scene of ERBE footprint is determined from collocated AVHRR infrared data.This clear ERBE footprint is compared with clear scene ID assigned by ERBE.The clear scene ID and clear scene which is determined by AVHRR show reasonable agreement in terms of both smaller visible reflectivity and smaller shortwave flux generally. However, the use of collocated AVHRR indicates better results, since it indicates which shows smaller short-wave fluxes (less contaminated with cloud).

References

Ackerman,R., A.Frey, and W. L. Smith,1992:Radiation budget studies using collocated observations from AVHRR,HIRS/2 and ERBE instruments. J.Geophys. Res. 97, 11 513-11 525.

Ackerman, S. A. and T. Inoue,1994: Radiation energy budget studies using collocated AVHRR and ERBE observations. J.Appl,Meteor.,33,370-378

Barkstrom,B.R.,E.F.,Harrison,G.Smith,R. Green, J.Kebler, R. Cess, and the ERBE Science Team, 1989: Earth Radiation Budget Experiment (ERBE) archival and April 1985 results. Bull Amer. Meteor.Soc., 70, 1254-1262.

Inoue,T.,1987:A cloud type classification with NOAA-7 split window measurements. J. Geophys. Res., 92, 3991-4000

Kopia,L.P.,1986:Earth radiation budget experiment scanner instruments. J.Geophys. Res., 24, 400-406.

Smith,G.L.,R.N.Green.E.Raschke,L.B.Avis,J.T.Suttles,B.A.Wielicki,and R.Davies,1986:Inversion methods for satellite studies of the earth's radiation budget:Development of algorithms for the ERBE mission. Rev. Geophys.,24, 407-421.

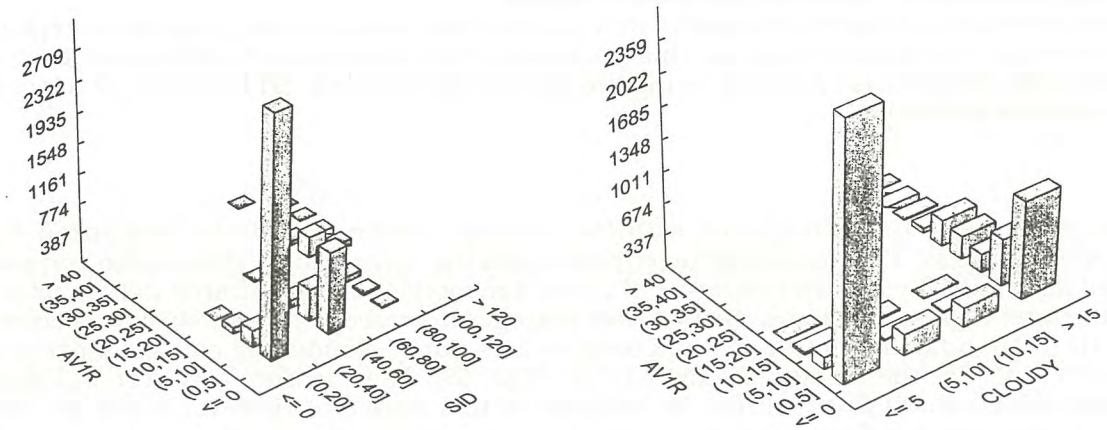


Figure 1-a(left), -b(right). The bivariate histogram for scene ID and visible reflectivity (left) and cloudiness(%) by collocated AVHRR (right).

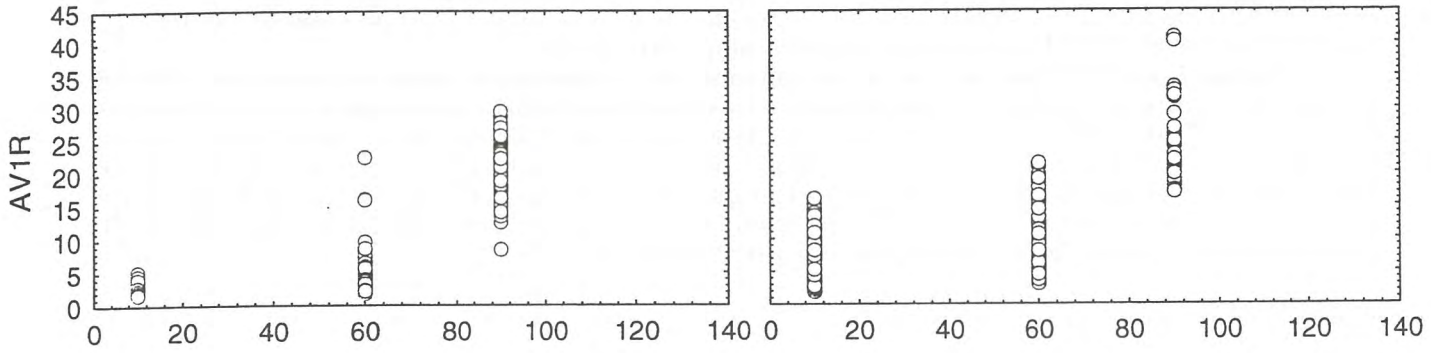


Figure 2 The scatter plots of visible reflectivity and scene ID for the data of January in 1986 (b) and other date(a).

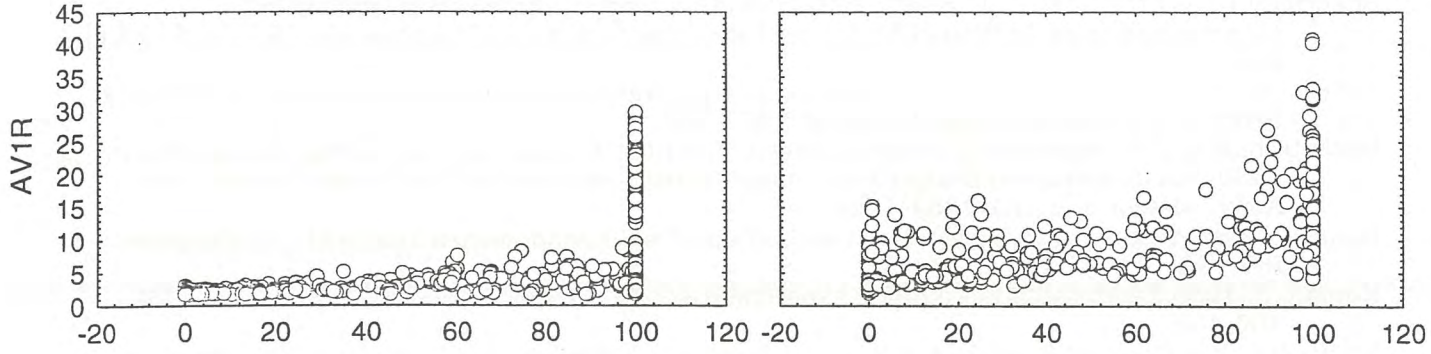


Figure 3 The scatter plots of visible reflectivity and cloudiness(%) for the data of January in 1986 (b) and other date(a).

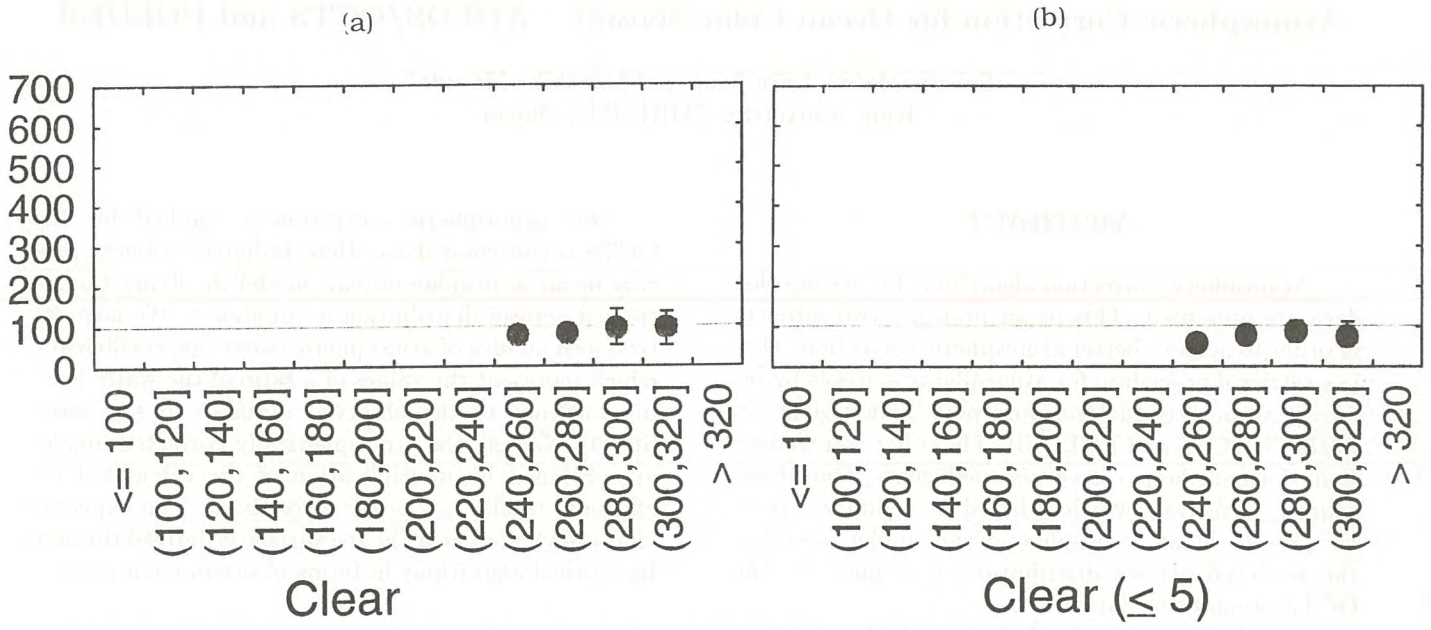


Figure 4 The short-wave flux (W/m*m) and long-wave flux (W/m*m) at the top of the atmosphere retrieved from ERBE observations for the clear scene ID (a) and clear scene by AVHRR (b).

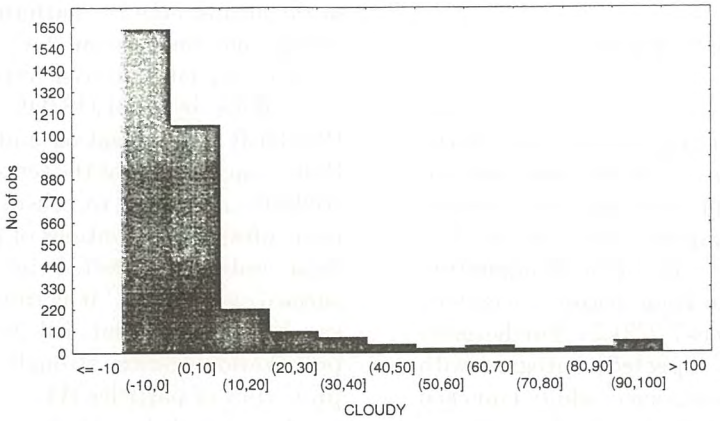


Figure 5-a The histogram of cloud cover determined from the collocated AVHRR for the clear scene ID footprint.

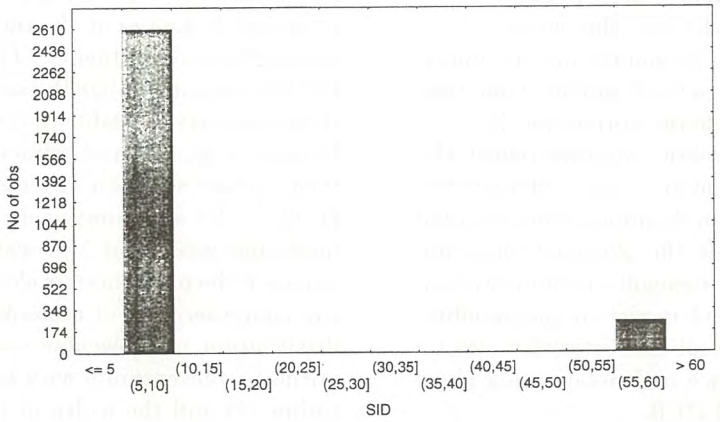


Figure 5-b The histogram of scene ID (10 is clear and 60 is partially cloudy) for the clear ERBE footprint which is covered by cloud less than 5% determined from collocated AVHRR data.

Atmospheric Correction for Ocean Color Sensors : ADEOS/OCTS and POLDER

Sonoyo Mukai, Itaru Sano and Kazuhiko Masuda*
Kinki University, *MRI/JMA, Japan

ABSTRACT

Atmospheric correction algorithms for ocean color data are presented. This paper proposes two subjects in order to achieve better atmospheric correction. One is a retrieval procedure for atmospheric aerosols by referring to both of radiance and polarization given by ADEOS/OCTS and POLDER. The other is introduction of atmospheric correction coefficients. Our atmospheric correction, which is based on radiative transfer process in an atmosphere-ocean model involving the retrieved aerosol distribution, is applied for the OCTS-ocean color data.

It is shown that retrieval of atmospheric aerosols is improved by combination use of radiance and polarization, and atmospheric correction process is progressed by using the correction coefficients.

1. INTRODUCTION

Atmospheric correction is the process of removal of contaminated atmospheric light from space-borne data. The Japanese satellite ADEOS was unfortunately ten-months life but provided us with valuable information of Earth environments since August 17th in 1996. ADEOS/OCTS(Ocean Color Temperature Scanner) is the second ocean color sensor in eighteen years since the first Nimbus-7/CZCS. Furthermore ocean color remote sensing is expected to progress with SeaWiFS of the USA, which was successfully launched on August 1 in 1997 [1]. At this time we focus our attention on atmospheric correction for ocean color data. Atmospheric correction is a key factor especially for ocean color analysis [2, 3], because the contribution of atmospheric light to the satellite data is about 80 to 90% in the visible wavelengths over the ocean.

Since atmospheric light is mainly due to multiple scattering by aerosols, aerosol model itself contributes greatly in atmospheric correction [4]. It is well known that atmospheric aerosols reflect the environmental change. Namely aerosol characteristics might change greatly in temporal and regional scales [5, 6, 7, 8]. Therefore the efficiency of atmospheric correction strongly depends on how we can set up an appropriate aerosol model to the satellite-image concerned. First aerosol characteristics are retrieved using both of radiance and polarization given by ADEOS/OCTS and POLDER.

Our atmospheric correction is applied for the OCTS ocean color data. Here radiative transfer process in an atmosphere-ocean model involving the retrieved aerosol distribution is simulated. We have introduced an idea of atmospheric correction coefficients, which represent the values of a ratio of the water leaving radiance to the observed radiance at the satellite [9]. Namely the atmospherically corrected images are obtained by multiplication of the calculated coefficients to the raw ocean color data. The expected chlorophyll map near the sea surface is derived through bio-optical algorithms in terms of ocean color data.

2. AEROSOL RETRIEVAL BASED ON ADEOS/OCTS AND POLDER DATA

It is well known that aerosols contribute greatly in the atmosphere by scattering and absorption in the visible and near infrared region of spectrum. This work partly cites aerosol retrieval using near-infrared data given by ADEOS/OCTS and POLDER. The POLDER (POLarization and Directionality of Earth Reflectance) is one of the sensors on board the satellite ADEOS, and aims to collect global-scale visible and near-infrared observations of polarized and directional solar radiance reflected by the Earth-atmosphere-surface system [10]. It is shown that aerosol retrieval can be efficiently pursued with polarization, because polarization feature strongly depends on the optical properties of particles [11].

It is found that, in the near-infrared wavelengths, a contribution of radiation out of the ocean to total radiation is negligibly small and optical thickness of the atmosphere is also small [12]. Therefore it is possible to assume that the images in the near infrared approximately represent the single scattering pattern by atmospheric constituents. Thus the measurements of OCTS- and/or POLDER- band 6 ($0.67\mu m$) and band 8 ($0.865\mu m$) are available to retrieve the aerosol characteristics, e.g., size and refractive index. A single scattering phase matrix is expressed by Stokes parameters (I, Q, U, V) and composed of Rayleigh scattering by molecular gases and Mie scattering by aerosols. The values of the phase matrix elements strongly depend on the characteristics of aerosols because of the uniform distribution of molecular gases. A single-mode log-normal representation with two parameters, the mode radius ($\bar{r}$) and the width of the log-normal curve (σ),

is considered here for one of the most widely used size distributions. Thus it becomes our purpose to retrieve $(\overline{r}, \sigma)$ for the log-normal distribution.

It is natural to consider that several kinds of aerosols could exist together in general. In this section, we take into account heterogeneous particles for maritime aerosol models. World Meteorological Organization [13] provides a standard maritime aerosol model, which is mainly composed of oceanic (OC) and water-soluble (WS) components. Oceanic type denotes sea-salt solution in water, and water-soluble type includes water-soluble substances consisting of ammonium sulfate, calcium sulfate and organic compounds. That is, we assume now the maritime aerosols are composed of oceanic component and water-soluble one. The mixing rules of several components into a spherical shaped heterogeneous particle have been presented by several authors, e.g. Maxwell-Garnett (MG) theory, Bruggeman theory and core-mantle type [14, 15]. Since these mixing rules have been already adopted for astrophysical grains, descriptions of each theory are omitted and MG theory is employed in our present simulations. That is, a heterogeneous grain model according to Maxwell-Garnett mixing rule as small water-soluble (WS) inclusions in an oceanic (OC) matrix where the volume fraction of WS-inclusions is represented by f, is examined for atmospheric aerosols.

Here an efficient algorithm for aerosol retrieval is developed using a ratio of the radiance data at band 8 to that at band 6 on each pixel of an image of interest. Namely the wavelength tendency is available to retrieve aerosol characteristics. On the other hands, view angles of sun and satellite on each pixel of the image correspond to angles of incident and scattered light in point of scattering process. In other words, each pixel of the image gives each scattering angle. In our simulations, a ratio of the scattered light at band 8 to that at band 6 can be calculated for an arbitrary scattering angle if a model of atmosphere involving aerosol model is set up. Therefore we can say that a scattering angle correlates radiance of a pixel of satellite image with a simulated value of atmospheric light, and so it is possible to determine the best aerosol parameters at each pixel by comparison of observations with simulations. Thus both of spectral information and directional information of the satellite data are used to retrieve aerosol distribution.

Fig.1 presents a retrieved distribution of the optical thickness of aerosols at a wavelength of 0.55 μm based on a ratio of band 8 to band 6 on each pixel of the OCTS image on April 26, 1997 over the Pacific Ocean near Japan. In this figure a heterogeneous model with $\{f = 0.1, (r = 0.25\mu m, \sigma = 2.2\mu m)\}$, which is named model-A hereafter, is selected as a good candidate for an aerosol model. Certainly some other grain models can also provide reasonable aerosol optical thickness. That is, model-A is one candidate to explain the OCTS-radiance data. Therefore the aerosol model-A is examined next using the polarization data simultaneously observed by POLDER. Fig.2a presents the observed polarization degree at a wavelength of $(0.67\mu m)$ on April 26 in 1997 and Fig.2b shows the simulated image using the model-A. By comparison with these two images, we found that the model-A can explain the POLDER-polarization data.

It is of interest to mention that any other grain models available to radiance data by OCTS are not impossible to interpret the polarization by POLDER. In other words model-A is an optimized aerosol model retrieved from both of OCTS and POLDER data based on scattering simulations in the polarization field. In general, it is natural to consider that not only optical thickness of aerosols but also their chemical composition and size distribution vary with pixel to pixel within an image. At any rate, such a present algorithm as both of images of radiance and polarization are interpreted by using the variation of optical thickness of one aerosol model is one approach to aerosol retrieval. Thus we can conclude that the model-A is a good aerosol model over the Pacific Ocean near Japan on April 26, 1997.

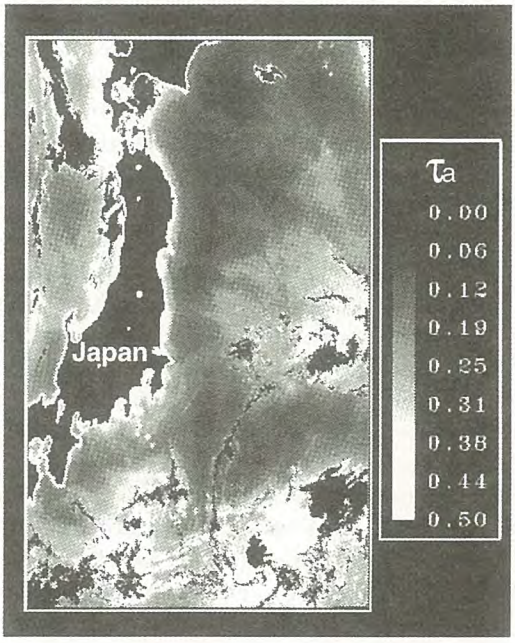


Fig. 1 A retrieved distribution of the optical thickness of aerosols at wavelength 0.55 μm based on a ratio of band 8 to band 6 on each pixel of the OCTS image on April 26, 1997 over the Pacific Ocean near Japan, where a heterogeneous grain with $\{f = 0.1, (r = 0.25\mu m, \sigma = 2.2\mu m)\}$ is set up for an aerosol model.

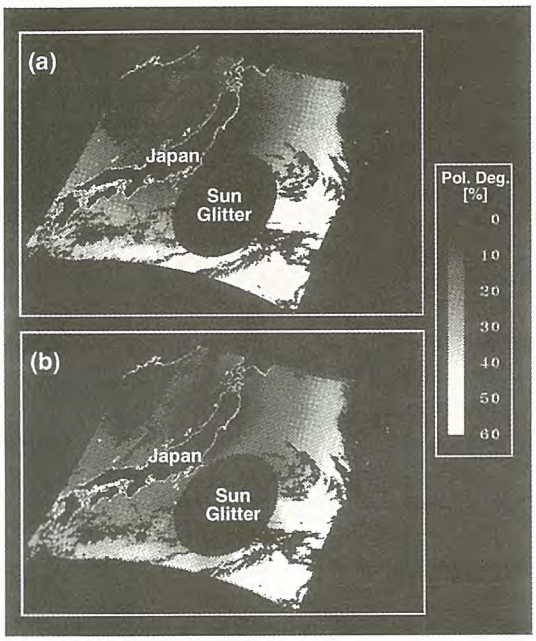


Fig. 2 Polarization degree at a wavelength of ($0.67\mu m$).
a: POLDER data observed on April 26, 1997 over the Pacific Ocean near Japan.
b: simulated results using the same aerosol model as Fig.1.

3. ATMOSPHERIC CORRECTION

Our atmospheric correction is based on multiple scattering calculations. Therefore radiative transfer problem in an atmosphere-ocean model involving the retrieved aerosol model has to be numerically solved to obtain the values of atmospheric correction coefficients C. The value of C is obtained from a ratio of the water leaving radiance to the observed radiance at the satellite. The C-values depend on the place of each pixel in a satellite image as well as wavelength. Atmospherically corrected images are obtained by multiplication of C-values to the raw satellite data.

In our present calculations, the model-A is employed for an aerosol model. The sea surface is simulated by multiple facets whose slopes vary according to the isotropic Gaussian distribution with respect to wind speed [16]. Wind speed is assumed to be $5m/sec$ as a typical value for a clear day. Several ocean models have been prepared. For example, one of them is a completely diffused model, namely upward radiance out of the ocean is represented by Lambert's law. Multiple scattering for the atmosphere-ocean model is solved by the adding-doubling method.

Chlorophyll density distribution near the sea surface is derived through bio-optical algorithms for ocean color data as follows;

$$Chlorophyll = 0.2818[(Rad_{0.520}+Rad_{0.565})/Rad_{0.490}]^{3.497}, \quad (1)$$

where Rad represents the radiance after atmospheric correction at wavelengths of 0.490, 0.520 and 0.565 μm [17, 18]. Fig. 3 represents the expected chlorophyll map in units of $\mu g/l$. From this figure we found that our treatment provides the intrinsic streams of Kuroshio (warm current) and Oyashio (cold current) in the Pacific Ocean. That is, the characteristic flow pattern of the sea surface in the late spring is clearly displayed, for example tidal front goes up to Sendai Bay and typical eddies are appeared off Sanriku coast etc.

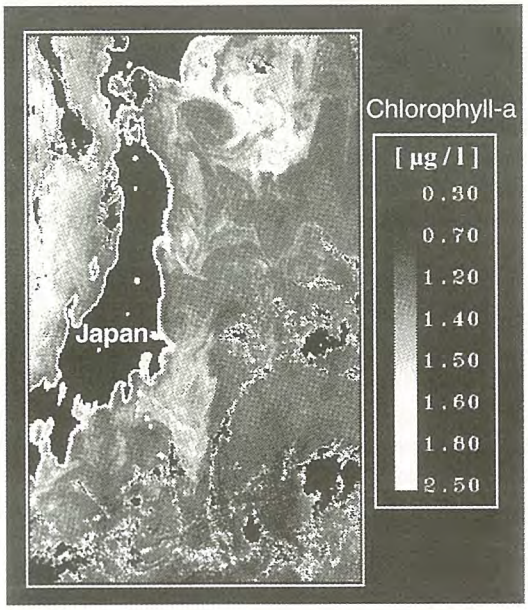


Fig.3 Expected chlorophyll map near the sea surface in units of $\mu g/l$ from the OCTS data on April 26, 1997.

4. DISCUSSIONS

It is found that an efficient atmospheric correction for ocean color data is pursued due to improved aerosol retrieval by combination of POLDER and OCTS, and employment of atmospheric correction coefficients.

It is natural to consider that several kinds of aerosol components exist together with. But it is difficult to determine the mixing structure of each components. At any rate, from present work, we can say that such a Maxwell-Garnett mixing rule as small water-soluble (WS) inclusions in an oceanic (OC) matrix is available to interpret the space-borne data, and polarization information is useful to improve the aerosol retrieval.

ACKNOWLEDGMENTS

POLDER data was distributed by CNES in France. This work was partially supported by NASDA (PSPC-20170), and also by scientific research funds from the Ministry of Education, Science and Culture of Japan (07640579).

References

[1] W. W. Gregg, F. S. Patt and R. H. Woodward, "Development of a Simulated Data Set for the SeaWiFS Mission", *IEEE Trans. Geosci. Remote Sensing*, vol.35, pp.421–435, 1997.

[2] H. R. Gordon, "Atmospheric correction of ocean color imagery in the Earth Observing System era," *J. Geophys. Res.*, vol.102, pp.17081–17106, 1997.

[3] H. Fukushima and M.Toratani, "Asian Dust Aerosol: Optical Effect on Satellite Ocean Color Signal and a Scheme of its Correction," *J. Geophys. Res.*, vol.102, pp.119-130, 1997.

[4] Y. J. Kaufman, D. Tanre, H. R. Gordon, T. Nakajima, J. Lenoble, R. Frouin, H. Grassl, B. M. Herman, M. D. King, and P. M. Teillet, "Passive remote sensing of tropospheric aerosol and atmospheric correction for the aerosol effect," *J. Geophys. Res.*, vol. 102, pp. 16815–16830, 1997.

[5] G. Dalu, R. Rao, A. Pompei, G. P. Boi, Tonna, and B. Olivieri, "Aerosol optical properties retrieved from solar aureole measurements over southern sardinia," *J. Geophys. Res.*, vol. 100, pp. 26135–26140, 1995.

[6] C. Pilinis, S. Pandis, and J. Seinfeld, "Sensitivity of direct climate forcing by atmospheric aerosols to aerosol size and composition," *J. Geophys. Res.*, vol. 100, pp. 18739–18754, 1995.

[7] P. S. K. Liu, W. R. Leaitch, C. M. Banic, S.-M. Li, D. Ngo, and W. J. Megaw, "Aerosol observations at chebogue point during the 1993 north atlantic regional experiment: Relationships among cloud condensation nuclei, size distribution, and chemistry," *J. Geophys. Res.* , vol. 101, pp. 28971–28990, 1996.

[8] G. R. Carmichael, M.-S. Hong, H. Ueda, L.-L. Chen, K. Murano, J. K. Park, H. Lee, Y. Kim, C. Kang, and S. Shim, "Aerosol composition at cheju island, korea," *J. Geophys. Res.*, vol. 102, pp. 6047–6061, 1997.

[9] S. Mukai, I. Sano, K. Masuda and T. Takashima, "Atmospheric correction for ocean color remote sensing : Optical properties of aerosols derived from CZCS imagery," *IEEE Trans. Geosci. Remote Sensing*, vol. 30, pp.818–824, 1992.

[10] P. Y. Deschamps, F. -M. Bréon, M. Leroy, A. Podarie, A. Bricaud, J. C. Buriez and Sèze, "The POLDER mission: Instrument characteristics and scientific objectives", *IEEE Trans. Geosci. Remote Sensing*, vol. 32, pp.598–615, 1994.

[11] S. Mukai, I. Sano and T. Takashima, "Investigation of Atmospheric Aerosols Based on Polarization Measurements and Scattering Simulations," *Opt. Rev.*, vol.3, pp.487-491, 1996.

[12] I. Sano, S. Mukai and T. Takashima, "Polarimetric properties of atmospheric aerosols", *Proc. SPIE'97*, vol.3121, pp.361–369, 1997.

[13] Radiation Commission, IAMAP, "A preliminary cloudless standard atmosphere for radiation computation," World Meteorological Organization, Geneva, WCP-112, WMO/TD-No.24, 1986.

[14] C. F. Bohren and N. C. Wickramasinghe, "On the computation of optical properties of heterogeneous grains," *Astrophys. Space Sci.*, vol.50, pp. 461–472, 1977.

[15] P. Chýlek and V. Srivastava, "Dielectric constant of a composite inhomogeneous medium," *Phys. Rev. B*, vol.27, pp. 5098–5106, 1983.

[16] C. Cox and W. Munk, "Measurements of the roughness of the sea surface from photographs of the sun's glitter," *J. Opt. Soc. Amer.*, vol.44, pp.838–850, 1954.

[17] M. Kishino, J. Ishizaka, S. Saitoh, Y. Senga and M. Utashima, "Verification plan of ocean color and temperature scanner atmospheric correction and phytoplankton pigment by moored optical buoy system," *J. Geophys. Res.*, vol.102, pp.17197–17207, 1997.

[18] NASDA, "ADEOS Reference Hand Book", Tokyo Japan, 1996.

V. Algorithm of Physical and Statistical Models

APPLIED MATHEMATICAL PROBLEMS OF ATMOSPHERIC CORRECTION AND FILTRATION OF MULTISPECTRAL SATELLITE DATA

OLEG I. SMOKTY

St. Petersburg Institute for Informatics and Automation
of Russian Academy of Sciences
39, Line 14th, PB 199178, St.Petersburg, Russia
Tel: +7-812-218-4900; FAX: +7-812-218-4450; e-mail: soi@iias.spb.su

Nowadays there are no doubts about the topicality and great significance of the problems connected with the atmospheric correction and filtration of multispectral satellite data, since the Earth's atmosphere not only transfer and treats substance and energy flows, but represents itself a spatial-frequency dynamic and informational filter as well. However, it's necessary to establish, that given problems in spite of their importance, hasn't obtained yet its own complete and detailed both theoretical and practical solutions.

It may be explained by real contents of the transfer function (operator) that is more deep and rich, than just a transformation of the natural formations' satellite brightness to the Earth's surface brightness [1]. As a matter of fact, the transfer function (operator) has to connect the radiation rejected by the Earth with its natural formation's state parameters. With this, mentioned connection has to be invariant in relation to the natural formation's sighting conditions and solar illumination.

In present time is clearly comprehensible, that for the atmospheric correction of satellite images and spectrums problems' solution of atmospheric spatial-frequency filtration it is necessary to attract the following means:

1. Advanced methods and algorithms for the solution of 3-D direct and inverse radiative transfer theory problems (for general case we take polarized radiation), taking into account refraction and turbulence effects inside a vertical-nonuniform atmosphere bounded from below by a horizontally-nonuniform anisotropically reflecting surface.
2. Linear systems and transformations theory methods for the construction of 3-D informational dynamic spatial-frequency filter of «the Earth's atmosphere-surface» system.
3. Advanced technological procedures, methods and algorithms for the satellite data automated processing and morphological (structural) transformations in the framework of its thematical interpretation, analysis and classification.

Taking into account the complex character of the atmospheric correction and filtration problems, for their solution it is necessary as well as to use natural formations brightness measurements taken at the test grounds, to work out the adaptive optical models of «the Earth's atmosphere-surface» system independently and to carrying out combined aircraft-satellite experiments in the Earth's environmental key zones.

It goes without saying, that it's impossible to consider all unsolved aspects of such complicated and complex problems as atmospheric correction and spatial-frequency filtration of the natural formations' satellite images and spectrums from the common methodological points of view in the same report. In this context only a certain part of the most actual, from applied mathematical point of view, and unsolved aspects of the problems, indicated above can be discussed.

For a general case, let us determine spectral transfer operator $\hat{\Pi}_\lambda$ of the «the Earth's atmosphere-surface» system according to the following relationship:

$$I_{sur,\lambda} = \hat{\Pi}_\lambda [\, I_{sat,\lambda} \,] \,, \tag{1}$$

where $I_{sat,\lambda}$ - is the Earth's surface spectral brightness, measured from a satellite and $I_{sur,\lambda}$ - is the natural formation's spectral brightness at the Earth's surface level. According to schemes, being proposed first of all a set of inverse problems is necessary to solve for the «atmosphere-underlying surface» system optical characteristics retrieving and afterwards solve appropriate direct transfer radiation problems connected with atmospheric correction and filtration of multispecial satellite data.

From the physical point of view a number of investigations on the atmospheric correction problems are regarded $I_{sat,\lambda}$ spectral brightness representation in the following form:

$$I_{sat,\lambda} = I_{atm,\lambda} + I_{sur,\lambda}\, T_\lambda + \hat{T}_{\sigma,\lambda}\left[I_{sur,\lambda}\right] \quad , \tag{2}$$

where $I_{atm,\lambda}$ - is atmospheric spectral brightness (without reflecting bottom), having been measured from a satellite, T_λ - is direct atmospheric spectral transparency for fixed sighting direction, $\hat{T}_{\sigma,\lambda}$ - is integral operator, determining the Earth's surface spectral brightness diffuse transfer to the upper level of the Earth's atmosphere. Let us note that in the case of orthotropical reflecting bottom only, the integral operator of $\hat{T}_{\sigma,\lambda}$ is transformed in the function $\hat{T}_{\sigma,\lambda}$, namely diffuse atmospheric spectral transparency. In this case simple factorization of $\hat{\Pi}_\lambda$ - spectral transfer operator is possible according to the following relationship:

$$\hat{\Pi}_\lambda \Rightarrow I_{sur,\lambda} = \frac{I_{sat,\lambda} - I_{atm,\lambda}}{T_\lambda + T_{\sigma,\lambda}} = \frac{I_{sat,\lambda} - I_{atm,\lambda}}{\mu_\lambda} \tag{3}$$

In practice, various approximate expressions for the $\hat{\Pi}_\lambda$ - spectral operator's components, based on the analytical, semi- analytical, numerical and empirical approaches are being used usually. We shall pay our attention to the construction of 1-D precise calibration model of a «vertically nonuniform atmosphere - nonorthotropically reflecting bottom» system's radiation field. Mathematical foundation of such calibration model can be Fredholm second kind of exact integral equations system for the azimuth brightness harmonics I^m_{sat}. of a vertically-nonuniforn atmosphere, bounded from below by an arbitrary anizotropically reflecting bottom having the following form [2]:

$$I^m_{sat}(\tau,\eta,\xi,\tau_0) = \frac{1}{2}\int_0^\tau \Lambda(\tau')\{\int_0^1 p^m(\tau',\eta,\eta')\, I^m_{sat}(\tau',\eta',\tau_0)\mathrm{d}\eta' +$$

$$+\int_0^1 p^m(\tau',-\eta,\eta')\, I^m(\tau',-\eta',\tau_0)\mathrm{d}\eta' + \frac{S}{2}\, p^m(\tau',\eta,\xi)\quad e^{-\tau'/\xi}\}\, e^{-\frac{(\tau-\tau')}{\eta}}\,\frac{d\tau'}{\eta} \quad , \tag{4}$$

$$I^m_{sat}(\tau,-\eta,\xi,\tau_0) = \frac{1}{2}\int_\tau^{\tau_0} \Lambda(\tau')\{\int_0^1 p^m(\tau',-\eta,\eta')\, I^m_{sat}(\tau',\eta',\xi,\tau_0)\mathrm{d}\eta' +$$

$$+\int_0^1 p^m(\tau',\eta,\eta')\, I^m(\tau',-\eta',\xi,\tau_0)\mathrm{d}\eta' + \frac{S}{2}\, p^m(\tau',-\eta,\xi)\, e^{-\tau'/\xi}\}\, e^{-\frac{(\tau'-\tau)}{\eta}}\,\frac{d\tau'}{\eta} +$$

$$+ I^m_{sur}(\eta,\xi,\tau_0)\, e^{-\frac{\tau_0-\tau}{\eta}} \quad , \quad m = 0,1,\ldots,M, \quad \tau\in[0,\tau_0], \quad \eta\in[0,1], \quad \xi\in[0,1], \tag{5}$$

$$\eta\, I^m_{sur}(\eta,\xi,\tau_0) = \int_0^1 y^m(\eta,\eta')\, I^m_{sat}(\tau_0,\eta',\xi,\tau_0)\eta'\mathrm{d}\eta' + \frac{S}{2}\, y^m(\eta,\xi)\xi e^{-\tau_0/\xi} \tag{6}$$

Here functions $I^m_{sat}, I^m_{sur}, p^m, y^m$ are determined according to well known relations as m-th azimuth's harmonic of brightness I_{sat} and I_{sur}, atmospheric and surface phase functions, correspondingly. The value of $\Lambda(\tau)$ is a single scattering albedo, $\arccos\eta = \theta$ is a vision angle and $\arccos\xi = \theta_0$ is an angle of Sun's position, τ and τ_0 are optical deepness and optical thickness of a slab, respectively, the solar constant is denoted as πS.

Integral equations system (4) - (6) is solving with help of the iterative method according to the following scheme:

$$I^m_{sat,(n+1)}(\tau,\pm\eta,\xi,\tau_0) = \hat{L}_{\pm}\{ I^m_{sat,(n)}(\tau,\pm\eta,\xi,\tau_0)\} + I^m_{sur,(n)}(\eta,\xi,\tau_0)\} e^{-\frac{\tau_0-\tau}{\eta}} \times \theta(\pm\eta), \quad (7)$$

where $\theta(+\eta) = 0$ and $\theta(-\eta) = 1$, $\eta \in [0,1]$, $\tau \in [0,\tau_0]$, $\xi \in [0,1]$, $m = 0,1,...,M$.

Let's choose the exact solutions of the integral equations system (4)-(6) for the primary atmospheric scattering and single reflection from an underlying surface as first iteration for the scheme (7):

$$I^m_{sat,(0)}(\tau,\eta,\xi,\tau_0) = I^m_{sat,1}(\tau,\eta,\xi,\tau_0), \qquad I^m_{sat,(0)}(\tau,-\eta,\xi,\tau_0) = I^m_{sat,1}(\tau,-\eta,\xi,\tau_0) \quad (8)$$

The intensities $I^m_{sat,1}(\tau,\pm\eta,\xi,\tau_0)$ may be calculated exactly for an arbitrary vertical atmospheric nonuniformity and any law of radiation reflection from an underlying surface [2]. It should be noted, that linear integral operators $\hat{L}_{\pm}$ and exact solutions $I^m_{sat,1}(\tau,\pm\eta,\xi,\tau_0)$ may be used for the calibration of approximate algorithms of atmospheric correction and filtration. Naturally, we may select arbitrary starting iteration, not only in the view of (8) but, for example, by using any approximate analytical, semi-analytical, numerical or empirical solutions for the brightness of a vertically nonuniform atmosphere with a nonorthotropical reflecting bottom, placed below. In this case the primary atmospheric light scattering and the single surface light reflection have to be estimated exactly at each separated iterative step. Thus, any approximate solution, have been used, may be improved in a final resulting radiation field model. Numerical data analysis demonstrates [2], that a vertical nonuniformity of the Earth's atmosphere is essential at small η and ξ values and actually doesn't show influence when η and ξ values are close to 1. Furthermore, when «m» azimuth's harmonics current number is increasing, the primary scattering input increases as well, and at $m \geq 50$, we may neglect the multiple scattering input in the accuracy limits of $\varepsilon \approx 10^{-4} \div 10^{-5}$. Actually this fact determines conditions of the informational radiation field compression according to appropriate Fourie harmonics reduction. Finally, the reflecting bottom anisotropy influence is more essential at atmospheric correction procedures, than vertical nonuniformity of the Earth's atmosphere (see also [1]).

However, it should be emphasized that correct atmospheric correction scheme may be provided at the base of unified, conciliated and closered mathematical approaches connected with the solutions of radiation transfer theory direct and inverse problems. The kernel of these approaches is determined by linear system's theory using and joint mathematical description for a board satellite sensors working and data measurements trends from the one hand, and the operators set of the direct-inverse problems solutions and «atmosphere - surface» system input optical models from another. Thus, it's necessary to provide unified and closered mathematical description of the following conciliated procedures:

$$G_{g\varepsilon} \Rightarrow \hat{L}_{g,\tilde{\varepsilon}}(G) \Rightarrow \hat{L}^{-1}_{\tilde{g},\hat{\varepsilon}}[\hat{L}(G)] \Rightarrow G^*_{g,\varepsilon^*} \quad (9)$$

on the base of reciprocal connection between $\hat{L}$-direct operators set construction and appropriate to their $\hat{L}^{-1}$ of inverse operators set in the framework of grid points $(g, \tilde{g})$ and errors level $(\varepsilon, \tilde{\varepsilon}, \hat{\varepsilon}, \varepsilon^*)$ being chosen [3]. In this context, probably, unique possibility may be realized only for mathematically strict reciprocal analytical description of the correlation $\hat{L}_{g,\tilde{\varepsilon}}(G) \Rightarrow \hat{L}^{-1}_{\tilde{g},\hat{\varepsilon}}[\hat{L}(G)]$. Namely, according to mathematical analysis given in [4], the correlation, mentioned above, may be provided by Ambarzumian's representation using, merely.

For the determination of informational contents connected with the atmospheric correction and filtration procedures it is necessary to establish the correspondence between current spatial angular discretization frequency (k) and highest spatial angular discretization frequency (M) for $I^m_{sat}(\eta,\xi,\tau_0)$. On the base of well-known Nyquist-Kotelnikov's theorem we have $k \geq 2M$. The comprehensive numerical modeling of $I^m_{sat}(\eta,\xi,\tau_0)$ shows that optimal correlation between M and k numbers in the framework of the accuracy $\varepsilon \sim 10^{-4}$ has to follow as $k \cong 2M+30$ for the primary atmospheric light scattering and single underlying surface light reflection [4]. For the multiple atmospheric light scattering and multiple bottom light reflection the empirical estimation given above in the framework of chosen accuracy can be weakened significantly due to significant compression for the total azimuth harmonics number - M carried out on the base of the estimation for primary scattering influence. Taking into account the Nuquist-Kotelnikov's theorem again and the possibility of remarked azimuth's harmonics total number compression we receive the final empirical

correlation between k and M according to the estimation $k \geq 2qM$ given in [4], where compression multiplier q is equal to 1/6 approximately. Accepting total azimuth's harmonics number of $M \cong 200\text{-}300$ for real atmospheric phase functions $x(\gamma)$, we have variations of grid points frequency up $k \cong 400 - 600$ to $k \cong 130\text{-}200$ for given beforehand approximation's accuracy of $\varepsilon \approx 10^{-4}$.

The analysis, given above, allows to formulate the high-accuracy method for the semi-analytical modeling of transfer operator $\hat{\Pi}_\lambda$ in the case of arbitrary atmospheric vertical nonuniformity and any reflecting bottom. It is primary atmospheric scattering and single reflecting from an underlying surface, that are calculated exactly, when multiply scattered and reflected ones are modeled approximately for a vertically uniform atmosphere and an orthotropically reflecting bottom. With all this fitting atmospheric phase function $x(\gamma)$ for the radiation field diffuse part is cramped in respect to total azimuth's harmonics in correspondence with ($m < 50$) estimation, given above.

At the Fig.1 normalized 1-D spatial-frequency atmospheric filter $|\hat{T}_{atm}(\nu,\omega|$ is represented according to parametrization and polynomial square approximation algorithms having been developed. In such a way the atmospheric filter is determined by direct and diffuse atmospheric transparencies as well as two empirical values of asympthotic spatial-frequencies ($\nu^*_{min} \sim 0.5$, $\nu^*_{max} \sim 3.5$):

$$|\hat{T}_{atm}(\nu,\omega| = \delta^*(\nu) + [1-\delta^*(\nu)]\,\frac{T_\lambda(\eta,\tau_0)}{\mu_\lambda(\eta,\tau_0)}\,, \qquad \delta^*(\nu) = 1 - \frac{(\nu-\nu^*_{min})^2}{(\nu^*_{max}-\nu^*_{min})^2} \tag{10}$$

Atmospheric filter performs starting from these asymptotic values ($\nu \leq \nu^*_{min}$, $\nu \geq \nu^*_{max}$) into atmospheric modulator:

$$|\hat{T}_{atm}(\nu \leq \nu^*_{min},\omega)| = 1, \quad |\hat{T}_{atm}(\nu \geq \nu^*_{max},\omega)| = \frac{T_\lambda(\eta,\tau_0)}{\mu_\lambda(\eta,\tau_0)} \tag{11}$$

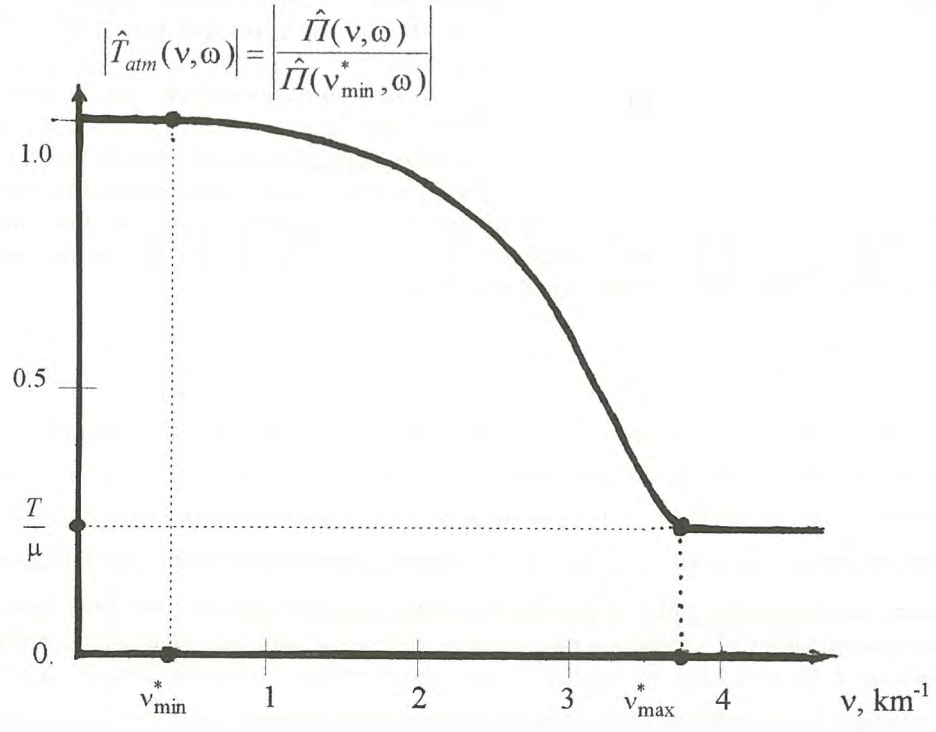


Fig.1. Parametrized and polynomial approximated spatial-frequency normalized transfer function $|\hat{T}_{atm}(\nu)|$ of the Earth's atmosphere.

The analysis of the total spatial-frequency normalized function $|\hat{T}_\Sigma(\nu,\omega)|$ carried out on the base of linear system theory application has shown that influence of a board satellite devices $|\hat{T}_{dev}(\nu,\omega)|$ is more significant than atmospheric turbulence $|\hat{T}_{turb}(\nu,\omega)|$. With another side the influence of $|\hat{T}_{turb}(\nu,\omega)|$ values is

more weak in comparison with multiple light scattering in the Earth's aerosol atmosphere $|\hat{T}_{atm}(\nu,\omega)|$. At Fig.2 the appropriate numerical results are given for λ=550nm, optical lens focus distance of satellite device F=0.3m, observation angle ω=2° and height satellite orbit H_{orb} = 100km [5].

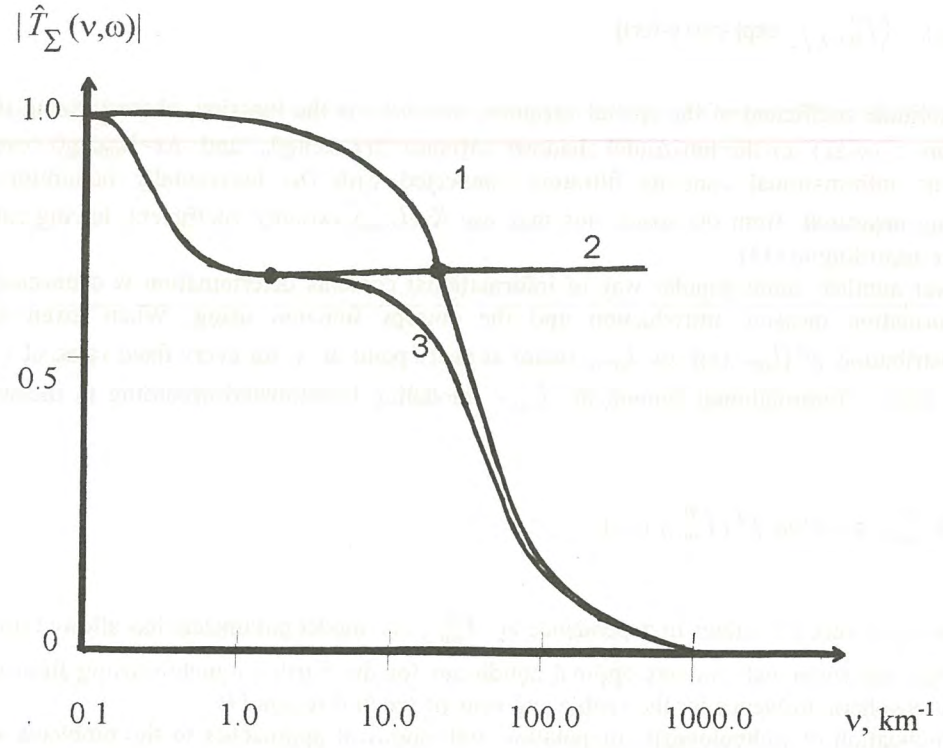


Fig.2. Total optical transfer function $|\hat{T}_{\Sigma}(\nu,\omega)|$ of "scattering aerosol-turbulence atmosphere" system. 1.$|\hat{T}_{turb}(\nu,\omega)|$ - turbulence atmosphere; 2. $|\hat{T}_{aer}(\nu,\omega)|$ - scattering aerosol atmosphere; 3.$|\hat{T}_{\Sigma}(\nu,\omega)| = |\hat{T}_{turb}(\nu,\omega)| \times |\hat{T}_{aer}(\nu,\omega)|$ - total case, λ=550nm, H_{orb}=100km, F=0.3m, ω=2°.

In the framework of the atmospheric correction and filtration problem being discussed the construction of optimal planes for the Earth's remote sensing conditions is very significant also. Important value $I^m_{atm,\lambda}$ for atmospheric correction procedures may be determined making use of the spatial fluctuations statistics for average azimuth brightness components $\langle I^m_{sat,\lambda}\rangle_x$, $\langle I^m_{sur,\lambda}\rangle_x$ and appropriate dispersions functions of $D[I^m_{sat,\lambda}]_x$, $D[I^m_{sur,\lambda}]_x$ on the base of following relationship [6]:

$$I^m_{atm,\lambda} = \langle I^m_{sat,\lambda}\rangle_x - \frac{D^{\frac{1}{2}}[I^m_{sat,\lambda}]_x}{K_\nu}, \qquad (12)$$

where K_ν is coefficient of the reflection variance of $\langle I^m_{sur,\lambda}\rangle_x$. Parametrization of values $\langle I^m_{sur,\lambda}\rangle_x$ making use of the following form

$$\langle I^m_{sur,\lambda}\rangle_x = r_{sur}(\lambda)\, R^m_{sur}(\eta,\xi), \qquad r_{sur}(\lambda) = A\, f(\lambda) + B \qquad (13)$$

allows to obtain linear regressive relationships for the calculations $\langle I^m_{atm,\lambda}\rangle_x$. For the spatial horizontally nonuniform underlying surface brightness variances modeling is necessary to use concrete reflection law of

$I^m_{sur,\lambda}(x\text{-}\Delta x,\eta,\xi)$ and spatial variance law for the indicated one. At the logarithmically current spatial distribution of brightness characteristics, being justified for the main part of the Earth's natural formations, the following representation of $I^m_{sur,\lambda}(x\text{-}\Delta x,\eta,\xi)$ is taken place:

$$I^m_{sur,\lambda}(x\text{-}\Delta x,\eta,\xi) = \left\langle I^m_{sur,\lambda} \right\rangle_x \exp[-\beta\alpha(x\text{-}\Delta x)] , \tag{14}$$

where . β - amplitude coefficient of the spatial variance, $\alpha(x\text{-}\Delta x)$ - is the function, characterizing the surface relief inclination $z_x'(x\text{-}\Delta x)$ or the horizontal shadows variance $z(x\text{-}\Delta x)\mathrm{tg}\theta_0$ and $\Delta x = H_{orb}\,\mathrm{tg}\theta\cos\varphi$. For the modeling of the informational contents filtration connected with the horizontally nonuniform surface brightness, being measured from the space, one may use $K_v(I_{\lambda,sur})$ variance coefficient, having calculated it obvious manner according to (12).

However another, more popular way of informational contents determination is connected with the Shannon's information measure introduction and the entropy function using. When given density of probabilistic distribution $\mathcal{P}[I_{sur,\lambda}(x)]$ of $I_{sur,\lambda}$ vector at every point of x, for every fixed value of λ - spectral channel being used, J informational content of $I_{sur,\lambda}$ modeling is estimated according to the well-known expression:

$$J = -\sum_{k=1}^{M} \mathcal{P}[I^m_{sur,\lambda}(x_k)] \log \mathcal{P}[I^m_{sur,\lambda}(x_k)] . \tag{15}$$

Obtaining of $\max\{J\}$ values in dependence of $I^m_{sur,\lambda}(x)$ model parameters has allowed to formulate according to their informational contents optimal conditions for the Earth's remote sensing from space with regard of the atmospheric influence for the visible and near IR spectral region [7].

The foundation of technological computation and empirical approaches to the problems solution of atmospheric corrections and spatial frequency filtration, discussed above, for low and middlespatial resolution of satellite data consists in using of following operations: the empirical and semi-empirical procedures, linear brightness transformations and atmospheric influence representation in a form of fitting coefficients for the initial satellite information expanded into a series according to an orthogonal polynomials as well as including of atmospheric correction and filtration procedures as a part of natural objects identification, classification and state estimation carried out on the base of automated schemes. Distinguishing features of the brightness transformations mathematical formalism, being used by us, are the input adaptive models of «atmosphere-underlying surface» system and preliminary solutions of the radiative transfer theory boundary value problems. According to developed algorithm actually radiative correction is carried out in two steps [1]. Physical sense of the first step consists in the account of the atmospheric haze brightness for the average albedo of underlying surface $\overline{A}$. As a result of mentioned step we may estimate the transformation of radiation fields multiply scattered by a vertically-nonuniform atmosphere and multiply-reflected by an underlying surface. At the second step of the atmospheric correction procedure the account of the spatial-frequency atmospheric characteristic's, connected with the horizontal nonuniformities of the underlying surface and the Earth's atmosphere is carried out. With all these the problem of multispectral satellite data atmospheric correction also may be solved successfully by using of input complex adaptive models for the «atmosphere-surface» system, which parameters are taken into account additionally respect to the place and moment of space survey.

Among the empirical procedures of the atmospheric correction using the rather transparent lake-sea waters and test grounds brightness measurements is very popular as well as the measurements of corresponding regressive models for the statistical description of the atmospheric haze influence. Another empirical possibility is determined by using of the spectral channels measurements combinations. For example in oxygen absorption band placed at λ = 760 nm and λ = 740 nm with further spectrums and images joint analysis. Using representation (2) for the Earth's surface space survey to the nadir condition (η=1), we have the following expression for the spectral atmospheric optical thickness of $\tau_{0,\lambda}$ (λ=760 nm) [1]:

$$\tau_{0,\lambda}(\lambda\text{=}760\text{ nm}) = \ln\left| \frac{T^{\max}_{atm} - T^{\min}_{atm}}{e^{-\tau^{\max}_{0,\lambda}(760)}\{T^{\max}_{atm} - T^{\min}_{atm}\} + \{e^{-\tau^{\max}_{0,\lambda}(760)} - e^{-\tau^{\min}_{0,\lambda}(760)}\}\{T_{atm} - T^{\max}_{atm}\}} \right| , \tag{16}$$

where T_{atm}, T_{atm}^{max} and T_{atm}^{min} are integral atmospheric transparencies being measured at meteorological station network.

Following steps of the atmospheric correction carrying out are connected with the optical thickness calculation for other spectral channels and atmospheric phase functions, corresponding to the spectral optical thickness way calculations, using a-priori information about the aerosol types and structures, aerosol particles refraction index and their distribution function. For example the important problem of atmospheric humidity influence on the input optical aerosol's characteristics for different meteorological range (visibility) may be solved by making use of well known Koshmider's relationship and two-layers structure of aerosol's particles (Fig.3) [8] with following application of modified Mie theory [9].

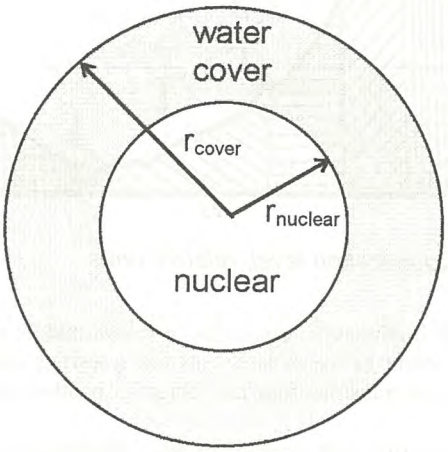


Fig.3. Imitative model of polydispertional two-layer aerosol's spherical particle of the Earth's atmosphere: $\varepsilon = r_{cover}/r_{nuclear}$ - fitting nonuniformity parameters for optical modeling of atmospheric humidity influence.

For this approach the optimization condition is used according to the following minimization relationship:

$$\min_{(\alpha,\lambda)} \sum_{n=1}^{D}\sum_{i=1}^{N}\sum_{k=1}^{L}\left|\tau_0^{exp}(\lambda_k)-\tau_0^{teor}(\alpha_i,\beta_n,\lambda_k)\right|^2 = \sigma_{\alpha\lambda}^2 , \qquad (17)$$

where β_n and α_i are a priory fixed and modeled fitting parameters set, respectively. In the framework of such approach refraction index and size distribution function view of aerosol particles have to be known beforehand.

Finally, at the last steps the satellite data reduction to the Earth's surface level with account of the Earth's surface albedo retrieval results and the underlying surface nonorthotropy factors being set a-priori is carried out. With all these a_k - fitting coefficients of the measured satellite brightness being approximated by the second-grade orthogonal polynomials $B_{1,2}$ (Chebyshev's polynomials) become the fitting parameters of the atmospheric correction and of the atmospheric filter, correspondingly [1]:

$$I_{kj}(\eta,\xi,\varphi\text{-}\varphi_0,A_j) = a_1+a_2B_1(A_j)+a_3B_1(\eta)+a_4B_1(\xi)+a_5B_1(\varphi\text{-}\varphi_0)+a_6B_2(A_j)+a_7B_1(A_j)B_1(\xi)+a_8B_1(A_j)B_1(\eta)+$$

$$a_9B_1(A_j)B_1(\varphi\text{-}\varphi_0)+a_{10}B_2(\xi)+a_{11}B_1(\xi)B_1(\eta)+a_{12}B_1(\xi)B_1(\varphi\text{-}\varphi_0)+a_{13}B_2(\eta)+a_{14}B_1(\eta)B_1(\varphi\text{-}\varphi_0)+a_{15}B_2(\varphi\text{-}\varphi_0), \qquad (18)$$

where k-index characterizes the aerosol's type in atmosphere vertical stratification, j - is the nonorthotropical surface reflection type, A - is underlying surface albedo, φ and φ_0 azimuths of vision direction and Sun's positions, respectively . Chebyshev's polynomials $B_{1,2}(x)$ determined according to following relationship: $B_1(x) = 2x - 1$, $B_2(x) = 2(2x - 1)^2 - 1$. The example of atmospheric correction procedure developed for the Earth's surface satellite multispectral images according to approach having been proposed is given at Fig.4 on the base of complex analysis.

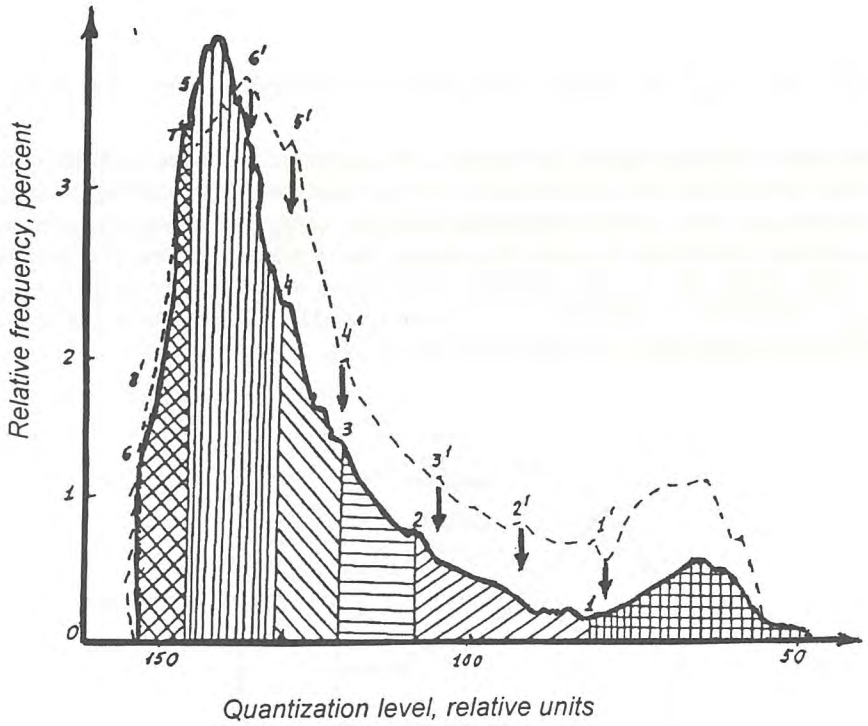


Fig.4. Histogram of the distribution of the brightness of objects on a spatial middle resolution image before atmospheric correction (*dashed*) and after it. *Figures* point to the existence of the resolving boundaries of the histograms *Arrows* correspond to the most probable boundaries of transition from one object to. another after atmospheric correction

In conclusion it should be noted that represented complex analysis was related exclusively to the scalar radiative fields. Polarization effects account for the atmospheric light scattering and reflection from real underlying surface essentially increases the informational contents of the Earth's remote sensing. That's why in this case significance of the atmospheric correction and filtration of multispectral satellite data is increasing in comparison with scalar case [10]. Taking into account the realization of such international programs as POLDER-ADEOS the development of advanced procedures and algorithms for the polarized radiation's atmospheric correction and spatial-frequency filtration become rather actual problems.

REFERENCES

1. K.Y.Kondratyev, V.V.Kozoderov, O.I.Smokty. Remote Sensing of the Earth from Space: Atmospheric Correction, Springer-Verlag, Berlin, 1992, 478 p.
2. O.I.Smokty. Multiple light scattering models for a nonuniform atmosphere with an arbitrary reflecting bottom, IMGA-CNR, Technical report No 3, Modena, 1994, 32 p.
3. O.I.Smokty. The determination of environment optical parameters in global ecological monitoring of the Earth from space. Proceedings of SEIKEN Symp., Tokyo, 1993, pp.40-65.
4. O.I.Smokty. The basic informational contents levels for satellite ecological investigations. Proceedings of International Conference on Informatics and Control (ICI&C'97), v.3, St.Petersburg, 1997, pp.1337-1344.
5. O.I.Smokty, R.Guzzi. The influence of the Earth's atmospheric turbulence on the optical system resolution. PIERS'94 (Progress in Electromagnetics Research Symposium), , Noordwijk, The Netherland.1994,11-15 July.
6. O.I.Smokty, G.A.Guseinov. Informational contents and optimal plans for the Earth's surface spectrophotometric remote sensing. Proceedings of St.Petersburg Institute for Informatics and Automation of Russian Acad. of Sci., N157, St.Petersburg, 1993, 74p.
7. O.M.Pokrovsky. Determination of informational characteristics of sounding systems from space. Journ. Atmospheric optics, Russian Acad. of Sci., N3, 1991, pp.227-235.
8. O.I.Smokty, N.V.Kobjakova. Advanced optical aerosol model for the environment forwad radiation fields computations, Technical Report N 4-95, IMGA-CNR, Modena, 1995.
9. K.Boren, D.Hafmen. Absorption and scattering of light by small particles. Publ.Co.Mir, Moscow, 1986,660p.
10. Y.Kawata, T. Kusaka, S.Ueno, O.Smokty. Atmospheric correction algorithm for remote sensing data with multiviewing angles IGARSS'93, Kogakuin Univ., Tokyo, v.4, 1993, pp. 1113-1115.

Single- and Multiple-Scattering Properties of Ice Crystals in 1.38 μm Wavelength and Its Potential Applications in Satellite Remote Sensing

Lisheng Xu[a,b], Tamio Takamura[a], Guotong Zhang [b]and Jilie Ding [b]

[a] Center for Environmental Remote Sensing, Chiba University, Chiba 263, Japan
[b] Atmospheric Radiation and Satellite Remote Sensing Laboratory
Chengdo Meteorological College, Chengdo, Sichuan 610041, China

ABSTRACT

An improved ray-optics theory and Mie theory for single scattering and the adding-doubling method for multiple scattering are used to study the interaction of radiation in the wavelengths of 1.38, 3.979, 6.5, and 11.03 μm and the microphysics of cirrus clouds. The study shows that the strong 1.38 μm water vapor band in the near-IR region is superior to the other three IR channels used in current operational satellites and has potential possibility of remote sensing of microphysical and optical properties of cirrus clouds.

1. INTRODUCTION

Remote sensing of cirrus cloud properties accurately is extremely important for cloud climatology and many other scientific disciplines. Although extensive observations and theoretical studies have been made recently, the cirrus cloud problem is still far from solved. Unlike water clouds, cirrus clouds are composed of nonspherical ice cryctals that have different densities, sizes, shapes, and orientations in space. Furthermore, cirrus clouds are often thin in optical thickness, with a variable IR emittance of less than 1. It has been realized that current operational satellites have some deficiencies in accurate detection of cirrus clouds, especially over land surface. Thus, it is important to seek new sounding channels and develop new sensors. Recently, during the NASA FIRE Phase II Cirrus field program, it was found by the measurements of the Airborne Visible Infrared Imaging Spectrometer (AVIRIS) that narrow channels near the center of the strong 1.38 μm water vapor band are very effective in detecting thin cirrus clouds[1-3]. And a near-IR channel centered at 1.375 μm has been selected for the Moderate Resolution Imaging Spectrometer (MODIS), which is one of the sensors on the Earth Observing System (EOS), for enhanced detection of cirrus clouds from space[2,4-5]. The sensitivity of the 1.375 μm MODIS channel to detect thin cirrus clouds is expected to be one to two orders of magnitude better than the current infrared emission techniques[2]. While initial results have been encouraging, further studies are needed.

2. CALCULATIONS

To study satellite remote sensing of cirrus clouds, two basic cloud microphysical parameters, i.e., the shape and size distribution of ice crystals, are needed. In this study, two specific crystal habits, randomly oriented hexagonal columns and plates, with a superposition of two modified Γ – function distributions are considered :

$$n(r) = w\,n_1(r) + (1-w)\,n_2(r) \qquad (1)$$

$$n_j(r) = c_j^{-1} r^{\alpha_j} \exp(-b_j r^{\gamma_j}) \quad (2)$$

$$b_j = (\alpha_j / \gamma_j) r_j^{-\gamma_j}$$

$$c_j = r_j^{-1} b_j^{-(\alpha_j + 1)/\gamma_j} \Gamma[(\alpha_j + 1)/\gamma_j]$$

$$j = 1, 2$$

where $0 \le w \le 1$, α and γ are shape factors, r_j corresponds to the size at which the peak in the respective distribution occurs, and $j = 1, 2$ corresponds to the small- and large-particle modes, respectively. To represent various microphysical characteristics of cirrus clouds in different developmental stages more really, we construct 20 particle size distributions including two types : (a) monomodal ; and (b) bimodal. Assume that the IWC ranges from 3×10^{-5} to 0.25 gm $^{-3}$.

The effective radius of the particles is defined as

$$r_e = \int_{r_1}^{r_2} \pi r^3 n(r)\, dr / \int_{r_1}^{r_2} \pi r^2 n(r)\, dr \quad (3)$$

Corresponding to the IWC mentioned above r_e ranges from 30 to 325 μm for columns and from 42 to 449 μm for plates.

For comparison, four wavelengths are considered simultaneously, i.e., 1.38, 3.939, 6.5 and 11.03 μm, in which 3.939 and 11.03 μm are the well-known atmospheric IR shortwave and longwave window channels used in the current satellites; 1.38 and 6.5 μm are located in the near-IR and IR water vapor bands, respectively.

The single scattering properties of ice crystals are calculated using the improved ray optics theory[6-7] for the dimension $L > 45$ μm and Mie scattering theory for $L \le 45$ μm . For a size distribution, the scattering and extinction coefficients of ice crystals are calculated, respectively, by

$$\beta_s = \int_{r_1}^{r_2} Q_s(r)\, n(r)\, dr \quad (4)$$

$$\beta_e = \int_{r_1}^{r_2} Q_e(r)\, n(r)\, dr \quad (5)$$

where Qs and Qe are the scattering and extinction efficients, respectively. The single scattering albedo ω_0 and asymmetry factor g are represented as

$$\omega_0 = \beta_s / \beta_e \quad (6)$$

$$g = 1/2 \int_{-1}^{+1} P_{11}(\theta) \cos\theta\, d(\cos\theta) \quad (7)$$

where P11(θ) denotes the scattering phase function, θ is the scattering angle. According to van de Hulst[8], " the similarity parameter"of ice crystals, is defined as

$$S = ((1-\omega_0)/(1-\omega_0 g))^{1/2} \quad . \quad (8)$$

For isotropic scattering, $S = (1 - \omega_0)^{1/2}$; for anisotropic scattering, S ranges from 0 ($\omega_0 = 1$) to 1 ($\omega_0 = 0$).The optical constants of ice are taken from Zhang and Xu [9]. The optical thickness within cirrus clouds is defined as

$$\tau_c = \int_{zb}^{Zt} (\beta_e + k_{gas})\, dZ \quad (9)$$

The cloud layer is considered as plane-parallel, horizontally homogeneous and vertically inhomogeneous with an improved two-layer ice model[10] being used. For multiple scattering calculations the adding/doubling method [11] is employed.

Four atmospheric models, namely, U.S. Standard Atmosphere, Tropical, Mid-latitude Summer, and Mid-latitude Winter are considered. Molecular scattering and absorption are taken into account, with the background stratospheric aerosols, which are calculated by LOWTRAN 7 Code [12].

3. RESULTS AND DISCUSSIONS

Figure 1 shows that the similarity parameters of both atmospheric IR window channels and 6.3 μm water vapor band are not sensitive to the particle effective radii. For $r_e > 60$ μm, the S values in these wavelengths are all larger than 0.90, especially at $\lambda = 11.03$ μm S is almost equal to 1.0. At $\lambda = 1.38$ μm, however, the S values are all less than 0.5. Moreover, the similarity parameter S increases regularly with the effective radius r_e , which indicates that for small ice crystals light scattering is dominant in extinction; with r_e increase the absorption of ice crystals increases. These illustrate that the similarity parameter S at 1.38 μm is well dependent on r_e .

We have studied how the phase function $P(\theta)$ of polydisperse ensembles of hexagonal ice crystals depends on the incident wavelength, particle shapes, and size distributions[13]. We found that the phase function pattern depends strongly on wavelengths. For $\lambda = 1.38$ μm, the phase function curve features are similar to those in visible, with the strong forward scattering, the secondary features at near 22^0 and 135^0, and the distinct backward scattering peak. The phase function patterns at 11 μm atmospheric window region represent the Christiansen effect , i.e., in there extinction is primarily due to absorption rather than scattering; thus, the backward scattering peak disapears. In addition, at the forward scattering ($\theta = 0^0$)the phase function peak is rather sensitive to the particle size r_e at $\lambda = 1.38$ μm .

These single scattering characteristics indicate the possibility of using 1.38μm band to detect microphysical properties of cirrus clouds.

Figures. 2 and 3 demonstrate the characteristics of the multiple scattering properties, i.e., the transmittance $\mathfrak{T}_c$ and reflectance $\mathfrak{R}_c$, of cirrus clouds in 1.38 μm wavelength varying with the cloud optical thickness , respectively. Fig.2 shows that with τ_c increasing, the transmittance, $\mathfrak{T}c$, of ice crystals decreases regularly. Compared with other wavelengths considered, the wavelength of 1.38 μm is the most transparent.

It is interesting to note from Fig. 3 that with τ_c increase the reflectance $\mathfrak{R}_c$ increases from the order of 10^{-3} to the order of 10^{-1}. The $\mathfrak{R}_c$ values of cirrus clouds in other wavelengths considered are less than those at 1.38 μm in the orders of $10^{-1} - 10^{-3}$. Moreover, in the investigated wavelengths only the $\mathfrak{R}_c$ values at $\lambda = 1.38$ μm vary with the optical thickness τ_c regularly.

These results demonstrate the potential application of 1.38 μm water vapor band to infer the optical thickness of cirrus clouds.

Gao and Kaufman[2] have pointed out that the strong 1.38 μm water vapor band is helpful for the detection of upper-level cirrus clouds. The signal received by the 1.375 μm channel from space depends on the scattering and absorption properties of cirrus clouds and water vapor absorption above, within, and below cirrus clouds. The two-way transmittance analyses for different atmospheric models with different precipitable water vapor values have shown that surface and clouds below 3 km are expected to produce little scattered signal at the satellite because the solar shortwave radiation reflected by surface is mostly absorbed by water vapor in the lower atmosphere , whereas clouds above 6 km are expected to produce more scattered

radiation at the satellite. Our results on single- and multiple- scattering by polydispersions of randomly oriented hexagonal ice crystals further demonstrate that the strong 1.38 μm water vapor band is superior to the atmospheric IR window channels and the 6.3 μm IR water vapor band not only in distinguishing cirrus clouds from satellite images, but also in its possibility of remote sensing of microphysical and optical properties of cirrus clouds from space. As EOS is planned to be launched in 1998, more studies on retrievals of cirrus cloud parameters using 1.38 μm band are particularly needed. Additional studies are under way and the results will be forthcoming.

4. CONCLUSIONS

Single- and multiple- scattering by different polydisperse ensembles of randomly oriented hexagonal ice crystals with two shapes, i.e., hexagonal columns and plates, and 20 particle size distributions are calculated for a near-IR channel centered at the strong 1.38μm water vapor absorption band by using an improved ray-optics theory and adding/doubling method. For comparison, both atmospheric IR windows and the 6.3μm water vapor IR absorption band used in current operational satellites are also investigated. The results show that at λ = 1.38μm the similarity parameter S of ice crystals is regularly dependent on the particle effective radius r_e ; and for r_e ranging from 30 to 330μm, the S values are all less than 0.5. Contrarily, the similarity parameters in both atmospheric IR. windows and 6.3μm band are not sensitive to r_e ; and their S values are considerably large, when $r_e > 60\mu m$, $S > 0.9$.

Moreover, at λ = 1.38μm , with the cloud optical thickness τ_c increase, the cloud transmittance $\mathfrak{T}_c$ decreases and the cloud reflectance $\mathfrak{R}_c$ increases regularly. At other three IR channels, there are no such as dependent relationships. In addition, the 1.38μm water vapor band is more transparent than the three IR channels; and also reflects more large radiation energy than the three IR channels in cirrus clouds.

These single- and multiple- scattering properties demonstrate that the strong 1.38μm water vapor absorption band is promising to be used in remote sensing of microphysical and optical properties of cirrus clouds.

ACKNOWLEDGMENTS

The research is supported by the National Natural Science Foundation of China under Grant NSFC-49675255 and the Foundation of Ministry of Education, Science, Sports and Culture of Japan under Grant N0. 08241104 .

REFERENCES

1. Gao, B.C., A.F.H. Goetz, and W.J. Wiscombe, Cirrus cloud detection from Airborne Imaging Spectrometer Data using the 1.38 micron water vapor band, J. Geophys. Ltr., 20, 301-304, 1993.
2. Gao, B.C. and Y.J. Kaufman, Selection of the 1.375-μm MODIS channel for remote sensing of cirrus clouds and stratospheric aerosols from space . J. Atmos. Sci. 52, 4231-4237, 1995.
3. Hutchison, K.D. and N. Choe, A quantitative assessment on the value of 1.38 micron imagery for the automated analysis of optically-thin cirrus in daytime imagery, in Proc. EUROPTO Series, SPIE 2578, 53-60, 1995.
4. King, M.D., Y.J. Kaufman, W.P. Menzel, and D. Tanre, Remote sensing of cloud, aerosol, and water vapor properties from MODIS, IEEE Trans. Geosci. Remote Sens., 30(1), 2-27, 1992.
5. NASA, 1995 MTPE/EOS Reference Handbook, NASA-GSFC, 1995.

6. Zhang, J. and L. Xu, Light scattering by absorbing hexagonal ice crystals in cirrus clouds, Appl. Opt., 34, 5867-5874, 1995.
7. Xu, L. and J. Zhang, Light scattering by randomly oriented hexagonal ice crystals: Improved diffraction computations and diffraction properties of ice crystals, Optik, 101, 161-165, 1996.
8. Van de Hulst H. C., Multiple Light Scattering, Tables, Formulas, and Applications. Vol.2, New York, Academic Press, 1980.
9. Zhang, G. and L. Xu, A study of the relationships between optical constants of ice and temperatures in the spectral region from the ultraviolet to the middle infrared ,Quart. J. Appl. Meteor. China, 3, 212-219, 1992.
10. Xu, L. and J. Zhang, Simulation of retrieval of the base height and thickness of cirrus clouds from satellite data, J. Opt. Soc. Am. A, 9, 1536-1546, 1992.
11. Lenoble, J., ed., Radiative Transfer in Scattering and Absorption Atmospheres : Standard Computational Procedures , Hampton , A. Deepak, 1985.
12. Kneizys, F. X., and Co-authors, Users Guide to LOWTRAN 7 , AFGL-TR-88-0177, AFGL/OPS, Hamscom AFB, MA01731, U.S.A, 1988.
13. Xu, L., G. Zhang, J. Ding and T. Takamura, Scattering phase function of polydispersions of randomly oriented hexagonal ice crystals. in Proc. on Aerospace Remote Sensing, EOS and SPIE, 1997.

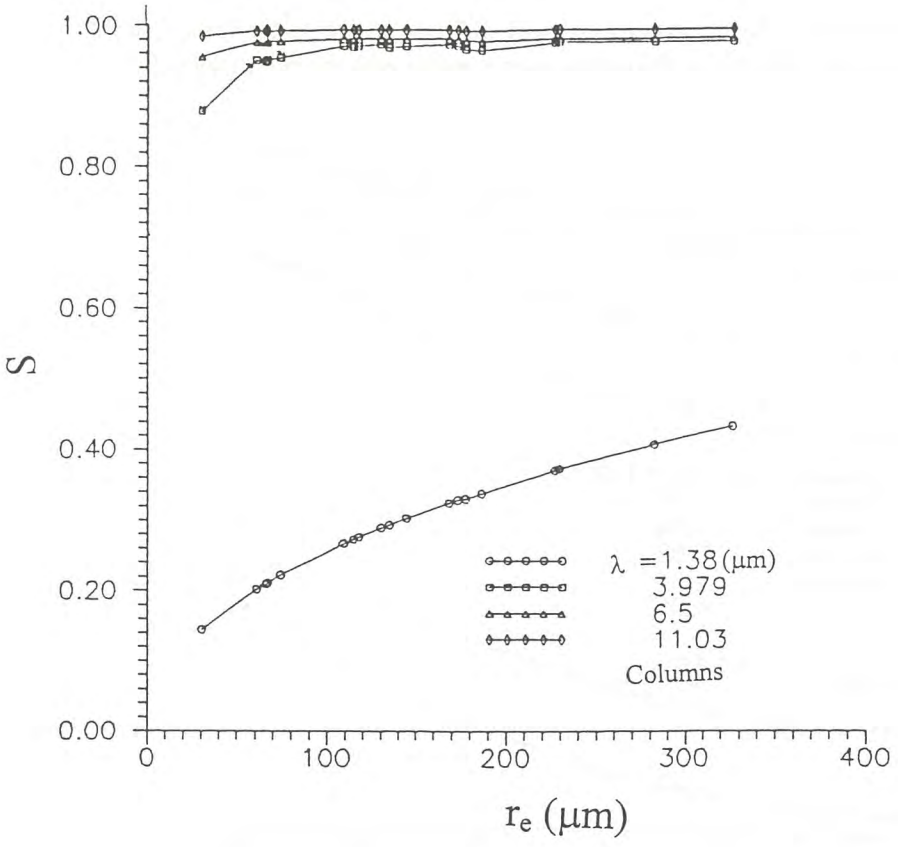


Figure 1. The similarity parameters, S , at $\lambda = 1.38$ μm and three IR channels, i.e., both atmostheric IR windows and 6.5 μm water vapor channel, versus the effective radii, r_e , of ice crystals.

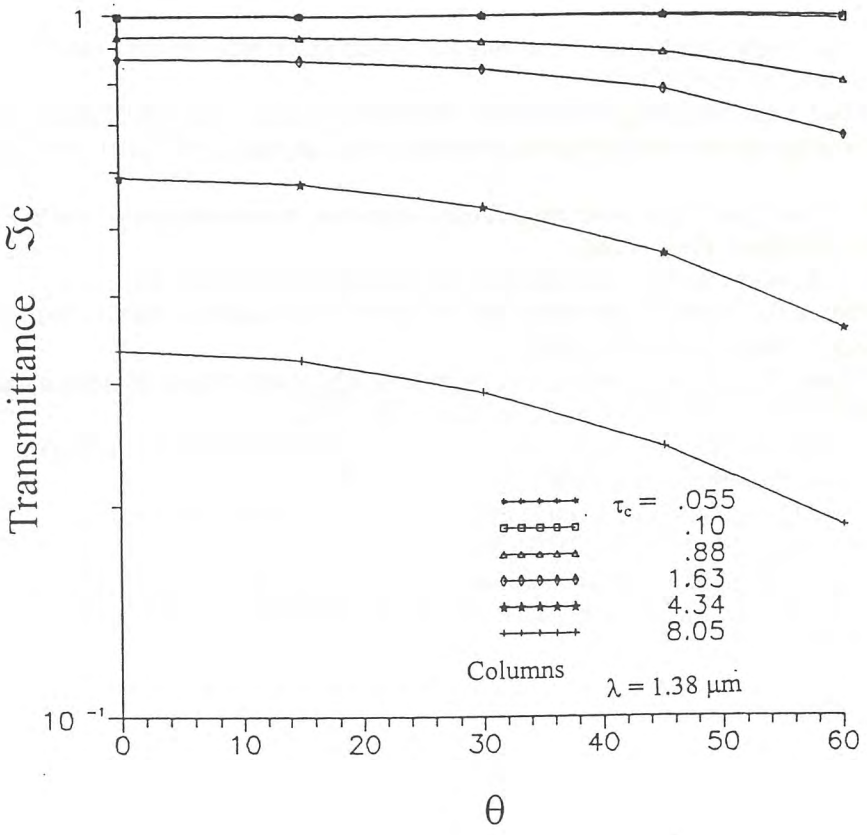


Figure 2. Transmittance $\mathfrak{Tc}$ of cirrus clouds with different optical thicknesses τ_c at the strong 1.38 μm water vapor absorption band varying with the zenith angle θ .

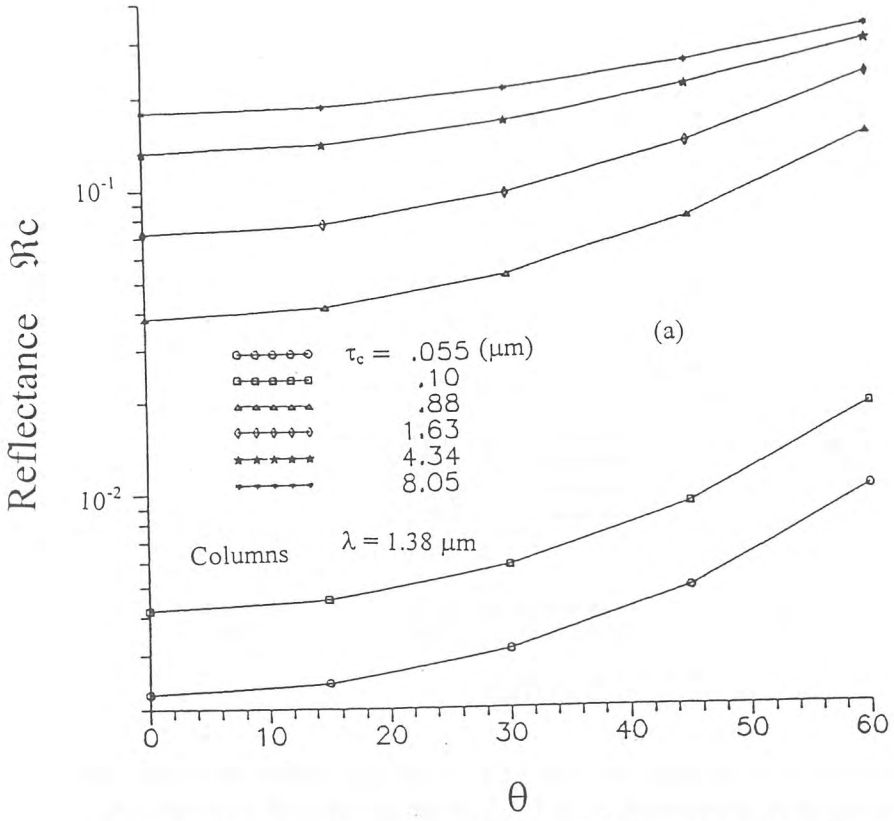


Figure 3. Reflectance $\mathfrak{Rc}$ of cirrus clouds with different optical thicknesses τ_c at the near-IR 1.38 μm band varying with the zenith angle θ .

Effects of adjacent clouds to satellite fields of view on the measurements of the surface reflectivity

Takahisa Kobayashi,
Kazuhiko Masuda,
and
Masayuki Sasaki
Meteorological Research Institute
1-1, Nagamine, Tsukuba, Ibaraki 305

In this paper we present multiple scattering effects in inhomogeneous atmospheres on estimating the surface reflectivity from space. It is well known that multiple scattering effects can not be negligible for accurate atmospheric corrections (Deschamps et al., 1983, Gordon et al., 1987). Extensive studies, therefore, have been undertaken on the radiative transfer simulations(Mitchell and O'brien, 1993, Hann et al.,1991, Gordon et al., 1997). These studies, however, assumed a plane-parallel atmosphere which is unlikely to occur in nature. Multiple scattering in highly inhomogeneous natural land surface and clouds lead to complicated problems to be solved for accurate atmospheric corrections, particularly for inhomogeneous surfaces (e.g. Kaufman and Sendra,1988). Radiation from surface areas adjacent to the target pixel enhances the radiance received at the satellite sensor by multiple-scattering processes, which is known to be so called adjacent effect (Reinersman and Carder, 1995). Similarly, scattered radiation from adjacent clouds, that is clouds in the vicinity of satellite field of view, enhances the radiance received at the satellite-borne sensor.

Clouds often appear to be broken on scales that defy high spatial resolution of recent satellite sensors. An assumption that the fields of view are over cast for cloud-contaminated field leads to bias in albedo (Coakley and Kobayashi,1989, Kobayashi, 1993). Even if the fields of view are cloud-free, clouds in the vicinity of the fields of view influence the

atmospheric scattering. Radiation scattered from the adjacent clouds enhances radiance detected at satellite-borne sensor and therefore may lead to bias in the retrieval.

Here we estimate the influence of the adjacent clouds to target pixel on the retrieval of the surface reflectivity by using a 3-D radiative transfer model. The estimate of the adjacent clouds effects which often occur in satellite images, will lead to a significant increase in an understanding of atmospheric correction and consequently will improve the retrieval of the surface reflectivity.

A 3-D radiative transfer model used here is based on the Monte Carlo technique. The model allows for the atmospheric inhomogeneity as well the surface one for visible wavelength bands. The radiance received at a satellite sensor at a wavelength of 0.49 μm and at a altitude of 500km was simulated. The solar zenith angle is 30 degree. The atmospheric model consists of stratified atmosphere of molecule and aerosols with optical thickness of 0.4 and cuboidal-long bar clouds with optical thickness of 9. An atmosphere in the target is assumed to be clear, but clouds in the vicinity of the target exist (Fig. 1).

Figure 2 shows sensor radiance as a function of cloud distance which defined as a length between a side of the target area and that of cloud. Clouds adjacent to the target area lead to significant enhancement of the radiance received by satellite-borne sensor. The enhancement, however, disappear drastically as the clouds separate from the target. Almost no effects of the clouds are observed at the distance of 10km.

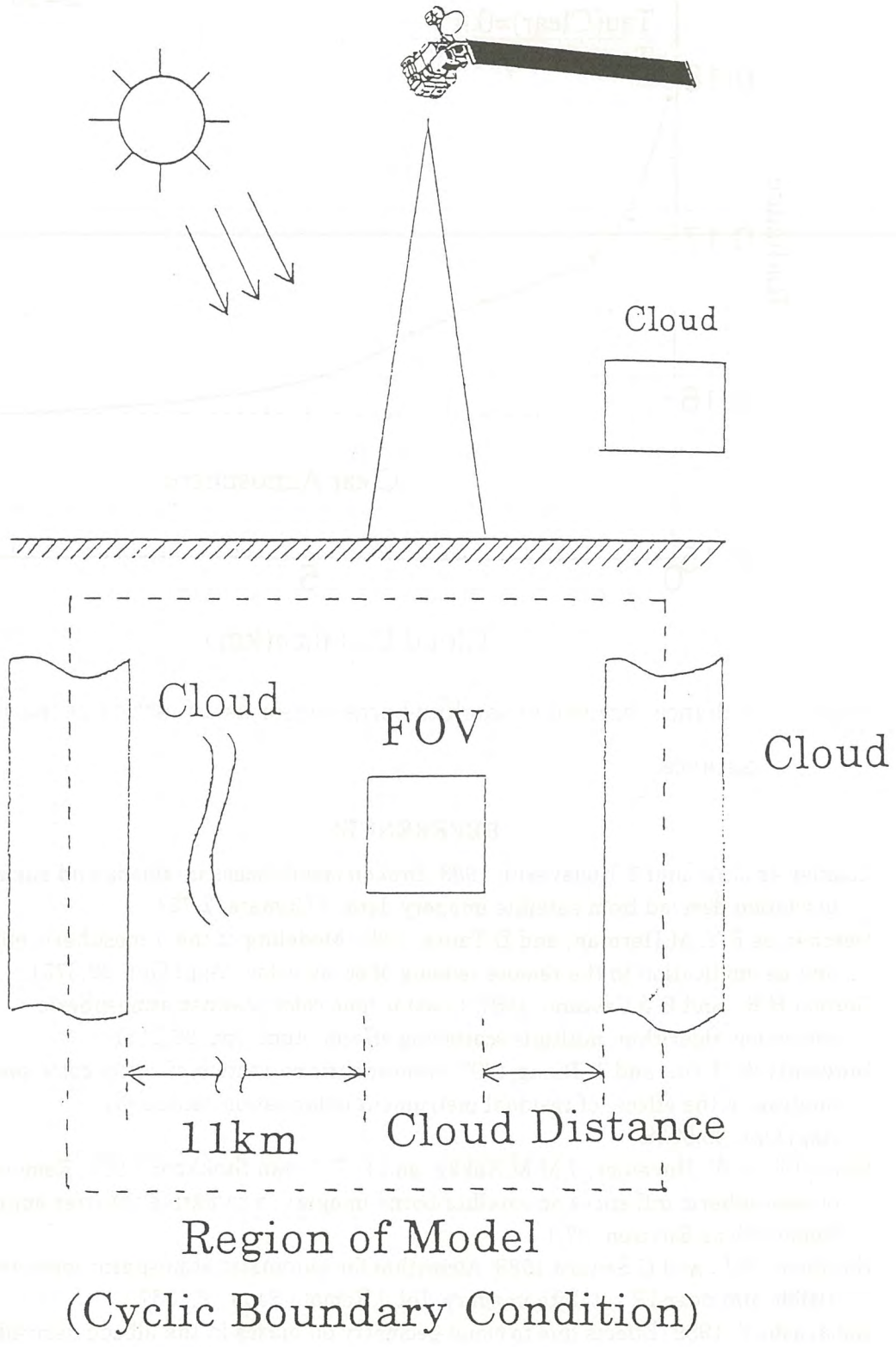


Fig.1 A schematic figure of model atmosphere. Side view (upper part) and top view (lower part) are plotted.

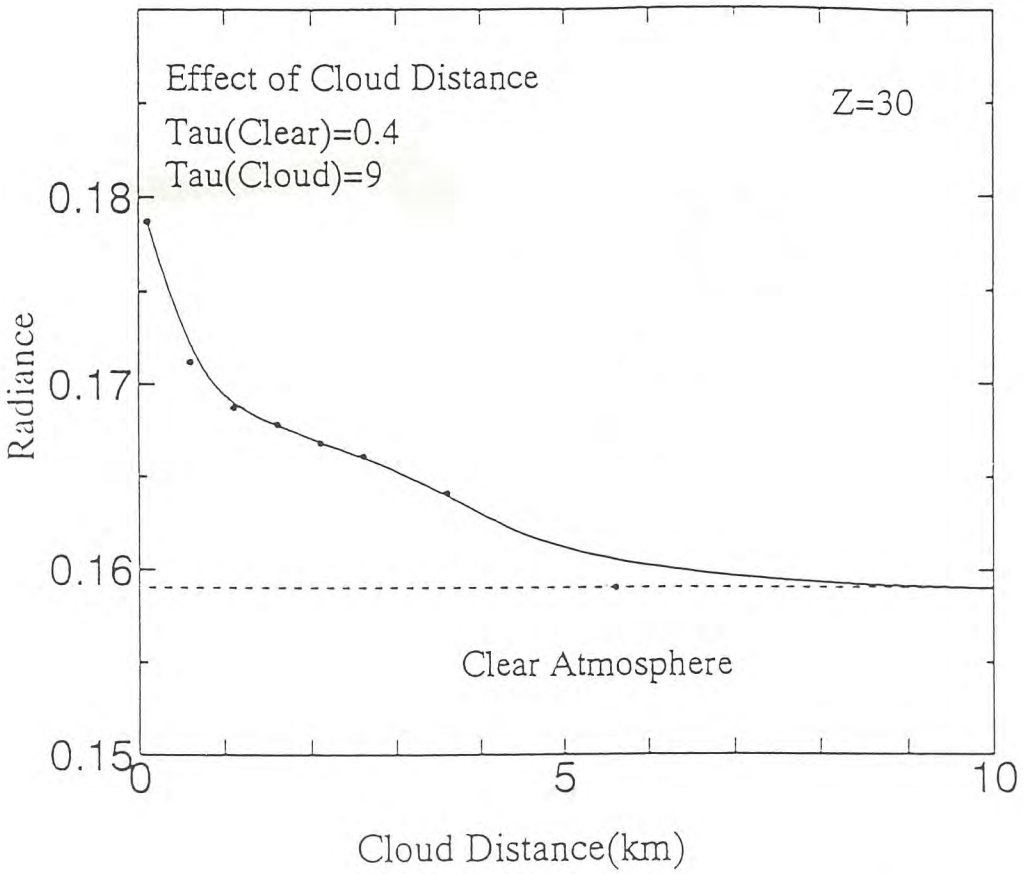


Fig.2 Radiance received at satellite-borne sensor as a function of the cloud distance.

REFERENCES

Coakley Jr.,J.A., and T.Kobayashi, 1989: Broken cloud biases in albedo and surface insolation derived from satellite imagery data, J.Climate, 2,721.

Deschamps,P.Y.,M.Herman, and D.Tanre, 1983: Modeling of the atmospheric effects and its application to the remote sensing of ocean color., Appl.Opt.,22,3751.

Gordon,H.R., and D.J.Castano, 1987: Coastal zone color scanner atmospheric correction algorithm: multiple scattering effects, Appl.Opt.,26,2111.

Gordon,H.R., T.Du, and T.Zhang,1997: Atmospheric correction of ocean color sensors: analysis of the effects of residual instrument polarization sensitivity, Appl.Opt.,36,6938.

Hann J.F., J.W.,Hovenier, J.M.M.Kokke, and H.T.C. van Stokkom, 1991: Removal of atmospheric infl ences on satellite-borne imagery: a radiative transfer approach, Remote Sens.Environ.,37,1.

Kaufman, Y.J., and C.Sendra,1988: Algorithm for automatic atmosphric correction to visible and near-IR satellite imagery, Int.J.Remote Sens., 9,1357.

Kobayashi,T.,1989: Effects due to cloud geometry on biases in the albedo derived from radiance measurements, J.Climate,6,120.

Mitchell,R.M., and D.M.O'brien,1993: Correction of AVHRR shortwave channels for the effects of atmospheric scattering and absorption. Remote Sens.Environ.,46,129.

Reinersman,P.N., and K.L. Carder, 1995: Monte Carlo simulation of the atmospheric point-spread function with an application to correction for the adjacency effect, Appl.Opt.,34,4453.

Sensitivity analysis of Temperature - emissivity separation relevant to the atmospheric correction

Masao Moriyama
Nagasaki University

1 Introduction

To estimate the land surface temperature and the spectral emissivity simultaneously (T/E separation), the new sensors and the new algorithms are under development. One the the sensor is ASTER onboard EOS-am1 will be launched 1998. As the pre-processing of the T/E separation, the atmospheric correction which uses the auxiliary atmospheric data such as the air temperature/humidity profile, ozone amount and aerosol and so on. Such atmospheric data will be from the sounder, assimilation data or climate dataset, it is expected that such data will contain the error. In this study, based on the error propagation theory, the relationship between the input (atmospheric data) error and the output (land leaving radiance) error of the atmospheric correction process. Also in the study, the simplified scheme to estimate the output error from the input error.

2 Atmospheric correction of ASTER/TIR

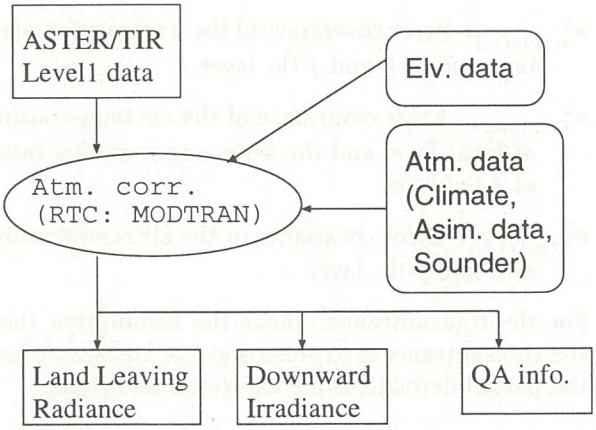


Figure 1: Schematic of ASTER/TIR atmospheric correction

For ASTER/TIR case, the atmospheric correction means the computation of the land leaving radiance from the atmospheric and elevation data from the radiative transfer code such as MODTRAN as Figure 1. The atmospheric correction is expressed as the following equation.

$$I_{si} = \frac{I_i - I_{ai}}{\tau_i} \quad (1)$$

I_{si}: Land leaving radiance at i-th. channel.

I_i: Satellite observed radiance at i-th. channel.

I_{ai}: Atmospheric radiance at i-th. channel.

τ_i: Total transmittance at i-th. channel.

And the land leaving radiance contains the radiation term and the reflection term as follows.

$$I_{si} = \varepsilon_i B_i(T_s) + (1 - \varepsilon_i)\frac{F_i}{\pi} \quad (2)$$

ε_i: Surface emissivity at i-th. channel.

T_s: Surface temperature.

F_i: Downward irradiance at i-th. channel.

As the atmospheric correction, τ_i, I_{ai} and F_i are computed from the atmospheric data and elevation data via the radiative transfer code (MODTRAN).

Since the ASTER/TIR spectral channels are in the windows spectrum, the air temperature/humidity profile, Ozone amount and aerosol type/amount are suitable as the atmospheric data. In Table 1, the atmospheric data and sources are summarized.

Table 1: Atmospheric data and sources

Data	Source
Air temp./humid.	Climate Assimilation data MODIS
Ozone	Climate TOMS MODIS
Aerosol	Climate MISR/MODIS ASTER

3 Sensitivity analysis

The ASTER land leaving radiance product will issue not only the LLR also the Downward irradiance and the uncertainties at each pixel. As the cause of the uncertainties, it is expected that atmospheric error is the dominant factor. In this study,the relationship between the atmospheric data error and the LLR error is formulated.

3.1 Relationship between the transmittance/atmospheric radiation error and the LLR error.

From Eq. (1), the transmittance and the atmospheric radiation are the independent variables, and the LLR is the dependent variable. In this case, the relationship between the error variance matrix of the independent variables S_i and the error variance of the dependent variable $\sigma^2_{I_{si}}$ can be expressed as follows [1].

$$\sigma^2_{I_{si}} = \nabla^t I_{si} S_i \nabla I_{si} \tag{3}$$

$$\nabla^t I_{si} = \left(\frac{\partial I_{si}}{\partial \tau_i}, \frac{\partial I_{si}}{\partial I_{ai}} \right) \tag{4}$$

$$\frac{\partial I_{si}}{\partial \tau_i} = -\frac{I_{si}}{\tau_i} \tag{5}$$

$$\frac{\partial I_{si}}{\partial I_{ai}} = -\frac{1}{\tau_i} \tag{6}$$

$$S_i = \begin{pmatrix} \sigma^2_{\tau_i} & \sigma^2_{\tau_i, I_{ai}} \\ \sigma^2_{\tau_i, I_{ai}} & \sigma^2_{I_{ai}} \end{pmatrix} \tag{7}$$

$\sigma^2_{\tau_i}$: Error variance of the transmittance at i-th. channel.

$\sigma^2_{I_{ai}}$: Error variance of the atmospheric radiance at i-th. channel.

$\sigma^2_{\tau_i, I_{ai}}$: Error covariance of the transmittance and the atmospheric at i-th. channel.

3.2 Relationship between the atmospheric data and the transmittance/atmospheric radiance

As the input of the atmospheric correction, the air temperature/humidity profile will be used. In this section, the formulation of the transmittance and the atmospheric radiance error relevant to these atmospheric data is discussed. In this case, the transmittance and the atmospheric radiance become the dependent variables, and the profiles are the independent variables. The error variance matrix of the transmittance and the atmospheric radiance S_i is expressed as the function of the error variance matrix of the air temperature/humidity profile $S_{T,u,i}$ and the Jacobian of the transmittance and the air temperature J_i.

$$S_i = J_i S_{T,u,i} J_i^t \tag{8}$$

$$J_i = \begin{pmatrix} \frac{\partial \tau_i}{\partial u(z_j)} (j = 1, \cdots, n) & \frac{\partial \tau_i}{\partial T(z_j)} (j = 1, \cdots, n) \\ \frac{\partial I_{ai}}{\partial u(z_j)} (j = 1, \cdots, n) & \frac{\partial I_{ai}}{\partial T(z_j)} (j = 1, \cdots, n) \end{pmatrix} \tag{9}$$

$$S_{T,u,i} = \begin{pmatrix} \sigma^2_{u(z_1)u(z_1)} & \cdots & \sigma^2_{u(z_1)T(z_n)} \\ \sigma^2_{u(z_1)u(z_2)} & \cdots & \sigma^2_{u(z_2)T(z_n)} \\ \vdots & \vdots & \vdots \\ \sigma^2_{u(z_1)u(z_n)} & \cdots & \sigma^2_{u(z_n)T(z_n)} \\ \sigma^2_{T(z_1)u(z_1)} & \cdots & \sigma^2_{T(z_1)T(z_n)} \\ \sigma^2_{T(z_2)u(z_1)} & \cdots & \sigma^2_{T(z_2)T(z_n)} \\ \vdots & \vdots & \vdots \\ \sigma^2_{T(z_n)u(z_1)} & \cdots & \sigma^2_{T(z_n)T(z_n)} \end{pmatrix} \tag{10}$$

n: Number of the atmospheric layer.

$T(z_j)$: Air temperature at j-th. layer.

$u(z_j)$: Water vapor mixing ratio at j-th. layer.

$\sigma^2_{u(z_k)u(z_j)}$: Error covariance of the water vapor mixing ratio at k and j-th. layer.

$\sigma^2_{T(z_k)u(z_j)}$: Error covariance of the air temperature at k-th. layer and the water vapor mixing ratio at j-th. layer.

$\sigma^2_{T(z_k)T(z_j)}$: Error covariance of the air temperature at k and j-th. layer.

For the transmittance, under the assumption that the transmittance is expressed as the Lambert's law the partial derivatives are expressed as follows.

$$\frac{\partial \tau}{\partial u} = -k\tau(u) \tag{11}$$

$$\frac{\partial \tau}{\partial T} = -u\tau(u)\frac{\partial k}{\partial T} \tag{12}$$

k: absorption coefficient.

3.3 Relationship between the atmospheric data and the downward irradiance

For the downward irradiance error, the same discussion as the transmittance/atmospheric radiance is effective. The error variance of the downward irradiance at i-th. channel σ^2_{Fi} is express as follows.

$$\sigma^2_{Fi} = \nabla^t(F_i) S_{T,u,i} \nabla(F_i) \tag{13}$$

$$\nabla^t(F_i) = \left(\frac{\partial F_i}{\partial u(z_j)} (j = 1, \cdots, n), \frac{\partial F_i}{\partial T(z_j)} (j = 1, \cdots, n) \right) \tag{14}$$

4 Partial derivative definition from the numerical simulation

Along with the above discussion, the partial derivatives of the transmittance and the atmospheric radiance is needed. The analytical definition of these values are very difficult, so the numerical simulation is made.

4.1 Conditions

The numerical simulation is made under the following conditions.

Air temperature/Humidity profile:
10 [deg.] interval logditual average of monthly mean NCEP[2] dataset.

Altitude: SFC, 850, 700, 500, 300 [hPa]

Difference interval: 1 % of the air temperature/water vapor mixing ratio.

4.2 Results

4.2.1 Transmittance

The absorption coefficient (Eq. (11)) and the partial derivative of absorption coefficient with the air temperature (Eq. (12))are listed in Table 2, 3.

Table 2: absorption coefficient [1/(g/kg)]

[hPa]	ch10	ch11	ch12	ch13	ch14
300	0.0119	0.00678	0.00353	0.00313	0.00413
500	0.0196	0.0122	0.00764	0.00892	0.0114
700	0.0237	0.0157	0.0110	0.0149	0.0188
850	0.0198	0.0128	0.00900	0.0134	0.0170
1013	0.00284	0.00184	0.00134	0.00228	0.00286

Table 3: partial derivative [1/(g/kg)/K]

[hPa]	ch10	ch11	ch12	ch13	ch14
300	0.000875	-0.000158	0.00029	0.000387	-3.57e-06
500	0.000370	5.14e-05	0.000145	7.97e-05	-7.01e-05
700	0.000192	4.07e-05	4.21e-05	-7.58e-05	-0.000162
850	-7.62e-05	-5.13e-05	-1.57e-05	-0.000140	-0.000214
1013	-8.26e-05	-4.46e-05	-2.06e-05	-5.60e-05	-7.48e-05

The partial derivative of absorption coefficient with the air temperature is nearly equals to zero, so in this spectrum the air temperature dependence of the transmittance can be neglected.

4.2.2 Atmospheric radiance

The partial derivertives of the atmospheric radiance are listed in Table 4, 5.

Table 4: Water vapor mixing ratio [W/cm2/sr/cm-1/(g/kg)]

[hPa]	ch10	ch11	ch12	ch13	ch14
300	-4.53e-08	-2.64e-08	-9.42e-09	-9.34e-10	-3.87e-09
500	-7.70e-09	7.09e-10	8.27e-09	2.59e-08	3.27e-08
700	3.18e-08	3.20e-08	3.31e-08	6.97e-08	9.08e-08
850	3.64e-08	3.32e-08	3.22e-08	7.30e-08	9.73e-08
1013	5.86e-09	5.48e-09	5.61e-09	1.42e-08	1.88e-08

Table 5: Air temperature [W/cm2/sr/cm-1/K]

[hPa]	ch10	ch11	ch12	ch13	ch14
300	9.26e-10	6.44e-10	3.22e-10	3.45e-10	2.69e-10
500	3.82e-09	2.57e-09	1.63e-09	1.63e-09	1.54e-09
700	7.61e-09	5.27e-09	3.70e-09	2.99e-09	2.91e-09
850	6.34e-09	4.59e-09	3.40e-09	1.68e-09	1.15e-09
1013	7.31e-10	7.68e-10	6.96e-10	-1.88e-10	-6.39e-10

4.2.3 Downward irradiance

Table 6: Water vapor mixing ratio [W/cm2/sr/cm-1/(g/kg)]

[hPa]	ch10	ch11	ch12	ch13	ch14
300	5.93e-09	4.67e-09	5.47e-09	1.15e-08	1.58e-08
500	2.44e-08	2.21e-08	2.40e-08	5.00e-08	6.54e-08
700	4.65e-08	4.53e-08	5.00e-08	1.05e-07	1.35e-07
850	4.20e-08	3.99e-08	4.25e-08	1.06e-07	1.40e-07
1013	7.10e-09	6.89e-09	7.46e-09	2.07e-08	2.73e-08

Table 7: Air temperature [W/cm2/sr/cm-1/K]

```
300  3.35e-10 3.12e-10 2.64e-10 3.02e-10 8.02e-11
500  1.56e-09 1.20e-09 1.05e-09 1.06e-09 3.55e-10
700  4.41e-09 3.16e-09 2.71e-09 1.75e-09 3.92e-10
850  5.51e-09 4.04e-09 3.49e-09 8.68e-10 -1.01e-09
1013 3.03e-09 2.04e-09 1.70e-09 8.49e-10 9.52e-10
```

Those irradiance are divided by π.

5 Example

As an example of the uncertainty computation, the numerical simulation under the following conditions are done.

Table 8: Downward irradiance uncertainties under tropic (Tr.) and US standard (US) atmosphere

S.D.[%]	F10	F11	F12	F13	F14
Tr. T(p):3K	14	18	21	22	20
Tr. u(p):10%	10	13	17	20	20
US. T(p):3K	15	18	17	20	18
US. u(p):10%	4	5	6	9	10

Table 9: Land leaving radiance uncertainties under tropic (Tr.) and US standard (US) atmosphere

S.D.[%]	Is10	Is11	Is12	Is13	Is14
Tr. T(p):3K	10	6	6	7	8
Tr. u(p):10%	8	6	5	5	6
US. T(p):3K	7	5	5	5	6
US. u(p):10%	3	3	2	3	4

Surface temperature: 284.15[K](US standard), 298.15[K](tropic).

6 Conclusion

The relationship between the error of the atmospheric dataset using ASTER/TIR atmospheric correction and the land leaving radiance and the downward irradiance are formulated. And the partial derivatives are defined at each levels.

References

[1] Nakagawa, Oyanagi, Experimental data analysis via the least squere method, Univ. of Tokyo pub., pp. 206, 1982.

[2] Schubert, S. D., J. Pjaendtner, and R. Rood, 1993. An assimilated data set for Earth science applications. Bull. Am. Met. Soc., 74:, 2331-2342.

A New Algorithm for Estimating Aerosol Optical Thickness from Satellite Image Data and Its Accuracy

Y. Kawata, A. Yamazaki, M. Imanaka and Mouri
Environmental Information Research Laboratory
Kanazawa Institute of Technology

Tel: +81-76-248-1100, Fax: +81-76-248-7753
E-mail: kawata@infor.kanazawa-it.ac.jp

Abstract: In the atmospheric correction for space remote sensing images, the aerosol optical thickness at the satellite observation time is critically needed. It is highly desirable to estimate this value from the satellite measured data themselves. In this study, we proposed a new algorithm for estimating the aerosol optical thickness from satellite image data alone. In this algorithm, the meteorological range, V, was used as a free parameter to compute the surface albedo distribution from satellite image data. The aerosol optical thickness value for each band can be computed from the meteorological range. The analytical approximation method for atmospheric correction and Modtran code were also utilized in our algorithm.

As for the algorithm validation, several simultaneous ground and sky measurements with LANDSAT/TM and ADEOS/AVNIR were conducted in 1996 and 1997. We found that the accuracy of the proposed algorithm is less than 0.04 in the aerosol optical thickness. The surface albedo distribution image computed from ADEOS/AVNIR data (taken on April 24, 1997) was presented, by using the estimated aerosol optical thickness values.

1. INTRODUCTION

It is well known that the removal of atmospheric effects from the satellite image data is necessary in the quantitative remote sensing analysis. There has been many works on the atmospheric correction in a flat terrain case of satellite measured images (Turner and Spencer (1972)[1] , Odell and Weinman, 1975[2]; Otterman and Fraser, 1976[3], 1979[4]; Kawata et al., 1978[5], Ueno et. al., 1979[6], Tanre et.al., 1981[7]; Ueno 1982[8]; Kaufman and Fraser, 1984[9], Kawata et. al. 1987[10]). The comprehensive book on this problem was published by Kondratyev et al. [11]. It has been clear now that the atmospheric correction is possible when the truth data with the aerosol optical thickness and the target surface albedo, or at least one of them are available. There are, however, few atmospheric correction works when no truth data. In this paper an new algorithm for estimating atmospheric optical thcikness from the satellite image data set alone was presented. The validation results of the algorithm were also presented.

2. ATMOSPHERIC CORRECTION ALGORITHM

Let us consider the radiative transfer model in the atmosphere bounded by a flat Lambertian

surface layer with a horizontally non-uniform albedo distribution. Let (x, y) and z are rectangular coordinates difining ground target position and height position in the atmosphere, respectively. We assume that atmospheric model is a plane paralell homogeneous, vertically inhomogeneous, and anisotropically scattering atmosphere with optical thickness of t, and parallel rays of a constant incident solar flux πF illuminates the top of the atmosphere($z=z_0$) from direction of Ω_0= (θ_0=cos$^{-1}\mu_0$,f_0), where μ_0 and f_0 are the cosine of the solar zenith angle and the solar azimuth angle, respectively.

The upwelling diffuse intensity $I(z_1, x, y, -\Omega)$ at the top of the atmosphere in the direction of $-\Omega$ can be expressed by Eq.(1) [12], allowing for a single reflection of radiation by the target surface (x, y) and up to double reflections of radiation by the adjacent surface,

$$I(z_1, x, y, -\Omega) = \mu_0 FR(\tau, \Omega, \Omega_0) + A_t(x, y) \times (s \cdot \overline{A} + t) + (p - s)\overline{A}^2 + (q - t)\overline{A} \quad (1),$$

where $A_t(x, y)$, $\overline{A}$, and $R(t, \Omega, \Omega_0)$ are the albedo of the target, the mean albedo of the adjacent surface, and reflection function of the atmosphere, respectively. Reflection function $R(t, W, W_0)$ can be computed by the Doubling and Adding method[13]. Furthermore, p, q, s, and t in Eq.(1) are the radiation cofficients which can be expressed by the reflection and transmition functions of the atmosphere[12]. The mean emergent intensity at the top of the atmosphere can be given approximately by Eq.(2).

$$\bar{I}(z_1, x, y, -\Omega) = \mu_0 FR(\tau, \Omega, \Omega_0) + p \cdot \overline{A}^2 + q \cdot \overline{A} \quad (2).$$

The mean albedo and the target albedo are given by Eq.(3) and Eq.(4), respectively.

$$\overline{A} = \frac{\left\{-q + \sqrt{q^2 - 4p \cdot (\bar{I}_{obs} - \mu_0 FR(\tau, \Omega, \Omega_0)}\right\}}{2p} \quad (3),$$

$$A_t(x, y) = \frac{\left\{I_{obs} - (p - s) \cdot \overline{A}^2 - (q - t) \cdot \overline{A} - \mu_0 FR(\tau, \Omega, \Omega_0)\right\}}{s \cdot \overline{A} + t} \quad (4).$$

The atmospheric correction algorithm is given as follows and the algorithm was tested against Landsat/ MSS, /TM, and MOS-1/MESSER data[11],[12]:

(1) Adopt an appropriate atmospheric model and its optical parameters.

(2) Compute the reflection and transmission functions, and the radiance coefficients, p, q, s, and t for a given incident solar illumination condition and a given wavelength band.

(3) Compute the mean adjacent albedo $\overline{A}$ from Eq.(3) by using $\bar{I}_{obs}$.

(4) Compute A_t(x, y) for each corresponding image pixel from Eq. (4) using the observed satellite-level intensity I_{obs}.

(5) Repeat the above steps (2) to (4) and compute A_t(x, y) for all image pixels in each wavelength

band.

3. METEOROLOGICAL RANGE ESTIMATION

In our proposed algorithm, all atmospheric optical parameters, except for aerosol amounts in the boundary layer (altitudes: 0 - 2 km), are assumed to be kept constant and they are given by MODTRAN code[14]. Sincethe aerosol optical thickness in the boundary layer can be found by inputting the meteorological range V at 0.55μm in MODTRAN code, we shall use V as a free varying atmospheric parameter, defining the atmospheric haze condition at the satellite observation time.

The estimation algorithm of V from the satellite data with n wavwlength bands is as follows:

(1) First, select appropriate atmospheric and aerosol models for a satellite measured scene, based on the measured date and geographic location.

(2) Set band number, i =1.

(3) When i > n, then move to step (6). Otherwise, go to step (4).

(4) Set an initial Meteorological Range for band i, V_0(i)= αand k = 1 , where α is a samall value in unit of [km].

   a. Compute the atmospheric optical parameters, using Modtran Code in the case of V_0(i) .

   b. Compute the surface albedo value for each pixel from the measured satellite data, by applying our atmospheric correction algorithm, using the atmospheric optical param eters found in (4)-a.

   c. When R > 0.01 and k = 1, then set V_0(i)= V_0(i) + ΔV_0 and go back to step (4)-a. Here, R is defined as a ratio of the number of pixels with negative albedo value to the total number of pixels within theimage. We suppose that the increment ΔV_0 takes a typical value of a few km. When R < 0.01 and k = 1, then move to step (4)-d. When R < 0.01 and k = 2, then go to step (5).

   d. Because we can judge that an appropriate value of V_0(i) exists between the present and previous ones, set V_0(i)= V_0(i) + ΔV_s and k = 2, whereΔV_s,= 0.1[km] and move to step (4)-a.

(5) Set i = i +1 and go back to step (3).

(6) Choose V = Max{ V_0(1), V_0(2),...., V_0(n)} as the appropriate Meteorological range and exit.

4. VALIDATION OF ALGORITHMS

We made the field experiments for the validation of our Meteorological Range retrieval algorithm at Heijo-Gu(the Old Palace Site) in Nara City, Japan on Dec.12, 1996 and at Meteorological Research Institute(MRI) in Tsukuba City, Japan on Jan. 8, 1997. Simultaneous ground measurements of the atmospheric optical thickness and surface reflectance at LANDSAT overpassing time were made on these dates. The sunphotometer (POM-01:Prede) and spectroradiometer (PS-1000: Ocean Optics) were used for the sky and surface albedo observations, respectively. The values of Meteorological Range for the test-site, obtained from the sunphotometer observations were V = 18.0 [km] and V = 50.0 [km] at Heijo-Gu and that at MRI, respectively. We showed the estimated values of Meteorological Range from TM data by applying our retrieval algorithm in the

band.

3. METEOROLOGICAL RANGE ESTIMATION

In our proposed algorithm, all atmospheric optical parameters, except for aerosol amounts in the boundary layer (altitudes: 0 - 2 km), are assumed to be kept constant and they are given by MODTRAN code[14]. Sincethe aerosol optical thickness in the boundary layer can be found by inputting the meteorological range V at 0.55μm in MODTRAN code, we shall use V as a free varying atmospheric parameter, defining the atmospheric haze condition at the satellite observation time.

The estimation algorithm of V from the satellite data with n wavwlength bands is as follows:

(1) First, select appropriate atmospheric and aerosol models for a satellite measured scene, based on the measured date and geographic location.

(2) Set band number, i =1.

(3) When i > n, then move to step (6). Otherwise, go to step (4).

(4) Set an initial Meteorological Range for band i, $V_0(i)= \alpha$and k = 1 , where α is a samall value in unit of [km].

   a. Compute the atmospheric optical parameters, using Modtran Code in the case of $V_0(i)$.

   b. Compute the surface albedo value for each pixel from the measured satellite data, by applying our atmospheric correction algorithm, using the atmospheric optical param eters found in (4)-a.

   c. When R > 0.01 and k = 1, then set $V_0(i)= V_0(i) + \Delta V_0$ and go back to step (4)-a. Here, R is defined as a ratio of the number of pixels with negative albedo value to the total number of pixels within theimage. We suppose that the increment ΔV_0 takes a typical value of a few km. When R < 0.01 and k = 1, then move to step (4)-d. When R < 0.01 and k = 2, then go to step (5).

   d. Because we can judge that an appropriate value of $V_0(i)$ exists between the present and previous ones, set $V_0(i)= V_0(i) + \Delta V_s$ and k = 2, whereΔV_s,= 0.1[km] and move to step (4)-a.

(5) Set i = i +1 and go back to step (3).

(6) Choose V = Max{ $V_0(1)$, $V_0(2)$,...., $V_0(n)$} as the appropriate Meteorological range and exit.

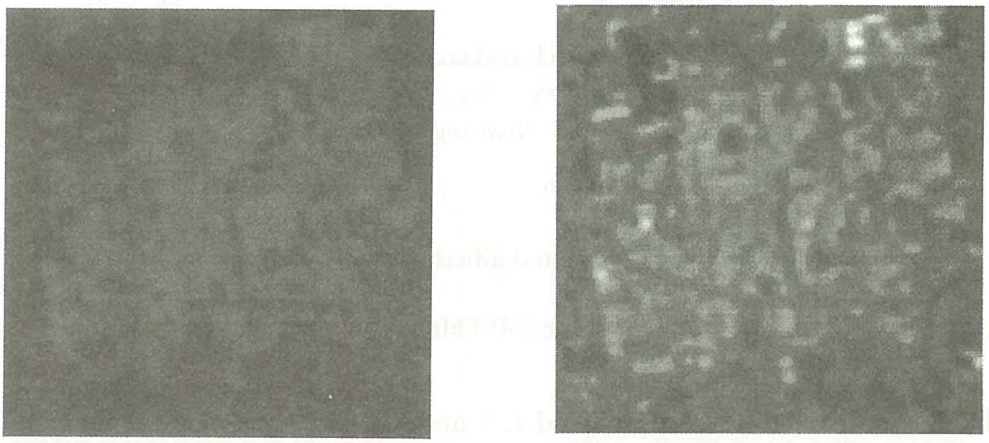
4. VALIDATION OF ALGORITHMS

We made the field experiments for the validation of our Meteorological Range retrieval algorithm at Heijo-Gu(the Old Palace Site) in Nara City, Japan on Dec.12, 1996 and at Meteorological Research Institute(MRI) in Tsukuba City, Japan on Jan. 8, 1997. Simultaneous ground measurements of the atmospheric optical thickness and surface reflectance at LANDSAT overpassing time were made on these dates. The sunphotometer (POM-01:Prede) and spectroradiometer (PS-1000: Ocean Optics) were used for the sky and surface albedo observations, respectively. The values of Meteorological Range for the test-site, obtained from the sunphotometer observations were V = 18.0 [km] and V = 50.0 [km] at Heijo-Gu and that at MRI, respectively. We showed the estimated values of Meteorological Range from TM data by applying our retrieval algorithm in the previous section in Table 1.

Table 1. Values of Meteorological Range for each band, by retrieval algorithm

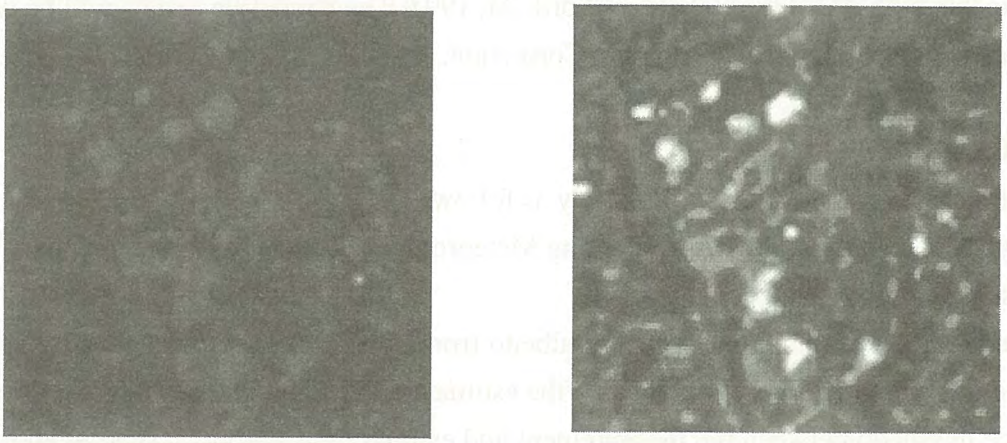
	Estimated meteorological range V [km]			
	Band 1	Band 2	Band 3	Band 4
Dec,12,1996	17.4	18.4	8.0	8.3
Jan, 8,1997	29.8	40.0	13.6	19.4

From Table 1, the appropriate Meteorological Ranges at Heijo-Gu (12/08/96)and MRI (01/08/97) are V = 18.4 [km] and V = 40.0 [km], respectively. We found that the agreement between the estimated and measured values is quite excellent. The differences in optical thickness between the measurement and estimation are less than 0.01 and less than 0.04 for Heijo-Gu and MRI cases, respectively.The target site in original TM band 4 image and in the albedo image (after the atmospheric correction, assuming V = 18.4 [km]) at at Heijo-Gu and MRI are shown in Fig. 1 and 2, respectively. The significance of the atmospheric correction is very clear by comparing two images (a) and (b).



(a) TM Band 4 image (b) Band4 albedo image

Fig. 1. The Landsat TM image and the estimated albedo image near Heijyougu.



(a) TM Band 4 image (b) Band4 albedo image

Fig. 2. The Landsat TM image and the estimated albedo image near MRI.

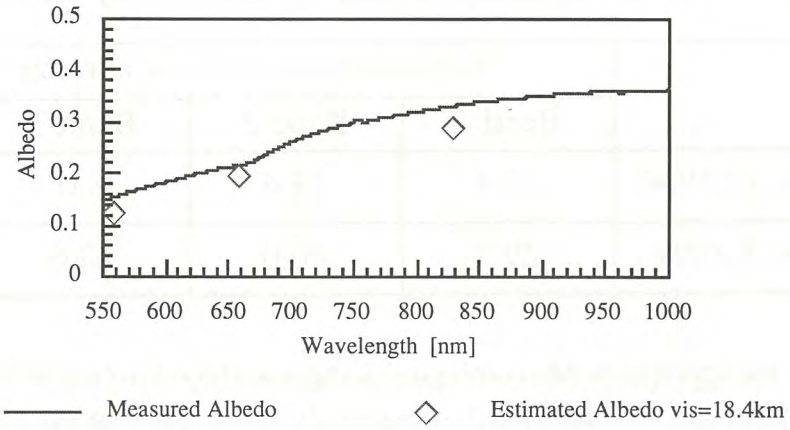


Fig. 3. Measured and estimated albedo values of dry grass at Heijyo-gu.

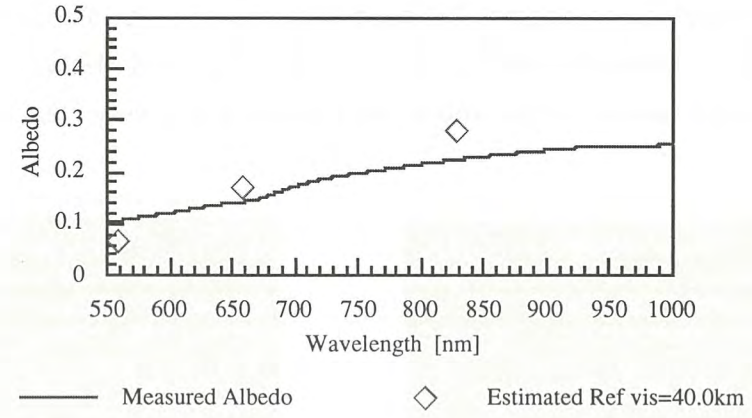


Fig.4. Measured and estimated albedo values of dry grass at MRI

Fig. 2. The Landsat TM image and the estimated albedo image near MRI.

We found that the albedo differences in band 2, 3, and 4 between the measurement and estimation are within ± 0.04 in the case of Heijyo-gu. We had similar results in the case of MRI, except for band 6, in which the difference is less than ± 0.06. We also made simultaneous sky observation measurements with ADEOS/AVNIR on April, 24, 1997. The validation results will be presented at the CERes Intl. meeting on Atmospheric Correction.

5. CONCLUSIONS

We came to conclusions by this study as follows:

(1) We presented an algorithm for estimating Meteorological Range(V) in the boundary layer from the measured satellite data alone.

(2) The estimation of the target's spectral albedo from the TM data set was done by applying our atmospheric correction algorithm by using the estimated Meteorological Range. We found that the difference in albedo between the measurement and estimation is within ± 0.06 in all bands.

(3) We also found that the estimated value of V depends on the size of a satellite image. We still have a problem how to treat with the variability of the atmospheric condition within a full scene. It

is certain that more simultaneous ground measurements with satellites should be done to establish an algorithm for retrieving aerosol optical thickness from satellite data alone.

This study was supported by the Research Contract No. NASDA-PSPC-18282, National Aeronautics and Space Developement Agency of Japan.

REFERENCES

[1] Turner, R.E., and Spencer, M.M., 1972. "Atmospheric model for correction of spacecraft data", Proc. of 8th Intl. Symp. on Remote Sensing of Environ., ERIM, pp.895-934.

[2] Odell, S.R., and Weinman, J.A., 1975. "The effect of atmospheric haze an image of the Earth's surface", J. of Geophys. Res., vol.80, pp.5035-5040.

[3] Otterman, J.,and Fraser, R.S., 1976. "Earth-atmosphere system and surface reflectivities in arid regions from Landsat MSS data", Remote Sensing of Environ., vol.5, pp.247-266.

[4] Otterman, J., and Fraser, R.S., 1979. "Adjacency effects on imaging by surface reflection and atmospheric scattering", Applied Optics, vol.18, pp.2852-2869.

[5] Kawata, Y., Haba, Y., Kusaka, T., Ueno, s., and Terashita, Y., 1978. "Atmospheric effects and their correction in airborne sensor and Landsat MSS data", Proc. of 12th Intl. Symp. on Remote Sensing of Environ., ERIM, pp.1241-1257.

[6] Ueno, S., Haba, Y., Kawata, Y., Kusaka, T., and Terashita, Y., 1979. "Theatmospheric blurring effect on renotely sensed Earth imagery", In Remote Sensing of Atmosphere, (Edited by Fymat, A.L. and Zuev, V.E., Elsevier(Amsterdam), pp.303-319.

[7] Tanre, D., Herman, M., and Deschamps, P.Y., 1981, "Influence of background contribution upon space measurements of ground reflectance", Applied Optics, vol.20, pp.3676-3684.

[8] Ueno, S., 1982. "Remote sensing-research experience and problem" In Marine Remote Sensing, (Edited by Vernberg, F.J., and Diemer, F.D.) Univ. of South Carolina Press, pp.451-510.

[9] Kaufman, y.J., and Fraser, R.S., 1984. "Atmospheric effect on classification of finite field", Remote Sensing of Environ., vol.15, pp.95-118.

[10] Kawata, Y., Kusaka, T., and Ueno, S., 1987. "Landsat Imaging:Removal of atmospheric effect", In Encyclopedia of Systems and Control, vol.4,(Edited by Siggh, M.) Pergamon Press, pp.2652-2655.

[11] Kondratyev, V.V. Kozoderov, and O.I. Smokty. 1992. Remote Sensing of the Earth from Space: Atmospheric Correction, Springer-Verlag, Berlin, 476p.

[12] Y. Kawata,and et.al. 1988, "Radiometric Correction for Atmospheric and Topographic Effects on Landsat MSS Images", Int. J. Remote Sensing, Vol.9,No.4, pp.729-748.

[13] J.E. Hansen, and L. Travis, "Light Scattering in Planetary Atmospheres, " Space Sci. Review , vol. 16, pp. 527-610, 1974.

[14] A. Berk, Bernstein,L.S.,Robertson,D.C. , "A Moderate Resolusion Model for LOWTRAN 7", GL-TR-89-0122, 1989.

A parameterized model for the atmospheric correction of satellite data

Qiu Jinhuan

Institute of Atmospheric Physics, Chinese Academy of Sciences, Beijing 100029, China

Abstract

Based on a lot of accurate radiance data, parameterized model for calculating outgoing radiance is developed. In the model, the outgoing radiance is analytically expressed in terms of atmospheric scattering phase function, surface reflectance, atmospheric optical depth, single scatter albedo, asymmetry factor and cosine of solar zenith angle. In the condition of aerosol optical depth less than unity, the solar zenith angle of <72.5° and viewing angle of <65°, the standard deviation of 39440 sets of radiance caculated by the parameterized model and the Gaus-Seidel itrative method is 4.2%.

1. Introduction

Atmospheric correction is of great importance for some applications of quantitatively remote sensing from space[1-3]. Two key points of atmosphere correction are relative scattering property of the atmosphere and available algorithm for calculating outgoing radiance. A simple but exact parameteriztion model for the radiance calculation would be very useful. Based on a lot of accurate radiance data and the radiance property, by using least square method and empirical fitting method, this paper develops a parameterized model of outgoing radiance is developed.

2. Parameteized upward radiance model

Under the assumption of no thermal radiation and the plane-parallel atmosphere, radiation transfer equation is

$$\mu\frac{dI(\tau,\mu,\phi)}{d\tau} = I(\tau,\mu,\phi) - \varpi\int_0^{2\pi} d\phi \int_{-1}^{1} d\mu\, P(\mu,\phi,\mu,\phi) I(\tau,\mu,\phi) - \varpi F \ell^{-\tau/\mu_0} P(\mu,\phi,-\mu_0,\phi_0), \quad (1)$$

where $I(\tau,\mu,\varphi)$ is radiance, τ is optical depth, μ is cosine of zenith angle, φ is azimuth angle, φ_0 is solar azimuth angle, μ_0 is cosine of solar zenith angle, ω_0 is atmospheric albedo, P is uniformed atmospheric scattering phase function, and F is extraterrestrial solar radiant intensity. In this paper p satisfies the following condition:

$$\frac{1}{2}\int_{-1}^{1} p(\cos\theta) d\cos\theta = 1, \quad (2)$$

Process in parameterizing upward sky radiance is divided into two steps. The first step only considers the condition when surface reflectance is zero. And, the second step considered the increasing of upward

sky radiance caused by surface reflection. At the point where single scattered radiance is more intensive, the contribution of multiple scattering should be larger. Thus, when surface reflectance A is zero, this paper selects parameterization model of outgoing upward sky radiance as follows:

$$\begin{aligned} I(\mu,\phi) &= I_s(\mu,\phi) + I_m(\mu,\phi) \\ &= I_s(\mu,\phi) + \left[1 + X_1 I_s(\mu,\phi)\right] X_2 X_2 X_3, \end{aligned} \tag{3}$$

In equation (3), $I_s(\mu,\phi)$ and $I_m(\mu,\phi)$ are single scattered and multiple scattered radiance, respectively; X_1, X_2, X_3 and X_4 are parameters to be determined. When phase function does not change with height, i. e., for homogenous atmosphere, $I_s(\mu,\phi)$ can be expressed as:

$$I_s(\mu,\phi) = \frac{F_0 \varpi \mu_0 p(\mu,\phi;\mu_0,\phi_0)}{\mu+\mu_0}\left[1 - \exp\left(-\frac{1}{\mu} - \frac{1}{\mu_0}\right)\right], \tag{4}$$

When surface reflectance is zero, $I(\mu,\phi)$ must satisfy the folowing relationship:

$$\int_0^{2\pi} d\phi \int_0^1 I(\mu,\phi)\mu d\mu = F_U(A=0), \tag{5}$$

where, $F_U(A=0)$ is exterrestrial upward radiation flux when A=0.

Combining equations (3) and (4), and supposing X_2=X_3=1, it is not dfficult to deduce that X_1 and X_2 satisfy the following relations:

$$X_2 = \frac{F_U(A=0) - F_{sU}}{\pi + X_1 F_{sU}}, \tag{5}$$

$$F_{sU} = \int_0^{2\pi} d\phi \int_0^1 I_s(\mu,\phi)\mu d\mu, \tag{6}$$

Where, F_{sU} is exterrestrial upward single scattered radiation flux.

Now X_1 is determined empirically on the basis of analyzing the dependence of upward radiance to atmospheric parameters again and again. X_2 is deduced using equation (5). Then, X_2 and X_3 are determined by combining least square method and empirical fitting method. At last, the increase of upward sky radiance $\Delta I_A(\mu,\phi)$ caused by surface reflectance is determined. The final parameterization model is:

$$I(\mu,\phi) = I_s(\mu,\phi) + \left[1 + X_1 I_s(\mu,\phi)\right] X_2 X_3 X_4 + \Delta I_A(\mu,\phi), \tag{7}$$

in which,

$$X_1 = 10(1 + 10g_0 + 810g_0^8)\left[F_{sU} / F_U(A=0)\right]^2, \tag{8}$$

$$X_2 = \frac{F_U(A=0) - F_{sU}}{\pi + X_1 F_{sU}}, \tag{9}$$

$$X_3 = X_{31}\left[2.3(1-\mu)\right]^{X_{32}} \exp(-X_{33}) - X_{34}X_{35}X_{36}\mu^{X_{37}} + 11(1-\mu)^8 (X_{38} - 1.4X_{39}), \tag{10}$$

$$X_{31} = 0.01(1 - 0.5\ell^{-\tau_t})\left[1.7 + 5(1-\varpi)\ell^{-4\tau_t^2)}\right]\left[5 + 105g_0^2 \exp(-120p_b^2)\right]\ell^{-\varpi^2 u_1}, \tag{11}$$

$$u_1 = 15\sqrt{g_0}\left[\mu_0 - 0.7\varpi \exp(-0.2\tau_s^2\right]^2\left[\sqrt{\mu_0}\exp(-\tau_t) + \mu_0^5 \exp(-8\tau_s^2)\right], \tag{12}$$

$$X_{32} = (1 + 1.5\mu^5)\exp\left[-486g_0^2 p_b^2 \mu_0^{12}\varpi^2 - 0.31\mu^3\mu_0(1-\alpha)^4\right] + \mu_0 g_0^{0.2}\ell^{-(0.1+15p_b\mu_0)\sqrt{\tau_s}}, \tag{13}$$

$$X_{33}=\left\{0.85(1-\alpha)^{u_2}(u_3+0.18\tau_t^2/\mu_0)\left[\sqrt{\mu_0}-(1-\mu_0)^4(1+\alpha/2)\right]+1.3\beta^{2.5}\right\}g_0 \\ -1.36(1-g_0)(1+\mu_0)u_3\sqrt{1-\mu_0}(1-\alpha+\beta/2), \tag{14}$$

$$u_2=2+\frac{0.18(2+\alpha)(2-\mu_0^2)\tau_t}{\mu_0(1+16\tau_t^4)}, \tag{15}$$

$$u_3=1-\sqrt{\tau_t}+0.38\tau_t, \tag{16}$$

$$X_{34}=\left[0.47+\frac{0.376g_0+1.6g_0^{12}\exp(9p_b)}{1+g_0}\right]\left[2-\varpi^{1/(1+3\mu_0\sqrt{\tau_t})}\right], \tag{17}$$

$$X_{35}=1-7.49g_0^{22}\mu_0^4\ell^{18p_b}+64g_0^8(1-1.25g_0)^2\mu_0^{30}\varpi^4-0.5(g_0-0.1)\ell^{-4g_0}, \tag{18}$$

$$X_{36}=1.026+0.06\exp(2p_b-8.6g_0^7)-0.95(1-g_0^{z_1})\tau_t+0.33(1-g_0^{z_2})(2\mu_0)^{0.3}\tau_t^2, \tag{19}$$

$$z_1=2.65-125g_0^{20}/(1+70p_b+1800p_b^2), \tag{20}$$

$$z_2=3.5-20g_0^{10}/(1+1900p_b^2), \tag{21}$$

$$X_{37}=z_3\left[z_4(1+z_5)+z_6\right], \tag{22}$$

$$z_3=1-0.5(1-\alpha\mu^{1-\alpha\mu^6})\left[1-\exp(-40+40\mu_0)\right]-0.25\mu^{(4-2\alpha)\mu^4}(1-\mu_0^4)\times(1-z_{31}+\beta^2), \tag{23}$$

$$z_{31}=\alpha\mu^{1-\alpha}\left\{1+0.4\exp\left[-35(1-\mu^{3+0.5\tau_t/\mu_0})\right](1-\alpha)^5\sqrt{\tau_t}/\sqrt{\mu_0}\right\}, \tag{24}$$

$$z_4=1.6\exp\left[-0.117+1.23\tau_s-0.507(1+g_0^8p_b)\tau_s^2\right]\left[g_0(2\mu_0)^{z_{41}}+1-g_0\right], \tag{25}$$

$$z_{41}=-3.2g_0\exp\left[-(1.1-16p_b)\sqrt{\tau_t}-g_0^4\right](1.25\mu_0)^{0.57+14p_t\tau_t}+3\exp\left[-34(1-\mu_0)-\tau_t\right], \tag{26}$$

$$z_5=19.5g_0^3(1-2.65g_0^6)\left[1-\exp\left(-\frac{98p_b}{1+2g_0^4}\right)\right]\exp(-23p_b), \tag{27}$$

$$z_6=33(1-\mu)^5\exp(g_0+12p_b), \tag{28}$$

$$X_{38}=\exp\left[-8.3g_0^3-2.2\tau_t^2\sqrt{\mu_0}/(1+0.5\tau_t^2)\right]+2(1-\varpi)\exp(-\tau_s/\mu_0)+ \\ g_0\mu_0^2\exp(-\tau_s/\mu_0+15p_b), \tag{29}$$

$$X_{39}=(g_0^{0.2}+77g_0^{20})(1-\mu_0)\left(1-\ell^{-2\tau_s/\sqrt{\mu_0}}\right)\exp\left[-0.06(1-\mu_0^2)(1+3200p_b^2)\tau_t\right]y, \tag{30}$$

$$y=23\exp\left\{-(2.7+8.2\mu_0)(1+\alpha)^3\left[1+30p_b(1-\mu_0)\sqrt{\tau_t}\right]\right\}(\mu_0^3+0.01)\ell^{-4\tau_t+1.9\tau_t^2}+1- \\ 2.9\exp\left[-8(1-\beta)^3-\sqrt{\mu_0}+22p_b-0.5\tau_t+y_1\right]-\frac{2.6\tau_t^2g_0^4\exp(-18p_b-19\sqrt{1+\alpha})}{(1+4\tau_t^4)(1-\mu_0^2)}, \tag{31}$$

$$y_1=0.49\sin^{20}(\phi-\pi/6)\exp(13p_b)(2-\sqrt{\mu_0})\exp(-4.5\tau_t+\tau_t^2)+ \\ \sin^8(\phi+\pi/4)(1+\alpha)^2(1.32+0.22\mu_0^2), \tag{32}$$

$$X_4=\exp\left[-0.74(1-\varpi)(1-\alpha)\sqrt{\tau_t}/\sqrt{\mu_0}/\mu\right], \tag{33}$$

$$\Delta I_A(\mu,\phi)=\frac{A}{\pi}F_D(A)\exp(-\tau_t/\mu)+\frac{y_A}{\pi}\left[F_U(A)-F_U(A=0)-AF_D(A)E(\tau_t)\right], \tag{34}$$

$$F_D=F_{dif}+\mu_0\exp(-\tau_t/\mu_0), \tag{35}$$

$$y_A = 1 - \exp(-\tau_t / \mu)\left[\mu - 0.84 + 0.24\exp(-2\tau_t^2)\right] / \mu^{0.8}, \quad (36)$$

$$E(\tau_t) = 2\int_0^1 \exp(-\tau_t / \mu)\mu d\mu. \quad (37)$$

In above equations, A is surface reflectance, τ_t is total optical depth, $\tau_s$is scattering optical depth, α=*cos*(ϕ), β=*sin*(ϕ), g_0 is asymmetry factor, F_U(A) upward flux at surface reflectance and atmospheric top, F_{dif}(A) is downward flux on the ground, p_b is scattering phase function at 180°. F_U(A) and F_{dif}(A) are calculated using a modified δ-Eddington approximation presented by Qiu[4].

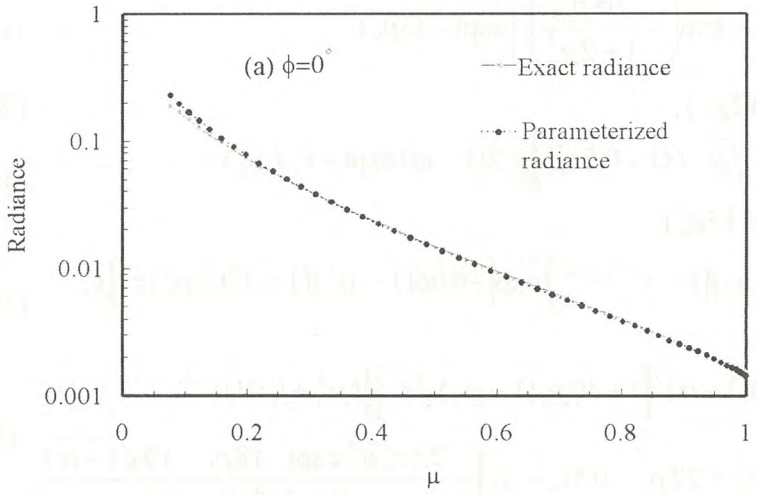
2. Numerical Test Result

Six aerosol or cloud phase functions are used in numerical experiments. Selected Junge size distribution is given by:

$$n(r) = \begin{cases} C(r/0.1)^{-(\nu^*+1)}, & \text{for } r > 0.1\mu\text{m}; \\ C, & \text{for } r \le 0.1\mu\text{m}. \end{cases}$$

ν^*=2, 3 and 4 are selected, and the corresponding distribution is marked as J2, J3 and J4. Another two aerosol size distributions are continent and marine haze models presented by Diermendjian[5], marked as DL and DM, respectively. Fair Weather Cumulus (FWC) model presented by Hasen[6] is also adopted.

Fig.1 compares the parameterized radiance with the radiance calculated by Gauss-Seidel iterative method[7] for μ_0=0.5 and τ_t=0.1. For three cases of φ=0°, 90° and 180°, agreement between them is very good.



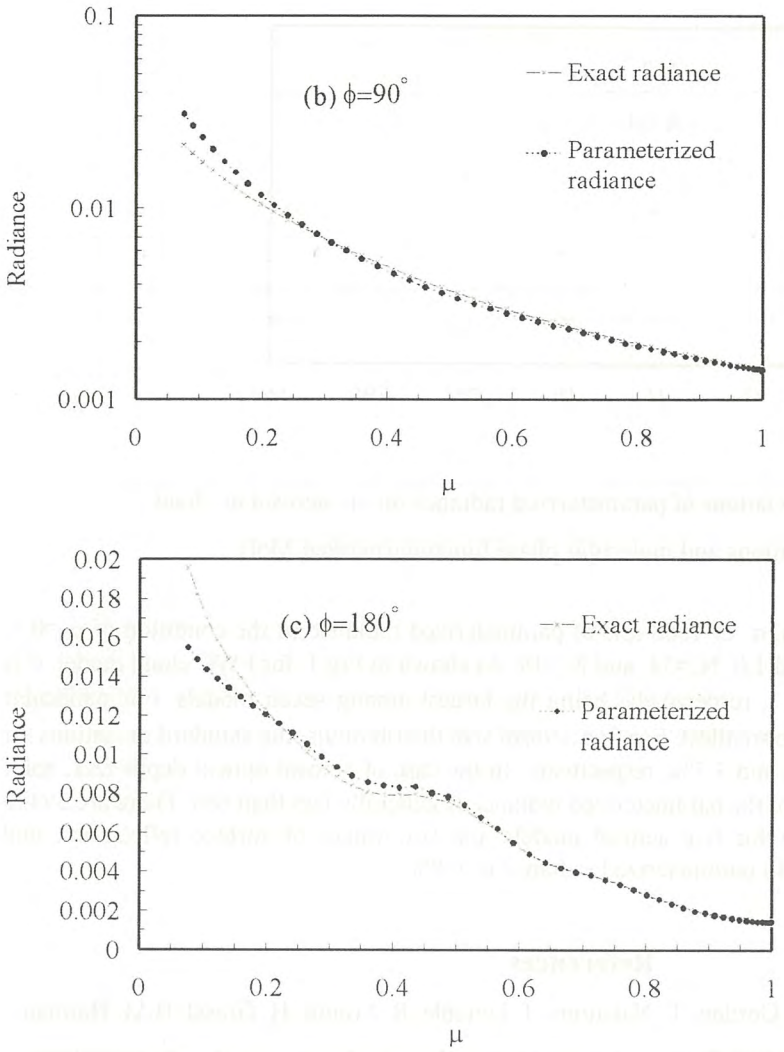


Figure 1 Comparison of radiance calculated by the parameterized model with the one by Gauss-Seidel iterative method for μ_0=0.5 and τ_t=0.1

Define percent standard deviation of parameterized radiance $I(\mu,\phi)$ as follows:

$$\sigma = \sqrt{\frac{1}{N_{\mu_0} N_\tau N_\mu N_\phi} \sum_{N_{\mu_0}} \sum_{N_\tau} \sum_{N_\mu} \sum_{N_\phi} \left[1 - \frac{I(\mu,\phi)}{I_{G-S}(\mu,\phi)} \right]^2} \%, \qquad (38)$$

where $I_{G\text{-}S}(\mu,\phi)$ is radiance calculated by Gauss-Seidel iterative method . N_{μ_0}, N_τ, N_ϕ and N_μ are numbers selected for solar zenith angle (or μ_0), optical depth τ_t, azimuth angle ϕ and μ. N_ϕ=19, ϕ is taken in the range of 0-180° and with a step of 10°. In this paper 120 streams on μ (Gauss integration) is taken, and 34 values of μ in the range from 1 to 0.432 (zenith angle changes from 0^0 to 65^0) are used in calculating standard deviation σ (N_μ=34). N_{μ_0}=4, μ_0=1.0, 0.8, 0.5 and 0.3 (solar zenith angle changes from 0° to 72.5°).

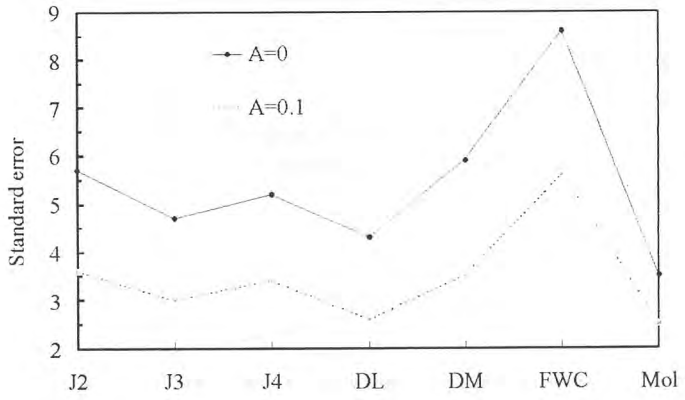


Figure 2 Standard deviations of parameterized radiance for six aerosol or cloud Size distributions and molecular phase function (marked Mol)

Fig.2 shows standard deviation, σ, of 7888 sets of parameterized radiance in the condition of μ_0=0.3, 0.5, 0.8 and 1.0, τ_t=0.1, 0.3, 0.5 and 1.0, N_μ=34, and N_ϕ=19. As shown in Fig.1, for FWC cloud model, σ is 8.6 % and 5.4 % for A=0 and 0.1, respectively, being the largest among seven models. For molecular model, the standard deviation is the smallest. For five aerosol size distributions, the standard deviations for A=0 and 0.1are all less than 5.9% and 3.7%, respectively. In the case of aerosol optical depth $\tau_t \leq 1$, solar zenith angle <72°, $\mu \leq 0.432$, error of the parameterized radiance is generally less than 6%. There are 39440 sets of comparative radiance data for five aerosol models and two values of surface reflectance, and standard deviation of the total 39440 parameterized radiance is 4.2%.

References

[1] Kaufman Y. J., D. Tanre, H.R. Gordon, T. Nakajima, J. Lenoble, R. Frouin, H. Grassl, B.M. Herman, M.D. King, and P. M. Teillet, 1997: Passive remote sensing of tropospheric aerosol and atmospheric correction for the aerosol effect, *J. Geophys. Res.*, Vol.102, No.d14, 16815-16830.

[2] Tanre, D., et al., 1992, Atmospheric correction algorithm for NOAA-AVHRR products: Theory and Application, IEEE Trans. Geosci. Remote Sens. 30(2), 231-248.

[3] Gordon, H. R., 1997, Atmospheric correction of ocean color imagery in the Earth observation System era, *J. Geophys. Res.*, Vol.102.

[4] Qiu Jinhuan, 1998: Two modified Delta-Eddington approximations for solar reflection, transmission and absorption calculations, submitted to *J. Atmos. Sci.*.

[5] Diermendjian, D., 1969, Electromagnetic scattering on spherical polydispersions, American Elsevier, New York, 290pp.

[6] Hansen, J. E., 1971: Multiple scattering of polarized light in planetary atmosphere, Part I: The doubling method, J. Atmos. Sci., 36, 508-51.

[7] Herman, B. M., and S. R. Browning, 1965: A numerical solution to the equation of radiative transfer, *J. Atmos. Sci.*, 22, 559-566.

Snow Surface Bidirectional Reflectance Effects on Atmospheric Correction based on Doubling- Adding Method

Satoshi TSUCHIDA

Geological Survey of JAPAN, Higashi 1- 1- 3, Tsukuba, Ibaraki 305- 8567, Japan
satoshi@gsj.go.jp

Snow surface bidirectional reflectance effects on atmospheric correction are studied for the snow reflectance estimation from satellite data and radiometric calibration of satellite optical sensor. The atmospheric correction based on doubling- adding method that has a potential to calculate multiple scattering between land surface and atmosphere are simulated with non- lambertian snow surface, and then the calculation error derived from lambertian assumption are estimated. The result shows that the non- lambertian surface model is necessary for the atmospheric correction over the snow, and it is better to account the multiple scattering between atmosphere and snow.

1.0 Introduction

Snow surface reflectance (and/or albedo) is one of the important parameters in the earth radiation balance, and vicarious and cross calibrations for optical sensor have been planned over the snow field for the precise analysis of the biological, chemical and geological process. The snow surface was assumed to be lambertian in many cases of atmospheric correction, though the snow surface shows departure from lambertian behavior. To avoid this non- lambertian problem for some land surface material, the previous studies carried out atmospheric correction with the measured (and/or modeled) bidirectional reflectance distribution function (BRDF) of the land surface and the single scattering calculation between surface and atmosphere. However, the snow surface shows high reflectance, therefore the multiple scattering between surface and atmosphere can not be ignored. In this study, snow surface bidirectional reflectance effects on atmospheric correction are estimated using doubling- adding method that has a potential to calculate multiple scattering between surface and atmosphere.

2.0 Radiative Transfer Simulation

The radiative transfer for atmosphere and snow is simulated for the estimation of the snow BRDF effects on atmospheric correction. The doubling- adding method[1] is used mainly, because the use of the doubling method[2] or discrete ordinate method[3] has been proposed for the snow BRDF simulation[4]. The modtran[5] and basic theories for atmosphere are also used in some processes (figure 1). This calculation flow is based on the atmospheric correction for the vicarious calibration which is shown in Tsuchida *et al.* (1997, 1998)[6],[7].

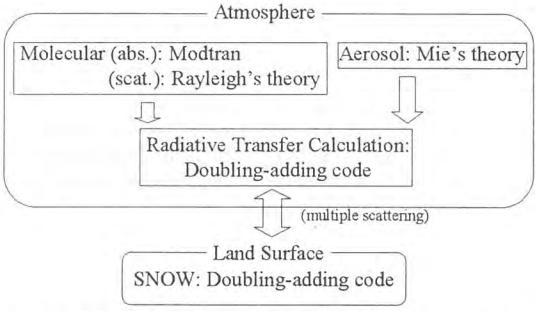


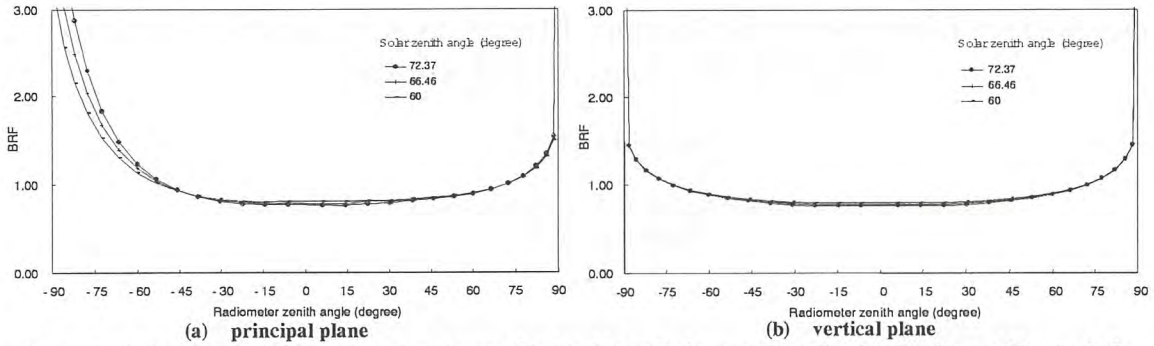
Figure 1 Calculation flow of the simulation of radiative transfer in atmosphere and snow

The input parameters are set for the snow field of Sarobetsu, Hokkaido in Japan, and then the radiative transfer of atmosphere and snow simulated using these codes. Atmospheric parameters are obtained from these models (Mid- latitude- Winter[5] and Water Soluble- Oceanic[8] mixed models) and some of them are changed with the *in- situ* measurement data[7]. Snow is assumed to be massive semi- infinity single layer, and

Table 1 Parameters of snow particle for snow surface BRDF simulation

Wavelength	560nm
Complex Index of Refraction*	1.3106-*i*8.290x10^{-9}
Size distribution	Uniform Function 50- 100μm

* Data from Warren (1982) [4]



(a) **principal plane** (b) **vertical plane**

Figure 2 Bidirectional reflectance factor over snow simulated by radiative transfer code with doubling- adding method.

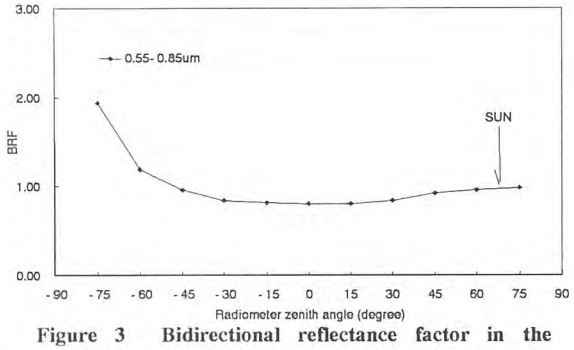


Figure 3 Bidirectional reflectance factor in the principal plane measured over snow near Logan Utah. USA (from Fig.8 of Solomonson and Marlatt, 1968)[9]. Solar zenith angle : 66 - 70 degree.

its parameters are shown in Table 1.

Figure 2 indicates the simulated reflectance factors of snow surface in the principal and vertical planes. The curved line of the reflectance factors versus observer (radiometer) zenith angle is very similar to one of the measurement data (the example under cloudless is shown in figure 3)[9].

3.0 Snow BRDF Effects

Snow surface BRDF effects on atmospheric correction based on doubling- adding method are estimated for vicarious calibration and satellite measurement. In this study, the percent differences of the results between the lambertian and non- lambertian surface models with multiple scattering calculation between snow and atmosphere are calculated as index for the effects.

3.1 Vicarious Calibration

Vicarious calibration[10] is the in- flight radiometric calibration for satellite optical sensor using the *in- situ* measurement data at the ground target. The reflectance factor of land surface $R(h(z)/0)$ (or $R(h(z)/d_{out})$) is measured by the field radiometer at the satellite overpass time, but it is for one direction (or few directions) in irradiance to snow surface, that is the solar zenith angle z at that time, where $h(z)$ is hemispherical input in solar zenith angle, d_{out} is output direction, and d_{out}=0 means the nadir direction. In many previous studies, the reflectance factor in nadir direction $R(h(z)/0)$ was used on the assumption that the land surface was lambertian, or the only single scattering between atmosphere and land surface is calculated using $R(h(z)/d_{out})$. For the calculation of the multiple scattering between atmosphere and snow, reflectance factors of the all directions in irradiance to snow surface and radiance from snow surface $R(d_{in}/d_{out})$ are necessary. It is impossible to measure all reflectance factors $R(d_{in}/d_{out})$ under the stable condition for atmosphere and snow, so the snow BRDF model will be used for this multiple scattering calculation.

To estimate the snow BRDF effects on the vicarious calibration, the radiances at the top of atmosphere and its percent differences are calculated from the ground measurement data in two cases that snow surface is assumed to be lambertian and non- lambertian (figure 4). The percent difference is very large (4 to 15 %) and smaller in larger solar zenith angle. The solar zenith angle at the snow field is generally 50 to 70 degree, and then the percent difference is almost 10 %.

As mentioned above, the same reflectance factor in the nadir direction $R(h(z)/0)$ is used in both cases as the *in- situ* measurement data, but the estimated snow surface reflectances $R(h(z)/h_{out})$ are difference (figure 5), where h_{out} is hemispherical output, and $R(h(z)/h_{out})$ in the lambertian model is equal to $R(h(z)/0)$. The surface

reflectance derived from non- lambertian model is almost stable in solar zenith angle, but the reflectance in lambertian model is getting smaller in larger solar zenith angle. The curved line of reflectance from the lambertian model in fig.5 is very similar to one of reference panel, i.e. Spectralon and $BaSO_4$[11] , except for the data of 80- 90 degree in solar zenith angle. Therefore the calibration error maybe decreased, if the reference panel s BRDF correction[11] is not carried out in vicarious calibration at the snow field. From this viewpoint, the reference panel BRDF effects was not corrected in previous vicarious calibration study at the snow field[6),7].

3.2 Satellite Measurement

Satellite measurement is to estimate the land surface reflectance $R(h(z)/h_{out})$ from the radiance at the satellite in this study. To estimate the snow BRDF effects on the satellite measurement, the snow surface reflectance and its percent differences are calculated from the satellite data in two cases that snow surface is assumed to be lambertian and non- lambertian (figure 6). The reflectances in the lambertian model exceed 100 % in 0 to 45 degree of the solar zenith angle, and it is rare case for the snow field that the solar zenith angle is smaller than 45 degree. Therefore the results in the range are not shown in fig.6. Figure 6 indicates that the percent differences are very variable (0 to 15 %) in the solar zenith angle and that the differnce is very small if the solar zenith angle is close to 60 degree.

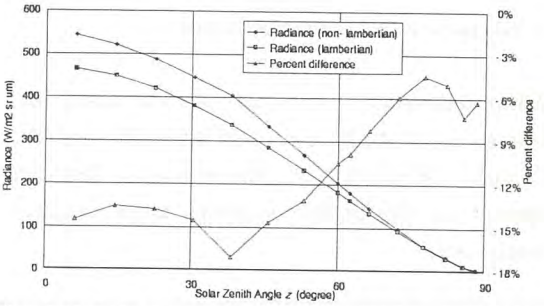


Figure 4 Radiances at the top of atmosphere calculated from the ground measurement data in two cases that snow surface is assumed to be lambertian and non- lambertian

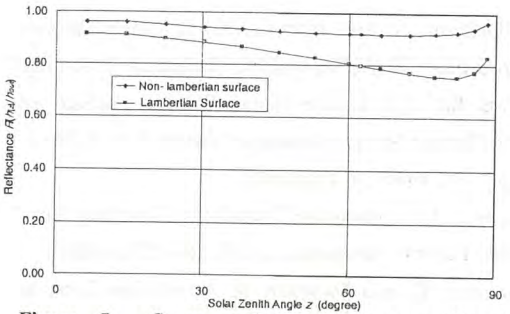


Figure 5 Snow surface reflectances $R(h(z)/h_{out})$ (hemispherical- hemispherical) calculated from the same reflectance factor $R(h(z)/0)$ in two cases that snow surface is assumed to be lambertian and non- lambertian

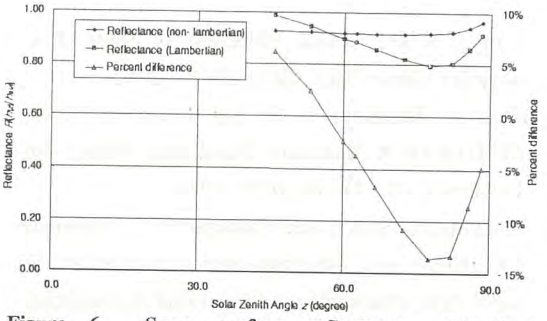


Figure 6 Snow surface reflectances $R(h(z)/h_{out})$ calculated from the satellite data in two cases that snow surface is assumed to be lambertian and non- lambertian

4.0 Concluding Remarks

The result of the simulations of the snow BRDF effects on atmospheric correction shows that the surface model with the BRDF parameters is necessary for this correction over the snow, and it is better to account the multiple scattering between the atmosphere and snow. To estimate the BRDF effects more precisely, more complicated snow model (multiple layers, including soot, and etc.) is used, and the simulation must be carried out in many cases. In the simulation for vicarious calibration, the percent differences of the radiance at the top of atmosphere between the lambertian and non- lambertian models with multiple scattering calculation between snow and atmosphere are very large (4 to 15 %). The effects on vicarious calibration can be decreased, if the complicated snow model is used. However, the calculated snow surface reflectance from the non-lambertian model must be nearly eqaul to measurement data. In the simulation for obtaining snow reflectance from satellite date, the percent differences of the snow reflectance (hemispherical- hemispherical reflectance) between the lambertian and non- lambertian surface models are very variable (0 to 15 %) in the solar zenith angle. The effects also can be decreased by the use of the snow BRDF model, if the input parameters of this

model can be obtain from satellite data.

Acknowledgments. I would like to thank Dr. Tsutomu TAKASHIMA of NASDA/EORC and Dr. Kazuhiko MASUDA of Meteorological Research Institute for the fruitful discussion about radiative transfer code.

5.0 Reference

1) Takashima, T. and Masuda, K., A Computational Procedure of the Upwelling Radiation Emerging from the Atmosphere-Ocean System, *Journal of the Remote Sensing Society of Japan*, Vol. 6, No.1, pp.5-35, 1986. (in Japanese)
2) Hansen, J. E., Radiative Transfer by Doubling Very Thin Layers, *Astrophys. J.*, 155, 565-573, 1969.
3) Stamnes, K. and Swanson, R. A., A New Look at the Discrete Ordinates Method for Radiative Transfer Calculations in Anisotropically Scattering Atmospheres, *J. Atmo. Sciences*, 38, 387-399, 1981.
4) Warren, S. G., Optical Properties of Snow, *Rev. Geophys. Space Phys.*, 20(1), 67-89, 1982
5) Berk, A., Bernstein, L. S., and Robertson, D. C., MODTRAN:A Moderate Resolution Model for Lowtran 7, GL-TR-89-0122, 1989.
6) Tsuchida, S., Sato, I. and Yamaguchi, Y., Vicarious Calibration with Doubling-adding method at the snow field, *Proceedings of the twelfth International Conference Applied Geologic Remote Sensing*, II, 317-322, 1997
7) Tsuchida, S., Sato, I., Yamaguchi, Y., Arai, K. and Takashima, T., Vicarious Calibration in the Visible to Infrared Region based on Reflectance-Based Method at the Snow Fields in Hokkaido, submitted to *Journal of the Remote Sensing Society of Japan*, 18(1), 1998. (in Japanese)
8) World Meteorological Organization, A Preliminary Cloudless Standard Atmosphere for Radiation Computation, *World Climate Programme*, WCP-112, WMO/TD-No.24, p.53, 1986.
9) Salomonson, V. V. and Marlatt, W. E., Anisotropic Solar Reflectance over White Sand, Snow, and Stratus Clouds, *J. Applied Meteorology*, 7, 475-483, 1968.
10) Slater, P. N., Biggear, S. F., Holm, R. G., Jackson, R. D., Mao, Y., Moran, M. S., Palmer, J. M. and Yuan, B., Reflectance- and Radiance-Based Methods for the In-flight Absolute Calibration of Multispectral Sensors, *Remote Sensing of Environment*, 22, 11-37, 1987.
11) Jackson, R. D., Clarke, T. R. and Moran, M. S., Bidirectional Calibration Results for 11 Spectralon and 16 BaSO4 Reference Reflectance Panels, *Remote Sensing of Environment*, 40, 231-239, 1992.

VI. Remote Sensing of Indonesian Forest Fire

FOREST/LAND FIRE IMPACT IN INDONESIA [1]

BY :
Muchlisin Arief Ph.D [2]
Bambang S. Tejasukmana Dipl. Ing [3]

Abstract

Indonesia is under influence of dry and rainy seasons. This year due to El-Nino, the dry season lasted longer than unusual, so that the forest fire that happened naturally and inflicted by human went out of control. In order to handle the fire effectively, an accurate and real time information is necessary.
Based on The measurement using the advanced very high resolution radiometer data from NOAA satelite, show that, the hot spots started on mars in sumatra, in kalimantan, sulawesi and the other island on may.
The area affected by burning related to the length of the dry season, so that The hot spots tended on increase maximum on the late september and after that tended on decrease.
Beside that, the monitoring of haze caused by forest fire has been conducted by LAPAN using NOAA-AVHRR and GMS satellite data.
In this paper presented the monitoring hot spots daily and distribution of haze has been done by LAPAN (National aeronautic and space institute Indonesia)

Key word

Forest fire, NOAA - AVHRR data , hot spots, haze, GMS data.

1. Presented in the CERes International Symposium on THE ATMOSPHERIC CORRECTION OF SATELITE DATA AND ITS APPLICATION TO GLOBAL ENVIRONMENT, Chiba university , January 21-23 , 1998.
2. , Head of Ground Station Environment and Weather Satelite LAPAN, Indonesia.
3. Director of Remote Sensing Application Center LAPAN, Indonesia.

I. Introduction

Indonesia is an archiphelogic country (including 17000 islands) and under two season (dry and rainy), located between two continents (Australia and Asia), two oceans (Hindia and Pacific ocean) and has two season: dry and rainy season, these seasons are controlled by many factor : both large and small scale of atmospheric, sea circulation such as: Asia monsoon, pacific and hindia circulation; and topographic factor control mainly on the intensity and the duration of those season.

The measurement from Advanced Very high Resolution Radiometer (AVHRR) data are among the most useful satellite data for land monitoring [1]. The NOAA satellite data can be received by the ground station at LAPAN are NOAA-12 and NOAA-14 which are passed on Indonesia four time on every days (4 time for each satellite). Based on satellite imagery monitoring using NOAA-AVHRR data, the fire occurred in Sumatra started in mars, in Kalimantan and other islands on may.

The monitoring of hot spots, haze and its impact caused forest and land fire from mars to November will be described in the next session.

II. Hot spots Monitoring

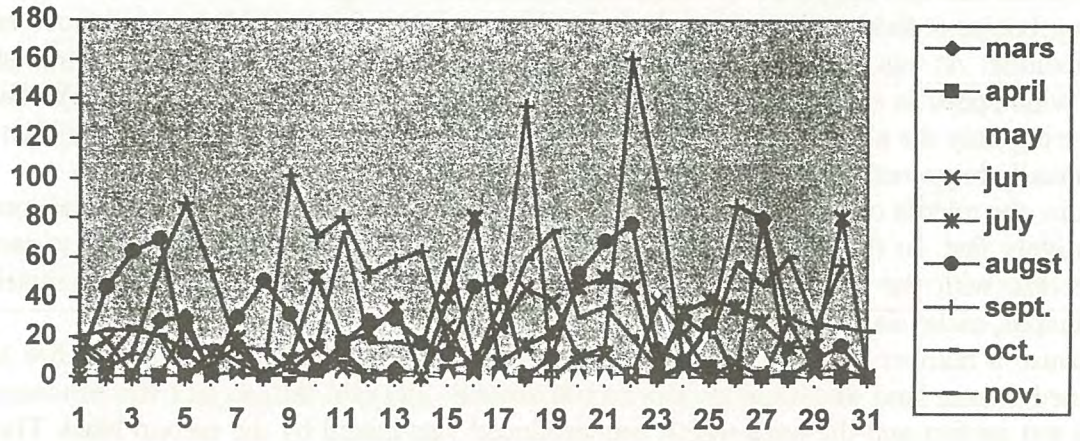
Normally, dry season is ended every September, so that at the end of October, the rain has been fallen in a large part of Indonesia territory, especially in Sumatra, Kalimantan and Irian Jaya.

Due to El Nino and the drought season, forest fire that usually occurs at the end of dry season become uncontrolled . This forest/land fire is categorized as national disaster.

The late of the starting rainy season has given impact to the forest/land fire was happened out of control. The forest/land fires occurred in Indonesia caused at first originated from new investment in agribusiness field and small scale individual society for land clearing purpose and agriculture. The forest/land fire can be identified by using NOAA-AVHRR data named as the hot spots.

Hot spots is an area on earth surface, which has correlated to its temperature. The hot spots indicated forest/land fires on earth surface, so that hot spots monitoring can be used as an early warning of forest/land fire.

Based on the satellite imagery analysis, the forest/land fire happened in Indonesia started on march in sumatra, in kalimantan and other island on may. The monitoring of hotspot frequence in sumatra and kalimantan daily respectively can be seen at the figure followed. (figure 1a and 1b)



Figur.1a. The frequency of hot spot daily in Sumatra.

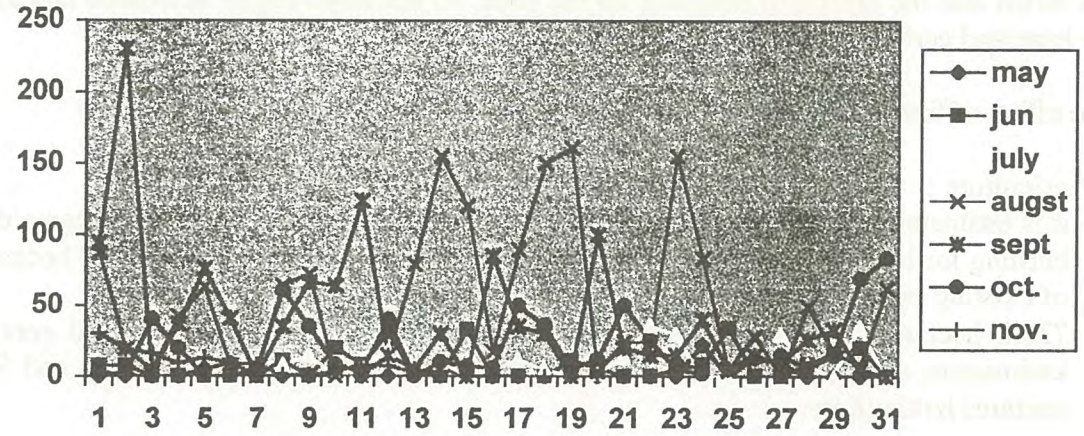


Figure. 1b. The frequency of hot spots daily in Kalimantan

From figure above, it can be seen that the fluctuation of daily hot spots during forest/land fires from march to may does not mean that the fire was extinguished but due to the capability of sensors in penetrating the haze to detect hot spot.
The hot spots are increasing in September, but there are decreasing in November. It is mean that the forest/land fore has been extinguished

III. Haze monitoring and impact

In haze monitoring and its impact, the information needed is area burned (location of longitude and lattitude), the kind material burned causing haze, wind condition.
The haze monitoring caused by forest/land fire has been conducted by LAPAN using NOAA-AVHRR data and GMS data since march 1997. Based on the monitoring from using AVHRR showed that:

The forest fire that happened in Indonesia caused at first originated from new investment in agribusiness field and small scale individual society for land clearing purpose and agriculture. At this moment, the material burned is only leaf and branch of the tree and the wind speed is slowly, so the land/forest fires relatively controllable and smoke/haze covering only the above area burned (in Kalimantan and sumatra only). This condition is cotinually happened until on the end of july.
But in the middle of August , the wind moved to the north-west direction with the speed relatively fast, so the fire was getting large, causing haze began to move to the same direction with the wing direction. This haze pass through the neighboring countries (singapor, malaysia)
Because a number of hot spots were increased in September (see fig. 1b) and fire has burned at peat land region, and also simultaneously the rain fell, so that fire processing was not perfect and the haze which was produced was mixed by the carbon black These conditions resulted the most Kalimantan and Sumatra was covered by haze and began unity of haze and carbon black.
In October, the efforts of government to extinguish the fire and simultaneously the rain has fallen and the efforts to brushing up the haze, so hot spots began decreased and also the haze and carbon black fell to earth surface.

The effect of forest/land fire are :

i) Agriculture :
a. it is estimated 121. 626 hectares has been burned consisting of : 22,816 hectares due burning for land clearing, 10,103 hectares due to spreding of fire and 88, 707 hectares of existing palnts
b. 730,5 hectares of food crop and holticulturred were burned in south and central kalimantan, south sumatra, 209 hectares rice crop 10.5 hectares second crop and 520 hectares holticulture.

ii) Transmigration:
a. 88 of 300 houses located on 300 hectares pieces of land in south tapanuli and north sumatra.
b. 149 houses burned on 800 hectares piece at muara dahup, lamunti, kuala kapuas and central kalimantan
c. 268 houses was destroyed by fire on 800 hectares of peat soil at pulau laut timur, kota baru and south kalimantan

iii) Forestry
a. 96,693 hectares of forest were burned consisting of: 10,552.30 hectares of protect forests, 70,259.20 hectares of productive forest, 3,890 hectares natural conservation forest, 1,724 hectares recreational forest, 10,222.09 hectares of natural park forest, 5 hectare of provincial recreational forest and 34.75 hectares of other natural forest, the timber and plantation estates (HTI) estimated loss RP. 45.7 billion.

iv) Transportation.

1,037 flight were cancelled at 11 air port in sumatra and 2,027 flight at 12 airportb in kalimantan

IV. Conclusion .

The land/forest fire in Indonesia caused at the drougth season lasted leonger than unusual and from new investment in agribusiness field and small scale individual society for land clearing purpose and agriculture.
The great losses of this occurrence was about 300.000 ha land and forest burned, 500 houses burned, bio organism extinguish decreases etc.

Bibliogrphy.

1. J.R.G. Townshead, et al.... " the 1 km resolution global dat set: need of the international Geosphere biosphere programme". Int. J. Remote Sensing. Vol.15, pp. 3417-3441, 1994.
2. ....., "agenda -21-Indonesia", State Ministry for Environment Republic of Indonesia, March, 1997.
3. ....., " Suara Merdeka " , tanggal 28 september 1997
4. Ir. Sumarsono et al... " Laporan Posko DIRJEN PHPA", 30 oktober 1997
5. Asean Development Bank, " Strennthening ASEAN's Capability to mitigate Transboundary Atmospheric Polution ", 3 th meeting asean senior official on environment (ASOEN) 18 November 1997.
6. Muchlisisn Arief, Muslich M, " Pemantauan kebakaran hutan di Indonesia semenjak bulan maret sampai dengan November 1997". Seminar ISRS(Indonesian Society for Remot. Sens.), Bandung Dec. 3-4, 1997.

Relation Between Continuity of Forest Fire and Forest Types in Indonesia

Haruo Sawada, Naoki Mitsuzuka
Forestry and Forest Products Research Institute
sawady@ffpri.affrc.go.jp, mituzuka@ffpri.affrc.go.jp

Tomoyuki Ueda
Forest Fire Prevention Management Project
tueda@indo.net.id

Abstract

Recently, big forest fires were reported in Indonesia every several years. According to the information from the Ministry of Forestry of Republic of Indonesia, the attacked areas were about 300 thousand, 162 thousand and 19 thousand hectors in 1997, 1994 and 1991, respectively.

Early detection of forest fires and early attack to them are considered important for preventing such big fires and a new satellite observation system coupled with NOAA and HIMAWARI(GMS) was installed in Bogor in July 1997 by the Japan International Cooperation Agency (JICA). The early detection system was developed and is being used in practical way for the project. The hot spots derived from NOAA data taken in midnight are overlayed on HIMAWARI images for observing smoke plumes and on TM with GIS information for identifying the ground conditions around the fires.

Estimation of danger of fire expansion, however, is required when we have to put priorities for attacking them. Then, as the first attempt for creating a fire danger map, we studied the relations between continuity of forest fires and soil types in Sumatra.

According to the observation of fires using this system in 1997, the fires on wetland forest area lasted for a long time expanding their areas. Smoke plumes from those area were also appeared very thick on HIMAWARI images.

Introduction

Wild fire is one of the matters of great concern in the world (Kasischke and French 1997, Ehrlich et al. 1997). Indonesia draw such a big concerns in 1997. Large forest fires periodically attack Indonesia with the interval of 3 to 5 years, due to unusual long dry seasons (Fig.1). It is well known that fire damaged 3.5 million hectors of forests in East Kalimantan in 1982 and 1983. Smoke from forest fires in 1991 and 1994 caused distarbances of air and marine traffic in neighboring countries. Based on the request from the Government of Indonesia, the Forest Fire Prevention Management Project commenced in 1996 as a technical cooperation between the Ministry of Forestry in Indonesia and Japan Cooperation Agency (JICA).

Fire (biomass burning) is considered a major source, on a global scale, of aerosols and various trace gases (Cuzen et al.) The overall goal of the project is to reduce the damage of forest fires in Indonesia, and thereby reduce forest devastation and environment disturbances caused by the smoke from them. In order to attain the above mentioned goal, the Project focused its activities on three fields as follows:

(1)To improve method of early warning and detection system by applying information from weather satellites, HIMAWARI and NOAA
(2)To support public relations and extension activities for forest prevention as well as training for initial suppression to local communities and local government staff
(3)To develop forest management techniques which are effective for forest fire prevention and make trials of green belt and fire break establishment in cooperation with concerned local communities .

Especially in the case of Indonesia, it is very difficult to suppress forest fires once they spread out, due to large forest areas and poor access roads and communication facilities. Early warning and detection can be the only possible way to effectively reduce the damage of forest fires.

Integration of remote sensing and GIS is suggested for fire management in developing countries (Flasse et al.). This report shows the development of the early detection system using NOAA and HIMAWARI satellites integrated with GIS data and the study on the relations between the continuity of forest fires and forest types which are considered useful for predicting the risk of big fires and/or severe smoke for each land cover types.

During the observation of NOAA and HIMAWARI images in August and September, we noticed that hot spots were found whole island in August but smoke covered Sumatra in September except the southern area and hot spots in the northern areas were not identified. Then we made the study on the relationship of soil types and forest fires using the data taken in August.

1. Development of Early Forest Fire Detection System

The conceptual idea of the developed system composed from the early warning system and the early detection system is shown in figure 1

We considered that the early fire detection system should include the prediction of expansion/reduction of the observed fires. Therefore early warning system which is based on the terrain conditions, phenological aspects and drought stress to vegetation is needed to be integrated into the system.

1.1 Information needed for early detection system

For creating the information system of the early fire detection, we thought that the information shown below are needed to be considered;

1) Active fires
 - detection and count
 - smoke condition
2) Geographic distribution
 - location of fires
 - distribution patterns
3) Temporal dimension
 - continuity
 - spatial dynamics (movement, expansion)
 - seasonal evolution and relationships with climate parameters
4) Target vegetation
 - type and biomass
 - seasonality, phenology
 - regrowth regeneration after fire
5) Land use
 - types of land use practices, tends
6) Impact
 - area affected by burn
 - severity of burn

1.2 Satellite Data Receiving System

Both NOAA receiving system (BURL: Bradford University Research Limited)and HIMAWARI receiving systems (SDP GMS System ,IN Technology) were introduced to the project in July 1997. Since then NOAA and HIMAWARI images were collected and stored as digital data. The NOAA data is found effective for identifying the forest fire because of its capability of the channel 3 and HIMAWARI is effectively used to interpret the smoke plumes every one hour.

1.3 Hot Spots observed by NOAA

Because bare lands with very high temperature in day time affect the NOAA data as "hot spots", the hot spots from NOAA taken in night time are considered showing forest fire. The process steps are shown as follows;

- set the threshold for temperature
- get the position of the hot spots with Latitude-Longitude system
- import the coordinates of hot spots to TNTmips as the points elements

1.4 Smoke Plume observed by HIMAWARI

Smoke plumes are identified on the HIMAWARI images which we can be obtained every one hour at the station in Bogor. The spectral resolution of the HIMAWARI is poor to identify ground conditions but smoke plumes are easily identified as follows;.

- check the cloud condition and select

appropriate images
- import these images to TNTmips as the raster objects
- correct geometry to the orthographic coordinate system (WGS1984, center [E140, N0])
- enhance [20, 40] to [0, 255] with Linear enhancement function

1.5 Integration of NOAA, HIMAWARI and other GIS data

The hot spot locations derived from NOAA satellite were converted into TNTmips software (GIS/Remote sensing software, Micro Image Inc.) as point data in a vector object with the coordinate system of Latitude-Longitude. Each HIMAWARI image was also converted to TNTmips file with orthographic coordinate system. Hot spot data were overlayed on HIMAWARI smoke images and severe smoke plumes from the hot spots were easily identified.

The HIMAWARI images observe the earth most frequently and it is considered to be the best way, as the routine work, to have the coordinate system of GIS suitable for the HIMAWARI images. Then, the coast lines, rivers and roads (DCW), geological data(GSU), Landsat images, soil type maps (FAO), elevation data and other related information are also converted to the same coordinate system, orthographic.

1.6 Forest Base Map derived from Landsat TM

Lack of systematic forest information system have caused poor accuracy of geometric condition of forest area. It is, however, necessary to have an accurate map for making a plan to suppress the fires. The geometric correction are applied to Landsat image of Jambi study area in Sumatra using the 1:50,000 topographic map and a large scale Landsat map was created for field study. The processing were carried out on the TNTmips.

1.7 Fire Information Transfer to Local Fire prevention office

We proposed that the local office should be installed with the same software TNTmips on a PC with a color printer. The hot spots location data will be sent by e-mail to the offices and overlayed on the base images which are installed together with the software. That makes it quite easy to identify the location and ground condition at the local office to make plan to attack the fires.

We also recommend that the home page of the fire detection and warning system should be established for making the fire information be easily accessed by local staffs and even by other officers.

2. Continuity of Forest Fires in Sumatra

2.1 Information used for the study

We analyzed the NOAA hot spots data taken in August 1997 as mentioned before. We checked the soil types and ground conditions of these places on the TNTmips system. The FAO digital soil map of the world (DSMW) used for this study is a vector type map based on the FAO/UNESCO soil map of the world, original scale 1:5,000,000.

The study area is around the Jambi province, central Sumatra and Landsat TM images were used to check the ground condition although the image were taken about several years ago.

2.2 Results

The result shows that there were 2,187 hot spots observed in August and most of them were not continued for more than two days. Fifty-six pixels of them were continuously shown for more than two days (Fig. 3). About 60% (33)of the continuous fire were occurred on the Dystric Histsols as shown on the table 1 although the ratio of the soil types in Sumatra is less than 20%.

Twenty-two of them were found near plantation forest (Oil Palm forest), eleven of them were at shifting cultivation area and six of them were next to forest road and the rest were not out of the Landsat images used (Table 2).

2.3 Discussions

These results show that human activities are closely related to the severe fire. Number of the continuous fires around big plantation

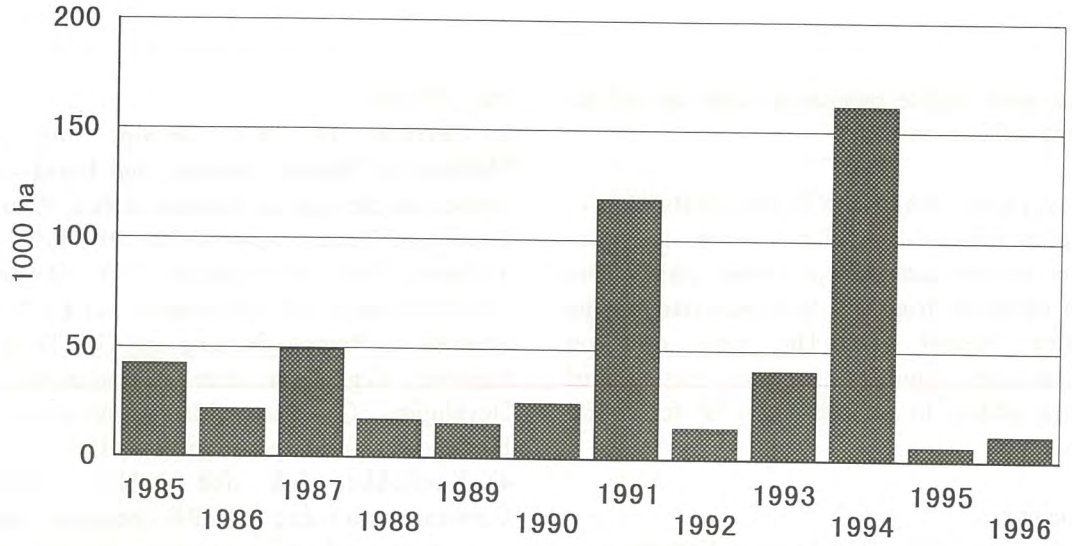


Figure 1. Forest Fire in Indonesia

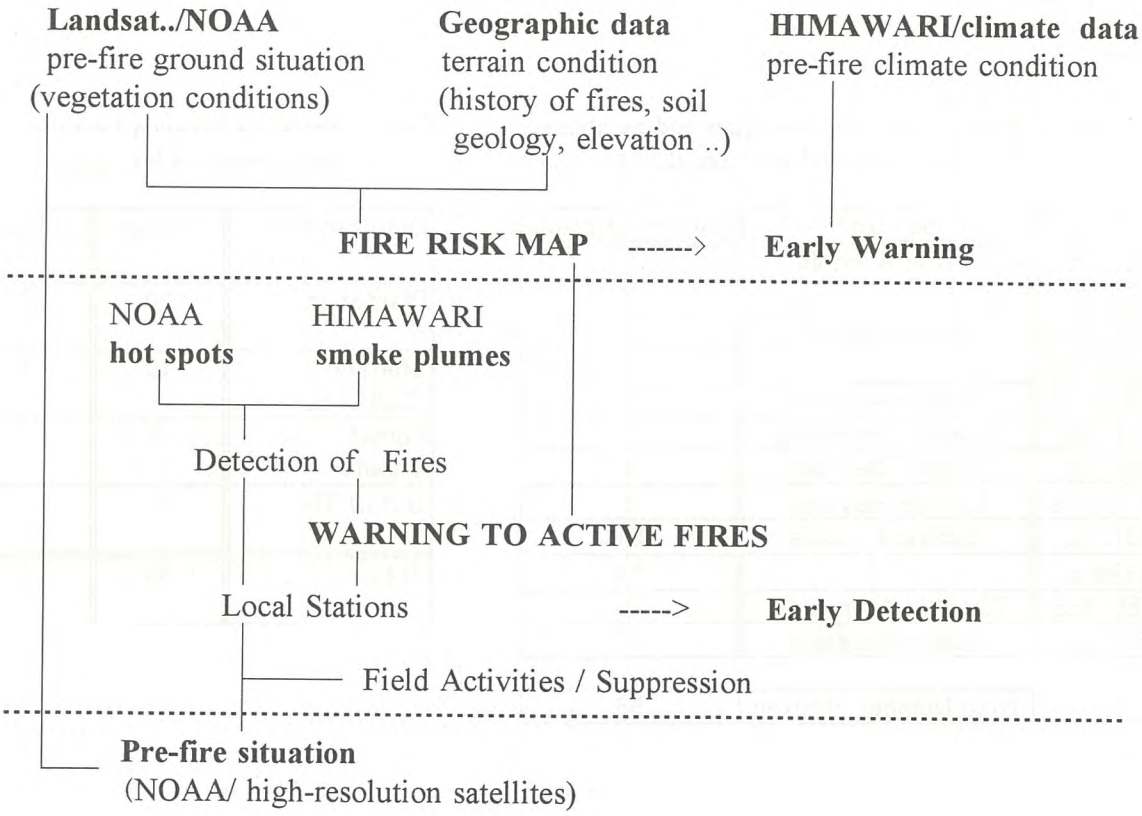


Figure 2. Early Warning / Detection System of Forest Fire

The concept of the developed system is shown. The early detection system depends on the early warning system which is built up by the information based on terrain conditions (soil, elevation, slope direction, slope angle, etc.) and phenological aspects and drought stress to the vegetation which will be obtained from the monitoring using satellite data.

areas were double comparing with that of the sifting cultivation areas.

Forest plantations on the Dystric Histsols have been established for oil palm trees in recent years in that area. Huge smoke plumes are also observed from the fires occurred on the Dystric Histsol soil. The early detection systems are requested to give the risk of smoke adding to the possibility of forest fire expansion.

References

1) Cruzen, P.J., Heid,L.E., Krasnec,J.P., Pollock, W.H. and Seiler,W.(1979) Biomass burning as a source of atmospheric gases CO, H, N2O, NO, CH3Cl and COS, Nature 282:253-256

2) Ehrlich, D., E.F.Lambin, and J-P Malingreau, Biomass burning and broad-scale land-cover changes in Western Africa, Remote Sensing of Environment, 61:201-209, 1997

3)Flasse, S.P., P. Ceccato, I.D. Downey, J.B.Williams, P. Navarro and M.A. Raimadoya, Remote Sensing and GIS Tools to Support Vegetation Fire Management in Developing Countries, 13th Conference on Fire and Forest Meteorology, 1-8, 1996

4) Kasischke, E.S and N.H.F. French, Constraints on using AVHRR composite index imagery to study patterns of vegetation cover in boreal forest, INt,J, Remote Sensing, 1997, Vol.18, No. 11, 2403 - 2426

Table 1. Relation between soil types and number of hot spots continued for more than two days

FAO Soil	Soil Unit	Number of pixels
Af55-3b	Ferric Acrisols	2
Af57-2a		4
Ao104-2/3c	Orthic Acrisols	1
Ao82-2/3b		5
Ap25-2/3a	Plinthic Acrisols	1
Fx32-2ab	Xanthic Ferralsols	1
Gh20-3a	Humic Gleysols	4
Jd12-2/3a	Dystric Fluvisols	3
Od19-a	Dystric Histsols	21
Od20-a		12
Qc59-1ab	Cambic Arenosols	1
Th17-2h	Humic Andosols	1
Total Number of pixels		56

Table 2 Relations between land use and number of hot spots

Duratoin days	2 Days	3 Days
Plantation	20	2
Shifting Cultivation	10	1
Forest Road	6	
Out of TM	17	
Total	53	3

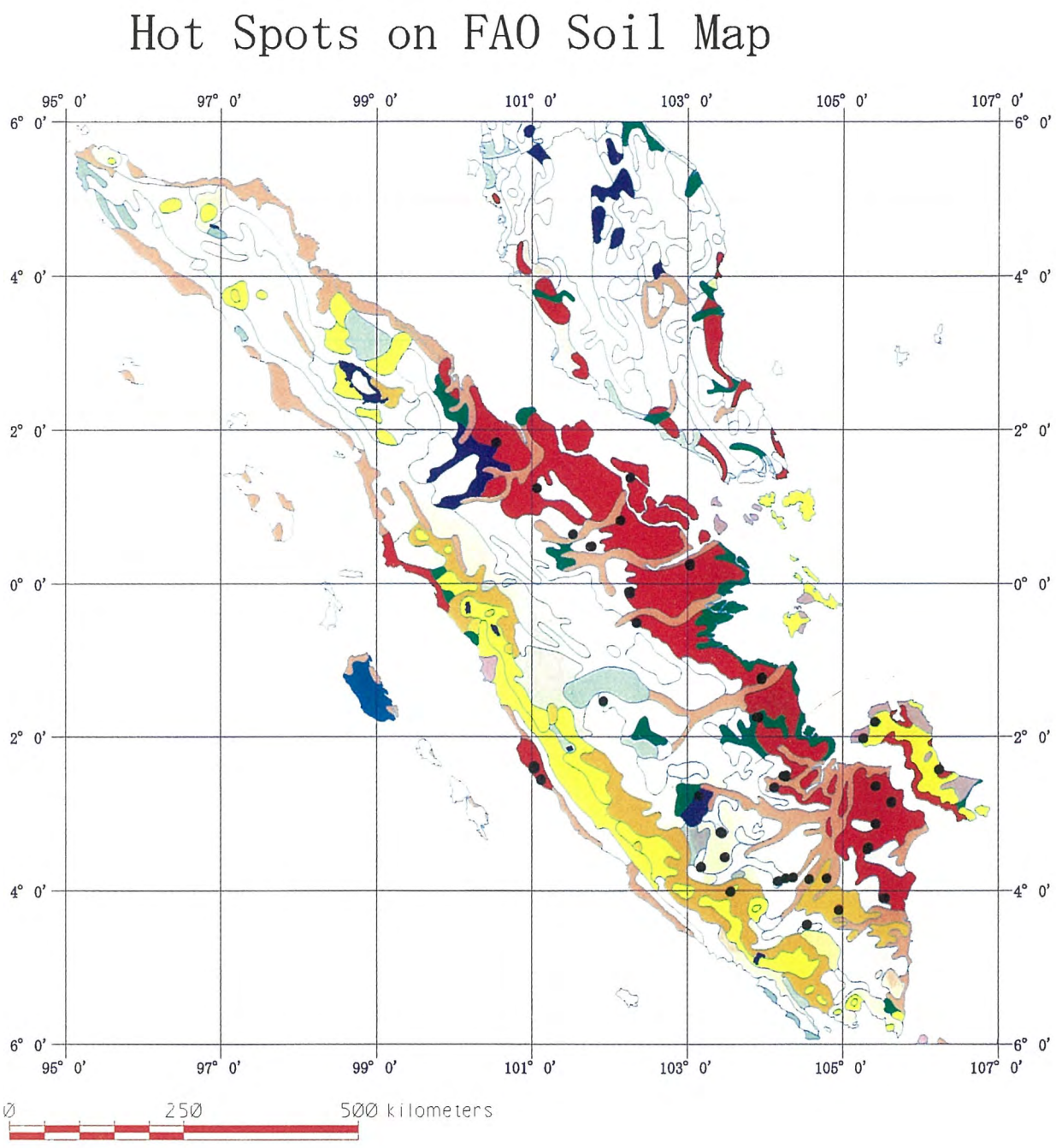


Figure 3. Hot Spots detected more than two continuous days in August 1997 by NOAA on the FAO Digital Soil Map

The Effect of Indonesian Forest Fire on Local Tropospheric Aerosol Optical Thickness by Using NOAA AVHRR data

Jianfei Ru[1], Mitsuo Minomura[1], Hiroaki Kuze[1] and Nobuo Takeuchi[1]
Akiko Higurashi[2] and Teruyuki Nakajima[2]
[1]Center for Environmental Remote Sensing (CEReS),
Chiba University, 1-33, Yayoi-cho, Inage-ku, Chiba, 263-8522 Japan
[2]Center for Climate System Research, University of Tokyo
4-6-1 Komaba, Meguro-Ku, Tokyo, 153, Japan
jru@rsirc.cr.chiba-u.ac.jp
January 22, 1998

1. Introduction

Aerosol particles affect the climate directly by interacting with solar and terrestrial radiation and indirectly by their effects on cloud microphysics, albedo, and precipitation. Biomass burning is a major source of not only trace gas emission into the troposphere but also organic hygroscopic particles. These smoke particles exacerbate the local ground visibility and give rise to the later increase of aerosol amount with smaller geometric radius during a relatively long period.

The Amazon basin atmospheric situation in Brazil had been noticed by many scientists and various kinds of researches were done on the effect of dry-season biomass burning. B.N. Holben and co-workers(1996) investigated the aerosol concentration and properties influenced by the biomass burning and their results showed the temporal and spatial variation of these parameters from 1992 through 1994.

The recent Indonesian forest fire started from August 1997 and lasted several months. The burning gave the local atmospheric conditions serious influences and affected the ecosystems. In order to find its effects on local tropospheric aerosol concentrations and related optical properties we have analyzed the NOAA AVHRR data of channel 1, 2 and 4. Color composed images are synthesized by red, green and blue to each channel to distinguish the smoke area, i.e. the smoke can be detected as yellow color while the cloud is colored as white or blue white. A retrieval algorithm has been established based on Mie theory calculation and the radiative transfer code (MODTRAN 3). With regard to the biomass burning aerosols the refractive index and aerosol size distribution have been taken from the previous works of Y.J. Kaufman, et al (1997). The NOAA AVHRR data on two separate days were obtained from the receiver station in Indonesia.

2. Algorithm description

The algorithm is composed of 3 parts. One is a computing program based on Mie theory. This is used to determine the particle scattering characters such as phase function, extinction and scattering factor, size distribution and asymmetry factor. The second one is MODTRAN3 software for the radiation transfer including the multi-scattering effect. The input parameters are the atmospheric model with user defined aerosol model,, wavelength integrating range, climate information such as the ground visibility, wind velocity and surface albedo. The last one is the smoke discrimination program according to the method mentioned above.

Before using the channel 1 and 2 data of NOAA AVHRR, the calibration of each pixel is necessary. In this paper we employ the following equation for the calibration

$$L_{pix} = (S \cdot DN + I)\frac{F}{100\pi \cdot W} \quad , \tag{1}$$

where L_{pix} is the pixel radiance, DN is the original digital number, S Slope, I Intercept, F integrated solar spectral irradiance and W equivalent width of the spectral response function. The value of the last four parameters are taken from NOAA calibration bulletin. For simplicity, only the atmosphere over the ocean part is considered because of the ease of surface albedo determination and its homogeneity. Equation (2) is used for the derivation of real sea surface albedo ρ .

$$\rho = \rho_0 \frac{L_{pix} - L_0}{L_{tot} - L_0} \quad , \tag{2}$$

where ρ_0 is the surface albedo assumed in MODTRAN3 simulation, L_{tot} the total radiance, and L_0 the path radiance calculated with the dark surface assumption (albedo=0). L_{pix} is the radiance of the pixel under consideration, given by eq. (1). Then, according to the radiative transfer equation, the direct reflected radiance from the surface is given by

$$L_{GD} = \frac{E_{ext}}{\pi} TT' \rho \cdot \cos\theta_Z \quad , \tag{3}$$

where E_{ext} is the solar irrandiance, T the vertical transmittance, T' the slant transmittance, θ_Z the solar zenith angle. From eq. (3), the aerosol optical thickness can be derived as

$$\tau = -\frac{1}{1+\sec\theta_Z} \ln\left(\frac{\pi \cdot L_{GD}}{E_{ext} \cdot \rho \cdot \cos\theta_Z}\right) \quad , \tag{4}$$

where $L_{GD} = L_{pix} - L_0$. The spectral optical thickness is used to compute the Ångström exponent which is defined as

$$\alpha = -\frac{\ln(\tau_1 / \tau_2)}{\ln(\lambda_1 / \lambda_2)} \quad . \tag{5}$$

3. Satellite data and Aerosol models

The satellite data involved in this research are shown in Figs. 1 and 2. The same area delineated by square boxes in Figs. 1 and 2 is selected over the sea surface. In Fig. 1, there is little smoke since it corresponds to the beginning of burning. On the contrary, in Fig. 2, the smoke is apparent and it covers large area over islands and sea.



Figure 1. Color composed AVHRR data of NOAA-14 taken at GMT 7:00, 1997/8/3 (before the fire).



Figure 2. Color composed AVHRR data of NOAA-14 taken at GMT 7:00, 1997/9/1 (during the fire).

For the data on 1997/8/3, a maritime aerosol model is assumed for computing the radiance in eq. (2) using MODTRAN 3. A user defined aerosol model described below is used for the data on 1997/9/1. Table 1 lists the relevant parameters employed in the calculation.

Table 1. The parameters needed in MODTRAN 3 calculation for 1997/8/3 and 1997/9/1

	Atmospheric model	Aerosol model	Albedo	Surface visibility	Solar zenith angle	Wind velocity	Season
97/8/3	Tropical	Maritime	0.07	20km	40	8 m/s	Spring-Summer
97/9/1	Tropical	Maritime + User defined	0.07	10km	35	5 m/s	Spring-Summer

In the present scheme, a biomass aerosol model is incorporated as the user-defined model. For the maritime and biomass burning aerosol model, the logarithmic size distribution defined by eq. (6) and the parameters listed in Table 2 are used to

Table 2. The related parameters used in the above calculation

Aerosol	r_g μm	σ μm	Refractive index	N_0
Biomass burning 1	0.14	0.22	1.43-0.0035i	26632.4
Maritime	0.0039 0.133 0.29	0.657 0.21 0.396	1.388-0.0003i	133 66.6 3.06
Biomass burning 2	0.14	0.22	1.43-0.0035i	13316.2

obtain the size distribution shown in Fig. 3.

$$\frac{dN(r)}{d\log r} = \frac{N_0}{\sqrt{2\pi}\sigma}\exp\left[-\frac{(\log r - \log r_g)^2}{2\sigma^2}\right] , \quad (6)$$

Here N_0 is the number of particles per cross section of the atmospheric column (cm^{-2}), σ the standard deviation of the logarithm of the radius, r the radius, r_g the modal radius of the number distribution.

In the simulation with MODTRAN 3 code, a modification of source code has to be introduced concerning the characteristics of biomass burning aerosol model. The Mie computation code is used for this purpose. The asymmetry factors associated with aerosol scattering phase function are calculated at several wavelengths for the biomass burning aerosol model. The result is shown in Fig. 4. In addition, the wavelength dependence factor of extinction coefficients is calculated with respect to the value at 550nm. This dependence varies according to the aerosol models and relative humidity (Fig. 5). During burning, the vertical profiles of aerosol concentration are modified to be homogeneous in the ground layer between 1 to 3km .

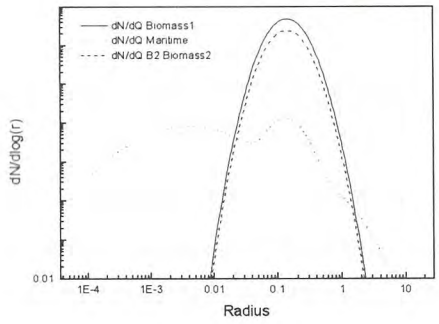


Figure 3. The aerosol size distribution of biomass burning aerosol model and maritime aerosol model.

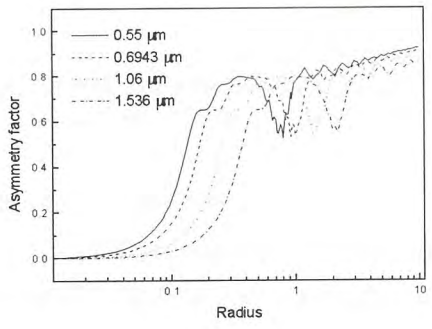


Figure 4. The asymmetry factors at 0.55, 0.69, 1.06 and 1.54 μm.

4. Results and Discussions

With the above algorithm the spatial distribution of aerosol optical thickness is retrieved for both 1997/8/3 and 1997/9/1 data. The results for channel 1 and 2 of AVHRR over the selected sea surface area are illustrated in Fig. 7. The statistical results over selected pixels are summarized in Tables 3 and 4. As can be seen from Fig. 6, the wavelength dependence of the average aerosol optical thickness changes between the

Table 3. The statistics of retrieved optical thickness results for ch.1

	Averaged Optical Thickness	Standard deviation	Maxium Value	Minium Value	Covered Area
1997/8/3	0.33	0.003	0.34	0.31	111x56 km^2
1997/9/1	0.40	0.002	0.40	0.38	111x56 km^2

Table 4. The statistics of retrieved optical thickness results at ch.2

	Averaged Optical Thickness	Standard deviation	Maxium Value	Minium Value	Covered Area
1997/8/3	0.198	0.008	0.22	0.15	111x56 km^2
1997/9/1	0.23	0.006	0.24	0.18	111x56 km^2

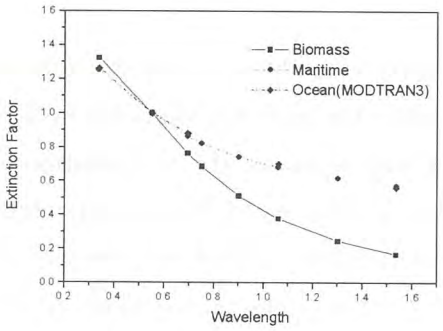


Figure 5. The wavelength dependency comparisons among different aerosol models.

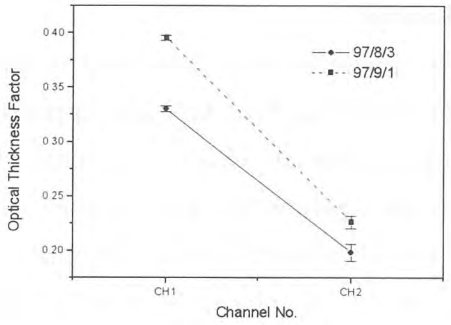


Figure 6. The wavelength dependence of optical thickness before & during fire.

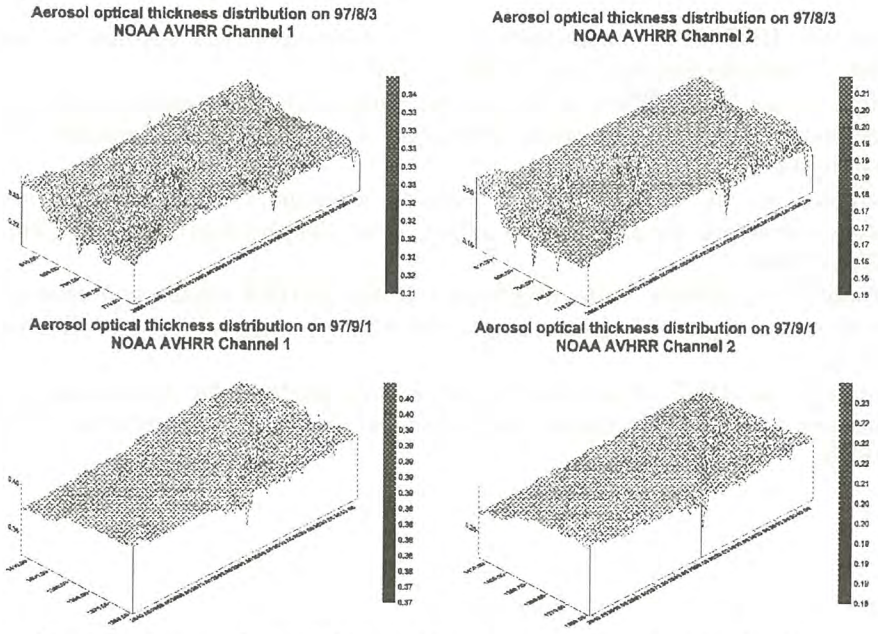


Figure 7. The aerosol optical thickness distributions derived from the algorithm

data before and during the fire. This indicates the change of aerosol characteristics due to the burning. The distributions of Ångström exponents are shown in Fig. 8. This figure implies the increase of smaller aerosol particles after the burning.

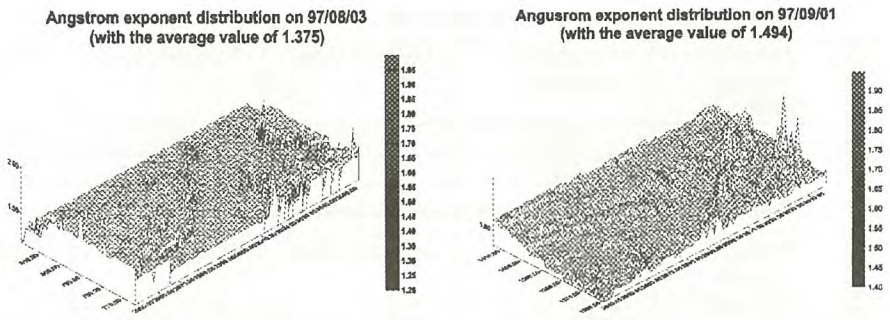


Figure 8 The Ångström wavelength exponents distributions.

5. Conclusions

In this paper we have described an algorithm for retrieving the atmospheric aerosol characters from satellite data and applied it to the processing of Indonesian forest fire. Assuming appropriate characteristics for biomass burning aerosols, the distribution of aerosol concentration over a certain sea surface area has been derived. The results show that the fire influenced both the amount of local aerosol distribution and the aerosol size distribution. We are planning to include the ground data to improve the accuracy of the satellite measurement.

References

1. Rudolf Richter, 1990: *A fast atmospheric correction algorithm applied to Landsat TM images*, Int. J. Remote Sensing, Vol. 11, No. 1, 159-166.
2. B.N. Holben, et al. 1996: *Effect of dry-season biomass burning on Amazon basin aerosol concentrations and optical properties, 1992-1994*. J. of Geophysical Research, Vol. 101, No. D14, p19465-19481.
3. Y.J. Kaufman, et al. 1997: *Passive remote sensing of tropospheric aerosol and atmospheric correction for the aerosol effect*, J. of Geophysical Research, Vol. 102, No. D14, p16815-16830.
4. Y.J. Kaufman, B.N. Holben, 1993: *Calibration of the AVHRR visible and near-IR bands by atmospheric scattering, ocean glint and desert reflection*, Int. J. Remote Sensing, Vol. 14, No. 1, p21-52.
5. W. A. Abdou, et al. 1997: *A modified linear-mixing method for calculating atmospheric path radiances of aerosol mixtures*, Journal of Geophysical Research, Vol. 102, No. D14, p16883-16888.

Climate-relevant Aerosol Parameters of South-East-Asian Forest Fire Haze

Wolfgang von Hoyningen-Huene, Universidade de Evora
Torsten Schmidt, Inst. f. Meteorologie, Universität Leipzig
Chan Ah Kee, Malaysian Meteorological Service

Abstract

A measurement campaign n in Malaysia with combined measurements of spectral aerosol optical thickness, sky brightness and down-welling fluxes have been carried out in the 1997 forest fire season in South-East Asia. The main measured parameters have been used for the derivation of the main climate-relevant aerosol parameters by the CIRATRA approach (Coupled Inversion Radiation Transfer). With this approach phase functions, real part of refractive index and single scattering albedo of the haze has been determined.

1. Introduction

Biomass burning in form of large forest fires is beside the other ecological consequences one of the global sources of atmospheric pollution. Especially, biomass burning is an appreciable aerosol source, the 3. strongest source after oceanic and mineral aerosols. Up to 30 % of this kind of pollution is assumed to be of man made origin, (*Hidy \& Wolf, 1995*). Generally sources of such dimensions have different impacts on climate by :
a) changes in the regional radiation balance by the increased turbidity,
b) changes in the cloud formation by the increase of the CCN within the haze.

The present aerosol models for radiative transfer calculation as well for climate modeling (e.g. *WCP-55, 1983*, *d'Almeida et al, 1991*, GADS (Global Aerosol Data Set), c.f. *Koepke et al., 1997*) as for solving remote sensing tasks do not include any parameters for this specific type of aerosols, produced by biomass burning processes. One can only refer to common pollution models, which do not consider the special conditions of the forest fire haze. Therefore in remote sensing approaches a dominating soot component with an absorption in the uv is assumed, c.f. *Hsu et al., 1996, Herman et al., 1997, Kaufman et al., 1992*. Here the logarithmic ratio between the observed radiance ratio of two uv wavelength and the radiance ratio derived from a model atmosphere is used as an aerosol index using the fact, that the aerosol absorption reduce in the radiance at the top of the atmosphere the contributions as well of the scattered light by the atmosphere as the surface reflectance. Differences resulting from different aerosol size distributions have been neglected.

The climate impact by the forest fire haze, especially the radiative effect is produced by the physico-chemical properties of the pollutants and their radiative properties in the ultraviolet, visible and infrared range of the incident solar radiation. From this point of view one aim of the global climate research activities has to be the determination of the main climate-relevant optical aerosol properties of the forest fire haze, used in climate research and satellite remote sensing: spectral optical thickness $\delta_A(\lambda)$, phase function $p_A(\theta)$ and single scattering albedo $\omega_A(\lambda)$ because the climatic effect of the biomass burning is not only an absorption effect and the scattering part changes the planetary albedo too. Therefore the situation of such large forest fires like in South-East Asia in autumn 1997 have been an opportunity to study this effects and complete the knowledge about the characteristic parameters of forest fires for the use in radiative transfer calculations and to estimate the effect on the radiation field.

For this purpose measurements in the South-East-Asian haze region in kind of a task force has been prepared. In a very short time with the finacial support of the German Ministry of Education and Research (BMBF) and the cooperation of the Malaysian Meteorological Service a short term measurement campaign in Malaysia has been installed, to obtain the main climate-relevant radiative aerosol parameters by a closure approach of different radiation measurements.

The approach in this campaign and first results of the radiative aerosol characteristics will be presented in this paper, to give base for the consideration of haze effects in radiative transfer on a experimental validated base.

2. Measurement Campaign and Haze Situation

The measurement campaign took place from 11.-24. October 1997. The site was at the meteorological station Subang Airport of the Malaysian Meteorological service (3.117 N, 101.6 E) near Kuala Lumpur in Malaysia. The weather situation has been determined by the inter monsoon time, with south-easterly winds, so that the situation there in Malaysia has been affected by forest fire haze from long range transports. Back trajectory calculations let identify fires in southern Kalimantan as responsible for the haze in this time.. The instrumentation used consists of:

- different ground based radoimeters for the determination of the data, necessary for the determination of the main climate-relevant optical aerosol parameters by the CIRATRA approach (Coupled Inversion RAdiation TRAnsfer), c.f. *Wendisch \& von Hoyningen-Huene, 1994*:
    1. spectral optical thickness δ_A (λ) by the spectral radiometer ASP with 80 calibrated channels between 0.35 and 1,1 µm,
    2. sky brightness in two channels (0.56 and 0.87 µm wavelength) by the sky scan in the almucantar in 24 angular steps between 3 and 180 degree at cloud free conditions, the part between 3 and 15 degree has a higher resolution and is used for the aureole brightness,
    3. integral short-wave down-welling flux measured with a common solarimeter
    4. spectral down-welling flux in 13 spectral channels between 0.365 and 1022 µm with a filter wheel radiometer SPA-1 (Schulz \& Partner),

- filter sampling system with a cyclone inlet for collecting aerosol samples of the sub-micron fraction and a later chemical analysis in cooperation with the Institute of Tropospheric Research Leipzig,
- standard meteorological data from radiosonde and trajectory calculations for the information about haze hight and origin of the haze.

3. Results of the Campaign

Until now the results consist of the determination of optical aerosol parameters of the haze situation in Malaysia able to use in radiative transfer calculations.

The optical data (spectral aerosol optical thickness, normalized sky brightness function and the integral down-welling flux) have been used until now for the determination of the climate relevant optical aerosol parameters with the CIRATRA approach to derive the other climate-relevant aerosol parameters as aerosol phase function and broadband single scattering albedo.

3.1. Aerosol Optical Thickness and Turbidity Parameter

The spectral aerosol optical thickness δ_A (λ) has been determined from the spectral optical thickness δ (λ) of the sun photometer measurements by eliminating the Rayleigh scattering and the contributions of ozone and water vapor.

In all cases of successful measurements slightly curved decreasing spectral slopes with increasing wavelength have been obtained. In the blue and the UV the decrease was smaller than in the red and NIR. Fig. 1 presents the daily averages of the spectral aerosol optical thickness. One can see, that the spectral behavior of the optical thickness is nearly stabile and is characteristic for the haze. Only the intensity of the haze has changed depending on the trajectories, crossing more or less strong source regions of the biomass burning. This curved spectral behaviour with a lower spectral decrease in the blue and uv also contributes to a reduced radiance at the top of atmosphere compared with the common assumption of the validity of the Angström power law in the whole spectral range. This reduction must not be associated only with an aerosol absorption as assumed in the mentioned above satellite retrievals, it has its origin as well in absorption as also in the scattering.

Nevertheless the presented spectra have not an ideal power law $\delta_A(\lambda) = \beta\ \lambda^{-\alpha}$, the Angström turbidity parameters α, the so called size coefficient or spectral slope and β, the turbidity coefficient, which is the aerosol optical thickness at a wavelength of 1 µm, have been determined. Fig. 2 presents the turbidity coefficients during the measurement campaign. Without less exceptions (if the measurements have been disturbed by real clouds) the α-value varies between 0.7 and 0.9 with an average of $\alpha = 0.79 \pm 0.11$ and has been a characteristics of the forest fire haze.

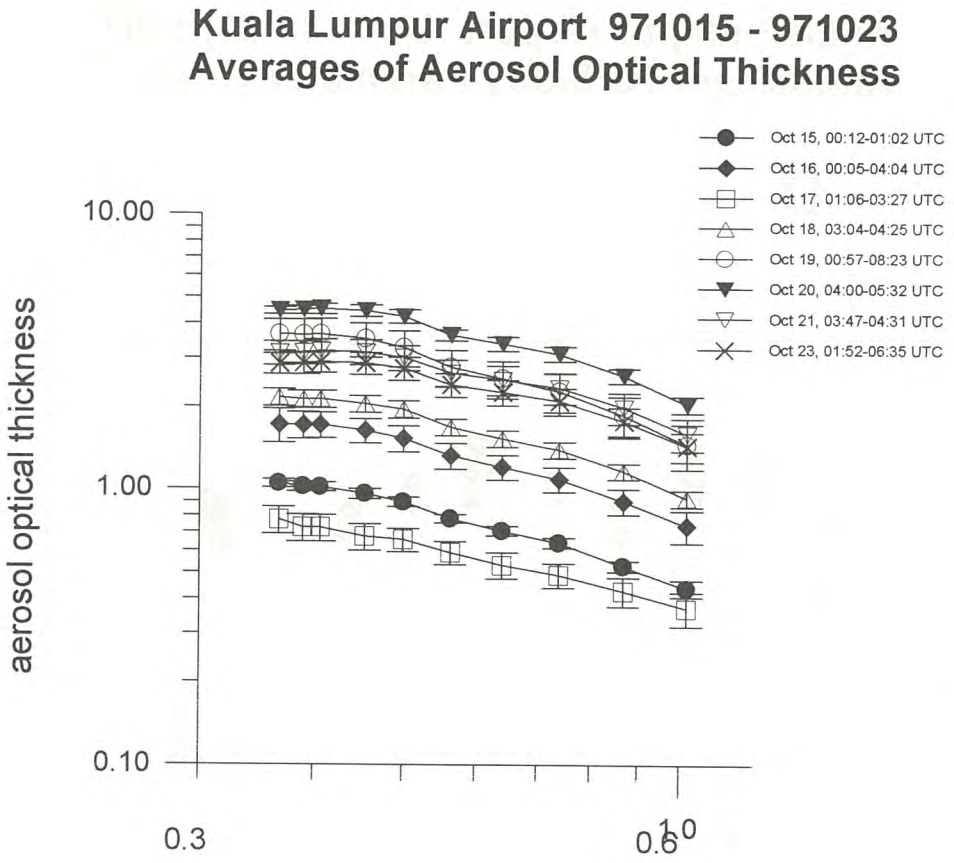


Fig. 1
Spectral aerosol optical thickness of the forest fire haze at Subang Airport (Kuala Lumpur) in October 1997.

The turbidity coefficient β changes from day to day parameter depending on the crossed source region at Kalimatan. Its range is from $0.35 < \beta$ 2.3. At the 24. Oct. even higher values have been measured (4.0), but it was unsure that it is a pure haze effect.

With such haze conditions, comparable with a thin cloud, some difficulties for the measurements have been connected: the contrast between sun disk and sky was so weak, that no automatic sun seeking program can be used. The sun position has to be pointed at first manually and the pointing has been made by an electromechnic parallactic sunfollower. Sometimes the pointing could be made first at sun elevations of $h \geq 20°$ because of missing shaddow for the pointing.

The height of the haze layer has been determined from aircraft pilot observations from Subang airport. The upper level of the haze has been observed between 2 and 2.5 km (6000 - 7500 ft). This layer is responsible for the optical characteristics found in this campaign.

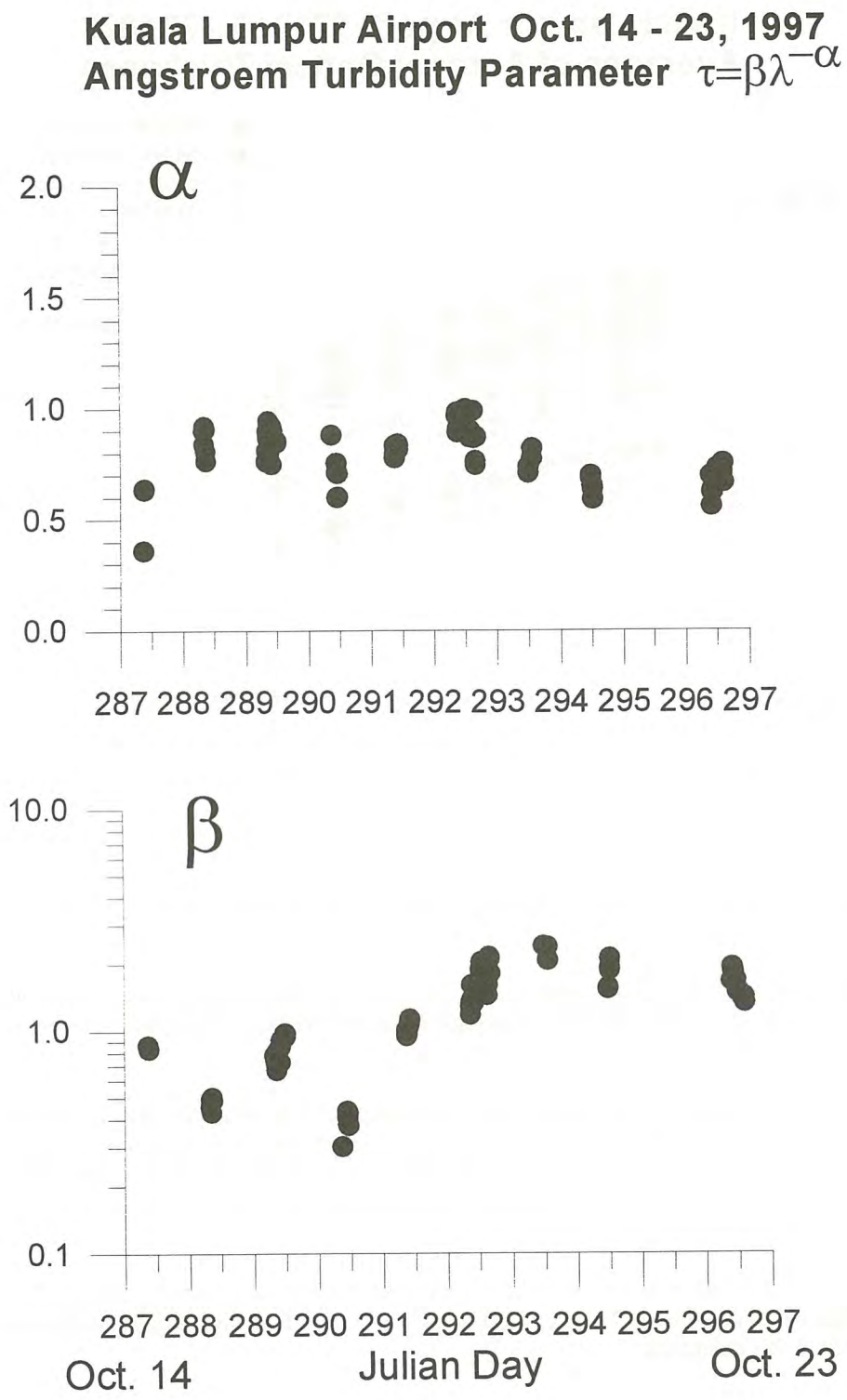


Fig. 2
Angström turbidity parameters for the measurement campaign at Subang Airport (Kuala Lumpur) during the forest fire season in October 1997 in South-East-Asia

3.2. Closures with the Sky Brightness Measurements

While the spectral optical thickness measurements can be made also at partly cloudy sky, if large enough cloud holes are existing, the sky brightness measurements require a totally cloudfree sky for the azimutal scan of the sky in the almucantar plane (same elevation as the sun). From the measurements the normalized sky brightness function is determined:

$$p^{sky}(\theta) = L(\theta) \; / \; \int_0^{\pi} \pi \, L(\theta) \sin\theta \; d\theta$$

This normalization gives a stabile angular light scattering characteristics of the atmosphere (aerosol scattering, Rayleigh scattering inclusive multiple scattering) independent of the illumination and the sun elevation. If this measurements are mad in spectral channels, where the Rayleigh scattering is weak (NIR), almost the aerosol characteristics can be seen. This normalized sky brightness function together with the spectral aerosol optical thickness are input data for the CIRATRA approach.

The normalized sky brightness function gives for constant optical conditions for all measurements the same function, if the normalization conditions can be fulfilled (integration between 0 and π. This requires an extrapolation of the measured radiance data from the minimal scattering angle measured (around 3°) to 0° and from the measured maximum scattering angle (180 - 2 h_o, h_o - solar elevation) to 180°. The problems occur with higher solar elevations ($h_o \geq 30°$), if the largest measured scattering angle is under 120° - the minimum of the aerosol phase function and the increase of the phase function to scattering angles toward 180° cannot be fitted from the measured data. Therefore the determination of the normalized sky brightness function is restricted to measurements at sun elevations $h_o \leq 30°$. The normalized sky brightness functions are presented together with the results of the CIRATRA approach in fig. 3.

The application of the CIRATRA approach allows to determine the main optical climate-relevant aerosol parameters: aerosol phase function, columnar size distribution, real part of the refractive index. In a first step all calculations have been made without an assumption for the aerosol absorption, because the normalization of the sky brightness function removes the single scattering albedo. The results of the approach are presented in fig. 3.

For all measurements Mie theory could be applied. This is an indicator for the sphericity of the particles. This may be caused by either dominant small particle, where this difference plays no role or by the high humidity, which leads to a water deposition on the haze particles.

The obtained real parts of the refractive index m vary between m = 1.37 and 1.55 with an average of m = 1.45. The higher values occur, if the relative humidity is decreased (e.g. at afternoon measurements). In the morning measurements the high relative humidity decrease the refractive index. This refractive index is much lower than expected, because the main assumption was a high soot content within the forest fire haze. This lower refractive index lead to the conclusion, that the haze over Malaysia, comes from relative complete burning processes and contains less soot than expected.

The phase functions for the most cases of the combined measurements are similar, except one situation in the afternoon of the 10. Oct. 97. This was the only more 'dry' situation. In all other cases the relative humidity was above 80 %. The asymmetry parameters, derived from the aerosol phase functions have an average of g = 0.69 ± 0.02.

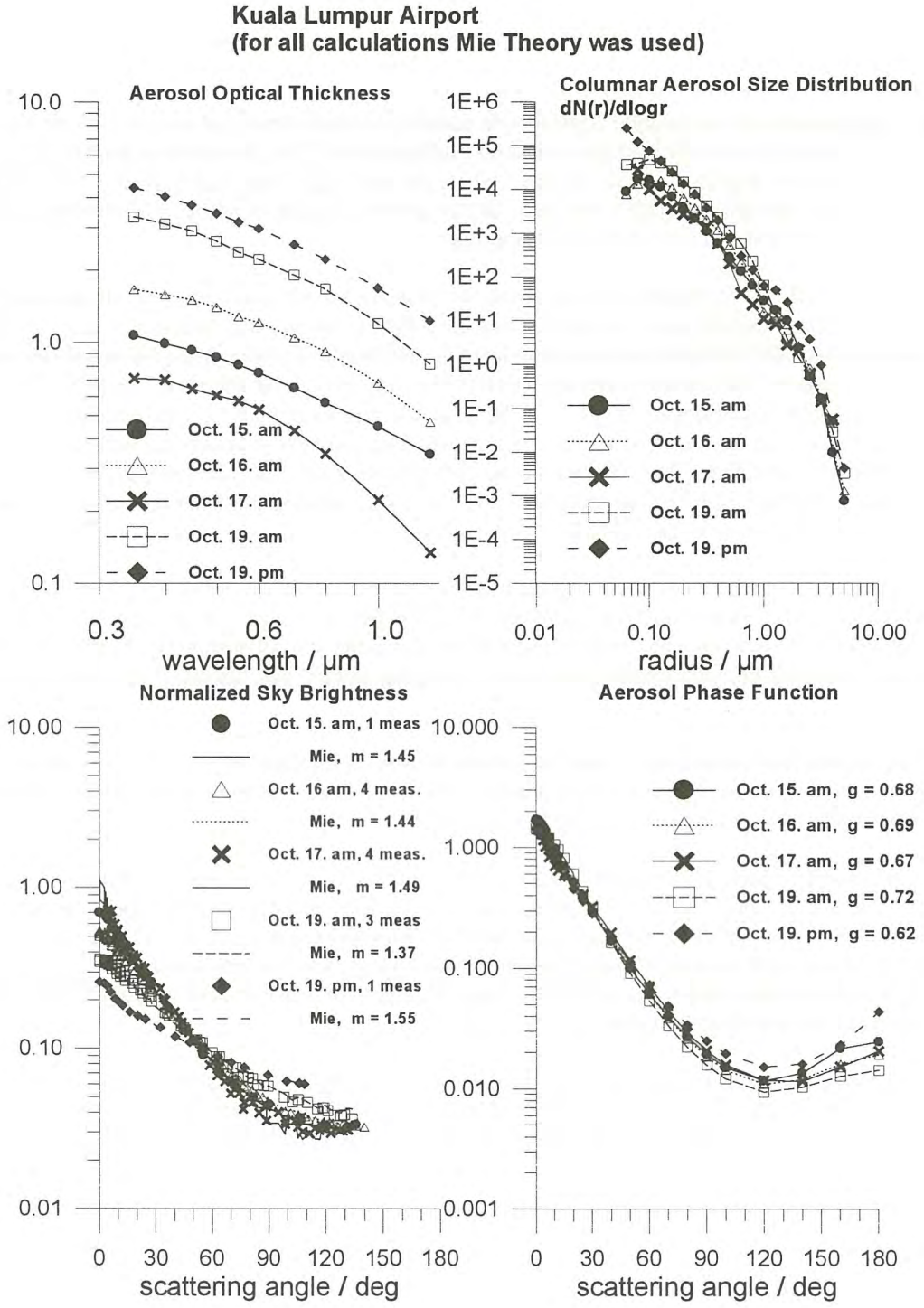


Fig. 3
Results of the combined measurements of spectral aerosol optical thickness (above, left) and sky brightness (below, left) for the climate-relevant aerosol parameters, columnar size distribution (above, right) and phase function (below, right)

3.3. Single Scattering Albedo

In a second step the single scattering albedo will be introduced again by the flux correlation. Here the down-welling fluxes between measurements and calculations have been used for the determination of the single scattering albedo with the flux correlation method, c.f. *von Hoyningen-Huene et al., 1996, von Hoyningen-Huene et al. 1998*. The calculations of the down-welling fluxes for the measurement times use the obtained results of the CIRATRA approach, which has been made first without consideration of the aerosol absorption.

In the broadband flux calculations water vapor is considered with ist spectral optical thickness obtained with HITRAN 92 on the base of the US tropical atmosphere. the HITRAN 92 results have been scaled with the measured water vapor optical thickness in the channel of 0.94 µm. These calculated broad-band fluxes are permanent higher than the measured ones, because they do not contain the aerosol absorption. The results of this extended CIRATRA approach for the data of the forest fire haze is presented in fig. 4.

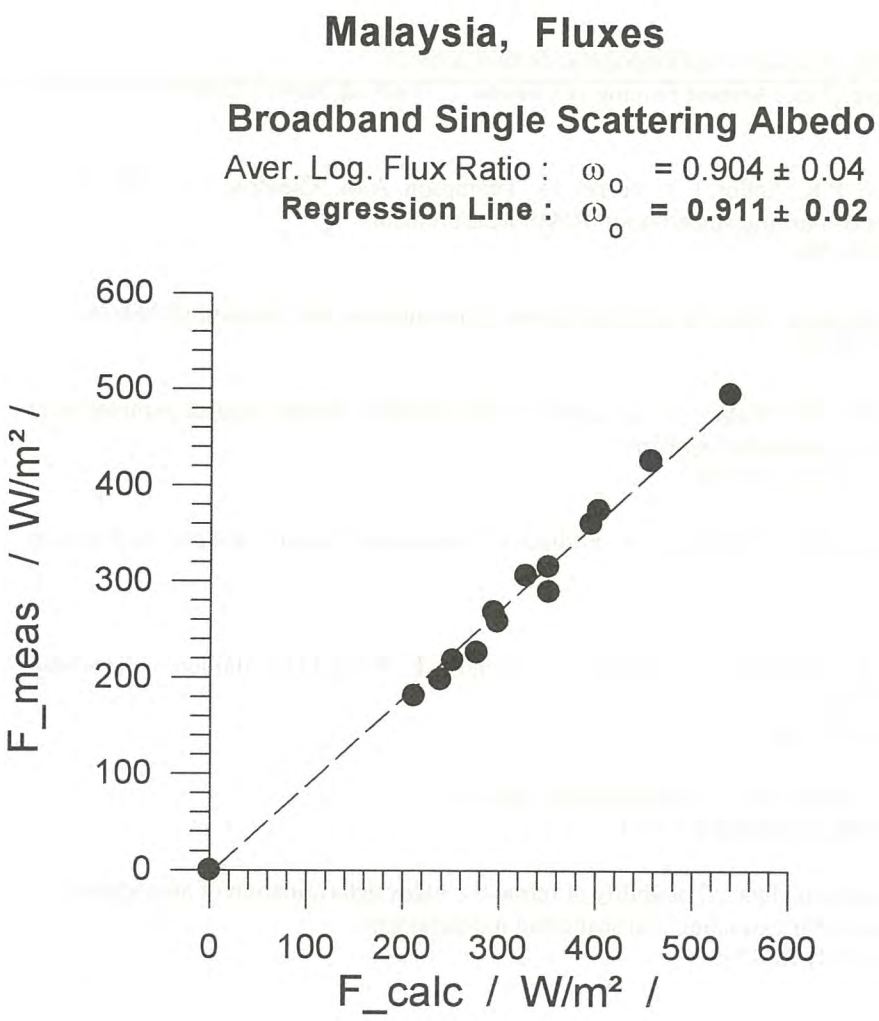


Fig. 4
Flux correlation between measured and calculated down-welling fluxes with the resulting broad-band single scattering albedo of the haze

Also this result is conform with the results to the real part of the refractive index. The obtained broad-band single scattering albedo of the haze is with $\omega_o = 0.90 \ldots 0.91$ higher tan expected, if a high soot content should be characteristic.

4. Conclusions

The measurement campaign gave radiation data for the forest fire haze in the autumn 1997 and are a contribution to the development of a radiative model for the forest fire haze. The spectral optical thickness gave a consistent characteristics over the whole measurement campaign, also the obtained phase functions with the CIRATRA approach. From these data it seems to be, that the aerosol absorption in the haze was lower than expected, the real part of the refractive index and the single scattering albedo obtained are indications for this.

References

d'Almeida, G.A., P. Koepke and E.P. Shettle: Atmospheric aerosol. Global climatology and radiative characteristics.
Deepak Publ, Hampton 1991.

Deepak, A. and H. Gerber: Report of the expert meeting on aerosols and their climatic effects.
WMO-Pub. WCP-55, 1983

Hidy, G.M., Wolf, M.: Projection of trends in anthropogenic aerosol sources.
In: R.J. Charlson, J. Heintzenberg (Eds.) Aerosol Forcing of Climate. J. Wiley \& Sons, Chichester 1995, pp 171-182

Hsu, N.C., Herman, J.R., Bhartia, P.K., Seftor, C.J., Torres, O., Thompson, A.M., Gleason, J.F., Eck, T.F., Holben, B.N.: Detection of biomass burning smoke from TOMS measurements.
Geophys. Res. Lett. 23 (1996) 745-748.

Kaufman, Y.J., et al.: Biomass Burning Airborne and Spaceborne Experiment in the Amazon (BASE-A).
Geophys. Res. 97 (1992) 14581-14599.

von Hoyningen-Huene, W., Stettler, M., Weller, M.: Determination of climate-relevant aerosol parameters in the vicinity of an industrial region in eastern Germany.
Meteorologist Zeitschrift N.F. 5 (1996) 269-278.

von Hoyningen-Huene, W., Wenzel, K., Schienbein. S.: Radiative Properties of Desert Dust and its Effect on Radiative Balance.
J. Aerosol Sci. (submitted 1998)

Herman, J.R., Bhartia, P.K., Torres, O., Hsu, N.C., Seftor, C.J., Celarir, E.: Global Distribution of absorbing aerosols from Nimbus-7/TOMS data.
J Geophys. Res. 102 (1997) 16911-16921.

Koepke, P., Hess, M., Schult, I., Shettle, E.P.: Global Aerosol Data Set.
Theoretical and Apllied Climatology (submitted 1997)

Wendisch, M. and W. von Hoyningen-Huene: Possibility of refractive index determination of atmospheric aerosol particles by ground based solar extinction and scattering measurements.
Atmospheric Environment 28 (1994) 785-795.

VII. Ground-based and Airborne Monitoring

Lidar Measurements of Stratospheric Aerosol over Hefei, China during 1991-1996

Huanling Hu, Jun Zhou, Yonghua Wu
Anhui Institute of Optics and Fine Mechanics
P.O.Box 1125, Hefei, Anhui 230031, China
Tel. +86-551-5591012 Fax +86-551-5591572
Email: hlhu@aiofm.hfcas.ac.cn

Abstract -- The violent eruption of Philippine volcano Pinatubo in mid June of 1991 caused a serious perturbation on the stratospheric aerosols for a long period. In the paper, we report L625 lidar observational results in the period of 1991-1996, including evolution of volcano Pinatubo cloud. The time variation and vertical distribution of the volcanic cloud height, thickness, peak scattering ratio, and integrated backscattering coefficients will be analyzed. L625 lidar measurement data of stratospheric aerosol reveal the characteristics of background period before the volcanic eruption, the evolution of the Pinatubo volcanic cloud, and present new background level.

INTRODUCTION

Variation of stratospheric aerosol affects atmospheric minor constituents and climate through changes in the radiation field as well as by dynamic and chemical processes. In order to estimate the impact quantitatively, it is very important to observe stratospheric aerosol vertical distributions and their time variations. Lidar is a very powerful remote sensing technique for monitoring the stratospheric aerosols with a high vertical and temporal resolution. This paper will analyze the variations of the stratospheric aerosol profiles measured by a L625 lidar over Hefei (31.9°N, 117.17°E), China, during 1991-1996.

L625 LIDAR AND MEASUREMENTS

L625 lidar system consists of a double frequency YAG laser (wavelength 532nm), emitting 100mJ per pulse at a repetition rate of 5Hz, a receiving telescope of diameter 625mm, and a photon counting unit. A mechanical chopper can cut the strong-intensity signal before it is amplified by the PMT (EMI9817B). The height resolution is 600m, normally. The whole system, which is controlled by a PC computer, is set on the top floor of a building with a dome ceiling at the suburb of Hefei city.

In order for one PMT to cover the whole signal range of about three orders of magnitude from 6km to 35km or higher, the measurement is divided into two steps. In the first step, an averaged profile, for about 1000 laser shots, of return signal is obtained at relatively low altitude (about 6-25km), when the chopper opens at 6km and a neutral attenuator with transmittance of 5% is inserted in front of the PMT. Thus, the photon arrival rate is small enough to eliminate the pulse-pair error. At the second step, the chopper is adjusted to cut off the return signals from the altitudes below 10km, and the attenuator is taken away, so that the return signal can be recorded from higher altitudes (10-35km). the whole measurement takes about 30 minutes. A 'grand composite' profile spanning the altitude region of interest between 6km and 35km can be formed by matching the above two profiles.

The lidar back-scattering ratio, R(z), is defined as

$$R(z) = [B_a(z) + B_m(z)] / B_m(z) = 1 + B_a(z) / B_m(z) \quad (1)$$

where $B_a(z)$, $B_m(z)$ are aerosol and molecular back scattering functions, respectively. The $B_m(z)$ can be calculated from radiosounde data or Elterman model. The backscattering ratio R(z) is calculated by evaluating

$$R(z) = k\, N_s(z)\, Z^2 / B_m(z) / Q^2(z) \quad (2)$$

where $N_s(z)$ is photon number of return signal, $Q^2(z)$ is the two-way atmospheric transmittance, and k is a system constant determined by normalizing the right-hand side of Eq. (2) to an expected minimum value (R_{min}=1.01) of R over a specified altitude range (28-32km). In calculation of the transmittance $Q^2(z)$, molecular extinction is from radiosonde or model, and aerosol extinction is calculated directly from the aerosol backscattering function by using extinction-backscattering ratio values[1] of 22, 40, 43 during the period of Pinatubo volcanic cloud (June of 1991 - June of 1994), and 34, 52, 58 during the period with normal situation, over the height ranges of 15-20, 20-25, and 25-30 km, respectively. The Eq.(2) is solved by using updated value of aerosol extinction for iterations. More than 400 profiles (nights) were obtained during 1991-1996.

VARIATION OF STRATOSPHERIC AEROSOLS DURING 1991-1996

The violent eruption of Philippine volcano Pinatubo in mid June of 1991 caused a serious perturbation on the stratospheric aerosols for a long period. L625 lidar was used at Hefei for measurement of stratospheric aerosol profiles in the period of 1991-1996, including evolution of volcano Pinatubo cloud.

Fig. 1 shows some typical profiles of stratospheric aerosols. The six years from 1991 to 1996 may be divided into three periods: (i) the background period from January to mid-June , 1991 before the eruption, (ii) the volcanic cloud evolution period from June of 1991 to mid-1994, and (iii) the present new background period since mid-1994. A profile taken on May 15, 1991 represents the background prior to the Pinatubo eruption, whose peak scattering ratio, R_{max}, is 1.21 only at 18.3 km altitude. The first increase of the aerosols from Pinatubo eruption was observed at 15.9 km with R_{max} of 4.54 at Hefei on June 27, 1991, just 12 days later after the eruption. On July 19, about a month after the eruption, a strong scattering layer was observed around 21 km. These results are similar with the data observed by MRI lidar system[2] at Tsukuba, Japan. On August 8, the value of R_{max} increased up to 37.62 at 22.5 km. From August 1991, the upper layer grew day by day over Hefei and merged into a broad layer together with the lower layer. Until the end of August of 1991 a double-layered structure could be observed, and since early September same year it was replaced by a single layer with a peak near 22 km. A profile taken on October 3, 1996 represents the nature in new background period, whose value of R_{max} is 1.27 at 17.6 km.

Fig. 2 shows the evolution of the maximum scattering ratio over Hefei. The values of R_{max} initially showed large fluctuation, reflecting inhomogeneity of the cloud distribution. It was confirmed by SAGE II measurements[3] from June to August of 1991 that the major part of the cloud was confined to an equatorial band 20°S to 30°N. Hefei is just located on the north boundary of the band. The large fluctuation was probably related to the forward and backward movement of the cloud around the equator. After

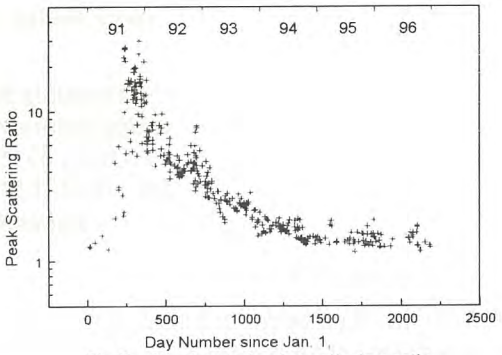


Fig.2 Maximum back scattering ratio

August 1991, the cloud was transported towards the north, the fluctuation became smaller and the peak scattering ratio generally varied between 10 and 20. It was about 10 in the early 1992, then decreased to about 5 in summer of 1992. The altitude of the peak scattering ratio, that is, the cloud height, over Hefei was mostly about 22 km. Positive correlation between peak scattering ratio and the cloud height was observed, i.e., a larger peak scattering ratio was located at higher altitude, generally.

The integrated backscattering coefficient (IBC) represents the total loading of aerosols. IBC is calculated from 16 km to 27 km. The IBC values are approximately 2.0×10^{-4} sr^{-1} and 3.0×10^{-4} sr^{-1} for pre-background period and present background period, respectively. During the effective period of Pinatubo volcano, the maximum value of IBC is 9.24 $\times$ 10^{-3} sr^{-1} on November 25, 1991. The maximum value of monthly average of IBC is 5.10×10^{-3} sr^{-1} for December of 1991. The e-folding decay time of IBC is estimated to be approximately 15 months. The IBC data are averaged for every half a year. Fig. 3 showed the variation of half-annual averaged IBC from 1991 to 1996. The maximum value emerged at the second half of 1991, and it decreased monotonously as time goes on, which reveals the evolution

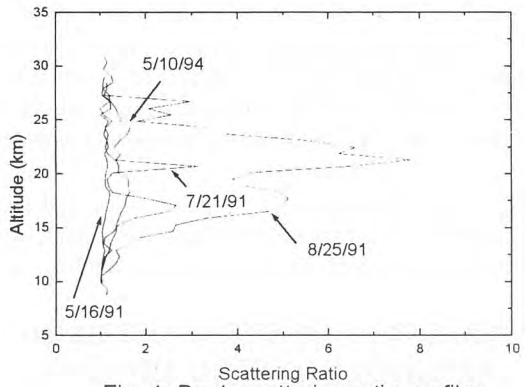


Fig. 1 Back scattering ratio profiles

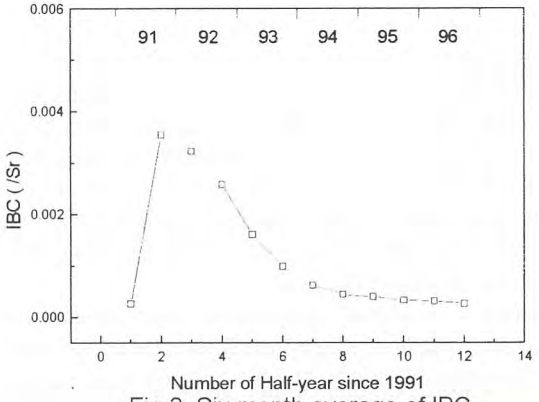


Fig.3 Six-month average of IBC

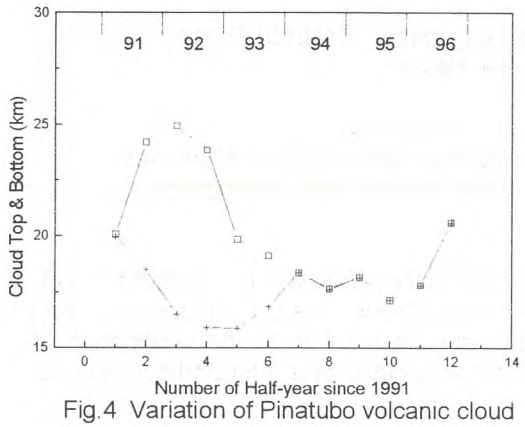


Fig.4 Variation of Pinatubo volcanic cloud

of Pinatubo volcanic cloud. Fig.4 showed the averaged heights of Pinatubo volcanic cloud top and bottom, whose scattering ratio values are defined to be more than 2.0. It can be deduced that the life of Pinatubo volcanic cloud is from June of 1991 to the middle of 1994 over Hefei. The cloud initially was thin layering and sometimes showed a double-peak structure during autumn of 1991. It became thicher and thicker with increasing time until autumn of 1992. The thick kept to be 8-9 km from winter of 1991 to autumn of 1992. The monthly average of cloud thick for April of 1992 was up to 9.8 km. The peak scattering ratio became less than 2.0 after the end of 1993.

REFERENCES

[1] H. Jager and D. Hofmann, "Midlatitude lidar backscatter to mass, area, and extinction conversion model on in situ aerosol measurements from 1980 to 1987", App. Opt., Vol.30, No.1, pp127-138, January 1991.

[2] O. Uchino "Lidar observations of the Pinatubo aerosol layers", Review of Laser Engineering, Vol. 23, No.2, pp161-165, February 1995.

[3] M. P. McCormick and R. E. Veiga, "SAGE II measurements of early Pinatubo aerosols", Geophys. Res. Lett., Vol.19, No.2, pp155-158, January 1992.

Lidar Measurements Synchronized with Satellite Overflights Acquired at 14.64N 121.07E

[1]Lorenzo de la Fuente, [2]Susana Dorado, [3]Nofel Lagrosas, [1]Columbo Enaje,
[3]John Holdsworth and [3]Minella Alarcon

[1]Manila Observatory, Quezon City, Philippines
[2]National Institute of Physics, University of the Philippines, Quezon City, Philippines
[3]Department of Physics, Ateneo de Manila University, Quezon City, Philippines

1. Introduction

Regular measurements using a Mie-scattering lidar have been obtained at a tropical location from July 1996 to December 1997. The measured backscatter intensity and linear depolarization ratio allow the calculation of extinction and backscatter coefficients. In addition to the verification of satellite observations these measurements characterize the local cloud and dust particulates and exhibit a seasonal variation.

2. Lidar system

The lidar site is located at 14.64 N 121.07 E within the Manila Observatory. A Q-switched Nd-YAG laser transmits an expanded, collimated and linearly-polarized 532 nanometer beam at 20 hertz. The backscatter is collected by a 28 centimeter diameter Schmidt-Cassegraine telescope in a biaxial vertical configuration, and directed through a collimating lens and a bandpass filter. From there the signal goes through a beamsplitter where parallel and orthogonal beam polarization components are directed to separate photomultiplier tubes (PMT). The analog voltage output from the two PMTs are digitized and averaged by a storage oscilloscope and saved using a microcomputer. Details of earlier configurations may be found in Alarcon et al. (1996).

3. Lidar observations

Figures 1 to 8 show time series plots of raw signal in volts for almost all measurement periods. Some measurement periods were not included because of insufficient duration, usually due to rain or equipment malfunction. The range gate most frequently used was 300 meters, but 600 and 1500 meter range gates were also used. Examples of high altitude measurements using a 1500 meter range gate are presented in De la Fuente et al. (1998). To make all time series plots intercomparable a voltage range of 0 to 0.2 volts was adopted for the Z-axis, an altitude range of 0 to 3000 meters for the Y-axis, and Local Standard Time (0800 LST is 0000 UTC) in decimal format for the X-axis. A summary of all modifications to the lidar equipment and measurement schedules that affected data acquisition is presented in Table 1. The schedule change on 14 January 1997 was implemented to accommodate a request from the Asian lidar network to make measurements that coincided with satellite overflights at the lidar site. Specific satellite platforms were not identified, but were probably polar orbiting satellites.

Table 1: Lidar system and schedule modifications

Date	Modification
05 December 1997	Q-switch failure
25 November 1997	data points changed 1000 points to 2500 points
21 November 1997	schedule changed 1930-2030 LST added
17 July 1997	operations resumed
22 May 1997	laser power supply failure
13 March 1997	configuration changed beamsplitter and depolarization PMT added
04 February 1997	configuration changed 20.33 centimeter diameter telescope to 27.94 centimeter diameter telescope
14 January 1997	schedule changed 0700-0900 and 1500-1700 LST to 0900-1000 and 1400-1500 LST
15 August 1996	regular schedule started 0700-0900 and 1500-1700 LST 20.33 centimeter diameter telescope single PMT installed 1000 data points

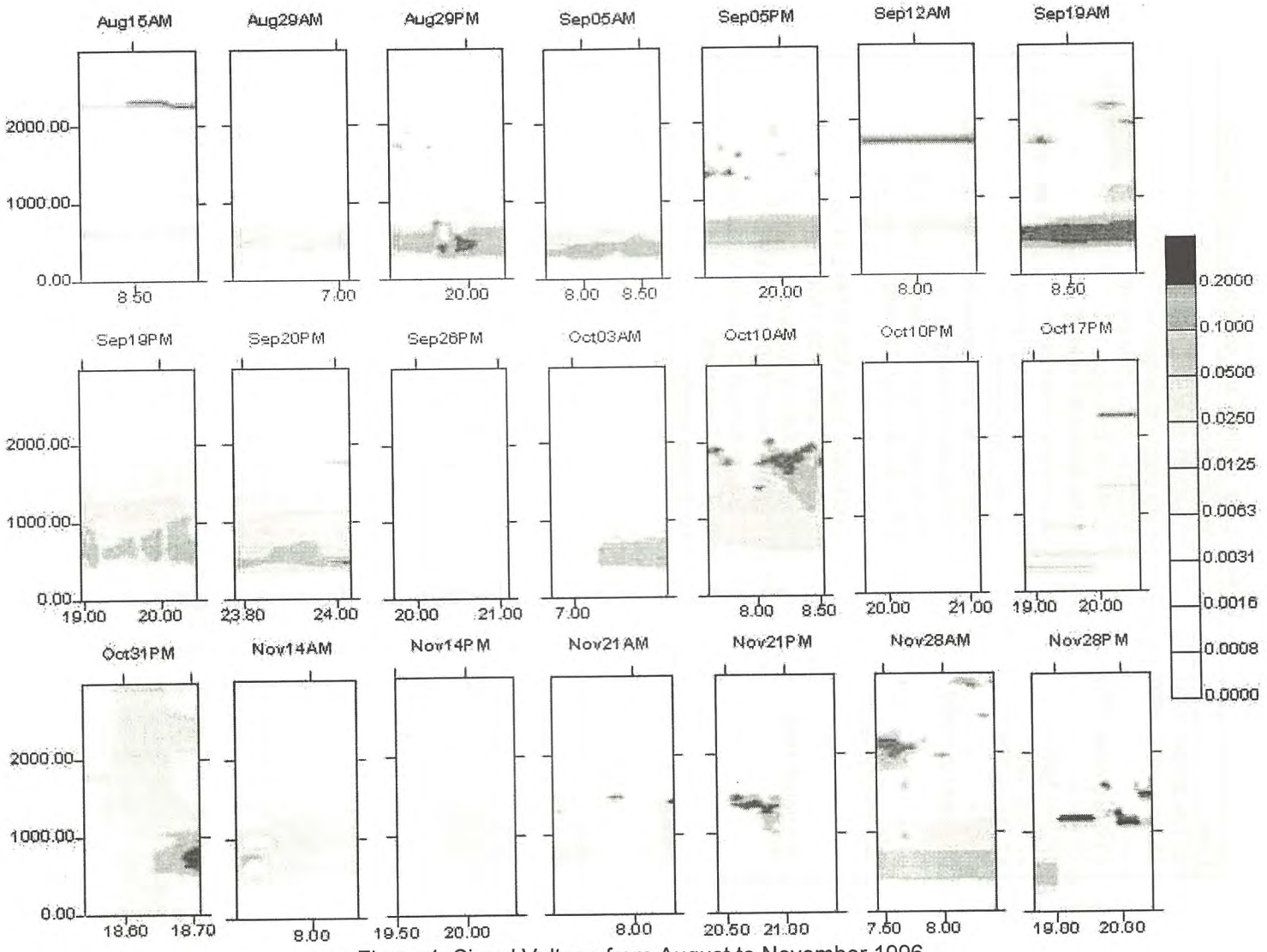


Figure 1: Signal Voltage from August to November 1996

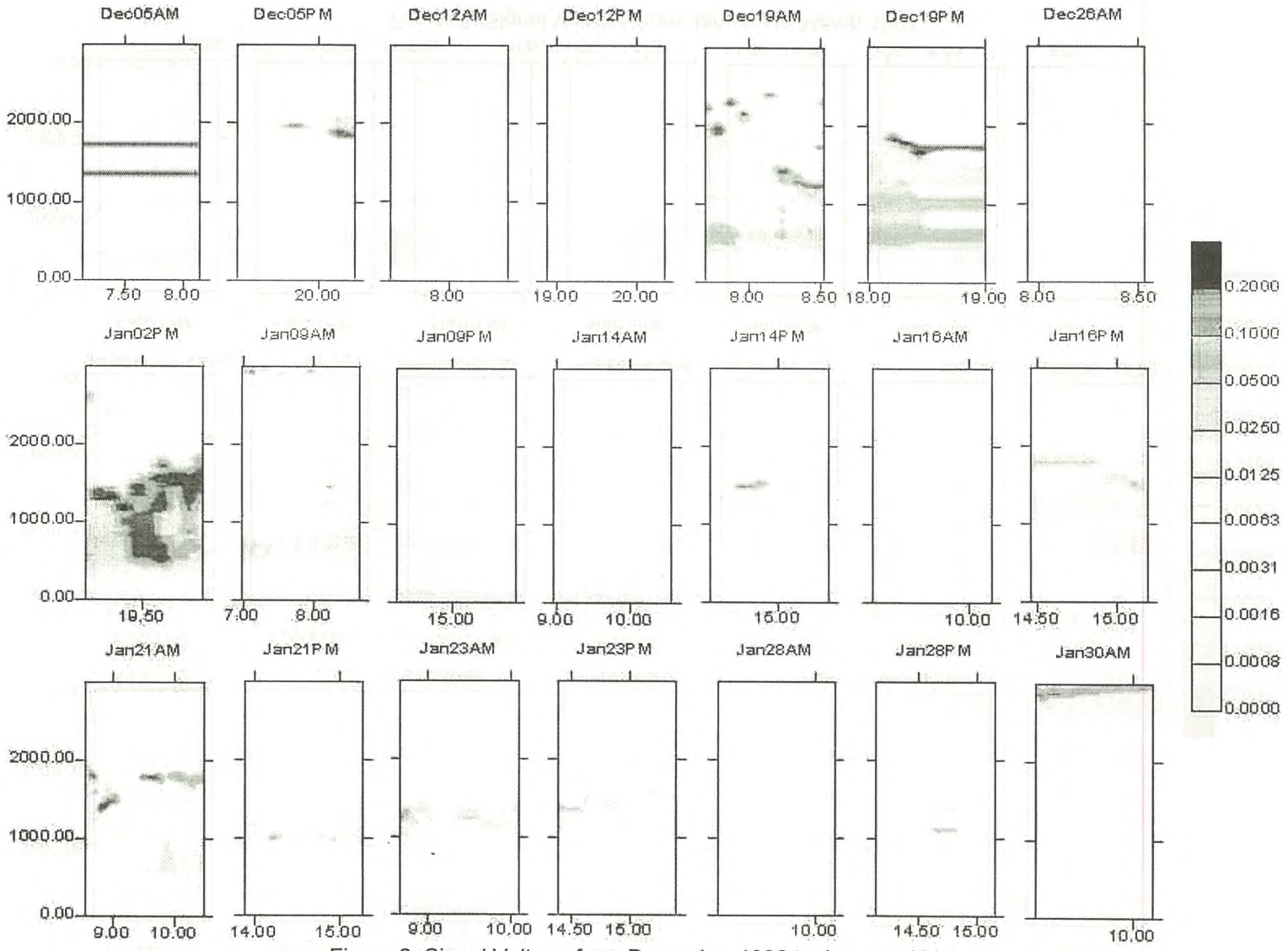


Figure 2: Signal Voltage from December 1996 to January 1997

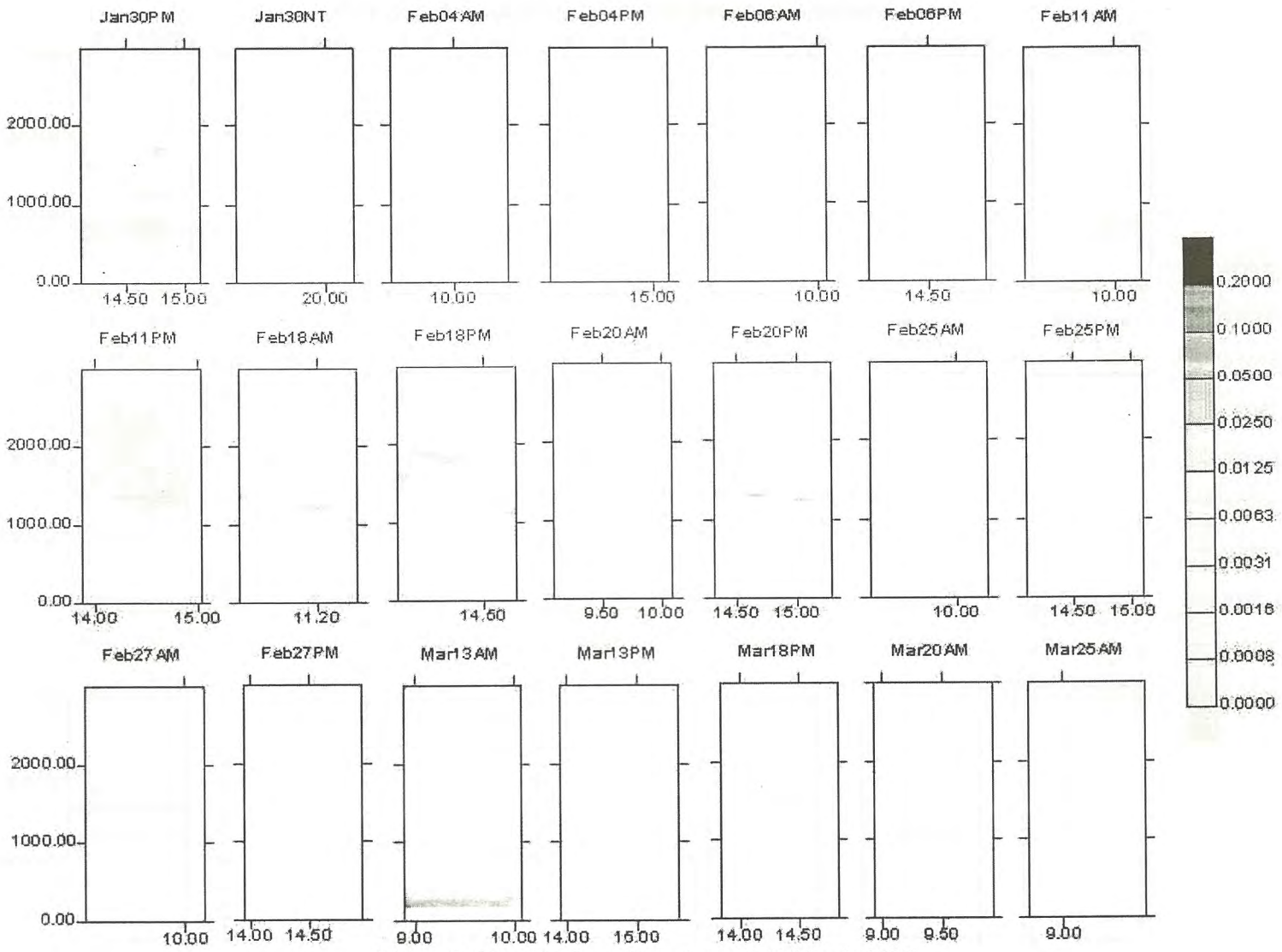


Figure 3: Signal Voltage from January to March 1997

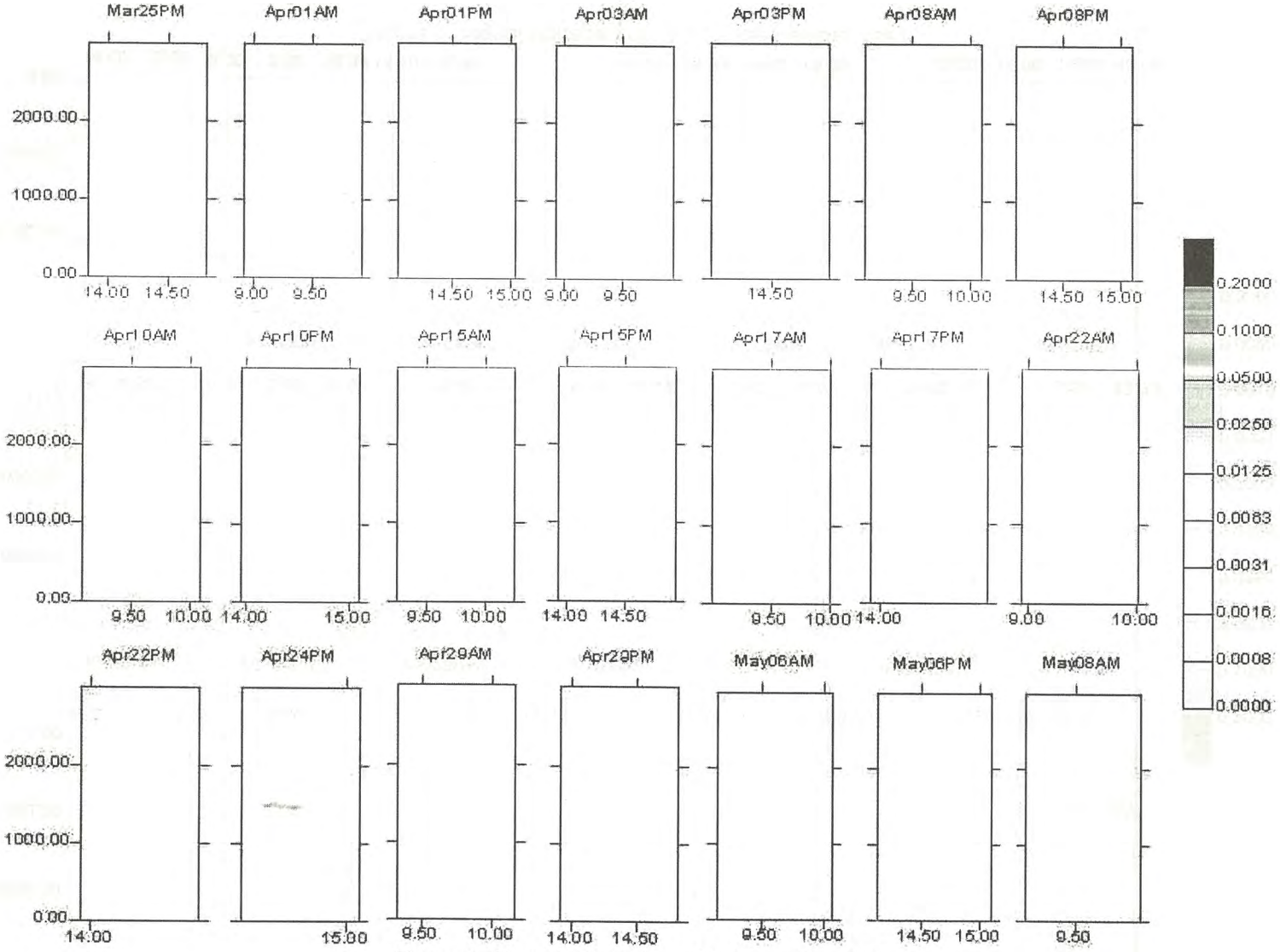


Figure 4: Signal Voltage from March to May 1997

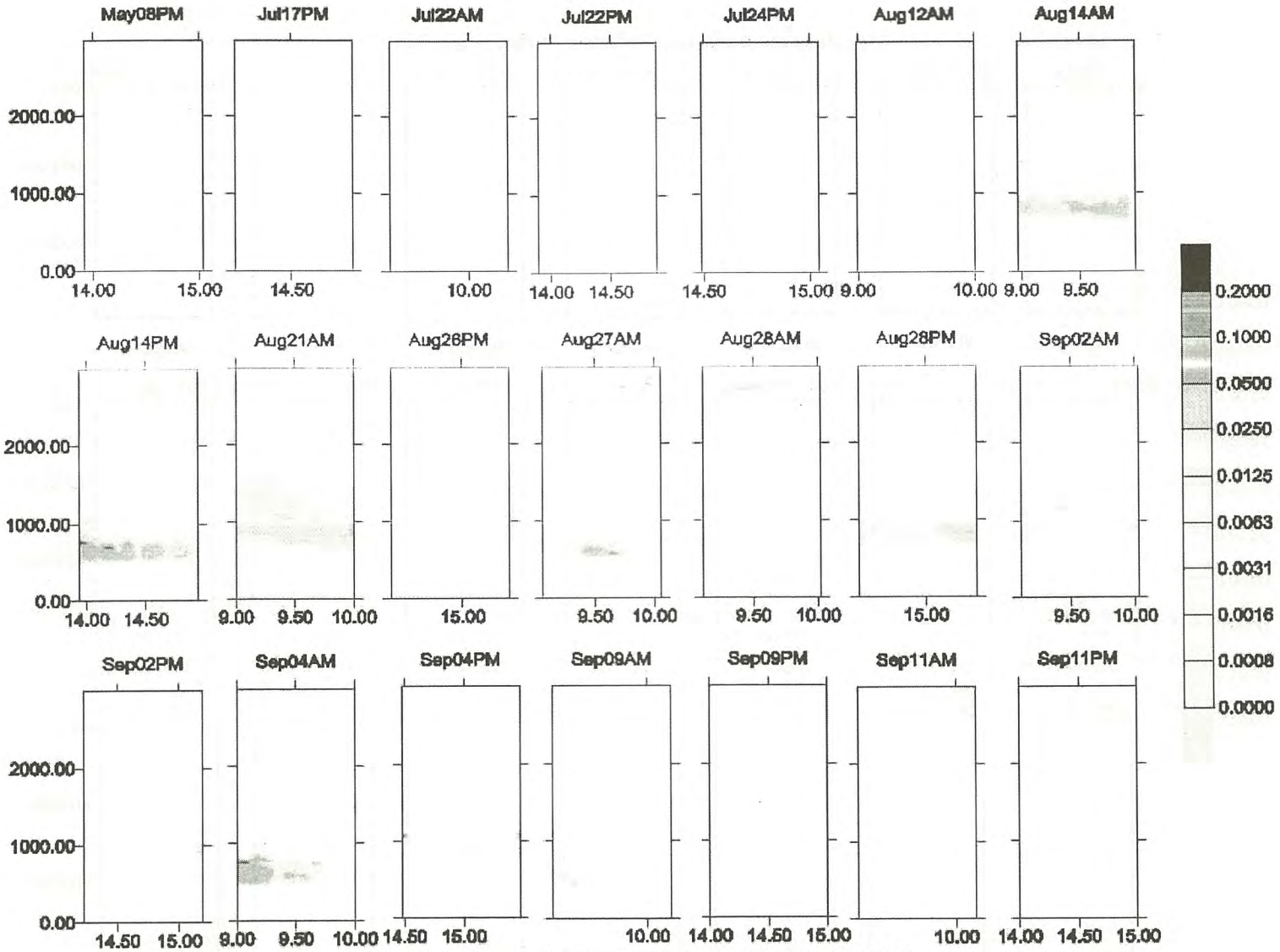


Figure 5: Signal Voltage from May to September 1997

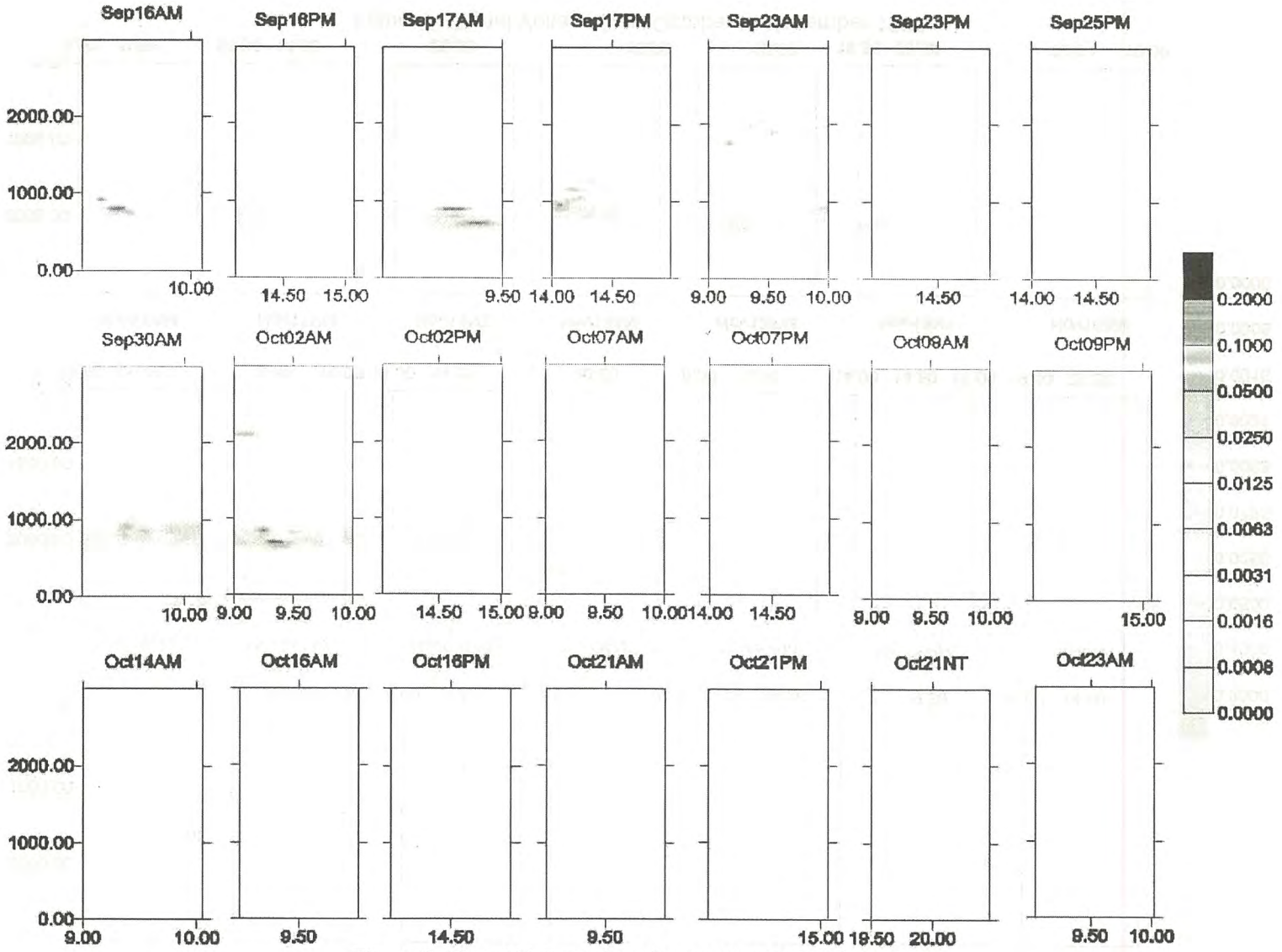


Figure 6: Signal Voltage from September to October 1997

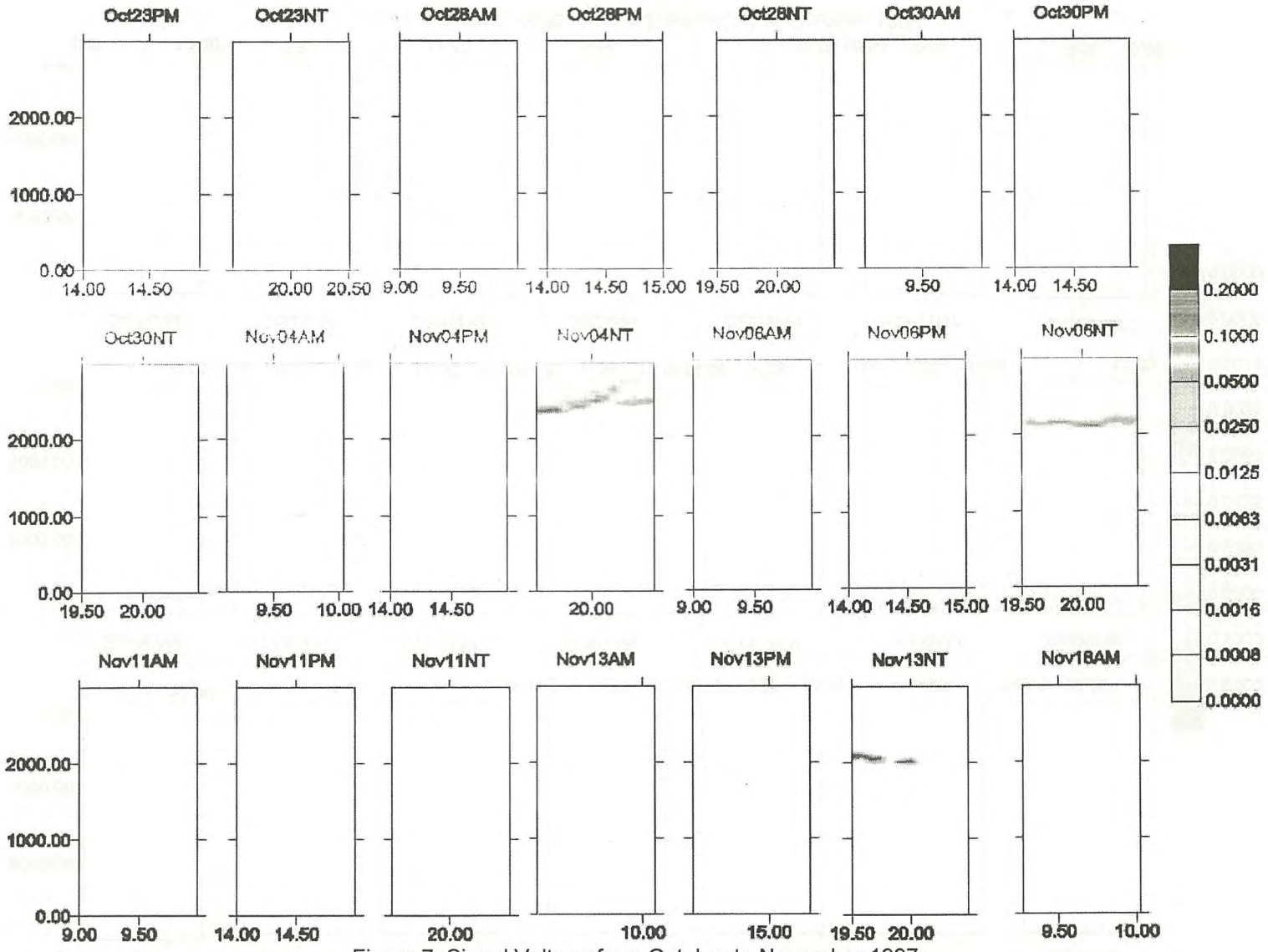


Figure 7: Signal Voltage from October to November 1997

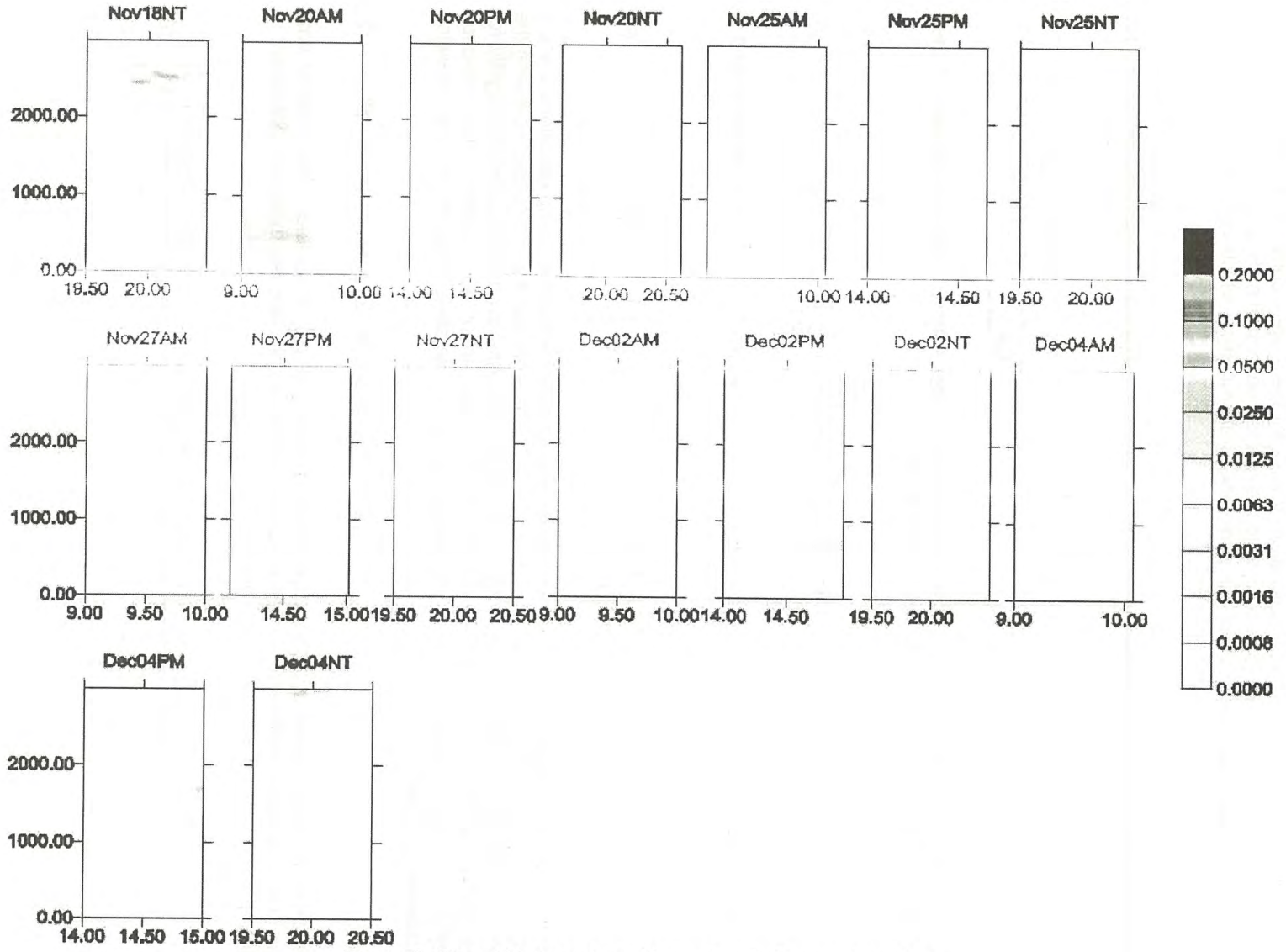


Figure 8: Signal Voltage from November to December 1997

4. Data inversion algorithms

Equipment and operational constraints introduce unavoidable variations in system parameters, which requires data to be constantly calibrated. Values for the system constant and backscatter to extinction ratio are then calibrated according to the method described by Russell et al. (1979). The following equations are expressions for particulate transmittance which may be combined to obtain an equation for the system constant:

$$R(r) = \frac{P(r)r^2}{K_{sys}T_R^2(r)T_P^2(r)\beta_R(r)} \quad (1)$$

$$T_P^2(r) = T_R(r)^{-\frac{3}{4\pi B}}\left[1 - \frac{2}{BK_{sys}}\int_0^r P(r')T(r')^{\frac{3}{4\pi B}-2}dr'\right] \quad (2)$$

Equation 1 may be solved for particulate transmittance. After setting it equal to equation 2 then solving for the system constant the equation becomes:

$$K_{sys} = \frac{P(r)r^2T_R(r)^{\frac{3}{4\pi B}}}{T_R^2(r)\beta_R(r)} + \frac{2}{B}\int_0^r P(r')T(r')^{\frac{3}{4\pi B}-2}dr' \quad (3)$$

The backscatter to extinction ratio is required in the computations for the system constant, and is determined using an equation derived from Fernald (1972):

$$B = \frac{1}{K_{sys}}\left[\int_0^r P(r')r^2T_R(r')^{\frac{3}{4\pi B}-2}dr'\right]\left[1 - T_P^2(r)T_R(r)^{\frac{3}{4\pi B}}\right]^{-1} \quad (4)$$

In order to solve for these parameters simultaneously an iterative process using equations 3 and 4 becomes necessary. The backscatter and extinction coefficients are then calculated following the method presented by Hughes et al. (1985). The laser-telescope overlap range varies slightly for each data collection period, but its altitude is generally about 500 meters. The extinction coefficient at the overlap range is calculated using an iterative method for the following transcendental equation:

$$k\ln\sigma(r_0) = S(r_0) + 2r_0\sigma(r_0) - \ln(K_{sys}B) \quad (5)$$

The extreme range varies with range gate setting, and is usually defaulted to the highest data point. The extinction coefficient at overlap range is used to calculate the extinction coefficient at extreme range using the following equation:

$$\sigma(r_f) = \left\{\exp\left[\frac{S(r_f) + 2r_0\sigma(r_0) - \ln(K_{sys}B)}{k}\right] - \frac{2}{k}\int_{r_0}^{r_f}\exp\left[\frac{S(r') - S(r_f)}{k}\right]dr'\right\}^{-1} \quad (6)$$

Finally, the extinction coefficients between the overlap and extreme ranges are calculated using the following equation developed by Klett (1981):

$$\sigma(r) = \frac{\exp\left[\frac{S(r) - S(r_f)}{k}\right]}{\frac{1}{\sigma(r_f)} + \frac{2}{k}\int_{r_0}^{r_f} \exp\left[\frac{S(r') - S(r_f)}{k}\right] dr'} \quad (7)$$

The backscatter coefficients are calculated from extinction coefficients using a power law with the exponent set to unity.

5. Discussion

Seasonal variations in lidar backscatter are apparent from the progression of time series profiles, and appear to correspond to increased cloudiness during the rainy season (June-November) and decreased cloudiness during the dry season (December-May). Using data in figures 1 to 4, similar observations were made by Dorado et al. (1998). Rainy season cloudiness for 1997 appears to be less distinct than for 1996, which may be due to currently occurring regional El Niño effects. There also appears to be evidence of a gradual decrease in laser output power when comparing peak signals from mid 1996 and late 1997. At 0000 UTC on 05 August 1997 a specially arranged radiosonde launch occurred within 100 meters of the lidar site, and the data used for figures 9 and 10. Sample range-corrected lidar signals from the parallel and orthogonal PMTs are shown in figure 9, where high linear depolarization ratios indicate either multiple scattering or non-spherical scattering particles which may be dust. Figure 10 shows sample extinction and backscatter coefficient profiles calculated using lidar backscatter from the parallel PMT. The behavior of extinction and backscatter coefficients may be inferred from figures 1 to 8, since these optical parameters are directly proportional to signal voltage as shown in figure 10. Depolarization, extinction and backscatter measurements from Dorado et al. (1998) also exhibit seasonal and height-dependent variability which may be partly due to dust transport from the surface. The rest of the data is currently being analyzed, so time series plots of backscatter and extinction coefficients should be available soon.

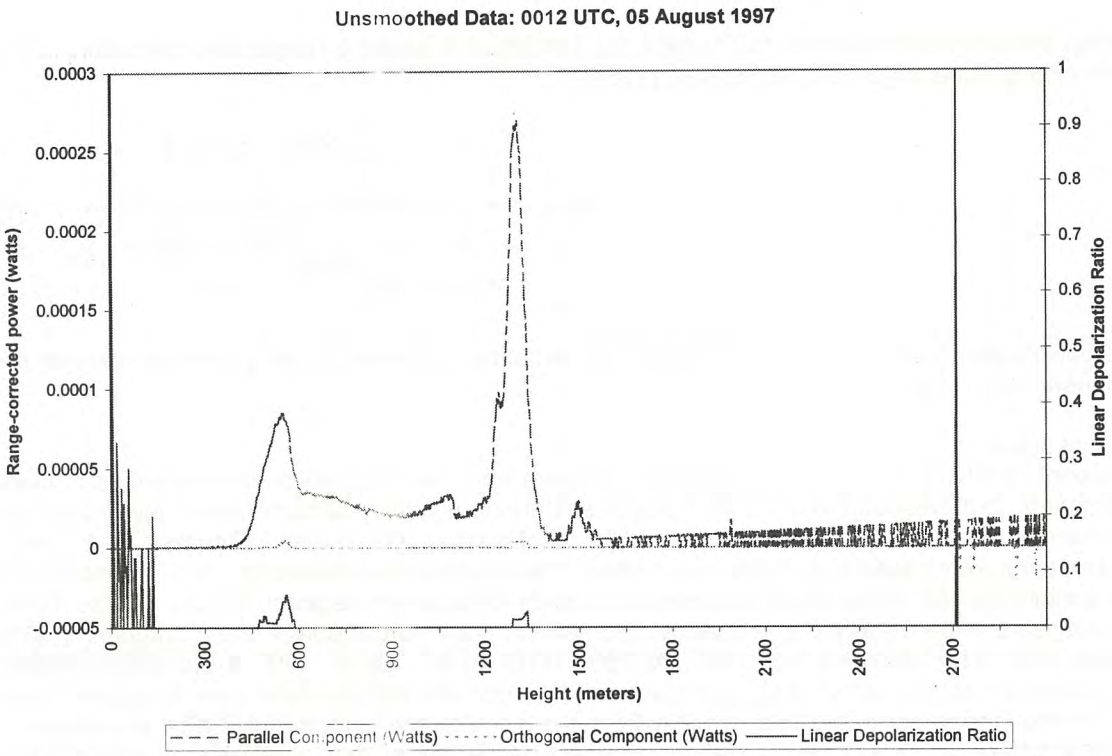


Figure 9: Range-corrected power and depolarization ratio for 0012 UTC, 05 August 1997

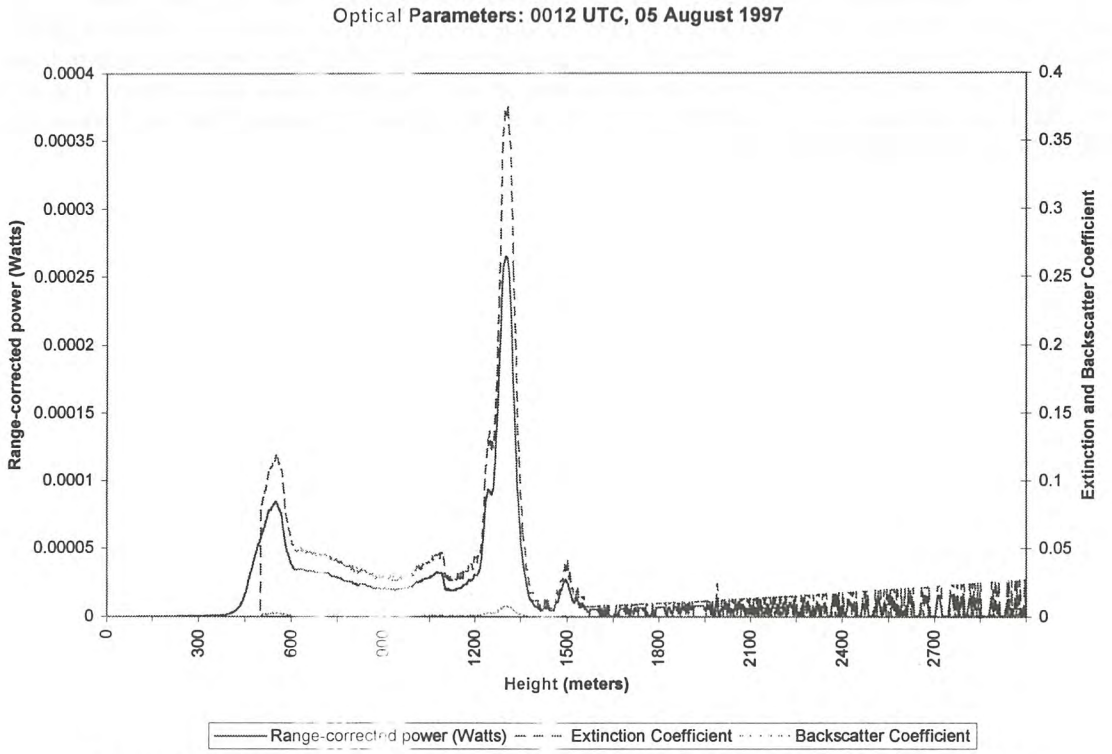


Figure 10: Extinction and Backscatter coefficients for 0012 UTC, 05 August 1997

References

Alarcon, M., S. Dorado, J. Holdsworth, B. Sychingiok, and D. McNamara. 1996: Mie lidar measurements in Metro Manila (14.64N, 121.07E). *Extended Abstracts, 18th Int. Laser Radar Conf.* Berlin, International Coordination Group on Laser Atmospheric Studies, 167

De la Fuente, L., M. Alarcon and S. Dorado. 1998: *Tropical Cloud Optical Phenomena and Pioneering Lidar Observations at the Manila Observatory.* Bull. Of the Amer. Meteor. Soc. 79, 5-7

Dorado, S., N. Lagrosas, L. de la Fuente, J. Holdsworth and M. Alarcon. 1998: *Mie Backscatter Intensity and Depolarization Measurements of Tropical Clouds at 14.64N 121.07E in the Philippines.* Submitted to J. of Atmos. Sci.

Fernald, F., B. Herman, and J. Reagan. 1972: *Determination of Aerosol Height Distribution by Lidar.* J. of Appl. Meteor. 11, 482-489

Hughes, H., J. Ferguson and D. Stephens. 1985: *Sensitivity of a Lidar Inversion Algorithm to Parameters relating Atmospheric Backscatter and Extinction.* Appl. Opt. 24, 1609-1613

Klett, J. 1981: *Stable Analytical Inversion Solution for Processing Lidar Returns.* Appl. Opt. 20, 211-220

Liou, K. 1980: *An Introduction to Atmospheric Radiation.* International Geophysics Series v.26. Academic Press. 392 pp.

Russell, P., I. Swissler and M. McCormick. 1979: *Methodology for Error Analysis and Simulation of Lidar Aerosol Measurements.* Appl. Opt. 18, 3738-3799

Climate Change and ENSO in Southern Thailand

Absornsuda Siripong
Marine Science Department, Faculty of Science
Chulalongkorn University, Bangkok 10330, Thailand.
e-mail: sabsorns@netserv.chula.ac.th
and
Phuwieng Prakhammintara
Meteorological Department
4353 Sukhumwit Road, Bangna, Khet Prakanong,Bangkok 10260, Thailand.
e-mail: phuwieng@hotmail.com

Presented at the **CEReS Symposium on the ATMOSPHERIC CORRECTION of SATELLITE DATA and ITS APPLICATION to GLOBAL ENVIRONMENT,**
January 21 – 23, 1998.
At Chiba University, Chiba, Japan

Abstract

The historical (1951 to 1996) yearly mean of air temperature and annual total of rainfall data from 21 meteorological stations in the Southern Part of Thailand were analyzed by time series plot of the anomaly from the baseline period (1961 to 1990) or from the whole period of records, and by variability of yearly mean and three-years running mean, in order to see the trends of these two climate elements. The stations are divided into two groups, the East coast and West coast of Southern Thailand, owing to the different physiography. The linkage of them with the ENSO events are also investigated. All stations except Phuket (West coast) show rising rainfall at present. Most stations show decreasing trend of air temperature except Ranong (West coast), Chumphon, Prachuap Khiri Khan and Surat Thani (East coast). During the ENSO years most stations show minus rainfall anomaly and at Upper South stations show plus rainfall anomaly, but Lower South stations show minus rainfall anomaly; and minus air temperature anomaly.

Introduction

Climate Change in IPCC (Intergovernmental Panel on Climate Change) usage refers to any change in climate over time whether due to natural variability or as a result of human activity. Climate has changed over the past century. At any one location year-to-year variations in weather can be large, but analyses of meteorological and other data over large areas and over periods of decades or more have provided evidence for some important systematic changes. Global mean surface air temperature has increased by between about 0.3 and 0.6 ^{0}C since the late 19th century; the additional data available since 1990 and the re-analyses since then have not significantly changed this range of estimated increase. Recent years have been among the warmest since 1860,i.e., in the period of instrumental record, despite the cooling effect of the 1991 Mt. Pinatubo volcanic eruption. Night–time temperatures over land have generally increased more than daytime temperatures. Regional changes are also evident.

Climate is expected to continue to change in the future. A general warming is expected to lead to an increase in the occurrence of extremely hot days and a decrease in the occurrence of extremely cold days. Warmer temperatures will lead to a more vigorous hydrological cycle; this translates into prospects for more severe droughts and/or floods in some places and less severe droughts and/or floods in other places. Several models indicate an increase in precipitation intensity, suggesting a possibility for more extreme rainfall events

The changes in sea surface temperatures in the Pacific Ocean (**El Nino** or **EN**) and changes in sea level atmospheric pressure across the Pacific basin (the **Southern Oscillation** or **SO**). These combined changes have come to be commonly referred to as **ENSO**. The associations between ENSO events and unusual changes in normal climate patterns (called anomalies) around the globe have been referred to by scientists as **"teleconnections"**. These are known connections between ENSO events and changes in distant weather or climate related processes. For example, there appears to be an association between ENSO events and droughts or floods in various parts of the globe.

ENSO is a natural phenomenon that recurs every few years. ENSO events wax and wane over time in their responses to climatic fluctuations. The ENSO may be called an anomaly. The *magnitude* of an El Nino is defined by degree of departure from a long-term average of anomalously warm sea surface temperatures in the central and eastern Pacific. *Frequency* relates to its return period in the

order of 2 to 20 years (more specifically, a major El Nino occurs every 8 to 11 years, and a minor one every 2 or 3 years). The *duration* of El Nino is 12 to 18 months, with a few notable exceptions. The *areal extent* could be interpreted to mean the spatial extent around the globe of the impacts of El Nino and its teleconnections. This would vary directly with the severity of the event, with major El Nino events being linked to major worldwide impacts and minor ones linked to localized or regional impacts. The *speed of onset* of El Nino is of the order of months. Occasionally, however, events have begun, only to collapse after a few months. *Spatial dispersion* refers to the area in the central and eastern Pacific that is encompassed by the anomalously warm sea surface temperatures. *Temporal spacing*, with respect to El Nino, refers to the return period which, on the average, is 4.5 years. The 1990 to mid-1995 persistent warm phase of the ENSO (which causes droughts and flood in many areas) was unusual in the context of the last 120 years.

Objectives of the Study

This paper is a preliminary study of climate change and the linkage of climate variability with ENSO in the Southern Part of Thailand.

The Study Area

From the physiographic feature, the Peninsular of Southern Thailand may be divided into two regions, i.e. the eastern and western sides. The high mountain ranges are the barrier for the passing of air masses. The East coasts are the emerged shoreline, while the West coasts are the submerged shoreline. The topography of both coasts is different from each other. The East coast is characterized with wider coastal plain, bordering the shallow Gulf of Thailand. The narrowest coastal plain is at Prachuap Khiri Khan Province and the widest are at Surat Thani and Nakhon Si Thammarat Provinces. Songkhla coast is a brackish lagoon and barrier beach system. The relatively short streams flow to the Gulf. Tapi River is the biggest river on this side. It flows to Ban Don Bay of Surat Thani Province, which is the biggest muddy bay in the South.There are two big islands, Ko Samui and Ko Pha-ngan, which belong to Surat Thani Province.

The characteristics of the West coast are drowned river valleys with many estuaries, bays and rugged coasts comparing to the more straight coastline of the East coast. The main islands are Phuket, Lanta, Tarutao. The relatively extensive and big mangrove trees are found along the rivermouths. The biggest river on this side is Kraburi river, which is the borderline of Thailand and Myanmar at Ranong Province. The continental shelf of the Andaman Sea is narrow and sloping down to the deeper part. The high mountain range is near the shoreline at Ranong. This causes the highest annual rainfall in Thailand at Ranong (4183.58 mm).

The physiographic feature of southern Peninsula causes the different climate from East and West coasts. The West coast receives heavy rain during the SW monsson season(May to October), while the East coast gets heavy rainfall during the NE monsoon (November to March). The monsoon season happens around September and October and this also causes heavy rain or sometimes flood in the east coast. The heaviest annual rainfall on the East coast is at Narathiwat Province (2460.02 mm), which is approximately half of Ranong.

From Koppen's classification of climate, the South has **Tropical Monsoon Climate: Am**. However, in some areas, the trend is **Tropical Rainforest: Af.** Ranong has the highest rainfall in the country and Phetchaburi Province receives the lowest rainfall (986.54 mm) in the South.

The air temperature in the South has rather low range compared to other parts of the country,i.e. 22.0 – 24.0 ^{0}C (Surat Thani – Phuket) and the range of the highest temperature is 31.2 – 32.3 ^{0}C (Chumphon – Trang). The highest mean of air temperature is at Phuket (28.15 ^{0}C) and the lowest is at Surat Thani (26.4 ^{0}C).

Methods of Study

The meteorological parameters are analysed only yearly mean of air temperature and annual rainfall amount from 21 stations. The longest periods for this study are from 1951 up to 1996. This period is long enough to cover the **baseline period** from 1961 to 1990 as recommended by IPCC. The yearly anomaly from baseline period for the stations where the data have been recorded from 1951 to present; or the period of the record for the stations where the data have been recorded recently, are plotted. The yearly mean and three-years running mean also are plotted to see the trend of both parameters. The comparison of anomaly values in ENSO years are shown to see the linkage among them.

Results of Study

Fig.1 is the location of the meteorological stations in Thailand which are organized by the Meteorological Department, only the Southern Part are studied.

The anomaly rainfalls and annual with three-years running mean for the East coast of Southern Thailand are shown from Figs 2 to 13 ; and for the West coast from Figs. 14 to 20. All stations except Hua Hin (East coast), Ranong and Phuket (West coast) show plus anomalies recently (upper mentioned figures).The rainfalls show increasing trends except Hua Hin, Ranong and Phuket (lower mentioned figures).

The anomaly of air temperatures and yearly mean with three-years running mean for the East coast of Southern Thailand are shown from Figs. 21 to 32; and for the West coast from Figs. 33 to 38. All stations except Chumphon, Prachuap Khiri Khan and Surat Thani (East coast) and Ranong (West coast) show minus anomalies recently (upper mentioned figures).The air temperatures show decreasing trends except Chumphon, Prachuap Khiri Khan Surat Thani and Ranong (lower mentioned figures).

The linkages of ENSO years with two meteorological parameter anomalies are listed in Tables 1 and 2. During ENSO years, most stations show minus rainfall anomaly and at Upper South stations show plus rainfall anomaly, but Lower South stations show minus rainfall anomaly; and most stations show minus air temperature anomaly.

Conclusion

The climate in the Southern Part of Thailand shows some variability due to the physiography. The rainfalls and air temperatures in many parts are decreasing . During the ENSO years, it is also the drier and colder years for most stations.

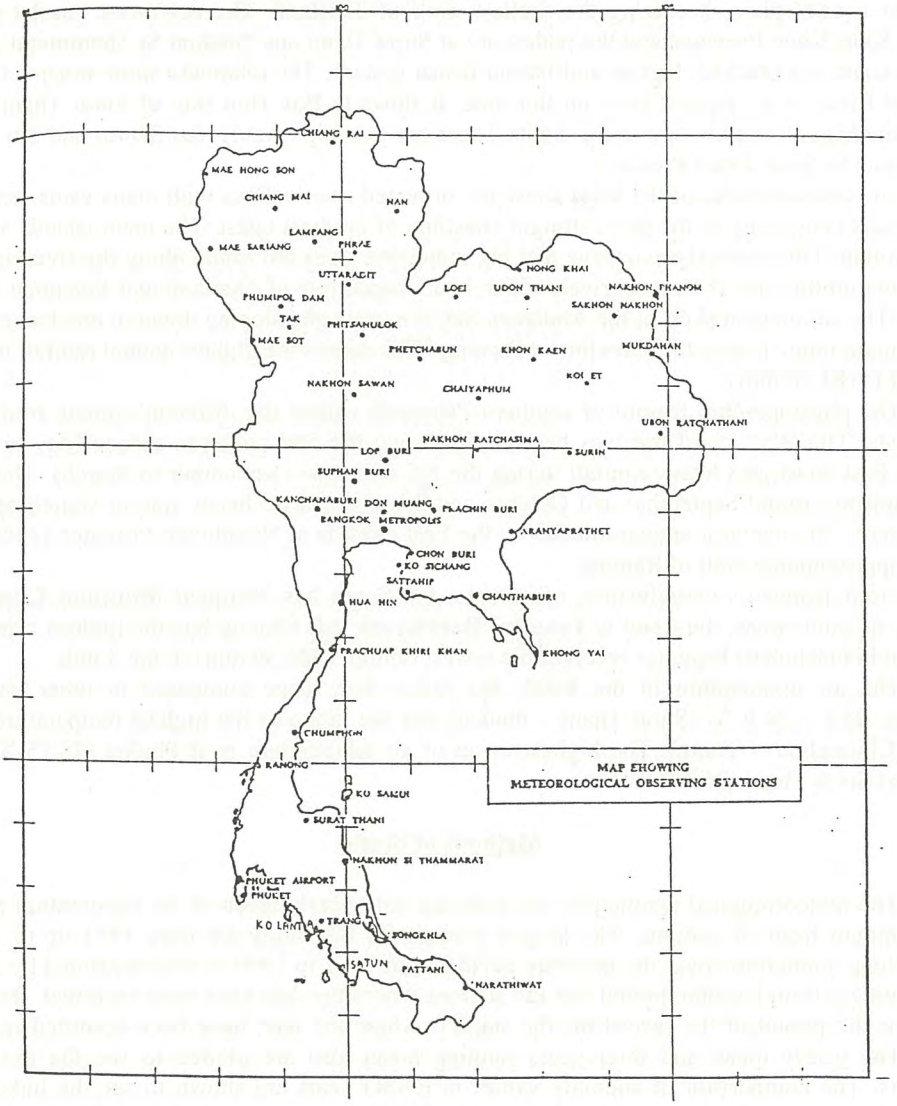
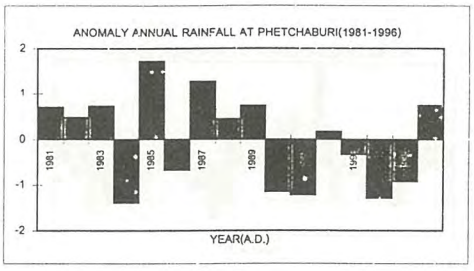


Fig. 1 . The meteorological stations in Thailand which are operated by the Meteorological Department.



MEAN PERIOD (1981-1996) = 986.5375 mm

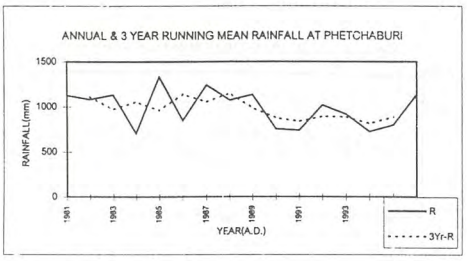
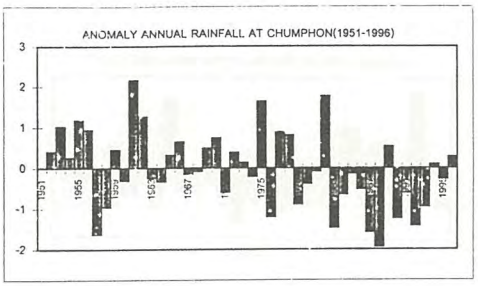


Fig. 2



BASELINE PERIOD (1961-1990) 1939.917 mm

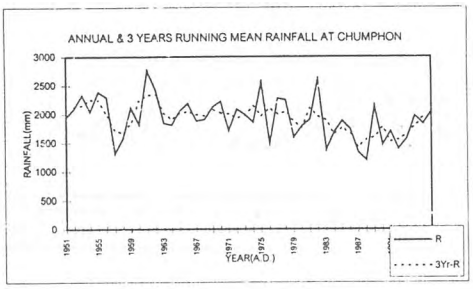
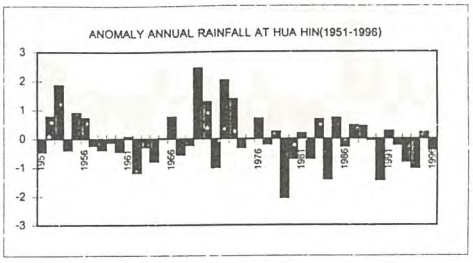


Fig. 5



BASELINE PERIOD (1961-1990) 998.4167 mm

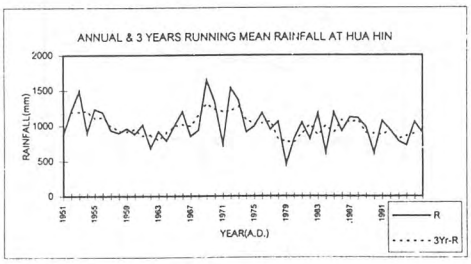
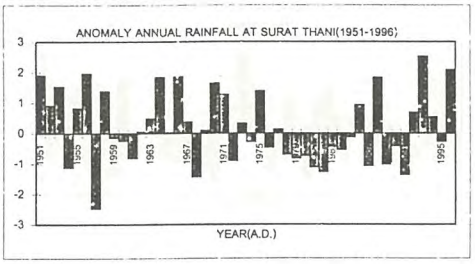


Fig. 3



BASELINE PERIOD (1961-1990) 1635.81mm

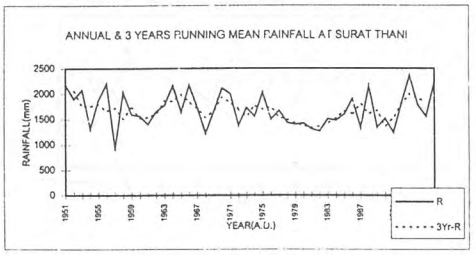
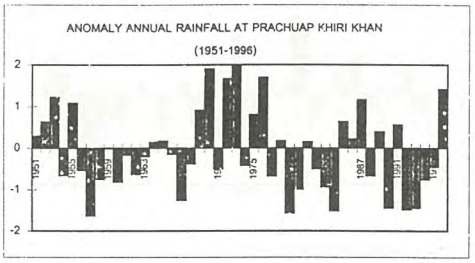


Fig. 6



BASELINE PERIOD (1961-1990) 1152.883 mm

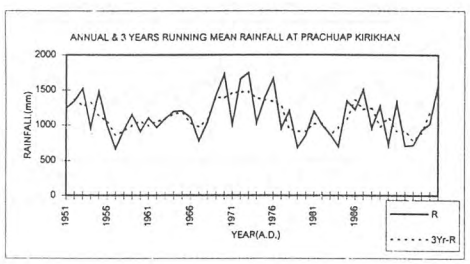
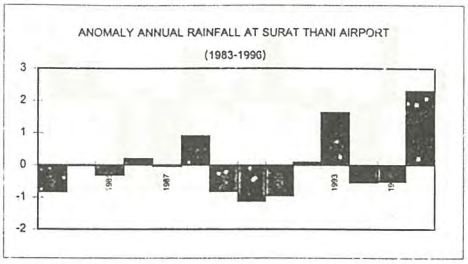


Fig. 4



MEAN PERIOD (1983-1996) = 1516.614 mm

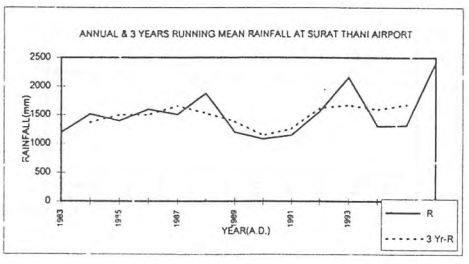
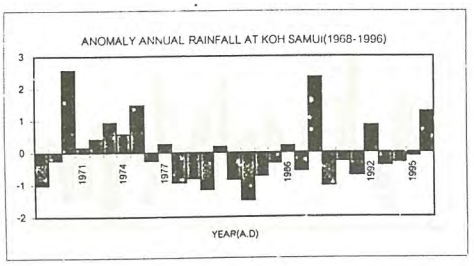


Fig. 7



MEAN PERIOD (1968-1996) = 1931.159 mm

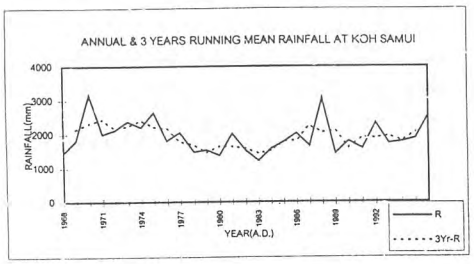
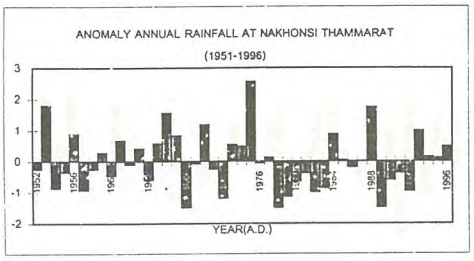


Fig. 8



BASE LINE PERIOD (1961-1990) 2381.363 mm

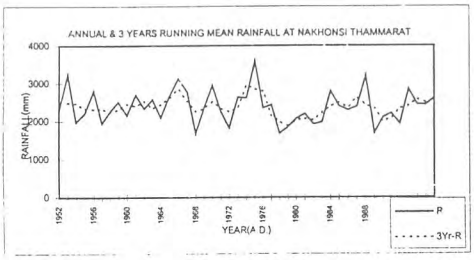
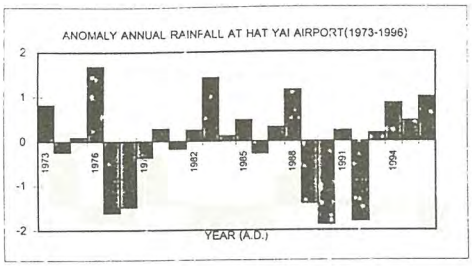


Fig. 9



MEAN PERIOD (1973-1996) = 1624.425 mm

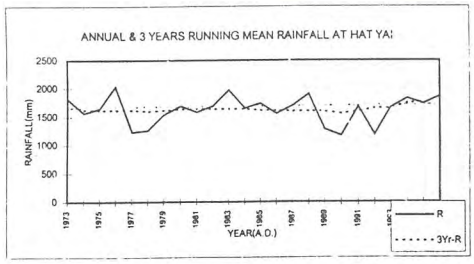
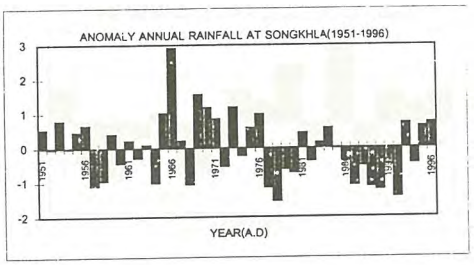


Fig. 10



BASELINE PERIOD (1961-1990) 2034.69 mm

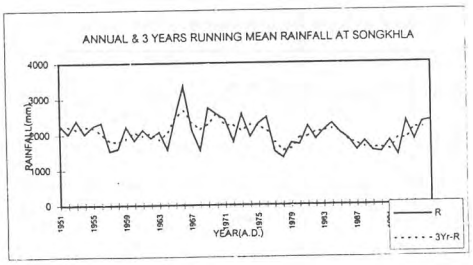
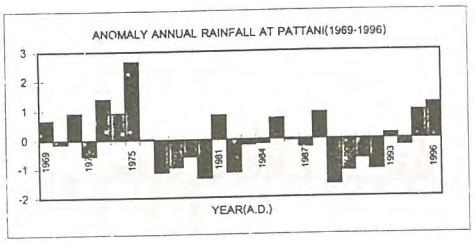


Fig. 11



MEAN PERIOD (1969-1996) = 1792.207 mm

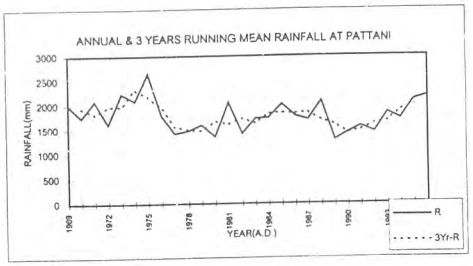
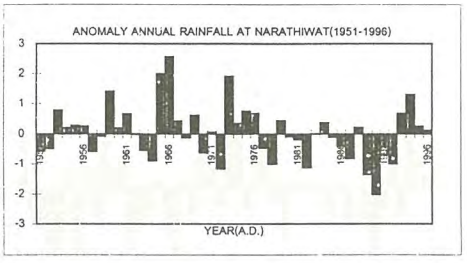


Fig. 12



BASELINE PERIOD (1961-1996) 2460.023 mm

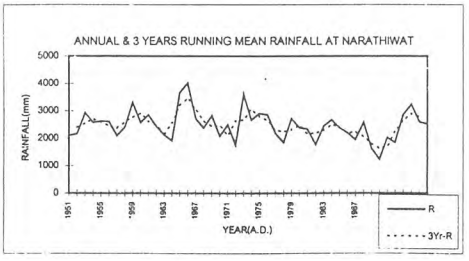
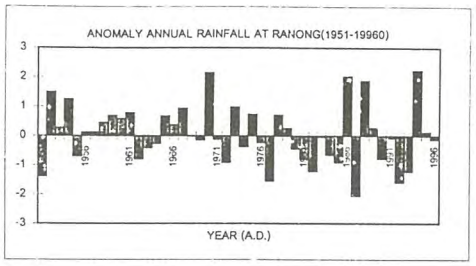


Fig. 13



BASELINE PERIOD (1961-1990) 4183.58 mm

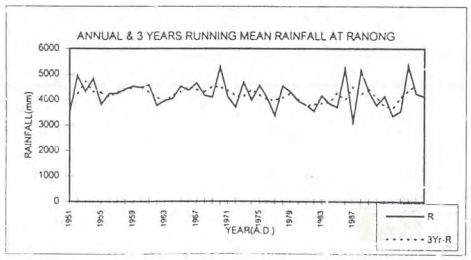
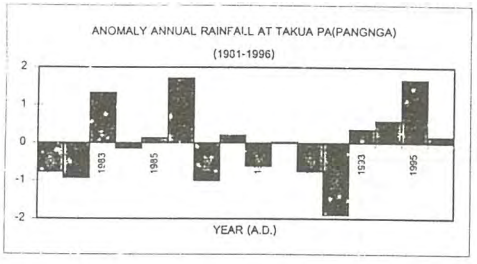


Fig. 14



MEAN PERIOD (1981-1996) = 3565.681 mm

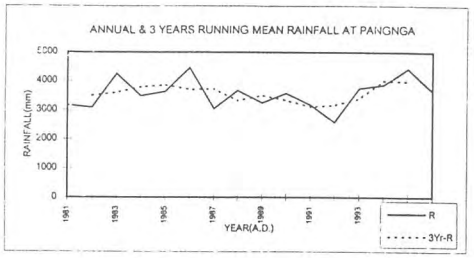
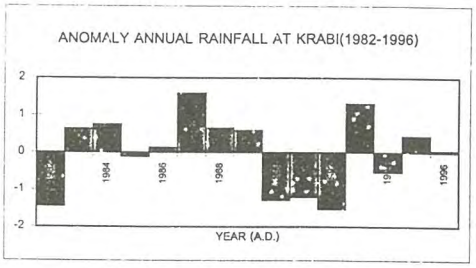


Fig. 15



MEAN PERIOD (1982-1996) = 2184.1 mm

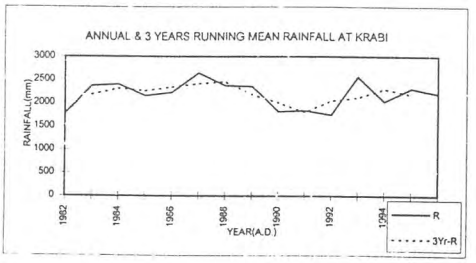
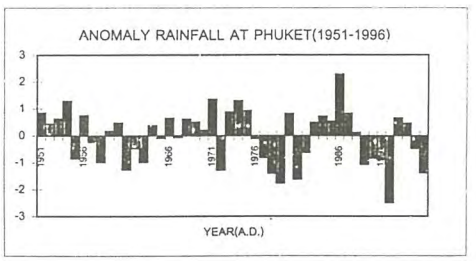


Fig. 16



BASELINE PERIOD (1961-1990) 2302.327 mm

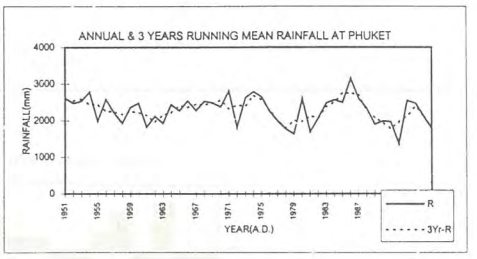
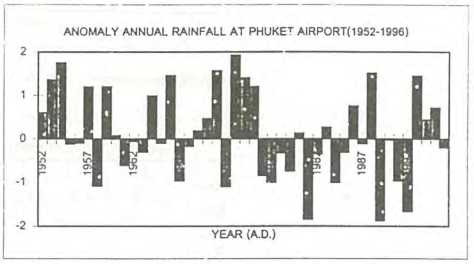


Fig. 17



BASELINE PERIOD (1961-1990) 2503.523 mm

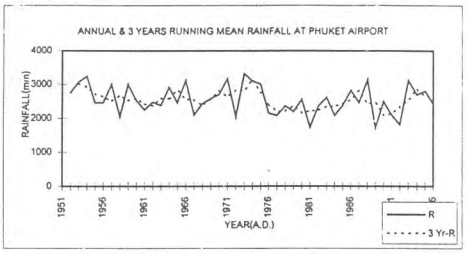
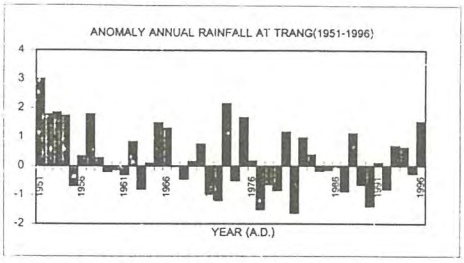


Fig. 18



BASELINE PERIOD (1961-1990) 2187.253 mm

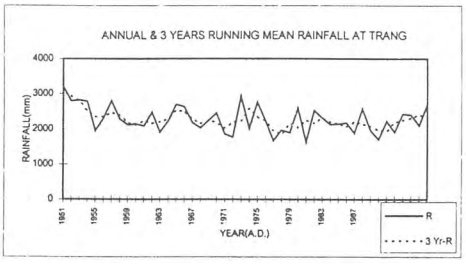
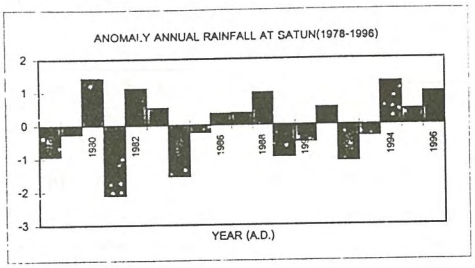


Fig. 19



MEAN PERIOD (1978-1996) = 2257.974 mm

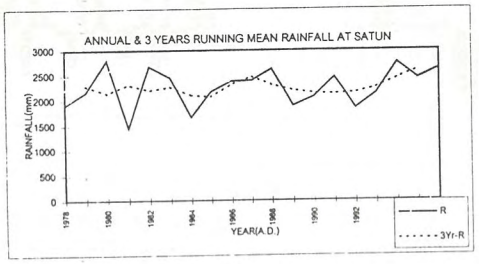
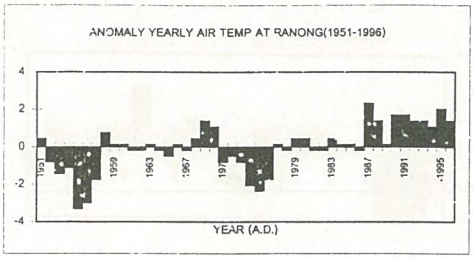


Fig. 20



BASELINE PERIOD (1961-1990) = 26.66 DEG.C

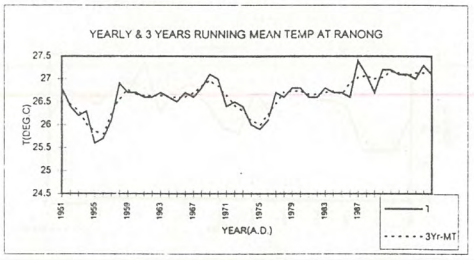
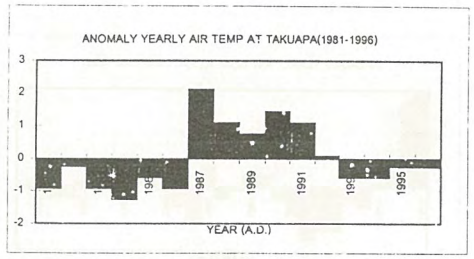


Fig. 33



MEAN PERIOD (1981-1996) = 27.075 DEG.C

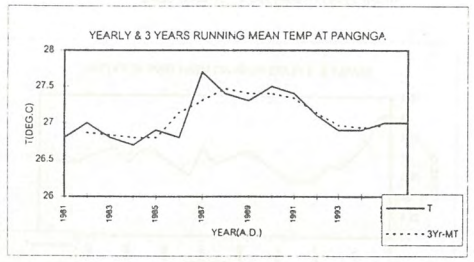
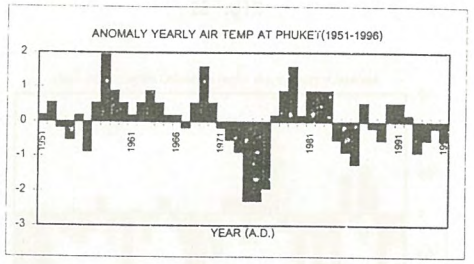


Fig. 34



BASELINE PERIOD (1961-1990) 28.15 DEG.C

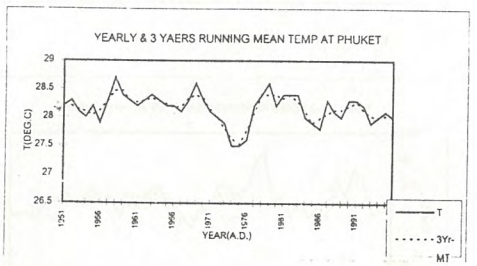
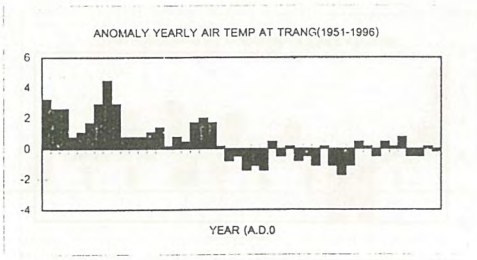


Fig. 35



BASELINE PERIOD (1961-1990) 27.05667 DEG.C

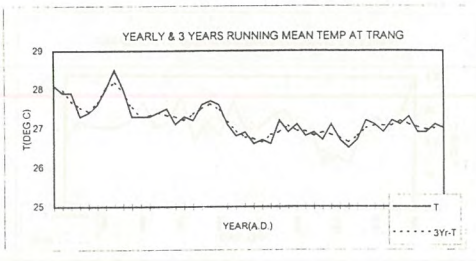
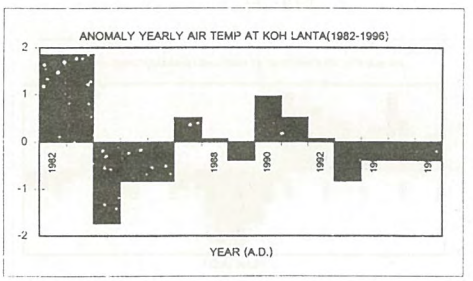


Fig. 36



MEAN PERIOD (1982-1996) = 27.98667 DEG.C

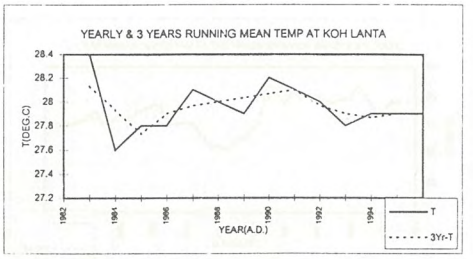
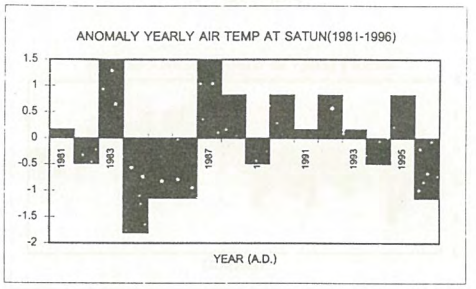


Fig. 37



MEAN PERIOD (1981-1996) = 27.475 DEG.C

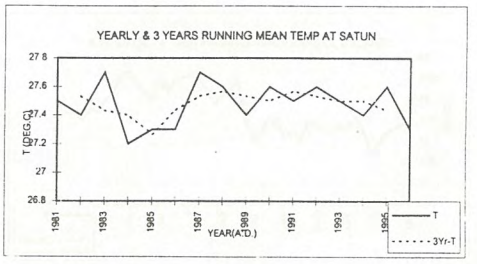
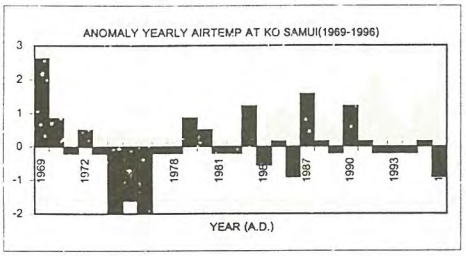


Fig. 38



MEANE PERIOD (1969-1996) = 27.75714 DEG.C

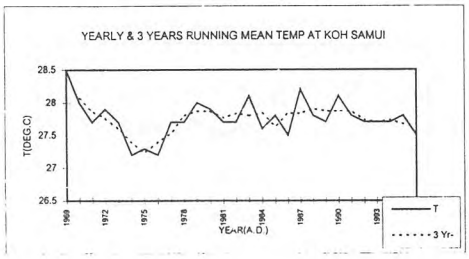
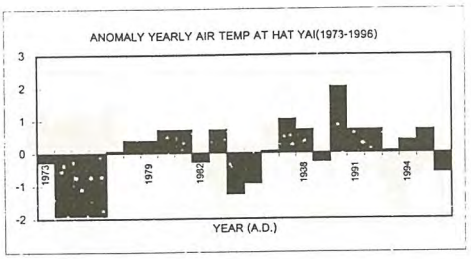


Fig. 27



MEAN PERIOD (1973-1996) = 26.78333 DEG.C

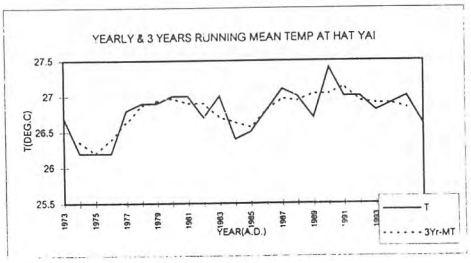
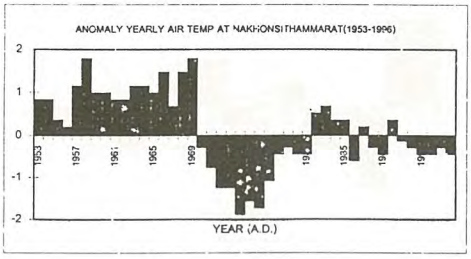


Fig. 30



BASELINE PERIOD (1961-1990) 27.28 DEG.C

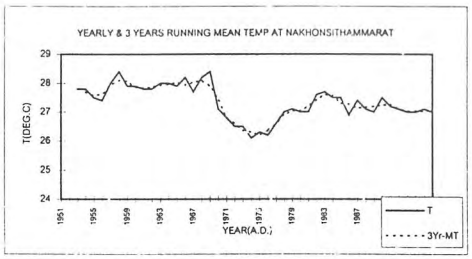
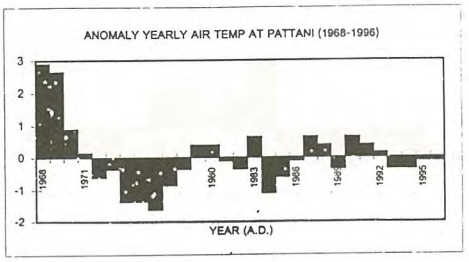


Fig. 28



MEANE PERIOD (1968-1996) = 26.94483 DEG.C

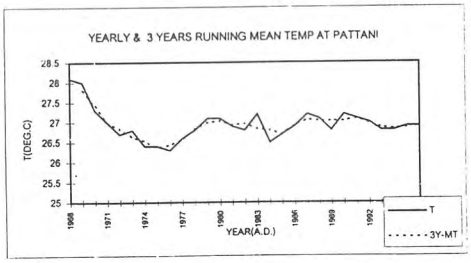
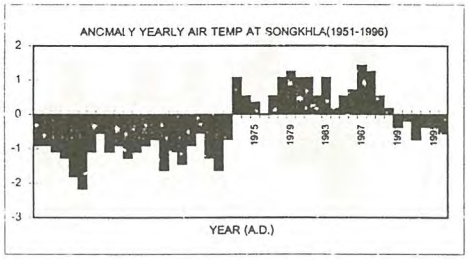


Fig. 31



BASELINE PERIOD (1961-1990) 27.90667 DEG.C

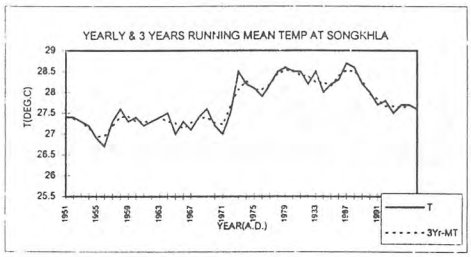
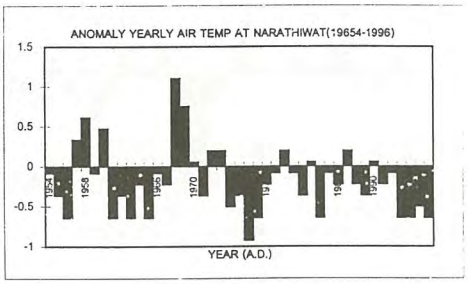


Fig. 29



BASELINE PERIOD (1961-1990) 27.23833 DEG.C

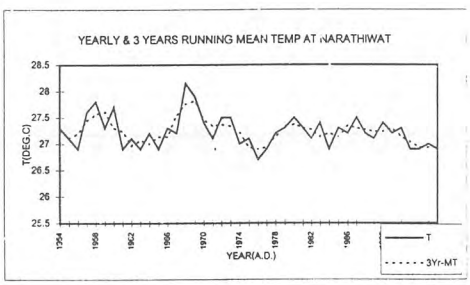
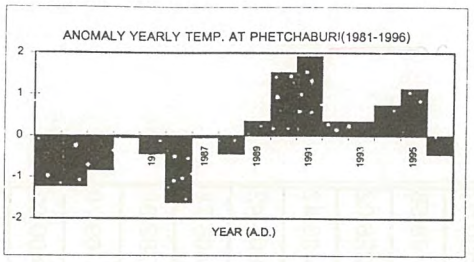


Fig. 32



MEAN PERIOD (1981-1996) = 27.7125 DEG.C

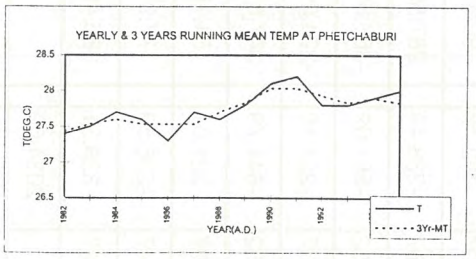
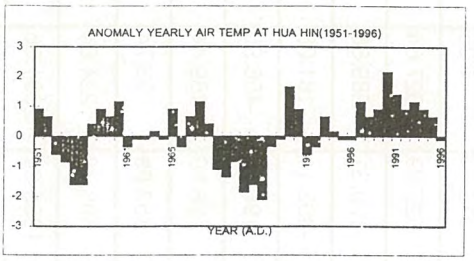


Fig. 21



BASELINE PERIOD (1961-1990) 27.54 DEG.C

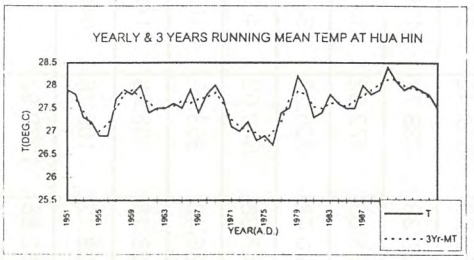
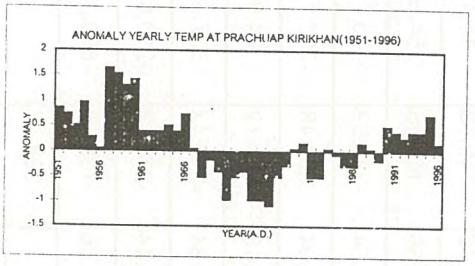


Fig. 22



BASELINE PERIOD (1961-1990)= 27.01333 DEG.C

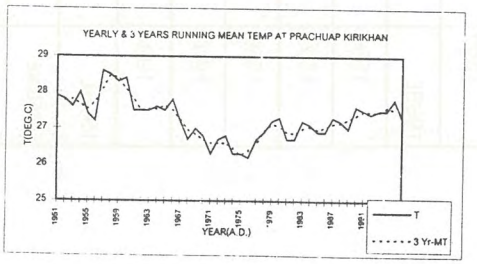
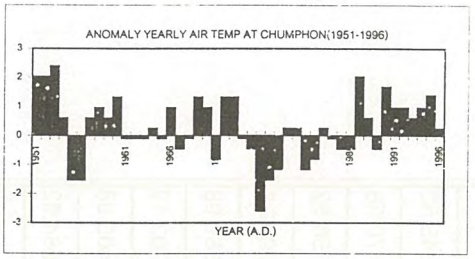


Fig. 23



BASELINE PERIOD (1961-1990) 26.73 DEG.C

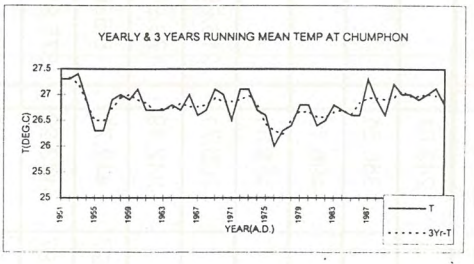
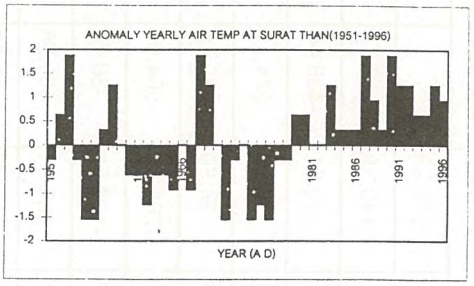


Fig. 24



BASELINE PERIOD (1961-1990)= 26.39667 DEG.C

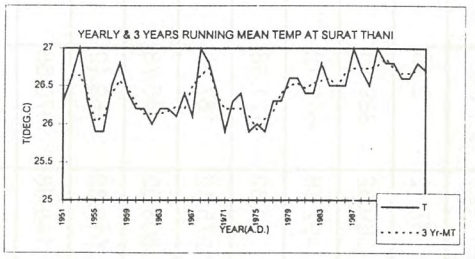
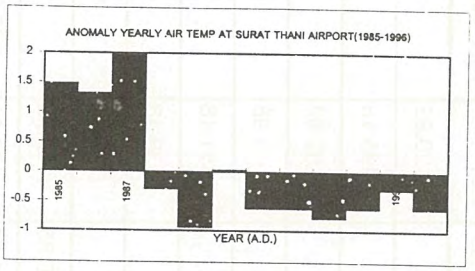


Fig. 25



MEAN PERIOD (1985-1996)= 26.98333 DEG.C

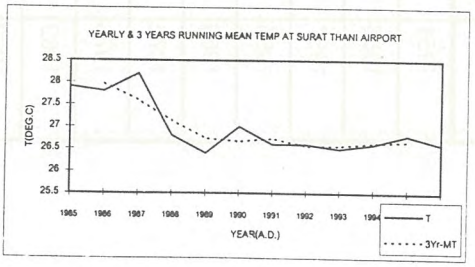


Fig. 26

TABLE 1A RAINFALL ANOMALY AT EAST COAST,SOUTHERN THAILAND IN ENSO YEAR

YEAR	PHETCHABUR 1981-1996	HUAHIN 1951-1996	SURAT AIRPORT 1983-1996	PRACHUAP 1951-1996	CHUMPHON 1951-1996	KOH SAMUI 1968-1996	SURATTHAN 1951-1996	NAKHONSI 1952-1996	HATYAI 1973-1996	SONGKHLA 1951-1996	PATTANI 1969-1996	NARATHIWAT 1951-1996
1951		-120.62		87.42	2.38		546.29			243.01		-346.52
1953		495.18		369.82	389.38		440.39	855.14		356.81		470.58
1957		-62.92		-492.18	-619.12		-712.91	-438.46		-496.19		-356.52
1965		3.98		50.62	121.68		5.39	274.54		459.41		1207.28
1969		651.18		275.12	187.08	-114.46	24.59	-39.16		705.71	216.99	369.98
1972		538.18		503.52	145.78	196.74	-260.01	-564.06		-242.19	-179.91	-703.12
1976		183.68		513.32	-459.12	-123.36	-134.91	-30.16	408.27	442.71	5.539	406.98
1982	96.86	-186.72		-149.98	670.58	-404.36	-366.31	-469.26	59.97	-173.29	-375.91	-684.32
1983	146.66	175.88	-323.91	-283.78	-560.42	-713.66	-126.71	-410.56	345.57	66.51	-61.51	-4.92
1987	255.76	119.48	-15.41	352.22	-601.42	-273.46	-310.11	-4.06	75.07	-492.49	-90.41	-500.52
1988L	89.56	112.18	354.59	-200.38	-738.72	1126.84	527.29	827.64	277.87	-238.49	287.59	128.58
1990	-231.64	-385.62	-435.71	-435.08	-472.82	-131.16	-120.31	-289.56	-456.52	-551.09	-360.81	-1226.02
1991	-245.94	67.48	-371.11	170.02	-236.22	-345.56	-393.11	-181.06	57.37	-227.19	-224.61	-426.42
1992	34.16	-60.72	34.99	-447.38	-540.62	403.94	196.59	-456.96	-437.52	-644.79	-347.61	-606.42
1993	-67.84	-218.42	637.49	-436.48	-363.52	-194.56	726.69	469.44	42.97	321.01	51.79	406.78
1994	-260.44	-274.82	-210.81	-228.28	33.58	-148.26	153.69	63.74	204.47	-206.59	-77.91	782.88
1996L	150.36	-102.12	898.12	428.12	105.18	608.84	598.79	224.64	239.87	328.31	385.49	69.78
BASELINE		998.42		1152.88	1939.92		1635.81	2381.36		2034.69		2460.02
MEAN PERIOD	986.54		1516.61			1931.16			1624.42		1792.21	

TABLE 1B RAINFALL ANOMALY AT WEST COAST,SOUTHERN THAILAND IN ENSO YEAR

YEAR	RANONG 1951-1996	TAKUAPA 1981-1996	PHUKET AIRPORT 1952-1996	PHUKET 1951-1996	KRABI 1982-1996	TRANG 1951-1996	SATUN 1978-1996
1951	-712.28			316.77		1030.65	
1953	140.92		567.48	234.97		631.95	
1957	60.42		498.48	-90.43		610.95	
1965	342.62		-42.42	-32.83		507.25	
1969	-75.38		74.78	187.27		50.25	
1972	-470.38		-462.52	-483.13		-412.15	
1976	-119.08		-356.02	-42.53		57.25	
1982	-623.88	-483.28	-147.82	-237.93	-417.1	332.15	425.93
1983	-22.98	681.82	108.48	179.57	182.6	128.85	201.13
1987	-1060.98	-520.58	-45.82	306.77	457.2	-303.35	236.03
1988L	964.02	105.22	632.38	41.17	187.7	382.25	370.93
1990	-402.08	8.32	-11.12	-317.43	-370.4	-478.65	-195.07
1991	-44.98	-389.98	-407.32	-335.33	-349.1	31.65	197.63
1992	-820.28	-984.28	-696.62	-936.43	-441.5	-276.85	-416.67
1993	-630.08	184.02	605.48	241.87	377.9	233.25	-129.27
1994	1147.12	301.02	183.58	168.27	-153.7	213.95	493.93
1996L	-63.18	81.92	-82.62	-521.63	11.3	518.65	369.93
BASELINE	4183.58		2503.52	2302.33		2187.25	
MEAN PERIOD		3565.68			2184.1		2257.97

TABLE 2A AIRTEMP ANOMALY AT EAST COAST,SOUTHERN THAILAND IN ENSO YEAR

YEAR	PHETCHABUR 1981-1996	HUAHIN 1951-1996	PRACHUAP 1951-1996	CHUMPHON 1951-1996	KOH SAMUI 1968-1996	SURAT AIRPORT 1983-1996	SURATTHANI 1951-1996	NAKHONSI 1952-1996	HATYAI 1973-1996	SONGKHLA 1951-1996	PATTANI 1969-1996	NARATHIWAT 1951-1996
1951		0.36	0.74	0.57			-0.1			-0.51		
1953		-0.24	0.44	0.67			0.6	0.52		-0.61		
1957		0.16	1.44	0.17			0.1	0.72		-0.61		0.24
1965		-0.04	0.34	-0.03			-0.3	0.62		-0.91		-0.46
1969		0.46	-0.16	0.37	0.74		0.4	1.12		-0.31	1.05	0.54
1972		-0.54	-0.46	0.37	0.14		-0.1	-0.78		-0.41	-0.24	0.14
1976		-0.84	-0.96	-0.73	-0.56		-0.5	-1.08	-0.58	-0.01	-0.64	-0.66
1982	-0.31	-0.14	-0.46	-0.23	-0.06		0.003	0.32	-0.08	0.29	-0.14	-0.26
1983	-0.21	0.26	0.04	0.07	0.34		0.4	0.42	0.22	0.59	0.25	0.04
1987	-0.01	0.46	0.14	0.57	0.44	1.21	0.6	0.12	0.32	0.79	0.25	0.14
1988L	-0.11	0.26	0.04	0.17	0.04	-0.18	0.3	-0.18	0.22	0.69	0.15	-0.16
1990	0.39	0.86	0.44	0.47	0.34	0.02	0.6	0.22	0.62	0.09	0.25	0.04
1991	0.49	0.56	0.34	0.27	0.04	-0.38	0.4	-0.08	0.22	-0.21	0.15	-0.16
1992	0.09	0.36	0.24	0.27	-0.06	-0.38	0.4	-0.18	0.22	-0.11	0.05	-0.06
1993	0.09	0.46	0.34	0.17	-0.06	-0.48	0.2	-0.28	0.02	-0.41	-0.14	-0.46
1994	0.19	0.36	0.34	0.27	-0.06	-0.38	0.2	-0.28	0.12	-0.21	-0.14	-0.46
1996L	-0.11	-0.04	0.14	0.07	-0.26	-0.38	0.3	-0.28	-0.18	-0.31	-0.04	-0.46
BASELINE		27.54	27.01	26.73	27.76			27.28		27.91		27.24
MEAN PERIOD	27.71					26.98	26.4		26.78		26.94	

TABLE 2B AIRTEMP ANOMALY AT WEST COAST,SOUTHERN THAILAND IN ENSO YEAR

YEAR	RANONG 1951-1996	TAKUAPA 1981-1996	PHUKET 1952-1996	TRANG 1951-1996	SATUN 1981-1996	KOH LANTA 1981-1996
1951	0.14		0.05	1.04		
1953	-0.46		-0.05	0.84		
1957	-0.56		0.15	0.94		
1965	-0.16		0.05	0.04		
1969	0.44		0.45	0.64		
1972	-0.16		-0.15	-0.26		
1976	-0.56		-0.55	-0.46		
1982	-0.06	-0.07	0.25	-0.36	-0.07	0.41
1983	0.14	-0.27	0.25	0.04	0.22	0.41
1987	0.74	0.62	0.15	0.14	0.225	0.11
1988L	0.44	0.32	-0.05	0.04	0.125	0.01
1990	0.54	0.42	0.15	0.14	0.125	0.21
1991	0.54	0.32	0.15	0.04	0.025	0.11
1992	0.44	0.02	0.05	0.24	0.125	0.01
1993	0.44	-0.17	-0.25	-0.16	0.025	-0.19
1994	0.34	-0.17	-0.15	-0.16	-0.075	-0.09
1996L	0.44	-0.07	-0.15	-0.06	-0.175	-0.09
BASELINE	26.66		28.15	27.06		
MEAN PERIOD		27.07			27.47	27.99

Tracking Urban Planetary Boundary Layer of Hong Kong by Aerosol Monitoring

K.M. Leung[1,2], T.M. Mok[2], K.Y. Chan[1], A.H.P. Ho[2], C. N. Ng[1,2], J.C.L. Chan[1,2], J.L. Gao[2]

[1] Centre for Environmental Science & Technology
[2] Department of Physics and Materials Science
City University of Hong Kong
83 Tat Chee Ave., Kowloon
Hong Kong, SAR, China

Abstract

Boundary layer has a diurnal variation of temperature near the ground with thickness variation ranging from hundreds of meters to a few kilometers. The dynamics of this layer can reveal the trapped pollutants related to atmosphere, climate, and human activities in urban areas of a city. In this paper, we present the first time a comprehensive result of tracking urban planetary boundary layer of Hong Kong (22.3N, 114.7E). The daily and seasonal variations of the mixing depth in the planetary layer over urban areas in Kowloon have been investigated using a ground-base Lidar station situated in the City University of Hong Kong to monitor relative aerosol concentration. The relationships between the aerosol profile, which is used to estimate the depth of the mixing layer, and the virtual potential temperature as well as relative humidity are examined. The Lidar observations and the radiosonde data obtained from the local meteorological station are in close agreement.

1. INTRODUCTION

In a populated city, aerosols are mainly formed by suspended particulates in the air. In particular, dust particles of less than 10 μm in diameter are easily inhaled and unhealthy to people with asthmatics and heart problems. Therefore, aerosol characteristics in the lower troposphere of a city become one of the significant atmospheric parameters in environmental monitoring. The atmospheric echo intensity in the lower troposphere is mainly the aerosol's back-scattered intensity which can in turn approximately represent the aerosol distributions. Hong Kong is a city full of environmental and geographical complexity. The essential geography of the city consists of an island (Hong Kong Island) ten miles wide, standing off the southern edge of a ragged peninsula (Kowloon) to form a long sheltered harbor in the strait with several developing satellite towns in the New Territories connecting the mainland China. Urban areas are characterised by a unique setting : situated on hillsides and facing the sea; mixture of many skyscrapers and clusters of residential quarters with the world's most populated areas where traffic is slow among many narrow streets. Because the International Kai Tak Airport is located in the Kowloon peninsula, the busy air traffic also frequently perturbs and pollutes the lower troposphere of Hong Kong.

Understanding the patterns of mixed layer depth variation in the planetary boundary layer (PBL), where most of the air pollution occurs, will improve our ability to forecast pollution events. Marsik et al. (1995) investigated the diurnal cycle of the mixing depth by several remote sensing techniques and suggested that different collecting systems should be used in order to give a more precise measurement. They also pointed out that it was difficult to determine the mixing depth in the late afternoon period when strong convective clouds developed. The diurnal variation of mixing depth is only a short-term characteristic of the mixed layer. In order to study the long-term patterns of its variation, the seasonal behavior of these patterns should also be examined. While such studies have been made in many places (Padilla et al. 1993, Glaser et al. 1993, Cooper and Enchinger 1994, etc.) these areas are mostly at the higher latitudes. Hong Kong is situated at the subtropical region so that a study of its monthly variation of the mixing depth may help to learn the seasonal behavior of the urban PBL in the lower latitudes. In this paper, we present the first time a comprehensive result of tracking urban PBL of Hong Kong (22.3N, 114.7E). The daily and seasonal variations of the mixing depth in the planetary layer over urban areas in Kowloon have been investigated using a ground-base Lidar station situated in the City University of Hong Kong to monitor relative aerosol concentration. In addition, since cold fronts occur quite often in the winter season in Hong Kong, the variations of the mixing depth in such meteorological events are also studied and will be presented separately.

2. THE LIDAR AEROSOL MONITORING SPECIFICS

In Hong Kong, the first Nd:YAG based lidar was established in 1996 at the City University of Hong Kong and commenced its aerosol monitoring in the middle of 1996. The Lidar system developed (Leung et al., 1994) by the Lidar group of the City University of Hong Kong, located on top of the tallest university building housed in an observational dome. Because of its relatively strategic location (58 m above sea level and near some of the busiest traffic clusters), the Lidar can scan the lower atmosphere of Kowloon urban areas horizontally as well as vertically. Measurements were mainly performed during the daytime. The Lidar transmitter is a Nd:YAG laser which is doubled to 532 nm with pulses of 10 ns at a repetition rate of 10 Hz. The scan-rate is 2-degree per sec. Data acquisition rate is 25 MHz, i.e., one data point per 6-meter. The analog signals collected by a high-gain photomultiplier are digitized using an 8-bit A/D converter and stored in a Pentium-Pro PC computer ready for data processing. A schematic diagram of the Lidar system is shown in Fig.1.

The back-scattered signals can be displayed in the form of aerosol intensity after making range and pulse-energy corrections, as well as noise-reduction processing. The calculation of the aerosol extinction coefficients was based on Klett's method (1980) of solving the Lidar equation. Assume that the ratio of the aerosol extinction coefficient and the back-scatter coefficient is independent of the spatial parameter, then Klett's solution for the aerosol extinction coefficients is :

$$\sigma(R) = \exp(S - S_m) / [(1/\sigma_m) + 2 \int_R^{R_m} \exp(S - S_m) dR'] \quad (1)$$

where $\sigma(R)$ is the extinction coefficient and $S \equiv S(R) = \ln[R^2 P(R)]$ with $P(R)$ to be the normalized Laser echo signal and $R^2 P(R)$, the intensity; $S_m \equiv S(R_m)$ and $\sigma_m \equiv \sigma(R_m)$ with R_m as the monitoring range of interest. For illustration, typical signal processing profiles are depicted in Fig.2.

To perform the tracking of the PBL in urban area of Hong Kong, we use the following strategy in Lidar monitoring of aerosol dynamics. Cooper and Enchinger (1994) have used vertical scan to observe the structure of the PBL and estimate the mixed layer depth over Mexico City. For this work, we have used both vertical and azimuthal scanning arrangements. The vertical scan appears as a wedge-shaped angle with the scan direction being perpendicular to the ground and the lidar is at the apex of the triangle while the Earth's surface is the base. A routine scanning arrangement was made from late September 1996 to January 1998 with some exceptions due to weather or instrumentation problems. To study the daily variation of the PBL, data were taken in approximately 3 hours interval (i.e., 0800, 1100, 1400, 1700, and 2000 Local Time) twice a week. Non-routine measurements were also made based on special meteorological forecast announced by the local meteorological station. For example, in Hong Kong a cold frontal passage is a common occurrence during the winter season. Northerly winds associated with such passages often carry large amount of pollutants from mainland China. The winds are also very strong and convective clouds usually occur with heavier precipitation. All of these can cause noticeable change in aerosol dynamics near the surface area of the city. We have attempted to monitor PBL as many cold frontal passages as allowable. Such measurements were made from one day before to one day after the passage at a 3-hours interval during the daytime. An illustration of these measurements will be presented in the following workshop.

3. TRACKING URBAN PBL OF HONG KONG BY AEROSOL MONITORING

a. Diurnal variation of mixing layer depth

It has been shown that the atmospheric PBL region can have a stratified structure which may respond to surface forcing with a time scale of about one hour or less (Stull, 1988). Forcing mechanisms may include contributions from frictional fog, evaporation, transportation, heat transfer, pollutant emission and other unknown atmospheric dynamics. An example of this stratified structure is shown in Fig. 3a, which displays a contour plot of the lidar backscattering coefficients profile at 1950LT on 11 January 1997. This is the averaging result of 12 vertical scans from 27° to 51° azimuth. Marked stratification can be found within the altitude range of 400-1800m, at the regions of 640-700m and 1100-1700m. Such clear stratified structure gives a good description of the atmospheric PBL over Hong Kong. This structure is in good agreement with the result obtained from the radiosonde data (Fig. 3b). Under the basic assumption that the top of the mixed layer is located at the position where the first sharp increase in virtual potential temperature is found, the mixed layer depth can be identified at 620m altitude, which is the height where a horizontal boundary is found

in Fig. 3a. This comparison demonstrates that the idea of applying lidar to track the PBL via aerosol monitoring is practical. In this work, we used the Lidar signal to estimate the mixed layer depth where the region having a sudden decrease in backscattering intensity which is consistent with Kaimal's work (1982).

A typical PBL pattern of the diurnal variation in Hong Kong tracked by Lidar aerosol signals is shown in Fig. 4. The tracking was performed on 16 December 1997 starting at 800LT with a shallow mixed layer developing near the ground as the sunlight began to warm-up the local surface. The mixed layer depth was estimated to be 500m and then increased quickly to 800m at 1400LT. In the early afternoon, the depth continued to increase and reach its maximum of about 1100m at around 1700LT. At that time, a capping layer stayed on the top of the mixed layer, and the aerosols were also much more concentrated in that region. The mixed layer depth remained almost constant over the afternoon. With the beginning of the sunset, the mixed layer depth decayed quickly to 700m by 2000LT.

b. Seasonal variation of mixing layer depth

In contrast to the diurnal variation of mixed layer depth, the seasonal variation may be driven by a long-term weather pattern that warrants a comparison to be made only between monthly data instead. The following analysis is based on the measurements from the late autumn of 1966 (early October) to the mid-winter of 1977 (end of January). The monthly averaged diurnal variation of the mixed layer depth shows that the average mixed layer depth decreases from the late autumn to mid-winter (Fig. 5) Such a pattern mainly results from the thermal energy exchange between the air in the mixed layer and the earth surface. In late autumn, the temperature at the earth surface is higher than that in winter, and the sum of the thermal energy emitted from the earth surface to the lower mixed layer is also much larger. The entrainment zone (EZ) may therefore appear at a higher altitude. Another reason affecting the mixed layer depth is the different azimuths of the sun in autumn and winter. An analysis of the rate of change of the mixed layer depth for the three months indicates that the mixed layer depth varies similarly. In general, in the late morning, the mixed layer depth increases at the fastest rate of 17-25 m per hour, and then continues increasing at the slower rate of 5-13 m per hour. The rate of change of the mixed layer depth reaches its maximum in the mid-afternoon and begins to decrease. At sunset time, it decreases at nearly the same rate of 37 m per hour. Such a periodic property describes the nature of the development of inversions. Table 1 summarizes the mixed layer depth for the late afternoon for a period of 3 months. The seasonal variation of the maximum mixed layer depth shows a declining trend of the mixed layer depth with time (Fig. 6).

Table 1. Summary of the late afternoon mixed layer depth tracked by Lidar aerosol monitoring.

Date	*Season*	*Mixed layer depth (m)*
12 Oct 1996	Autumn	1400
19 Oct 1996	Autumn	1300
26 Oct 1996	Autumn	1000
30 Nov 1996	Early winter	1300
05 Dec 1996	winter	700
14 Dec 1996	winter	1200
17 Dec 1996	winter	1000
19 Dec 1996	winter	1200
30 Dec 1996	winter	500
31 Dec 1996	winter	800
07 Jan 1997	winter	900
09 Jan 1997	winter	600 and 1000
11 Jan 1997	winter	700 and 1200

c. Comparison between the radiosonde data and lidar tracking urban PBL

To understand the urban PBL structure, radiosonde data are often used to identify the mixed layer depth. In our work, comparisons between the virtual potential temperature, relative humidity, wind speed and lidar backscattering data are also made. From the radiosonde data, the inversion region can be defined as the location where a sharp increase in virtual potential temperature or decrease in relative humidity first occurs.

In general, it is difficult to identify the fine structure of the lidar extinction coefficient profile due to its low signal to noise ratio in daytime tracking. Late-afternoon Lidar data is easier for such comparison. However, a qualitative correlation of the mixed layer depth can be realized. An illustrated comparison is shown in Fig. 7.

4. CONCLUSIONS

Although the report of the Lidar measurements and data analysis of urban PBL of Hong Kong for this study is preliminary, this is the first time a comprehensive result of tracking urban PBL of Hong Kong (22.3N, 114.7E) for a long-term observation. Hong Kong is situated at the subtropical region so that a study of this kind may help to learn the seasonal behavior of the urban PBL in the lower latitudes. The diurnal variation of the mixed layer depth has been verified to be consistent with the changes in virtual potential temperature and relative humidity provided by the radiosonde measurements. Analyses of the seasonal variation of the mixed layer depth basically depends on the energy exchange between the earth surface and the mixed layer. The rate of change of the mixed layer depth changes faster in the warmer days than in cooler ones. The mixed layer depth is much more stable in the mid-afternoon than in the morning or night unless rapid change of weather episodes occur such as a cold frontal passage. As a result, such a property indicates the capping inversion is more stable at the top of the mixed layer in the mid-afternoon and such inversions become less active in winter. In addition, from autumn to winter, a decreasing trend of the mixed layer depth was found. To improve our understanding of the urban PBL of Hong Kong, further work needs to be pursued. For example, we plan to obtain more Lidar data during the coming spring and summer which may provide further information of the mixed layer in the subtropical region.

ACKNOWLEDGEMENTS

The authors wish to thank Mr. T. J. Lin, Mr. J. Zhu, and Mr. Y. M. Lee for their contributions in the initial PBL measurements. This work was supported by the Strategic Research Grants of the City University of Hong Kong (Grants 7000429 and 7000646) with additional support provided by the Faculty of Science and Technology of the City University of Hong Kong.

REFERENCES

Cooper, D. I. and W.E. Enchinger, "Structure of the Atmosphere in an Urban Planetary Boundary Layer from Lidar and Radiosonde Observations", J. Geophys. Res., **99**, 22, 937-22, 948, 1994.

Glaser, E., N. Dagan, O. Furer, M. Gamliel, A. Yogev, S. Fastig, U. Dayan, and Y. Benayahu, "A comparison of balloon soundings and lidar scans for measuring the height of the turbulent mixed layer at a coastal site in Israel", *Wat. Sci. Tech.* **27**, 271-278, 1993.

Kaimal, J. C., N. L. Abshire, R. B. Chadwick, M.T. Decker, and W. H. Hildebrand, "Estimation the depth of the daytime convective boundary layer", *J. Appl. Meteor.*, **21**, 1123-1129, 1982.

Klett, J. D., "Stable analytical inversion solution for processing lidar returns", Applied Optics **2**, 211-220, 1980.

Leung, K. M., T. J. Lin, and J. C. L. Chan, "Lidar measurement of wind velocity by tracking a single cloud movement", Abstracts of Papers of the 17th International Laser Radar Conference, 575-577, Sendai, Japan, 25-29 July 1994.

Marsik, F. J., K. W. Fischer, T. D. McDonald, and P. J. Samson, "Comparison of methods for estimating mixing height used during the 1992 Atlanta Field Intensive", *J. Appl. Meteor.*, **34**, 1802-1814, 1995.

Padilla, H. G., A. C. Leyva, and P. A. Mosino, "An analysis of Daily Humidity Patterns at a Mountainous and Urban Site in a Tropical High-Altitude Region", *J. Appl. Meteor.*, **32**, 1638-1646, 1993.

Stull, R. B., "An Introduction to Boundary Layer Meteorology", Kluver Academic Press, Chs.1, 11, 12, 1988.

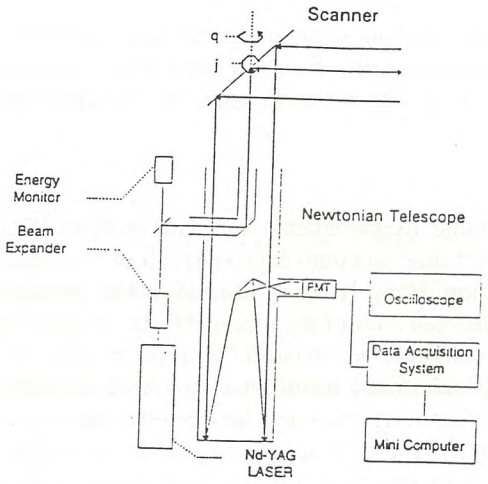


Fig. 1. Schematic diagram of the Lidar system at the City University of Hong Kong.

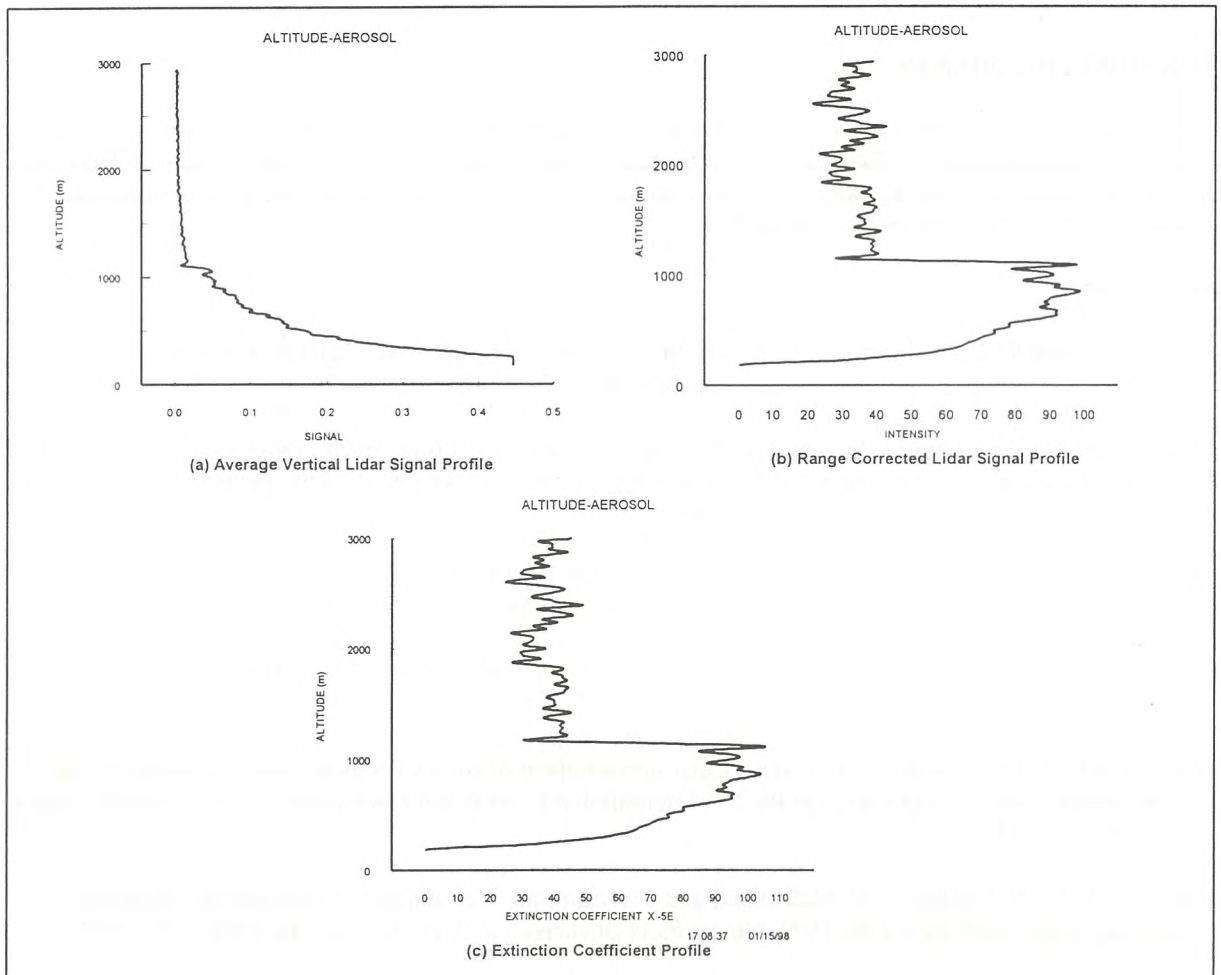


Fig. 2. Different profiles derived from Lidar backscattering signals.

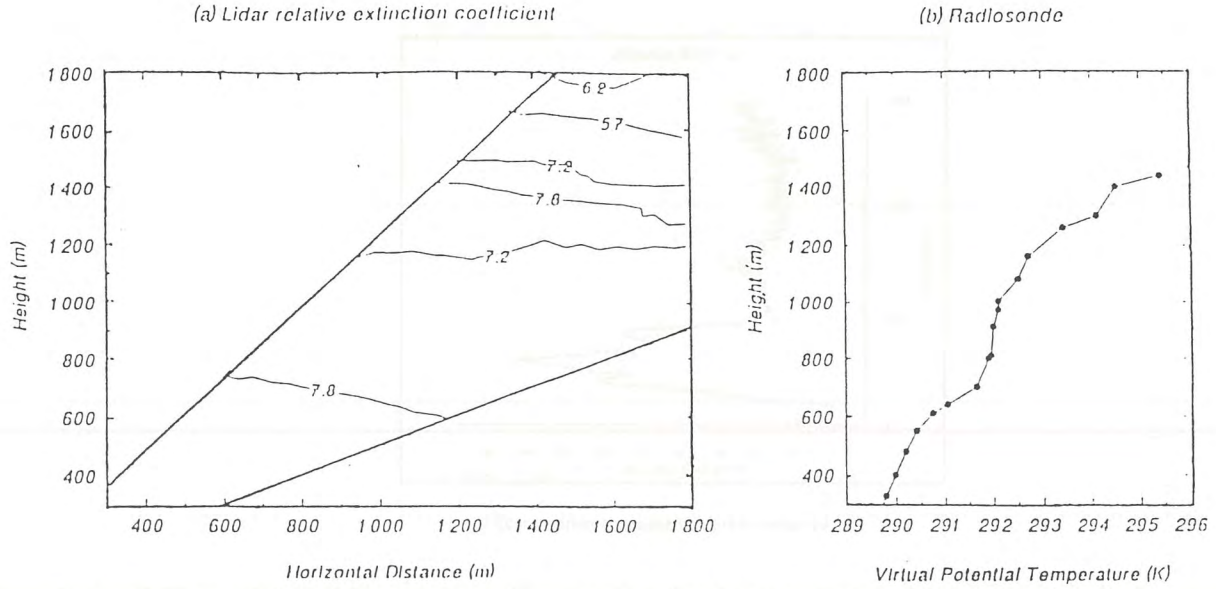
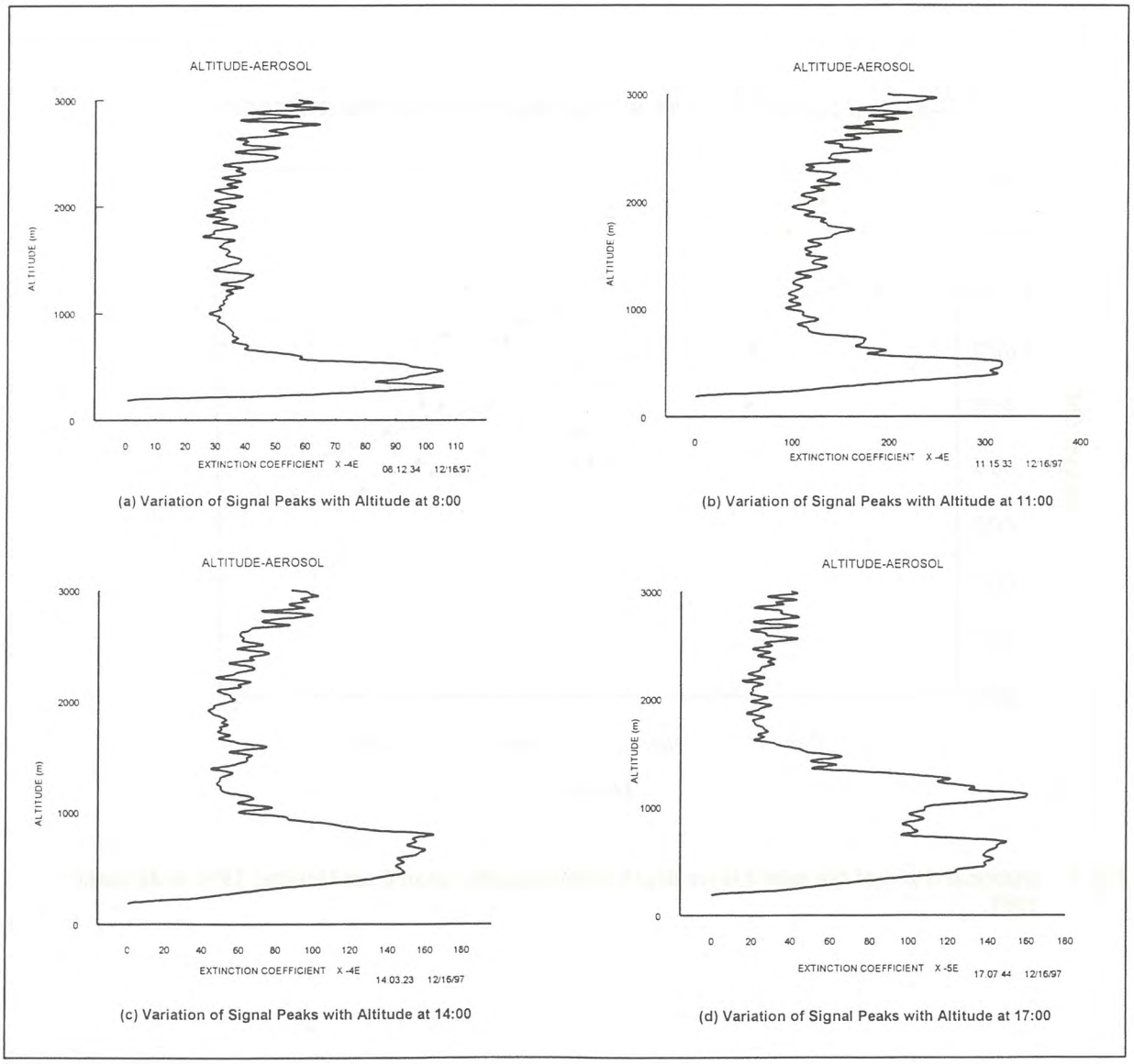
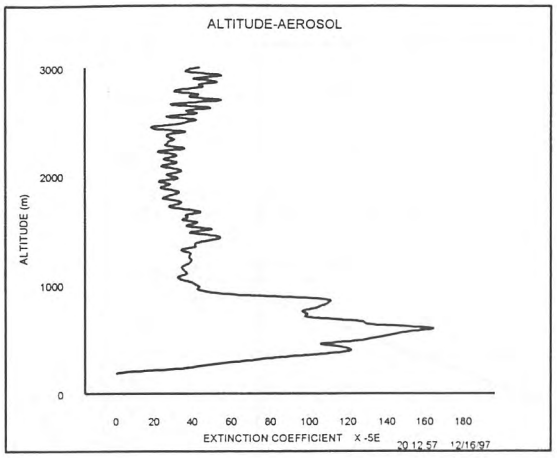


Fig. 3. (a) 2-D contour map of Lidar aerosol extinction coefficients of the mixed layer; and (b) Vertical variation of virtual potential temperature with height from radiosonde data at 2000LT on 11 January 1997.





(e) Variation of Signal Peaks with Altitude at 20:00

Fig. 4. Daily variation (a) to (e) of aerosol extinction profiles measured by Lidar on 16 December 1997.

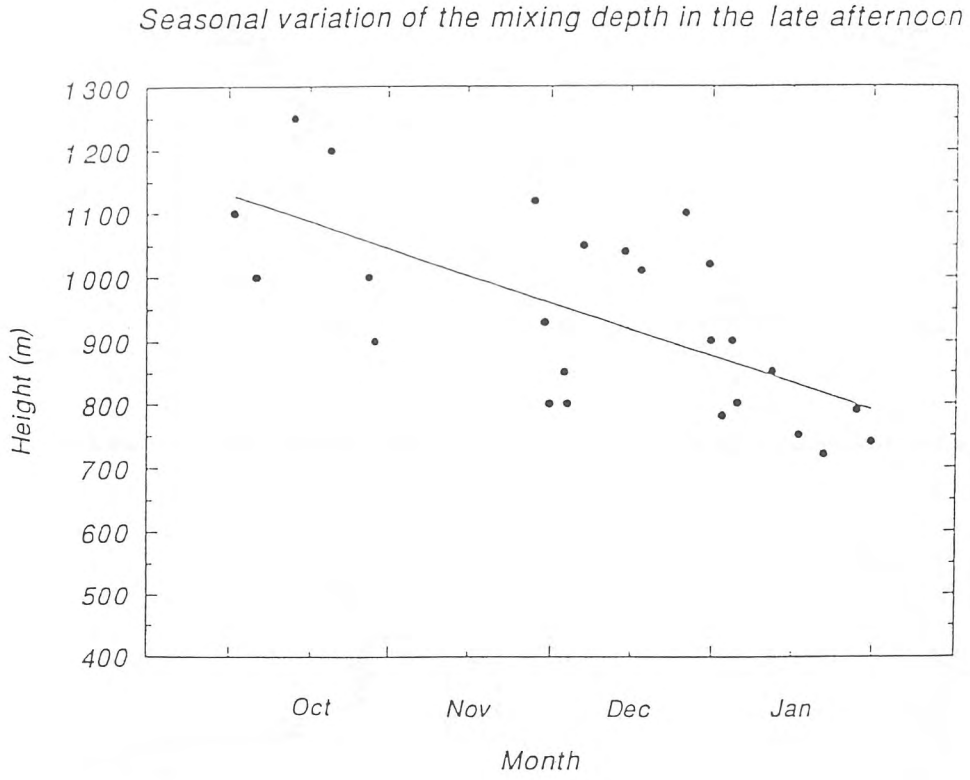


Fig. 5. Seasonal trend of the mixed layer depth in the late afternoon from October 1996 to January 1997.

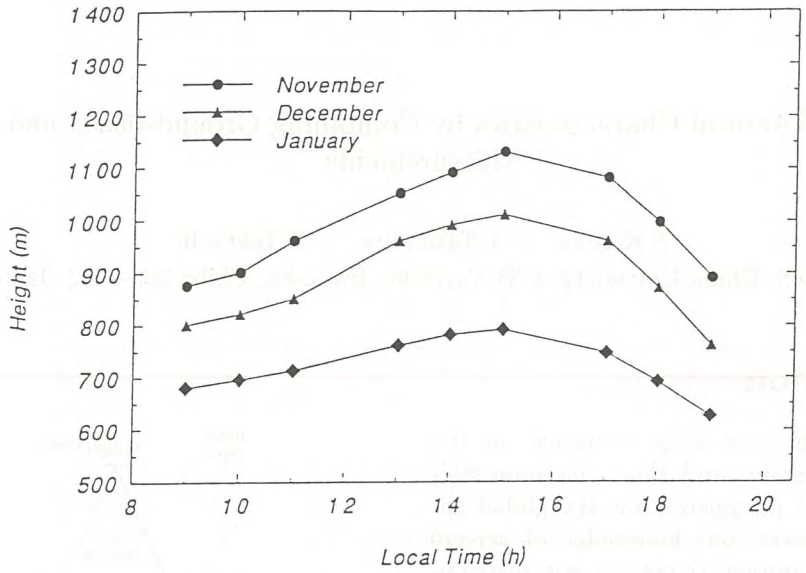


Fig. 6. Monthly average of the mixed layer depth from November 1996 to January 1997.

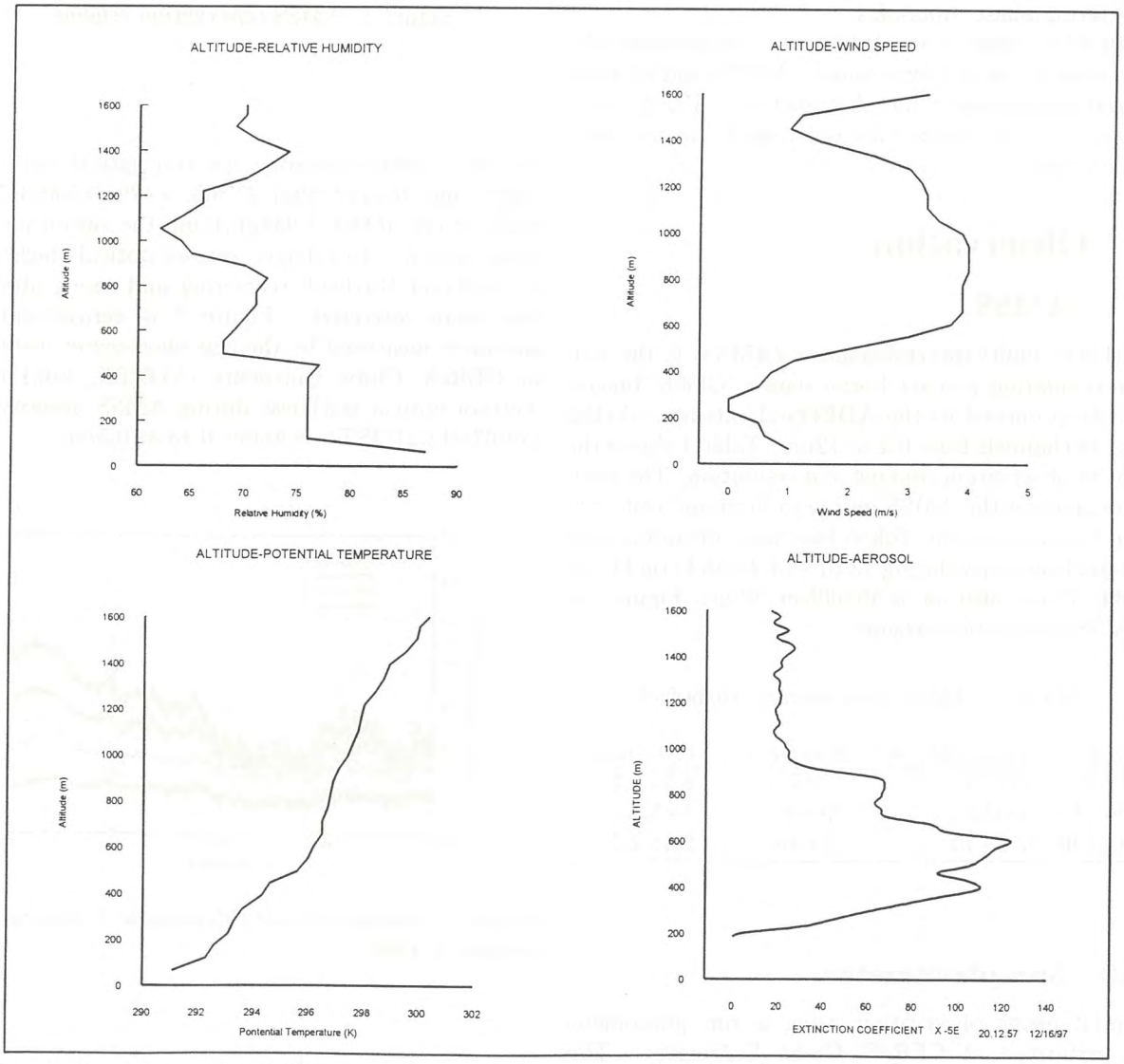


Fig. 7. Comparison of variation of radiosonde data with Lidar monitored aerosol extinction coefficient profile measured at 20:00LT on 16 December 1997.

Retrieval of Aerosol Characteristics by Combining Ground-based and airborne Measurements

S.Kaneta T.Takamura N.Takeuchi
CEReS, Chiba University, 1-33 Yayoicho, Inage-ku, Chiba 263-8522, Japan

1 Introduction

Atmospheric aerosols have large influence on the earth-atmosphere system, and their characteristics are one of important parameters for the global climate system. However, our knowledge of aerosol characteristics (e.g., optical thickness, size distribution etc.) and their spatial and temporal variation is still not enough. There are many literatures about studies of global aerosol properties using space-borne sensor [6, 5, 2]. But these methods require assumed aerosol parameters (such as size distribution function, scattering phase function.)

In this studies we carried out the simultaneous observation by an airborne sensor (AMSS) and ground-based instrument (sun photometer). Using these data, we try to estimate aerosol optical thickness over Tokyo bay.

2 Observation

2.1 AMSS

Airborne multi-spectral scanner (AMSS) is the sensor simulating a space-borne sensor, Global Imager (GLI), proposed to the ADEOS-II satellite. AMSS has 46 channels from 0.4 to 12μm. Table 1 shows the AMSS observation channel and resolution. The measurements of the AMSS on-board in an aircraft were carried out over the Tokyo bay area, including over Chiba University during 13:07~13:21(JST) on Dec 3, 1996. Flight altitude is 19500feet (6km). Figure 1 is AMSS observation scheme.

Table 1. AMSS resolution at 19500feet

ch.#	wavelength(μm)	pixel size(m)	IFOV(mrad)
1~37	0.4~1	15×7	2.5×1.2
38~42	1~3.7	30×30	5×5
43~46	7.5~10	15×15	2.5×2.5

2.2 Sun photometer

Simultaneous observation using a sun photometer is performed at CEReS, Chiba University. This

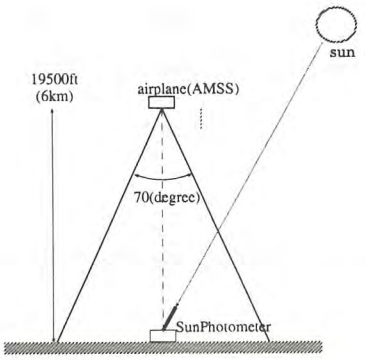


Figure 1. AMSS observation scheme

sun photometer measured spectral optical thickness with 8 interference filter (0.368, 0.420, 0.500, 0.532, 0.675, 0.778, 0.880, 1.033μm) and the silicon photodiode sensor. To retrieve aerosol optical thickness, we subtract Rayleigh scattering and ozone absorption were corrected. Figure 2 is aerosol optical thickness measured by the sun photometer installed at CEReS, Chiba University (35.620N, 140.120E). Aerosol optical thickness during AMSS observation (13:07~13:21(JST)) is about 0.15 at 0.5μm.

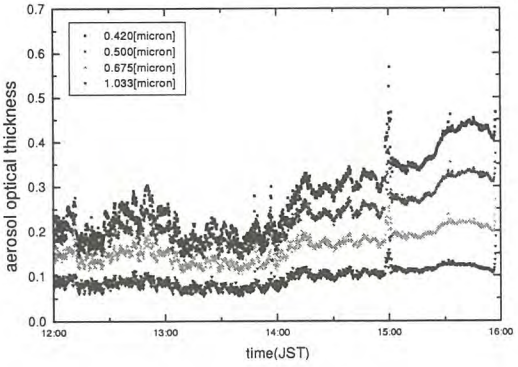


Figure 2. Aerosol optical thickness at Chiba on December 3, 1996

3 Analysis of AMSS data

To retrieve aerosol optical thickness over Tokyo bay from the aircraft data, some aerosol basic parameters, such as single-scattering albedo, asymmetry factor, were assumed using the grand-based data of the sun photometer. The flow of data analysis is shown in Figure 3.

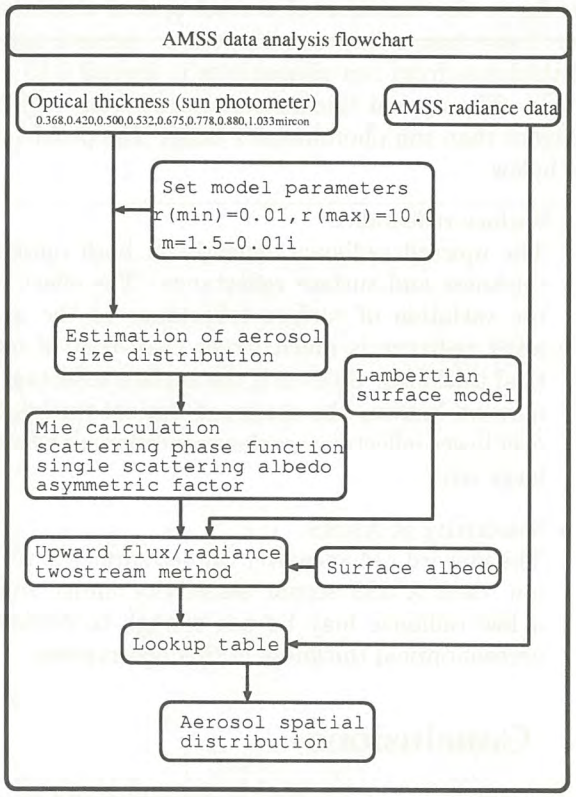


Figure 3. Aerosol data analysis flowchart

3.1 Aerosol size distribution

The relation of aerosol optical thickness and aerosol size distribution can be written as [3]

$$\tau_A(\lambda) = \int_0^\infty \pi r^2 Q_{\rm ext}(r, \lambda, m) n_c(r) dr, \qquad (1)$$

where r is particle radius, m is the refractive index of the aerosol particles, λ is wavelength of incident illumination, and $Q_{\rm ext}(r, \lambda, m)$ is the extinction efficiency factor from Mie theory. $n_c(r)$ is the columnar aerosol size distribution. In present studies we assume $m = 1.5 - 0.01i$, and particle size range is $0.01 \leq r \leq 10.0\mu$m. By inverting equation (1) then we can estimate aerosol size distribution (Figure 4).

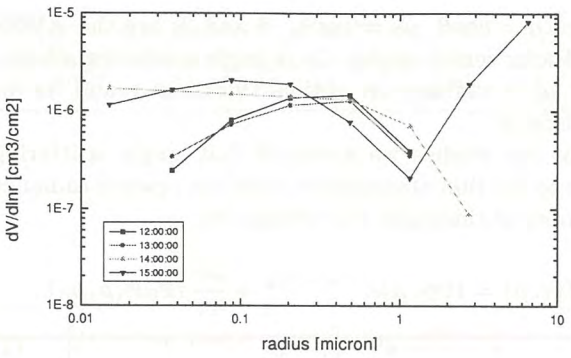


Figure 4. Aerosol size distribution at Chiba on December 3, 1996

3.2 Aerosol phase function

Aerosol phase function were calculated from Mie theory using aerosol size distribution estimated by inversion of aerosol spectral optical thickness [1]. In this calculation the complex refractive index of aerosol is assumed to be $1.5\text{-}0.01i$. Figure 5 shows the scattering phase functions for several wavelengths. These are not so serious difference between each wavelengths for the sharp forward scattering.

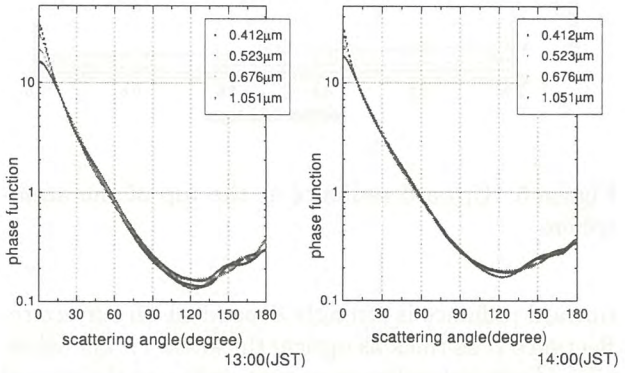


Figure 5. Scattering phase functions at Chiba on December 3, 1996

3.3 Upward radiance at AMSS altitude

The azimuthally independent radiative transfer equation for diffuse radiation can be written as [4]

$$\mu \frac{dI(\tau,\mu)}{d\tau} = I(\tau,\mu) - \frac{\tilde{\omega}_0}{2} \int_{-1}^{1} I(\tau,\mu') P(\mu,\mu') d\mu' - \frac{\tilde{\omega}_0}{4\pi} \pi F_0 P(\mu,\mu_0) e^{-\tau/\mu_0}. \qquad (2)$$

Here $\mu = \cos\theta$, $\mu_0 = \cos\theta_0$, θ and θ_0 are the AMSS and solar zenith angles. $\tilde{\omega}_0$ is single scattering albedo. $I(\tau, \mu)$ is radiance at optical thickness τ and its direction μ.

In our studies we assumed that single scattering due to the thin atmosphere, then the upward radiance at optical thickness τ is written by

$$I(\tau,\mu) = I(\tau_0,\mu)e^{-(\tau_0-\tau)/\mu} + \frac{\tilde{\omega}_0}{4\pi}\pi F_0 P(\mu,\mu_0) \times \frac{\mu_0}{\mu+\mu_0}e^{\tau/\mu}\left[1-e^{-(1/\mu+1/\mu_0)(\tau_0-\tau)}\right]. \quad (3)$$

In equation (3), we calculated the upward radiance $I(\tau_0, \mu)$ by two-stream approximation [4] with assumption of Lambertian surface. Figure 6 represents relation of optical thickness and upward radiance in each surface reflectance. In Figure 6, it is clear that

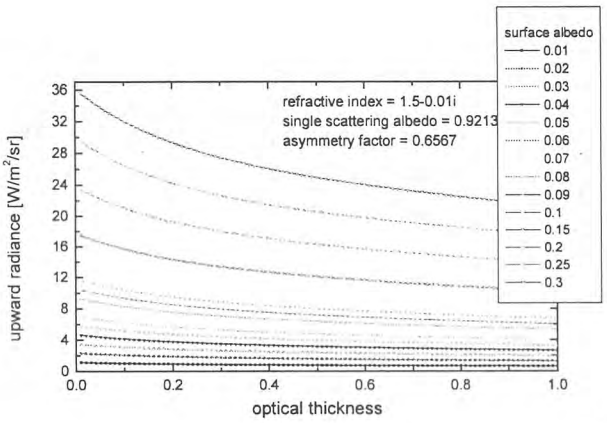


Figure 6. Upward radiance at the top of the atmosphere

upward radiance is strongly dependent on surface reflectance R as thick as optical thickness τ. The variation of upward radiance corresponding to the optical thickness is quite small, as shown in Figure 6. It should be noted to take care of this relation on retrieving aerosol optical thickness from AMSS data. That is,

- Over the land surface, the surface reflectance varies very wide range then we must know the surface reflectance in advance.
- Over the sea surface, it is easier to get the precise surface reflectance, but it is so low that the sensor sensitivity should be required to be high.

In our study we try to retrieve aerosol optical thickness over sea surface (Tokyo bay) according to the flow in Figure 3. Using the lookup tables, we evaluate AMSS's upward radiance data, with the surface reflectance R, 0.06.

4 Results

We retrieved aerosol optical thickness over Tokyo bay. The retrieved aerosol optical thickness is shown in Figure 7. The top of this figure is Yokosuka (south bound), and the bottom region is Chiba (north bound). The dark region (optical thickness is 0) is land surface, where aerosol optical thickness can not retrieved because of high surface reflectance. In this figure the variation of aerosol optical thickness over Tokyo bay is between 0.2 to 0.8. Aerosol optical thickness from sun photometer is around 0.15 at 0.5μm. The optical thickness retrieved from AMSS is higher than sun photometer's value. The problems are below.

- Surface reflectance
  The upward radiance depends on both optical thickness and surface reflectance. The effect of the variation of surface reflectance to the upward radiance is much larger than that of optical thickness. So even if the surface reflectance may be known, the retrieved optical thickness over lower reflectance surface condition may have large error.
- Sensitivity of AMSS
  The upward radiance over the sea surface is very low then AMSS sensor sensitivity under such a low radiance may be not enough to retrieve aerosol optical thickness in this observation.

5 Conclusions

Using airborne and grand-base measurements data, we tried to retrieve an aerosol optical thickness over Tokyo bay. The preliminary results were not so good accordance with the ground-based observations. For more accurate retrieval, we continue the following analysis.

- Using two altitude data
  In this observation we performed measurement at two altitude. We can reduce the influence of surface reflectance with those data.
- Using multi-spectral data
  But AMSS has 46 channels, can be used to retrieve aerosol optical thickness more accurately.
- Using aerosol vertical profile (LIDAR) data
  Aerosol vertical profile is very useful for retrieval. We should use those data.

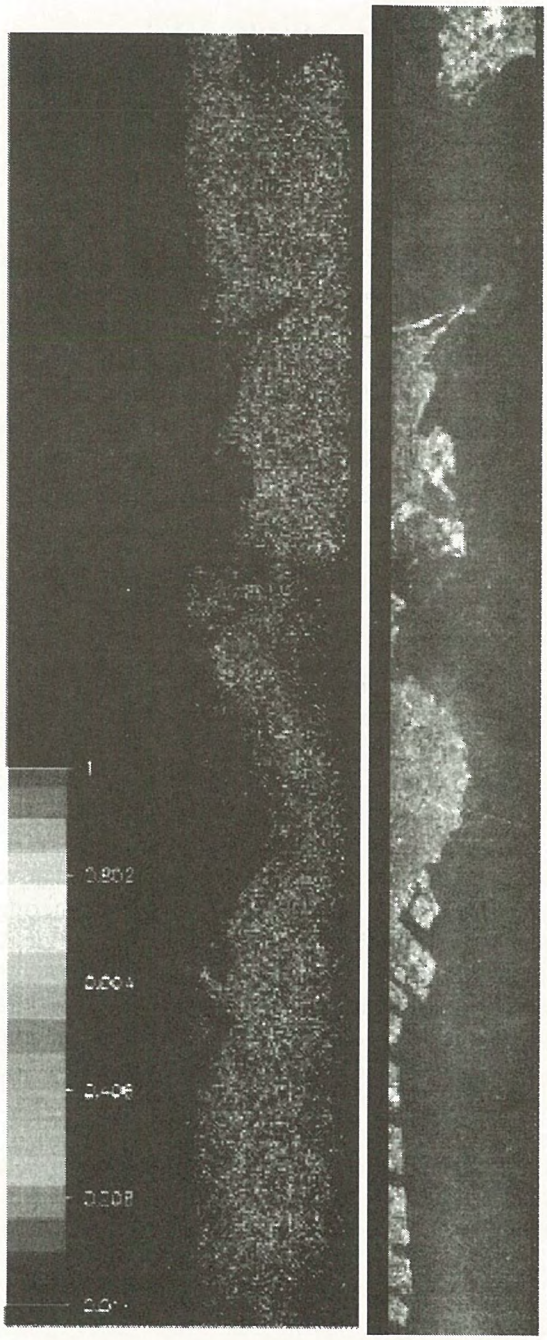


Figure 7. Retrieved optical thickness over Tokyo bay (left side), right side is AMSS radiance image as same place as left one, where λ=0.5228μm $\tilde{\omega}_0$=0.9213 g=0.6874 R=0.06

References

[1] Barber, P. W., and Hill, S. C. *Light Scattering by Particles: Computational Methods.* World Scientific Publishing, 1990.

[2] Isakov, V. Y., Feind, R. E., Vasilyev, O. B., and Welch, R. M. Retrieval of aerosol optical thickness from aviris data. *International Journal of Remote Sensing* **17**, (1996), 2165–2184.

[3] King, M. D., Byrne, D. M., Herman, B. M., and Reagan, J. A. Aerosol size distributions obtained by inversion of spectral optical depth measurements. *Journal of the Atmospheric Sciences* **35**, (1978), 2153–2167.

[4] Liou, K. N. *An Introduction to Atmospheric Radiation.* New York: Academic Press, 1980.

[5] Rahman, H. Atmospheric optical depth and water vapour effects on the angular characteristics of surface reflectance in noaa avhrr. *Internatinal Journal of Remote Sensing* **17**, (1996), 2981–2999.

[6] Wang, M., and Gordon, H. R. Estimating aerosol optical properties over the oceans with the multiangle imaging spectroradiometer: some preliminary studies. *Applied Optics* **33**, (1994), 4042–4057.

An Attempt for Ground Truth Validation of MOS-B Radiance Data

Wolfgang von Hoyningen-Huene, Universidade de Evora
Peter Posse, DLR, Institut for Space Sensor Technology Berlin

Abstract

Combined measurements of spectral aerosol optical thickness, angular sky brightness together with spectral water leaving radiance are used to produce a complete set of experimental based input data to be used for the solution of the radiative transfer equation. The up-welling radiances for the top of the atmosphere obtained with the IMS program of Nakajima & Tanaka (1988) are compared with experimental data from two MOS-B overpathes in the German Baltic Sea and North Sea region. In the first case (Ruegen island, Baltic Sea) the ground based data are obtained at continental-marine-mixed aerosol conditions and have been far away of radiation conditions of the commonly used aerosol properties: no power-law-like spectral behavior of the aerosol optical thickness, increased side scattering compared with the most used assumption of validity of Mie-scattering. In the second case (Helgoland, North Sea) a wet marine situation was characteristic.

1. Introduction

An essential step in the validation of satellite radiances, the evaluation of their information content and the development of retrieval procedures for atmospheric and surface properties is their intercomparison with ground truth data. Therefore ground truth experiments have to be a integrated part of the technical and methodical improvement of the data processing on different levels and the quality assurance of the satellite data.

In most cases the attempt is made, to reproduce the satellite radiances by model assumptions of radiative properties of the atmosphere and the surface as spectral optical thickness, phase function, single scattering albedo and bidirectional surface reflection function. Here either radiation models for aerosols, as e.g. *Shettle & Fenn, 1979, d'Almeida et al., 1991*, c.f. *Heinemann, 1995* or correlative relationships between optical thickness and the atmospheric path radiance are used *Wilson, 1979* or spectral ratios between different spectral channels *Gordon et al., 1978, 1987, 1989, 1991,* are used, to estimate the atmospheric contribution within the satellite radiance. All these ways assume more or less stabile aerosol conditions and idealized aerosol models and neglect the temporal and spatial variability of the aerosol.

Therefore the reproduction of satellite radiances is a process of tuning of a number of open parameters without knowing the real atmospheric conditions. Though only ground truth experiments give the opportunity to connect satellite radiances with the real atmospheric and surface conditions and helps in the further development of atmospheric correction models.

Satellite ground truth validations can be carried out as a physical closure experiment between experimental radiances obtained by the space borne radiometer (here MOS-B spectral radiance data) and the modeled up-welling radiances basing on complete sets of spectral atmospheric and surface parameters determined by ground based radiation measurements. Basics is a complete experimental data set of ground based radiation data of atmospheric as well as surface properties to modelize the up-welling radiances to the satellite position by an exact enough radiation transfer routine including multiple scattering.

This contribution presents the approach and first results of two ground truth experiments integrating atmospheric and surface radiative measurements in a kind presented before during MOS overpathes.

2. Description of the Ground-Truth-Experiment and Results

One first ground-truth experiment, carried out during an overpath of MOS/IRS at 23. September 1996, consists of different measurements of the main atmospheric optical parameters by spectral sun- and sky radiometers and the spectral water leaving surface reflectance. The location within the Greifswald Bight at the German Baltic Sea coast near the island of Ruegen. The positions of atmospheric measurements by the University of Leipzig

and the DLR and the connected ship measurements of the water reflectance made by the Institute of Baltic Research are shown in fig 1.

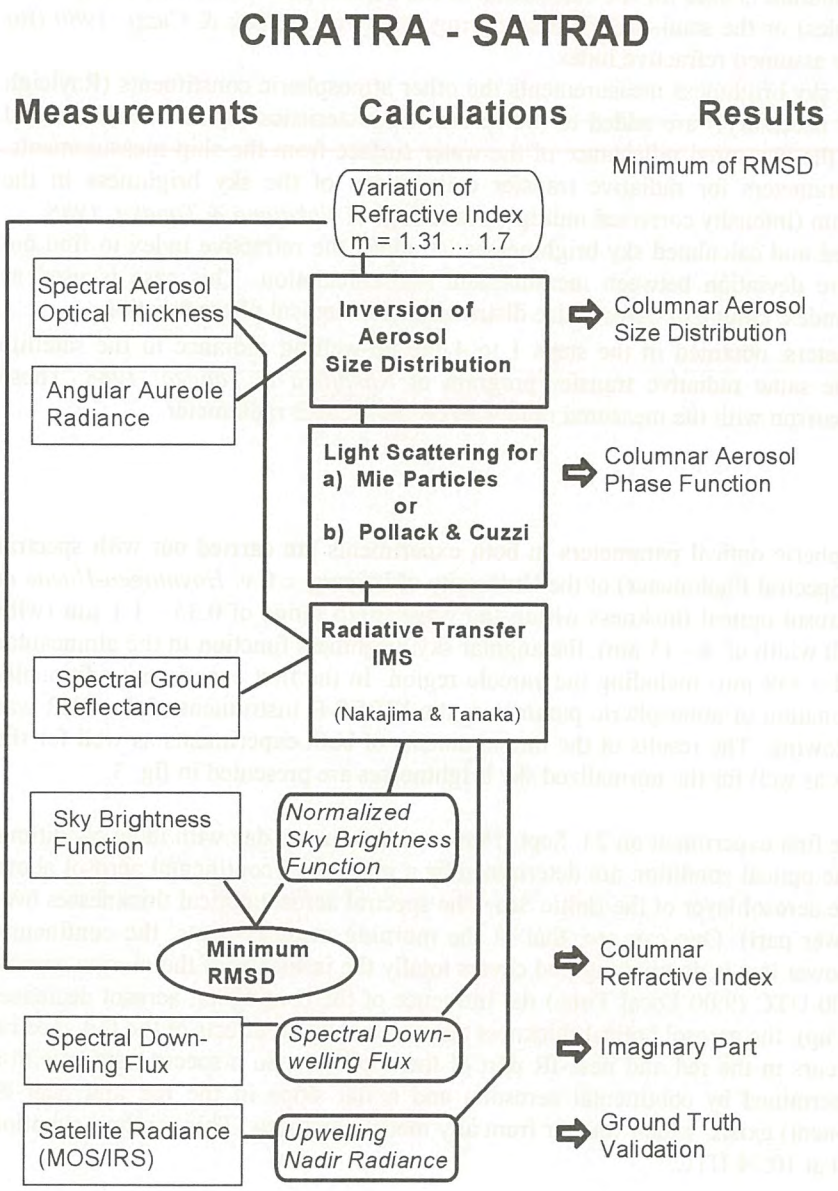


Fig. 2
Closure scheme of the interaction between experimental data (left) and the coupled inversion radiation transfer (CIRATRA) approach for the determination of up-welling radiances and the result output for aerosol parameters (right).

The second experiment has been taken place at Helgoland island in the North Sea during an overflight of MOS/IRS at the 9. March 1997 with a similar approach. The situation there was characterized by wet marine air, which has been followed shortly after the overpath by a large fog field.

The optained measurements have been connected by the modified CIRATRA-SATRAD analysis model (Coupled Inversion RAdiation TRAnsfer prorgam for SATellite RADiances), basing on the ground version, presented by *Wendisch & von Hoyningen-Huene, 1994, von Hoyningen-Huene & Wendisch 1994.*. The scheme

of the complete closure experiment, showing the interchanges between experimental input data and the main modeling steps in the CIRATRA program is shown in fig. 2. The main steps are following:

1. Spectral aerosol optical thickness and angular aureole brightness are used to invert columnar aerosol size distributions under assumption of a real part of the refractive index of the aerosol particles.
2. The columnar aerosol size distribution is used for the calculation of the aerosol phase function, using either Mie theory (for spherical particles) or the semi-empirical scattering theory of *Pollack & Cuzzi, 1980* (for non-spherical particles) with the assumed refractive index.
3. For the spectral channels of the sky brightness measurements the other atmospheric constituents (Rayleigh scattering, ozone absorption (if necessary)) are added to the aerosol characteristics (optical thickness and phase function). Together with the measured reflectance of the water surface from the ship measurements, the data are used as input parameters for radiative transfer calculations of the sky brightness in the almucantar with the IMS program (intensity corrected multiple scattering) of *Nakajima & Tanaka, 1988.*
4. The comparison of the measured and calculated sky brightnesses let adjust the refractive index to find out the minimum root mean square deviation between measurement and calculation. This case is used as ground-truth data of refractive index, columnar aerosol size distribution and aerosol phase function.
5. With these atmospheric parameters, obtained in the steps 1 to 4 the up-welling radiance to the satellite direction is calculated with the same radiative transfer program of *Nakajima & Tanaka, 1988.* These radiences are used for the comparison with the measured radiances of the MOS-B radiometer.

Atmospheric Measurements

Measurements of the main atmospheric optical parameters in both experiments are carried out with spectral radiometers ASP-3 (Atmospheric Spectral Photometer) of the University of Leipzig, c.f. *v. Hoyningen-Huene et al. 1991* consist of the spectral aerosol optical thickness within the wavelength range of 0.35 - 1.1 μm (with approximately 80 channels of a half width of 8 - 15 nm), the angular sky brightness function in the almucantar at 3 wavelength (0.863, 0.683 and 0.538 μm) including the aureole region. In the first experiment aditionally another instrument for the determination of atmospheric parameters the HIRES-B instrument of the DLR was used. The obtained results are following: The results of the measurements of both experiments as well for the spectral aerosol optical thicknesses as well for the normalized sky brightnesses are presented in fig. 3.

The meteorological situation of the first experiment on 23. Sept. 1996 was a clear sky day with ideal conditions for a ground-truth experiment. The optical condition are determined by a mixture of continental aerosol above the surface layer and a thin marine aerosol layer of the Baltic Sea. The spectral aerosol optical thicknesses over the day is presented in fig. 3 (lower part). One can see, that in the morning measurements, the continental aerosol with is nearly Angström power law is dominating and covers totally the influence of the marine aerosol of the Baltic Sea. But around 7:00 UTC (9:00 Local Time) the influence of the continental aerosol decreases more and more (may be by drying up), the aerosol optical thickness decreases and the effects of the flat spectral decrease of the marine aerosol occurs in the red and near-IR part of the spectrum. So a spectral slope with a decrease in the blue and uv (determined by continental aerosols) and a flat slope in the red and near-IR (determined by the marine component) exists, which was far from any model situations. This mixture situation was characteristic for the overpath at 10:34 UTC.

The second experiment has a clear marine air mass situation with a high relative humidity (rh > 85 % increasing).
The spectral aerosol optical thickness has a flat spectrum with a slope $\alpha \approx 0.2$ (for the overflight time $\alpha \approx 0.35$). The normalized sky brightness is more asymmetric than in the first case. The shortly after the overpath following fog has been stopped the sun- and sky-radiometer measurements, but the first fog results are included in the fig. 3.

The sky brightness functions for the measurements during the both cases are presented in fig. 3 (upper part). The measured angular behavior in the almucantar plane in the first case (Ruegen island) cannot be obtained by the assumption of spherical super-micron particles within a realistic refractive range. Only if we assume a non-spherical scattering for the super-micron particles of the marine component, calculated with the semi-empirical scattering theory of *Pollack & Cuzzi*, the observed increased side scattering of dried marine aerosols could be reproduced within realistic refractive indices. The average relative humidity was here under 50 %. Same results are also obtained in different measurement campaigns carried out under clear marine environments at Helgoland island within the German North Sea, c.f. *von Hoyningen-Huene & Posse, 1997.*

In the second case (Helgoland island), with the wet clean marine conditions, the normalized sky brightness functions could be reproduced with the assumption of Mie-theory within an RMSD between measured and calculated sky brightnesses of 2.9 %. Until now only the clear sky conditions have been considered, nevertheless also fog data have been obtained.

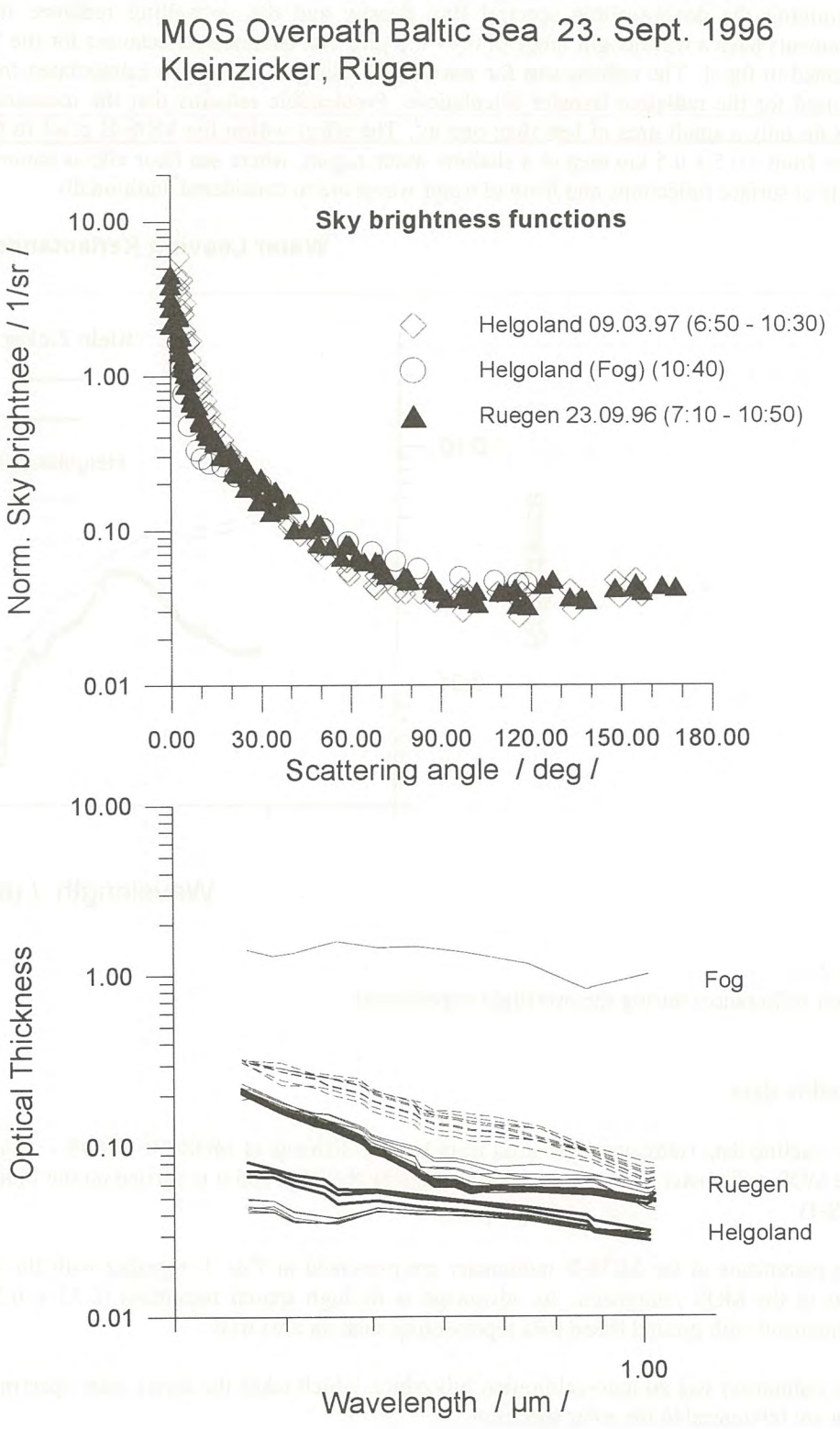


Fig.:3
Atmospheric data of both overflight experiments (Ruegen island, 23. Sept. 1996 and Helgoland, 3. March 1997). Normalized sky brightness (above) and spectral aerosol optical thickness (below). The optical thickness conditions during the overpath time (10:30 LT) are marked with thick lines.

Water Reflectance

For the measurements of the water reflectance two instruments are used: 1. a down-looking instrument (of the DLR, HIRES-ES) hanging from the ship over the water surface, measuring the incident solar spectral flux density and the nadir radiance leaving the water surface. The other instrument was a swimming instrument, determining the down-welling spectral flux density and the up-welling radiance inside the water. Both instruments have a wavelength range of 0.4 - 0.8 µm. The obtained reflectances for the MOS/IRS overpath are presented in fig. 4. The reflectances for wavelength's larger 0.8 µm are extrapolated from these measurement and used for the radiative transfer calculations. Problematic remains that the measured raflectance data are valid for only a small area of less than one m^2. The effect within the MOS-B pixel in the Ruegen experiment comes from a 0.5 x 0.5 km area of a shallow water region, where sea floor effects cannot be excluded and also effects of surface reflections and foam of water waves are to considered additionally.

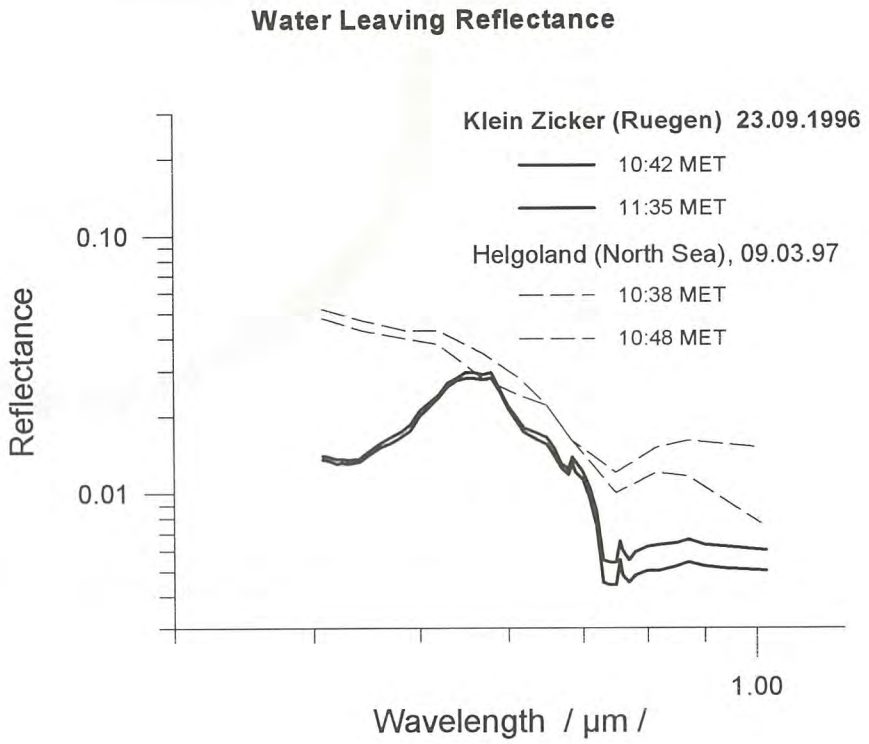


Fig. 4
Water reflectances during the overflight experiments

Satellite data

The satellite data (radiances) are used from the 13 channels of MOS/IRS (MOS - Modular Optical Scanner). The MOS-radiometer is developed and operated by the DLR and it is carried on the Indian Research Satelite - 1 (IRS-1).

The parameters of the MOS-B radiometer are presented in Tab. 1. together with the parameters of the other parts of the MOS radiometer. Its advantage is its high spatial resolution (0.52 x 0.52 km) which allows a comparison with ground based data representing such an area well.

The radiometer has an auto-calibration procedure, which takes the direct solar spectrum at each path and the data are referenced to the solar spectrum.

Channel 12 is within the water vapor band and has been not considered for the inter-comparisons. In the channels 4 - 8 the ozone absorption of the Chappius band has to be considered for the inter-comparison.

Channel 7 seems to be uncalibrated, because the data of this channel have been much outside (to low radiances) of the ranges of the other channels. Therefore it also has been skipped within the comparisons as the water vapor channel.

Tab. 1
Parameters of the MOS-radiometer on IRS-P3

Parameter	Channel	MOS-A	MOS-B	MOS-C
Spectral Range (µm)		0.755 - 0.768	0.408 - 1.011	1.600
No of Channels		4	13	1
Wavelength (µm)	1	0.7568	0.4080	1.600
	2	0.7606	0.4436	
	3	0.7635	0.4846	
	4	0.7663	0.5208	
	5		0.5705	
	6		0.6153	
	7		0.6503	
	8		0.6853	
	9		0.7497	
	10		0.8141	
	11		0.8683	
	12		0.9439	
	13		1.0111	
Characteristics		O_2-A-band	Aerosol H_2O-vapor water content	SWIR
Band width (nm)		1.4	10	100
FOV				
along track (deg)		0.344	0.094	0.14
across track (deg)		13.6	14.0	13.4
Swath width (km)				
Pixel size (km x km)		1.57 x 1.4	0.52 x 0.52	0.52 x 0.62
Radiance range				
Min / Max		0.1	0.2	0.5
(µW/(cm² nm sr)		40	65	18

Comparison of Ground Truth and Satellite Radianaces

For the overpath time, the spectral aerosol optical thickness, the aerosol phase function, obtained from the CIRATRA approach and the water reflectance in nadir direction are used within the radiative transfer program to calculate the up-welling nadir radiance at the top of the atmosphere for all spectral channels of the MOS-B-radiometer. Within channels with ozone absorption, the ozone optical thickness from the ASP radiometer in the Chappius band is used, water vapor is still not considered. Therefore also the channel at 0.938 µm is excluded from the comparison. The comparison results for both experiments are shown in fig. 5. In the first experiment (Ruegen island) both cases of inversion results: 1. assumption of spherical aerosol particles (Mie-theory) and 2. best fit inversion using the semi-empirical scattering theory of *Pollack & Cuzzi* are presented, because Mie-theory gave insufficient results for the closure between measured and calculated sky brightness functions of the ground based measurements. In the second experiment (Helgoland island) the Mie theory could be used, therefore no calculations with the *Pollack & Cuzzi* approximation have been used.

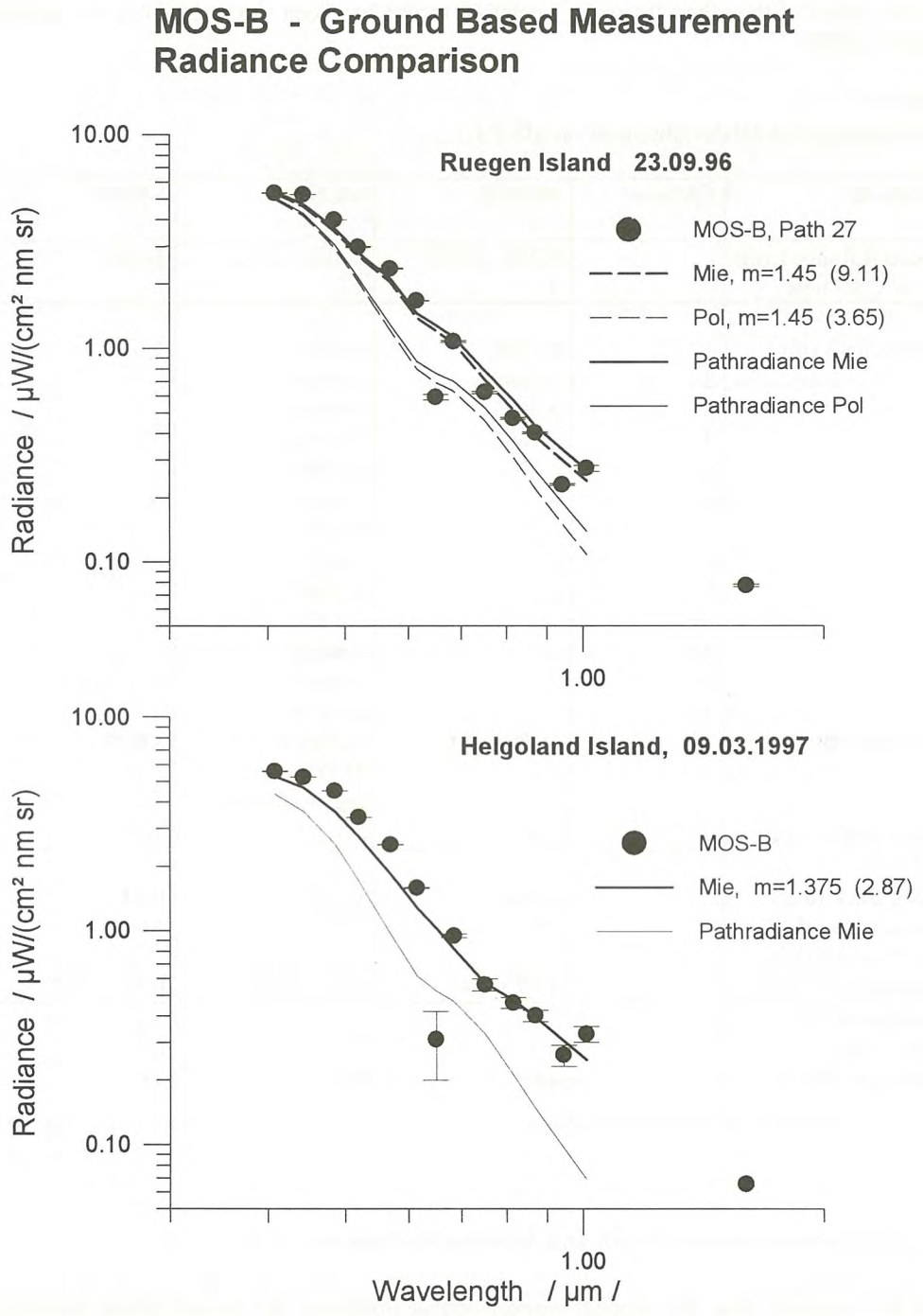


Fig. 5
Inter-comparison of the nadir radiances at the top of the atmosphere for both overpathes: Ruegen island, 23. Sept. 1996 (above) and Helgoland island, 9. March 1997 (below)

Generally the measured by MOS-B satellite radiances for both overpathes in the wavelength range $\lambda < 0.6$ µm are larger than the calculated ones, but the result with the phase function of the non-spherical particles are closer to the measured ones. But it still remains a difference of 10 % and more, which would be to large for a retrieval of small water reflectances or even aerosol parameters. A better estimation of the phase function in this wavelength range with also non-sphericity effects could be a contribution to reduce this difference. But between 0.45 and 0.55 µm the difference couldn't be produced by the atmospheric aerosol (optical thickness and phase function) alone, because the most effect of the path radiance comes from the Rayleigh scattering.

The spectral channels of 0.68 to 0.86 give for the first attempt a close coincidence. For this channels the measured sky brightness functions have been obtained directly by the measurements. For the other channels the phase functions from these channels (0.68 and 0.86 μm) have been transferred to the wavelength of the channels. Within these channels also the best results for the phase functions by the CIRATRA program are obtained. For the wavelength larger 0.8 μm the missing measured values for the water reflectance are a factor of incertainty in the inter-comparison. The channel 7 of MOS-B shows generally to low radiances. This channel wavelength should be out of a strong absorption line, so it seems to be probabely a calibration error.

3. Conclusions

In this very first attempt the ground truth measurements could reproduce in the most channels the main spectral features of the MOS-B radiances within few percents and show the connection between the satellite data and the ground based measurements. This could be a base for retrieval procedures for the determination of aerosol parameters, such as spectral decrease with the wavelength and resulting from this main aerosol type. Nevertheless the differences between the radiances, measured by the satellite and the calculations from the ground based measurements (with several percents) are still to large for an accurate retrieval of so small reflectances of a water surface, because this effect is within the deviations. The investigation of the reasons of these differences should be used for the improvement of as well as the ground truth approach with all its experimental results as the quality of the satellite data.

But the experiments show very clearly: the obtained experimental data for the atmospheric parameters by the ground measurements are far of that of the normally used aerosol model types: The one situation was a mixture of continental and marine aerosol and non-spherical particle scattering has to be used for the super-micron aerosol fraction. Therefore assumptions of a certain aerosol model as for instance that of *d'Almeida et al, 1991* alone are a real source of incertainty for a retrieval of spectral water reflectances.

Refereces

d'Almeida, G.A., Köpke, P., Shettle, E.P.: Atmospheric aerosol. Global Climatology and radiative characteristics.
Deepak Publ., Hampton 1991.

Gordon, H.R.: Removal of atmospheric effects from satellite imaginary of the oceans.
Apll. Optics 17 (1978) 1631-1640

Gordon, H.R., Castano,D.J.: Coastal zone color scanner atmospheric cerrection algorthm: multiple scattering effects.
Appl. Optics 26 (1987) 2111-2122.

Gordon, H.R., Castano, Aerosol analysiswith CZCS: a simple method for including multiple scattering effects.
Appl. Optics 28 (1989) 1320-1326.

Gordon, H.R.: Radiative Transfer in the atmosphere for correction of the ocean color remote sensors.
In: Theory and Application in a decade of CZCS experience. Report of JRC CEC, Ispra, October 1991.

Heinemann, T.: Satellitengestützte Fernerkundung von Aerosolen. In: Strahlung in Atmosphäre und Ozean, Beiträge zur Fernerkundung (Ed. J. Fischer) Veröffentlichungsreihe des Institut für Weltraumwissenschaften, Freie Universität Berlin,
Heft 1,1995, 144 p.

von Hoyningen-Huene, W., Bohmann, W., Rehnert, J.:Spektralfotometer ASP-2 zur Bestimmung spektraler atmosph"arischer Parameter.
Geophysik und Geologie 4 (1991) H. 3, 23-34.

von Hoyningen-Huene, W., Wendisch, M.: Variability of Aerosol Optical Parameters by Advective Processes.
Atmospheric Environment 28 (1994) 923-933.

von Hoyningen-Huene, W., Posse, P.: Nonsphericity of Aerosol Particles and Their Contribution to Radiative Forcing.
J. Quant. Spectr. Rad. Trans. 1997 in press.

Kaufman, Y.J., Fraser, R.S., Ferrare, R.A.: Satellite measurements of large scale air pollution: Method.
J. Geophys. Res. 95 (1990) 9895-9909.

Kaufman, Y.J., Sendra, C.: Algorithm for automatic corrections to visible and near-IR sattelite imaginary.
Int. Journ. of Remote Sensing 9 (1988) 1357-1381.

Nakajima, T., M. Tanaka: Algorithms for radiative intensity calculations in moderately thick atmospheres using a truncation approximation.
J.Quant.Spectrosc.Radiat.Transfer 40 (1988) 51-69.

Pollack, J.B. and J.N. Cuzzi: Scattering by nonspherical particles
of size comparable to a wavelength: a new semi-empirical theory and its
application to tropospheric aerosols.
Journal of the Atmospheric Sciences, 37 (1980) 868-881.

Wendisch, M., von Hoyningen-Huene, W.: Possibility of Refractive Index Determination of Atmospheric Aerosol Particles by Ground-Based Solar Extinction and Scattering Measurement.
Atmospheric Environment 28 (1994) 785-792.

Wilson, W.H.: Measurements of atmospheric transmittance in a maritime environment.
In: Atmospheric Effects on Radiative Transfer, SPIE 195 (1979) 153-159.

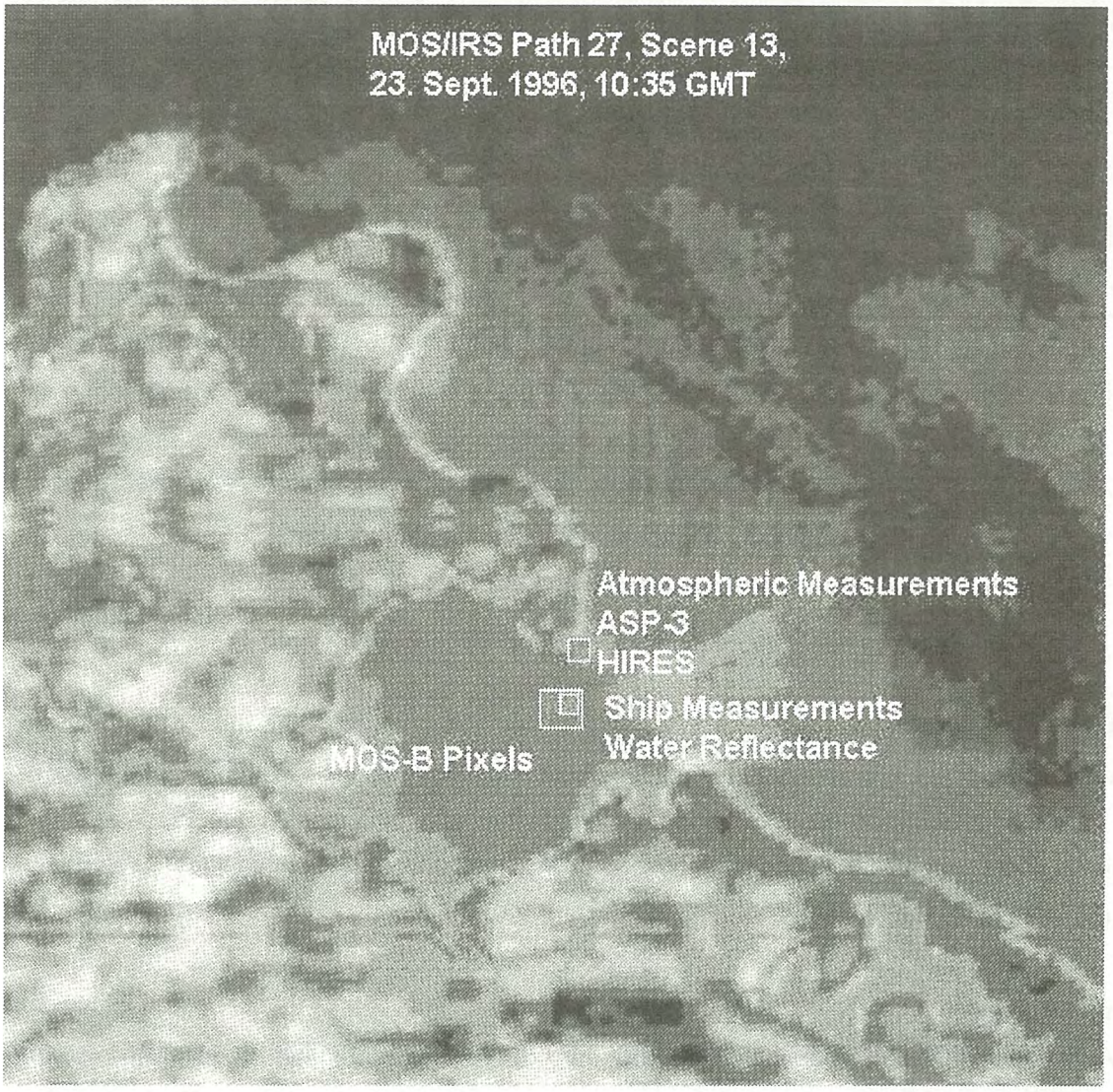


Fig. 1
Part of a composite image of MOS radiance data of the Path 23 on 23. Sept. 1996 with the Positions of the measurement sites during the overpath. The part shows the Baltic Sea region around the island Ruegen with the Greifswald bight in northern Germany.

Lidar Network for Observation of Asian Dust (Kosa) in Japan

T. Murayama [1)], N. Sugimoto [2)], I. Matsui [2)], K. Arao [3)], T. Sakai [4)], S-A Kwon [4)], H. Adachi [4)], K. Aoki [5)], M. Abo [6)], H. Kuze [7)], N. Takeuchi [7)], A. Nomura [8)], Y. Saito [8)], T. Kawahara [8)], K. Asai [9)], R. Koga [10)], M. Fujiwara [11)], K. Shiraishi [11)], R. Imasu [12)], K. Kai [13)]

[1] Tokyo Univ. of Mercantile Marine, [2] National Inst. for Environmental Studies, [3] Faculty of Environmental Science, Nagasaki Univ., [4] STE labo., Nagoya Univ., [5] Inst. of low temperature science, Hokkaido Univ., [6] Faculty of Engineering, Tokyo Metropolitan Univ., [7] CEReS, Chiba Univ., [8] Faculty of Engineering, Shinshu Univ., [9] Faculty of Engineering, Tohoku Inst. of Technology, [10] Faculty of Engineering, Okayama Univ., [11] Faculty of Science, Fukuoka Univ., [12] National Inst. of Resources and Environment, [13] Inst. of Geoscience, Univ. of Tsukuba

e-mail: murayama@ipc.tosho-u.ac.jp

Abstract: We have organized a lidar network for the observation of Asian dust in the spring, March to May, of 1997 in Japan. Owing to the communication through the internet e-mail we effectively obtained some coincident observation of Kosa aerosol layers. We have compared the ground-based data in Tokyo with a satellite observation, TOMS. Further continuation and wide coverage of the network are desired.

1. Introduction

Asian dust (Kosa in Japanese); falling out of yellow sands has been well-known meteorological phenomenon in western Japan especially during the spring. The origin is yellow sands of spread desserts in the continent, which are blown up by surface wind and delivered in free troposphere by westerly jet. Much meteorological research on Kosa has been made to survey its effect on radiation, the character of the aerosols, the mechanism of the transportation, etc., in last decades. However, the quantitative information of Kosa is still not well known. From the point of view of global environment, Kosa is an interesting target to study the global transportation of troposheric aerosols.

Lidar is a unique remote-sensing technique to obtain the height distribution and various optical properties of atmospheric aerosol. The lidar group of Nagoya University has intensively observed Kosa layers [1]. It was found that Kosa aerosol layer often had the multiple structure. Numerical simulations based on trajectory analysis and tracer model reproduced the multiple structure in some cases [2]. However, simultaneous lidar observation of Kosa aerosol layer in a scale as large as Japan is desired to figure out the net structure of Kosa and survey its transport mechanism. Such a lidar network observation is mutually complementary to the satellite observation.

Recently, there are increasing lidar groups who routinely observe the troposphere in Japan. Thus we have tentatively organized Lidar Network for the observation of Kosa in Japan (LINK-J) in the spring, March 1 to May 31, of 1997. The participants are listed in authors and the sites are indicated in Fig. 1. We have exchanged information about Kosa through the e-mail. Because upper Kosa layers often remain for more than one-day long, such a communication measure was efficient. In this paper, we will briefly present an example of the measurement, a preliminary comparison with Total Ozone Mapping Spectrometer (TOMS) aerosol data and perspective.

2. Observational results in 1997

Unfortunately, Kosa events in 1997 were less than usual. Here we present an example of the network observation of weak Kosa layer that has a multiple structure on April 1, 1997. The lidar data continuously obtained at Tsukuba and Tokyo are shown in Fig. 2 and 3, respectively. We recognize two isolated aerosol layers around 3.5 km and 5 km. A descent process of the upper layer is clearly seen. High depolarization ratio in these layers as shown in Fig. 3 indicates a typical non-sphericity of Kosa dusts. The lower aerosol layer was also detected by a Micro Pulse Lidar in Chiba. The aerosol layer with high depolarization ratio more than 10% was observed in Nagoya at the night. Similar data were obtained on the previous day, March 31. A weak Kosa event was recorded by a particle counter at Nagasaki on March 30.

3. Comparison with TOMS data

By the courtesy of Dr. J. Herman in JSFC/NASA, we have made a comparison between our observation and EARTH PROBE, TOMS data; it passes over Japan at 11:17 JST everyday. The analysis by using TOMS two UV-channels can derive an aerosol index (AI) for UV-absorbing aerosols above 2 km in altitude [3]. In the east Asian area, Asian dust and coal-burning smoke are probable UV-absorbing aerosols. On March 31 and April 1, 1997, there have not been obtained significant AI over Japan. The reason is probably due to the small amount of aerosols; the integrated optical depth over 2 km on both days is about 0.1. Then we have examined for the other days when the AI near Japan is large: on May 10 and 12; the data are shown in Fig. 4. We show corresponding lidar and sky radiometer [4] data in Tokyo on these days in Fig. 5 and 6, respectively. In Tokyo, the AI is between 0.50 to 0.75 on May 12, but less on May 10. The high-altitude aerosol layer around 7 km on May 12 might be detected by TOMS. On the other hand, there was a larger amount of aerosol below 5 km on May 10. The reason may be explained by the height dependent sensitivity of AI and the difference of optical properties on both days; the later is indicated by the lidar depolarization ratio and retrieved results from sky radiometer.

4. Summary and Perspective

We have demonstrated the lidar network observation of Kosa aerosol in the spring of 1997. The continuous observation and depolarization measurement are useful to detect Kosa aerosol layers. We have made a preliminary comparison between TOMS observation and lidar and sky radiometer data in Tokyo. Such a comparison seems quite important to validate satellite data even at particular sites. We will continue the seasonal campaign, LINK-J in the following years. It must be promising to expand the network to international collaboration and also to join ACE-3 (Asia) programmed in 2,000 year.

References

[1] *e.g.*, Y. Iwasaka *et al.*, "Transport of Asian dust (KOSA) particles; importance of weak KOSA events on the geochemical cycle of soil particles.", Tellus 40B (1988) pp.494-503.

[2] K. Kai *et al.* , "Lidar Observation and Numerical Simulation of a Kosa (Asian Dust) over Tsukuba, Japan during the Spring of 1986", J. Meteorol. Soc. Jpn. 66 (1988) pp.457-472.

[3] J. R. Herman *et al.*, "Global distribution of UV-absorbing aerosols from Nimbus 7/TOMS data", J. Geophys. Res. 102 (1997) pp.16911-16922.

[4] T. Nakajima *et al.*, "Use of sky brightness measurements from ground for remote sensing particulate polydispersions", App. Optics 35 (1996) pp. 2672-2686.



Fig. 1 Observation sites in LINK-J.

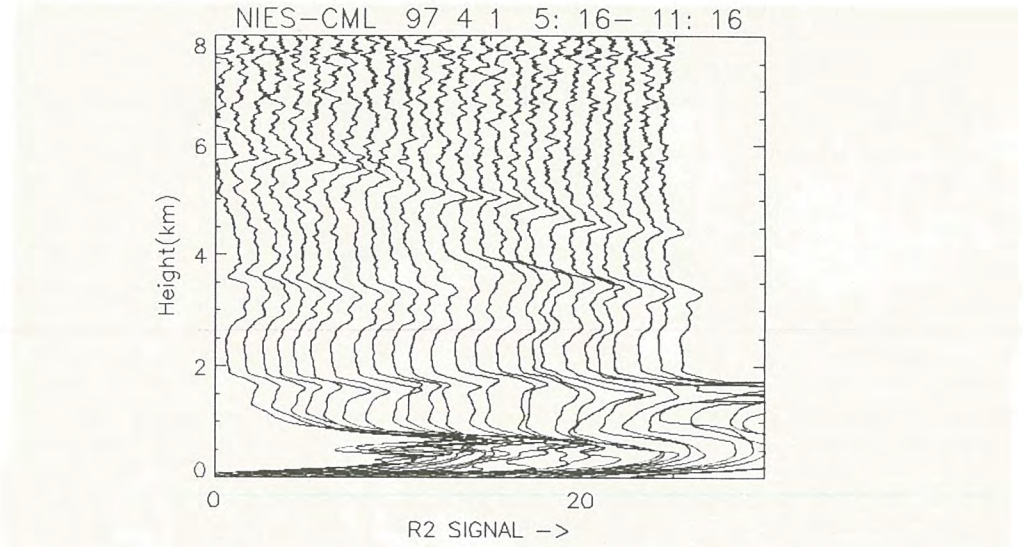
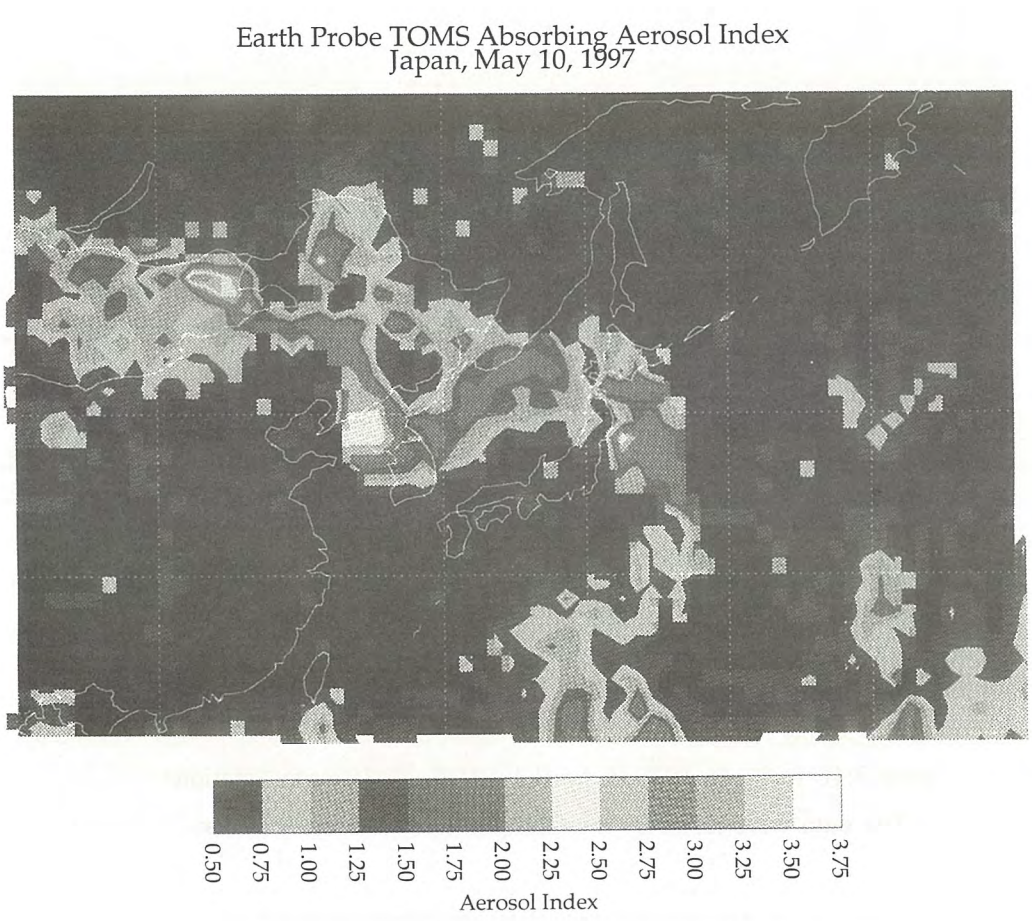


Fig. 2 Profiles of range-corrected backscatter intensity obtained at NIES in Tsukuba from 5:16 to 11:16 JST on April 1, 1977. (THI representation)
The data were taken by the Compact Mie-scattering Lidar.

Fig. 3 Profiles of range-corrected backscatter intensity (left) and depolarization ratio (right) obtained at TUMM in Tokyo from 5:47 to 10:06 JST on April 1, 1997.



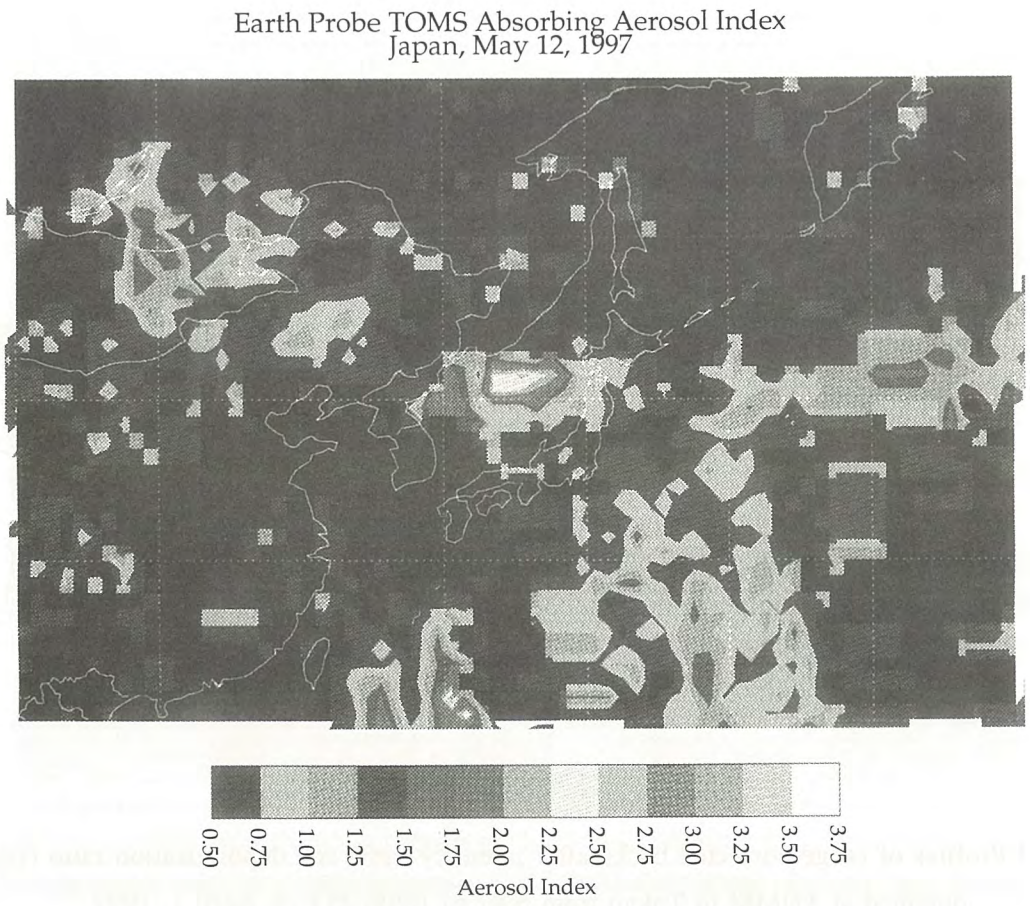


Fig. 4 Map of TOMS UV-absorbing aerosol index over Japan on May 10 (upper) and 12 (lower), 1997. (by the courtesy of Dr. J. Herman)

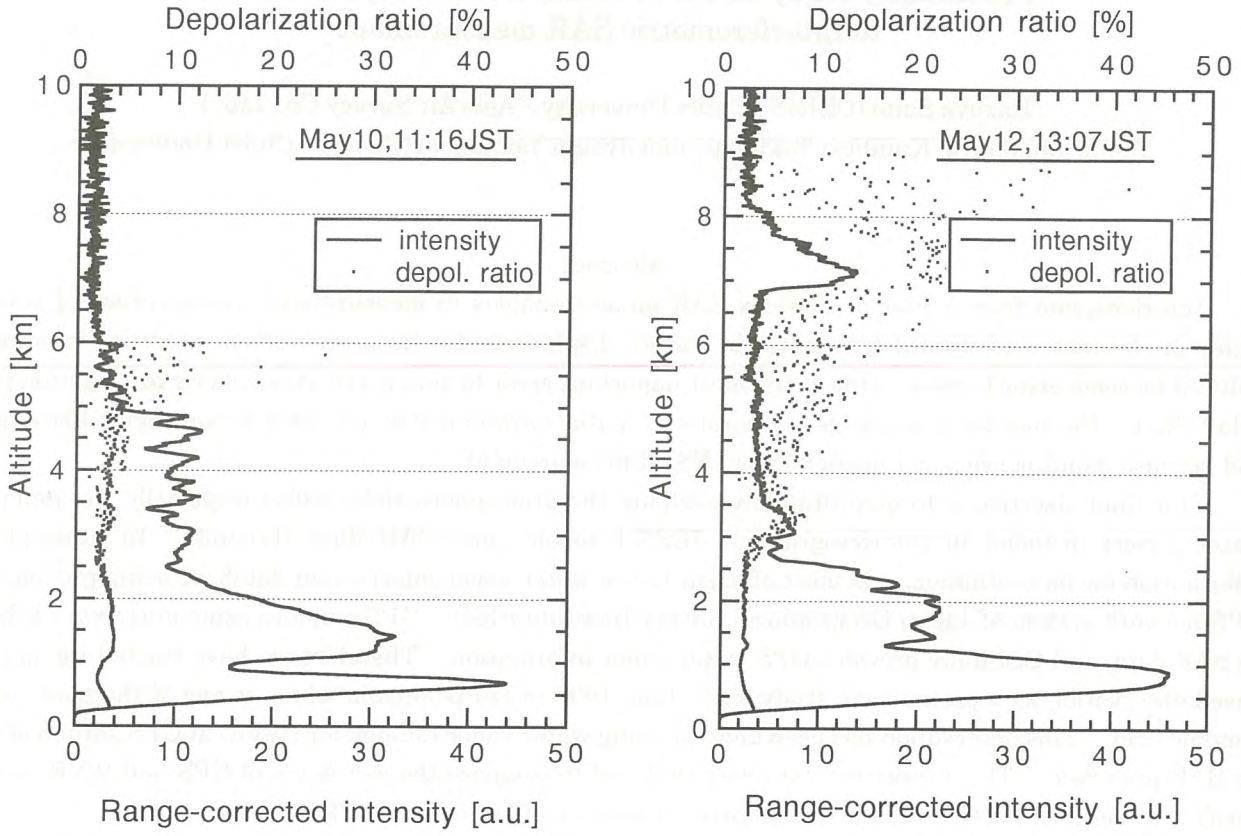


Fig. 5 Lidar data at TUMM in Tokyo on May 10 (left) and May 12 (right), 1997.

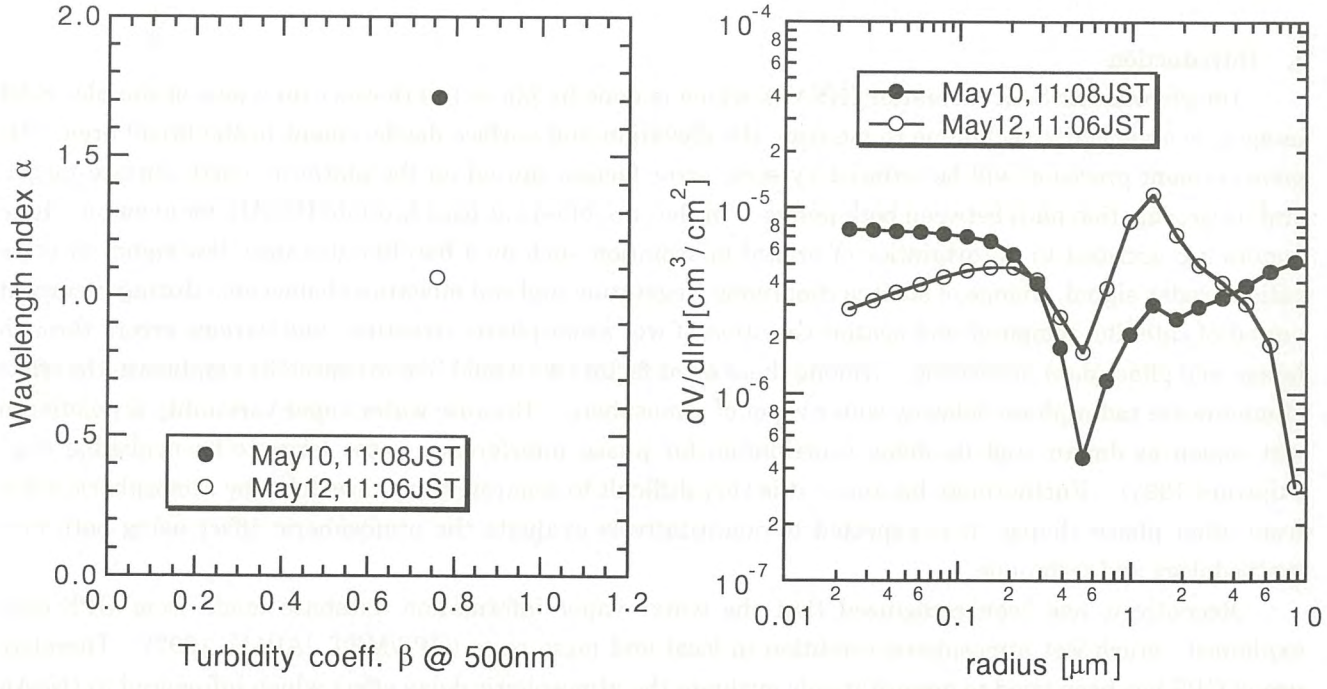


Fig. 6 Retrieved optical thickness, Angstrom index (left) and volumue size distribution (right) from the sky radiometer at TUMM on May 10 and 12, 1997.

Preliminary study on the evaluation of atmospheric effect to Interferometric SAR measurement

Kazuya Saito (CEReS , Chiba University／Asia Air Survey Co., Ltd.)
Tamio Takamura, Kunihisa Takimoto, and Jyouta Yamamoto (CEReS , Chiba University)

Abstract

Interferogram from a pair of complex SAR images enables to measure with the accuracy of several meter in elevation and several centimeter in surface displacement. Its measurement precision is actually reduced by some error factors. One of the most important error factors is the atmospheric propagation path delay effect. Because there is a large temporal and spatial variation of water vapor in wet region like Japan, and because its influence is not negligible for INSAR measurement.

Our final objective is to quantitatively evaluate the atmospheric delay effect (especially wet delay by water vapor) included in interferogram of JERS-1 repeat pass SAR data (L-band). In atmospheric information for its evaluation, it is most efficient to use water vapor information database being provided by GPS network system of Japan Geographical Survey Institute (GSI). GPS employs same microwave L-band as SAR data, and GSI daily provides GPS water vapor information. Therefore we have started the ground based observation as a preliminary study since June 1997 in Izu peninsula where is one of the most active tectonic field. This observation has been done by using water vapor radiometer (WVR) at GPS station of GSI on SAR pass date. The acquisition data was analyzed to compare the wet delay of GPS and WVR, and to verify the usefulness of GPS for the quantitative evaluation of atmospheric effect.

These observation results indicate that the wet delay of GPS corresponds well with WVR delay (correlation coefficient is 0.996, rms delay is about 1.8cm), and that GPS database is very useful in the quantitative evaluation of atmospheric delay effect. The difference of wet delay between summer and autumn observation using GPS becomes very large (more than 20 cm), and moreover its spatial distribution reveals a large variation. This suggests that a local variation in water vapor content often bring the severe height and surface displacement error for INSAR measurement.

1. Introduction

Interferometric SAR (hereafter INSAR), which is done by phase interference on a pair of complex SAR images, is an effective technique to measure the elevation and surface displacement in the broad area. Its measurement precision will be reduced by some error factors caused on the platform, earth surface target, and its propagation path between both points. In the case of repeat pass satellite INSAR, for example, those factors are ascribed to uncertainties of orbital information such as a baseline distance, low signal to noise ratio of radar signal, change of surface conditions (vegetation and soil moisture change etc.) during recurrent period of satellite, temporal and spatial variation of wet atmospheric structure, and various errors through image and phase data processing. Among these error factors we would like to especially emphasize the effect of microwave radar phase delay by water vapor of atmosphere. Because water vapor variability is popular in wet region as Japan, and its delay contribution for phase interference is too large to be negligible (e.g., Fujiwara,1997). Furthermore because it is very difficult to separate the phase delay by atmospheric effect from other phase change, it is expected to quantitatively evaluate the atmospheric effect using both new methodology and technique.

Recently it has been recognized that the water vapor information database made from GPS data explained much wet atmospheric condition in local and meso scale (GPS/MET JAPAN, 1997). Therefore use of GPS has been tried to quantitatively evaluate the atmospheric delay effect which influenced to INSAR measurement. In order to extract and quantitatively evaluate the atmospheric delay effect to INSAR measurement, it is most effective and efficient to positively utilize the wet delay data induced from GPS SINEX data of Japan Geographical Survey Institute (GSI). These water vapor information are daily provided as a zenith wet delay which indicates residuals from initial value of correction parameter at the

standard atmospheric model. We use this GSI troposphere data, and make quantitatively clear the relationship between GPS and INSAR delay for atmospheric correction on SAR interferogram.

2. Measurement error by atmospheric delay effect

SAR signal causes the atmospheric phase delay through microwave radar propagation pass. Total atmospheric delay Δx consists of hydrostatic delay $(\Delta x)_{dry}$ by dry atmosphere and wet delay $(\Delta x)_{wet}$ by water vapor as follows:

$$\Delta x = (\Delta x)_{dry} + (\Delta x)_{wet} \quad (1)$$

These delay terms depend on atmospheric pressure, temperature, and water vapor pressure on the propagation path. If these meteorological parameters have the regularity with respect to height from the sea level, total zenith delay Δx will be easily approximated by ground observation value (Saastamoinen,1972; Zebker,1997).

$$\Delta x = (2.277\times10^{-3}-1.11\times10^{-5}\cos\Lambda)Ps+2.277\times10^{-3}\,[0.05+1255/Ts]\,Es \quad (2)$$

where Λ, Ps, Ts, and Es show latitude, atmospheric pressure, temperature, and water vapor pressure at the observation point. First term of (2) indicates the hydrostatic delay by dry atmosphere. Although the value itself becomes very large (more than 2 m), it is not always necessary to consider the influences of atmospheric effect. Because the difference of hydrostatic delay between two SAR images is not so large in spatial distribution. Even if there were several hPa change of atmospheric pressure, hydrostatic delay will be less than 2 cm (about 2mm delay for 1hPa change). Most important effect is the water vapor delay described as second term of (2). Wet delay value itself is not so large (several 10 cm), but temporal and spatial variation becomes complicated. The SAR measurement error by wet delay strongly depends on the difference of spatial distribution of phase delay.

For wet delay of the SAR data, measurement error is represented as follows: If σ_z is the elevation error and σ_d is the surface displacement error towards look direction,

$$\sigma_z = 2\Delta x\,[\,\rho\sin\theta / B\cos(\theta-\alpha)\cos\eta\,] = 2\Delta x\,\rho\sin\theta / Bp\cos\eta \quad (3)$$

$$\sigma_d = 2\Delta x / \cos\eta \quad (4)$$

where ρ is the distance between satellite and surface target (called slant range), θ is the look angle, η is the incident angle, B is the orbital separation length (called baseline distance), Bp is the perpendicular component of baseline distance, and α is the angle between baseline and horizontal line.

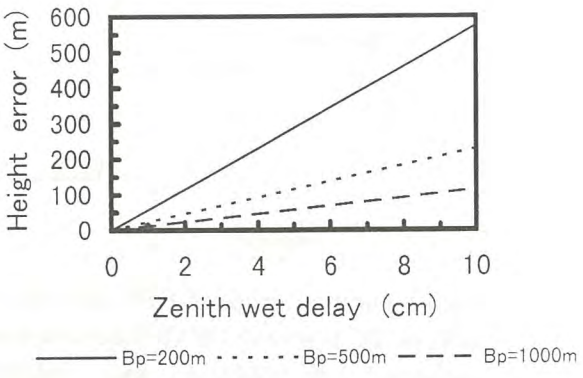


Fig.1 Height error by wet delay effect

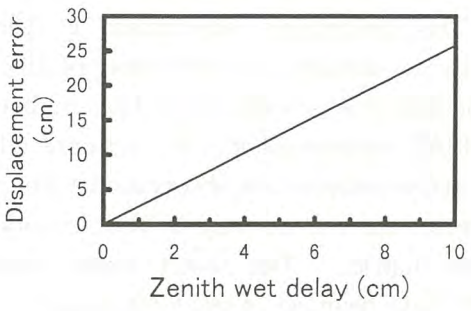


Fig.2 Displacement error by wet delay effect

Although wet delay in surface displacement analysis nearly becomes to the measurement error ($\cos\theta$ means the projection to SAR look direction), the elevation error severely depends on baseline change. Inserting typical JERS-1/SAR parameter (ρ = 709km, θ = 35deg, η =39deg) into (3) and (4), the error estimation for wet delay may be illustrated in Fig.1 and 2. Fig.1 indicates that height error is represented as a function of baseline distance, and that smaller distance produces larger error. Large Bp, however, reduces the capability of interference in terms of degradation of coherence between both images. Optimum combination of SAR images for height measurement will not be always determined by only baseline distance, but the atmospheric conditions must be considered at the same time. On the contrary, phase delay of surface displacement just directly reveals the measurement error. The atmospheric effect is very meaningful for extracting several cm order change such as a coseismic fault displacement of intermediate shock or a symptomatic crustal deformation just before a large shock. However these measurement errors may have maximum value when zenith wet delay is equivalent to $\lambda \cos\eta /4 \times n$ (n is an integer) because of phase periodicity.

The phase delay or measurement error by wet delay generally means the result of only one image (one day data). As repeat pass satellite INSAR needs a pair of images (two day's data), we can replace the phase delay of one image to the difference of phase delay for two images. An important problem is the local characteristics of phase delay difference between both days. It is remarkable that the accuracy is not apparently reduced if there is no difference of wet delay in spatial distribution.

3. Use of GPS network data of GSI

In the quantitative evaluation of atmospheric delay effect to INSAR measurement, it is most effective and efficient to use wet delay data of GPS network database provided by Japan Geographical Survey Institute (GSI). The water vapor information by GSI indicates residuals from initial value which is a correction parameter for determination of GPS station coordinates at the standard atmospheric model (atmospheric pressure: 1013hPa, temperature: 18℃, relative humidity: 50% on the ground). Therefore wet delay data of GSI is not equal to actual wet delay content. It is necessary to be recalculated by the following correction.

$$\Delta xw = \Delta x - \Delta xd + \Delta xt \qquad (5)$$

where Δxw represents the actual wet delay at GPS station. Δx, Δxd, and Δxt show the total delay by standard atmospheric model (see (2)), the hydrostatic delay based on actual atmospheric pressure, and the wet delay provided by GSI. Δxd needs the ground based atmospheric pressure observation value at GPS station.

4. WVR observation at SAR data acquisition time

This preliminary experiment is devoted to identify the usefulness of GPS data provided by GSI for the quantitative evaluation of atmospheric effect to INSAR measurement. We compare GPS data with other independent observation value. Fig. 3 illustrates the location map of GPS network station in Izu district. Two water vapor radiometers (WVR) have been set at two GPS stations (AMAGI and OHHITO) in Izu peninsula where is one of the most active tectonic field. Atmospheric pressure is measured at an either station.



Fig.3 Location map of GPS network (by GSI) in IZU peninsula. WVR observation was performed at AMAGI and OHHITO. Parentheses show station height (m).

Table.1 Dates and conditions of data acquisition

Date	Weather	GPS data By GSI	WVR direction	Pressure gauge location	JERS-1/SAR path-row
Jun.27	fine	not provided	zenith	AMAGI	D64-242
Jun.28	rain	not provided	zenith	AMAGI	D65-242
Aug.10	cloudy/rain	provided	zenith	AMAGI	D64-242
Aug.11	rain/cloudy	provided	zenith	AMAGI	D65-242
Sep.23	rain	provided	cancelled	cancelled	D64-242
Sep.24	rain/fine	provided	scanned	OHHITO	D65-242
Nov. 6	cloudy	provided	scanned	OHHITO	D64-242
Nov. 7	cloudy/fine	provided	scanned	OHHITO	D65-242

"scanned" means that WVR have several direction data by scanning towards east-west.
Each elevation angle is 25, 30, 35, 40, 50, 60, 75, 90deg (zenith).

Other observation such as temperature, humidity, and brightness temperature of thermal infrared towards zenith are complemented at both stations. Table.1 shows the observation results and conditions at the present. These radiometers (WVR-1100 by Radiometrics Corp.) obtain downward radiation in two frequency bands of 23.8 and 31.4 GHz. The wet delay by WVR Δw is calculated by the following linear retrieval equation using an optical thickness in each frequency.

$$\Delta w = c_0 + c_1 \tau_{23.8} + c_2 \tau_{31.4} \quad (6)$$

where $c_0 \sim c_2$ are calibration values which indicate 0.077, 139.691, -81.466. τ_i is represented as follows:

$$\tau_i = \ln [(Tm_i - Tc) / (Tb_i - Tc)] \quad (7)$$

where i shows frequency band, Tm_i is 279.06 and 277.73 in each frequency as an average atmospheric radiation temperature (K). Tc shows outer space black body temperature (2.73K), and Tb_i is the observational brightness temperature at GPS point.

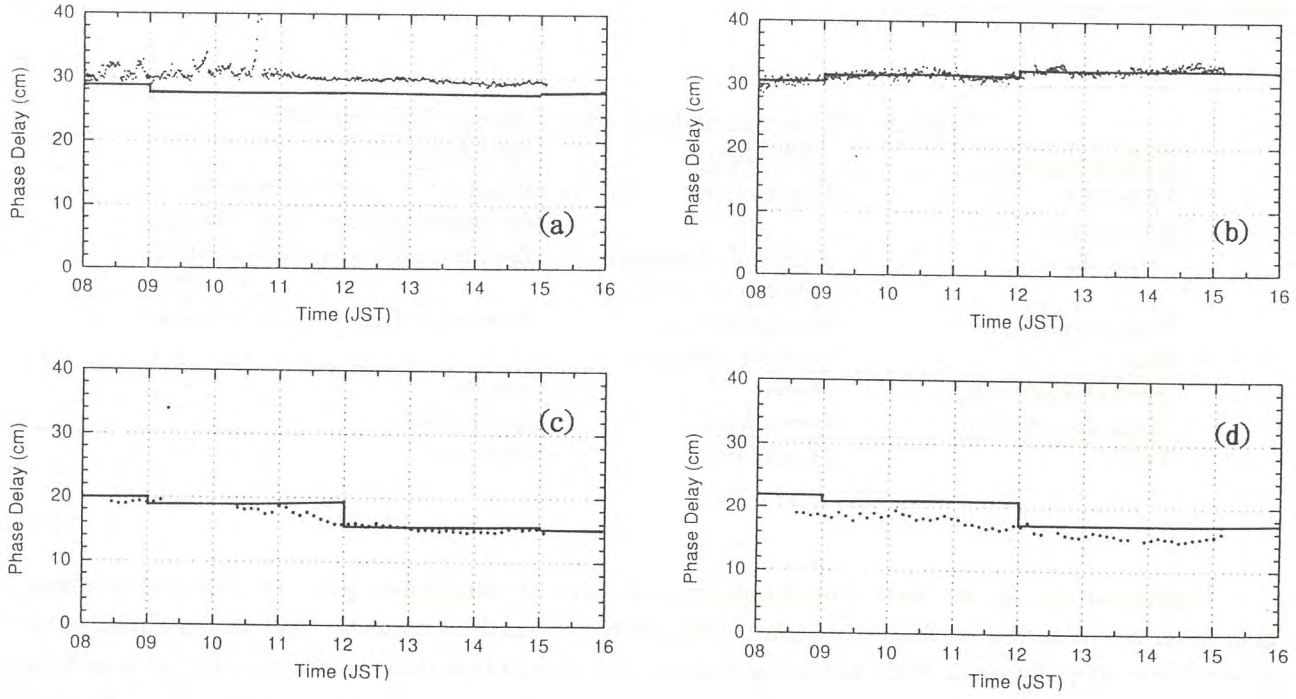


Fig.4 Temporal comparison of corrected GPS data and WVR observation data. (a) 8/11/97 AMAGI (b) 8/11/97 OHHITO (c) 9/24/97 AMAGI (d) 9/24/97 OHHITO. Plot data shows WVR, and solid line shows GPS at every three hours.

Fig.4 shows the comparison between GPS corrected by (5) and WVR wet delay at AMAGI and OHHITO in time series. Examples demonstrates the typical summer (Aug.11) and autumn (Sep.24) data which have a large difference of water vapor content. Both days are SAR data acquisition date. Solid line indicates the corrected GPS delay and Plot data does WVR delay. Each figure reveals a good correspondence in spite of the independent observation value. Next we represented the comparison of GPS and WVR wet delay acquired at 10:30 (SAR pass time) and 13:30 of Aug.10～ Nov.7 (except Sep.23) at each station (Fig.5). The results showed correlation coefficient 0.996 and rms delay error about 1.8cm. This comparison implies the capability of employment of GPS data to evaluate SAR phase delay, and the efficiency to process a lot of GPS station data on wide area.

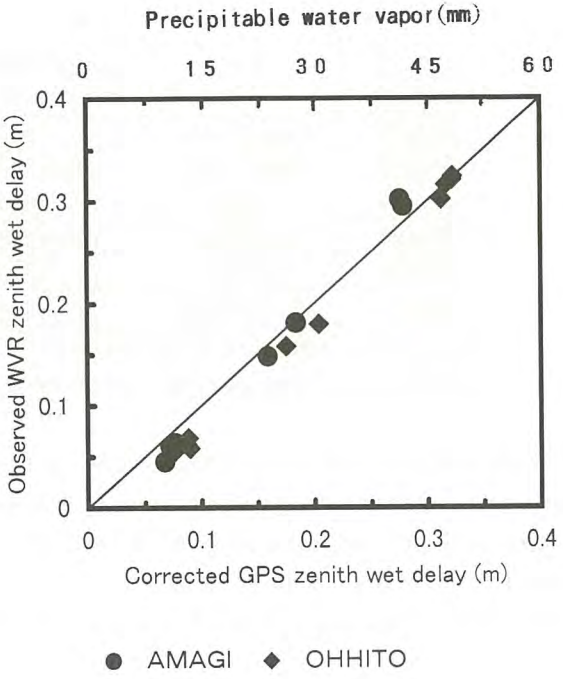


Fig.5 Wet delay compared between GPS and WVR at 10:30 (SAR pass time) and 13:30. Precipitable water vapor is about a factor of 0.15 of wet delay.

5. Application to SAR data

Wet delay corrected by (5) is a spatial average value within a volume above the GPS station. To apply this GPS delay to JERS-1/SAR data, the different characteristics of delay effect between SAR and GPS have to be made clear as shown by Table.2. It is very important to identify the difference of propagation path, delay direction, data acquisition time and data spatial distribution.

Table.2 Differences of delay effect between SAR and GPS

Different point	SAR delay	GPS delay
Observed parameter	Phase change	Residual of a correction term for determination of coordinates
Delay direction	SAR look direction (35deg for JERS-1)	Zenith direction at GPS station
Data acquisition time	Instantaneous (several seconds)	Average value for every 3 hours
Spatial information (data distribution)	Dense (area data)	Sparse (point data)
Path	Round-trip	One-way

Unfortunately, as no good interferogram has been accomplished yet, we can not perform the quantitative evaluation of SAR wet delay. Therefore we tried to estimate the measurement error for atmospheric effect by using GPS wet delay data on the assumption that we obtain a useful interferogram For the sake of its spatial error estimation, local distribution of wet delay has been illustrated in Fig.6 for Izu peninsula area. The combined data shown in Fig.6 is a pair of Aug.11 and Nov.7 which are the largest difference of wet delay. Small wet delay can be seen in the area from central Izu to north-east direction.

The largest delay value appears at NSHIIZU, and smallest does at AMAGI. Its delay difference is about 5.6 cm. Assuming that AMAGI is the control (zero level) point, the error of NSHIIZU relatively becomes to 116 m in height and 14.4cm in displacement for 500m baseline distance. In the case of combination of 9/24 and 11/7 which is the smallest delay, however, the measurement error becomes 35m in height and 4.2cm in displacement at the same point. Hence the difference of wet delay by temporal and spatial variation of water vapor heavily depends on the accuracy of INSAR measurement.

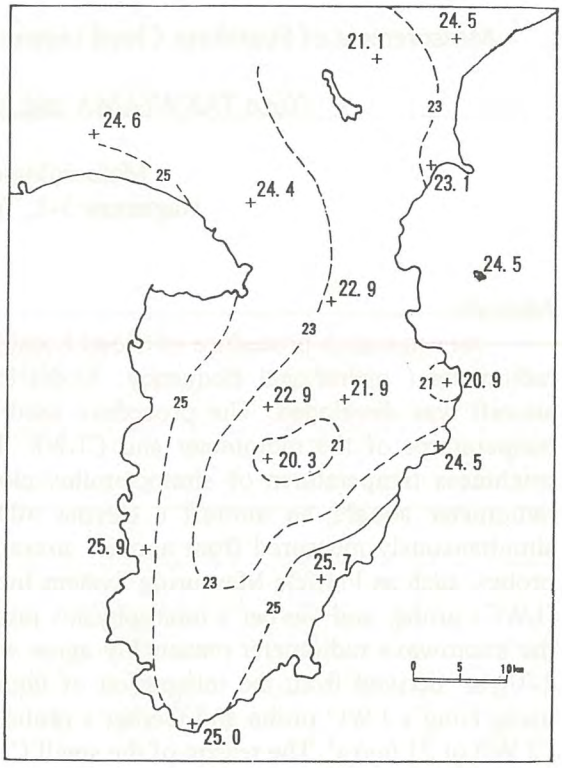


Fig.6 Local wet delay (cm) distribution in IZU peninsula. Used data is 8/11 and 11/7 pair which have the largest difference of wet delay.

6. Conclusion

We have preliminarily analyzed to quantitatively evaluate the atmospheric effect to interferometric SAR measurement using microwave radiometer observation and GPS network data by GSI.

We conclude through these analyses as follows:

(1) The observation results indicate that the wet delay of GPS corresponds well with WVR delay (correlation coefficient is 0.996, rms delay is about 1.8cm), and that GPS database is very useful in the quantitative evaluation of atmospheric delay effect.

(2) The difference of wet delay between summer and autumn observation becomes very large (more than 20 cm), and moreover its spatial distribution reveals a large variation. This suggests that a local variation in water vapor content often bring the severe height and displacement error for INSAR measurement.

(3) If we could obtain the useful interferogram, it is very important to check the relationship between SAR phase delay and GPS phase delay. Finally we have to also consider the algorithm how to develop the sparse GPS data to two dimensional distribution.

References

Fujiwara,S., P.A.Rosen, T.Tobita, and M.Murakami, Crustal deformation measurements using repeat-pass JERS-1 SAR interferometry near the Izu, Japan, J.G.R., 1997. (in press)

GPS/MET JAPAN, Database of precipitable water vapor information in Japan by GPS and application to Meteorology, Environmental Science, and Hydrology, GPS Meteorology workshop in Chiba University, 1997.

GPS/MET JAPAN, Water vapor information system and application to Meteorology, Geodesy, and Hydrology, GPS Meteorology workshop in Kyoto University, 1997.

Radiometrics Corp., WVR-1100 Water Vapor and Liquid water Radiometer, User's Manual, 1997.

Saastamoinen,J., Atmospheric correction for troposphere and stratosphere in radio ranging of satellites, in The Use of Artificial Satellites for Geodesy, Geophys. Monogr. Ser. Vol.15, 247-252, 1972.

Zebker,H.A., P.A.Rosen, and S.Hensley, Atmospheric effects in interferometric synthetic aperture radar surface deformation and topographic maps, J.G.R., Vol.102, No.B4, 7547-7563, 1997.

Measurement of Stratiform Cloud Liquid Water Path from Airborne Microwave Radiometer

Yozo TAKAYAMA and JACCS Aircraft Observation Group

Meteorological Research Institute
Nagamine 1-1, Tsukuba, Ibaraki 305 Japan

Abstract

An estimation procedure of Cloud Liquid Water Path (CLWP) from a dual-frequency microwave radiometer (operational frequency: 23.8GHz and 31.4GHz, Radiometric WVR-1100) aboard an aircraft was developed. The procedure used non-linear regression method between the brightness temperatures of the radiometer and CLWP. The derived CLWP by applying this procedure to the brightness temperatures of stratocumulus cloud over the sea, which were taken by a microwave radiometer aboard an aircraft (Cessna 404 aircraft) over the sea, was compared with those simultaneously measured from another aircraft (Beechcraft B200 aircraft) equipped with the cloud probes, such as Particle Measuring System Inc. (PMS) 1D- and 2D-probes, King's Liquid Water Path (LWC) probe, and Gerber's microphysics probe (PVM-100A). The estimated CLWP of 178g/m^2 by the microwave radiometer reasonably agree with the integrated cloud water contents of 102g/m^2 and 170g/m^2 derived from the integration of liquid water contents given by the sounding measurement using King's LWC probe and Gerber's probe, respectively. The PMS probe, however, showed small CLWP of 21.6g/m^2. The reason of the small CLWP from the PMS probe due to the calibration problem or a size range of this instrument.

1. Introduction

Cloud liquid water path (CLWP) is one of the most important parameters for cloud physics and for study climate change. The accurate method for measuring the CLWP is by using well-calibrated airborne cloud probe. This method, however, is limited in measurement area and in frequency, because of economical limitation. The method of retrieving CLWP from the brightness temperature measured by a microwave radiometer has been developed and has been used from spacecraft, aircraft and ground base measurements (e.g. M. A. Janssen ed. 1993). The usefulness of this method is widely accepted, but the verification of the performance of the microwave method is still difficult and experimental comparisons has been limited in number. Therefore, number of experiment for the verification of the microwave CLWP retrieval methods has been required (Curry et.al. 1990).

We have studied the relation between the layered water cloud structure and its radiative properties, based on aircraft observation using cloud probes, visible, infrared and microwave radiometers. In this study, we developed a retrieval method of CLWP from an airborne dual-frequency microwave radiometer manufactured by Radiometric Inc., and verified the retrieval method by comparing the CLWPs from microwave estimated and from cloud probes such as King's cloud water probe, PMS probe and FSSP probe.

2. Aircraft observation and measurement of cloud liquid water path

In the experiment, two aircraft were used. An aircraft was Beechcraft 200 Super King Air (B200) equipped with cloud probes such as PMS FSSP-100, PMS OAP-2D-C, King's cloud liquid water probe, and AVIOM. This aircraft was used to measure cloud physical parameters by going through a cloud layer from the top of a cloud layer to its base. The other aircraft Cessna 404 Titan (C404) equipped down looking radiometers such as an IR radiometric thermometer, a FTIR radiometer and a dual-frequency microwave radiometer, and one set of Multi-channel Cloud Pyranometer for upward and downward spectral flux measurement. This aircraft was used for measure the radiation from cloud and surface by flying over the cloud layer.

The characteristics of the microwave radiometer is shown table 1. The microwave radiometer (WVR1100) was installed on C404 aircraft, looking nadir to measure the upwelling microwave radiation from the surface, atmosphere and cloud underlying the aircraft. The radiometer has two frequency channels, horizontal polarization 23.8GHz and vertical polarization 31.4GHz, but measure the radiation by two channels in time sharing base. Therefore the time difference is exist about

0.5secand between the measurements in two channels. To retrieving cloud liquid water path from the microwave radiometer, a nonlinear regression algorithm had been developed through simulation study. Comparison of the cloud liquid water path between the estimated using this algorithm and the given values for various atmosphere and cloud models is shown in figure 1. The estimation error of the cloud liquid water path is expected to be about 8%.

We had two simultaneous measurements for stratocumulus cloud using the two aircraft over ocean in January 20 1996 at off-Wakasa bay in Honshyu and in January 22 1997 off-Kagoshima in Kyushyu. Figure 2 shows the vertical distribution of the cloud particle radius (a) and cloud water content distribution (b) measured by the cloud particle probes in the 1997measurement (related information shows in table 2). The cloud layer is roughly uniform in cloud particle size with mean radius of 7μm but had a large variation in liquid water content due to rapid vertical change in its particle number density. For the 1996 measurement, the cloud layer was nearly the same size distribution with the mean radius of 7.5μm but moderate change in cloud water content.

Figure 3 shows the time sequences of the cloud liquid water paths for the 1996 measurement (a) and for the 1997 measurement (b) derived from the microwave radiometer, respectively. The horizontal bars in the figures show the simultaneously measured cloud liquid water paths by the cloud particle probes, the bar lengths show the co-located cloud sounding area/time corresponding to simultaneous measurements by the two aircraft. The negative value of the cloud water path is mainly due to the deviation in observation angle of the microwave radiometer from the nadir direction for C404 aircraft to turn flight course. The cloud liquid water paths derived from the microwave radiometer data reasonably agree with those given by the cloud particle probe measurements. This experimental study shows that the microwave radiometer measurement of a water cloud by using non-linear regression equation gives reasonable estimate of the cloud liquid water path.

3. Conclusion

From simultaneous measurement of stratiform water cloud by microwave radiometer and by cloud particle probes, the microwave radiometer gives reasonable cloud liquid water path was verified. Therefore the microwave radiometer data would provide useful reference information for cloud study.

References

Curry, J.A, C.D. Srdeel and L. Tian, Liquid water content and precipitation characteristics of stratiform clouds as inferred from satellite microwave measurement, J. Geophys. Res., 95, D10, 16659-16671, 1990.

Atmospheric remote sensing by microwave radiometry, Janssen, M. A., Ed. 1993, John Wiley & Sons. 1-572.

Table 1 Characteristics of a dual-frequency microwave radiometer WVR1100

Operational frequency	23.8GHz and 31.4GHz, time-shared
bandwidth	400MHz (double-side band)
receiver	total-power receiver
antenna	6" Gaussian lens antenna and corrugated feed horn
antenna gain	32dBi
beam width	5.7/4.4 degree for 23.8 and 31.4GHz (full angle at half power)
radiometric accuracy	1K
measurement range	0-500K
sampling time	1 sec.
polarization	linear: vertical/horizontal
calibration	blackbody, noise diode and tipping curves
scanning resolution	0.45 degree

Table 2 Cloud Liquid Water Path (g/m^2) of stratocumulus cloud derived from vertically summing up cloud water density measured by aircraft sounding using King LWC, PVM-100A, FSSP probes and microwave radiometer in 1997. 1. 22 at local time of 12.29 – 12.32

cloud layer height	1.78 (top) – 1.14 (base) km
10um IR cloud top brightness temperature	-5.7C
10um IR sea surface brightness temperature	17.3 – 11.3 C
air temperature at cloud top	-9.0 C
air temperature at cloud base	-5.5 C
sounding area latitude	31.41- 31.30 N
longitude	129.48-129.53 E
mean diameter of cloud particle	7.0μm (PVM)
	5.5μm (FSSP)
CLWP	g/m^2
Aircraft: Beechcraft B200	
King LWC	102.1
Gerber PVM-100A	169.6
FSSP	21.6
Aircraft: Cessna C404	
Microwave Radiometer	182.7
(averaged value retrieved CLWP over sounding area)	

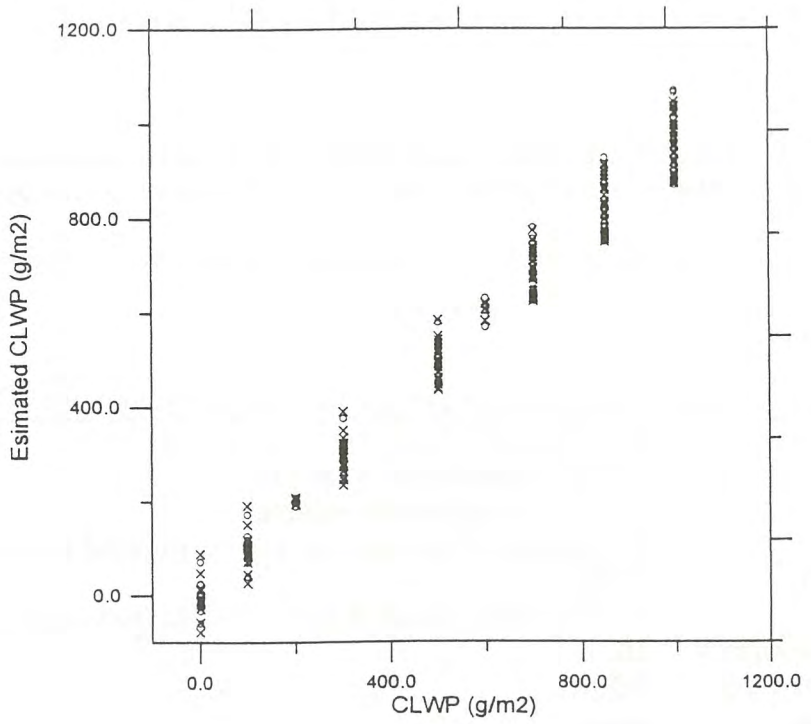


Figure 1 Estimated cloud liquid water path by using the non-linear regression algorithm for WVR1100 airbone microwave radiometer

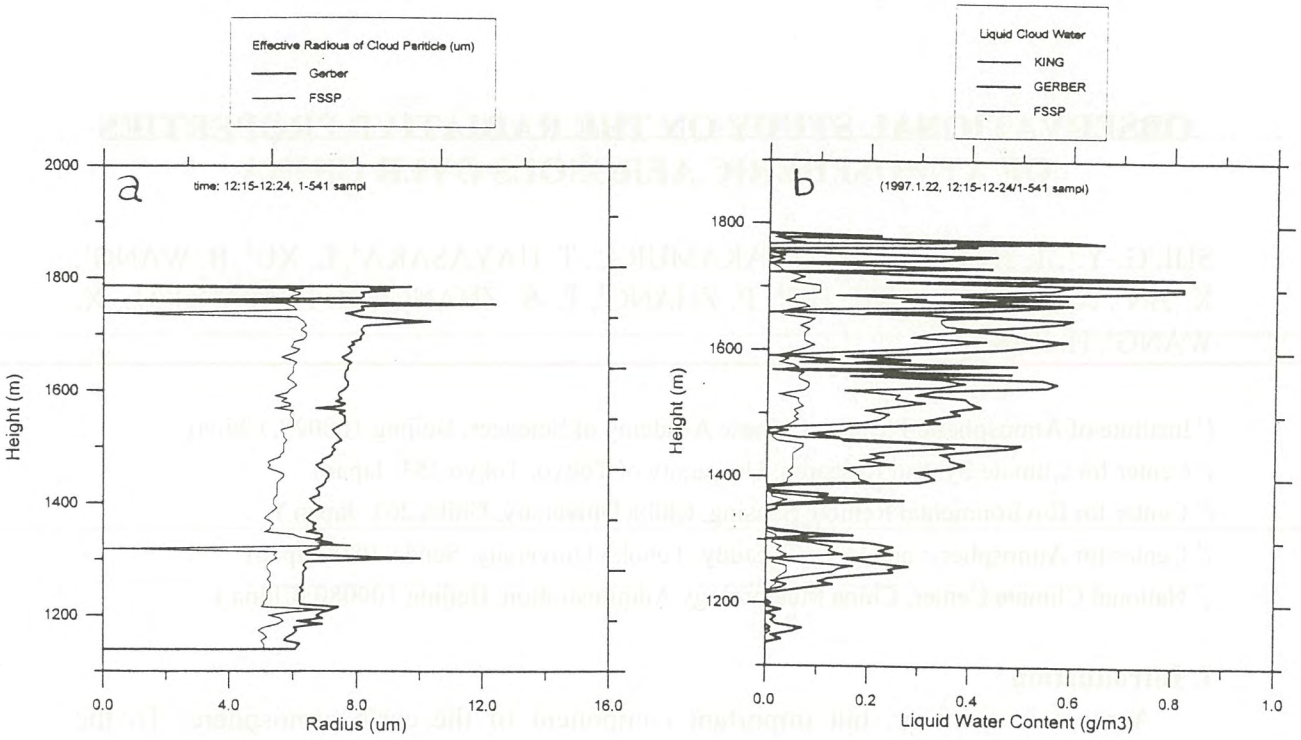


Figure 2 Vertical cloud particle radius distribution of stratocumulus cloud layer (a) and its cloud liquid water content distribution measured by the cloud particle probes.

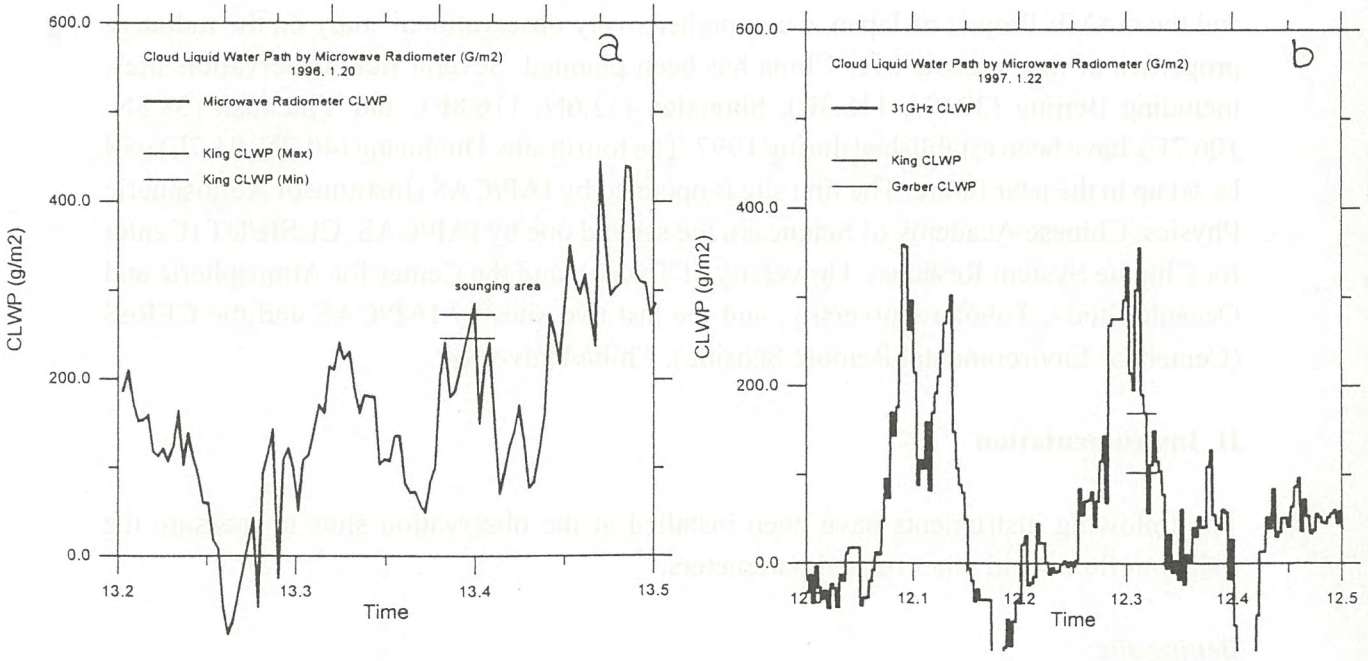


Figure 3 Cloud liquid water path retrieved from the microwave radiometer data and measured by the cloud probes.

OBSERVATIONAL STUDY ON THE RADIATIVE PROPERTIES OF ATMOSPHERIC AEROSOLS OVER CHINA

SHI, G.-Y.[1], T. NAKAJIMA[2], T. TAKAMURA[3], T. HAYASAKA[4], L. XU[5], B. WANG[1], X. JIN[1], X.-B. FAN[1], R.-M. HU[1], P. ZHANG[1], L.-S. ZHANG[1], X.-H. WANG[1], L.-X. WANG[1], H. ZHANG[1]

([1] Institute of Atmospheric Physics, Chinese Academy of Sciences, Beijing 100029, China)
([2] Center for Climate System Research, University of Tokyo, Tokyo 153, Japan)
([3] Center for Environmental Remote Sensing, Chiba University, Chiba 263, Japan)
([4] Center for Atmospheric and Oceanic Study, Tohoku University, Sendai 980, Japan)
([5] National Climate Center, China Meteorology Administration, Beijing 100080, China)

I. Introduction

Aerosol is a minor, but important component of the earth atmosphere. To the atmospheric sciences, the importance of the aerosols is not only represented in their effects on the climate change through both of their direct and indirect radiative forcing, but also in that they can affect the interpretation of satellite remote sensing data through their interference in the atmospheric radiation field.

Under the supports of NSFC (National Natural Science Foundation of China), NASDA, and the GAME Project of Japan, a comprehensively observational study on the radiative properties of the aerosols over China has been planned. Several field observation sites, including Beijing (39.9N, 116.3E), Shouxian (32.6N, 116.8E), and Yinchuan (38.5N, 106.2E), have been established during 1997. The fourth site, Dunhuang (40.2N, 94.7E) will be set up in the near future. The first site is operated by IAP/CAS (Institute of Atmospheric Physics, Chinese Academy of Sciences), the second one by IAP/CAS, CCSR/UT (Center for Climate System Research, University of Tokyo), and the Center for Atmospheric and Oceanic Study, Tohoku University, and the last two sites by IAP/CAS and the CEReS (Center for Environmental Remote Sensing), Chiba University.

II. Instrumentation

The following instruments have been installed at the observation sites to measure the radiation fluxes and other related parameters.

Beijing site:

Sky radiometer, Sunphotometer, Pyrheliometer for direct solar radiation, Pyranometers for global solar radiation, Pyranometer for downward flux with shadow disk, Pyranometer for reflected solar radiation, Optical Particle Counter

Shouxian site:

Sky radiometer, Pyrheliometer for direct solar radiation, Pyranometer for downward

flux with shadow disk, Pyranometer for reflected solar radiation, Pyrgeometer for downward thermal radiation, Pyrgeometer for ground emitted radiation

Yinchuan site:

Sky radiometer, Pyranometer for downward solar flux, Pyrgeometer for downward thermal, sensors for temperatures and humidity

III. Preliminary Results

The observations at Beijing, Shouxian and Yinchuan sites began in May, August and December 1997, respectively. The data from Beijing site have been analyzed tentatively.

From data obtained from Sky radiometer, the daily averaged column aerosols' optical depths can be found a large variation from day to day, with the large and small extremes of 1.2 and 0.2, respectively. The diurnal variation of column aerosols is relatively stable. In this period, typical bi-modal spectrum of aerosol particle size were observed, with the mode radius near 0.05 and 3 μm. As an illustration, Fig.1 shows the spectral distribution of optical depths, size distribution and phase functions on two selected days, in which we can notice that the larger optical depths are corresponding to the larger particle size and hence the stronger forward scattering, which is a common phenomenon over Beijing area.

With data obtained from sunphotometer, we retrieved the optical thickness of aerosols and their daily average values.

OPC observation is an *in situ* measurement of surface aerosols, which are always influenced by environment and weather condition around this area. However, further comparison between the results of sky radiometer, sunphotometer and OPC associated with data of conventional weather observation will reveal more interesting information.

With pyrheliometer and pyranometer, the solar radiation from 6 a.m. to 18 p.m. for every day was observed once a minute. Fig.2a shows an example of clear day. It can be seen that the observed global fluxes are close to the theoretical values for Middle Latitude Summer Atmosphere. Fig.2b shows a typical cloudy day, the diffuse flux is significantly larger than that of above, and the direct flux is much weaker. Around the mid-day, the shadowing and scattering effects of clouds are most significant. During an overcast day, the discrepancy between the theoretical values for Middle Latitude Summer Atmosphere and observation is very large (Fig.2c). These examples suggest that ground-based observation of solar radiation may contain useful information about clouds; further analysis combined with radiation transfer theory will arrive at some useful empirical relation and prompt the application of surface observation of radiation.

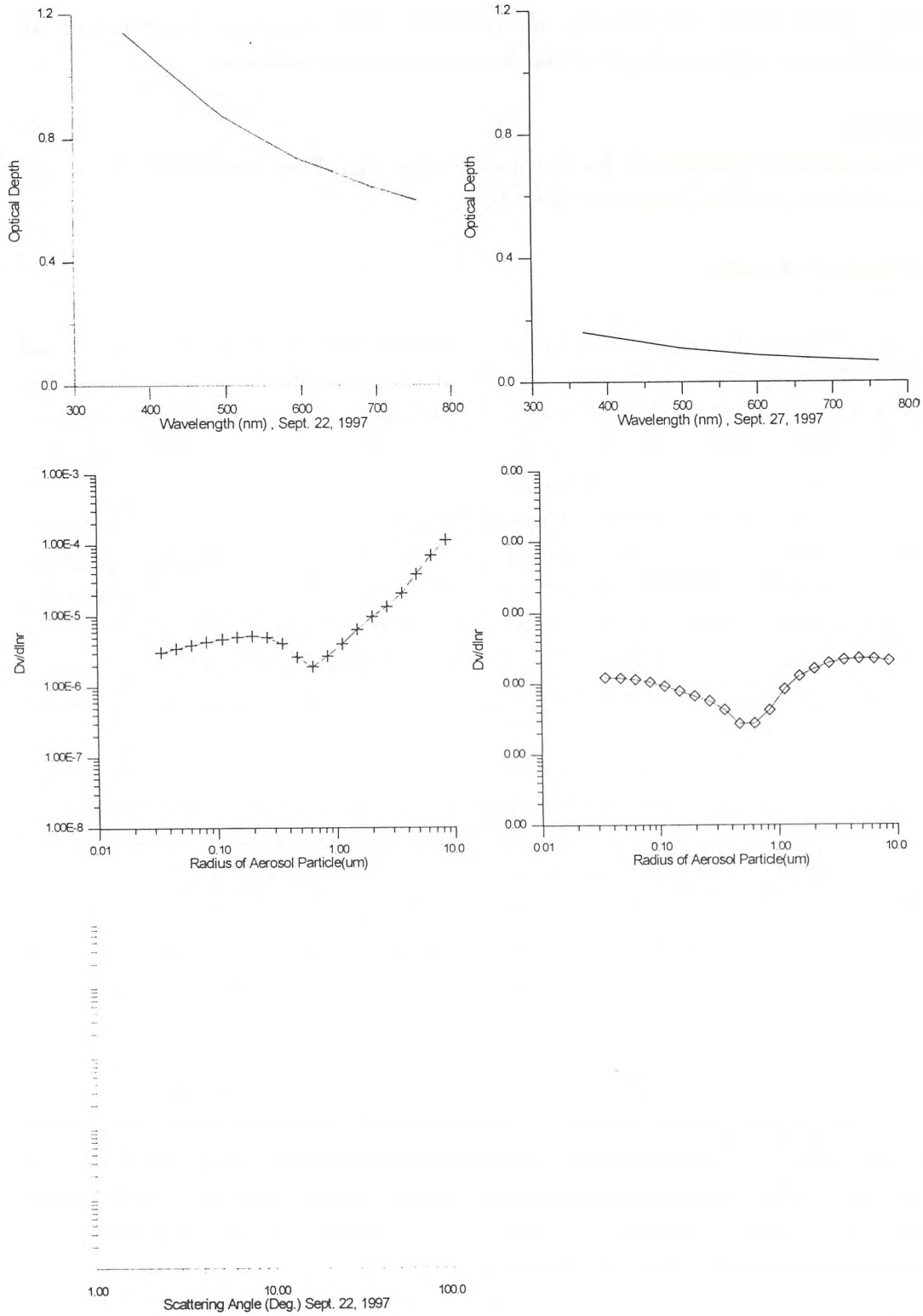


Fig.1. Optical depths, size distribution and phase functions of aerosol on two days, Beijing.

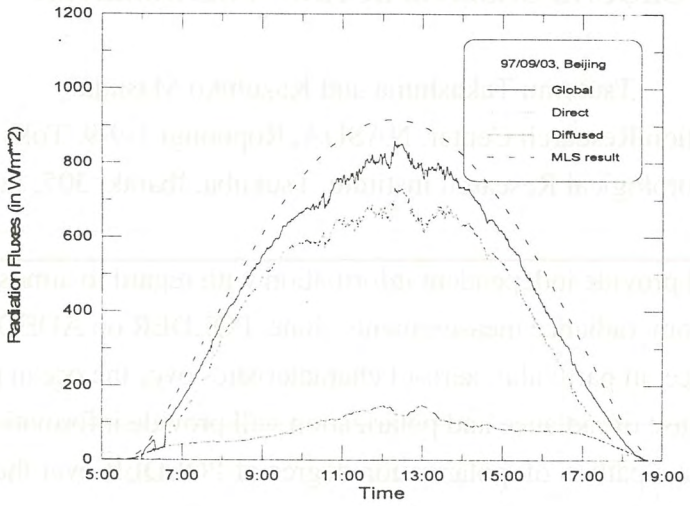


Fig.2a. Surface solar radiation, Beijing, Sept. 3, 1997.

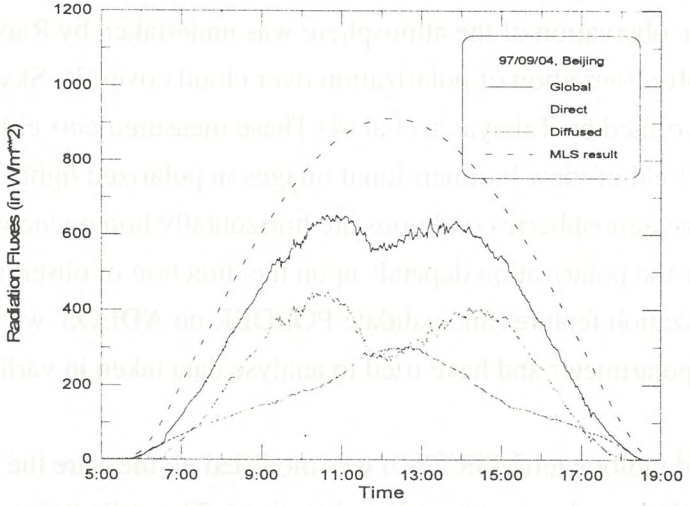


Fig.2b. Surface solar radiation, Beijing, Sept. 4, 1997.

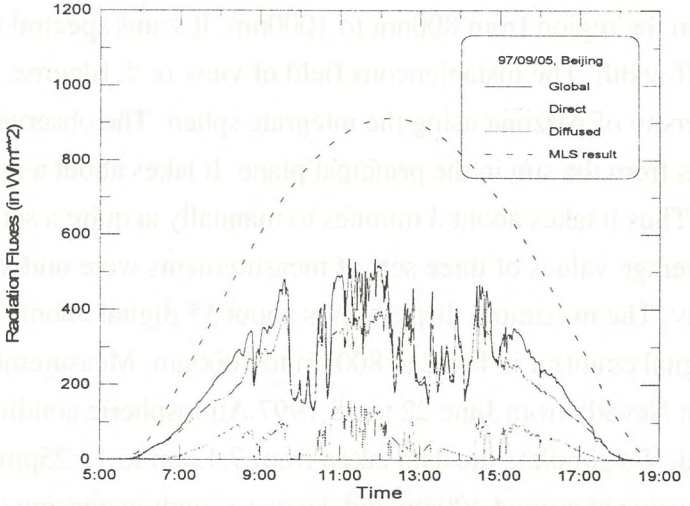


Fig.2c. Surface solar radiation, Beijing, Sept. 5, 1997.

ATMOSPHERIC AEROSOL PROPERTIES OVER LUNAR LAKE,NEVADA USING THE GROUND BASED SPECTRO－POLARIMETER

Tsutomu Takashima and Kazuhiko Masuda*
Earth Observation Research Center, NASDA, Roppongi 1-9-9, Tokyo 106, Japan
* Meteorological Research Institute, Tsukuba, Ibaraki 305, Japan

Polarization would provide independent information with regard to atmosphere-surface system than can be deduced from radiance measurements alone. POLDER on ADEOS is first trial to derive Earth system from space, in particular, aerosol characteristics over the ocean more precisely. Therefore a combined use of radiance and polarization will provide information on aerosols among others.When we look at a pattern of polarization degree of POLDER over the ocean, we noticed neutral points that could be from the interaction of radiation between atmosphere and ocean.

In the polarization community, there is a limited number of atmospheric measurements. For example, balloon borne obsrvation of the atmosphere was undertaken by Rao et al.(1) and Deuze et al.(2), as well as aircraft observation of polarization over cloud cover(3). Skylight measurements on the vessel were performed by Takayama et al.(4).These measurements either scan the principal plane or observe wide field of view bidimensional images in polarized light. These would provide useful information if the atmospheric conditions are horizontally homogeneous. Otherwise, these are rather tedious since the polarization depends upon the direction of observation.

To understand polarization features and validate POLDER on ADEOS, we have developed ground based spectro-polarimeter and have tried to analyse data taken in various atmospheric and surface conditions.

A multipurpose field radiometer(MSR7000) was modified to measure the degree of polarization and radiance of the skylight at the corresponding direction. The radiometer covers the spectral region ranging from 400nm to 1000nm. The detectors are photomultiplier in the region from 400nm to 800nm and silicon in the region from 800nm to 1000nm. It scans spectral range with 1nm intervals with 5nm half width. The instanteneous field of view is ±1degree. The radiometer was calibrated at the University of Arizona using the integrate sphere.The observation direction is set manually to 90 degrees from the sun in the principal plane. It takes about a minute to measure a polarized component. Thus it takes about 3 minutes to manually acquire a set of polarization measurements. The average values of three sets of measurements were undertaken. Dark current was checked frequently. The maximum dispersion is about 15 digital counts at 400 to 800nm (mostly less than 5 digital count);it is 1 to 2 at 800nm to 1000nm. Measurements were undertaken over the Lunar Lake in Nevada from June 22 to 28,1997.Atmospheric condition is clear in the morning without cloud. We simulate the data taken from 7:13am to 13:25pm on June 24. The radiance hits the peak value at around 400nm and decreases with increasing the wavelength, exhibiting some drops in the region (from 410nm to 550nm). The corresponding polarization degrees to these drops are rather insensitive. Therefore these drops are due to the Fraunhofer lines.

Polarization degrees exhibit scattered values in the wavelength regions longer than 750nm in the data of early morning(7:13,7:35 and 8:00). However, it was converged within the small region afterwards. Polarization exhibits rather sensitive to the atmospheric parameters such as water vapor, oxygen and aerosols. In the above wavelengthe region, a number of water vapor absorption bands exist. Thus water vapor amount might be decreased or aerosol might be smoothed out. A vertical profile of these mixed gases play an important role on polarization features. Note that when three sets of polarization data taken at 7:13 was compared, higher polarization of first data set corresponds to that of second and third data set. This indicates that scattered values could not be noise. Polarization degree increases with increasing wavelength and reaches maximum at 500nm. At 7:35, it is a little over 70%. And then it decreases with increasing wavelength. It decreases sharply beyond 700nm.This indicates that the optical thickness of the aerosol in the atmosphere could not decrease with increasing wavelength.

Fig.1 shows one of example of observation(radiance and polarization degree) to angle of 90 degree from the sun in the principal plane. Symbols,x and o are simulation at the corresponding POLDER polarization channels,443nm,670nm and 865nm. They are aerosol optical thicknesses,0 & 0.25(dust-like model). The surface is assumed to be Lambertian. SZA denotes solar zenith angle.The radiance R exhibits well correspondence to the measurement at 670nm, but it is lower at 865nm and higher at 443nm. The polarization degree is a little lower than the measurement at 443nm and 670nm, but higher at 865nm. Simulation exhibits that the reflected radiance by the surface play an important role, since the reflectance is rather high(up to 45% according to Dr.S. Tsuchida). To validate the surface reflectance properties, we observed the reflected radiation at two directions. Fig.2 shows illustration of measurements of surface reflection properties. Rb and Rf denote radiance to backward and forward directions with regard to the solar direction. The corresponding polarization degree is Pb and Pf. The nadir angle of observations changes with a change of solar zenith angle.Fig.3 shows one of example of radiance and polarization degree. Rb is 15～20% higher than Rf.This reflection property differs clearly that of Lambertian. The reflected radiation by the Lunar lake exhibits little polarization.It is less than 5% for Pf and practically zero for Pb.This is close to Lambertian characteristics.

References

(1) Rao,C.R.N.,T.Takashima and R.B.Toolin; Measurements and interpretation of the polarization of radiation emerging from the atmosphere at an altitude of 28km over south-western New Mexico(USA), Q.J.Roy.Met.Soc.,99,pp294-302,1973.

(2) Deuse,J.L.,Devaux,C.,Herman,M.,Santer,R.,Balois,J.Y.,Gonzalez,L.,Lecomte,P., and Verwaerde,C.; Photopolarimetric observations of aerosols and clouds from balloon, Remote Sens.Environ. 29,93-109, 1989.

(3) Goloub,P.,Deuze,J.L., Herman,M. and Fouquart,Y; Analysis of POLDER polarization measurements performed over cloud covers, IEEE Trans.Geosci.Remote Sens. 32,78-88,1994.

(4) Takayama,Y.K.Masuda and T.Takashima; Polarimetric investigation of the atmospheric aerosols over the Pacific ocean, Int.J.Remote Sens.,12,969-983,1991.

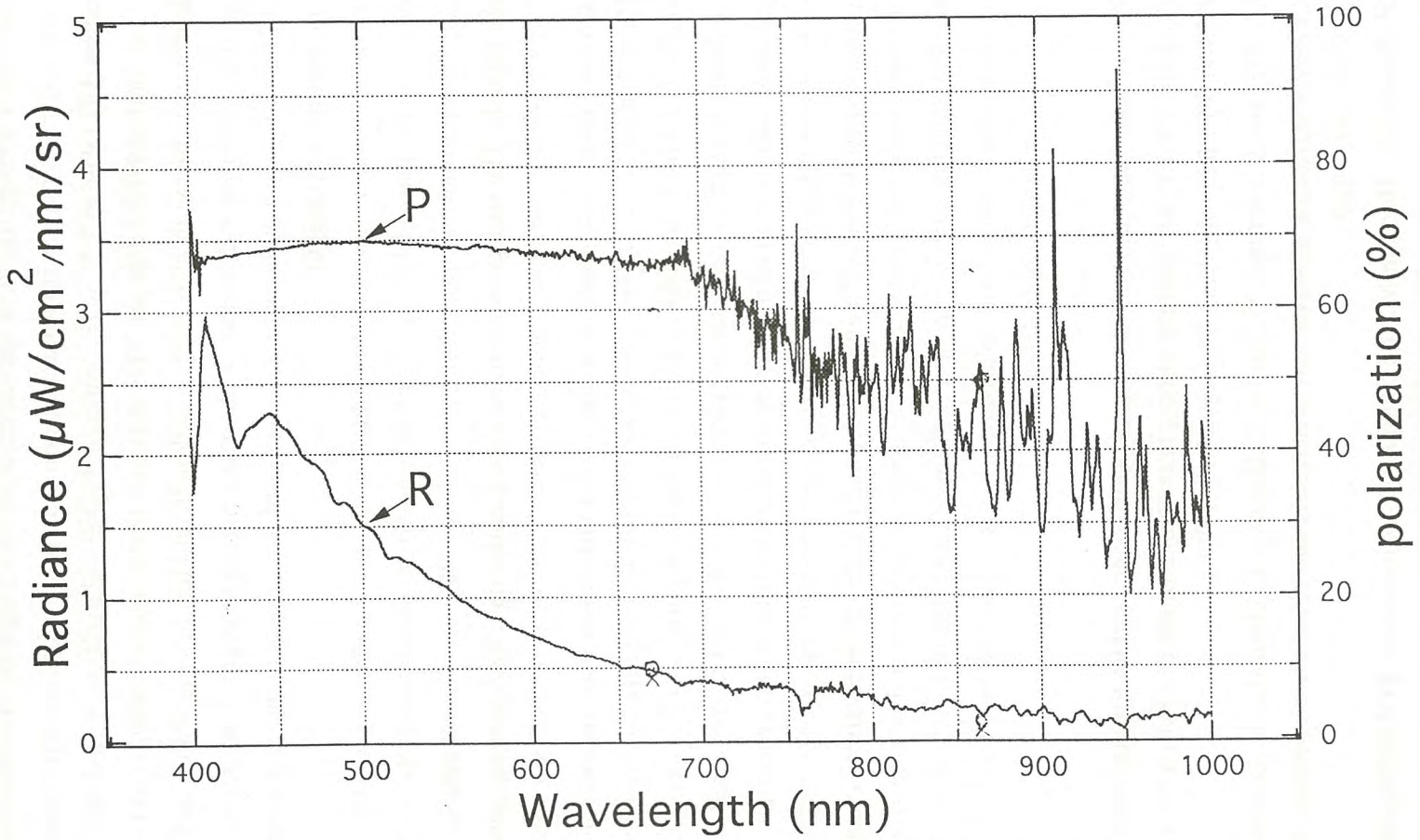


Fig.1 shows one of example of observation(radiance and polarization degree) to angle of 90 degree from the sun in the principal plane. Symbols,x and o are simulation at the corresponding POLDER polarization channels. They are aerosol optical thicknesses,0 & 0.25(dust-like model). SZA denotes solar zenith angle.

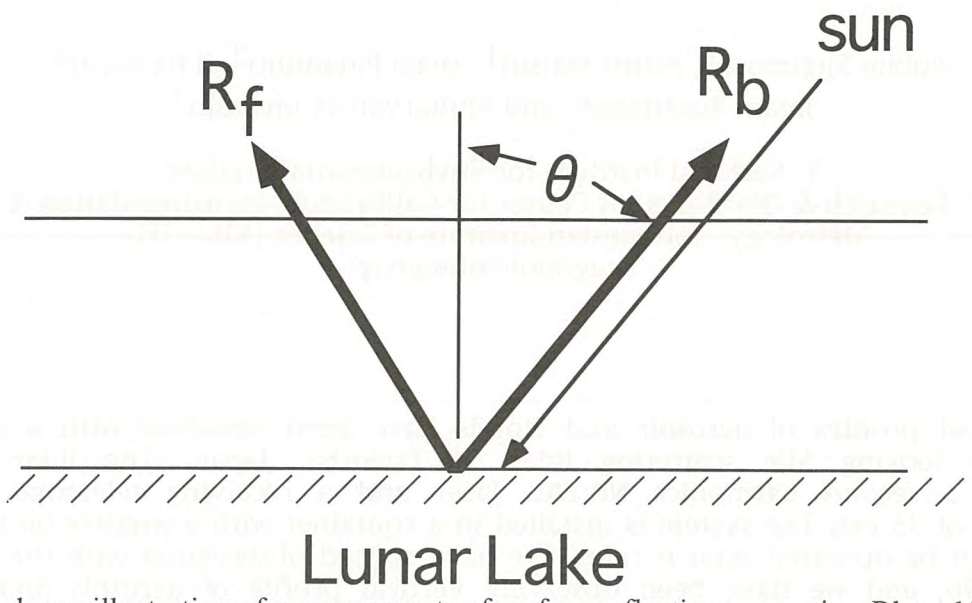


Fig.2 shows illustration of measurements of surface reflection properties. Rb and Rf denote radiance to the backward and forward directions with regard to the solar direction. The nadir angle of observations changes with a change of solar zenith angle.

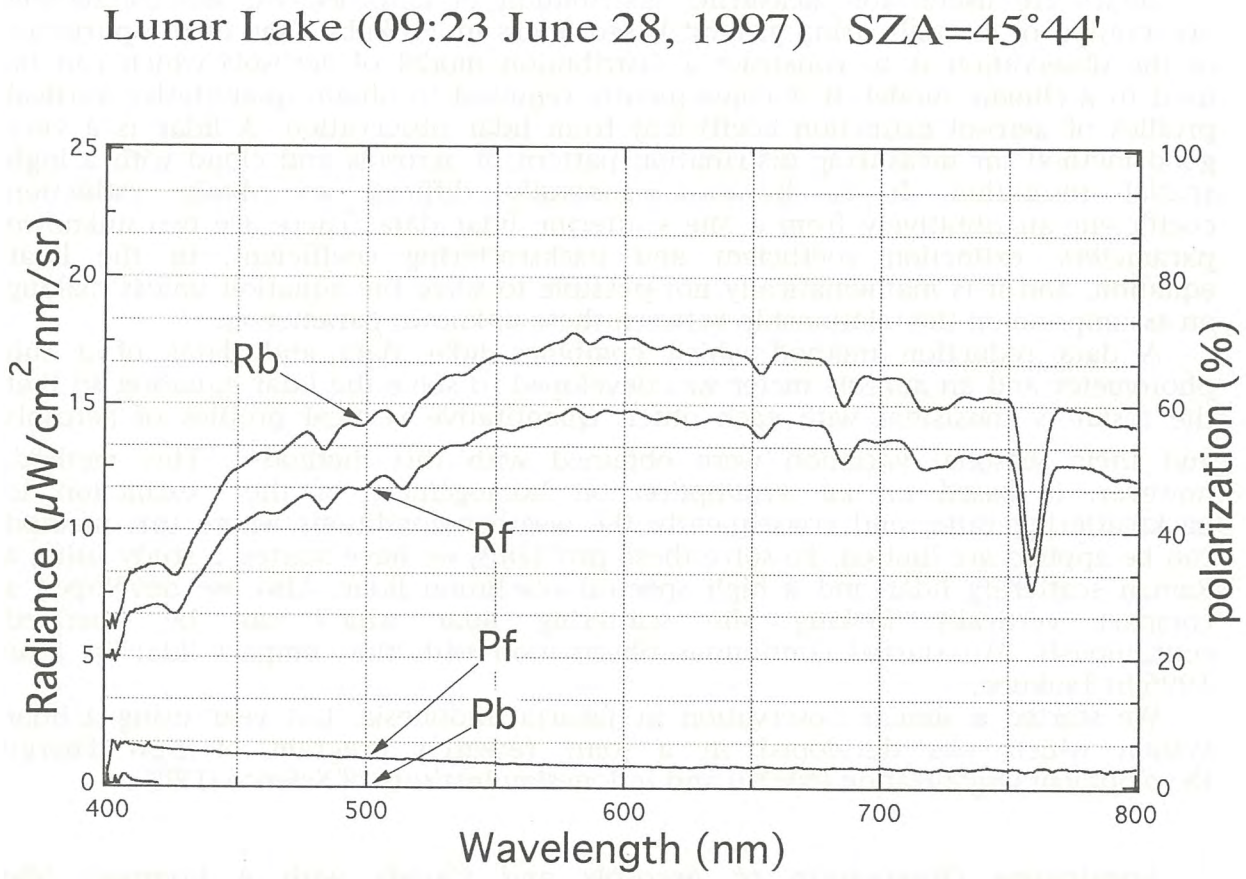


Fig.3 shows one of example of radiance and polarization degree. Rb is higher than Rf. The reflected radiation by the Lunar lake exhibits little polarization.

Continuous observation of aerosols and clouds with ground based lidars in Tsukuba, Japan and in Jakarta, Indonesia

Nobuo Sugimoto[1], Ichiro Matsui[1], Mego Pinandito[2], Ii Hydayat[2], Imam Rosananto[2] and Muharyan Syamsudin[2]

1. National Institute for Environmental Studies
2. Reaearch & Development Center for Calibration, Instrumentation & Metrology, Indonesian Institute of Science (KIM-LIPI)
nsugimot@nies.go.jp

Abstract

Vertical profiles of aerosols and clouds have been observed with a compact vertically looking Mie scattering lidar in Tsukuba, Japan. The lidar system employs a second harmonics Nd:YAG laser and a receiving telescope with a diameter of 35 cm. The system is installed in a container with a window on the loof, and it can be operated even it rains. We have started observation with the lidar in June 1996, and we have been observing vertical profile of aerosols and clouds continuously over Tsukuba. Typical diurnal variation of the atmospheric boundary layer structure and changes with longer time scales are observed. We have recently started similar observation in Jakarta, Indonesia.

1. Introduction

Lidars are useful for measuring distribution of aerosols. We are conducting observation of aerosols using ground based lidars in Tsukuba. One of the purposes of the observation is to construct a distribution model of aerosols which can be used in a climate model. It is consequently required to obtain quantitative vertical profiles of aerosol extinction coefficient from lidar observation. A lidar is a very good method for measuring distribution pattern of aerosols and cloud with a high spatial resolution. It is, however, generally difficult to obtain extinction coefficient quantitatively from a Mie scattering lidar data. There are two unknown parameters, extinction coefficient and backscattering coefficient, in the lidar equation, and it is mathematically not possible to solve the equation unless making an assumption on the relationship between these unknown parameters.

A data reduction method which combines lidar data and datas of a sun photometer and an aureole meter was developed to solve the lidar equation so that the result is consistent with each other. Quantitative vertical profiles of aerosols and their seasonal variation were obtained with this method[1)]. This method, however, is based on an assumption on homogeniety of the extinction to backscattering ratio, and consequently the weather conditions where this method can be applied are limited. To solve these problems, we have started a study using a Raman scattering lidar and a high spectral resolution lidar. Also, we developed a compact vertically looking Mie scattering lidar which can be operated continuously. We started continuous observation with the compact lidar in June 1996 in Tsukuba.

We started a similar observation in Jakarta, Indonesia, last year using a lidar system which was developed in a joint research program of New Energy Development Organization (NEDO) and Indonesian Institute of Science (LIPI) .

2. Continuous Observation of Aerosols and Clouds with a Compact Mie Scattering Lidar

The compact Mie scattering lidar employs a second harmonics Nd:YAG laser as a light source. The receiving telescope has a diameter of 35 cm. The system is

installed in a container with a window on the loof.[2] Observation is being carried out continuously. Vertical profiles of aerosols averaged 5 minutes are recorded every 15 minutes. Figure 1 shows an examples of a range corrected time-height indication during one month. Signal intensity is higher in the brighter areas in the figure. The strong signals indicate scattering at cloud bases. Diurnal variation of aerosol profile is seen in Fig. 1. Also changes in aerosol distribution with a time scale of several days is seen in Fig. 1. Changes in cloud base hight associated with passage of warm fronts are also seen in Fig.1.

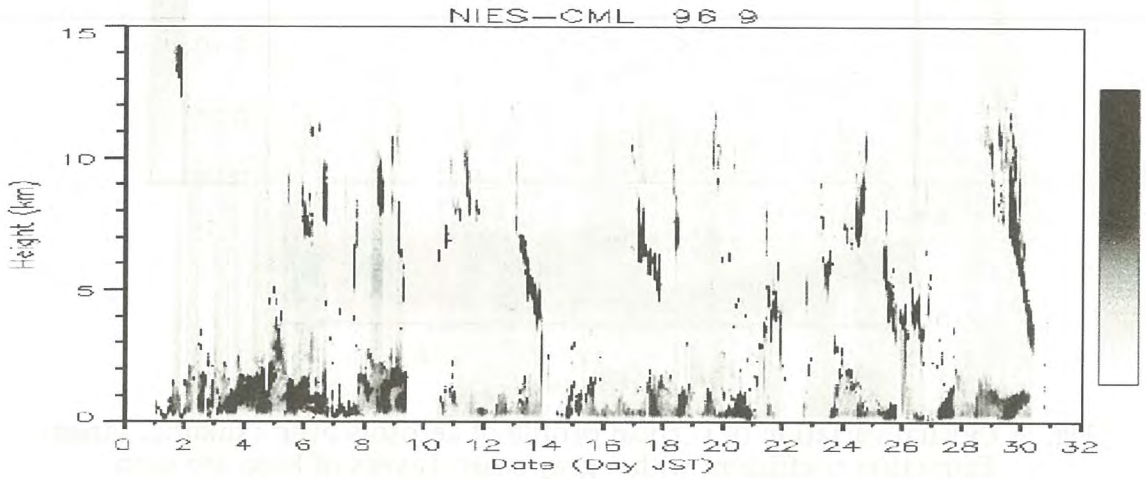


Fig. 1 Variation of vertical profile of aerosols and clouds during a month.

Figure 2 shows seasonal variation of cloud base height. It can be seen that cloud base height of high altitude clouds is higher in the summer and lower in the winter. On the other hand, cloud base height of lower clouds is lower in the summer.

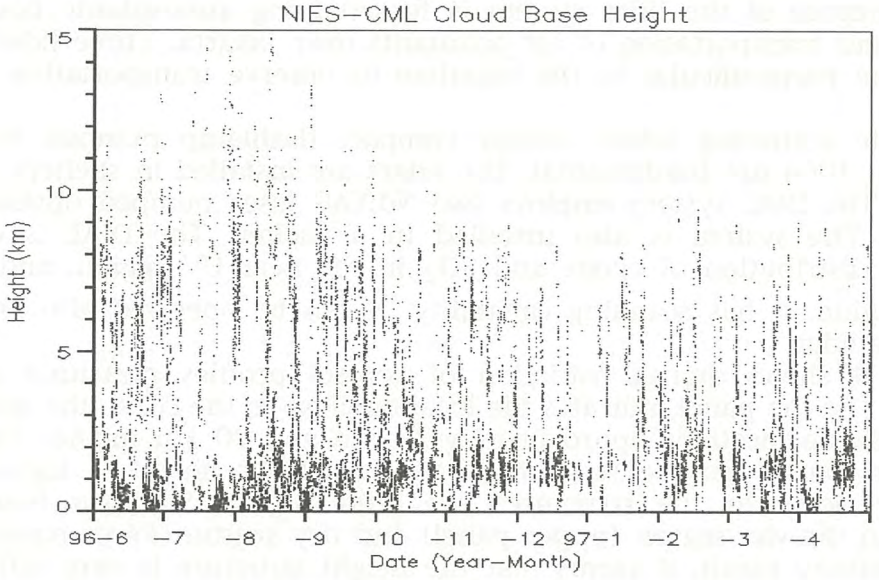


Fig. 2 Seasonal variation of cloud base height.

Vertical profiles of aerosol extinction coefficient were obtained using the Fernald's method. Figure 3 shows an example. In this example layers of Kosa or Asian dust are observed. We are conducting climatological study using these data.

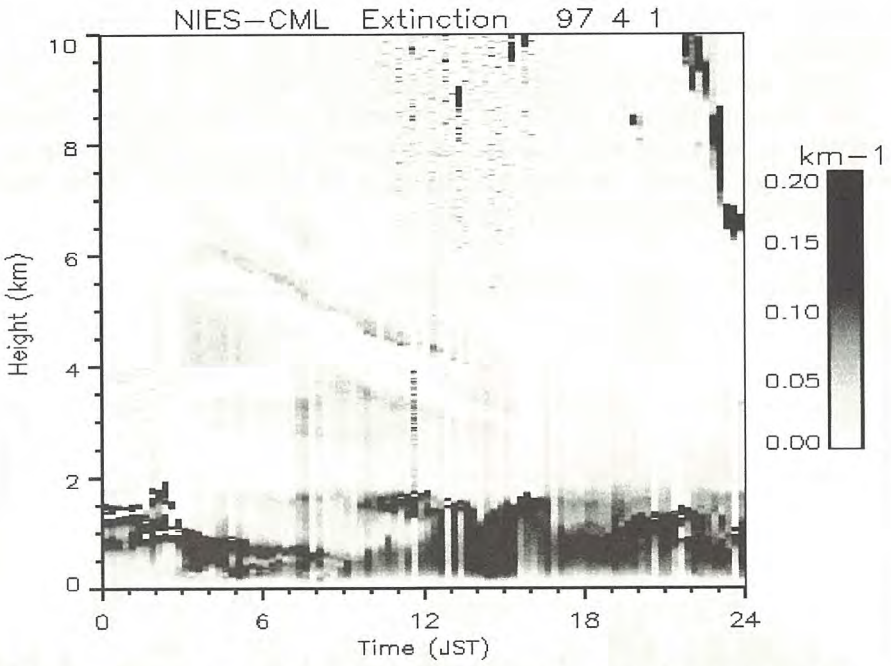


Fig. 3 Diurnal variation of vertical profile of aerosols over Tsukuba, Japan. Extinction coefficient with a gray scale. Layers of Kosa are seen at around 3-8 km altitude.

3. Observation of Aerosols and Clouds with Mie Scattering Lidars in Jakarta

We recently started lidar observation in Jakarta, Indonesia in the NEDO-LIPI joint program. The lidar system consists of three lidars, two Mie scattering lidars and one differential absorption lidar (DIAL) installed at three locations in Jakarta. Primary purpose of the lidar system is for studying atmospheric boundary layer structure and transportation of air pollutants over Jakarta. Three lidar are located along a line perpendicular to the coastline to observe transportation by sea/land breeze.

The Mie scattering lidars employ compact flashlamp pumped Nd:YAG lasers operated at 1064 nm fundamental. The lidars are installed in shelters and directed vertically. The DIAL system employs two Nd:YAG laser pumped optical parametric oscillators. The system is also installed in a shelter. The DIAL is designed for measuring distribution of ozone and SO_2 in the near UV region, and NO_2 in the 450-nm region. It has scanning capability. It can be operated also as a vertically looking Mie lidar.

Figure 4 shows diurnal variation of aerosol profiles measured at the three locations. The top panel indicates the location close to the coast, the middle and the bottom indicate locations approximately 10 km and 20 km inland. The structures are similar, but it can be seen that boundary layer height is higher in inland. Also, time delay in the structures are seen. Figure 5 shows boundary layer structure in the wet season (upper panel) and dry season (lower panel). Though it is a preliminary result, it seems that the height structure is very different in wet and dry seasons. We plan to continue observation and climatological study.

References

1) Sasano, Y., Tropospheric Aerosol Extinction Coefficient Profiles Derived from Scanning Lidar Measurements over Tsukuba, Japan, from 1990 to 1993, Appl. Opt. 35 (24) 4941-4952 (1996).
2) Matsui, N. Sugimoto, S. Maksyutov, G. Inoue, E. Kadygrov, and S. Vyazankin,

Comparison of Atmospheric Boundary Layer Structure Measured with a Microwave Temperature Profiler and a Mie Scattering Lidar, Jpn. J. Appl. Phys. 35, 2168-2169 (1996).

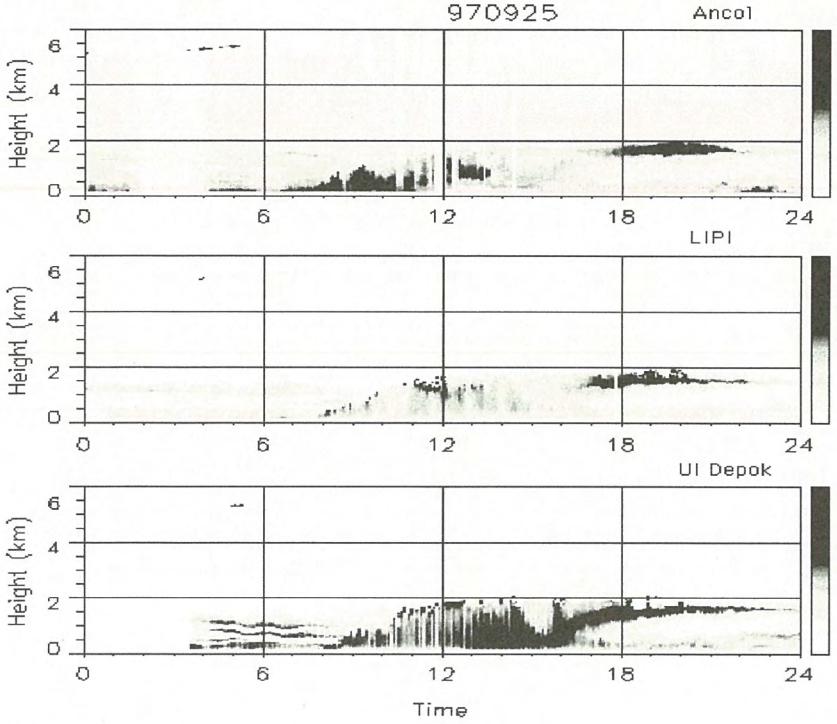


Fig.4 diurnal variation of aerosol profiles measured at the three locations in Jakarta.

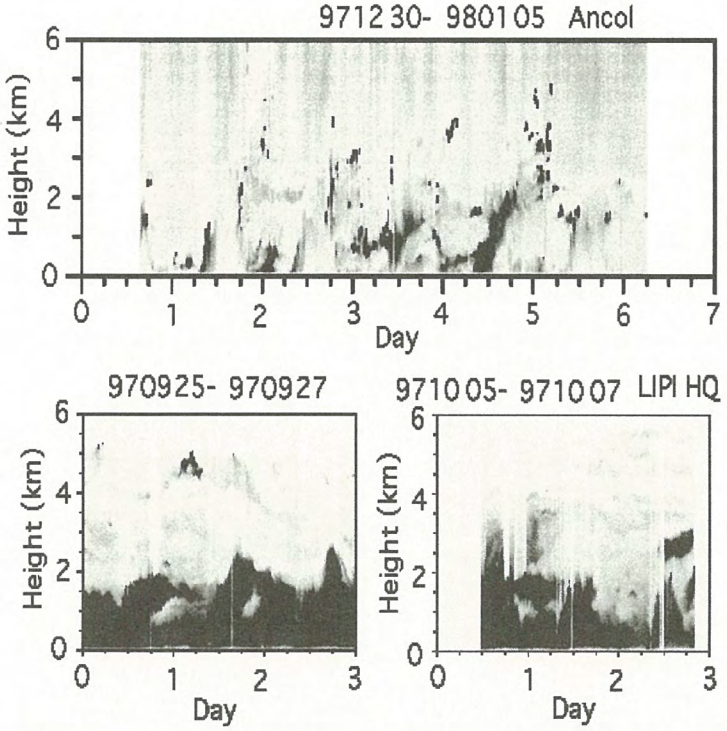


Fig.5 Preliminaly result showing difference in boundary layer structure in the wet season and dry season in Jakarta.

Satellite Workshop :
The Accuracy of Optical Thickness Derived from Lidar Observation

Calibration of the vertical lidar measurement of tropospheric aerosol extinction coefficients

Hideki Kinjo*, Hiroaki Kuze, Hiroaki Matsusima and Nobuo Takeuchi
CEReS, Chiba University, 1-33 Yayoi-cho, Inage-ku, 263-8522 Japan
*e-mail: wood@rsirc.cr.chiba-u.ac.jp

In the derivation of aerosol profile from lidar data one has to assume an appropriate value for the aerosol extinction coefficient at a critical range which is usually set at a distance well outside the detection range. Since this value influences the absolute magnitude of the aerosol extinction through the atmosphere, it is desirable to have a means for calibration. Here we propose the use of ground-level extinction coefficient measured with an integrated nephelometer. For the calibration of atmospheric data collection lidar (ADCL) data the additional information obtained using a portable lidar is found to be useful for connecting the ground-level value with the retrieved value at the lowest altitude (ca. 100m) determined by the overlapping of the laser beams with telescope field-of-view.

1. Introduction

Recently we have constructed an atmospheric data collection lidar (ADCL) to obtain the aerosol data needed to perform the atmospheric correction to satellite remote-sensing data. To obtain good precision in inverting the ADCL data for the case that the condition of a large optical thickness cannot be fulfilled, here we propose to use the calibration value obtained with an integrated nephelometer set at ground level. In the case of our atmospheric data collection lidar the lowest altitude determined by the overlapping of the laser beams with telescope field-of-view is approximately 400 m above ground level in vertical measurement with 3 mrad field-of-view. This lower limit, which is introduced to prevent the saturation of the detection system, can be alleviated by employing a larger field-of-view angle, but cannot be eliminated completely. In order to obtain the relevant information between the ground level and the overlapping point we make use of a portable lidar set at an elevation angle of 20 degrees. In the actual process it is assumed that the medium between the laboratory level (about 60 m above sea level) and the full overlap point of the portable lidar (about 160 m above sea level) is homogeneous.

2. Experimental situation

Figure 1 shows the schematic diagram of the experiment.

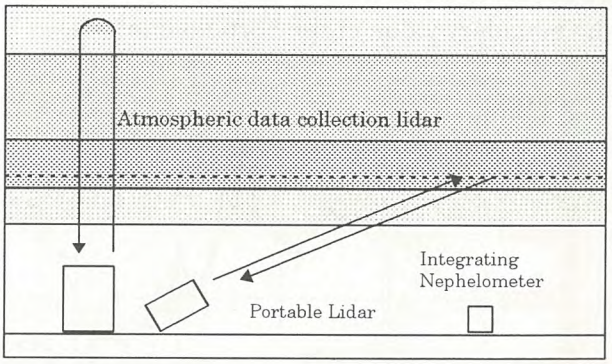


Fig.1 Schematic diagram of the experiment. All the instruments are located at an elevation height of approximately 60 m above mean sea level.

Aerosol vertical profile measurement at the Nd:YAG laser wavelength of 532 nm has been performed using our atmospheric data collection lidar. Simultaneously a portable lidar with a Nd:YAG laser; wavelength 532 nm at an elevation angle of 20 degree has been employed to collect the atmospheric information below the full overlap point of ADCL. To calibrate the lidar-derived extinction coefficient, an integrating nephelometer is operated continuously at the ground level. All the instruments are located at an elevation height of approximately 60 m above mean sea level, in our

laboratory at Chiba University, located 30 km east of Tokyo.

3. Portable lidar measurement

First we examine whether it is reasonable to calibrate the portable lidar data by means of the ground level extinction coefficient measured with the integrating nephelometer. Figure 2 is the plot of aerosol extinction at the ground level measured with the two instruments. In the analysis of the lidar data with Fernald's inversion method[1], the boundary value is assumed to be constant, 0.00022 m^{-1}. The reference altitude is chosen to be 500 m (1462 m slant range). For the extinction-to-backscattering ratio we have assumed S_1=30 through the lidar path. The lowest altitude of the interval considered is 100 m (292 m slant range) with a receiver field-of-view of 4 mrad. If the medium between the ground and this lowest altitude is assumed to be homogeneous, we can expect a value at the lowest altitude in agreement with the nephelometer-derived extinction data. This gives rise to a constraint with regard to the choice of the boundary value in the Fernald analysis.

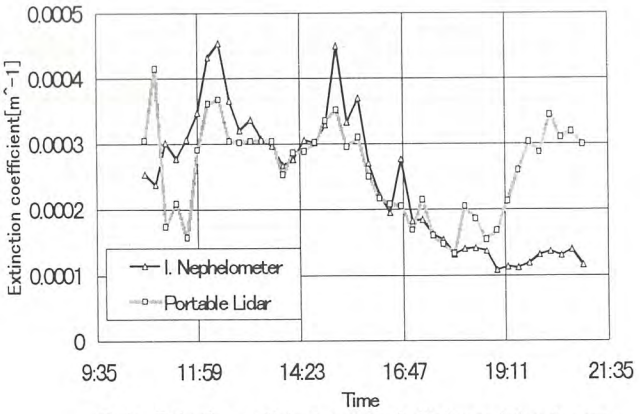


Fig2 Extinction coefficients measured with the nephelometer near ground level (60 m ASL) and the portable lidar. The latter is at 160 m altitude derived from Fernald method. (12 August 1997. S1=30.)

Two results agree well around 14:00, when the atmospheric condition at the reference altitude (500 m) is considered to be stable with time.

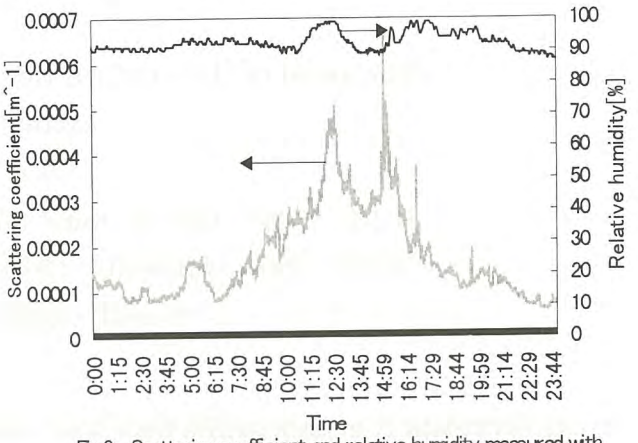


Fig3 Scattering coefficient and relative humidity measured with the integrating nephelometer on 12 August 1997.

Since the mean value of the relative humidity observed on the experimental day at our laboratory is approximately 92% (Fig.3), the value of single-scattering albedo is considered to be high. It is reasonable to suppose that the ground-level extinction value can serve as the calibration value in the analysis of the portable lidar data.

4. Calibration of the ADCL data

Figures 4 and 5 show the range corrected profiles measured with the two lidars (19:15JST, 13 August, 1997). The profile associated with an aerosol layer is observed between the altitude of 300 m to 600 m in both cases.

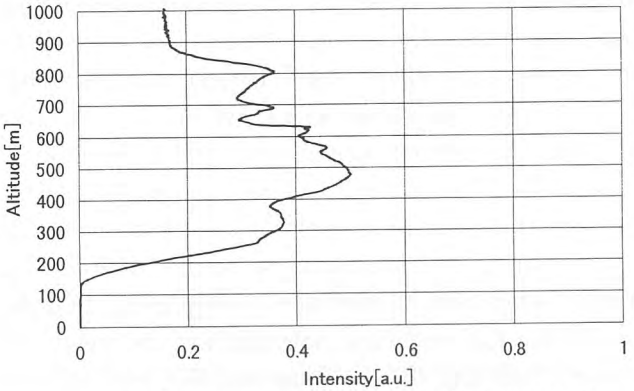


Fig. 4 Range corrected signal measured with an atmospheric data colleciton lidar at 19:15 on 13 Augst 1997.

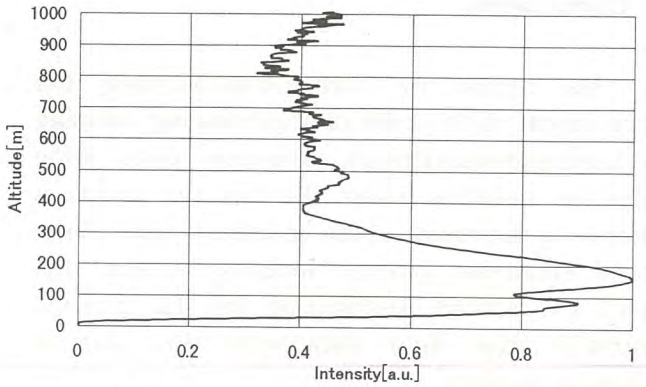


Fig.5 Range corrected signal measured with a portable lidar at 19:15 on 13 Augst 1997.

The vertical extinction profiles in Figs.6 and 7 have been composed from the atmospheric data collection lidar measurement in the altitude between 400 m and 3500 m and the portable lidar measurement in the altitude between 100 m and 400 m. The boundary value at 400 m altitude for the inversion of the portable lidar data is chosen utilizing the ground-level calibration value. This boundary value also serves as a calibration value for the inversion of the ADCL data. Below 100 m the aerosol extinction coefficient is assumed to be constant. Figure 8 exhibits the change of the extinction coefficient between Fig.6 (19:15JST, 13 August, 1997) and Fig.7 (19:30JST, 13 August, 1997). The mean value of the relative humidity observed on the relavant day at our laboratory is approximately 93%.

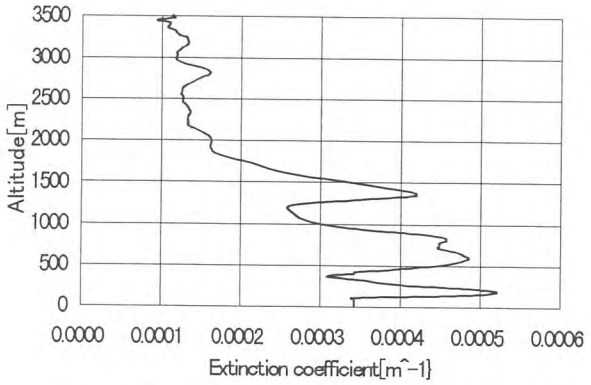


Fig.6 Aerosol extinction coefficint with Fernald method from multi-wavelength and portable lidar return measured at 19:15 on 13 August 1997. S1=30.

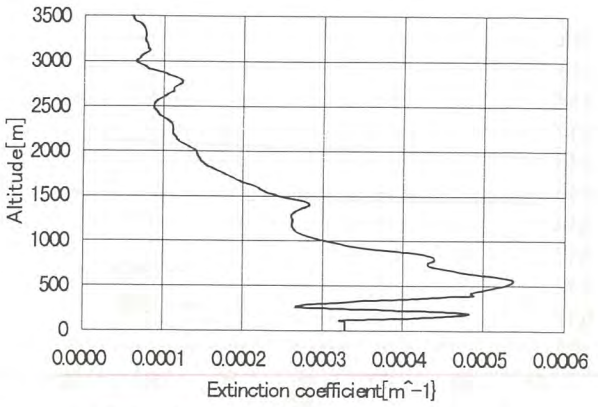


Fig.7 Same as Fig.6 at 19:30 on13 August 1997.

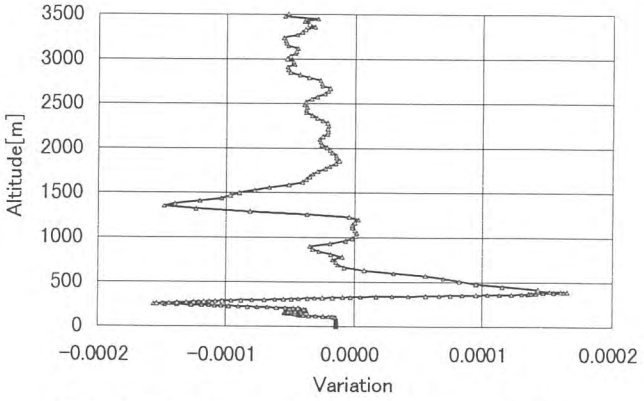


Fig.8 Variation of extinction coefficient between Fig.5 and Fig.6.

We can see a multi-layered structure of aerosols which changes rapidly with time. The growth of the layer thickness between the altitude of 300 m to 1000 m is explained by the descent of the concentrated aerosol layer.

5. S_1 dependence of optical thickness

The two profiles shown in Figs.6 and 7 are calculated with the extinction-to-backscattering ratio of 30 in the lidar path. In this section, we investigate the S_1 dependence of the optical thickness. The optical thickness between 0 and 3500 m is calculated with the S_1 value between 30 and 60. The results show an increase of 3.6% in the case of 19:15 data (Fig.6), while there is 2.2% increase in the case of 19:30 data (Fig.7). Owing to the high value of the relative humidity, it appears that the change of S_1 parameter does not affect the resulting optical thickness significantly.

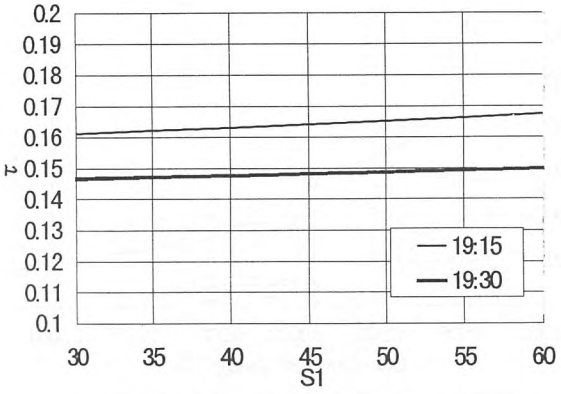


Fig.9 Effect of extinction to backscattering ratio S1 on the optical thickness. S1is assumed to be constant over any interval measured with the two lidars.

6. Conclusions

In this report we have demonstrated the improvement of the lidar-data processing utilizing the nephelometer-derived extinction data. Even under the situation where the inverted profile is sensitive to the choice of the boundary value of the aerosol extinction (optical thickness is less than unity), the aerosol distribution can be inverted accurately from lidar data with this type of calibration method.

1)F.G.Fernald , "Analysis of Atmospheric Lidar Observations : Some Comments", Appl.Opt.23,652 (1984)

H-S method for deriving aerosol extinction coefficient profile from lidar observation

Qiu Jinhuan
Institute of Atmospheric Physics, Chinese Academy of Sciences, Beijing, China

1. Introduction

The backward integration (Klett) algorithm to lidar equation is generally more stable than the forward integration algorithm[1-2], but there is a key difficulty to determine the far-end boundary value. In this paper, a new method for lidar equation, i.e. so-called H-S method, is proposed. The H-S method demands lidar return signals along both Horizontal path and slant (or vertical) path, and it uses Horinzontal signals as additional information in determining the far-end aerosol extinction coefficient and then extinction coefficient profile along the slant path without an assumption on the homogeneous atmosphere. The analytical soluttion of the H-S method, including an analytical expression of the optical thickness derived from lidar observations, and some applications are presented.

2 H-S Method

The lidar equation can be written as

$$P(r) = \frac{CE[\beta_m(r) + \beta_a(r)]}{r^2} e^{-2\int_0^r [\sigma_m(r') + \sigma_a(r')]dr'} \tag{1}$$

where P(r) is the lidar return signal from the atmosphere at the distance r, C is a constant of lidar system, E is laser output energy, $\beta_m(r)$ and $\sigma_m(r)$ are molecular backscatter coefficient and extinction coefficient, and $\beta_a(r)$ and $\sigma_a(r)$ are aerosol backscatter and extinction coefficients, respectively.

It can be derived from Eq.(1) that

$$\int_0^r k_a(r')S(r') \exp\left\{2\int_0^{r'}[1 - k_a(r'')/k_m]\sigma_m(r'')dr''\right\}dr'$$

$$= \frac{CE}{2}\left\{\exp[-\alpha_0 - 2\tau_a(0, r_0)] - \exp\left[-2\tau_a(0, r) - \frac{2k_a(r)}{k_m}\tau_m(0, r)\right]\right\}$$

where $\alpha_0 = \frac{2k_a(r_0)}{k_m}\tau_m(0, r_0)$, $k_a(r)$ and k_m are aerosol and morecular extinction to backscatter ratios. τ_a and τ_m are aerosol and molecular optical depths, and $S(r)=P(r)r^2$.

Combining Eq.(1) and (2) yields

$$\sigma_a(r) = -\frac{k_a(r)}{k_m}\sigma_m(r) + S(r)k_a(r)\{\exp[2\tau_m(0, r)$$

$$+2\tau_a(r_0, r) - \frac{2k_a(r_0)}{k_m}\tau_m(0, r_0)] - \exp[2\tau_m(0, r) \tag{3}$$

$$-2\frac{k_a(r)}{k_m}\tau_m(0, r)]\} / \int_0^r 2S(r')k_a(r') \exp\left\{2\int_0^{r'}\left[1 - \frac{k_a(r'')}{k_m}\right]\sigma_m(r'')dr''\right\}dr'$$

Similarly, from horizontal lidar return signals it can be derived

$$\int_0^{\bar{r}_1} \bar{S}(r)\,\exp[2(1-\frac{\bar{k}_a}{k_m})r\overline{\sigma_m}]dr$$

$$= \frac{C\bar{E}}{2\bar{k}_a}\{\exp[-2\bar{\tau}_a(0,r_0) - \frac{2\bar{k}_a}{k_m}\overline{\sigma_m}r_0] - \exp[-2\tau_a(0,\bar{r}_1) - \frac{2\bar{k}_a}{k_m}\overline{\sigma_m}\bar{r}_1]\} \quad (4)$$

where parameters with the bar are the horizontal ones. and constant aerosol extinction to backscatter ratio along horizontal path is assumed. Here same near-end distance r_0 is taken in both cases of horizontal and slant laser path. but different far-end distances are considered.

Combining Eq.(2) and (4). the aerosol optical depth $\tau_a(r_0, r_1)$ between r_0 and far-end distance r_1 along the slant path is

$$\tau_a(r_0, r_1) = \frac{k_a}{k_m}\tau_m(r_0, r_1) - 0.5\ln\left\{1 - \left[e^{2\overline{\tau_a}(r_0,\bar{r}_1)} - \frac{2\overline{k_a}}{k_m}\overline{\tau_m}(r_0, \bar{r}_1)\right]f(r_1)/b\right\} \quad (5)$$

where $f(r_1)=\dfrac{\int_{r_0}^{r_1} S(r')\,k_a(r')\exp\left\{2\int_0^{r'}[1-k_a(r'')/k_m]\sigma_m(r'')dr''\right\}dr'}{\int_{r_0}^{\bar{r}_1}\bar{S}(r)\overline{k_a}\exp[2(1-\overline{k_a}/k_m)\bar{\sigma}_m r]dr}$

$$b = \exp\left[2\overline{\tau_a}(0,r_0) + \frac{2\overline{k_a}}{k_m}\overline{\sigma_m}r_0 - 2\tau_a(0,r_0) - \frac{2k_a(r_0)}{k_m}\tau_m(0,r_0)\right]E/\bar{E}$$

A key question by using Klett's method is how to exactly determine the far-end extinction coefficient (boundary value). Next. how to determine the coefficient in the two cases is studied.

Case I : ***Height-independent aerosol extinction to backscatter ratio*** k_a

In the case, according to Eq.(3) and (5). the far-end boundary value (extinction coefficient $\sigma_a(r_1)$) along the slant path can be determined as follows:

$$\sigma_a(r_1) = -\frac{k_a}{k_m}\tau_{m\tau}(r_1) + S(r_1)\left\{\exp\left[2\tau_{m\tau}(0,r_1) - \frac{2k_a}{k_m}\tau_{m\tau}(0,r_0)\right]\right.$$

$$\left.+2\tau_{m\tau}(r_0,r_1) - \exp\left[2\tau_{m\tau}(0,r_1) - \frac{2k_a}{k_m}\tau_{m\tau}(0,r_1)\right]\right\} \Big/ \quad (6)$$

$$\int_{r_0}^{r_1} 2S(r)\exp\left[2\int_0^r\left(1-\frac{k_a}{k_m}\right)\sigma_m(r')dr'\right]dr$$

$$\text{with}\quad \begin{cases} \tau_a(r_0, r_1) = -\dfrac{k_a}{k_m}\tau_m(r_0, r_1) - 0.5\ln\left[1 - Gf(r_1) / b\right] \\ G = 1 - \exp\left[-2\overline{\tau_a}(r_0, \overline{r_1}) - \dfrac{2k_a}{k_m}\overline{\tau_m}(r_0, \overline{r_1})\right] \\ f(r_1) = \dfrac{\int_{r_0}^{r_1} S(r)\, k_a \exp\left[2(1 - k_a / k_m)\sigma_m(r)\right]dr}{\int_{r_0}^{r_1} \overline{S}(r)\, k_a \exp\left[2(1 - k_a / k_m)\overline{\sigma_m}(r)\right]dr} \\ b = \exp\left[2\overline{\tau_a}(0, r_0) - 2\tau_a(0, r_0) + 2\dfrac{k_a}{k_m}\overline{\sigma_m} r_0 - 2\dfrac{k_a}{k_m}\tau_m(0, r_0)\right]\dfrac{E}{\overline{E}} \end{cases}$$

If k_a is known, f(r_1) can be determined, and G can be derived by determining the aerosol optical depth $\overline{\tau_a}(r_0, \overline{r_1})$ from horizontal lidar return signals. In the case of small r_0 or basically homogeneous aerosol extinction coefficient between 0 and r_0, $b \approx E / \overline{E}$. As f($r_1$), G and b are determined, $\tau_a(r_0, r_1)$ and then the far-end boundary value $\sigma_a(r_1)$ can be derived. Then the slant aerosol extinction coefficient solution using the value $\sigma_a(r_1)$ is :

$$\sigma_a(r) = -\alpha\,\sigma_m(r) + \frac{S(r)\exp\left[2(\alpha - 1)\int_r^{r_1}\sigma_m(r')dr'\right]}{S(r_1) / \left[\sigma_a(r_1) + \sigma_m(r_1)\right] + 2\int_r^{r_1} S(r')\exp\left[2(\alpha - 1)\int_{r'}^{r_1}\sigma_m(r'')dr''\right]dr'} \qquad (7)$$

with $\alpha = k_a / k_m$.

Case II : ***Height-independent aerosol extinction to backscatter ratio k_a and no molecular scatter***

In the case, Eq.(6) can be greatly simplified as :

$$\sigma_a(r_1) = S(r_1)\left\{\exp\left[2\tau(r_0, r_1)\right] - 1\right\} / \int_{r_0}^{r_1} 2S(r)dr \qquad (8)$$

$$\text{with}\quad \begin{cases} \tau_a(r_0, r_1) = -0.5\ln\left[1 - Gf(r_1) / b\right] \\ G = 1 - \exp\left[-2\overline{\tau_a}(r_0, \overline{r_1})\right] \\ f(r_1) = \int_{r_0}^{r_1} S(r)dr \,/\, \int_{r_0}^{r_1} \overline{S}(r)dr \\ b = \exp\left[2\overline{\tau_a}(0, r_0) - 2\tau_a(0, r_0)\right]\dfrac{E}{\overline{E}} \end{cases}$$

2. **Some applications**

The H-S method was used in deriving aerosol extinction coefficient profiles from a ruby-lidar observations during a dust storm happened in Beijing on April of 1988. Fig. 1 shows lidar-detected horinzontal (curve 1) and vertical (curve 2) aerosol extinction coefficient distributions made in April 14, 1988. Figs.2-3 shows aerosol extinction coefficient profiles made in April 11 and 12. As shown in Figs.2-3, there were two passages of the sand particles on April 11, which were at the levels of 2-3km and 3.5-6km.

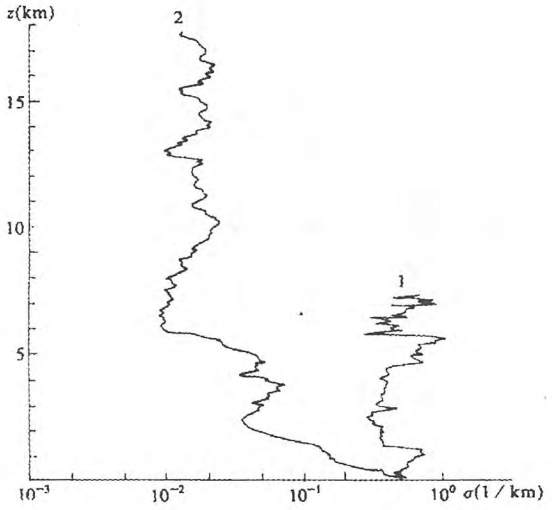


Fig.1 Aerosol extinction distributions in April 14, 1988. 1:horinzontal distribution; 2: vertical distribution

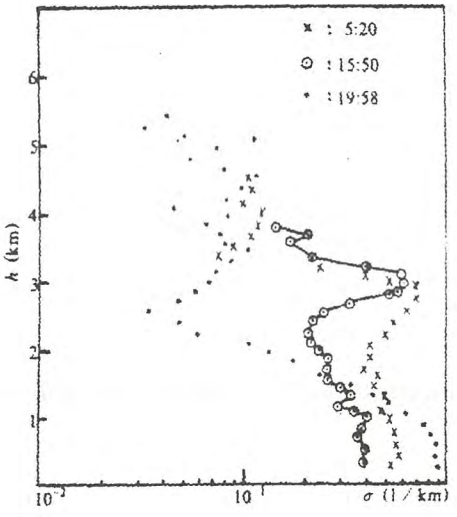


Fig.2 Aerosol extinction coefficient profiles for 1520-1958 BST, April 11, 1988

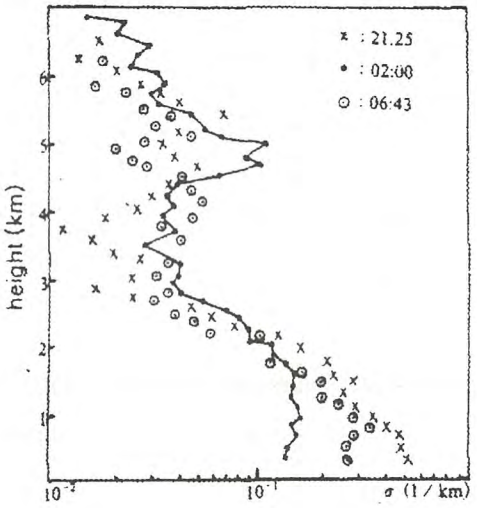


Fig.3 Aerosol extinction coefficient profiles during from 2125 on April 11 to 0643 on April 12, 1988

References

[1]Klett,J.D.,1981, Stable analytical inversion solutions for processing lidar returns, Appl. Opt., 20,211-220.

[2] Qiu Jinhuan and Lu Daren, 1988: A study of inversion algorithm for spaceborne lidar measurements of aerosol extinction coefficient profile, Chinese J. of Atmos. Sci., Special Issue, 258-270.

Lidar measurements of tropospheric aerosol over Hefei

Jun Zhou
Anhui Institute of Optics & Fine Mechanic
Chinese Academy of Sciences

1. Introduction

Tropospheric aerosols absorb and scatter both the incoming solar radiation and the emitted infrared energy from the earth. They are also involved in forming processes of cloud, fog and haze. Therefore, tropospheric aerosol particles produce a very significant effect on climate. For example, the aerosol absorption of sunlight can produce significant atmospheric heating within the aerosol layer. Depending on the altitude of the aerosol layer, this perturbation of the atmospheric temperature profile may affect the atmospheric stability and thereby alter atmospheric circulation. Thus it is important to observe the vertically resolved aerosol extinction in the troposphere (1).

Lidar has been shown to be effective for the measurements of aerosol vertical distributions. Since the ground-based lidar can be operated as long as the weather conditions permit, a large amount of data can be accumulated from many observations (2).

Troposphere is characterized by large aerosol content and therefore is a good target of lidar aerosol measurements. In recent years, many lidar systems have been developed for tropospheric aerosol measurements. However, there still has been a lack of long-term or even middle-term observational studies on spatial and temporal distributions of tropospheric aerosols.

This paper describes the lidar observational results of tropospheric aerosol extinction at 532 nm wavelength in nearly one year period of time. The measurement site is located at Anhui Institute of Optics & Fine Mechanics, 15 km west of Hefei ($31.31^{o}N, 117.17^{o}E$), China. The characteristics of the Mie scattering lidar is briefly introduced. Observation and dada processing methods are described. Some typical and seasonal average extinction coefficient profiles of tropospheric aerosol are presented and discussed.

2. L300 lidar

Table 1 lists important parameters for the L300 lidar system operating at Hefei. Figure 1 shows the schematic diagram of the lidar system.

Table 1. Characteristics of L300 Lidar

Laser type and wavelength:	Nd:YAG 532 nm / 1064 nm
Laser energy/pulse:	70 mJ / 150 mJ
Laser repetition:	10 Hz
Measurement range:	15 km
Space resolution:	30 m
Receiver configuration:	300 mm Cassegrainian
Receiver field-of-view:	4 mrad
Receiver bandwidth:	1 nm
Detector used:	Hamamatsu R1333/7102
Signal processing:	Analog DSP2210
Computer:	Pentium 586

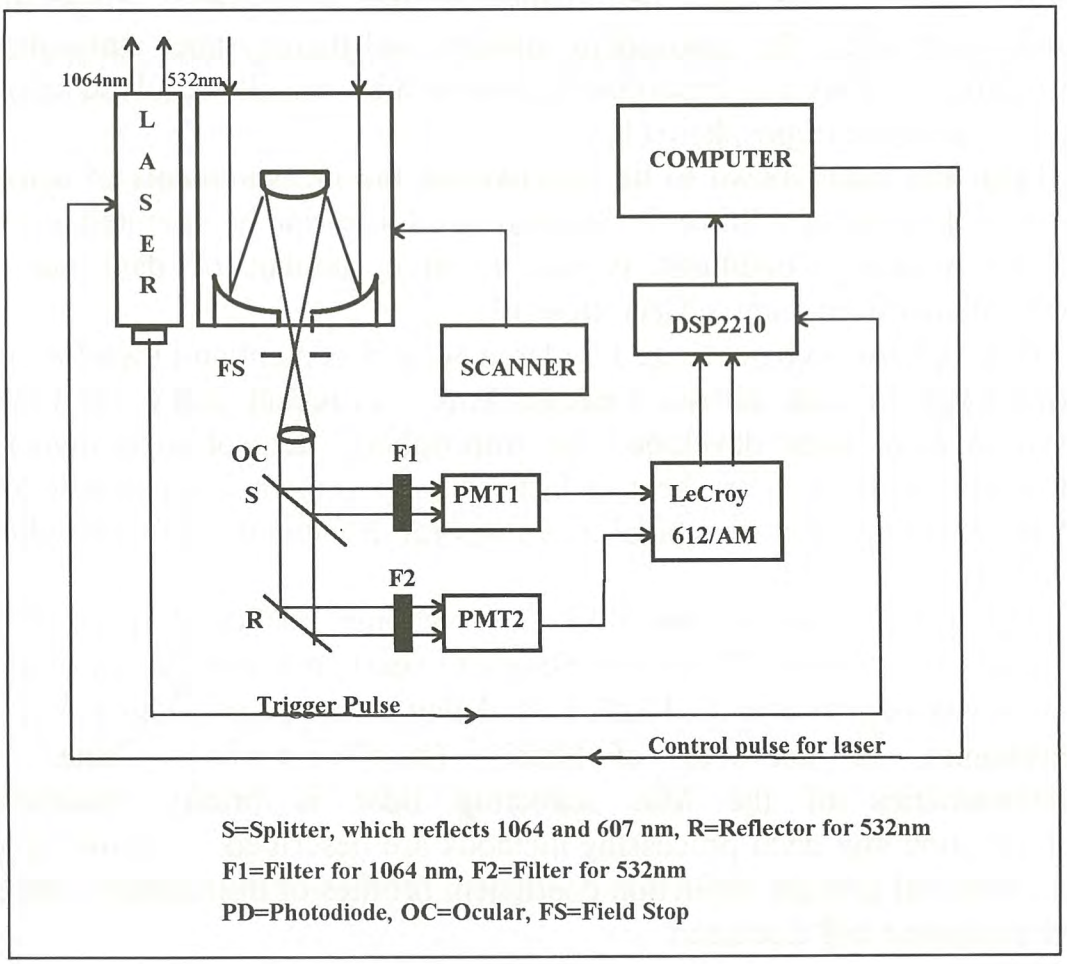


Fig. 1. Schematic diagram of L300 lidar

3. Measurement and data processing

Tropospheric aerosol measurements were routinely carried out every clear night. To deal with large dynamic range of received signal, two

section measurements were made. Typical 5000 laser shots were fired for close range through setting an attenuator and 10000 laser shots were fired for far range without attenuator. In the second section, the switching circuit set in the PMT housing was used to cut the strong intensity signal under 2 km altitude. The two profile sections were linked to construct a complete signal profile from earth surface to 15 km altitude.

Fernald solution for the two-component lidar equation was used to process the lidar signal data (3). For this purpose, a constant extinction to backscattering ratio $S_1 = 50$ was used. The extinction coefficients of air molecular $\alpha_2(z)$ were calculated using U. S. Standard Atmospheric Model. The boundary value $\alpha_1(Z_{cb})$ was determined through the matching method. This method assumes a clear layer at a certain altitude around the tropopause where the aerosol backscattering ratio is assumed to be 1.01.

4. Results and discussion

Figure 2 shows the aerosol extinction coefficient profile (solid line) derived from the measurement on October 22, 1997. As comparison, the air molecular extinction coefficient profile is also presented in the Figure (dashed line). It is evident that there was a well-defined mixed layer and its height was about 3 km, where the aerosol extinction coefficient also got close to the value of air molecular or less. Moreover, there were several aerosol layers, located at about 5, 9, 10.5 km, respectively, indicating

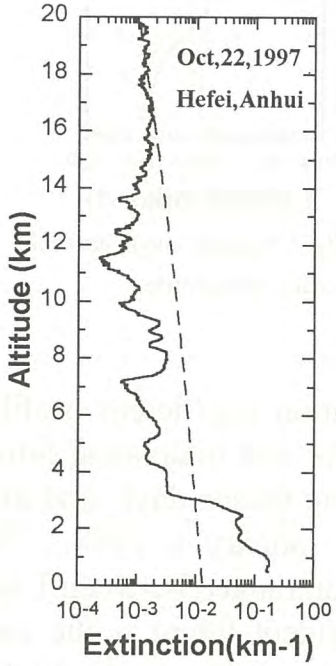


Fig.2. Aerosol extinction coefficient profile on Oct. 22, 1997.

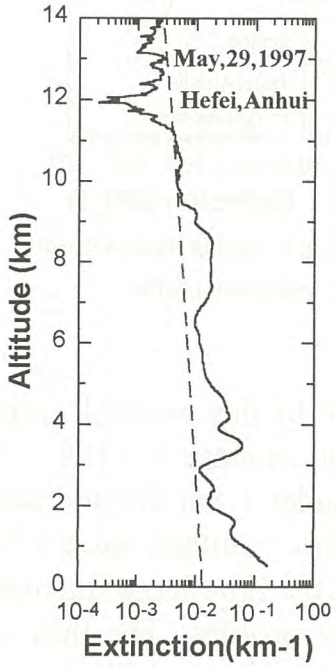


Fig. 3. Aerosol extinction coefficient for May 29, 1997.

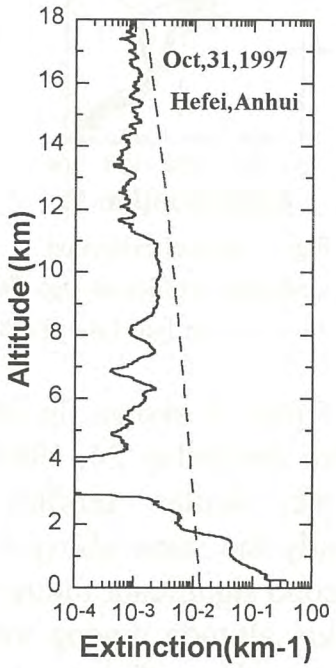


Fig. 4. Aerosol extinction coefficient on Oct. 31, 1997.

existence of high loading aerosol over there. This stratification structure indicates vertical inhomogeneity in the aerosol content. From the figure, It can also be seen that the clear layer was located at about 12 km altitude.

Figure 3 shows the aerosol extinction coefficient profile derived from the measurement on May 29, 1997. Its significant future was larger values of aerosol extinction coefficients in the midtroposphere from 3 to 10 km range. The crossing level with the air molecular extinction coefficient was nearly 9 km . This usually happened during the spring time.

Figure 4 shows the aerosol extinction coefficient profile derived from the measurement on October 31, 1997. In this Figure, there was a low aerosol extinction regime just between an altitude of 3-4 km. This case happened seldom.

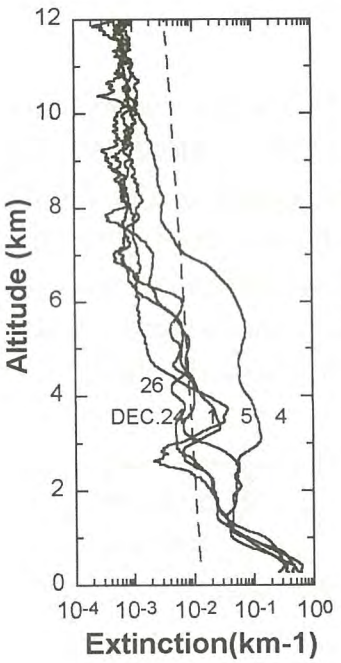


Fig. 5. Aerosol extinction coefficient profiles on Dec. 24, 26, 1997 and Jan. 1,4,5, 1998.

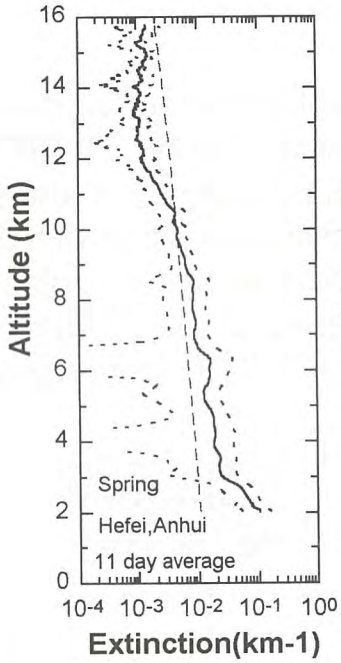


Fig.6. Spring mean aerosol extinction profile.

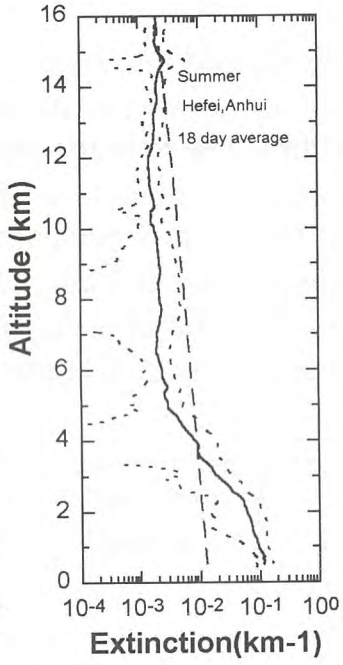


Fig.7. Summer mean aerosol extinction profile.

Figure 5 shows the day to day aerosol extinction coefficient profiles from December 24, 1997 to January 5, 1998. The first interesting future is their similar profiles under 1 km altitude during theses days, and also nearly the same above 8 km altitude except for January 4, 1998. The second significant future is the little large fluctuation ranged between 1 and 6 km altitude among these profiles. The third evident future is the very large values of aerosol extinction coefficients from 1 km up to 10 km altitude on January 4, 1998, comparing with the values of the other winter month measurements. On January 2 and 3, 1998, a cold front was passing from northern China to Hefei area. Very strong northern wind swept

across this area during the two days. The aerosol particle uplifted in the northern China and dust particles along the current path were all transported to Hefei area by the front activity. This dust storm event contributed significantly to the values of aerosol extinction coefficients in the low and middletroposphere range on January 4, 1998. This wide aerosol layer disappeared at night on January 5, 1998.

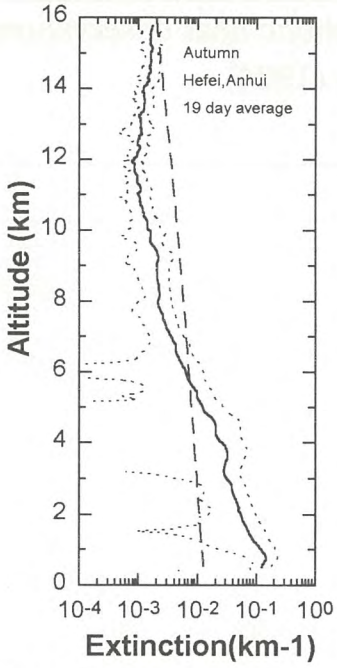


Fig.8. Autumn mean aerosol extinction profile.

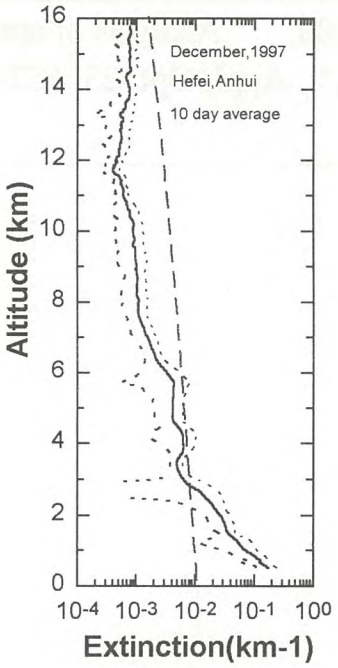


Fig.9. December mean aerosol extinction profile.

Figures 6,7,8 show average extinction coefficient profiles of tropospheric aerosol for spring, summer, autumn of 1997, respectively, and Figure 9 depicts the one for December of 1997 (solid lines). The dashed lines in these Figures are standard deviation in corresponding time period. It can be seen that larger aerosol extinction coefficients were found in the midtroposphere form 4 to 9 km in the spring rather than in any other season. The mean aerosol extinction coefficients got close to the corresponding value of air molecular or less at about 2-6 km altitude range, except for the spring time, during which the crossing level was rather higher at 9 km altitude. It can also be seen that for all the seasons the aerosol profiles in the lower and middle troposphere usually appeared larger fluctuations because of their bigger standard deviation. In the upper troposphere this variation was rather small.

References

1. David M. Winker, " Space lidar mission concepts for climate studies," presented at the European Symposium on Aerospace Remote Sensing, 22-26 September 1997, London.
2. Yasuhiro Sasano, " Tropospheric aerosol extinction coefficient profiles derived from scanning lidar measurements over Tsukuba, Japan, from 1990 to 1993," Appl. Opt. 35, 4941-4952 (1996).
3. F. G. Fernald, " Analysis of atmospheric lidar observations: some comments," Appl. Opt. 23, 652-653 (1984).

Diurnal Measurements of the Planetary Boundary Layer over Hong Kong Derived from Lidar Observations

K.M. Leung and T.M. Mok
Department of Physics and Materials Science
City University of Hong Kong
83 Tat Chee Avenue, Kowloon
Hong Kong, SAR, China
e-mail: aplkml@cityu.edu.hk

Abstract

The diurnal variation of the planetary boundary layer (PBL) over Hong Kong was studied by means of lidar and radiosonde. Aerosol monitoring was performed for a period of 24 hours using a ground-base lidar developed at City University of Hong Kong for atmospheric study based on a Nd:YAG laser operated at 532 nm. The lidar signal is a combination of the backscattering signal, atmospheric background radiation and thermal system noise, etc.. In this paper, the analysis of a typical pattern of the diurnal variation of the ML depth in Hong Kong during the winter season will be presented. Comparisons between this result and the radiosonde data will also be discussed.

1. Introduction

The diurnal variation of planetary boundary layer in the atmosphere has long been recognized. When high pressure crosses over the land surface, the PBL shows a well-defined structure that varies with diurnal cycle. During a typical cycle one can observed that a mixed layer (ML) forms just before sunrise and reaches its maximum in the late afternoon. Soon after sunset, the ML starts to decline and stays at some height within the PBL or simply disappears. Based on this diurnal change PBL can then be divided into three major components, namely, the ML, the residual layer, and the stable boundary layer. If clouds are present within the ML, further divisions are the cloud layer and subcloud layer (Stull 1988; Garratt 1992; Kaimal and Finnigan 1994). The structure and evolution of these layers are important in atmospheric and environmental research because of the optical thickness of the ML would limit the vertical extent to which the pollutants emitted from the ground.

Observational studies of the diurnal variation of the PBL at coastal region (Sasano et al. 1973; Glaser et al. 1993) are relatively few in number when compared to the number of published studies on the mid-latitude PBL (Uthe 1972; Lenchow and Stankov 1979; Mahrt 1981; Devara et al. 1995; Grant 1997).

In this paper the lidar observations of the PBL at the subtropical coastal urban city, and its preliminary analysis are discussed. The measurements obtained during a 36-hour period at an interval of 3-hour are used to analyze the variation of the depth of the ML. The data were collected on January 4 and 5 1998 using the lidar located at the City University of Hong Kong (Leung et al. 1994).

2. City University of Hong Kong Lidar

The lidar station at the City University of Hong Kong is a Mie-scattering aerosol lidar, consisting of a frequency-doubled Nd:YAG laser operated at 532 nm wavelength and 10 Hz repetition rate. The laser beam was expanded to 30 mm in diameter and collimated to about 0.2 mrad of beam divergence by a beam expander. The beam is reflected to the atmosphere by a 300 mm stepping angular scanner (vertical and horizontal). The receiver consists of a 0.25 m Newtonian telescope, where a backscattering signal is collected and measured with a photomultiplier tube (PMT), an interference filter whose 532 nm centre wavelength and 1 nm bandwidth used to reduce the background light. Light signals were converted to

electrical current by the PMT. The current was transformed to output voltage signal by the operational amplifier and recorded as well as displayed on the digital storage oscilloscope (DSO). A PIN photo-diode detector besides the reflecting mirror fed the trigger signal of the DSO. Averaged data in the DSO were automatically transferred to a Pentium-Pro based personal computer via a GPIB interface. The minimum detectable range is about 300 m. In addition, a CCD camera is used for viewing where the target of the laser beam is pointing in the atmosphere.

The lidar is situated inside a dome on top of a nine-storey building. The dome location is estimated at latitude 20°20′6″N and longitude 114°10′18″E, and at an elevation of 57 metres above mean sea level, or within the Kowloon city centre of Hong Kong. The site is about 3 km Northwest of the Hong Kong Observatory where radiosondes are routinely released twice a day.

3. Data Processing

The lidar signal profile is set to an average of 10 pulses. The profile is digitized into 500 values to get a maximum range of 3 kilometres with a resolution of 6 metres. A data set is comprised with 5 consecutive profiles at a given instant (see figure 1).

As the noise is much greater at the far end of the profile, the mean of the last ten data points has chosen to be the lidar baseline noise level. Each data point in the data set subtracts this mean in order to minimize the noise. The backscattering signal intensity is normalized by its corresponding laser transmitted intensity and the maximum intensity in the reference channel is used to calibrate the fluctuation in the laser pulse.

Since the inverse square law defines the propagation of light in the atmosphere, a lidar profile is also calibrated by multiplying each data point to the square of its corresponding range value. The algorithm of Klett [1981] is applied to derive the extinction coefficient.

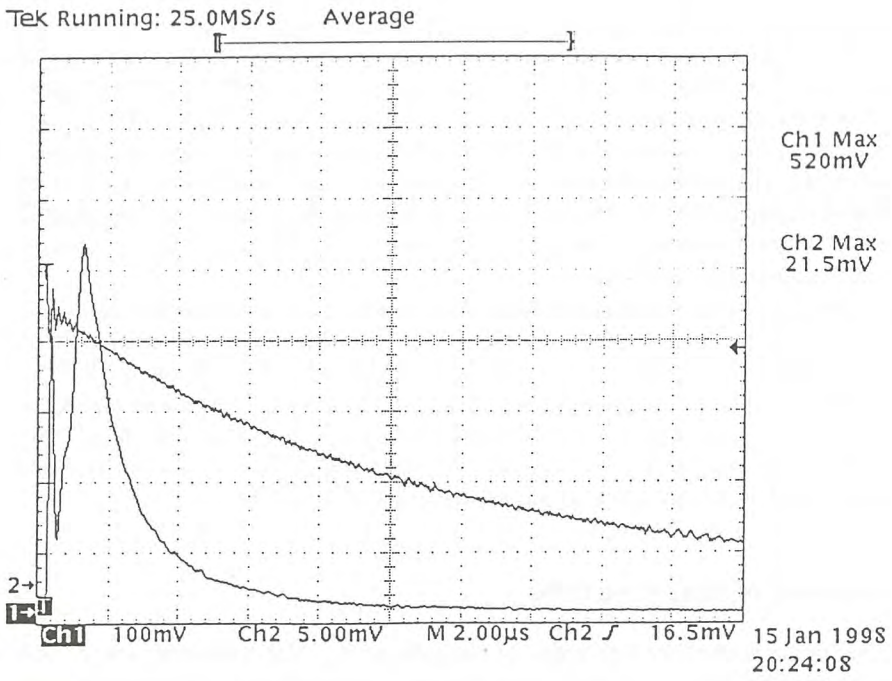


Figure 1. The lidar signal profile displayed on DSO.

4. Synoptic Conditions of a Diurnal Measurement

On January 4 and 5 1998 the Southeast China coastal region was under the influence of cold front which brought the cold air from the Northwest. The front was moving away from the region in the evening of January 6. There is variable of cloud cover, consisting mainly of cumulus and stratocumulus clouds. On January 4 the weather was generally sunny, the daytime boundary layer strongly convective, and the ML ranged from 500 m to 1300 m. The clouds were formed at mid-night associated with the approaching front. Clouds cover the region was continuously throughout the night till just before noon of January 5.

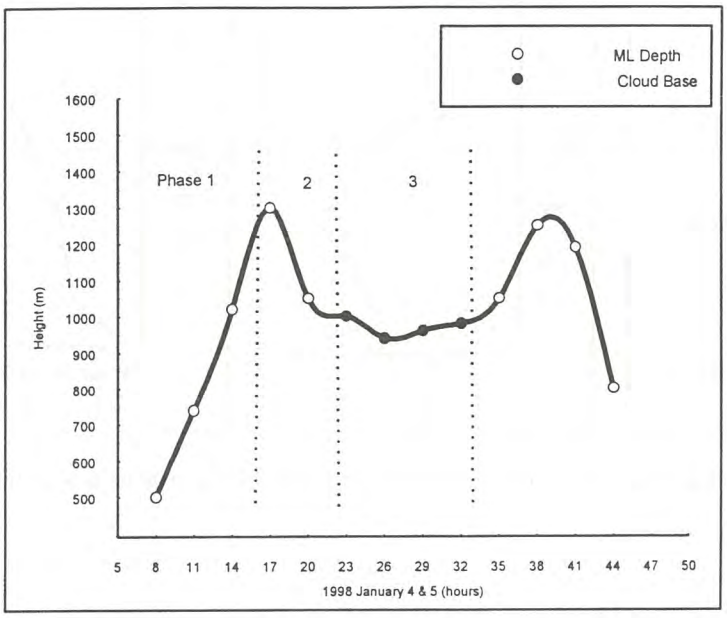


Figure 2. The diurnal variation of the depth of mixed layer on January 4 and 5 1998.

5. Discussion

Figure 2 shows the diurnal variation of the depth of the ML in the presence of a cold front. The data were obtained over a 3-hour interval starting from local times 08:00 of January 4 to 20:00 of January 5. The steep rise indicates strong turbulent convection in the ML for the whole morning. The depth of the ML starts to decline just before sunset. Then the inversion stays at that altitude and the clouds are forming, attains at the level for the entire evening and morning. This was associated with a cold front approaching to the region bringing the clouds covered. In the late afternoon of January 5 the depth grows up again to its maximum and a distinct drop after sunset. This is mainly due to the cold front passage carried the cold air down from the North.

In summary, the sinusoidal pattern can easily be observed even though in the presence of a cold front. By considering the daytime observation, which is consistent with Wilde et al. [1985] findings in their study in mid-latitude. But the formation of the ML in our region is much more rapidly deepened at an approximate rate of 80 metres per hour.

Figure 3 and 4 present the lidar and radiosonde measurements, respectively, of aerosol content and of temperature and humidity, which were employed to identify the ML and the top of the PBL. Since the instrument is relatively a crude sampling device, the resolution is one order of magnitude less than the lidar data. The top of the inversion (e.g. PBL) was detected from radiosonde data as the region where the first increase in potential temperature and sharply coincident as decrease in relative humidity was found over isothermal layer (Wyngaard, 1986). The mixing profiles of potential temperature and relative humidity tend to be constant with height.

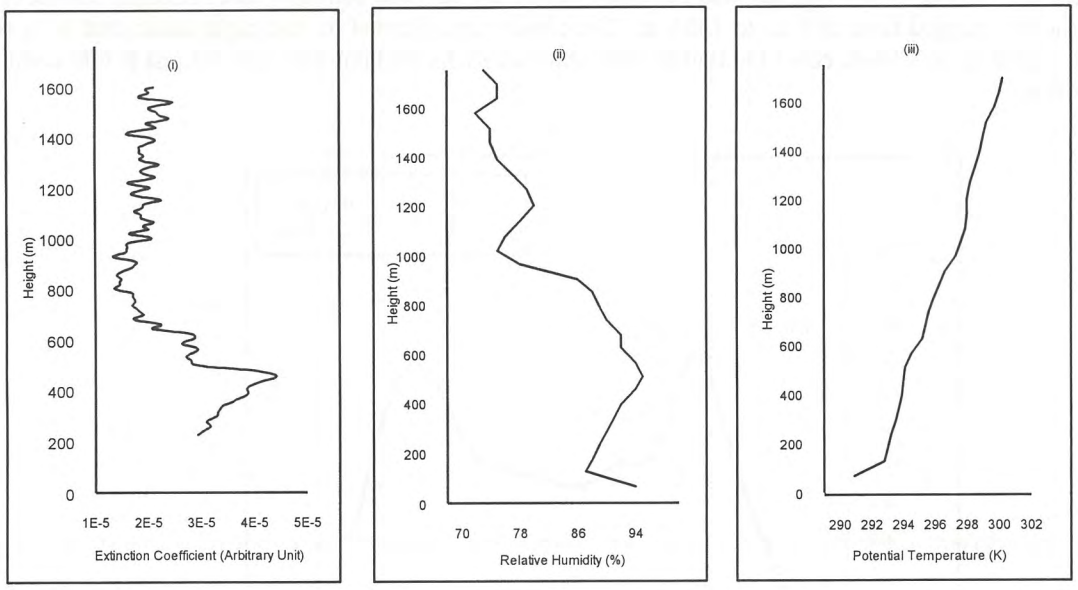


Figure 3a. Comparison between lidar (i) and radiosonde (ii)&(iii) observations at 08:00 on 4 January 1998.

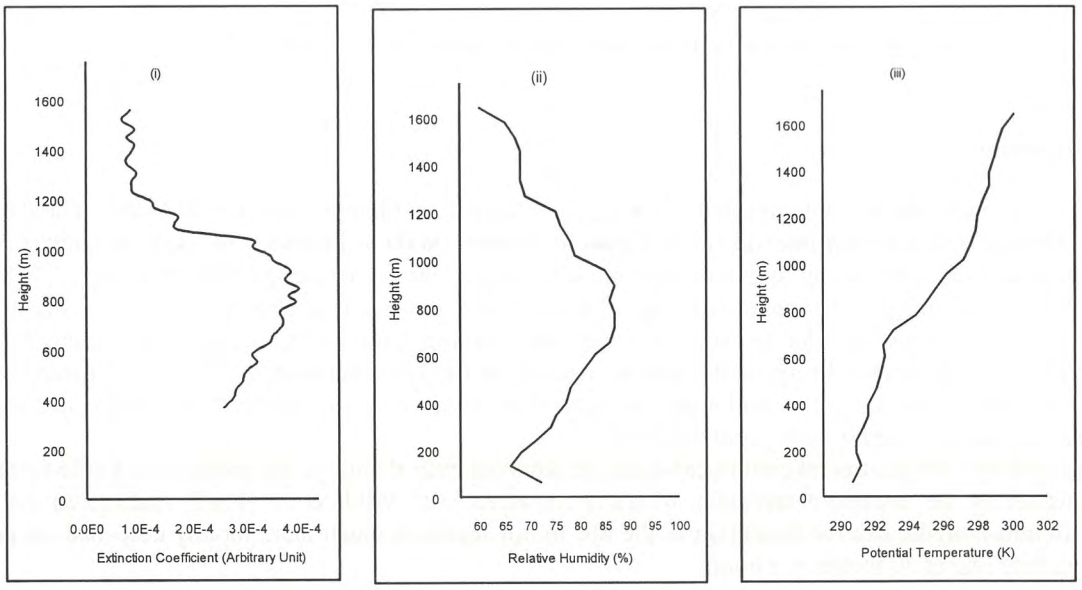


Figure 3b. Comparison between lidar (i) and radiosonde (ii)&(iii) observations at 20:00 on 4 January 1998.

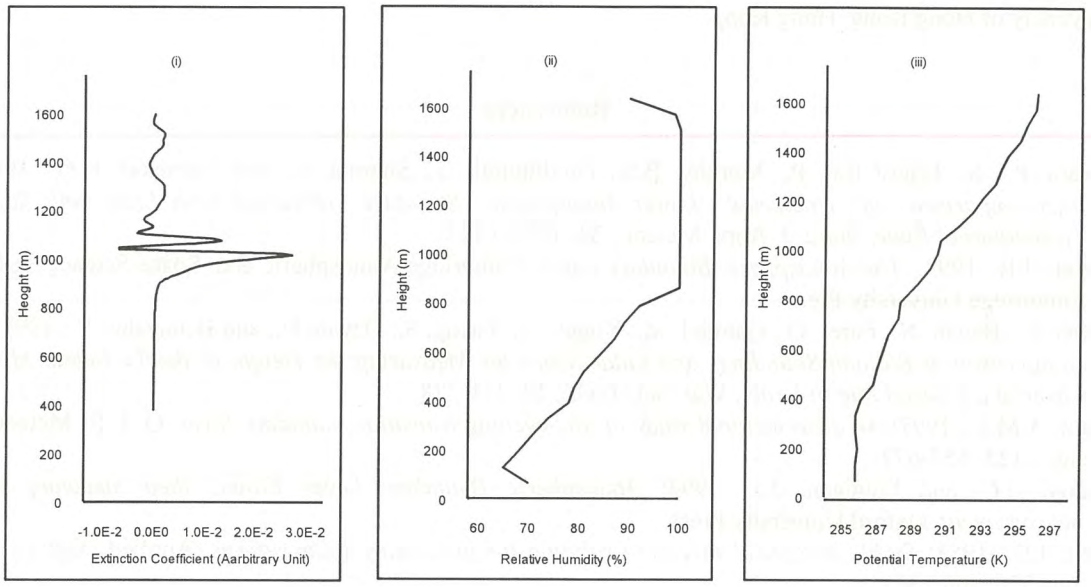


Figure 4a. Comparison between lidar (i) and radiosonde (ii)&(iii) observations at 08:00 on 5 January 1998.

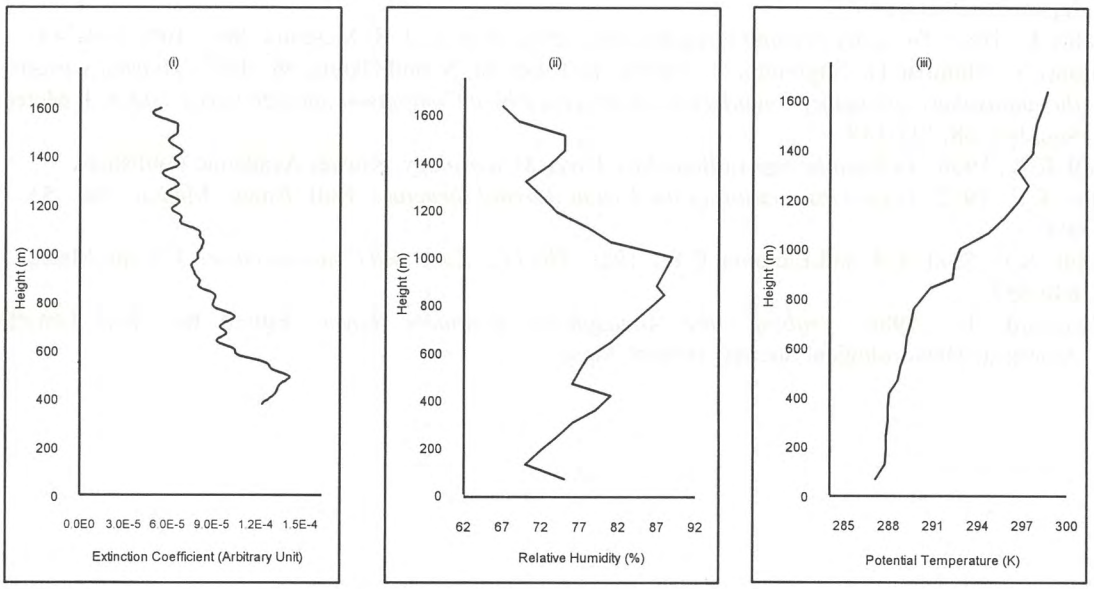


Figure 4b. Comparison between lidar (i) and radiosonde (ii)&(iii) observations at 20:00 on 5 January 1998.

Acknowledgements

We are grateful to Professor J.C.L. Chan, Drs A.H.P. Ho and C.N. Ng for many helpful discussions, to Mr. K.Y. Chan and Mr. J.L. Gao for assistance during the measurements. Thanks are also extended to the Hong Kong Observatory for providing the Radiosonde data. This work was sponsored by the Strategic Research Grants (Grants 7000429 and 7000646) and the Falcuty of Science and Technology, City University of Hong Kong, Hong Kong.

References

Devara, P.C.S., Ernest Raj, P., Murphy, B.S., Pandithurai, G., Sharma, S., and Vernekar, K.G., 1995: *Intercomparison of Nocturnal Lower-Atmospheric Structure Observed with Lidar and Sodar Techniques at Pune, India.* J. Appl. Meteor., **34**, 1375-1383.

Garratt, J.R., 1992: *The Atmospheric Boundary Layer.* Cambridge Atmospheric and Space Science Series, Cambridge University Press.

Glaser, E., Dagan, N., Furer, O., Gamliel, M., Yogev, A., Fastig, S., Dayan, U., and Benayahu, Y., 1993*: A Comparison of Balloon Soundings and Lidar Scans for Measuring the Height of the Turbulent Mixed Layer at a Coastal Site in Israel.* Wat. Sci. Tech., **27**, 271-278.

Grant, A.M.L., 1997: *An observational study of the evening transition boundary-layer.* Q. J. R. Meteorol. Soc., **123**, 657-677.

Kaimal, J.C. and Finnigan, J.J., 1994: *Atmospheric Boundary Layer Flows; their structure and measurement.* Oxford University Press.

Klett, J.D., 1981: *Stable analytical inversion solution for processing lidar returns.* Applied Optics, **20**, 211-220, and 1981.

Lenschow, D.H., Stankov, B.B., and Mahrt, L., 1979: *The Rapid Morning Boundary-Layer Transition.* J. Atmos. Sci., **38** . 2108-2124.

Leung, K.M., Lin, T.J., and Chan, J.C.L., 1994: *Lidar measurement of wind velocity by tracking a single cloud movement*, Abstracts of Papers of the 17th international laser Radar conference, 575-577, Sendai, Japan, 25-29 July, 1994.

Mahrt, L., 1981: *The early evening boundary-layer transition.* Q. J. R. Meteorol. Soc., **107**, 329-344.

Sasano, Y., Shimizu, H., Sugimoto, N., Mutsui, I., Takeuchi, N. and Okuda, M., 1973: *Diurnal variation of the atmospheric planetary boundary layer observed by a Computer-controlled laser radar.* J. Meteorol. Soc. Jpn. **58**, 143-148.

Stull, R.B., 1988: *An Introduction to Boundary Layer Meteorology.* Kluwer Academic Publishers.

Uthe, E.E., 1972*: Lidar Observation of the Urban Aerosol Structure.* Bull. Amer. Meteor. Soc., **53**, 358-360.

Wilde, N.P., Stull. R.B. and Eloranta, E.W., 1985: *The LCL Zone and Cumulus Onset.* J. Appl. Meteor., **24**, 640-657.

Wyngaard, J.C., 1986: *Probing the Atmospheric Boundary Layer.* Edited by D.H. Lenschow, American Meteorological Society, Boston, Mass..

Lidar Monitoring of Atmospheric Aerosols in Seoul using a Micro Pulse Lidar

Soon-Chang Yoon, Jae Guang Won
Department of Atmospheric Sciences
Seoul National University, Seoul 151-742, Korea

Abstract: Vertical profiles of light extinction coefficient by atmospheric aerosols are measured continuously day and night in Seoul using a micro pulse lidar(MPL) during Fall 1997. The ratio of the light extinction coefficient to the backscattering is calculated from the Mie theory with the aerosol characteristics measured in Seoul. The extinction to backscattering ratio turns out to be a nearly constant value of 25 in Seoul for the relative humidity of 30 to 70% range. For the relative humidity greater than 70%, the ratio decreases linearly down to 20 at relative humidity near 100%. With this value of the extinction to backscattering ratio the light extinction coefficient by aerosols in each layer of 30m thick is computed up to 5km height. Numerous vertical profiles are examined to investigate the variation of the tropospheric aerosol profiles in conjunction with meteorological field. The temporal variation of the planetary boundary layer(PBL) height could be obtained from the numerous consecutive profiles, which reveals the existence of residual layer in PBL in the evenings which can hardly be identified by the conventional soundings by the air sondes.

1. Measurements

The MPL system is manufactured by the SES Inc. and it's specifications are listed in table 1. Details of the system are given in Lee et al.(1997).

Table 1. MPL system parameters (Spinhirne et al., 1995 ; SES Inc., 1996)

Laser	Nd:YLF (Spectra-Physics 7300)
Wavelength	523.5nm
Laser Energy	1W
Pulse Energy	4-5 μJ
Pulse Repetition Frequency	2000Hz (adjustable)
Resolution	30m (adjustable)
Telescope Diameter	20cm
Transmitter Field of View	50 μrad
Receiver Field of View	100 μrad
Detector	EG&G SPCM-PQ GAPD

The monitoring site is located at the skirt of Mt. Kwanak in the campus of Seoul National University. Day and night continuous measurements were done except on rainy days during September to November 1997. The lidar data were averaged every 10 minutes.

Aerosol size distributions are measured with an optical particle counter (HIAC/ROYCO Inc., Model 5230), which measures the number concentration of the particles ranging 0.32㎛ ~ 25㎛ into 8 channels(Table 2). Also, the aerosols are sampled by a high volume sampler and analysed by an ion chromatography for the ion components analysis.

Table 2. Particle size intervals of OPC(Optical Particle Counter)

channel	1	2	3	4	5	6	7	8
range (diameter,㎛)	0.32-0.45	0.45-0.7	0.7-1.0	1-1.5	1.5-2.5	2.5-5	5-10	10-25

2. Data analysis

One of the major parameters required for the computation of light extinction coefficient from the lidar data is the ratio of the light extinction coefficient to the backscattering coefficient, which is typically in a range of 15 to 60 in many applications of aerosol lidars. Light extinction and backscattering coefficient for a single spherical particle can be computed numerically for a given wavelength if the refractive index of aerosols and the relative humidity are provided(Bohren and Huffman, 1983). Using the refractive index of each aerosol component given in Table 3, the mean refractive index of aerosols is obtained by a weighted averaging of refractive indices for each aerosol components as listed in Table 4. By this way the daily mean refractive index can be obtained as in Table 5. The arithmetic mean of the refractive index of aerosols in Table 5 becomes $1.510-0.612i$, which is similar to the result of Kim et al.(1990) for urban air when the relative humidity is about 50%.

Table 3. Refractive indices and densities of aerosol materials (Pitts, 1986 ; Reist, 1993)

Material	Cl^-	NO_3^-	SO_2^{-2}	TOC	IC	Metal
Real	1.381	1.559	1.528	1.450	1.600	1.550
Imagin.	-3.7e-9	-1.0e-9	-1.0e-9	-1.0e-9	-5.0e-1	-1.0e-9
Density(g/㎤)	1.33	1.73	1.77	1.60	1.20	2.50

With the mean refractive index and the particle size, the extinction to backscattering ratios are computed for a single particle from the Mie scattering program, BHMIE subroutine in Bohren & Huffman(1983). Multiplying this value by

Table 4. Volume ratios of aerosol materials measured in Autumn 1995 and 1996

Date\Material(%)	NO_3^-	SO_4^{2-}	Cl^-	TOC	IC
95/10/13	35.2	26.7	7.8	21.4	3.4
95/10/14	18.2	30.5	12.1	19.9	13.9
95/10/16	10.1	42.8	10.0	21.1	12.1
95/10/17	21.2	26.1	13.7	25.4	8.6
95/10/18	14.1	23.8	13.7	21.2	22.0
95/10/19	7.0	28.8	19.5	20.2	21.1
95/10/21	22.1	24.2	9.8	27.2	11.3
95/10/23	25.8	22.6	11.1	23.3	11.6
95/10/25	32.4	25.1	16.1	13.3	7.6
96/10/12	28.6	27.9	6.1	23.0	9.8
96/10/13	20.1	35.8	6.0	22.8	9.7
96/10/14	16.7	38.1	7.9	23.0	9.8
96/10/15	10.1	34.7	12.1	22.0	16.5
96/10/16	16.1	30.3	11.1	22.3	16.7
96/11/12	10.3	40.5	12.0	22.7	9.7
96/11/15	10.4	34.7	12.4	22.2	16.7
96/11/22	26.7	27.1	9.6	23.0	9.8
96/11/25	26.3	25.9	9.3	22.3	9.5

the number of the aerosols in each interval, the extinction to backscattering ratios are computed for the given values of relative humidity. Fig. 1 shows the extinction to backscattering ratio vs relative humidity. Its mean value turns out about $25 \pm 10\%$ when the relative humidity is below 70%, and it decreases down to 20 as the relative humidity approaches 100%. Since the relative humidity tends to decrease with height, we have used the constant value of 25 for the extinction to backscattering ratio. However, this ratio is supposed to vary with height because of the variation of refractive index of aerosols and their size distribution with height. But, since we have no such data in the upper air, we are forced to use the constant value.

The boundary condition for the computation of lidar constant is given as $\beta_p = 0.2\beta_m$ at 5 km, where β_p and β_m are the backscattering coefficient by the particles and by the molecules, respectively. The lidar constant is computed by the iteration method introduced in Fernald(1984).

Fig 2. shows typical profiles of the light extinction coefficient. The decay of raw data caused by the unfocused lidar signal near the ground is corrected by the overlap correction method introduced by Spinhirne(1995). A comparison of the light extinction

coefficients thus obtained at the ground level with those computed from the Mie scattering theory is shown in Fig. 3. The extinction coefficient computed from MPL data is much higher than the one computed from the Mie theory. However, their temporal variations matches very well.

Table 5. Refractive indices of aerosols in Seoul measured in Autumn 1995 and 1996

Date	Real	Imaginary	Date	Real	Imaginary
95/10/13	1.514	-0.0169	**96/10/12**	1.518	-0.0492
95/10/14	1.511	-0.0698	**96/10/13**	1.515	-0.0488
95/10/16	1.509	-0.0605	**96/10/14**	1.511	-0.0491
95/10/17	1.502	-0.0429	**96/10/15**	1.509	-0.0825
95/10/18	1.513	-0.1100	**96/10/16**	1.512	-0.0835
95/10/19	1.502	-0.1054	**96/11/12**	1.503	-0.0486
95/10/21	1.508	-0.0565	**96/11/15**	1.508	-0.0833
95/10/23	1.511	-0.0583	**96/11/22**	1.512	-0.0492
95/10/25	1.510	-0.0383	**96/11/25**	1.513	-0.0479

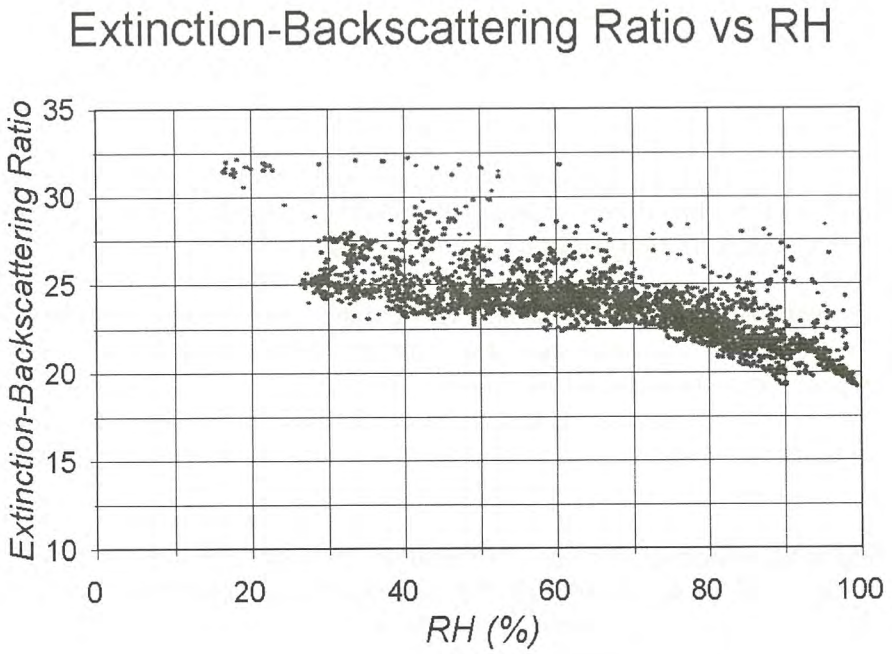


Fig 1. Dependency of extinction-backscattering ratio on the relative humidity(R.H.) computed from Mie theory using the aerosol characteristics measured in Seoul.

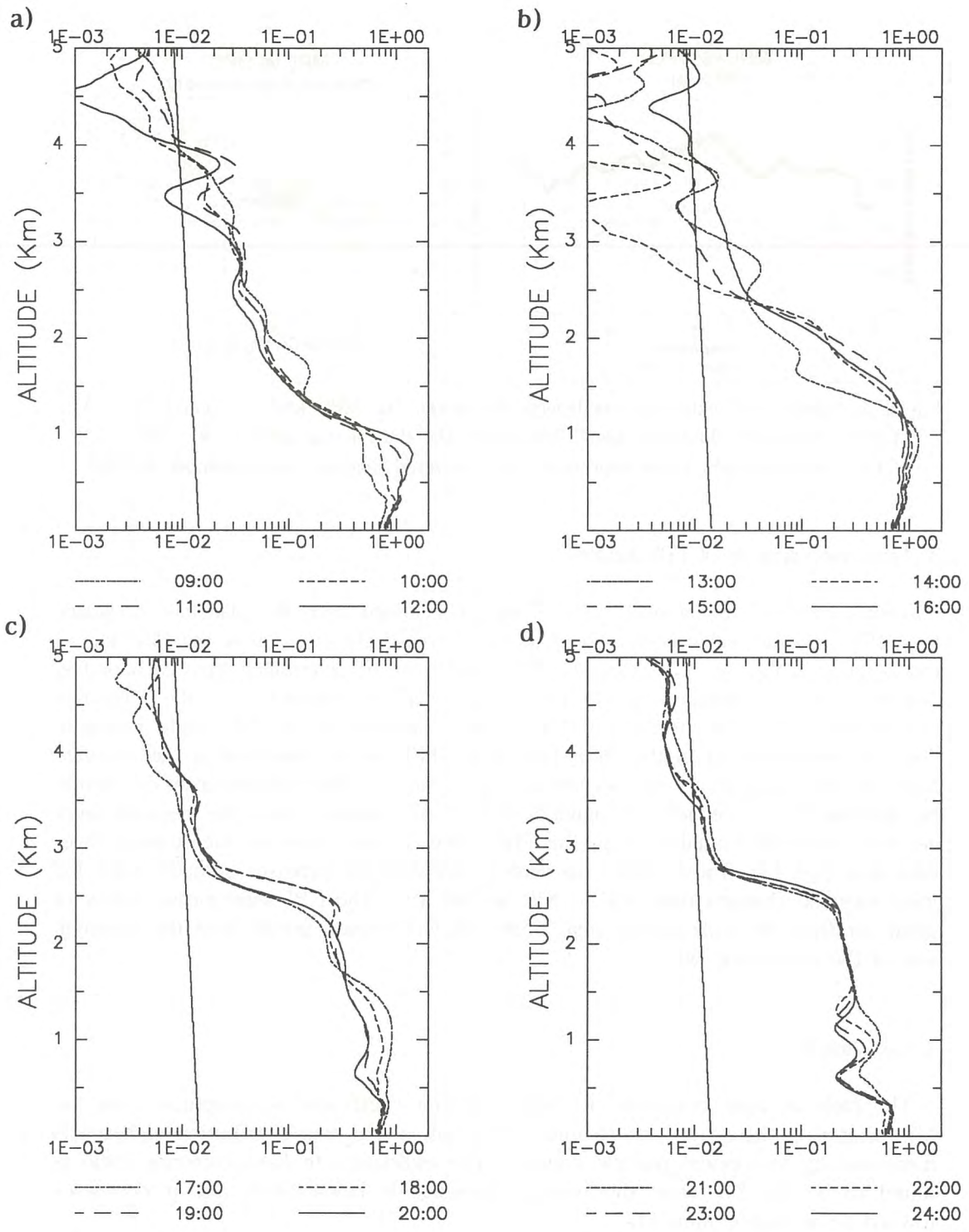


Fig 2. Profiles of aerosol extinction coefficients during the day of September 30, 1997 ; at a) 09:00, 10:00, 11:00, 12:00, b) 13:00, 14:00, 15:00, 16:00, c) 17:00, 18:00, 19:00, 20:00, d) 21:00, 22:00, 23:00, 24:00 ; straight line is Rayleigh scattering coefficient

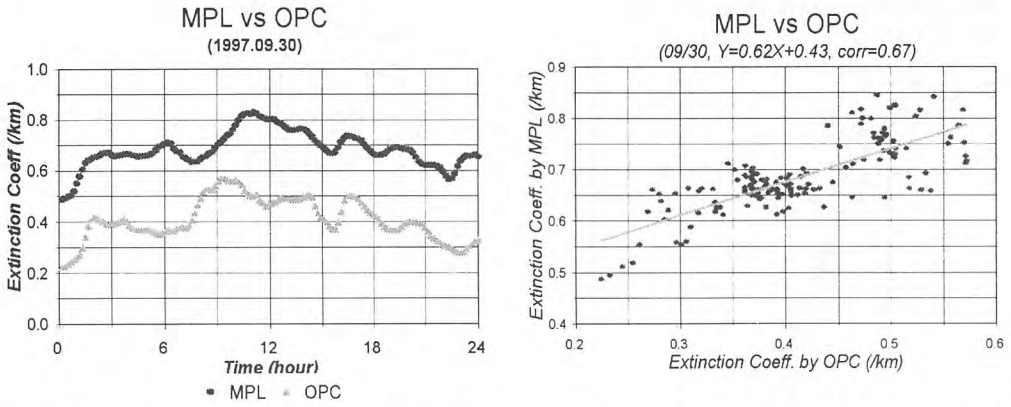


Fig 3. Comparison of extinction coefficients measured by MPL and computed from Mie theory with OPC data; left panel represents the diurnal variation (·····●····· MPL, ·····▲····· OPC), and the right panel represents the scattered diagram on September 30, 1997.

3. Temporal variation of PBL height

Since most of the aerosol mass is mostly confined with the planetary boundary layer(PBL), the aerosol concentration tends to decrease abruptly across the PBL top as can be seen in Fig. 2. Therefore, the PBL height can be determined from each profile, and the temporal variation of the PBL height can be obtained from the numerous consecutive profiles for each a day. Fig. 4 shows an example of PBL height variation. Also, the residual layer in the upper part of the PBL can be identified in the evenings from the MPL profiles as can be seen in Figs 2 and 5. This residual layer can hardly be detected by conventional soundings such as air sondes. Once the residual layer develops, air pollution piles up in the PBL since it stays there in the residual layer until next day. Fig. 5 also shows the aerosol concentration increases abruptly when the wind direction changes from SW to NW at 9:00 a.m.. The NW wind means inflow of urban air from the metropolitan area, while SW wind means inflow from the mountain side of the monitoring site.

4. Conclusion

The ratio of light extinction to backscattering coefficient is computed from the Mie scattering theory for the chemical composition and size distribution of aerosols measured by an optical particle counter. The extinction to backscattering ratio is found to be 25 ± 2.5 when the relative humidity is below 70%, and it decreases toward 20 at higher humidity.

Temporal variation of PBL height can be obtained from the numerous consecutive profiles, and the residual layer in the upper part of PBL can be detected from MPL profiles.

References

Bohren, C. F. and Huffman, D. R., 1983 ; Absorption and Scattering of Light by Small Particles, *John Wiley & Sons, Inc.*

Fernald, F. G., 1984 ; Analysis of Atmospheric Lidar Observations : Some Comments, *Appl. Opt.* Vol. 23, No. 5, pp 652-654

Kim, Y. J. and Boatman, J. F., 1990 ; Size Calibration Corrections for the Forward Scattering Spectrometer Probe (FSSP) for Measurement of Atmospheric Aerosols of Different Refractive Indices, *J. Atmospheric and Oceanic Technology, Vol. 7,* pp 681-688

Lee, H. S. et al., 1997 ; Micro Pulse Lidar for Aerosol and Cloud Measurement, *Advances in Atmospheric Remote Sensing with Lidar, Selected Papers of the 18th International Laser Radar Conference.* pp 7-10

Pitts, B. J, and Pitts, J. N, 1986 ; Atmospheric Chemistry : Fundamentals and Experimental Techniques, *A Wiley-Interscience Publication,* John Wilye & Sons

Reist, P. C., 1993 ; Aerosol Science and Technology, *McGraw-Hill, Inc.*

SES Inc., 1996 ; *Micro Pulse Lidar Instruction Manual*

Spinhirne, J. D., 1995 ; Compact Eye Safe Lidar Systems., *The Review of Laser Engineering, Vol. 23, No. 2,* pp 112-118

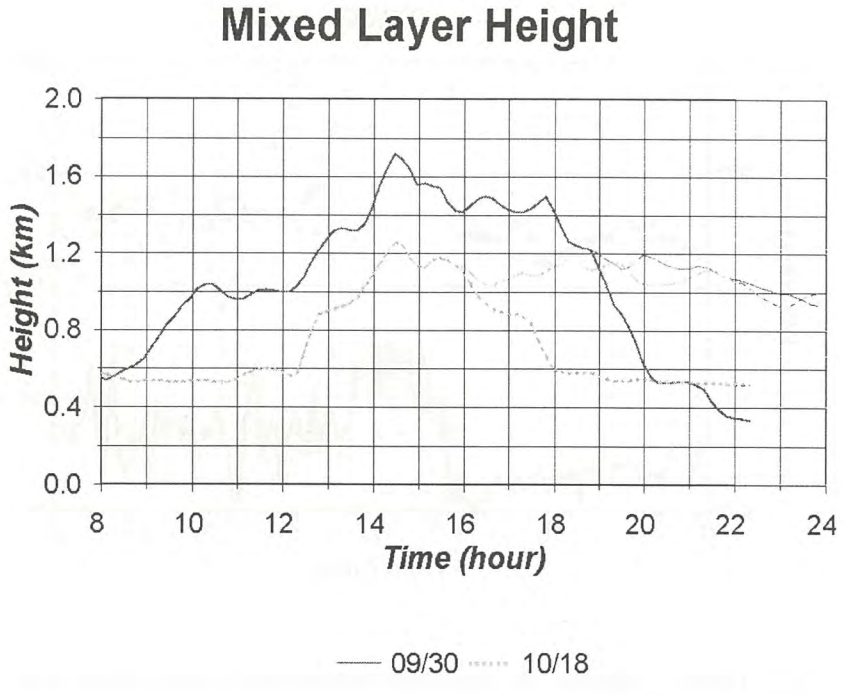


Fig 4. Diurnal variations of mixed layer height September 30 and October 18, 1997 where the thin lines in the evening represent residual layer heights.

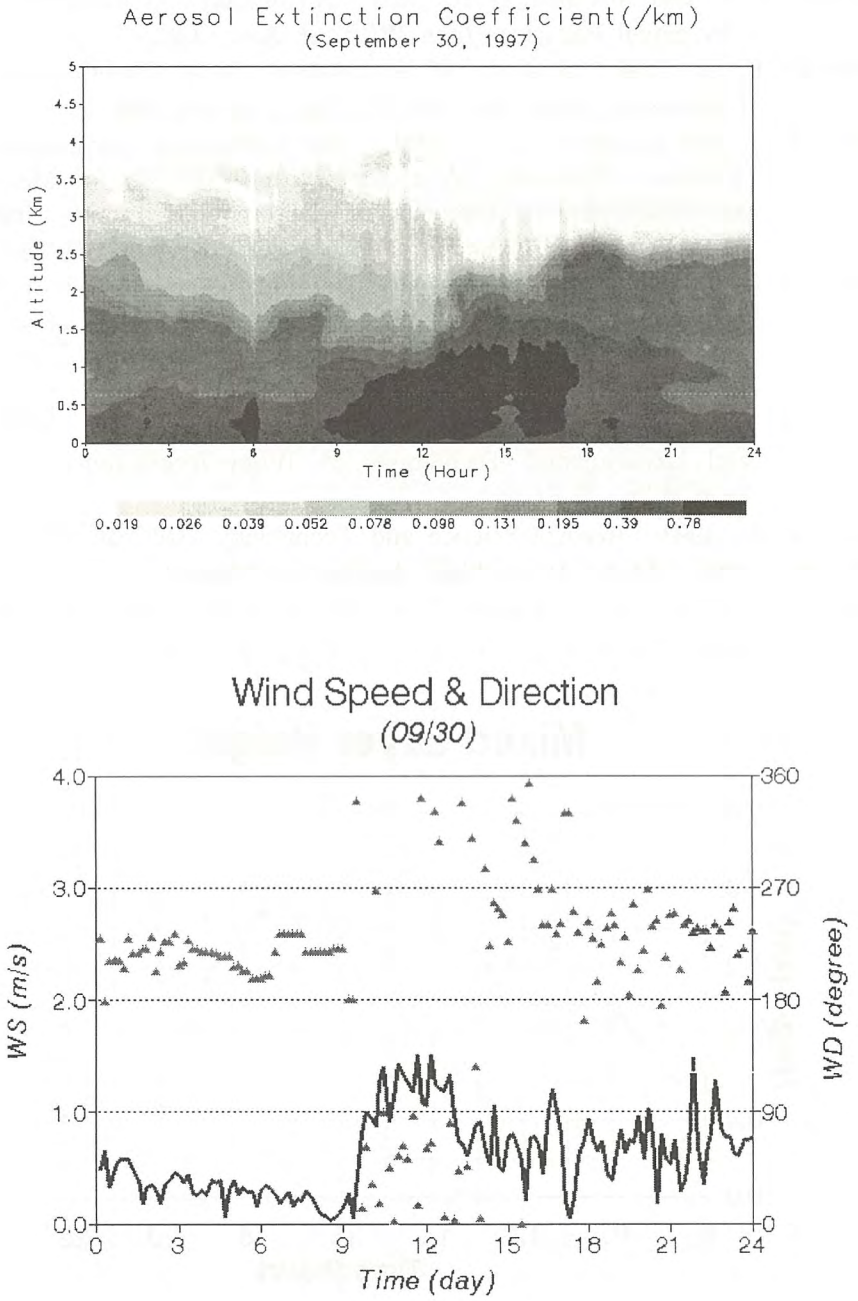


Fig 5. Diurnal variation of aerosol extinction coefficient profile(upper panel), and wind direction and speed(lower panel) on September 30, 1997.

INDEX

Abo, M. 264
Adachi, H. 264
Alarcon, M. 214
Arief, Muchlisin 183
Aoki, K. 264
Aoki, Tadao 25
Aoki, Teruo 25
Arai, Kohei 112
Arao, K. 264
Asai, K. 264

Chan, J.C.L. 242
Chan, K.Y. 242
Ding, Jilie 106, 151
Dorado, S. 214
Enaje, C. 214

Fan, X.B. 280
Fuente, L.Dela 214
Fujiwara, M. 264
Fukabori, Masashi 25
Fukushima, Hajime 125
Gao, J.L. 242

Hayasaka, T. 280
Higurashi, Akiko 51, 195
Ho, A.H.P. 242
Holdsworth, J. 214
Honda, Yoshiaki 71
Hoyningen-Huene, W. 201, 254
Hu, Huanling 211
Hu, R.M. 280
Hydayat, Ii 288

Iino, N. 37
Imanaka, M. 165
Imasu, R. 264
Inoue, Toshiro 132
Ishida, Hiroshi 45
Iwabuchi, T. 65
JACCS Group 276
Jin, X. 280

Kai, K. 264
Kajiwara, Koji 71
Kaneta, S. 250
Kaufman, Yoram J. 89
Kawahara, T. 264
Kawata, Y. 165
Kawamoto, Kazuaki 77
Kinjo, Hideki 295
Kinoshita, K. 37

Kobayashi, Takahisa 157
Kohno, J. 37
Koga, R. 264
Kondoh, Akihiko 59, 65
Kozai, Katsutoshi 121
Kuze, Hiroaki 102, 195, 264, 295
Kwon, S-A. 264

Lagrosas, N. 214
Leung, K.M. 242, 309
Liu, Dongqi 59

Ma, Q. 3
Matsushima, Hiroaki 295
Masuda, Kazuhiko 45, 136, 157, 284
Matsui, I. 264, 288
Menenti, M. 59
Minomura, Mistuo 102, 195
Mitomi, Yasushi 125
Mitsuzuka, Naoki 188
Miyazaki, S. 65
Mok, T.M. 242, 309
Mori, A. 37
Moriyama, Masao 161
Mouri, K. 165
Mukai, Sonoyo 136
Murao, Naoto 17
Murayama, T. 264

Naito, I. 65
Nakajima, Teruyuki 51, 77, 195, 280
Ng, C.N. 242
Noguchi, Toshimitsu 125
Nomura, A. 264

Ogino, Kiyofumi 81
Ohta, Sachio 17
Okada, Itaru 81
Okayama, Hiroshi 11
Oppenheimer, C. 55
Otani, R. 65

Pinandito, Mego 288
Prakhammintara, P. 228
Qiu, Jinhuan 31, 171, 299
Ru, Jianfei 102, 195
Rosananto, I. 288

Saito, Kazuya 270
Saito, Y. 264
Sakai, T. 264
Sasaki, Masayuki 45, 157
Sano, Itaru 136
Sawada, Haruo 188

Siripong, Absornsuda 228
Shi, G.Y. 280
Shiraishi, K. 264
Smokty, I.Oleg 143
Sugimoto, N. 264, 288
Syamsudin, Muharyan 288

Takamura, Tamio 81, 106, 151, 250, 270, 280
Takashima, Tsutomu 45, 284
Takayama, Yozo 276
Takeuchi, Nobuo 102, 195, 250, 264, 295
Takimoto, Kunihisa 270
Tamaru, Hideki 81
Tejasukmana, B.S. 183
Tipping, R.H. 3
Toratani, Mitsuhiro 125
Tsuchida, Satoshi 177

Ueda, Tomoyuki 188
Uno, I. 37

Watson, I.M 55
Wang, B. 280
Wang, Jiemin 59
Wang, Li-Zhong 11
Wang, L.X. 280
Wang, X.H. 280
Winardi 121
Won, Jae Guang 315
Wu, Yonghua 211
Xu, L. 280
Xu, Lisheng 106, 151

Yamazaki, A. 165
Yamamoto, Hirokazu 71
Yamamota, Johta 270
Yoon, Soon-Chang 315

Zhang, H. 280
Zhang, Guotong 106, 151
Zhang, L.S. 280
Zhang, P. 280
Zhou, Jun 211, 303